12th International Symposium on High-Temperature Metallurgical Processing

EDITED BY

Zhiwei Peng
Jiann-Yang Hwang
Jesse F. White
Jerome P. Downey
Dean Gregurek
Baojun Zhao
Onuralp Yücel
Ender Keskinkilic
Tao Jiang
Morsi Mohamed Mahmoud

TMS

Springer

The Minerals, Metals & Materials Series

Zhiwei Peng · Jiann-Yang Hwang · Jesse F. White · Jerome P. Downey · Dean Gregurek · Baojun Zhao · Onuralp Yücel · Ender Keskinkilic · Tao Jiang · Morsi Mohamed Mahmoud
Editors

12th International Symposium on High-Temperature Metallurgical Processing

TMS

Springer

Editors
Zhiwei Peng
Central South University
Changsha, China

Jesse F. White
Elkem Carbon Solutions
Kristiansand, Norway

Dean Gregurek
RHI Magnesita
Leoben, Austria

Onuralp Yücel
Istanbul Technical University
Istanbul, Turkey

Tao Jiang
Central South University
Changsha, China

Jiann-Yang Hwang
Michigan Technological University
Houghton, MI, USA

Jerome P. Downey
Montana Technological University
Butte, MT, USA

Baojun Zhao
Jiangxi University of Science
and Technology
Ganzhou, China

Ender Keskinkilic
Atilim University
Ankara, Turkey

Morsi Mohamed Mahmoud
King Fahd University of Petroleum
and Minerals
Dhahran, Saudi Arabia

ISSN 2367-1181 ISSN 2367-1696 (electronic)
The Minerals, Metals & Materials Series
ISBN 978-3-030-92387-7 ISBN 978-3-030-92388-4 (eBook)
https://doi.org/10.1007/978-3-030-92388-4

This Springer imprint is published by the registered company Springer Nature Switzerland AG
The registered company address is: Gewerbestrasse 11, 6330 Cham, Switzerland

Preface

This book presents selected papers submitted for the 12th International Symposium on High-Temperature Metallurgical Processing at The Minerals, Metals & Materials Society (TMS) Annual Meeting & Exhibition held in Anaheim, California, USA in 2022. The symposium created a platform for presenting ongoing research on the analysis, development, and/or operation of high-temperature processes that involved processing of mineral resources, production, and treatment of metals, alloys, ceramic materials, etc. It also provided a space for reporting fundamental and applied research related to metallurgical waste generation, characterization, minimization, collection, separation, treatment, and disposal. Moreover, it was open to people who are interested in integrating experiment and computation to solve enduring engineering problems due to the high complexity, high cost, and high energy consumption of metallurgical process and to those who work on improving practical metallurgical processes based on techno-economic and life cycle analyses for commercial-scale production, which identify how to enhance economic feasibility and minimize environmental impact. At the TMS 2022 Annual Meeting & Exhibition, this symposium received a total of 73 abstracts from authors from around the world, of which 68 submissions were accepted. After peer review, 58 papers were included in the book.

This book is expected to serve as a treasured reference for academia and industry covering a wide range of research fields. Educators, researchers, professionals, and students will enjoy the diversity of topics that reflect brilliant achievements of the authors on developing innovative and sustainable technologies and routes for minerals processing, physical metallurgy, process metallurgy, and materials science and processing.

The editors of this book would like to express their gratitude to the authors for their contribution and willingness to share their research findings and to the reviewers

for their time and effort that ensured the quality and timeliness of the publication. The editors would also like to thank the Pyrometallurgy Committee and Extraction and Processing Division of TMS for sponsoring the symposium and Springer for publishing the book.

Zhiwei Peng
Jiann-Yang Hwang
Jesse F. White
Jerome P. Downey
Dean Gregurek
Baojun Zhao
Onuralp Yücel
Ender Keskinkilic
Tao Jiang
Morsi Mohamed Mahmoud

Contents

Part VII Poster Session

About the Editors

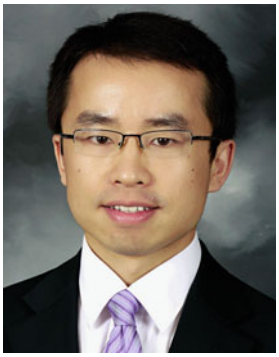

Zhiwei Peng is a professor in the School of Minerals Processing and Bioengineering at Central South University, China. He received his B.E. and M.S. degrees from Central South University in 2005 and 2008, respectively, and his Ph.D. degree in Materials Science and Engineering from Michigan Technological University, USA, in 2012. His research interests include dielectric characterization, ferrous metallurgy, microwave processing, comprehensive utilization of resources, waste valorization, powder agglomeration, low-carbon technology, process simulation, electromagnetic shielding, and synthesis of functional materials.

Dr. Peng has published over 170 papers, including more than 120 peer-reviewed articles in journals such as *International Materials Reviews*; *Journal of Hazardous Materials*; *ACS Sustainable Chemistry & Engineering*; *Resources, Conservation & Recycling*; *Journal of Cleaner Production*; *Waste Management*; *Metallurgical and Materials Transactions A*; *Metallurgical and Materials Transactions B*; *JOM*; *Journal of Power Sources*; *Fuel Processing Technology*; *Energy & Fuels*; *IEEE Transactions on Magnetics*; *IEEE Transactions on Instrumentation and Measurement*; *Ceramics International*; *Powder Technology*; and *Separation and Purification Technology*. He holds 56 Chinese patents and has served as an associate editor for *Mining, Metallurgy & Exploration*, as a guest editor for *JOM* and *Metals*, and as an editor for *PLOS ONE* and *Cogent Chemistry*. He has also been a member of editorial boards of *Scientific Reports*, *Journal of Central South*

University, and *Journal of Iron and Steel Research International*, and has served as a reviewer for more than 70 journals.

Dr. Peng is an active member of The Minerals, Metals & Materials Society (TMS). He has co-organized 10 TMS symposia and co-chaired 24 symposia sessions since 2012. He is a member of the Pyrometallurgy Committee and the vice chair of the Materials Characterization Committee. He was a winner of the TMS EPD Young Leaders Professional Development Award in 2014 and the TMS EPD Materials Characterization Award Best Paper—1st Place in 2020.

Jiann-Yang Hwang is a professor in the Department of Materials Science and Engineering at Michigan Technological University. He is also the Chief Energy and Environment Advisor at the Wuhan Iron and Steel Group Company, a Fortune Global 500 company. He has been the editor-in-chief of the *Journal of Minerals and Materials Characterization and Engineering* since 2002. He has founded several enterprises in areas including water desalination and treatment equipment, microwave steel production, chemicals, fly ash processing, antimicrobial materials, and plating wastes treatment. Several universities have honored him as a guest professor, including the Central South University, University of Science and Technology Beijing, Chongqing University, Kunming University of Science and Technology, and Hebei United University. Dr. Hwang received his B.S. from National Cheng Kung University in 1974, M.S. in 1980 and Ph.D. in 1982, both from Purdue University. He joined Michigan Technological University in 1984 and served as its Director of the Institute of Materials Processing from 1992 to 2011 and the Chair of Mining Engineering Department in 1995. He has been a TMS member since 1985. His research interests include the characterization and processing of materials and their applications. He has been actively involved in the areas of separation technologies, pyrometallurgy, microwaves, hydrogen storage, ceramics, recycling, water treatment, environmental protection, biomaterials, and energy and fuels. He has more than 28 patents and has published more than 200 papers. He has chaired the Materials Characterization Committee and the Pyrometallurgy Committee in TMS and has organized several symposia.

He is the recipient of the TMS Technology Award and of Michigan Tech's Bhakta Rath Research Award.

Jesse F. White holds a Ph.D. in Materials Science and Engineering from the KTH Royal Institute of Technology, an M.Sc. in Metallurgical and Materials Engineering from the Colorado School of Mines, and a B.S. in Metallurgical Engineering from the South Dakota School of Mines and Technology. He began his career in 1996 as a Process Engineer at the Kaiser Aluminum Mead Works. In 1997, he moved to Luleå, Sweden, and began as a Research Engineer at MEFOS working mainly in strip casting of steel. In 2002, he moved to Oslo, Norway and spent 5 years at Alstom as a Project Engineer designing, building, commissioning, and troubleshooting gas treatment systems for aluminum smelters around the world. Since 2007, he has been employed by Elkem in Kristiansand, Norway, starting out at Elkem Solar as a Research Engineer specializing in silicon refining, later moving to Elkem Technology, and since 2015 at Elkem Carbon. He is currently Technology Director at Elkem Carbon, supporting the production facilities in Brazil, China, Malaysia, Norway, and South Africa. In parallel, Dr. White is also currently an Affiliated Faculty Member of the Materials Science and Engineering Department at the KTH Royal Institute of Technology in Stockholm, where he teaches thermodynamics and conducts research in the areas of high-temperature experimental thermodynamics and metallurgical reactor design.

Jerome P. Downey earned his Ph.D. in Metallurgical and Materials Engineering at Colorado School of Mines and his B.S. and M.S. degrees in Metallurgical Engineering at Montana Tech. Dr. Downey is a Registered Professional Engineer with active licenses in Colorado and Montana. He has over 40 years of professional experience that includes industrial operations, applied process research and development, and corporate management. His technical expertise includes chemical and metallurgical thermodynamics, thermal processing, materials synthesis and processing, and hazardous materials treatment.

Dr. Downey is presently the Goldcorp Professor of Extractive Metallurgy at Montana Tech where he serves

as Department Head of Metallurgical and Materials Engineering as well as the Campus Director of the Montana University System Materials Science Ph.D. program. Dr. Downey's research efforts are currently focused on the study of fundamental properties of slags, molten salts, and glasses; vapor phase extraction and refining of rare earth elements; synthesis and sintering of non-oxide ceramic and composite materials; and applications of nanocomposite particles for water remediation.

Dean Gregurek is a senior mineralogist in the RHI Magnesita Technology Center, Leoben, Austria since 2001. Dr. Gregurek received his M.Sc. degree at the University of Graz in 1995 and his doctorate degree in Applied Mineralogy from the University of Leoben in 1999. Prior to RHI Magnesita, he worked for two years for Luzenac Europe in talc business. His current research interests and technical expertise are focused on chemical and mineralogical studies related to interactions between refractories, molten metals, and slags from pyrometallurgical furnaces. Dr. Gregurek has been a TMS member since 2012, *JOM* advisor (2014–2017), chair of the Pyrometallurgy Committee (2018–2020), and a co-organizer for the 7th–12th International Symposium on High-Temperature Metallurgical Processing (TMS Annual Meetings 2016–2021) and Furnace Tapping (TMS Annual Meeting 2022).

Baojun Zhao is a Professor in the College of Materials, Metallurgy and Chemistry at Jiangxi University of Science and Technology, Ganzhou, China. His primary fields of research are fundamental and applied investigations relevant to high-temperature processing of metals and materials. He has developed a series of novel research techniques to enable high-quality research to be carried out. A large number of experimental data on phase equilibrium and viscosity from his research directly supported industrial operations and development of thermodynamic and viscosity modeling. He has published over 200 refereed journal and conference papers and received several international awards to demonstrate his leading research achievements. He has long-term collaborations with many international

companies on metallurgy and resources to support efficient utilization of low-grade minerals and optimization and development of pyrometallurgical processes.

Onuralp Yücel completed his technical education with a Ph.D. in Metallurgical Engineering from Istanbul Technical University (ITU) where he has held the post of Professor since 2002. He was a Visiting Scientist at Berlin Technical University between 1987 and 1988. He carried out postdoctoral studies at the New Mexico Institute of Mining and Technology, Socorro, USA between 1993 and 1994. Prof. Yücel has as many as 400 publications/presentations to his credit, which include topics like technological developments in the production of a wide range of metals, ferroalloys, advanced ceramic powders, and application of carbothermic and metallothermic processes, among others. He was the vice chairman of ITU, Metallurgical and Materials Engineering Department (MMED) between 2004 and 2007. He has been a director of ITU, Applied Research Center of Material Science & Production Technologies between 2006 and 2012. He was the chairman of ITU, MMED between 2016 and 2018.

Prof. Yücel is a member of the international advisory board of the International Symposium on Boron, Borides and Related Materials (ISBB), International Symposium on High-Temperature Metallurgical Processing organized by TMS, International Symposium on Self Propagating High-Temperature Synthesis (SHS), and International Metallurgy and Materials Congress (IMMC).

Dr. Yücel's areas of interest include:

Pyrometallurgy; Pretreatment of concentrates (production of WO_3, Sb_2O_3, As_2O_3, MoO_3, ZnO), smelting and reduction of slags, production ferroalloys, alloys and metals carbothermic and metallothermic processes (SHS) in EAF or in ladle (Mg, Ca, Sr, Cu, Co, V, Cr, W, Zn, ferroboron, cobaltboron, nickelboron, ferronickel, nickel pig iron, ferrotungsten, ferromolybdenum, ferromanganese, silicomanganese, ferrovanadium, ferrochromium, iron-nickel-chromium-molybdenum, and aluminum-titanium-boron alloys).

Ceramic Powder Production and Processing; Production of carbide, nitride, boride powders and

their processing by explosive consolidation or sintering techniques (B_4C, TiB_2, ZrB_2, SiC, $CrB_{2,}$).

Beneficiation of Industrial Wastes; Production of metals and compounds from aluminum dross, steel scale and EAF dust, Waelz slag, galvanizing ash, brass production wastes, and vanadium sludge produced aluminum production, and grit production from aluminum, copper, and steel slags.

Ender Keskinkilic earned his undergraduate degree in 1999 from the Department of Metallurgical and Materials Engineering of Middle East Technical University (METU), Ankara, Turkey. He continued his M.S. and Ph.D. studies in the same department and worked as a Research Assistant in METU between 1999 and 2003. After receiving his master's degree in 2001, he progressed further in the field of extractive metallurgy. During the Ph.D. period, Dr. Keskinkilic moved to Eregli-Zonguldak in 2003 and worked in the Quality Metallurgy and RD Department of Eregli Iron and Steel Works Co. (ERDEMIR), which is the leading steel company in Turkey for the qualities produced and the production capacity. After earning his Ph.D. in 2007, he returned to university and to work in the Department of Metallurgical and Materials Engineering of Atilim University, Ankara, in 2008. Dr. Keskinkilic has been working as faculty in Atilim since 2008 and has been a full-time professor since 2020. His primary field of interest is extractive metallurgy and more specifically pyrometallurgical processes such as iron- and steelmaking, ladle metallurgy, ferroalloy production, and non-ferrous extractive metallurgy. He has been acting as the Chairperson of the Department of Metallurgical and Materials Engineering since July 2018 and as the Director of Graduate School of Natural and Applied Sciences since April 2021.

Tao Jiang received his M.S. in 1986 and Ph.D. in 1990, both from Central South University of Technology. Then he joined the university and served as an assistant professor (1990–1992) and full professor (1992–2000). From 2000 to 2003, he was a visiting scientist to the Department of Metallurgical Engineering, the University of Utah. Since 2003, Dr. Jiang has been a Professor in the School of Minerals Processing & Bioengineering at Central South University. He has been Specially Appointed Professor of Chang Jiang Scholar Program of China since 2008 and dean of the school since 2010.

His research interests include agglomeration and direct reduction of iron ores and extraction of refractory gold ores. He has undertaken more than 50 projects from the government and industry, including the National Science Fund for Distinguished Young Scholars Program. He and co-workers invented the direct reduction process of composite binder pellets, and three plants were set up in China based on the invention. He proposed the innovative composite agglomeration process of iron ore fines, which was put into production in Baotou Steel Company, China. He is actively involved in the areas of utilization of non-traditional ferrous resources such as complex ores and various solid wastes. He has published 320 technical papers and 6 books including *Direct Reduction of Composite Binder Pellets and Use of DRI*, *Principle & Technology of Agglomeration of Iron Ores*, *Chemistry of Extractive Metallurgy of Gold*, and *Electrochemistry and Technology of Catalytical Leaching of Gold*. He holds 35 patents and has more than 30 conference presentations.

Morsi Mohamed Mahmoud joined the Mechanical Engineering Department at King Fahd University of Petroleum and Minerals (KFUPM), Saudi Arabia, in August 2016. He also holds an Associate Professor position at the Advanced Technology and New Materials Research Institute (ATNMRI), City for Scientific Research and Technological Applications (SRTA City), Egypt. From December 2009 until August 2016, he worked as a Visiting Assistant Professor and then as a Senior Scientist at Institute of Applied Materials—Applied Materials Physics (IAM-AWP) at Karlsruhe Institute of Technology (KIT), Germany. Dr. Mahmoud

earned his Ph.D. and M.Eng. degrees in Materials Science and Engineering from Virginia Tech, Blacksburg, USA in 2007. He has accumulated unique experience and skills in advanced materials processing techniques such as microwave processing, glasses, ceramics, and structure–property processing relationship in materials, in addition to a deep knowledge in materials characterization techniques. He also has had experience organizing and editing several technical publications, conferences, web-seminars, and scientific events. He served as the Chairman and the Organizer of the Processing and Performance of Materials Using Microwaves, Electric and Magnetic Fields, Ultrasound, Lasers, and Mechanical Work at the Materials Science & Technology Technical Meeting and Exhibition 2019 (MS&T19), USA. Furthermore, he served as a Co-editor for nine books and published 32 technical papers in the top 10 ISI ranked journals in Materials Science and Engineering. He was given several prestigious awards such as Virginia Tech Citizen Scholar Award; an Honor Scholarship from Virginia Tech Graduate School, USA; and Two German Academic Exchange Service (DAAD) Fellowships.

Part I
Simulation of High-Temperature Processes

3D Experimental Model Study on Gas–Solid Flow of Raceway in BF

Cong Li, Qingguo Xue, Xing Peng, Haibin Zuo, Xuefeng She, Guang Wang, and Jingsong Wang

Abstract The transfer phenomenon and chemical reactions happening in raceway play a key role in both metallurgical principle and industrial operation of blast furnace (BF). Hot air with high blasting velocity resulting in efficient gas–solid motion, which determines the velocity field and furthermore temperature field, influences the total rate of chemical reaction. A 1/3rd scale 3D cold sector experimental model taking blast air kinetic energy as similarity criterion is built to study the gas–solid motion phenomenon by using 80–110 m/s gas inflow and real coke granule (average dimeter: 10–12 mm). The results indicate that, to study the movement inside of raceway, using the blast air kinetic energy as similarity criterion is much more reasonable than the Reynolds number or Froude number.

Keywords Raceway · Blast air kinetic energy · Cold experimentation · Gas–solid interaction

Introduction

In BF production, the transmission phenomenon and chemical reaction in raceway are very important and have always been the focus of research. For example, raceway in actual BF by microwave reflection method is directly measured [1]. Through the cold physical model, the different effects of two-dimensional slot model and three-dimensional sector model in whole furnace model are studied [2, 3]. The application of numerical simulation can comprehensively study the multiphase flow, temperature field, transmission phenomenon, composition distribution, and chemical reaction in BF [4, 5].

In the cold simulation of physical model, the commonly used coke particle substitutes are glass beads, plastic balls, beans, and grains. The density, equivalent diameter, and internal friction coefficient of these particles are very different from those of coke.

C. Li · Q. Xue · X. Peng · H. Zuo · X. She · G. Wang · J. Wang (✉)
State Key Laboratory of Advanced Metallurgy, University of Science and Technology Beijing, Beijing 100083, China
e-mail: wangjingsong@ustb.edu.cn

Z. Peng et al. (eds.), *12th International Symposium on High-Temperature Metallurgical Processing*, The Minerals, Metals & Materials Series,
https://doi.org/10.1007/978-3-030-92388-4_1

Besides, the selected similarity criterion is generally Reynolds number or Froude number, and thus, the blast speed is low. There are some deficiencies in revealing the particle motion under the interaction of gas–solid, especially the high-speed motion [2, 6].

In this paper, using blast air kinetic energy as similarity criterion and coke as filler, a 1/3rd scale 3D sector physical model is established to simulate the gas–solid flow in the lower part of BF at four blast speeds of 80, 90, 100, and 110 m/s, with emphasis on the particle movement in the raceway. Experiments show that it is reasonable to use blast air kinetic energy as similarity criterion and coke as filler, which can more accurately reflect the actual situation in the raceway of BF tuyere and improve the reliability of physical cold simulation.

Model Description

Model Geometry

A cold sector model scale of 1/3rd was determined. The basic geometric dimensions of the model are as follows. The cold model is made of plexiglass, and measurement holes with an alignment of 10 × 10 cm are reserved on one side wall, as shown in Fig. 1 (Table 1).

Fig. 1 3D model experimental facility (empty and charged)

Table 1 Dimension of real industrial BF and model (unit: mm)

	Real industrial BF	Model
Hearth radius	2600	867
Hearth height[a]	2900	540
Bosh height	3000	1000
Belly radius	3000	1000
Belly height	1200	100
Tuyere diameter	100	35
Tuyere central line height	2500	400
Raceway depth[b]	998	350
Raceway height	865	300
Raceway width	563	200

[a] Hearth is shortened for the reason of no hot metal liquid
[b] Raceway parameter is calculated according to literature [7, 8]

Table 2 Blast air kinetic energy real industrial BF and model

	Real industrial BF	Model
Tuyere diameter (mm)	110	35
Real blast speed (m/s)	190	110
Mass flow (kg/s)	1.136[a]	0.1275
Blast air kinetic energy (kJ/s)[b]	20.495	0.771

[a] The effects of blast pressure and temperature are considered
[b] The ratio of is 26.58

Taking Blast Air Kinetic Energy as the Similarity Criterion

In this experiment, the blast air kinetic energy is used as the similarity criterion when determining the blast speed. The size of coke particles should also be one-third of the actual coke, so the mass of actual coke in industry is 27 times that of the coke particles used in this model. The blast air kinetic energy should also be reduced to one twenty seventh of actual BF (Table 2).

Particle Physical Properties and Measuring Devices

According to the real density and volume, six kinds of particles are selected: hollow alumina ball, coke (average diameter 12 mm), chickpea, black bean, red bean, and mung bean. The physical properties are shown in Table 3.

The density and average equivalent diameter of coke and chickpea are similar. Therefore, when filling the model, gray chickpea is used to replace some coke particles, which not only ensures the accuracy and reliability of physical simulation, rather

Table 3 Particle physical properties

	Real density (kg/m^3)	Average single particle mass (kg)	Average single particle volume (m^3)	Average equivalent diameter (m)
Alumina ball	2435	1.35E−03	5.56E−07	0.0102
Coke	1280	7.92E−04	6.19E−07	0.0106
Chickpea	1242	6.54E−04	5.26E−07	0.0100
Black bean	1163	2.10E−04	1.80E−07	0.0070
Red bean	1302	1.31E−04	1.01E−07	0.0058
Mung bean	1360	6.15E−05	4.52E−08	0.0044

than hollow alumina ball, chickpea, black bean, red bean, or mung bean, but also plays a role of tracing.

Use L-shaped pitot tube + digital display instrument and hot air velocimeter to measure the gas flow velocity in the model. Use a high-speed industrial camera to capture particle motion and obtain motion data, and the image storage interval is 25 ms.

Results and Discussion

Gas Superficial Velocity Distribution

After obtaining the velocity values in the horizontal and vertical directions, the contour map of gas flow superficial velocity distribution on the vertical plane passing through the tuyere central line is drawn, as shown below (Figs. 2, 3, 4, 5, 6, 7, 8 and 9).

It can be seen from the contour map that after the core air flow enters the model from the tuyere, because the space expands instantaneously, the kinetic energy decays rapidly, and the velocity gradient is large. The core air flow quickly decays from high speed to 25–40 m/s differently. When approaching the end wall, the horizontal speed further decays to 3–7 m/s differently. Finally, subject to the obstruction of the end wall, the core air flow turns to the vertical direction.

Motion of Single Particle Under the Interaction of Gas–Solid

Through a pipe above the tuyere, a single particle of six kinds is put into airflow. A horizontal section is set when making the pipeline, so as to avoid friction and gravity to the greatest extent. Record the horizontal position of particles between two contiguous pictures (the scale plate in the image below is 5 × 5 cm), and the

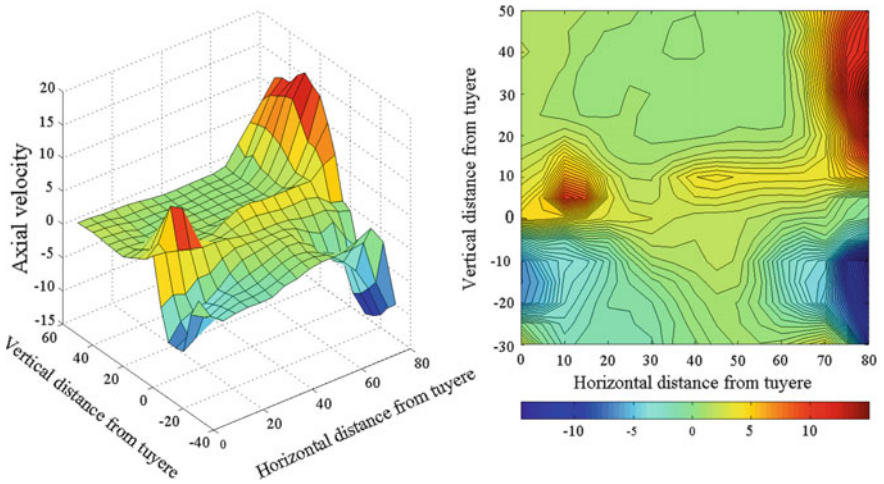

Fig. 2 Contour of axial velocity in plane *XY* through tuyere central line (blast speed: 80 m/s, *X* and *Y* axes unit: cm)

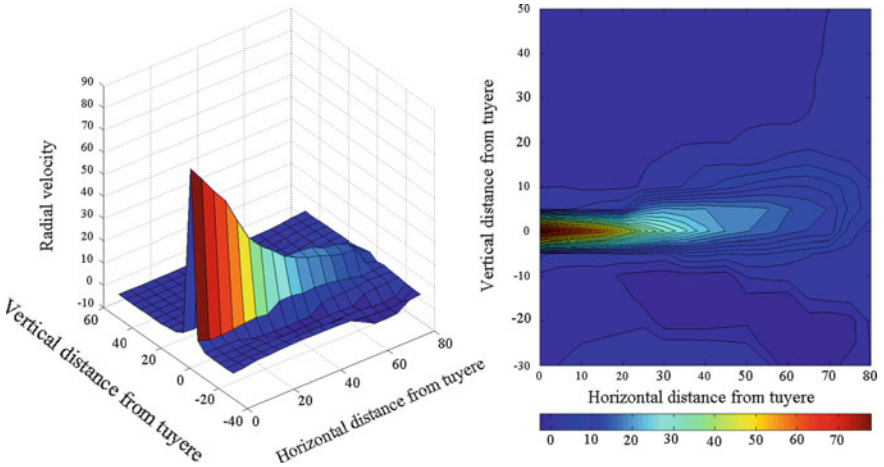

Fig. 3 Contour of radial velocity in plane *XY* through tuyere central line (blast speed: 80 m/s, *X* and *Y* axes unit: cm)

storage interval of two contiguous pictures is 25 ms, so as to obtain the particle movement speed (Fig. 10).

The moving speed of particles is measured for many times, and the average value is taken to obtain the results, as shown below (Fig. 11).

It can be seen from the above figure that with the increase of blast speed, the particle movement speed increases obviously, and the movement speed of particles with low density and small equivalent diameter, such as mung bean and red bean,

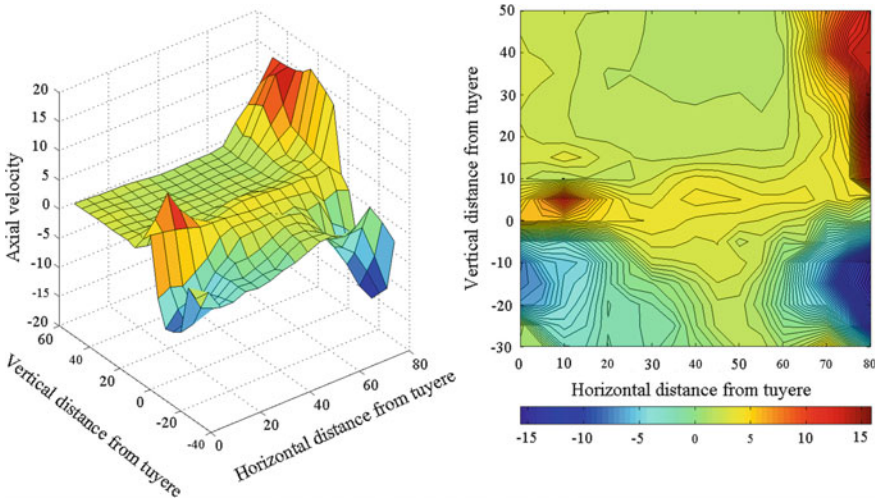

Fig. 4 Contour of axial velocity in plane *XY* through tuyere central line (blast speed: 90 m/s, *X* and *Y* axes unit: cm)

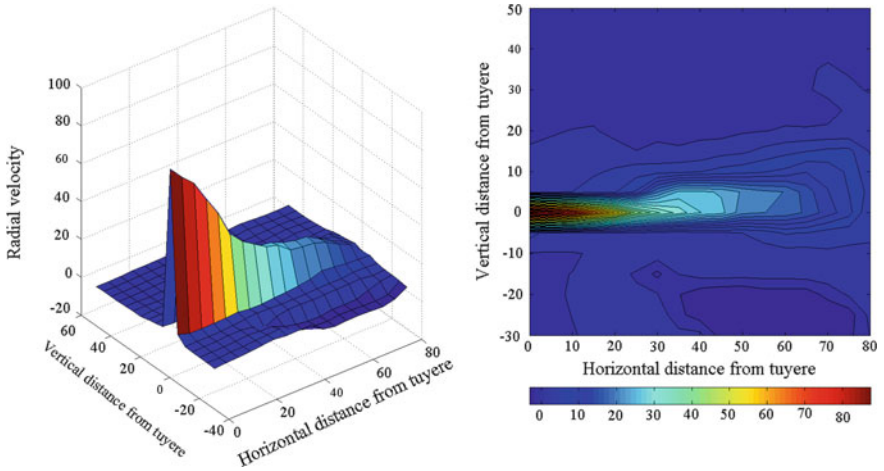

Fig. 5 Contour of radial velocity in plane *XY* through tuyere central line (blast speed: 90 m/s, *X* and *Y* axes unit: cm)

increases more obviously. This is consistent with the sharp increase of the specific surface area of powdered charge ($\leq$5 to 8 mm) and the easy fluidization of powdered particles.

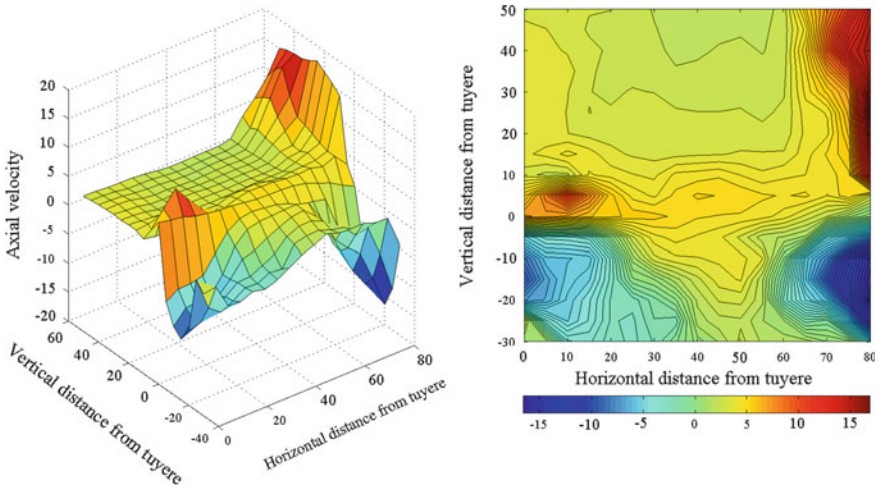

Fig. 6 Contour of axial velocity in plane *XY* through tuyere central line (blast speed: 100 m/s, *X* and *Y* axes unit: cm)

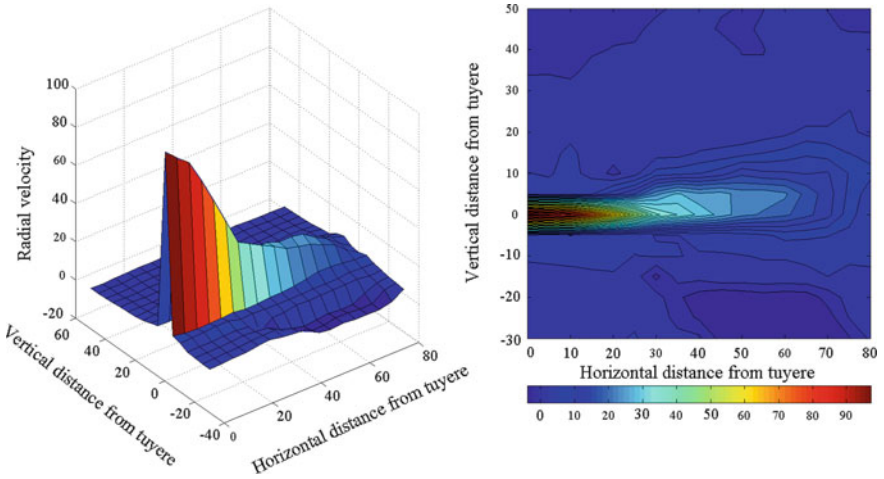

Fig. 7 Contour of radial velocity in plane *XY* through tuyere central line (blast speed: 100 m/s, *X* and *Y* axes unit: cm)

Multi-particle Motion Under Gas–Solid Interaction

Multi-particle motion experiments were carried out under four blast speeds: 80, 90, 100, 110 m/s. Three kinds of particles: alumina ball, chickpea, and coke are put into it (Fig. 12).

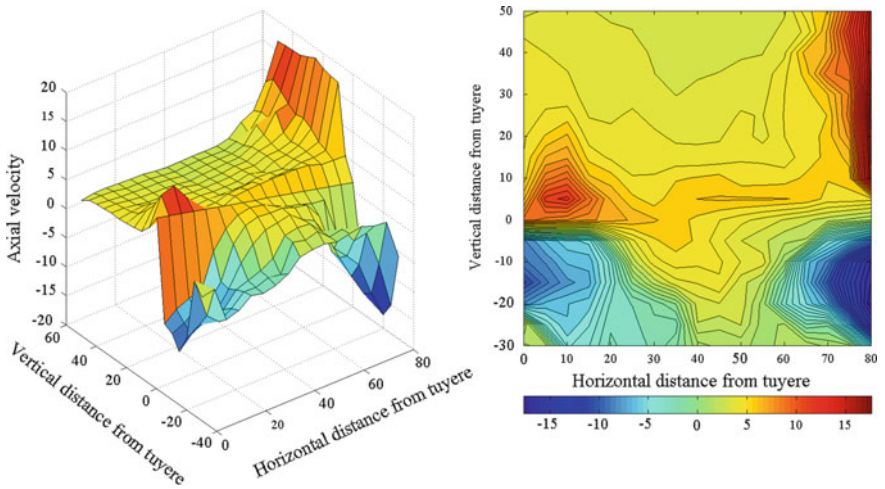

Fig. 8 Contour of axial velocity in plane *XY* through tuyere central line (blast speed: 110 m/s, *X* and *Y* axes unit: cm)

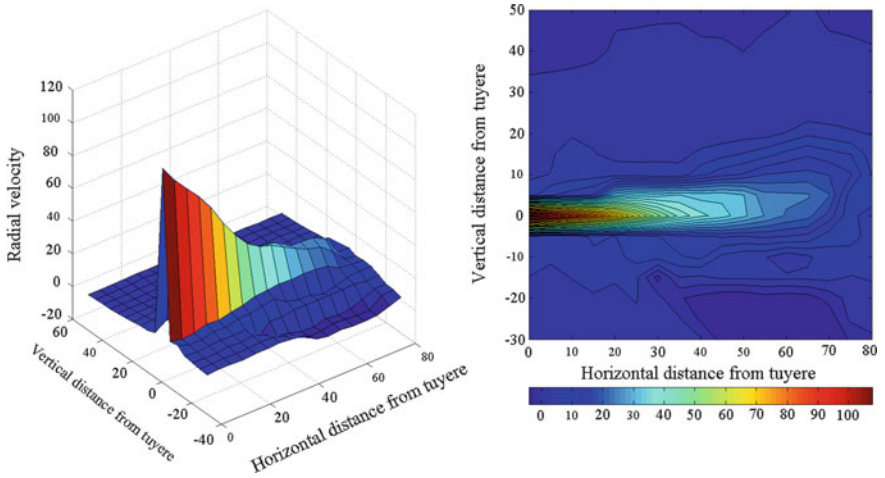

Fig. 9 Contour of radial velocity in plane *XY* through tuyere central line (blast speed: 110 m/s, *X* and *Y* axes unit: cm)

After obtaining the position information, similar to the motion of a single particle, the motion speed of particle can be calculated, as shown in Table 4.

Because of the elastic collision force between particles, the velocity of most coke particles is lower than that of single particles. At 100 m/s and 110 m/s, there are more moving particles, and the particle velocity decreases significantly. The frequency of particle at 100 m/s entering in the middle low-speed region is more than 110 m/s (Fig. 13).

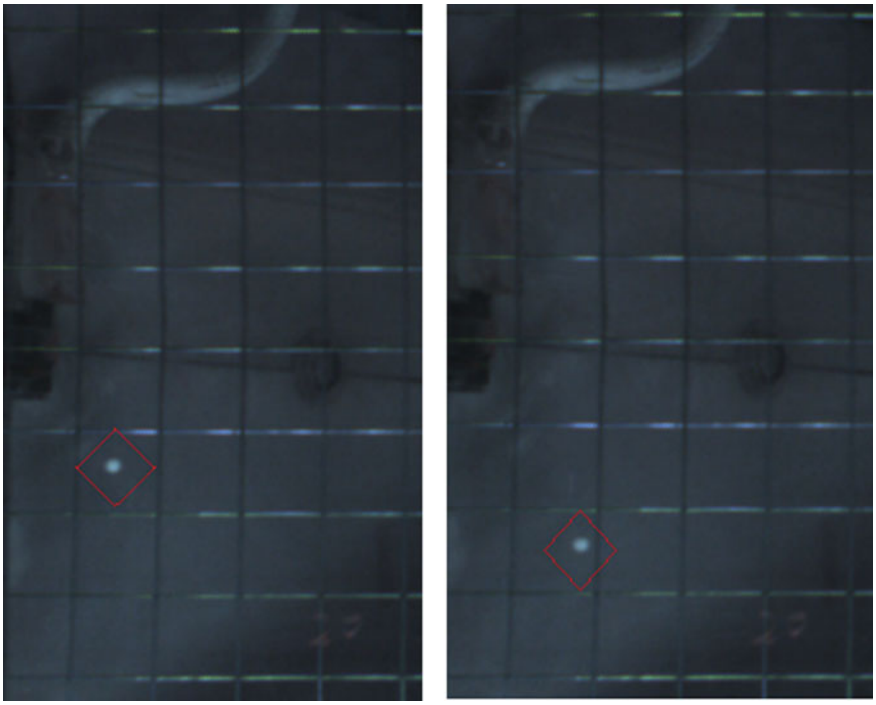

Fig. 10 Two contiguous images of alumina ball at 80 m/s blast speed

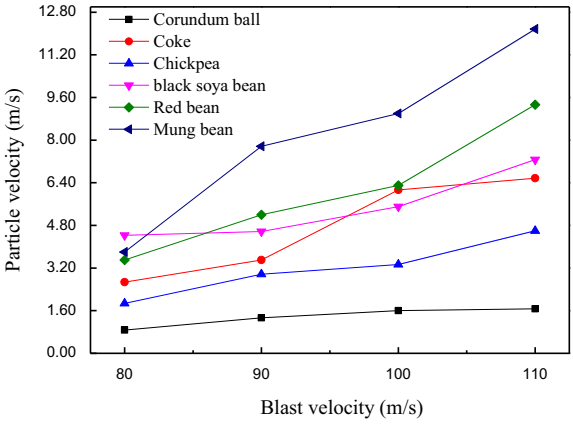

Fig. 11 Particle velocity under different blast speeds

According to the particle velocity and direction, the raceway can be divided into four regions: the lower rightward region, the upper leftward region, the right upward region, and the middle low-speed region.

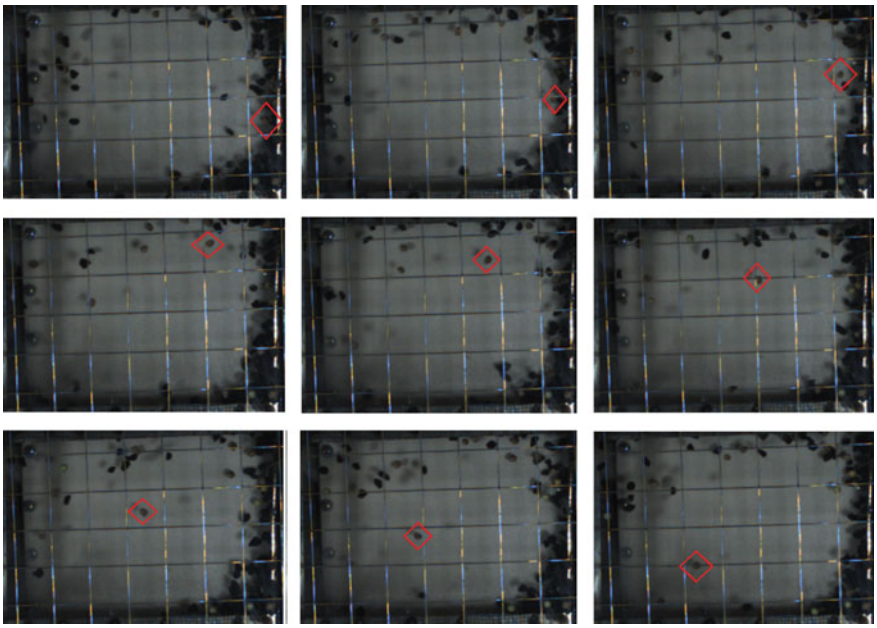

Fig. 12 Particle motion and identification at 100 m/s blast speed

Table 4 Particle speed in four zones at different blast speeds

	80[a]	90	100	110
Bottom rightward	–	5.00	3.20	3.60
Top leftward	–	–	1.40	3.00
Right upward	–	3.00	1.00	1.80
Middle slow	–	–	0.80	0.60

[a] No moving particles have been found at 80 m/s. And size of moving particles at 90 m/s is particularly small (it maybe the granule resulting from friction)

Conclusions

The conclusions are as follows:

- Coke particles circle obviously in raceway at blast speed of 100 m/s and 110 m/s. This proves the rationality of choosing blast air kinetic energy as the similarity criterion to establish the cold raceway model of BF.
- Small coke particles are selected as the filler based on the same physical parameters and density. The geometric size is strictly scaled to meet the similarity criteria as much as possible, which can improve the reliability of physical simulation.

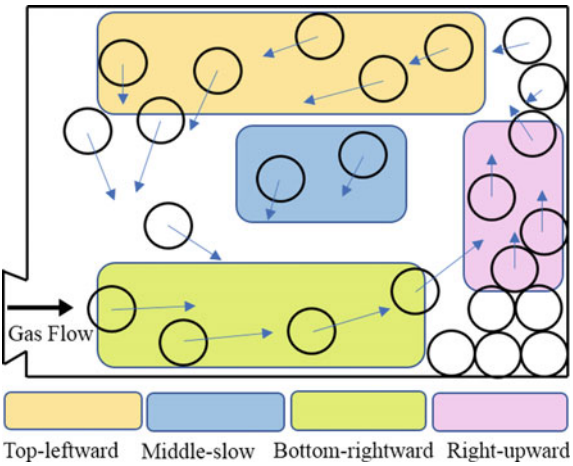

Fig. 13 Different motion zones in raceway

- For the movement speed of single particle, the influence of particle real density is greater at low blast speed, while the influence of equivalent diameter is greater at high blast speed.
- The multi-particle motion in the raceway under the interaction of gas–solid can be divided into four regions with significantly different velocities and directions.

Acknowledgements The authors acknowledge the financial support from National Natural Science Foundation of China (U1960205) gratefully.

References

1. Matsui Y, Yamaguchi Y, Sawayama M, Kitano S, Nagai N, Imai T (2006) Analyses on blast furnace raceway formation by micro wave reflection gunned through tuyere. Tetsu-to-Hagane 92(12):919–925
2. Wright B, Zulli P, Zhou ZY, Yu AB (2011) Gas–solid flow in an ironmaking blast furnace-I: physical modelling. Powder Technol 208(1):86–97. https://doi.org/10.1016/j.powtec.2010.12.006
3. Hatano M, Fukuda M, Takeuchi M (1976) An experimental study of the formation of raceway using a cold model. Tetsu-to-Hagane 62(1):25–32
4. Zhou ZY, Zhu HP, Wright B, Yu AB, Zulli P (2011) Gas–solid flow in an ironmaking blast furnace-II: discrete particle simulation. Powder Technol 208(1):72–85. https://doi.org/10.1016/j.powtec.2010.12.005
5. Yu X, Shen Y (2018) Modelling of blast furnace with respective chemical reactions in coke and ore burden layers. Metall Mater Trans B 49(5):2370–2388. https://doi.org/10.1007/s11663-018-1332-6
6. Guili M, Pinti M, Federico G, Salvatore E (1990) Investigation on burden descent in the blast furnace. In: Proceedings of the sixth international iron and steel Congress, Nagoya, Japan, vol 2, pp 521–526

7. Nomura S (1986) A simple treatment on the geometry of raceway zone. Trans Iron Steel Inst Japan 26(2):107–113. https://doi.org/10.2355/isijinternational1966.26.107
8. Michiharu Hatano BH, Fukuda M, Masuike T (1976) Analysis of the combustion zone in the experimental blast furnace. Tetsu-to-Hagane 62(5):505–513

Modelling of Permanent Magnetic Field for Its Application in Electroslag Remelting

Guotao Zhou, Shenyang Song, Wei Yan, and Jing Li

Abstract A high-efficiency and low-power consumption permanent magnetic technology was proposed to modify the poor control of structure and primary carbide of high-carbon stainless steel. One key point of the better application of permanent magnetic technology is the generation of magnetic field with stronger intensity and more even distribution using less magnet. In this study, the permanent magnetic field under varying arrangement, thickness, number, and arc degree of magnets was modelled. The results indicated that adjacent magnets with same polarization mode have stronger magnetic field intensity. All the greater magnet thickness, greater arc degree of single magnet and less magnet number under same sum of total arc degree can increase field intensity. The arrangement mode of two 40 mm-thickness magnets with arc degree of 120 and different polarization mode among more than 20 arrangement modes has strongest field intensity and widest range of intensive magnetic flux density along radial direction.

Keywords Permanent magnetic field · Magnet arrangement · Electroslag remelting

List of Symbols

μ_0	Vacuum permeability
B	Magnetic flux density
M	Magnetization intensity
H	Magnetic field intensity
V_m	Magnetic scalar potential
μ_r	Relative permeability

G. Zhou · S. Song · W. Yan (✉) · J. Li
University of Science and Technology Beijing, Beijing, China
e-mail: weiyan@ustb.edu.cn

Z. Peng et al. (eds.), *12th International Symposium on High-Temperature Metallurgical Processing*, The Minerals, Metals & Materials Series,
https://doi.org/10.1007/978-3-030-92388-4_2

Introduction

Electroslag remelting (ESR) has been receiving increasingly widespread application during production of special steels and alloys due to its excellent performance in increasing cleanliness, solidification structure refinement, and homogeneity of metal materials. High-carbon martensitic stainless steels have broadly used in production of high-grade knives because of high hardness, abrasive resistance, and corrosion resistance. They are always produced through ESR to improve cleanliness and structure. However, the coarse primary carbides are observed frequently in ESR ingots due to high carbon and alloy contents, this would deteriorate the product performance and service life. The primary carbide is especially difficult to be eliminated completely during subsequent process, it is therefore ESR process is the critical step to control the primary carbide.

Many measurements have been proposed and tried to adjust the segregation and primary carbide through process parameter optimization, alloying treatment of steel, and development of new ESR technique. Suh [1] found that increase of melting rate could decrease the size of primary carbide on the surface but increase the size of primary carbide in the zone of 1/2 radius and core of high-speed steel ESR ingot. Chumanov [2] investigated the primary carbide of semi-heat-resistant steel prepared by ESR through rotating a consumable electrode and found the carbide became fine and uniform, he contributed this to the increasing uniformity of pool temperature and cooling rate. Chang [3] adopted the similar method with Chumanov during ESR of bearing steel; as a result, the segregation of carbon and chromium was decreased, and the primary carbide was restrained. Boccalini [4] found that addition of rare earth promoted the formation of M6C carbide and attributed this to the formation of more nucleation sites in the case of rare-earth oxysulfide.

Ultimately, formation of primary carbide is the result of interdendritic enrichment of carbide-forming elements in the solidification front. To control primary carbide should first control the interdendritic segregation of carbide-forming elements. Dong [5] reported that element segregation decreases with the decrease of dendrite spacing in electroslag remelted cold roller steel and concluded that solidification segregation of ESR ingot could be suppressed through control of secondary dendrite spacing. Despite some methods as above have been investigated and employed, however, these measurements are always conducted through changing the process parameters of ESR, most of time they have not obvious effect especially for large-size ingot limited by the solidification mode of ESR. External field control of metal solidification represented by electromagnetic field has been utilized widely during continuous casting of steel and received good effectiveness. Some researchers [6, 7] have applied electromagnetic stirring during centrifugal casting of high-speed roller steel and mould casting of high-speed steel. The results indicated that the carbide became finer and distributed more uniformly. The application of electromagnetic field during ESR is rarely reported. Murgas [8] and Wang [9] reported that the solidification structure became fine and dendrite spacing decreased after application of electromagnetic field during ESR of M2 high-speed steel and H13 die

steel. Considering the relationship between primary carbide and element segregation and dendrite spacing, the electromagnetic field may be effective for primary carbide control. Permanent magnetic field has more advantages such as high field intensity, low energy consumption, and simple equipment structure, so it may be more suitable for large section and high-alloy electroslag remelted steel compared to electromagnetic field. Permanent magnetic field is generated from permanent magnet, the size, number and arrangement mode of permanent magnet are the designing keys for generation of high permanent magnetic field intensity in the case of less magnet number. The present study aims to propose an optimum arrangement mode of permanent magnet for subsequent application during ESR.

Modelling Description

The COMSOL Multiphysics (COMSOL) software was employed in the present study to conduct the modelling and computation. The geometrical model can be built through COMSOL software with same height of 200 mm but varying permanent magnet number, thickness, arc degree, arrangement mode, and polarization direction. N38 permanent magnet (sintered NdFeB) with a magnetic flux density of 1.26 T and a relative permeability of 1.05 was used in the modelling. In the case of magnetic system simulated with permanent magnets, the AC/DC module with the magnetic field no current (MFNC) physics was utilized. The surrounding air layer of the permanent magnet model with a thickness of 20 mm and a relative permeability of 1.0 was set as the insulation surface in the model, and this means that the magnetic induction line cannot penetrate the air layer or a magnetic vector potential is zero. The steel with a relative permeability of 1.0 and a conductivity of 7.14×10^5 S/m was used as the material between the magnets. Then, the model was meshed. Figure 1 presents the mesh example for the arrangement mode of NSNS (N and S represent the polarization direction of north and south, respectively) used in the modelling.

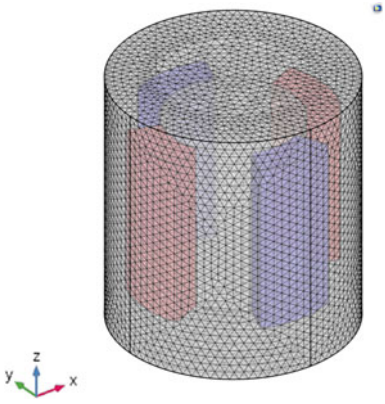

Fig. 1 Mesh of the permanent magnet model

In the area with no current, Maxwell–Ampere's law for the system can be simplified as follows.

$$\nabla \cdot \left(\frac{1}{\mu_0} B - M \right) = \nabla \cdot H = 0 \tag{1}$$

The following equation can be obtained according to the Gauss magnetic law.

$$\nabla \cdot B = 0 \tag{2}$$

The magnetic scalar potential can be defined using the following equation.

$$H = -\nabla V_m \tag{3}$$

The constitutive relation equation for surrounding air area can be written as follows.

$$B = \mu_0 \mu_r H \tag{4}$$

The constitutive relation equation for permanent magnet can be obtained through a combination of the above Eqs. (1–3).

$$B = \mu_0 (H + M) \tag{5}$$

where μ_0 is vacuum permeability, B is magnetic flux density, M is magnetization intensity, H is magnetic field intensity, V_m is magnetic scalar potential, and μ_r is relative permeability.

Results and Discussion

Effect of Polarization Direction on Permanent Magnetic Field

The generation and magnitude of magnetic field are related to the polarization direction. This is because the polarization direction affects the transmit–receive and distribution of magnetic lines. In order to investigate the effect of polarization direction of magnet on permanent magnetic field, two polarization direction modes of magnets including "North–South-North–South (NSNS)" and "North–North-South-South (NNSS)" were modelled. All magnets used in the model have same thickness of 40 mm, same arc degree of 45°, and same height of 200 mm. The modes can be expressed simply as 4-60-NSNS-40 and 4-60-NNSS-40 (magnet number–arc degree–polarization mode–thickness). Figure 2 indicates the calculated coupled

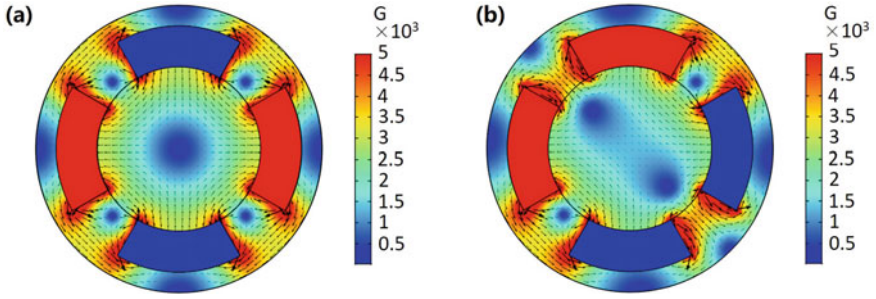

Fig. 2 Magnetic flux density and vector for **a** 4-60-NSNS-40 and **b** 4-60-NNSS-40 mode

figures of magnetic flux density and magnetic vector. In the figure, red and blue represent the south magnetic pole (S) and the north magnetic pole (N), respectively.

It can be found from Fig. 2a, b that the distribution of magnetic lines from the model with NSNS polarization mode is very different from that from the model with NNSS polarization mode. The magnetic lines are sparse in the core but dense around the magnets for NSNS mode, while the magnetic lines are denser in the core for NNSS mode than that for NSNS mode. This result can be observed more visually from Fig. 3, which gives the change relationship of magnetic flux density with radial distance of pair magnet pole. The magnetic flux density of core is almost 0 for NSNS mode, while it is up to 1350 G for NSNS mode. This is because the magnetic lines are inclined to enter the nearest magnet with the opposite polarization mode. The magnet arrangement of NSNS mode is easier to receive the magnetic lines from the adjacent magnets than the NNSS mode.

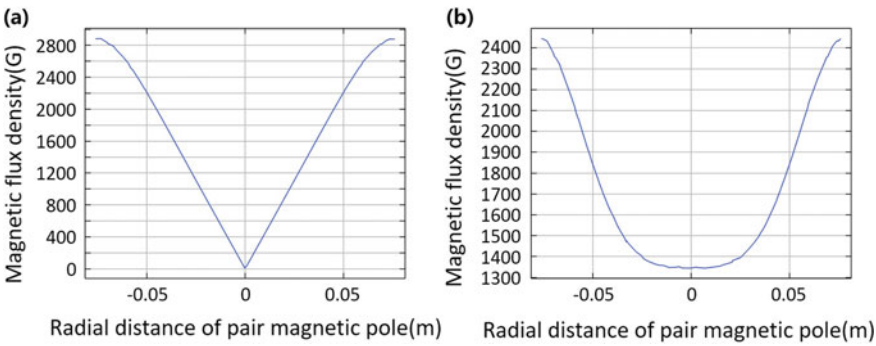

Fig. 3 Magnetic flux density along radial distance of magnetic pole for **a** 4-60-NSNS-40 and **b** 4-60-NNSS-40 mode

Effect of Magnet Thickness on Permanent Magnetic Field

As shown in Fig. 4, the permanent magnetic field was modelled using the magnets with thickness of 20 mm and 40 mm but same arrangement mode (NNSS) and number of four. The modes can be expressed simply as 4-60-NNSS-20 and 4-60-NNSS-40. It can be seen from Fig. 4 that the magnetic flux density in the core and around the thinner magnets is obviously lower than that generated by the thicker magnets. In details, the magnetic flux density increases by double with a doubling of the magnet thickness according to Fig. 5. But the range of intensive magnetic field along the radial direction has no apparent change. Therefore, application of thick magnet is one way to strengthen magnetic field.

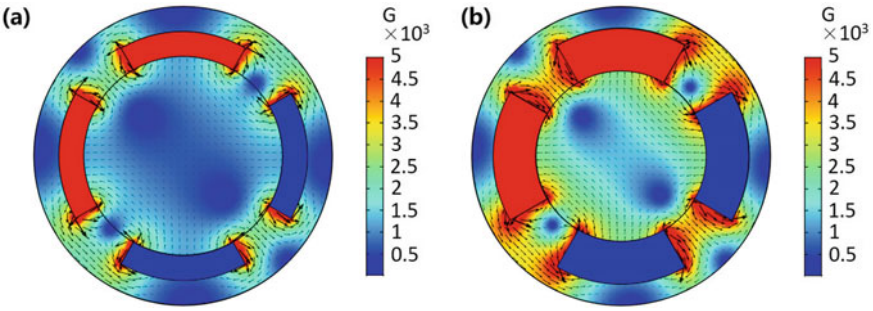

Fig. 4 Magnetic flux density and vector for **a** 4-60-NNSS-20 and **b** 4-60-NNSS-40 mode

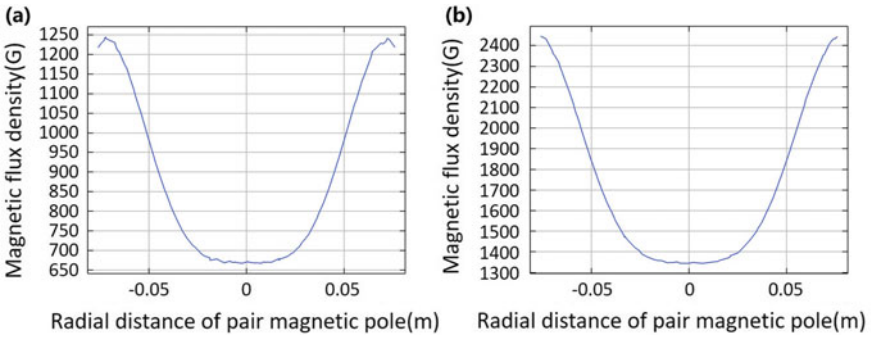

Fig. 5 Magnetic flux density along radial distance of magnetic pole for **a** 4-60-NNSS-20 and **b** 4-60-NNSS-40 mode

Effect of Magnet Number on Permanent Magnetic Field

In order to evaluate the single effect of magnet number on the permanent magnetic field, the effect of the magnet number on magnetic field was investigated in the case of same total arc degree of magnet, same magnet thickness as well as same polarization direction with a symmetrical distribution.

Figure 6 presents the calculated coupled figures of magnetic flux density and magnetic vector. Two magnets with single arc degree of 120° and thickness of 40 mm (2-120-NS-40) were used in the modelling for Fig. 6a, while four magnets with single arc degree of 60° and thickness of 40 mm (4-60-NS-40) were used in the modelling for Fig. 6b. It can be seen that both magnetic flux density and magnetic vector are different with each other despite of same and total arc degree of 240°. Figure 7 shows the change of magnetic flux density with radial distance of pair magnetic pole. It can be found that the core magnetic flux density of 2-120-NS-40 mode is up to 1650 G, which is stronger than 1350 G of 4-60-NS-40 mode. This is because the magnetic lines from the N pole tend to enter the nearest S pole, this phenomenon just agrees with the magnet arrangement mode as shown in Fig. 6b. It should be stressed that

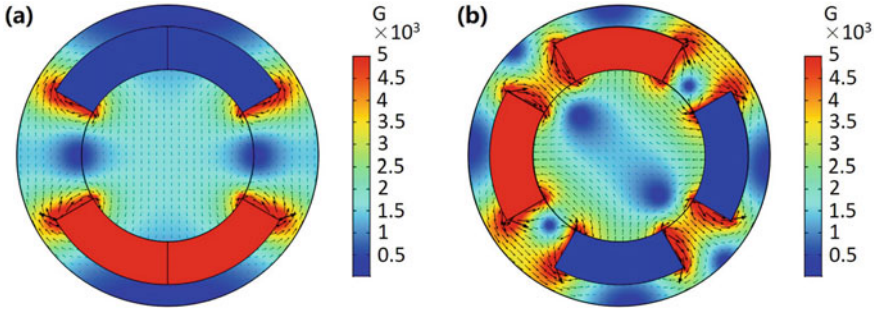

Fig. 6 Magnetic flux density and vector for **a** 2-120-NS-40 and **b** 4-60-NNSS-40 mode

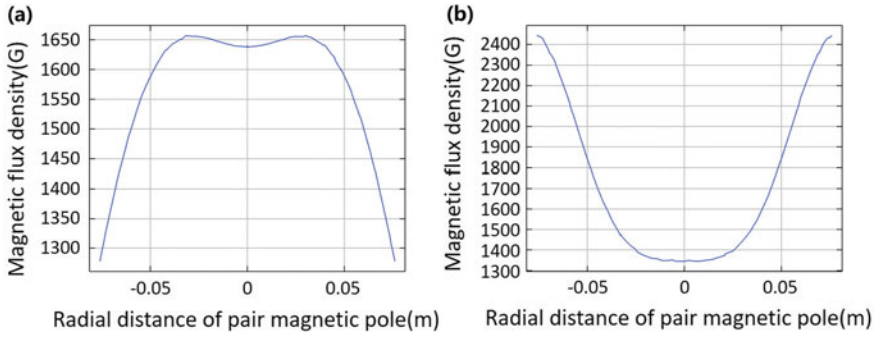

Fig. 7 Magnetic flux density along radial distance of magnetic pole for **a** 2-120-NS-40 and **b** 4-60-NNSS-40 mode

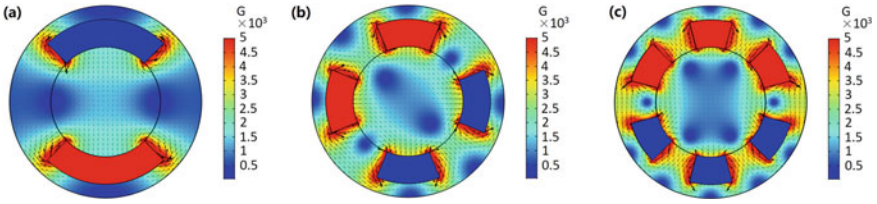

Fig. 8 Magnetic flux density and vector for **a** 2-90-NS-40, **b** 4-45-NNSS-40, and **c** 6-30-NNNSSS-40 mode

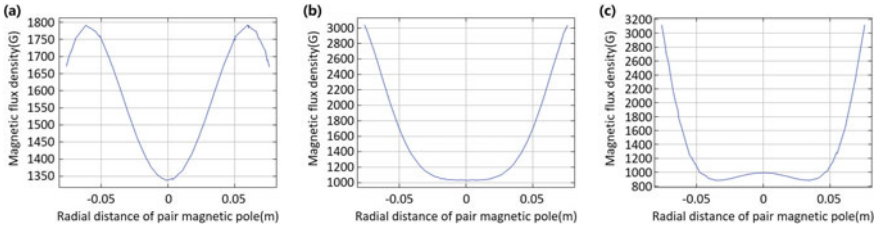

Fig. 9 Magnetic flux density along radial distance of magnetic pole for **a** 2-90-NS-40, **b** 4-45-NNSS-40, and **c** 6-30-NNNSSS-40 mode

the magnetic flux density in the core zone is important because the molten pool is in the core zone during ESR, and high magnetic flux density means strong magnetic force to affect the solidification process of steel.

The permanent magnetic field was further modelled in the case of same total arc degree of 90° made up of two 90-arc degree magnets (2-90-NS-40 mode), four 45-arc degree magnets (4-45-NNSS-40 mode), and six two 30-arc degree magnets (6-30-NNNSSS-40 mode). Figures 8 and 9 present the calculated coupled figures of magnetic flux density and magnetic vector as well as the change relationship of magnetic flux density with radial distance of pair magnetic pole. As magnet number increases, it can be seen from Figs. 8 and 9 that the magnetic lines passing through the core zone become less and less, the core magnetic flux density decreases from about 1350 G for 2-90-NS-40 mode to about 1000 G for 4-45-NNSS-40 mode and 6-30-NNNSSS-40 mode, but the range of intensive magnetic field along the radial direction decreases.

Effect of Magnet Arc Degree on Permanent Magnetic Field

Figure 10 shows the calculated coupled figures of magnetic flux density and magnetic vector for the mode with same magnet number of two and same magnet thickness of 40 mm but different arc degree of 30° (Fig. 10a 2-30-NS-40 mode), 45° (Fig. 10b 2-45-NS-40 mode), and 60° (Fig. 10c 2-60-NS-40 mode). It can be seen from Fig. 10a–c

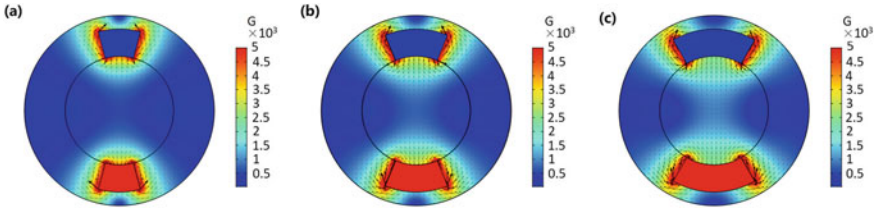

Fig. 10 Magnetic flux density and vector for **a** 2-30-NS-40, **b** 2-45-NS-40, and **c** 2-60-NS-40 mode

that more magnetic lines pass through the core zone with increasing arc degree. This is because larger arc degree of pair magnet pole can emit and receive more magnetic lines. In combination with Fig. 11, it can be found that the core magnetic flux density increases from about 500 G to about 700 G and then to about 950 G with the increase of arc degree from 30° to 45° and then to 60°. But the range of intensive magnetic field along the radial direction decreases. In combination with Figs. 6a and 8a, the magnetic flux density increases by 1150 G when the arc degree increases from 30° to 120°.

Figure 12 shows the similar change tendency of magnetic lines and magnetic flux density with modelling results of those modes shown in Fig. 10. Compared with modes presented in Fig. 10, the arc degrees are still same, but the magnet number increases from two to four. According to Fig. 13, the core magnetic flux density increases from about 700 G to about 1000 G and then to about 1350 G, but the range

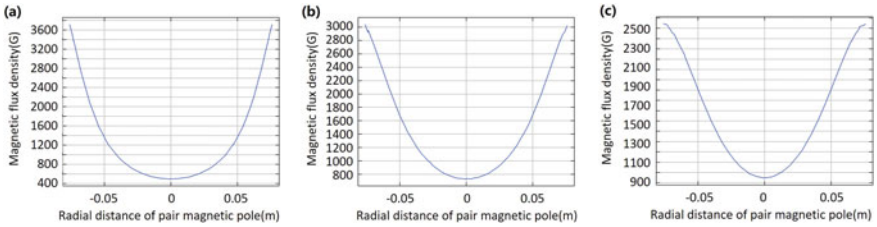

Fig. 11 Magnetic flux density along radial distance of magnetic pole for **a** 2-30-NS-40, **b** 2-45-NS-40, and **c** 2-60-NS-40 mode

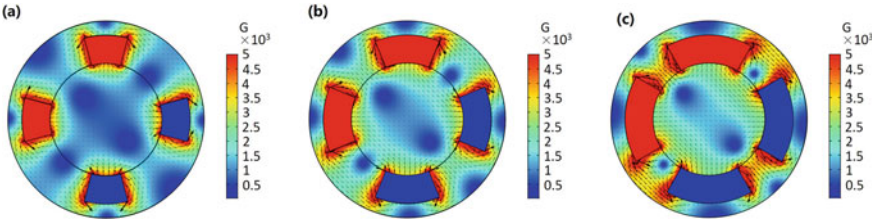

Fig. 12 Magnetic flux density and vector for **a** 4-30-NNSS-40, **b** 4-45-NNSS-40, and **c** 4-60-NNSS-40 mode

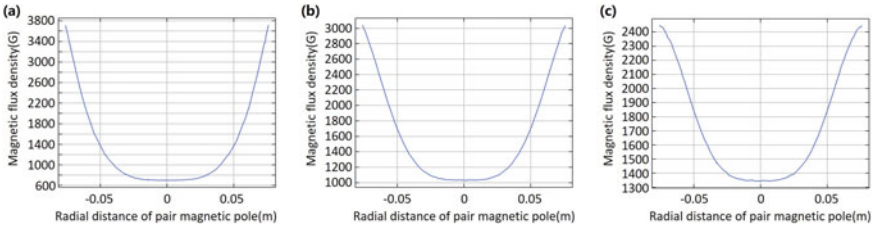

Fig. 13 Magnetic flux density along radial distance of magnetic pole for **a** 4-30-NNSS-40, **b** 4-45-NNSS-40, and **c** 4-60-NNSS-40 mode

of intensive magnetic field along the radial direction decreases with increasing arc degree.

For ESR of large-size ingots, the high core magnetic flux density is necessary to generate large magnetic force to control the solidification process during ESR. According to the above modelling results, it can be found that the core has higher magnetic flux density in the case of same polarization direction of adjacent magnets. The core magnetic flux density increases with the increase of magnet thickness, arc degree, and less magnet number in the case of same total arc degree.

Concluding Summary

Same polarization direction of adjacent magnets is beneficial for increase of magnetic flux density. The core magnetic flux density is stronger for thicker magnet when the magnet arrangement and number are same. The core magnetic flux density becomes stronger with increasing total magnet arc degree in the case of same magnet arrangement and number. The core magnetic flux density also becomes stronger when the magnet number is less, but the total arc degree is same. Among these modes, the mode of 2-120-NS-40 has largest core magnetic flux density of about 1650 G, the modes of 2-90-NS-40 and 4-60-NNSS-40 have similar core magnetic flux density of about 1350 G, but the 4-60-NNSS-40 mode has wider range of intensive magnetic field along the radial direction. The corresponding arrangement mode of magnet can be chosen according to the ingot size, demand for magnetic flux density, and magnet saving.

Acknowledgements The authors express their gratitude to the financial support from National Natural Science Foundation of China (Grant No. 51904022) and help from Dr. Xiaobin Zhou from Anhui University of Technology.

References

1. Suh SH, Choi J (1986) Effect of melting rate on the carbide cell size in an electroslag remelting high speed steel ingot. Trans ISIJ 26(4):305–309
2. Chumanov VI (2011) Control of the carbide structure of tool steel during electroslag remelting: part I. Rus Metal (Metally) 6:515–521
3. Chang LZ, Shi XF, Cong JQ et al (2014) Effects of relative motion between consumable electrodes and mould on solidification structure of electroslag ingots during electroslag remelting process. Ironmak Steelmak 41(8):611–617
4. Boccalini M, Corrêa A, Goldenstein H (1999) Rare earth metal induced modification of γ-M_2C, γ-M_6C, and γ-MC eutectics in as cast M2 high speed steel. Mater Sci Tech 15:621–626
5. Dong YW, Jiang ZH, Xiao ZX et al (2009) Influence of ESR process parameters on solidification quality of remelting ingots. J Northeast Univ 30(11):1598–1601
6. Deng AY et al (2015) Effects of electromagnetic stirring on cast structure of high-carbon high-speed steel. Paper presented at the 8th International Conference on Electromagnetic Processing of Materials, Cannes, France, 12–16 Oct 2015
7. Zhang TM, An YT, Song XT (2012) Influence of magnetic flux on microstructure and properties of high carbon high speed steel made by centrifugal casting. J Iron Steel Res 24(5):35–40
8. Murgas M, Chaus AS, Pokusa A (2000) Electroslag remelting of high-speed steel using a magnetic field. ISIJ Int 40(10):980–986
9. Wang Q, Yan HG, Wang F et al (2015) Impact of electromagnetic stirring on grain structure of electroslag remelting ingot. JOM 67(8):1821–1829

Numerical Simulation of the Effect of Bed Height Diameter Ratio on Gas–Solid Flow Characteristics in a Side Stirred Fluidized Bed

Chuanfu Li, Yan Liu, Ting'an Zhang, Ning Li, and Shengyu Zhang

Abstract Fluidized bed reactor has become an important branch of non-blast furnace ironmaking due to its high heat and mass transfer efficiency, simple equipment structure, and low cost. In view of the uneven distribution of gas–solid two-phase in the traditional fluidized bed fluidization process, this paper puts forward a new idea that side stirring is applied to the fluidization iron making process to inhibit the sticking. The bed height diameter ratio is a structural factor which has great influence on the hydrodynamic performance of fluidized bed. In this paper, the three-dimensional numerical simulation of gas–solid fluidized bed is carried out by using Eulerian–Eulerian two-fluid model under the same inner diameter of fluidized bed reactor to study the effect of bed height diameter ratio on two-phase flow in gas–solid fluidized bed.

Keywords Fluidization ironmaking · Side stirring · Numerical simulation · Bed height diameter ratio

Introduction

At present, blast furnace ironmaking technology has almost reached a perfect level [1]. However, problems such as resources and environment are becoming increasingly tense. The fluidized ironmaking technology can directly reduce hematite by carbon monoxide or hydrogen. The reduction kinetic conditions are better, which can not only reduce resource consumption, but also reduce environmental pollution. The research shows that using H_2 instead of CO as reducing agent in the process of iron ore reduction can effectively improve the reaction rate and further reduce CO_2 emission [2, 3]. However, in industrial production, it is prone to slugging, channeling, and sticking problem. The uneven distribution of gas–solid two phases

C. Li · Y. Liu (✉) · T. Zhang · N. Li · S. Zhang
Key Laboratory of Ecological Metallurgy of Multi-Metal Intergrown Ores of Ministry of Education, Special Metallurgy and Process Engineering Institute, Northeastern University, Shenyang 110819, China
e-mail: liuyan@smm.neu.edu.cn

Z. Peng et al. (eds.), *12th International Symposium on High-Temperature Metallurgical Processing*, The Minerals, Metals & Materials Series,
https://doi.org/10.1007/978-3-030-92388-4_3

reduces the fluidization quality and the efficiency of heat and mass transfer. Song [4] added a vertical stirring device to the fluidized bed of ultrafine iron oxide powder and concluded that the addition of stirring device can significantly improve the fluidization quality of iron oxide powder. Wang [5] numerically simulated the flow behavior of particles in a gas–solid stirred fluidized bed with frame agitator. The results show that the transverse motion of particles is enhanced by mechanical stirring. Although adding vertical stirring device in fluidized bed can improve the degree of gas–solid mixing to a certain extent, the action area of agitating vane is small and can only affect the movement of gas–solid two phases in horizontal direction, and the effect is limited. In order to further improve the effect of stirring device, a new idea of using side stirring to inhibit particle sticking in fluidized ironmaking process is proposed in this paper. The bed height diameter ratio is one of the structural factors that have a great influence on hydrodynamics. Sathiyamoorty and Horio [6] verified through experiments that the influence of height diameter ratio of fluidized bed on the uniform distribution of gas–solid two-phase cannot be ignored. Zhang et al. [7] studied the influence of bed height on pressure fluctuation in a fluidized bed filled with Geldart B particles and found that there was obvious gas–solid heterogeneity when the height diameter ratio was 6. Gokon [8] determined the appropriate particle size range and bed height diameter ratio for the design of fluidized bed reactor.

In this paper, the three-dimensional numerical simulation of the fluidization process in a side stirred fluidized bed reactor at room temperature is carried out by using the Eulerian–Eulerian two-fluid model. The effect of bed height diameter ratio on gas–solid two-phase flow characteristics in a side stirred fluidized bed was investigated. It provides data support for the next high temperature experiment of hydrogen reduction of hematite.

Simulation Calculation Models and Parameters

Mathematical Model Basic Assumptions

In this paper, the Eulerian–Eulerian two-fluid model coupled with kinetic theory of granular flow is used to simulate the side stirred fluidized bed. In order to save calculation resources, the quantities that have little impact on gas–solid two-phase flow are simplified, so the following assumptions are made:

(1) The slip action between wall and gas–solid two-phase is not considered;
(2) The lift force between gas and solid is not considered;
(3) Due to the large density difference between gas and solid, the virtual mass force is not considered;
(4) The dispersive force of turbulence is not considered.

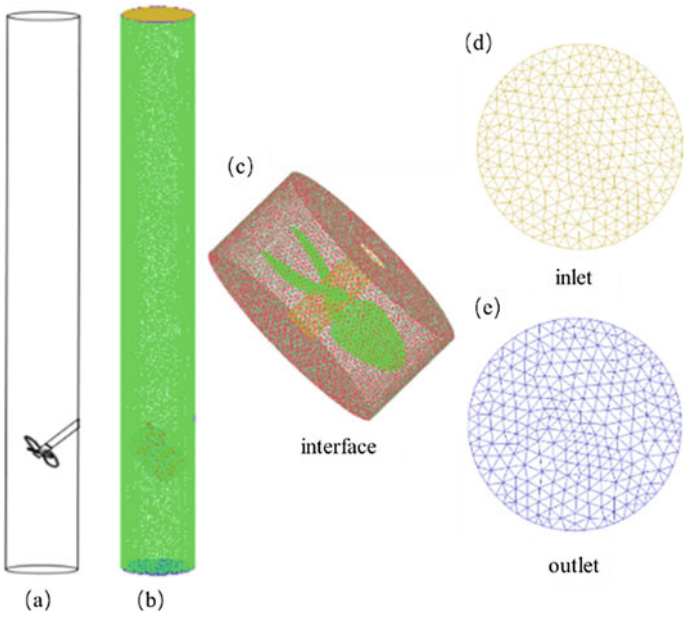

Fig. 1 Physical model and mesh. **a** Schematic diagram of the side agitated fluidized bed **b** Meshing of the fluidized bed **c** Meshing of agitator **d** Inlet **e** Outlet

Physical Model and Mesh Model

Figure 1 shows the geometric model and mesh model of the side stirred fluidized bed. The inner wall diameter D of the fluidized bed is 0.1 m, the agitating vane diameter is 0.07 m, and the agitator shaft is inserted into the fluidized bed at 45°. The distance between the center of the agitating vane and the bottom of the fluidized bed is 0.2 m.

Boundary Conditions and Related Simulation Parameters

Table 1 shows the physical parameters, operating parameters, and boundary conditions of simulation calculation of solid particle fluidization process in a side stirred fluidized bed under different bed height diameter ratio.

RNG k-ε is selected as turbulence model. The wall of fluidized bed and the wall of agitator adopt non-slip boundary for gas–solid two-phase flow. The operating pressure is set to 101.325 kPa. The momentum transfer between gas and solid phases mainly depends on the drag force [9]. Aiming at the decrease of drag force caused by particle agglomeration in a specific particle concentration range, based on the characteristic analysis of the traditional drag force model in different particle concentration ranges, the drag force model suitable for different particle concentration ranges is

Table 1 Physical parameters and operation parameters

Calculating parameters	Parametric values
Particle density, ρ_s (kg/m^3)	2840.200
Gas density, ρ_g (kg/m^3)	1.225
Average particle diameter, d_s (μm)	500
Apparent gas velocity, u_g (m/s)	0.500
Stirring speed, N (rpm)	160
Initial static bed height, H_0 (mm)	200, 300, 400, 500
Inlet type	Velocity-inlet
Outlet type	Pressure-outlet
Time step, Δt (s)	0.001
Particle collision coefficient, e_{ss}	0.900

selected, and the modified drag force model is obtained through the smooth function connection [10]. The modified drag model is imported into FLUENT software by user-defined (UDF) program.

Simulation Results and Analysis

Effect of Bed Height Diameter Ratio on Bed Pressure Drop

The variation of bed pressure drop with time in side stirred fluidized bed under different bed height diameter ratio is shown in Fig. 2. The figure reflects the fluctuation of bed pressure in side stirred fluidized bed. The change of gas volume fraction caused by the interaction between gas and solid particles and the bed vibration caused

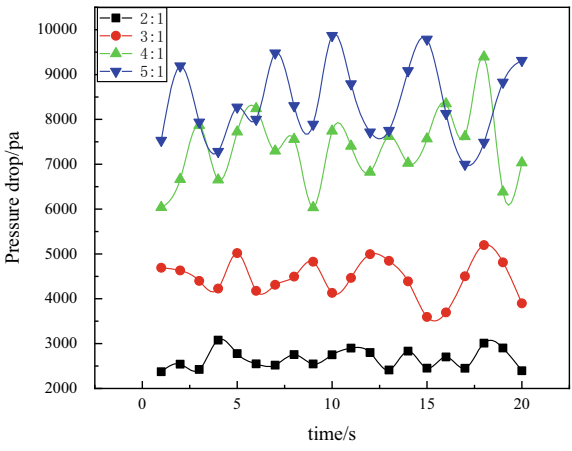

Fig. 2 Variation of bed pressure drop with time in side stirred fluidized bed with different height diameter ratio

Table 2 Variation of average deviation of bed pressure drop with height diameter ratio

Bed height diameter ratio	Average deviation of bed pressure drop (%)
2:1	7.24
3:1	7.53
4:1	8.46
5:1	8.69

by the collision between solid particles and side agitator, solid particles, and wall can lead to the fluctuation of bed pressure in the bed. It can be seen from the figure that with the increase of the bed height diameter ratioC, the pressure drop in the bed gradually increases, and the stronger the pressure fluctuation in the fluidized bed. When the bed height diameter ratio is 2:1 and 3:1, the bed pressure fluctuation is small, while when the bed height diameter ratio is 4:1 and 5:1, the bed pressure fluctuation is more intense. This is due to the increase of the bed height diameter ratio and the mass of the added solid particles, resulting in the gradual increase of the average pressure drop of the fluidized bed. Through calculation, the average deviation of bed pressure drop under the condition that the height diameter ratio of fluidized bed is 2:1, 3:1, 4:1, and 5:1 is shown in Table 2. It can be seen that the average deviation of bed pressure drop increases with the increase of bed height diameter ratio. When the height diameter ratio of fluidized bed is 2:1 and 3:1, the fluctuation of bed pressure drop in side stirred fluidized bed is smaller, and the operation is more stable.

Characteristics of Gas Radial Velocity Distribution

Figure 3 shows the gas velocity distribution along the radial direction of the fluidized bed at 10 s with axial heights of 0.1, 0.2, 0.3, 0.4, and 0.5 m, respectively. According to the cloud diagram of solid particle volume fraction distribution at different bed height diameter ratios in Fig. 6, when the axial height is 0.1 m, the fluidization state of fluidized beds with different bed height diameter ratio is similar, and the distribution of gas and solid is relatively uniform. Since the agitating vane is located at axial height of 0.2 m, the gas velocity distribution is complex, generally showing a higher central velocity and a lower velocity on both sides. During the mixing process, the momentum of the gas increases. When the axial height is 0.3 m and the bed height diameter ratio is 2:1, the gas velocity is small, and when the ratio is 3:1, the gas velocity is large due to the formation of bubbles on the left and right sides. When the axial height is 0.4 and 0.5 m and the bed height diameter ratio is 5:1, the maximum gas velocity reaches 3.66 m/s due to the formation of bubbles on the right side.

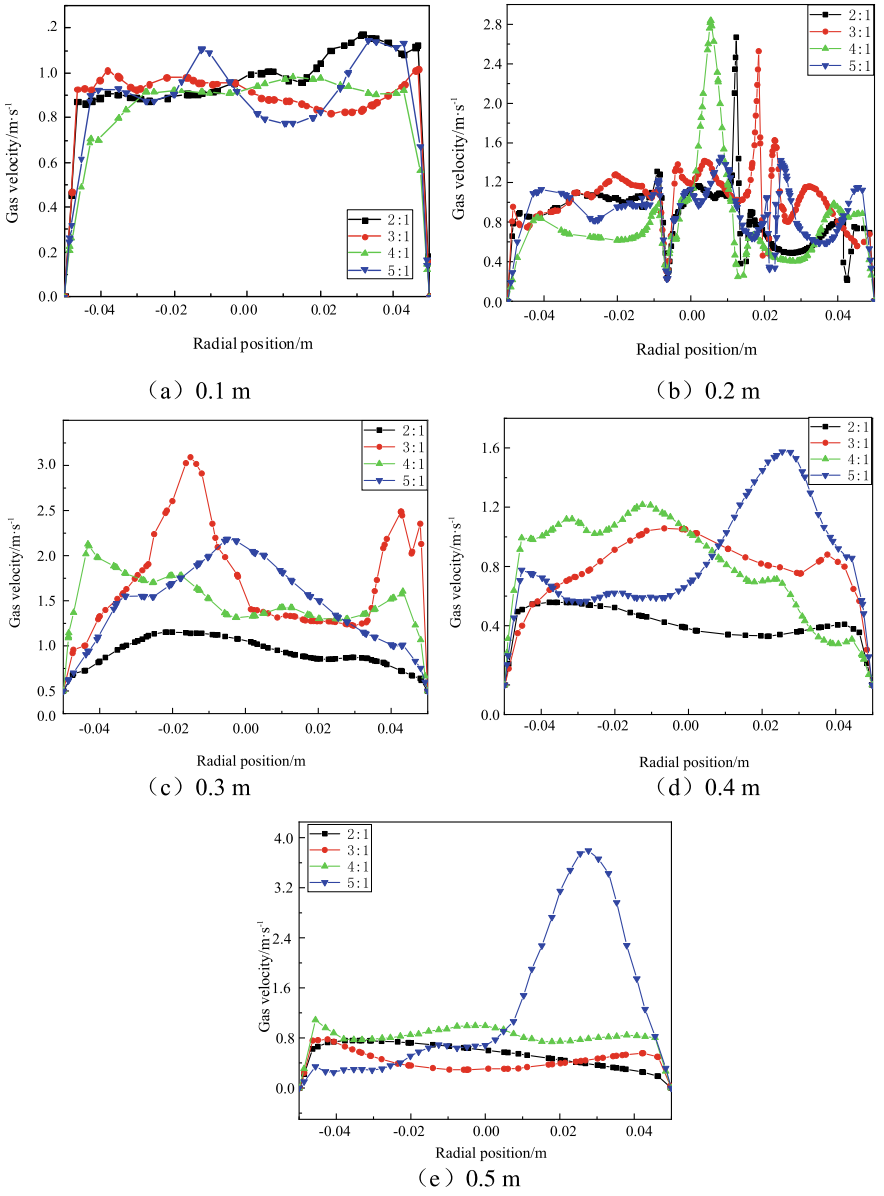

Fig. 3 Gas velocity distribution at different axial height under different bed height diameter ratio

Characteristics of Particle Axial Velocity Distribution

Figure 4 is the cloud diagram of solid particle velocity vector distribution under different bed height diameter ratio at 10 s. It can be seen from the figure that under the four bed height diameter ratios, the momentum of bubbles increases due to the action of the agitating vane, which drives the movement of solid particles. Therefore, the velocity of solid particles above the agitating vane is large. Vortices are generated in the lower part of the fluidized bed and the upper part of the agitator when the height diameter ratio of the bed is 4:1 and 5:1. When the bed height diameter ratio is 5:1, two vortices are formed on both sides above the impeller due to the formation, growth, and floating of bubbles above the impeller.

Figure 5 shows the particles axial velocity distribution along the radial direction of the fluidized bed at 10 s with axial heights of 0.1, 0.2, 0.3, 0.4, and 0.5 m, respectively. When the axial height is 0.4 m and the bed height diameter ratio is 2:1, the particle volume fraction is 0 because the position is above the bed layer. Similarly, when the axial height is 0.5 m and the height diameter ratio is 2:1 and 3:1, the particle volume fraction is 0. At the axial height of 0.1, 0.2, and 0.3 m, the fluidized bed particles with different bed height diameter ratio show similar axial velocity distribution. When the axial height is 0.4 and 0.5 m and the bed height diameter ratio is 5:1, vortices are generated in the fluidized bed. According to Sect. 3.2, the gas velocity on the right side of the fluidized bed is large, so it drives the solid particles to move upward and has a large axial velocity. In the gas vortex, the axial velocities of solid particles are positive on the right and negative on the left. The gas drives the particles to move counterclockwise. It can also be seen from the figure that among the absolute values of solid particle velocity, the particle velocity in the center is larger, and the particle velocity near the side wall of the fluidized bed is smaller. This is because the resistance increases and the particle velocity near the wall is relatively small due to the influence of boundary viscous force and particle adhesion.

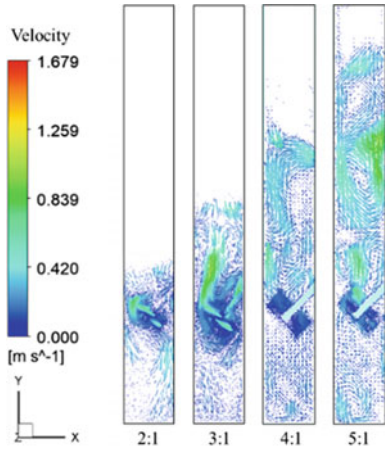

Fig. 4 Velocity vector distribution of particles under different bed height diameter ratio

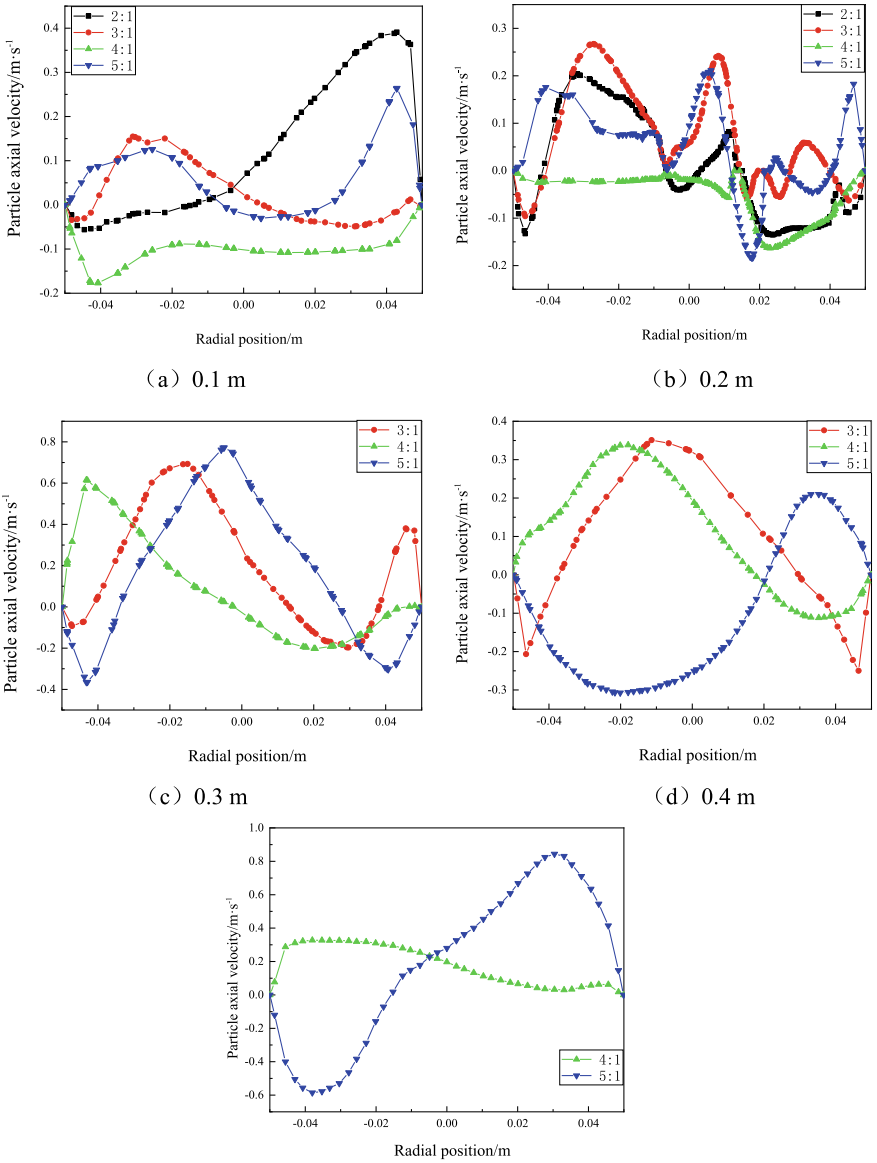

Fig. 5 Particles axial velocity distribution along the radial direction of the fluidized bed under different bed height diameter ratio

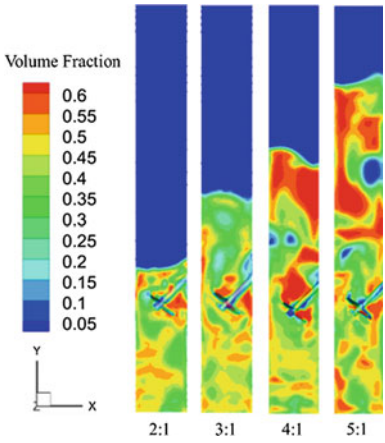

Fig. 6 Distribution of particle volume fraction under different bed height diameter ratio

Distribution Characteristics of Solid Particle Volume Fraction

The cloud diagram of solid particle volume fraction can more intuitively see whether the gas–solid mixing is uniform, the accumulation of particles, and the existence of bubbles. Figure 6 shows the distribution of solid particles radial volume fraction on the section with axial height of 0.1, 0.2, 0.3, 0.4, and 0.5 m under different bed height diameter ratio at 10 s. It can be seen from the figure that under the conditions of different bed height diameter ratio, the lower part of the fluidized bed has better fluidization effect than the upper part. With the increase of height diameter ratio, the accumulation of particles in the upper part of the fluidized bed becomes more serious. Small bubbles are formed above the agitating vane. With the increase of the bed height diameter ratio, the bubbles in the upper part of the bed continue to grow and have a large size because they exceed the action range of the agitating vane.

Figure 7 shows the radial volume fraction distribution of solid particles at different bed height diameter ratios at 10 s with axial heights of 0.1, 0.2, 0.3, 0.4, and 0.5 m, respectively. In order to further analyze the distribution of solid particles in fluidized bed, the radial volume fraction distribution of solid particles at different axial heights was compared. The bed height diameter ratio condition with solid particle volume fraction of 0 is not shown in the figure. When the bed height diameter ratio is 3:1 and 4:1, the fluidization state is relatively stable when the axial height is 0.1 m. At the axial height of 0.2 m, the gas volume fraction in the fluidized bed changes sharply due to the action of the agitating vane. When the axial height is 0.4 m and the bed height diameter ratio is 4:1, the volume fraction of solid particles in the middle of the fluidized bed is evenly distributed, with an average value of about 0.414, and the volume fraction of solid particles near the side walls on both sides of the fluidized bed is large, When the axial height is 0.5 m and the bed height diameter ratio is 5:1, the volume fraction of solid particles on the right side of the fluidized bed is low and that on the left side is high due to the floating of bubbles on the right side and the falling of solids on the left side. The main reason for the non-uniformity of radial

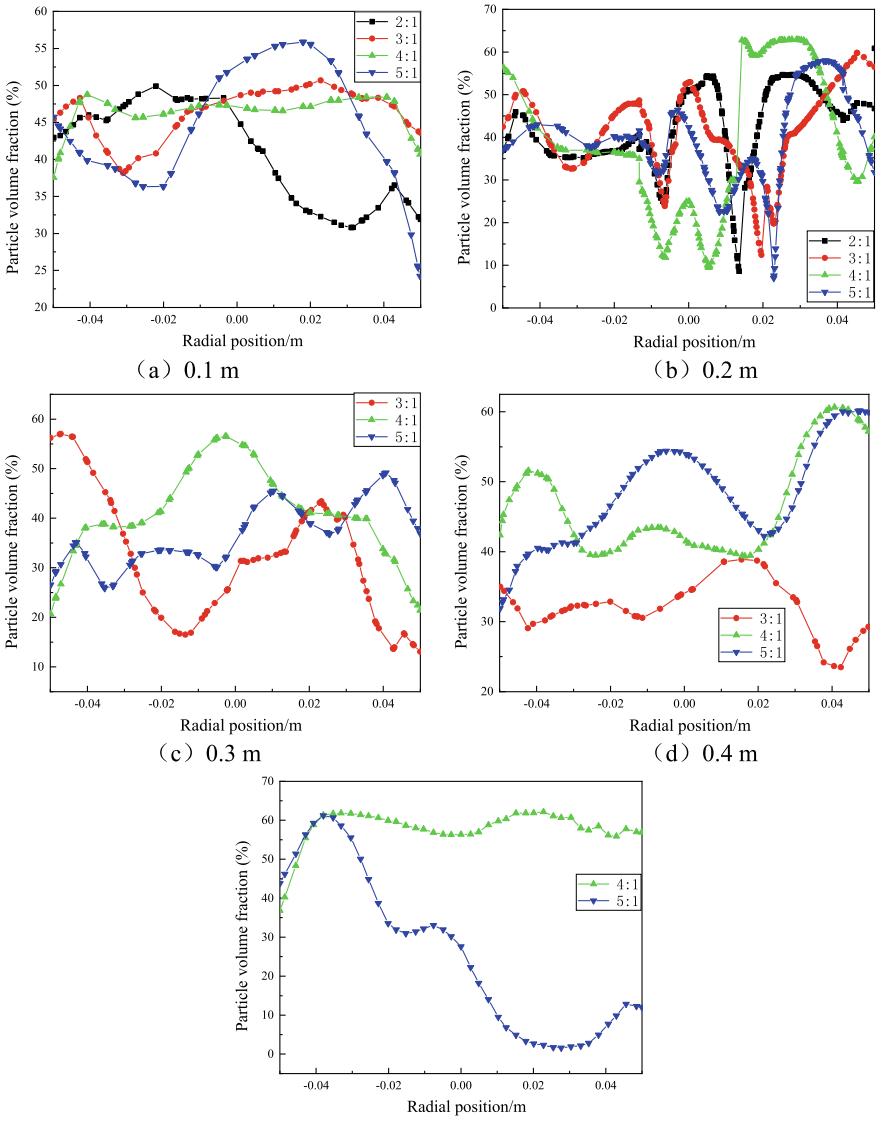

Fig. 7 Volume fraction distribution of particle at different axial heights under different bed height diameter ratios

solid particle volume fraction distribution is the accumulation of particles in the fluidized bed, which makes the gas volume fraction at the local position significantly lower and causes the radial solid particle volume fraction distribution to fluctuate greatly. In addition, due to the different bed height diameter ratio, the resistance of gas passing through the solid particle bed is different, which makes the difference of gas–solid two-phase mixing in the fluidized bed.

Conclusions

In this paper, the effect of bed height diameter ratio on gas–solid two-phase fluidization characteristics in side stirred fluidized bed was studied by numerical simulation. The results show that when the bed height diameter ratio is 2:1 and 3:1, the fluctuation of bed pressure drop in side stirred fluidized bed is small, and the operation is stable.

The radial distribution of gas–solid two-phase velocity and volume fraction distribution on different sections in the side stirred fluidized bed were obtained. Due to the different bed height diameter ratio, the resistance of gas passing through the solid particle bed is different, which makes the mixing of gas–solid two phases in the fluidized bed different. In order to make the distribution of gas–solid two-phase in the fluidized bed more uniform, no large bubbles are formed in the bed and give full play to the role of the agitating vane, and therefore, the fluidized bed with a bed height diameter ratio of 3:1 has better fluidization effect and smaller particle accumulation area.

References

1. Zhang H (2019) Current situation of non blast furnace ironmaking in the world. Shanxi Metall 42(01):71–73
2. Spreitzer D, Schenk J (2019) Reduction of iron oxides with hydrogen—a review. Steel Res Int 90(10)
3. Long H (2017) Research of reduction reaction and movement behavior of gas-solid in the hydrogen shaft furnace. Yanshan University
4. Song Y, Zhu Q (2011) Experimental study on fluidization and reduction of ultrafine iron oxide powder in stirred fluidized bed. Chin J Process Eng 3:5–11
5. Wang S, Chen Y, Jia Y et al (2018) Numerical simulation of flow behavior of particles in a gas-solid stirred fluidized bed. Powder Technol 338:S0032591018305187.
6. Sathiyamoorthy D, Horio M (2003) On the influence of aspect ratio and distributor in gas fluidized beds. Chem Eng J 93(2):151–161
7. Zhang CX, Qian WZ, Wei F (2015) Direct Lyapunov method to analysis mal-distribution of gas solids flow through parallines. In: The 8th Sino-US joint conference of chemical engineering, Shanghai, China
8. Gokon N, Tanabe T, Shimizu T et al (2016) Cold test with a benchtop set-up for fluidized bed reactor using quartz sand to simulate gasification of coal cokes by concentrated solar

radiation. In: Solarpaces: international conference on concentrating solar power & chemical energy systems. AIP Publishing LLC
9. Li L, Bo Z, Lu L (2018) Influence of drag model on the numerical simulation of fluidized two-phase flow. Energy Conserv Technol 36(05):54–57
10. Zheng X, Pu W, Yue C et al (2015) Simulation of fluidization characteristics of 2D bubbling fluidized bed by improved drag model. Chin J Process Eng 15(05):737–743

First-Principles Calculations of Adsorption Reactions of C and Cl_2 on TiO_2 (001) Surface with Bridge-Oxygen Defect in Fluidized Chlorination

Fan Yang, Liangying Wen, Qin Peng, Yan Zhao, Meilong Hu, Shengfu Zhang, and Zhongqing Yang

Abstract Based on the first-principles calculations of the density functional theory, the reaction mechanism of carbochlorination of TiO_2 with bridge-oxygen defect was studied. The results show that the presence of C promotes the carbochlorination reactions. When C and Cl_2 co-adsorbed on the bridge-oxygen defect of TiO_2 (001) surface, Cl_2 molecules dissociate, and all C atoms bond to Ti or O atoms on the surface. In the adsorption reactions, O2c atoms are the electron acceptors, and Ti5c(r) atoms are the electron providers. The adsorption energy of the structure that CO formed by C and O2c, and two Cl atoms bonded with Ti5c on both sides is low, and the adsorption energy of this structure is −11.78 eV.

Keywords Defects · Adsorption · Fluidized chlorination · Surface

Introduction

Titanium dioxide is widely used in coating, papermaking, and printing. $TiCl_4$ is an important raw material for the production of the titanium dioxide by chlorination. At present, the carbochlorination process is widely used to prepare $TiCl_4$ by mixing titanium containing materials and petroleum coke and sending them to a fluidized chlorination furnace at high temperature for reaction. There are obvious interactions among C, Cl_2, and TiO_2 particles in the chlorination process. The Ti–O bond on the surface of TiO_2 will break, and bridge-oxygen defects will inevitably appear on

F. Yang · L. Wen (✉) · Q. Peng · Y. Zhao · M. Hu · S. Zhang
School of Materials Science and Engineering, Chongqing University, Chongqing 400044, People's Republic of China
e-mail: cquwen@cqu.edu.cn

Chongqing Key Laboratory of Vanadium-Titanium Metallurgy and Advanced Materials, Chongqing University, Chongqing 400044, People's Republic of China

Z. Yang
School of Power Engineering, Chongqing University, Chongqing 400044, People's Republic of China

Z. Peng et al. (eds.), *12th International Symposium on High-Temperature Metallurgical Processing*, The Minerals, Metals & Materials Series,
https://doi.org/10.1007/978-3-030-92388-4_4

the surface. The appearance of these defective surfaces has a certain impact on the chlorination process. Therefore, it is of great significance to explore the adsorption behavior and mechanism of C and Cl_2 on the defect surface of TiO_2 to regulate and control the chlorination reaction process and efficiently prepare $TiCl_4$.

The first-principles calculations of the density functional theory (DFT) are used to explore the interactions among the materials at the microscopic level. In recent years, many scholars have studied the adsorption behaviors of the molecules or atoms on the surface of metal compounds by DFT. Guo et al. [1] studied the adsorption behavior of H_2O_2 on CuO (111) and Ag/CuO (111) surfaces. It was found that the small molecules dissociated from H_2O_2 had the highest adsorption stability on CuO (111) and Ag/CuO (111) surfaces. The adsorption energy of H, O, OH, and OOH on Ag/CuO (111) surface was higher than that on CuO (111) surface. Zhong et al. [2] studied the adsorption behavior of CO on FeO surface. It was found that CO was more inclined to form C–Fe bond with Fe atoms on FeO (100) and (110) surfaces. Yang et al. [3, 4] studied the adsorption behaviors of C and Cl_2 on TiO_2 surfaces. It was found that the presence of C could promote the adsorption of Cl_2 on the surface of TiO_2, and C atom was more conducive to the adsorption of Cl_2 on the surface of TiO_2 (100) than CO molecule. With the increase of the proportion of C atoms in the reaction process, the possibility of Cl atoms being completely adsorbed on TiO_2 (110) surface has increased. Rutile TiO_2 contains three low index surfaces, which are (110), (100), and (001) surfaces, respectively. Among them, TiO_2 (001) has higher surface activity and possibility of oxygen defects. At present, the adsorption process of TiO_2 (001) surface with bridge-oxygen defect is rarely reported. Therefore, it is of great significance to explore the adsorption behavior and mechanism of C and Cl_2 on TiO_2 (001) surface with bridge-oxygen defect to enrich and perfect the fluidized chlorination theory.

In this work, based on the first-principles calculations, we have investigated the separate adsorption and co-adsorption behaviors of C and Cl_2 on TiO_2 (001) surface with bridge-oxygen defect. By analyzing the adsorption energy, Mulliken charge and density of states, the adsorption mechanism of C and Cl_2 on TiO_2 (001) surface with bridge-oxygen defect has been studied, and it provides a deeper theoretical basis for the further study of the chlorination reaction behavior.

Calculation Method and Models

The separate adsorption and co-adsorption processes of C and Cl_2 on TiO_2 (001) surface with bridge-oxygen defect were calculated by Castep module in Material Studio software. The ultra-soft pseudopotential of plane wave was used to describe the electron interactions in the calculation processes. The exchange correlation functional used the GGA-PBE [5, 6]. The model of TiO_2 (001) surface with bridge-oxygen defect was 2×2 supercell, which composed of seven layers of atoms. The bottom four atomic layers were fixed, and the other three atomic layers were relaxed. K point and energy cutoff were set to $3 \times 3 \times 1$ and 400 eV, respectively. The thickness of

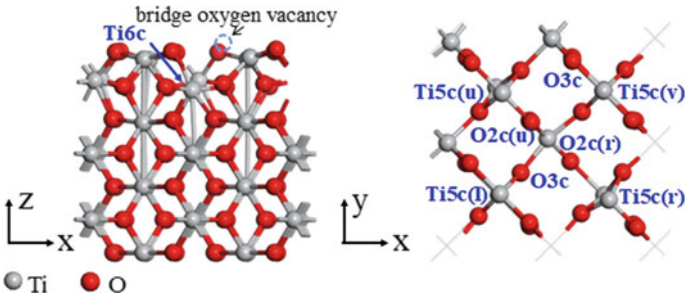

Fig. 1 Optimized TiO_2 (001) surface with bridge-oxygen defect. The left is the front view, and the right is the top view

the vacuum layer was set to 15 Å. Figure 1 shows the optimized structure of TiO_2 (001) surface with bridge-oxygen defect. In the calculation, the adsorption energy E_{ads} of X ($X = Cl_2$, $C + Cl_2$) is defined as follows.

$$E_{ads} = E_{TiO_{2+X}} - (E_{TiO_2} + E_X) \tag{1}$$

where $E_{TiO_{2+X}}$ represents the surface energy of X ($X = Cl_2$, $C + Cl_2$) adsorbed on TiO_2 surface with bridge-oxygen defect, and E_{TiO_2} represents the energy of TiO_2 surface with bridge-oxygen defect, and E_X represents the energy of X ($X = Cl_2$, $C + Cl_2$).

Results and Discussion

Adsorption Structures

Figure 2 shows the structures of Cl_2 adsorbed on TiO_2 (001) defect surface. The chemical bonds of Cl_2 molecules in both structures are broken, and the distances between the dissociated Cl atoms extend to 3.35 Å and 3.62 Å, respectively. A dissociated Cl atom bonds with the surface Ti5c(r) in structure a, and the bond length is 2.22 Å. The two dissociated Cl atoms bond with Ti5c on both sides in structure b, and bond lengths of them are 2.25 Å and 2.22 Å, respectively. The adsorption energies of the structures a and b are −3.20 eV and −5.71 eV, respectively. Among them, the adsorption energy of the structure b is lower, indicating that the stability of the structure with both Cl atoms bonded to the surface is higher. By analyzing the Mulliken charge of these two adsorption structures, Ti5c(r) is electron provider, and Cl_2 is electron acceptor.

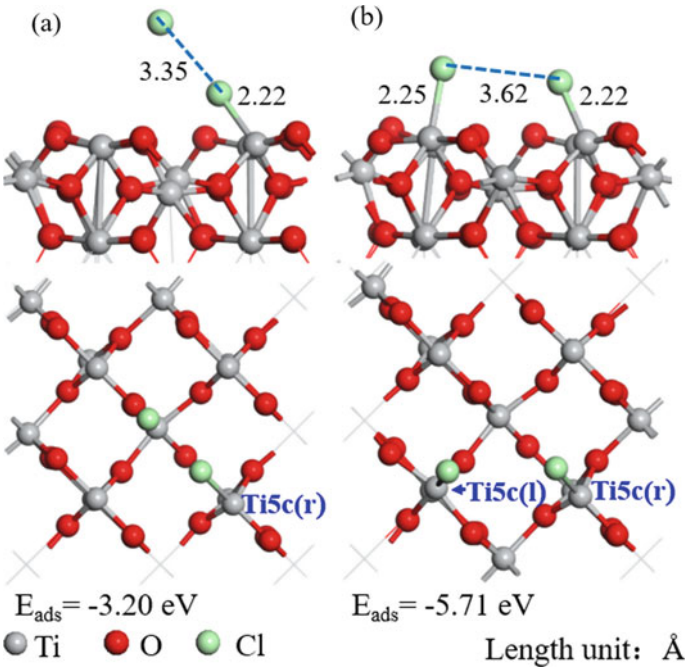

Fig. 2 Adsorption structures of Cl_2 on TiO_2 (001) surface with bridge-oxygen defect

Figure 3 shows the adsorption structures of C and Cl_2 on TiO_2 (001) surface with bridge-oxygen defect. O2c(s) moves upward from the surface under the action of C and Cl_2 in structure a. The dissociated Cl atoms bond with Ti5c(r) and C, and the bond lengths are 2.25 Å and 1.83 Å, respectively. The dissociated Cl atoms in structure f bond with Ti5c on both sides, and the bond lengths of them are 2.33 Å and 2.23 Å, respectively. In structure g, C and Ti5c(r) form Ti5c(r)–C bond with the bond length of 2.03 Å. After dissociation, both Cl atoms bond with C atoms, and the chemical bond lengths are 1.75 Å and 1.80 Å, respectively. The bond length of Ti5c(r)–C in the structure i is 2.14 Å. The dissociated Cl atoms bond with Ti5c(l) and C, and the bond lengths are 2.27 Å and 1.67 Å, respectively.

The adsorption energies of these structures in Fig. 3 are −9.29 eV, −8.45 eV, −8.84 eV, −11.48 eV, −7.68 eV, −11.78 eV, −9.91 eV, −11.57 eV, and −9.02 eV, respectively. Among them, the adsorption energy of structure f is low, indicating that the adsorption structure of CO formed by C and O2c, and two Cl atoms bond with Ti5c on both sides is stable. Compared with the structures b, c, and e, the structures a, d, f, g, h, and i have lower adsorption energies and higher stabilities, indicating that the bond of the dissociated Cl atom with Ti or C atoms on the surface can improve the stability of the adsorption structures. Compared with the adsorption energies of −3.20 eV and −5.71 for Cl_2 adsorbed on TiO_2 (001) surface,

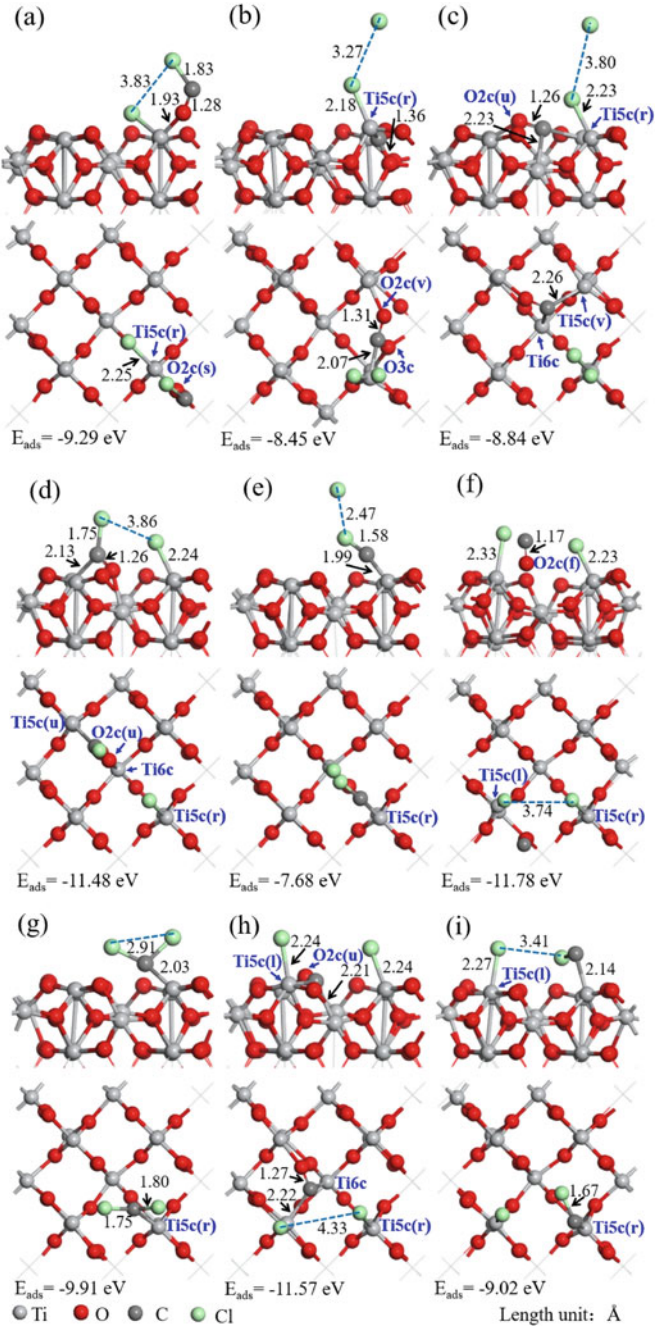

Fig. 3 Adsorption structures of C and Cl_2 on TiO_2 (001) surface with bridge-oxygen defect

Table 1 Mulliken charge analysis of C and Cl_2 adsorbed on TiO_2 (001) defect surface

No.	C		O2c		Ti5c(r)		Cl_2	
	q(e)	Δq(e)	q(e)	Δq(e)	q(e)	Δq(e)	q(e)	Δq(e)
a	3.90	0.10	6.55	−0.55	10.80	1.20	14.38	−0.38
b	3.92	0.08	6.57	−0.57	10.87	1.13	14.70	−0.70
c	4.10	−0.10	6.49	−0.49	10.82	1.18	14.73	−0.73
d	4.09	−0.09	6.49	−0.49	10.85	1.15	14.36	−0.36
e	4.56	−0.56	/	/	10.77	1.23	14.03	−0.03
f	3.59	0.41	6.45	−0.45	10.83	1.17	14.70	−0.70
g	4.57	−0.57	/	/	10.76	1.24	13.98	0.02
h	4.08	−0.08	6.51	−0.51	10.81	1.19	14.67	−0.67
i	4.40	−0.40	/	/	10.69	1.31	14.17	−0.17

q(e) is the total amount of the electrons. Δq(e) represents gain or loss electrons. Negative value represents gain electrons, and positive value represents loss electrons. O2c in structures a, b, c, d, f, and h are O2c(s), O2c(v), O2c(u), O2c(u), O2c(f), and O2c(u)

the addition of C can promote the occurrence of the adsorption reaction of Cl_2 on TiO_2 (001) defect surface.

Charge Analysis

Table 1 shows the Mulliken charge analysis of C and Cl_2 adsorbed on TiO_2 (001) surface with bridge-oxygen defect, where a, b, c, d, e, f, g, h, and i correspond to the structures a, b, c, d, e, f, g, h, and i in Fig. 3, respectively. O2c is electron acceptor, while Ti5c(r) is electron provider in these structures. In structures a, b, and f, C atoms are the electron providers. C atoms are the electron acceptors in structures c, d, e, g, h, and i. Cl_2 in the structures a, b, c, d, e, f, h, and i are electron acceptors. The amounts of the electrons obtained by Cl_2 are 0.38e, 0.70e, 0.73e, 0.36e, 0.03e, 0.70e, 0.67e, and 0.17e, respectively. Among the above structures, after the dissociation of Cl_2 molecules in the structures e and g, Cl atoms bond with C or enter the vacuum layer, and there is no Ti–Cl bond in the structures. The amounts of electrons obtained or lost by Cl_2 in both structures are less, indicating that it is difficult for Cl_2 to obtain more electrons when there are no Ti–Cl bonds in the adsorption structures.

Density of State

Figure 4 shows the partial density of states of C and Cl_2 adsorbed on TiO_2 (001) surface with bridge-oxygen defect. Resonance peaks may exist between C and O2c, Ti5c and Cl, and C and Cl in the different adsorption structures. The Cl atoms in

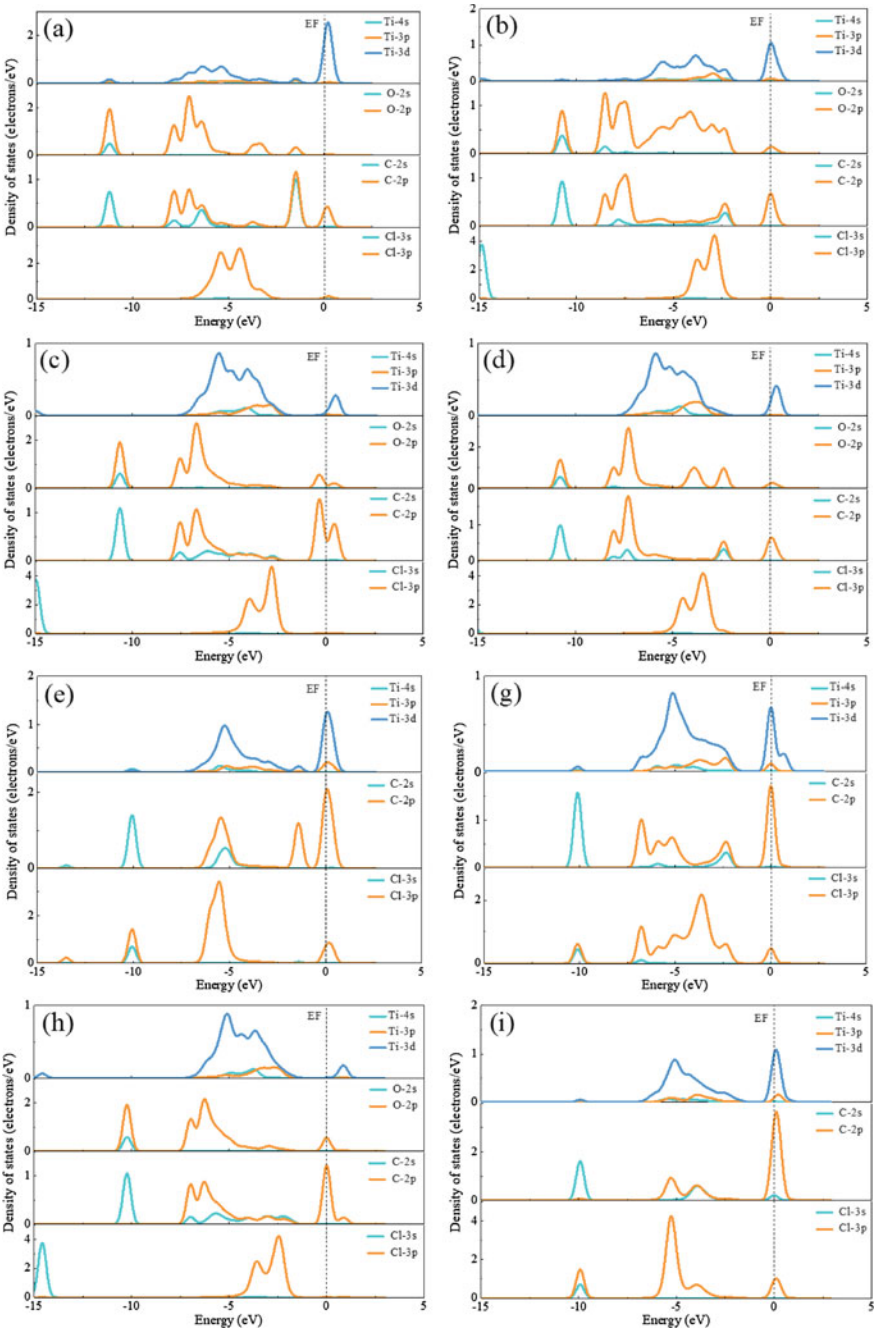

Fig. 4 Partial density of states of C and Cl_2 adsorbed on TiO_2 (001) defect surface. The structures **a**, **b**, **c**, **d**, **e**, **g**, and **h** are corresponding to the structures **a**, **b**, **c**, **d**, **e**, **g**, **h**, and **i** in Fig. 3, respectively. Where Ti atoms all refer to Ti5c(r), O atoms in the structures a and b refer to O2c(s) and O2c(v), and O atoms in the structures **c**, **d**, and **h** refer to O2c(u), respectively

the structures a, b, c, d, and h are all bonded with Ti5c(r), and the Cl atoms in the structures e, g, and i are the right Cl atoms bonded with C atom. Compared with the structures a, b, c, d, and h, the density of states peaks of Ti5c(r) in the structures e, g, and i near −5.00 eV on the left side of Fermi level is sharp, indicating that the electron localizations around Ti5c(r) in the adsorption structures without C–O bond are strong and the electron activities are low. In the structures e and i, C atoms only bond with two other atoms, which are Ti5c(r) and one of the dissociated Cl atoms, respectively. In the density of states diagrams of the two structures, the density of states peak of Cl atom on the left side of Fermi level is sharp near −5.30 eV, indicating that the electron delocalization around Cl atom is weak.

Conclusions

Based on the first-principles calculations, the separate adsorption and co-adsorption models of C and Cl_2 on the rutile TiO_2 (001) surface with the bridge-oxygen defects are established, and their adsorption behaviors are studied. Cl_2 molecules dissociate when they adsorbed alone on TiO_2 (001) defect surface. In the adsorption reactions, Ti5c(r) is the electron providers, and Cl_2 atoms are the electron acceptors. When C and Cl_2 co-adsorbed on TiO_2 (001) surface, Cl_2 molecules are dissociated, and C bonds with the surface atoms. The presence of C promotes the chlorination reaction. In the adsorption reaction, O2c is the electron acceptor, and Ti5c(r) is the electron provider. There are resonance peaks between C and O2c or between Ti5c and Cl atoms. In the adsorption structures without C–O bond, the electron localizations around Ti5c(r) are strong, and the electron activities are low.

Acknowledgements The work is supported by the National Natural Science Foundation Project of China (51674052, 51974046) and by graduate scientific research and innovation foundation of Chongqing, China (Grant No. CYS20003).

References

1. Guo YX, Hu RM, Zhou XL, Yu J, Wang LH (2019) A first principle study on the adsorption of H_2O_2 on CuO(111) and Ag/CuO(111) surface. Appl Surf Sci 479:989–996
2. Zhong H, Wen LY, Li JL, Xu J, Hu ML, Yang ZQ (2016) The adsorption behaviors of CO and H_2 on FeO surface: a density functional theory study. Powder Technol 303:100–108
3. Yang F, Wen LY, Peng Q, Zhao Y, Xu J, Hu ML, Zhang SF, Yang ZQ (2021) Prediction of structural and electronic properties of Cl_2 adsorbed on TiO_2 (100) surface with C or CO in fluidized chlorination process: a first-principles study. J Cent South Univ 28(1):29–38
4. Yang F, Wen LY, Peng Q, Zhao Y, Zhang SF, Yang ZQ (2020) Prediction of structural and electronic properties of C and Cl_2 adsorbed on the rutile TiO_2 (110) surface. ACS Omega 5(45):29002–29008

5. He P, Zhu JY, Chen YZ, Chen F, Zhu JL, Liu MF, Zhang K, Gan M (2021) Pyrite-activated persulfate for simultaneous 2,4-DCP oxidation and Cr(VI) reduction. Chem Eng J 406:126758
6. Yang C, Zhao ZY, Wei HT, Deng XY, Liu QJ (2021) DFT calculations for single-atom confinement effects of noble metals on monolayer g-C_3N_4 for photocatalytic applications. RSC Adv 11(7):4276–4285

Research on Cost System of Total Scrap EAF Steel-Making Process

Bo Li, Ling-zhi Yang, Yu-feng Guo, Shuai Wang, and Hang Hu

Abstract EAF steel-making process is a discrete and complex process with complex equipment and wide professional coverage, resulting in many data sources and poor authenticity, accuracy, and real-time performance. In the process of product production, the enterprise's operating capital flow is not clear, and the cost accounting is rough, which seriously affected the cost management of the steel mill. This paper is based on multivariate data acquisition and feature preprocessing. Using Visual Studio 2013 development tools and Microsoft SQL Server 2012 database technology, the cost data collection module, cost real-time monitoring and calculation module, process cost module, cost composition and trend analysis module, and historical cost inquiry module were developed, and the full cost analysis model was built to realize the dynamic analysis and optimization of costs in steel-making and production.

Keywords EAF steel-making · Total scrap · Cost analysis · Model

Introduction

As one of the two main steel-making methods, the electric arc furnace (EAF) steel-making has the advantages of short process, less investment, fast construction, and outstanding energy saving effect [1, 2]. In recent years, the proportion of EAF steel-making in China has gradually increased. With the continuous accumulation of scrap resources in China and the continuous development of EAF steel-making technology [3, 4], how to effectively control the cost of EAF steel-making process has become an important work. At present, the main factors affecting the cost of EAF steel-making process are scrap and electric energy. Therefore, how to accurately and timely collect the real-time smelting consumption of each station in the EAF steel-making process and provide the basis for optimizing the cost accounting of the EAF steel-making process is a problem to be solved.

B. Li · L. Yang (✉) · Y. Guo · S. Wang · H. Hu
Central South University, Changsha 410083, China
e-mail: yanglingzhi@163.com

Z. Peng et al. (eds.), *12th International Symposium on High-Temperature Metallurgical Processing*, The Minerals, Metals & Materials Series,
https://doi.org/10.1007/978-3-030-92388-4_5

Some researchers have done a lot of researches on cost accounting of EAF steel-making process in iron and steel plants, mainly through collecting on-site smelting data, applying computer technology, developing software with cost statistics function for managers to view and analyze. Based on the blast furnace data acquisition system of Shougang Jingtang Iron and Steel Plant, Li and Zhu [5] proposed a cost data acquisition scheme based on OPC technology. Song [6] used the method of DBLink and Kepware to collect, store, and display data in real time and realized the self-steel-making of varieties of steel under double slag mode, which achieved good results in Hebei Steel Tube Company. Mao et al. [7] put forward the industrial gateway data acquisition system, which can realize multi-source heterogeneous data acquisition and provide a unified basis for enterprise resource management system and energy management system. For iron and steel enterprises, Li [8] established a cost management system based on ERP and MES system, which achieved the integration and sharing of data, realized the dynamic control and prediction of the cost of iron and steel enterprises, and improved the informatization level of iron and steel enterprises. Liu et al. [9] used PowerBuilder 10.5 and MS SQL Sever2005 technology to develop a set of steel industry cost prediction system. The system can provide detailed cost prediction information for managers and assist managers to make cost decisions. Hu et al. [10] based on material balance and heat balance, combined with the actual situation of a steel plant, according to the target requirements of steel composition, determined the converter end-point control and alloy charging, calculating the total cost of LF.

In this paper, the EAF steel-making process of a steel plant is taken as the research background. The real-time cost data collection module is developed by KEPServer. The cost analysis model system is developed by Visual Studio 2013 development software. The collected smelting data are systematically analyzed to optimize the smelting operation of EAF steel-making process, providing theoretical basis for reducing smelting cost for iron and steel enterprises.

Establishment of Cost Analysis Model System

EAF short steel-making process with its advantages in investment, efficiency, and environmental protection has become one of the two main processes of world steel production. For iron and steel enterprises, the smelting cost directly affected the efficiency of enterprises. In order to monitor the smelting cost in real time and reduce the smelting cost in the production process, it is necessary to develop the cost analysis model system of EAF steel-making process based on the actual smelting situation.

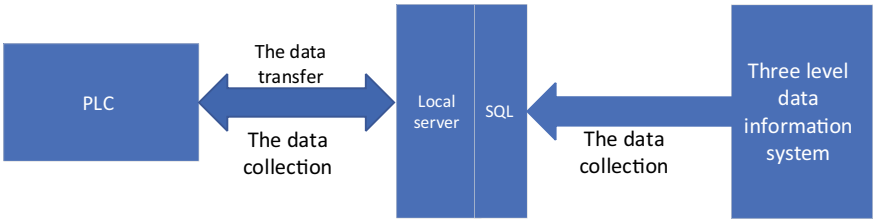

Fig. 1 Real-time cost data collection module structure diagram

Real-Time Cost Data Collection Module

The online operation of the cost analysis model system required the support of on-site real-time production data. The smelting process of EAF steel-making process includes many process data and cost parameters, including scrap charging, power consumption, injection consumption, lime consumption, and other data. These data directly reflected the real-time cost of EAF steel-making process. Therefore, it is necessary to collect real-time smelting data of EAF steel-making process, developing real-time cost data collection module, and provide data services and support for cost analysis model system.

The production data in the EAF steel-making process are mainly from the three-level data information system and PLC production data, and KEPServerEX software is selected as the third-party OPC server to construct the data collection platform [11, 12]. The software can ensure the stability and convenience of real-time cost data collection, reduce the difficulty of module development, and shorten the time of module development. The real-time cost data are saved in Microsoft SQL Server 2012. The database software can provide a comprehensive view of all real-time data and help ensure data confidence through integration, purification, and management. In hardware, choosing a good performance server for data storage is the core of the cost model. The structure of real-time cost data collection module is shown in Fig. 1.

The Structure of Cost Analysis Model System

With the continuous development of computer technology, it is easier to verify the on-site smelting cost. In order to optimize the smelting cost, the collected real-time cost data are systematically analyzed to facilitate real-time comparison of the cost of each smelting furnace and each station.

Due to the large amount of cost data collected, it is necessary to display and analyze the cost from the dimensions of furnace, time, and cost composition according to the cost data. The cost analysis model system is divided into five modules, includes cost inquiry module, process cost module, material composition module, trend analysis

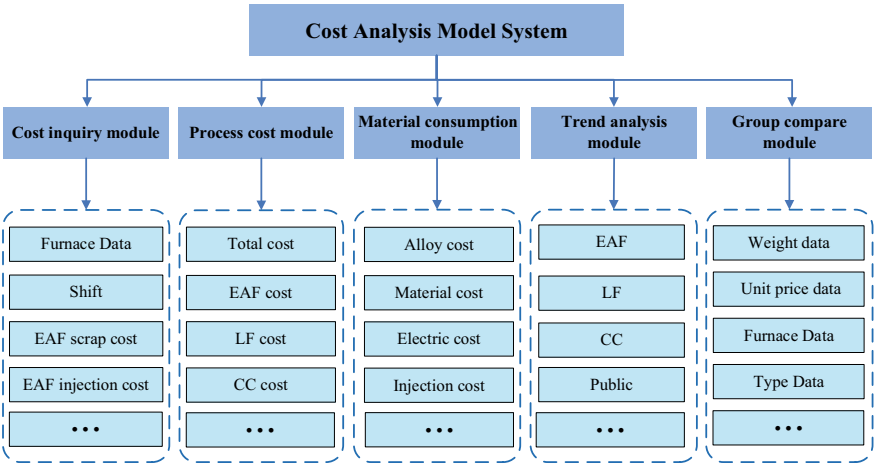

Fig. 2 Structure of cost analysis model system

module, and group compare module. The system structure of cost analysis model system is shown in Fig. 2.

Cost Inquiry Module

The cost inquiry module obtains various raw material consumption data through the real-time cost data collection module and obtains the cost data through the module calculation. The cost inquiry module can query the cost data of the EAF steel-making process through the time range or the furnace range (smelting steel, shift group, EAF charging cost, EAF scrap cost, EAF power supply cost, EAF injection cost, EAF consumables cost, LF charging cost, LF power cost, LF injection cost, LF consumables cost, etc.).

Process Cost Module

The process cost module disposals the data according to the scrap feeding data, auxiliary feeding data, temperature measurement paper tube consumption, and the consumption number of other spare parts in each process of each furnace under the query conditions, calculates the process cost, and draws the histogram. The process cost of each smelting furnace under the query condition is intuitively reflected.

Material Consumption Module

The material composition module is according to the query conditions of each EAF process, LF process, CC process of metal material feeding data, auxiliary alloy feeding data, electric energy and injection and consumption of public supplies and other information for data processing, calculation cost composition and automatic generation of pie chart.

Trend Analysis Module

The trend analysis module is according to the query conditions of each EAF process, LF process, CC process of metal material feeding data, auxiliary alloy feeding data, electric energy and consumption of public supplies and other information for data analysis, forming a line chart, intuitively view the trend of cost consumption of each material in each process.

Group Compare Module

The group compare module conducts data analysis according to the metal material feeding data, auxiliary material alloy feeding data, electric energy and injection number as well as the consumption number of public spare parts, and consumables generated in each process of the furnace under the corresponding query conditions, and shown the consumption trend of each material in each furnace. In the production process, if the material weight exceeds the standard, the red background will be displayed; if the material weight exceeds the standard, the green background will be displayed. The module is convenient for operation to adjust the weight of each material in time.

Cost Analysis Model System

Development Tools

The cost analysis model system is developed with C# language on the Visual Studio 2013 platform. C# programming language is the mainstream programming language at present, which is a fully object-oriented programming language. C# is designed to be a “simple, modern, and universal” and object-oriented programming language. The implementation of this language should provide support for

the following software engineering elements: strong type checking, array dimension checking, uninitialized variable reference detection, and automatic garbage collection (garbage collection refers to an automatic memory release technology). Software must be strong, durable, and have strong programming productivity. This language provides suitable component development applications for development in distributed environments.

Visual Studio 2010 integrates access to objects, relational data, and XML in a more concise language. This software provides wizards, tools, and components that simplify the development of code to build and manage SQL Server databases, Windows workflow applications, Enterprise Server solutions, etc. [13].

System Interface and Function

The cost analysis model system is developed by Visual Studio 2013 software. The system consists of five modules, which can monitor the cost of EAF steel-making process in real time, draw the cost composition diagram under different conditions and processes, and analyze the cost benchmarking. The interface diagram of each module is shown in Figs. 3, 4, 5, 6 and 7.

The cost analysis model system is a complex system composed of five different modules. By using this system, operators can timely adjust the cost consumption under the steel-making process of the whole scrap EAF through historical cost data, so as to minimize the consumption of furnace raw materials and reduce the smelting cost.

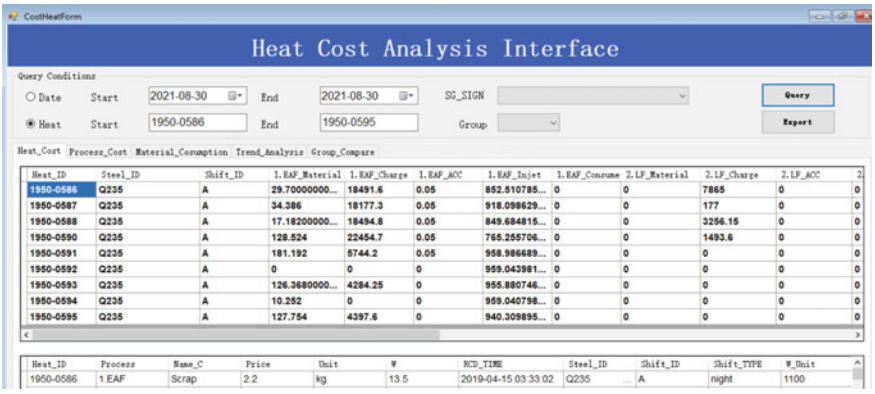

Fig. 3 Interface of cost inquiry module

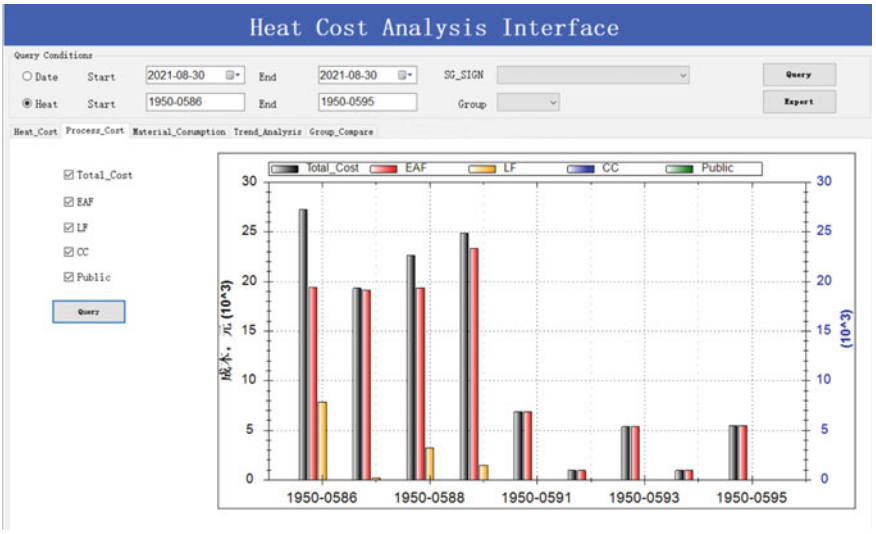

Fig. 4 Interface of process cost module

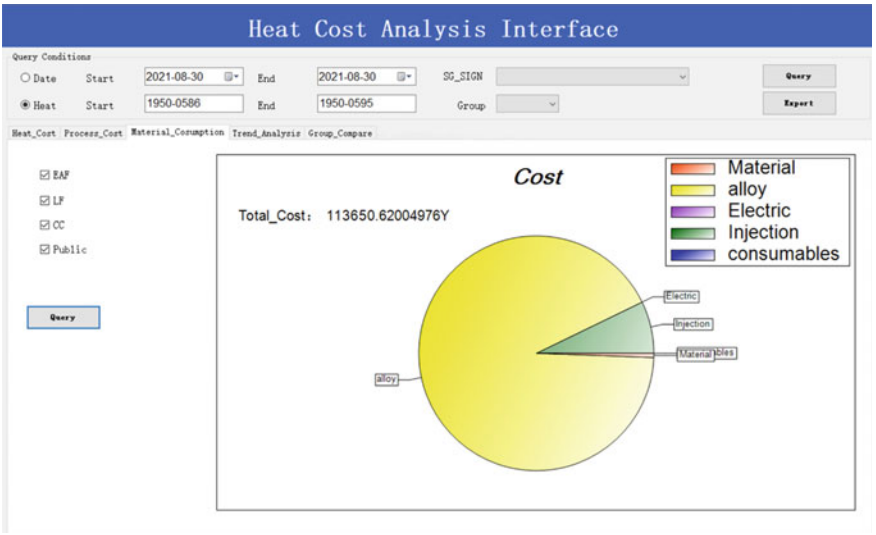

Fig. 5 Interface of material consumption module

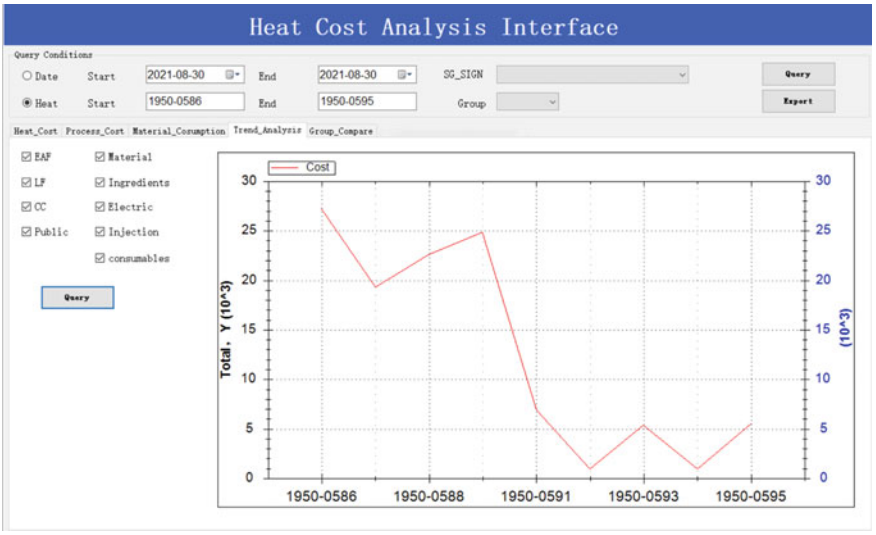

Fig. 6 Interface of trend analysis module

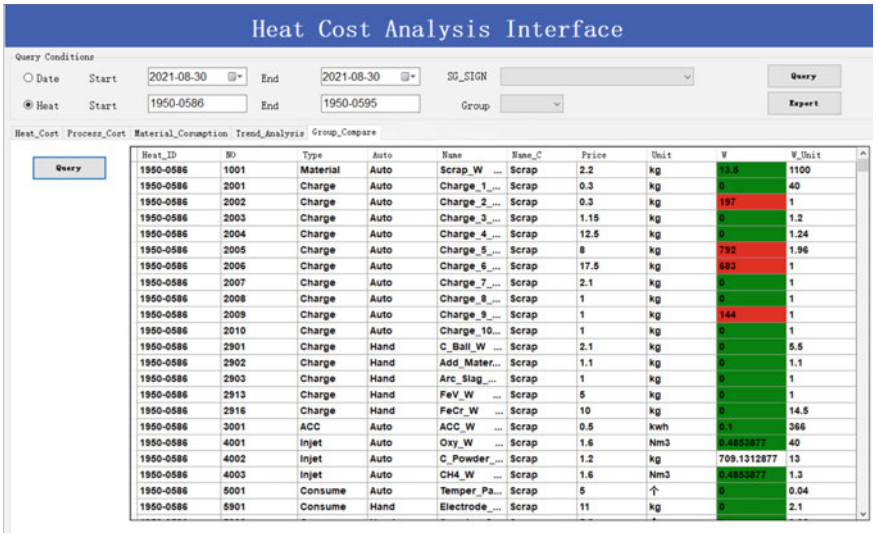

Fig. 7 Interface of group compare module

System Analysis and Discussion

The cost analysis model system based on real-time cost data collection module consists of cost inquiry module, process cost module, material consumption module, trend analysis module, and group compare module, which effectively solves the problems of unclear operating capital flow and rough cost accounting in EAF steel-making process enterprises.

(1) Through the cost analysis model system, it is convenient for enterprises to monitor the cost in real time and provide the basis for the development of intelligent cost platform.
(2) Through the cost analysis model system, the smelting operation of EAF steel-making process is optimized, and different charging guidance is provided according to different types of steels.
(3) The cost analysis model system calculated the cost composition of each station and realized the dynamic analysis and optimization of cost in steel-making production process.

Conclusion and Further Research

Due to the complexity of EAF steel-making process, the cost accounting of steel-making process in iron and steel plants is rough, which seriously affected the benefits of iron and steel plants. With the development of computer technology, more detailed real-time cost data collection will be needed in the future, and use the big data platform to analyze the cost data in real time.

In this paper, KEPServerEX software is used as the third-party OPC server to build a data collection platform, construct a real-time cost data collection module, and store it in Microsoft SQL 2012 database. The cost analysis model system is developed by using Visual Studio 2013. The system consists of cost inquiry module, process cost module, material consumption module, trend analysis module, and group compare module. The system can be used for real-time cost data analysis of EAF steel-making process and provide a theoretical basis for iron and steel enterprises to reduce smelting costs.

In the future, the smelting operation of EAF steel-making process can be optimized according to the cost data of multiple furnaces, and the charging optimization operation system can be built according to the needs of different steel types to realize dynamic cost control of EAF steel-making process.

References

1. Jiang Z, Kang C, Liu F, Dong Y, Geng X (2021) Development trend of special melting and remelting production process. J Mater Metall 20(01):1–8+22

2. Li W, Cao L, Xu Y, Cheng J (2020) Cost analysis and competitiveness evaluation of EAF steel-making. Ind Heat 49(09):29–31+36
3. Li X, Zhou Y, Hao Y, Peng F (2018) Analysis of present situation and development trend of Steel-making process in China. Metall Econ Manage 03:51–55
4. Wu Y, Xiao B, Zhu L, Wang Y (2021) Current situation analysis and prospect of iron and steel raw material for electric arc furnace steel-making. Iron Steel-Making 21(09):1–9
5. Li Q, Zhu Z (2013) Application of OPC technology in data acquisition of blast furnace. Ke Ji Feng 13:119
6. Song M (2020) Development of data management platform for secondary steel-making system. Hebei Metall 09:44–48
7. Mao S, Song Y, Liu L (2015) Real-time data acquisition technology of iron and steel enterprise based on industrial gateway. Internet Things Technol 5(12):10–12
8. Li K (2018) Research on cost control of iron and steel enterprise based on ERP system. Master of Thesis, North China University of Science and Technology
9. Liu Q, Zhang Z, Pan K (2014) The cost forecasting model of key products of steel enterprises and system development. Manuf Autom 36(15):28–33
10. Hu X, Fu S, Xiong H (2020) Development and application of steel cost prediction model. Hebei Metall (11):16–19+33
11. Shen W (2017) Application of OPC technology in power energy data exchange of MES system in steel enterprises. Metall Power 05:59–62
12. Zhou Q (2014) Research on the process control system and the scheduling system based on the simulation platform of steelmaking-continuous casting. Master of Thesis, Northeastern University
13. Xue B, Yang L, Guo Y, Chen F (2020) Research on the database construction of furnace material consumption in EAF steel-making process. Paper presented at the 11th International Symposium on High-Temperature Metallurgical Processing, TMS 2020

Study on Stress–Strain and Deformation Behavior of Bloom in the Heavy Reduction Process Under Single Roll

Yizhe Du, Songyuan Ai, Yanhong Fang, Mujun Long, and Dengfu Chen

Abstract In order to obtain the key parameters of the bloom heavy reduction process in continuous casting, the mathematical model of solidification heat transfer of bloom continuous casting was established by using the general simulation software of billet secondary cooling. Then, combined with Abaqus finite element software, the stress–strain and deformation behavior of billet was investigated in detail. The results demonstrated that the calculation error tends to stabilize when the size of the reduction roll unit is below 15 mm. The stress of billet is distributed symmetrically along the thickness direction, and decreases from the inner arc and the outer arc to the center. The maximum stress increases from 119 to 140 MPa in the range of 10 to 30 mm reduction amounts, resulting in the increase of the corner crack tendency. The reduction amount shall be greater than 10 mm to effectively improve the internal quality of the billet. In addition, the side strain of the billet is basically consistent with the deformation distribution in the width direction and has a good linear relationship.

Keywords Bloom · Heavy reduction · Error analysis · Stress · Deformation behavior

Introduction

Due to the large section size of bloom, slow solidification and uneven cooling often occur, which lead to serious central segregation and central porosity in the continuous casting process. These defects will deteriorate the quality of subsequent products. Traditional soft reduction technology has limited ability to improve the internal quality problems of blooms. Therefore, in order to improve the quality of billet, people have proposed heavy reduction technology on the basis of soft reduction.

Y. Du · S. Ai · Y. Fang · M. Long · D. Chen (✉)
Laboratory of Materials and Metallurgy, College of Materials Science and Engineering, Chongqing University, Chongqing 400044, China
e-mail: chendfu@cqu.edu.cn

Chongqing Key Laboratory of Vanadium-Titanium Metallurgy and New Materials, Chongqing University, Chongqing 400044, China

Z. Peng et al. (eds.), *12th International Symposium on High-Temperature Metallurgical Processing*, The Minerals, Metals & Materials Series,
https://doi.org/10.1007/978-3-030-92388-4_6

However, with the increase of the reduction amount, the tendency of cracks in the billet also increases. In order to clarify the implementation effect of the heavy reduction process and avoid the appearance of surface or internal cracks, it is necessary to conduct an in-depth study on the stress–strain behavior and deformation of the cast billet during the reduction process.

At present, a large number of scholars have carried out a series of simulation and experimental investigation on the heavy reduction process. Wu et al. [1] studied the closing behavior of internal porosity during blooms under heavy reduction and found that large deformation is beneficial to the elimination of porosity. Ji et al. [2] explored the influence of blooms on the internal quality of billet through a combination of experimental and numerical simulation. The results show that heavy reduction can effectively increase the internal density of the cast billet. A two-stage reduction method is also proposed in their study. Cheng et al. [3] compared the difference in the effect of single-roll reduction and multi-roll reduction on the internal quality of blooms and indicate that single-roll reduction can more effectively close the internal pores of the billet.

Although there has conducted in-depth research on the process of casting billet heavy reduction, the calculation errors caused by different element sizes in the finite element simulation are often ignored. Therefore, in order to clarify the influence of varying element sizes on the calculation results, we firstly conduct mesh convergence analysis to select the best element size. Then we use Abaqus finite element software to explore the high-temperature stress and strain behavior of bloom. In addition, we quantitatively analysis the deformation in the width direction of the side of the cast billet during the heavy reduction process. The research results can provide some valuable information for the selection of key parameters in the heavy reduction process and design of the reduction device.

Model and Method

The research objective of this paper is GCr15 bloom from a factory. The main chemical composition and parameters involved in the continuous casting process are shown in Tables 1 and 2.

Table 1 Main chemical composition of the GCr15 (mass fraction)/%

Steel	C	Si	Mn	P	S	Cr
GCr15	0.95–1.05	0.15–0.35	0.25–0.45	≤0.025	≤0.025	1.40–1.65

Table 2 Parameters for the GCr15 bloom continuous casting process

Parameters	Value
Transverse section size (mm × mm)	420 × 530
Casting speed (m/min)	0.45
Machine radius (m)	16.5
Reduction roll diameter (mm)	500
Reduction position (fs)	1.0

Mathematical Model of Solidification Heat Transfer

The temperature field information of the bloom is the basis for the accurate construction of the high-temperature stress–strain model. In order to save calculating costs and obtain accurate initial temperature information under heavy reduction, the three-dimensional heat transfer problem is transformed into two-dimensional, and the billet size change caused by solidification and cooling shrinkage is ignored, and the solidification heat transfer of continuous casting is considered as a steady-state heat transfer process. The effect of forced convection of molten steel on the heat transfer of the cast billet is processed into the effective thermal conductivity of molten steel. Taking into account the influence of molten steel flow on heat transfer, the equivalent specific heat Ce is used to replace the specific heat C of steel in the two-phase zone [4]. According to the relationship of the pulling speed $v = \partial Z/\partial\tau$, the basic differential equation of heat transfer in bloom solidification can be obtained:

$$C_e\rho\frac{\partial t}{\partial\tau} = \frac{\partial}{\partial x}\left(\lambda_e\frac{\partial t}{\partial x}\right) + \frac{\partial}{\partial y}\left(\lambda_e\frac{\partial t}{\partial y}\right) \tag{1}$$

where t is temperature, K; τ is time, s; ρ is density of steel, kg/m^3; C_e is effective specific heat, J/(kg °C); λ_e is the thermal conductivity, W/(m °C).

The model includes four heat transfer modes of the cast billet during continuous casting which are cooling water impact, cooling water evaporation radiation heat transfer, and contact between the cast billet and the roller. At the same time, it also considers that the difference in water flow density distribution and the difference between inner and outer arcs to ensure the temperature distribution during continuous casting can be accurately calculated [5, 6]. The high-temperature physical property parameters of GCr15 steel involved in the calculation are shown in Table 3.

In this paper, the general simulation software of the secondary cooling developed by the 2M laboratory from Chong Qing University [7] was used to simulate the solidification and heat transfer behavior of the bloom during the entire continuous casting process. As shown in Fig. 1, the temperature calculation results in the thickness direction of the billet at the time of reduction are imported into Abaqus as the initial temperature field conditions of the stress–strain model in Section "High-Temperature Stress–Strain Mathematical Model". On this basis, the stress–strain and deformation behavior of the billet under different reduction conditions is calculated and analyzed.

Table 3 GCr15 steel thermophysical parameters

Parameters	Value
Liquidus temperature (°C)	1345
Solidus temperature (°C)	1455
Density (kg/m^3)	7883.24–0.34421T
Specific heat (J/kg °C)	479.95544 + 0.15426T
Thermal conductivity (w/m °C)	44.350–0.0169T
Freezing latent heat (kJ/kg)	236,500

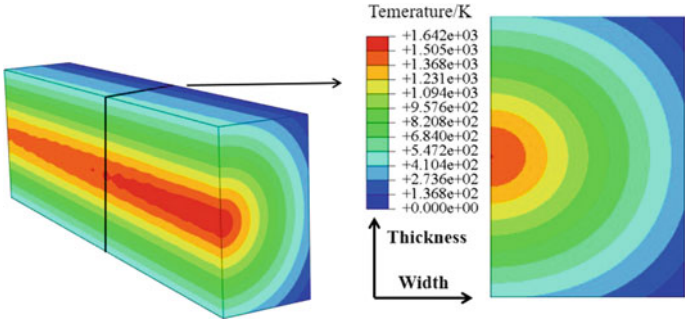

Fig. 1 Temperature distribution of heavy reduction position

High-Temperature Stress–Strain Mathematical Model

Model Descriptions

The composition and mesh distribution of the model are shown in Fig. 2. Based on the symmetry in the width direction, a 1/2 model is established along the center line of the drawing direction. Considering that there will be a certain flow in the front and rear

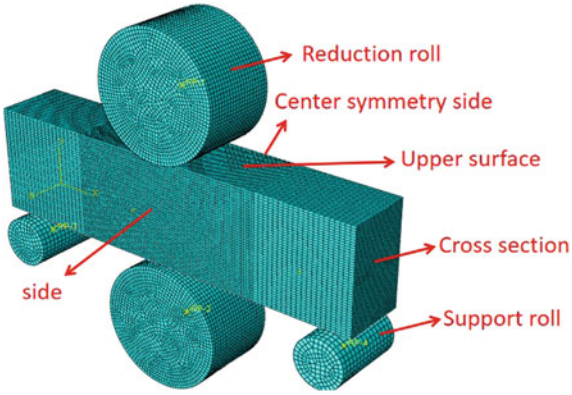

Fig. 2 3D FEM model of heavy reduction

direction of the cast billet during the reduction process, the model is appropriately lengthened along the drawing direction, and finally, 1600 mm is selected as the length of the cast billet model. At the beginning of calculation, the upper roll firstly reduction a suitable amounts (10–30 mm) at a position of 800 mm away from the end of billet. Then, the upper and lower rollers roll 200 mm in the opposite direction of the billet to obtain the stress and strain information of the cast billet in this process. Since the stress only acts on the solidified shell, this model considers the influence of the hydrostatic pressure of the liquid steel by setting different material properties. When the solid ratio in the reduction region is greater than that corresponding to the zero strength temperature, the influence of the hydrostatic pressure of the steel is not considered.

The model adopts a structured grid division and selects indirect thermal–mechanical coupling to calculate. Among them, the heat transfer model adopts the DC3D20 hexahedral quadratic integration unit; In the stress–strain model, the cast billet adopts the method of sparse and dense grid division, and adopts the C3D8RH hexahedral linear hybrid formulation unit combined with reduced integration unit. The average unit size is 15 mm. The rolls adopt C3D8R hexahedron linear reduced integration unit.

In order to reduce the calculation cost, the following assumptions are made under the premise of ensuring the accuracy of the calculation: ① The casting billet is isotropic and composed of continuous medium. ② The mechanical properties of the billet are only a function of temperature. ③ The billet is an elastoplastic material, the rolls are an elastic material, and the elastic modulus of the rolls is much greater than that of the casting billet.

Boundary Conditions

The displacement and rotation of the roller are set as boundary conditions during the simulation. Assuming that the billet does not move, the upper and lower rollers also rotate in the opposite direction of the billet. The roller is set to contact with the billet surface, the normal direction is set to "hard" contact, the tangential direction is set to Coulomb friction, and the friction coefficient is 0.3 [8]. The temperature field in the region under heavy reduction is extracted, set as a predefined field, and loaded into the heat transfer model as the initial temperature field of the stress–strain model.

In addition to the thermal stress caused by temperature drop, the billet will be subjected to great reduction force and large deformation. The total strain increment $d\varepsilon$ include thermal $d\varepsilon_T$, elastic strain increment $d\varepsilon_e$, and plastic strain increment $d\varepsilon_p$ [9], i.e.:

$$d\varepsilon = d\varepsilon_T + d\varepsilon_e + d\varepsilon_p \tag{2}$$

Mechanical Performance Parameters

In the stress–strain model, the main mechanical property parameters include elastic modulus, Poisson's ratio, coefficient of thermal expansion, and plastic deformation parameters, which are closely related to temperature. Therefore, in order to improve the accuracy of simulation results, the accurate mechanical property parameters should be provided. The plastic deformation parameters of GCr15 steel can be obtained from the literature [10], and the variation law of thermal expansion coefficient can be obtained from the research results of Qian et al. [11].

Results and Discussion

Error Analysis

The unit size is a critical factor affecting the accuracy of the calculation results. Therefore, it is necessary to analyze the convergence of mesh before calculation. As shown in Fig. 3, in order to facilitate statistics, taking the 30 mm units as the benchmark, the error analysis is carried out by comparing the tangential force and normal force received by the upper roll during heavy reduction. The billet unit size is kept unchanged in this process. The results demonstrate that the error curve of tangential force and normal force is obviously divided into three regions. Among them, when the unit size of the reduction roll is less than 15 mm, the calculation errors of normal force and tangential force are relatively stable. When the unit size of the reduction roll is in the range of 15–25 mm, the calculation error increases rapidly with the decrease of the unit size. Besides, the error of calculation results is

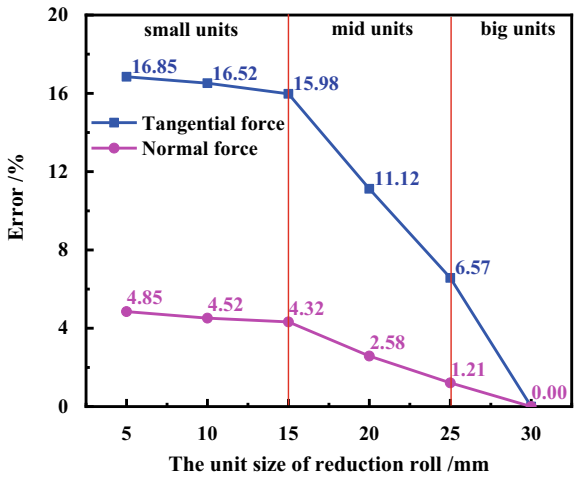

Fig. 3 Error analysis with varying unit sizes

relatively large when the unit size is greater than 25 mm. This is because when the size of reduction roll unit is too large, the stress on it cannot be fully captured, leading to the deviation of the calculation results from the reality. Consequently, considering the calculation cost and accuracy, the reduction roll unit size of 15 mm is finally used for simulation.

Stress Analysis

In order to obtain the stress distribution of the billet and evaluate the tendency of surface cracks, the stress distribution was quantitatively analyzed with the reduction of 30 mm as an example. Figure 4a, b, respectively, shows the stress distribution on the upper surface and cross section of the billet at the reduction position. It can be seen that the stress distribution in the non-corner area on the upper surface of the billet is relatively uniform, and the corner stress value at the position where the roller is pressed down reaches the maximum. Combined with the temperature distribution of the billet cross section (i.e. Fig. 1), it can be obtained that the stress distribution is directly related to the temperature distribution. The lower the temperature, the stronger the deformation resistance and the greater the stress. The temperature in the central area of the billet is the highest, and the stress is the lowest.

Figure 4c, d shows the stress distribution on the side of the billet and the central symmetrical side at the reduction position, respectively. It can be concluding that although only the upper roller is reduction, the deformation of the inner and outer arcs of the billet is extraordinary similarity, and the stress distribution also has good symmetry. The stress decreases from the inner and outer arc to the center as a whole. The temperature of the billet side is lower, and the overall stress is greater than that of central symmetrical side. At the side of the billet, the maximum stress at the corner reaches 140 MPa, and there is stress concentration. On the central symmetrical side of the billet, with the deepening into the billet, the stress decreases sharply, up

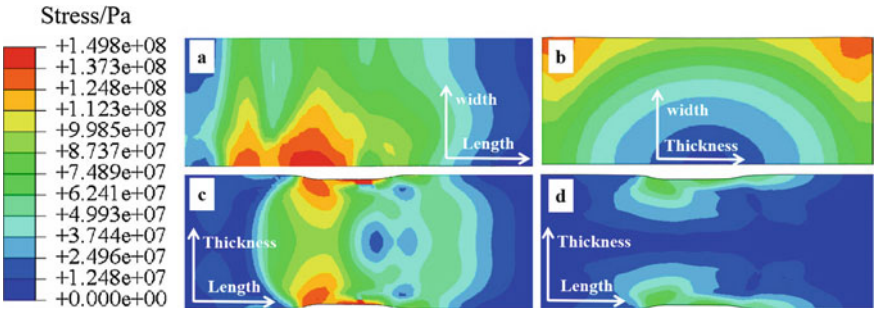

Fig. 4 Distribution of stress of different position of GCr15 bloom **a** upper surface **b** cross section **c** side **d** center symmetry side

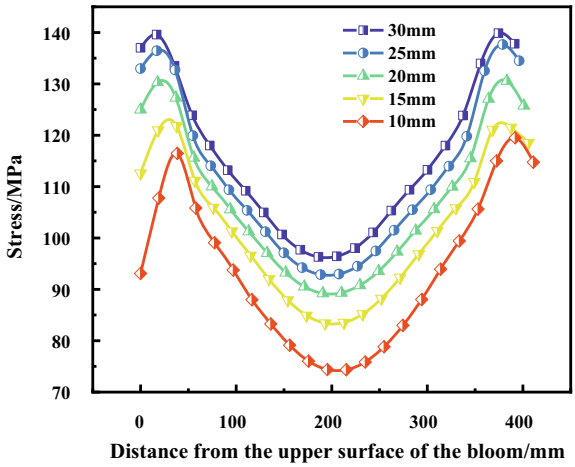

Fig. 5 Distribution of stress along thickness direction of billet

to 87 MPa, and there is almost no stress in the center. This shows that the heavy reduction process is mainly the stress on the outer shell, especially in the corner area.

Figure 5 shows the distribution of billet side stress along the thickness direction at the pressing position when the reduction amount is 10–30 mm. It can be seen that change law of billet stress is consistent in the thickness direction. The overall stress increases firstly and then decreases, reaching the maximum in the range of 17–38 mm from the upper and lower surfaces and the minimum in the center. The maximum stress increases from 119 to 140 MPa in the range of 10 mm–30 mm reduction amounts. Therefore, with the increase of the reduction amount, it is necessary to follow the growth of stress in the corner of billet to avoid the occurrence of surface cracks caused by stress concentration.

Strain Analysis

Due to the high temperature in the central of the billet and poor resistance to deformation, the strain during the reduction process is large, which may result in internal cracks. In addition, the heavy reduction process will cause the billet to deform in varying directions. Among them, the investigation on the deformation of billet in width direction can not only judge the reduction effect of heavy reduction to a certain extent, but also provide a reference for the design of the supporting device of reduction roll. Consequently, in order to clarify the deformation of the billet and the tendency of internal cracks, the deformation behavior and strain distribution were analyzed quantitatively.

Figure 6a shows the distribution of equivalent strain of billet cross section under the 30 mm reduction amounts. In the width direction, the strain in the non-corner area remains basically stable, and the equivalent plastic strain in the center is evenly

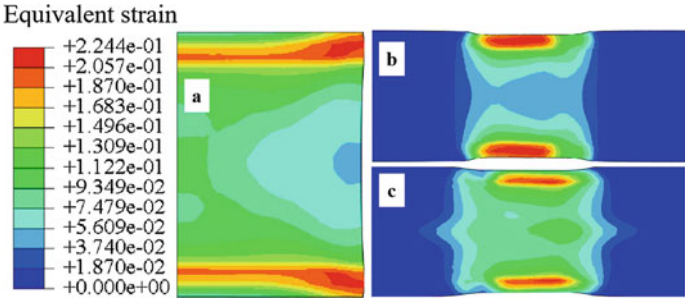

Fig. 6 Distribution of equivalent strain of varying position of GCr15 bloom. **a** cross section **b** side **c** center symmetry side

distributed, all above 0.05, indicating that the strain can be effectively transmitted to the center at this reduction. Figure 6b, c shows the distribution of equivalent strain on the side and central symmetrical side of the billet at the reduction position, respectively. With the reduction of the upper roll, the strain of the billet increases gradually, and the equivalent plastic strain distribution of the outer side and the central symmetrical side of the billet maintains central symmetry in the thickness direction. From the upper and lower surfaces to the center, the strain first increases, then decreases, and remains stable in the central region. In the side thickness direction, the maximum equivalent plastic strain is distributed in the area 30–60 mm thick from the upper and lower surfaces, and the maximum value is 0.23; the central symmetrical side is the largest in the range of 40–60 mm. This is because the temperature of the outer side of the billet is lower than that of the central side, so the stress change of the central side is easy to transfer to the billet center, which is consistent with the above analysis results.

Figure 7a, b shows the strain distribution along the thickness direction on the side of the billet and the variation of deformation in the width direction at different

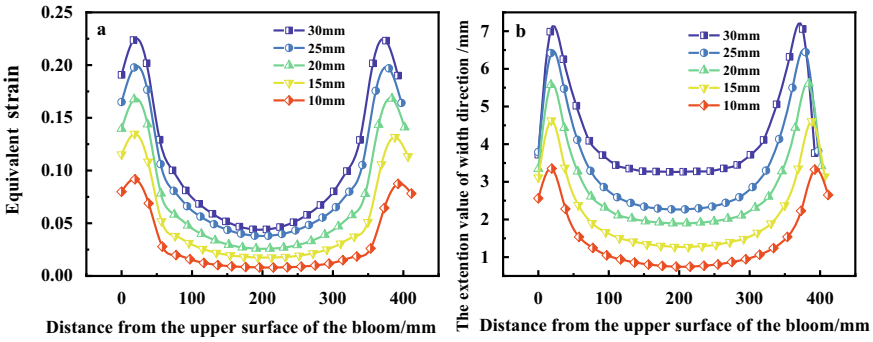

Fig. 7 Strain distribution **a** and the broadening amount distribution **b** in the side width direction of billet within the range of reduction amounts of 10–30 mm

positions on the side. It can be seen that the distribution law of slab strain and deformation is completely consistent, both of which are approximately in "M" shape. When the reduction amount is 10 mm, the central strain of billet is almost 0. This shows that it cannot be effectively transferred to the center of the billet, and the reduction effect is poor. Therefore, for the target steel grade and section, in order to improve the internal quality of the billet, the reduction amount in the heavy reduction process should be greater than 10 mm. However, while increasing the reduction amount, it is necessary to pay attention to the growth of the internal strain of the billet and control it within the critical strain range to avoid the occurrence of internal cracks. By observing Fig. 7b, it can be seen that the sides of the billet are deformed to varying degrees during the reduction process. The maximum deformation in the width direction of slab side increases from 3.4 mm to 7.2 in the range of 10–30 mm reduction amounts. Thus, when designing the supporting device of holding down roll, it is necessary to reserve enough roller length according to the broadening amount of the billet, so as to achieve the purpose of effective reduction.

Figure 8a shows the variation of the maximum strain on the side of the billet and the maximum deformation in the width direction within the reduction range of 10–30 mm. With the increase of the reduction amount, the side strain and broadening amount increase, and the increase decreases, which is consistent with the research results of Wu et al. [1]. This is mainly because with the increase of the reduction amount, the deformation resistance of billet increases, resulting in the difficulty of billet deformation. As shown in Fig. 8b, the quantitative relationship between the billet strain and the deformation in the width direction is obtained, that is, $y = 0.798 + 28.303x$, $R^2 = 0.99$. It can be seen that the lateral strain of the billet is basically linear with the deformation in width direction.

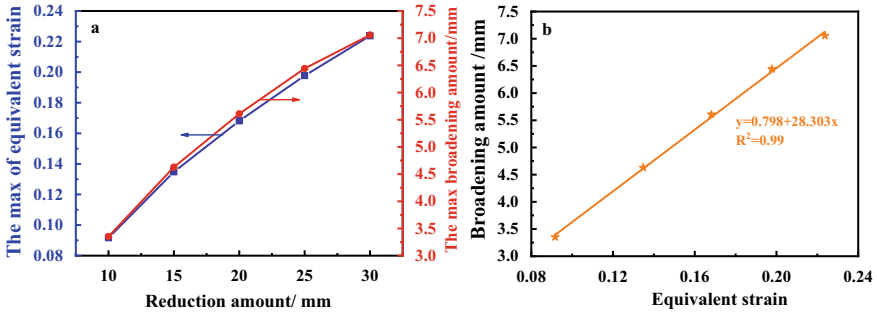

Fig. 8 **a** Variation law of maximum strain and maximum broadening amount of billet side. **b** The relationship between strain and broadening amount

Conclusions

By establishing the high-temperature stress–strain mathematical model of bloom under heavy reduction pressing, the stress–strain and deformation behavior is studied, which provides some valuable information for the selection of key process parameters and the design of related devices. The specific conclusions are as follows:

(1) The unit size of the model will directly affect the calculation accuracy. On the premise that the billet unit size remains unchanged, by comparing the tangential force and normal force received by the reduction roll in the heavy reduction process, it is finally concluded that the calculation error tends to be stable when the unit size of the reduction roll is less than 15 mm.
(2) The stress of the billet is symmetrically distributed along the center in the thickness direction, and the stress decreases from the inner and outer arc to the center. In the range of 10–30 mm reduction amounts, the maximum stress of billet increases from 119 to 140 MPa. With the increase of the reduction amount, the tendency of corner cracks increases.
(3) Under the working condition of this investigation, the reduction amount shall be greater than 10 mm to improve the internal quality of the billet. But at the same time, we should pay attention to the growth of internal strain of the billet and control it within the critical strain range to avoid the occurrence of internal crack. In addition, the distribution law of billet side strain and broadening amount at different positions is basically the same, and they have a good linear relationship.

Acknowledgements The authors gratefully acknowledge the financial support provided by the National Natural Science Foundation of China, project No. 52074053.

References

1. Wu C, Ji C, Zhu M (2019) Closure of internal porosity in continuous casting bloom during heavy reduction process. Metall Mater Trans B 50(6):2867–2883
2. Ji C, Wu C, Zhu M (2016) Thermo-mechanical behavior of the continuous casting bloom in the heavy reduction process. JOM 68(12):3107–3115
3. Cheng R, Zhang J, Zhang L, Ma H (2018) Comparison of porosity alleviation with the multi-roll and single-roll reduction modes during continuous casting. J Mater Process Tech 266:96–104
4. Li J, Chen D, Wu G (2014) Secondary cooling system of continuous casting round billet of 37Mn2 steel. Steel 49(1):45–51
5. Long M, Chen D, Zhao Y (2011) Heat transfer simulation software based on improving central segregation of continuous casting slab. Continuous Cast S1:406–412
6. Du Y, Li L, Wang Q, Chen D (2021) Analysis of slab temperature and stress under single roll heavy pressing of extra thick slab. Continuous Cast 01:47–54
7. Chen D, Long M, Pan Y (2005) Design and development of general simulation software for secondary cooling of slab continuous casting. Continuous casting secondary cooling technology exchange meeting. Jiuquan, Gansu, China

8. Fu J, Li J, Zhang H (2010) Viscoelastic plastic analysis of slab widening in secondary cooling zone of continuous casting. J Metals 01:91–96
9. Yu S, Long M, Wang Q, Chen D, Wu S (2019) Effect of the strand corner structure on the corner stress during the bending and straightening processes in slab continuous casting. J Manuf Process 48:270–282
10. Ji C, Wang Z, Wu C, Zhu M (2018) Constitutive modeling of the flow stress of GCr15 continuous casting bloom in the heavy reduction process. Metall Mater Trans B 49(193):1–16
11. Qian D, Peng Y, Deng J (2017) Hot deformation behavior and constitutive modeling of Q345E alloy steel under hot compression. J Cent South Univ 24:284–295

Decarburization and Chromium Conservation Model in AOD Refining Process of 304 Stainless Steel

Jun Cai and Jing Li

Abstract Decreasing chromium loss in the decarburization stage of the argon oxygen decarburization (AOD) refining process is one of the key technologies of 304 stainless steel smelting. In this paper, based on the theoretical conditions and production status of a 75 t AOD furnace, a decarburization and chromium conservation mathematical model of 304 stainless steel was established. Using this model, conditions of chromium oxidization in different situations can be predicted, and the required CO partial pressure as well as the gas supply parameters of decarburization and chromium conservation under different smelting conditions can also be calculated. Applying the model on a 75 t AOD furnace, the side and top combined blowing parameters in AOD refining process were optimized, and the burning loss of chromium in molten steel was also reduced obviously. In addition, a 379.2 kg decrease of the average consumption of ferrosilicon in the reduction stage has been achieved using the model, and the average smelting cycle was shortened by 6.4 min.

Keywords Decarburization and chromium conservation model · Argon oxygen decarburization · 304 stainless steel

Introduction

Nowadays, approximately 70% of world's stainless steel is produced through the electric arc furnace (EAF) → argon oxygen decarburization (AOD) process [1]. Due to the relatively high carbon content of austenitic stainless steel, to speed up the smelting rhythm, most production enterprises adopt this process [2–5]. As a typical austenitic stainless steel, 304 stainless steel is widely used owing to the characteristics of corrosion resistance, low temperature plasticity, easy forming, and good weldability. As one of the key links, AOD refining process directly affects the molten steel quality and cost-effectiveness of 304 stainless steel, such as burning loss

J. Cai · J. Li (✉)
State Key Laboratory of Advanced Metallurgy, University of Science and Technology Beijing, Beijing 100083, China
e-mail: lijing@ustb.edu.cn

Z. Peng et al. (eds.), *12th International Symposium on High-Temperature Metallurgical Processing*, The Minerals, Metals & Materials Series,
https://doi.org/10.1007/978-3-030-92388-4_7

of chromium [6] and ferrosilicon consumption [7]. Moreover, the decarbonization efficiency in AOD refining process has a significant influence on the smelting cycle, which is considered as an essential impact of operation-level performance [8].

During the research work of the past few decades, many mathematical models in AOD refining process of stainless steel production were established, such as decarburization rate [9], heat balance calculation [10], and temperature prediction [11, 12], which have also been applied to industrial production successfully [13]. However, few works about the decarburization and chromium conservation model in the AOD refining process of 304 stainless steel were reported, especially the dynamic control of decarburization and chromium conservation by determining blowing parameters through model calculation. For different initial molten steel conditions, as the blowing goes on, the temperature and composition of molten steel were different and changed dynamically at different blowing periods. Correspondingly, these differences caused a change kinetic and thermodynamic conditions of the decarburization and chromium conservation, furthermore, greatly affects the quality control of 304 stainless steel in AOD refining process. Therefore, the establishment of decarburization and chromium conservation calculation model is complex and is of great significance for the actual production of 304 stainless steel. Based on the actual operations, thermodynamic and kinetic conditions of the blowing process of refining 304 stainless steel in the 75 t AOD converter, a mathematical model of molten steel decarburization and chromium conservation in the decarburization process of 304 stainless steel was established in this paper. According to determined conditions of initial molten steel and blowing parameters, the model can be used to judge whether chromium burning loss occurs, calculate and determine the relative process parameters for controlling chromium burning loss. Moreover, through using the calculation results of the model, the gas supply parameters required for the molten steel decarburization and chromium conservation were determined in the decarburization stage of the AOD refining process. Combined with the mathematical model of decarburization and chromium conservation and the actual operating conditions of the 75 t AOD converter refining 304 stainless steel, the purpose of decarburization and chromium conservation in the decarburization stage was achieved by adjusting the gas supply parameters, and the burning loss of chromium in molten steel was minimized, which has essential guiding significance for the optimization of gas supply parameters in the actual production process of 304 stainless steel.

Establishment of Decarburization and Chromium Conservation Model

Process Introduction

In this paper, the 304 stainless steel is produced by the process of EAF → AOD → LF (Ladle Furnace) → CC (Continuous Casting), and the process schematic diagram is shown in Fig. 1.

The decarburization and chromium conservation model was established on the basis of the refining of AOD refining process of 304 stainless steel. The mixture of inert gas and oxygen was blown into AOD refining furnace through side–top combined blowing, in which oxygen is mainly used for decarbonization and inert gas (argon or nitrogen) is mainly used to reduce the partial pressure of carbon monoxide. AOD refining process can be divided into four stages, namely steel melting stage, decarburization period I, decarburization period II, and reduction stage. Before the reduction stage, nitrogen is used to replace expensive argon, and pure argon is blown on the side in the reduction stage. In the steel melting and decarburization stage, due to the side–top combined blowing and six branch gas supply, the gas stirs the molten bath strongly, and the dynamic conditions are good.

In the steel melting stage, the initial molten steel, slag, scrap, alloy, and other furnace charges are mixed into the AOD furnace. Because of high contents of carbon and silicon in the initial molten steel and a low molten bath temperature, pure oxygen and the mixture of oxygen and nitrogen are blown into AOD refining furnace to heat up the bath rapidly through top blowing and side blowing, respectively. In the actual production process, in order to protect the side blowing elements, furnace lining, and safe production, a certain flow of nitrogen (>16 Nm/min) is necessary to be blown as the protective gas through side blowing, and the maximum value of R, the mass ratio of oxygen to nitrogen, is 8.5.

The decarburization stage includes decarburization period I and II. The side–top combined blowing process is adopted for decarburization, and the gas supply parameter R can be adjusted online. As the progress of decarburization reaction progresses, the carbon content in steel gradually decreases, and the bath temperature increases. When the carbon content drops to a certain value and the temperature meets the requirements, the R value is decreased to reduce metal burning loss and control the excessive temperature of the molten bath. When the decarburization stage ends

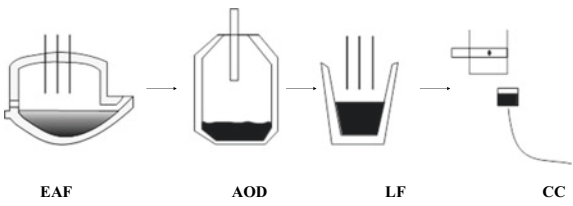

Fig. 1 Production process schematic diagram of stainless steel

and enters the reduction stage, stop top blowing and side blowing with pure argon. Moreover, alloy, lime, etc., were added into molten bath to adjust the composition of molten steel and refining slag, in which ferrosilicon was added to reduce (Cr_2O_3) in the slag to [Cr] and back to the molten steel. After the temperature and composition of molten steel meet the target requirements, the tapping operation was carried out.

Competitive Oxidation of Carbon and Chromium in AOD Decarburization Stage

In the decarburization stage of AOD refining process, based on the industrial site gas supply intensity, when the molten steel carbon concentration is high (high carbon area), the molten steel decarburization reaction rate is mainly determined by the oxygen supply intensity. When the molten steel carbon concentration is low (low carbon area), the molten steel decarburization reaction rate is mainly determined by the mass transfer rate of [C] from the molten steel to the gas–liquid reaction interface. There is a critical carbon concentration corresponding to the oxygen supply intensity. When the carbon concentration is higher than the critical value, the oxygen blown into the bath reacts with carbon without chromium burning. When the carbon concentration of molten steel is lower than the critical value, the competitive oxidation of carbon and chromium occurs, and chromium was oxidized to Cr_2O_3, resulting in the burning loss of chromium. The changing curve of conversion temperature of competitive oxidation of carbon and chromium during decarburization in AOD refining process of 304 stainless steel is shown in Fig. 2.

According to Fig. 2, in the process of competitive oxidation of carbon and chromium, the increase of [C] content and temperature are beneficial to decarburization and chromium reservation in the molten bath. As the content of [C] decreases, the conversion temperature of competitive oxidation of carbon and chromium gradually increases. When the content of [C] in molten steel is greater than 0.3%, the

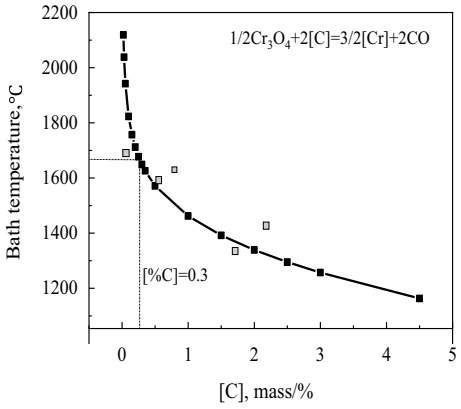

Fig. 2 Curve of conversion temperature of competitive oxidation of carbon and chromium

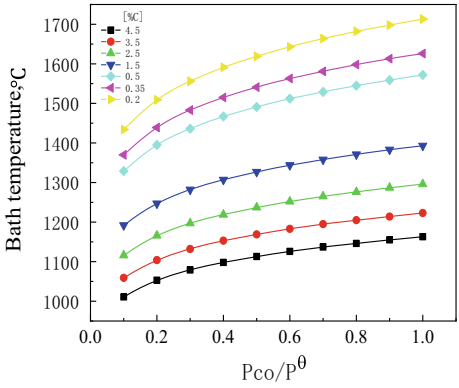

Fig. 3 Equilibrium relationship between CO partial pressure and temperature of carbon and chromium competitive oxidation reaction

conversion temperatures are below 1680 °C. When the content of [C] in molten steel reduces to less than 0.3%, the conversion temperature rapidly increases to above 1680 °C. When the carbon content in molten steel decreases below the critical value, the molten bath temperature cannot meet the temperature requirements of decarburization and chromium reservation, and [Cr] oxidation occurs in molten steel. In this case, to continue decarburization, it is necessary to improve the stirring strength in the furnace and reduce the partial pressure of CO for reducing chromium burning loss in the molten bath.

Under different carbon content conditions, the relationship between CO partial pressure and bath temperature when the carbon and chromium competitive oxidation reaction reaches equilibrium is shown in Fig. 3.

It can be seen from Fig. 3, as the bath temperature increases, the equilibrium partial pressure of CO increases. At a certain temperature, the [C] content of molten steel decreases, and correspondingly, the equilibrium partial pressure of CO decreases rapidly. In addition, as the content of [C] decreases, decarburization and chromium reservation have strict requirements for reducing CO partial pressure.

Determination of Critical Carbon Content

The oxidative reactions of the carbon and chromium can be written as follows:

$$[\mathrm{C}] + \frac{1}{2}\mathrm{O_2} = (\mathrm{CO}) \tag{1}$$

$$\frac{2}{3}[\mathrm{Cr}] + \frac{1}{2}\mathrm{O_2} = \frac{1}{3}(\mathrm{Cr_2O_3}) \tag{2}$$

Combining Eqs. (1) and (2), the decarburization and chromium reservation reaction in AOD refining process of 304 stainless steel can be expressed as Eq. (3):

$$\frac{1}{3}(Cr_2O_3) + [C] = \frac{2}{3}[Cr] + CO \tag{3}$$

When the reaction achieves equilibrium, the equilibrium constant (K_1) can be determined by Eq. (4) [14]:

$$\lg K_1 = \lg \frac{f_{[Cr]}^{2/3}[\%Cr]^{2/3} p_{CO}}{f_{[C]}[\%C]} = -\frac{13114}{T} + 8.38 \tag{4}$$

The activity (a_i) of elements in molten steel can be expressed by Eq. (5):

$$a_i = f_i \cdot [\%i] \tag{5}$$

According to the thermodynamic manual, the activity interaction coefficients of each component to C and Cr ($f_{[C]}$ and $f_{[Cr]}$) in molten steel are found, and they can be calculated by Eqs. (6) and (7), respectively:

$$\lg f_{[C]} = 0.14[\%C] - 0.024[\%Cr] + 0.012[\%Ni] + 0.08[\%Si] - 0.012[\%Mn] \tag{6}$$

$$\lg f_{[Cr]} = -0.12[\%C] - 0.0003[\%Cr] + 0.0002[\%Ni] - 0.0043[\%Si] \tag{7}$$

The activities of carbon and chromium were calculated by Eqs. (5) to (7). Then, by substitute the calculation result into Eq. (4), the following result can be obtained:

$$\begin{aligned} &0.22\%[C] + \lg \%[C] - \lg p_{CO} - 0.024\%[Cr] + 0.012\%[Ni] + 0.08\%[Si] \\ &- 0.012\%[Mn] - 0.67 \lg \%[Cr] = \frac{13,114}{T} - 8.38 \end{aligned} \tag{8}$$

According to Eq. (8), p_{CO} can be obtained by R, and the actual smelting parameters can be substituted into Eq. (8) to obtain the critical carbon content, so as to judge whether the burning loss of chromium occurs in molten steel.

Application of Decarburization and Chromium Reservation Model

Optimization of Gas Supply Parameters

Taking 304 stainless steel produced by 75 t AOD furnace for 3 heats in a stainless steel production enterprise as an example, high oxygen nitrogen ratio ($R = 8.5$) blowing was used in the decarburization stage. The critical carbon content of decarburization period I and decarburization period II was calculated through the model.

Under a certain R, there is a critical carbon content correspondingly. In the actual production process, it is necessary to blow a certain flow of nitrogen (>18 Nm/min) as the protective gas during gas supply. Therefore, the actual value of R has an adjustable range. Correspondingly, there is a controllable range of critical carbon content for decarburization and chromium reservation. The controllable range of critical carbon content of decarburization period I and decarburization period II is shown in Table 1.

It can be seen from Table 1 that when the actual production heats of the 3 heats are blown with $R = 8.5$, at the end of decarbonization period II, the critical carbon contents of the 3 heats are 0.363%, 0.428%, and 0.382%, and the actual carbon contents are 0.110%, 0.093%, and 0.121%, respectively. The carbon content is lower than the critical carbon content. In the decarburization stage, when the carbon content is reduced to the critical carbon content value, the critical carbon content can be reduced by adjusting R online to reduce the burning loss of chromium in molten steel as much as possible.

Before optimizing the blowing parameters, the 75 t AOD converter adopts the gas supply mode of subsection regulation R, namely stepped gas supply, as shown in Fig. 4a. According to the mathematical model of decarburization and chromium reservation and the actual operating conditions, the gas supply mode was optimized as curved gas supply, as shown in Fig. 4b. It can be seen from Fig. 4b, when the

Table 1 Range of relevant gas supply parameters of AOD blowing

Heat	R	Pco/p^{θ}	Critical carbon content, mass pct	End of decarburization period II, mass pct
C02	0.2–8.5	0.429–1.416	0.124–0.363	0.110
C05	0.2–8.5	0.429–1.416	0.149–0.428	0.093
C06	0.2–8.5	0.429–1.416	0.131–0.382	0.121

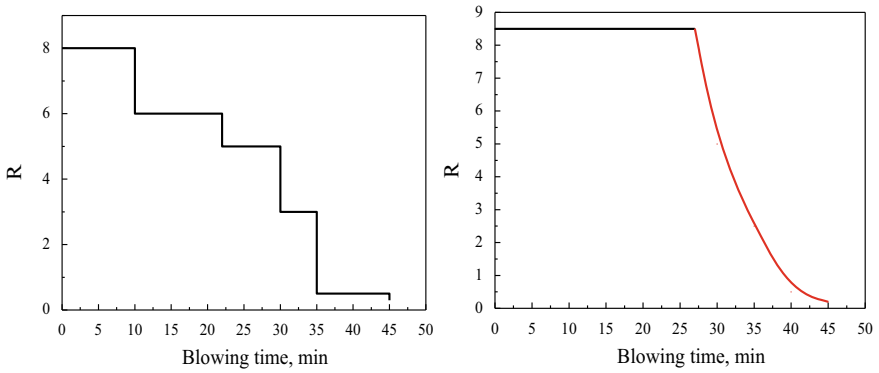

(a) stepped mode (b) curve mode

Fig. 4 Gas supply mode of the AOD blowing

carbon content of molten steel is greater than the critical value, the gas supply adopts a high *R*. On the contrary, the *R* is adjusted online, namely curve gas supply.

Model Application Results

In the process of AOD decarburization, the critical carbon content at each sampling point was calculated using the model. In the initial stage of blowing, high *R* was adopted to improve the decarburization efficiency, which is conducive to a rapid temperature rise of molten bath and shortening smelting cycle. When the carbon content in steel drops to a critical value, the AOD blowing adopts the curve mode of gas supply for decarburization and chromium reservation. In a stainless steel production enterprise, the optimized AOD gas supply scheme was adopted to smelt 10 heats of 304 stainless steel in the 75 t AOD furnace. Compared with 10 heats with similar initial boundary conditions without optimizing gas supply, their relevant production indexes are shown in Table 2.

According to Table 2, compared with the conventional stepped gas supply under similar initial boundary conditions, after optimizing the gas supply parameters, the burning loss of molten steel chromium was significantly reduced, the ferrosilicon consumption of each furnace was reduced, and the smelting cycle was shortened. After optimizing the gas supply parameters, in the initial stage of blowing, the oxygen supply intensity was improved, the decarburization speed was accelerated, and the average smelting cycle was shortened by 6.4 min. In the later stage of blowing, the curve gas supply was adopted. Compared with the conventional gas supply mode, namely stepped mode, the burning loss of chromium was reduced by 1.86%. In the reduction stage, ferrosilicon was added to reduce (Cr_2O_3) in the slag. By optimizing the gas supply parameters, the average consumption of ferrosilicon per heat was reduced by 379.2 kg (34.3%).

Conclusions

In this study, a decarburization and chromium reservation model in AOD refining process of 304 stainless steel was established. By using this model, *R* adjustment in the refining process was guided, and the optimization of gas supply has achieved good metallurgical results. The following conclusions were drawn: Firstly, according to the theory of competitive oxidation of carbon and chromium, in the process of decarburization in the AOD furnace, increasing the bath temperature and reducing p_{CO} are beneficial to the decarburization and chromium reservation of molten steel. The value of p_{CO} is controlled by *R*, and adjusting *R* can achieve the purpose of decarburization and chromium reservation. Secondly, there is a critical carbon content for decarburization and chromium reservation of refining 304 stainless steel

Table 2 Relevant data for refining process of 304 stainless steel 75 t AOD furnace

Heat	Mass of steel, t	End of blowing (Cr_2O_3), Mass Pct	Ferrosilicon consumption, kg	Smelting cycle, min
1	73.5	5.35	1350	95
1’	72.8	2.13	805	78
2	75.6	4.52	1642	86
2’	75	4.30	1350	74
3	78	6.03	1602	90
3’	77.8	2.49	1190	79
4	74	5.64	1410	89
4’	74.7	3.60	1000	89
5	74	4.77	1474	67
5’	74.5	3.56	1015	66
6	72	4.31	1377	78
6’	73.1	2.95	1180	75
7	70	6.07	1236	77
7’	71.9	4.83	1125	71
8	75	5.25	1467	80
8’	74.3	3.73	1096	76
9	76	5.82	1580	83
9’	75.7	3.58	1230	81
10	79	5.13	1695	88
10’	78	3.15	1050	80

1–10: The optimized gas supply of blowing
1’–10’: The conventional gas supply of blowing

in the 75 t AOD furnace. This critical value can be calculated by the decarburization and chromium reservation model, to reduce the oxidation of chromium in blowing. Thirdly, compared with the conventional gas supply mode, the burning loss of chromium can be reduced by 1.86% through optimizing the gas supply parameters, the average ferrosilicon consumption per heat was reduced by 379.2 kg (34.3%), and the average smelting cycle can be shortened by 6.4 min.

Acknowledgements The work supported by the Fundamental Research Funds for the Central Universities (Grant No. FRF-AT-20-13).

References

1. Pariser HH, Backeberg NR, Masson O et al (2018) Changing nickel and chromium stainless steel markets—a review. J South Afr Inst Min Metall 118(6):563–568

2. Chen XR, Cheng GG, Hou YY et al (2019) Oxide-inclusion evolution in the steelmaking process of 304L stainless steel for nuclear power. Metals 257(9):1–11
3. Chen XR, Cheng GG, Hou YY et al (2020) Influence of refining process and utilization of different slags on inclusions, titanium yield and total oxygen content of Ti-stabilized 321 stainless steel. J Iron Steel Res Int 27(8):913–921
4. Kim WY, Nam GJ, Kim SY (2021) Evolution of non-metallic inclusions in Al-killed stainless steelmaking. Metall Mater Trans B 52(3):1508–1520
5. Wei W, Gustavsson J, Samuelsson PB et al (2021) Prediction of nitrogen behaviour in the AOD process by a time-dependent thermodynamic model. Ironmaking Steelmaking 1–13
6. Mani C, Karthikeyan R, Davim JP (2020) A review on austenitic stainless steel-based dissimilar metal welding using gas tungsten Arc welding. J Manuf Technol Res 12(1/2):65–82
7. Liu YL, Guo GC, Bin H et al (2018) Formation of non-metallic inclusions of Si-killed stainless steel during GOR refining process. High Temp Mater Processes (London) 37(6):521–529
8. Andersson N, Tilliander A, Jonsson LTI et al (2012) Investigating the effect of slag on decarburization in an AOD converter using a fundamental model. Steel Res Int 84(2):169–177
9. Andersson N, Tilliander A, Jonsson L, Jönsson PG (2012) An in-depth model-based analysis of decarburization in the AOD process. Steel Res Int 83(11):1–14
10. Deo B, Kumar S (2013) Dynamic on-line control of stainless steel making in AOD. Adv Mater Res 794:50–62
11. Wei JH, Zhu DP (2002) Mathematical modeling of the argon-oxygen decarburization refining process of stainless steel: part I. Mathematical model of the process. Metall Mater Trans B 33(1):111–119
12. Pisilä SE, Järvinen MP, Kärnä A et al (2011) Fundamental mathematical model for AOD process: part II: model validation. Steel Res Int 82(6):650–657
13. Wei JH, Zhu DP (2002) Mathematical modeling of the argon-oxygen decarburization refining process of stainless steel: part II. Application of the model to industrial practice. Metall Mater Trans B 33(1):121–127
14. Chen C (2005) Application of the selective oxidation in carbon elimination and chromium conservation of stainless steel. Sci/Tech Inf Dev Econ 58(2):40–46(7)

Part II
Energy Efficient Clean Metallurgical Technologies

Removal of Arsenic from Leaching Residue of Tungsten

Liqiang Xu, Chunfa Liao, Sui Xie, and Baojun Zhao

Abstract After years of exploitation of tungsten ore in China, the average grade of tungsten ore has decreased obviously, and the contents of impurities are getting higher and higher. Arsenic is commonly present in wolframite [(Fe, Mn)WO_4] resulting in As-containing leaching residue. The residue is therefore classified as hazardous waste due to its heavy metal content, especially the arsenic content up to 2 wt%. The arsenic has to be removed before the residue can be used or treated. A technique involving sodium carbonate roasting–water leaching has been developed to remove arsenic from tungsten leaching residue efficiently. The optimized parameters were determined experimentally, and the reaction mechanisms have been analyzed by FactSage 8.1. The results show that the arsenic content in the residue can be reduced below 0.1% and the tungsten in the residue is also recovered in the same time.

Keywords Tungsten · Leaching residue · Arsenic · Roasting · FactSage

Introduction

Tungsten is one of the critical minerals with wide applications. The most common tungsten minerals are wolframite (Fe,Mn)WO_4 and scheelite $CaWO_4$ [1–3]. Leaching of the tungsten minerals is the key process in production of the final products. The leaching residue is increasing continuously since the grade of the tungsten ore is decreasing [4, 5]. Due to the complexity of the ores and processes used, 2–5 wt% WO_3 and other valuable elements are remained in the leaching residues [5].

L. Xu · S. Xie · B. Zhao (✉)
International Research Institute for Resources, Energy, Environment and Materials, Jiangxi University of Science and Technology, Ganzhou, China
e-mail: bzhao@jxust.edu.cn

L. Xu · C. Liao · S. Xie · B. Zhao
College of Materials, Metallurgy and Chemistry, Jiangxi University of Science and Technology, Ganzhou, China

Z. Peng et al. (eds.), *12th International Symposium on High-Temperature Metallurgical Processing*, The Minerals, Metals & Materials Series,
https://doi.org/10.1007/978-3-030-92388-4_8

With nearly 1 million tons of the leaching residue in stock, approximately 70,000–80,000 tons residue is producing annually in China. Treatment of these residues to recover valuable elements has attracted extensive researches [4–7].

Arsenic is commonly present in the wolframite resulting in arsenic-containing residue [8, 9]. The leaching residue containing over 0.1 wt% As is defined as dangerous waste since arsenic is harmful to human health [10, 11]. With the decrease of tungsten ore grade, the impurities including arsenic in tungsten ore are increasing continuously [12–14]. It is urgent to develop a suitable process to efficiently treat the residue and recover the valuable elements. A high-temperature process to treat the tungsten leaching residue under reducing condition has been developed recently [15–17]. W–Fe–Mn alloy can be produced from the process and used for production of cast iron. However, it was found that the arsenic from the leaching residue can also come to the alloy, causing the alloy to be contaminated with arsenic [15]. It is essential to remove arsenic before alloy production for efficient utilization of the leaching residue.

It was observed that arsenic is present in the leaching residue as FeAsS which is the same mineral from the tungsten ore [15]. This confirms that FeAsS did not react with any other components during the leaching process. Thermodynamic analyses indicate that arsenic can be removed from the residue at different conditions. High-temperature experiments were carried out to evaluate these methods.

Methodology

Three approaches were considered to remove arsenic from tungsten leaching residue based on the thermodynamic analyses. Three series of experiments have been conducted in different conditions to evaluate the approaches proposed. The composition of the leaching residue from industry is given in Table 1. The residue contains 0.8 wt% As_2O_3 and 3.8 wt% WO_3. 18.2 wt% MnO and 39.5 wt% Fe_2O_3 indicate that the residue was mainly resulted from wolframite (Fe,Mn)WO_4, and certain amount of scheelite $CaWO_4$ was also involved as 15.3 wt% CaO is present. As-received leaching residue consisted of significant moisture. The residue was dried completely for all experiments, and the composition given in Table 1 does not include water.

In the first series of experiments, 60 g dry residue sample placed in an alumina crucible was heated at 800 °C for 4 h under high-purity argon flow. Po_2 was estimated to be 10^{-5} atm according to the O_2 and H_2O concentrations in the gas. After cooling, the sample was then ground for further reduction experiments. 10 g sample was mixed with 1 g SiO_2 and 1 g graphite powder and pelletised. The pellets placed

Table 1 Composition of the dry tungsten leaching residue

Sample	WO_3	Na_2O	Al_2O_3	SiO_2	SO_3	K_2O	CaO	MnO	Fe_2O_3	As_2O_3
WZ1	3.8	3.6	3.9	10.4	4.9	0.4	15.3	18.2	39.5	0.80

in an alumina crucible were heated to 1450 °C for 60 min under high-purity argon flow. The sample was rapidly cooled on the bottom of the furnace with argon gas flashing. The alloy and slag were removed from the crucible and crushed to analyse their compositions by XRF.

In the second series of experiments, 20 g dried leaching residue was pelletised and heated to 1000 °C or 1100 °C for 2 or 4 h. Alumina crucible was used for the experiments, and mixtures of air and N_2 were used to obtain the oxygen partial pressure between 0.02 and 0.1 atm. After heat treatment under controlled oxygen partial pressures, the samples were cooled on the bottom of the furnace and then removed from the crucible for XRF analysis.

The third series experiments were sodium carbonate roasting followed by water leaching. 50 g dried leaching residue was mixed with sodium carbonate according to the required ratios. The mixed sample in alumina crucible was heated in a muffle furnace at 700–900 °C for 1–2 h. The heated samples were ground and leached with water. The second leaching residue was dried for XRF analysis.

FactSage 8.1 software was used in the thermodynamic calculations [18]. The databases selected in FactSage 8.1 for calculations were "FactPS" and "FToxide". The solution phases selected in the calculations included "FToxid-SLAGA", "FToxid-SPINA", and "FToxid-MeO".

Results and Discussion

It has been confirmed from the analysis of tungsten leaching residue that FeAsS from the tungsten ore did not react with other components and air during high-temperature leaching process [15]. The first and second series of experiments were planned based on the assumption that FeAsS will only react with the gas at relatively lower temperatures. The products of the reactions will be As and As_2O_3 vapors leaving the condensed system.

Removal of Arsenic as Decomposition Product

Thermodynamic analysis by FactSage 8.1 [18] indicates that FeAsS is completely decomposed into solid FeS and gas As at temperatures above 614 °C:

$$\mathrm{FeAsS(s)} \rightarrow \mathrm{As(g)} + \mathrm{FeS(s)} \tag{1}$$

After the residue was heated at 800 °C for 4 h under high-purity argon flow, 10 g heated sample was mixed with 1 g SiO_2 and 0.8 g, 1 g and 1.2 g graphite powder, respectively. Three samples were treated at 1450 °C for 60 min in high-purity argon atmosphere. The compositions of the alloys and slags from three experiments are given in Table 2. It can be seen that the alloy mainly consists of Fe and W when carbon

Table 2 Compositions of the slags and alloys analysed by XRF

Alloy	W	Na	Al	Si	S	K	Ca	Mn	Fe	As
1	9.9	0.0	0.0	0.0	0.3	0.0	0.0	0.1	87.8	1.6
2	8.7	0.0	0.0	0.0	0.2	0.0	0.0	0.5	89.1	1.3
3	7.6	0.0	0.0	0.0	0.0	0.0	0.0	13.4	77.9	0.9
Reduced slag	WO_3	Na_2O	Al_2O_3	SiO_2	SO_3	K_2O	CaO	MnO	Fe_2O_3	As_2O_3
1	0.8	3.9	19.7	27.2	0.5	0.5	18.4	21.2	7.8	0.0
2	0.1	4.0	22.1	28.8	0.4	0.6	19.4	22.0	2.6	0.0
3	0.0	4.2	22.0	33.1	0.8	0.6	22.3	16.8	0.2	0.0

is lower than 1 g. 13.4 wt% Mn is present in the alloy if carbon is increased to 1.2 g. Unfortunately, 0.9–1.6 wt% As is present in all alloys. The arsenic concentration in the alloy decreases with increasing carbon. It is clear that the arsenic in the leaching residue was not removed according to Reaction 1. It seemed that FeAsS reacted with other components such as Na_2O, K_2O, and CaO. It is noted from Table 2 that all arsenic was removed from the slag during the reduction process. All iron and tungsten are recovered in the alloy with addition of 1.2 g carbon for 10 g residue.

Removal of Arsenic as Oxide

FactSage calculations indicate that As_2O_3 can be formed under controlled oxygen partial pressures and vaporized at the temperature above 465 °C:

$$FeAsS(s) + O_2(g) \rightarrow As_2O_3(g) + Fe_3O_4(s) + SO_2(g) \quad (2)$$

Analyses of the second series of samples indicate that, after heat treatment at temperatures 1000–1100 °C under oxygen partial pressure 0.02 to 0.1 atm, the As_2O_3 in the samples is still 0.6–0.7 wt%. This means that the arsenic was not removed according to Reaction 2. Again, it seems that the assumption of FeAsS not reacting with other components was not correct. If the residue composition given in Table 1 is used for FactSage calculations to consider the oxidation of FeAsS, the results are shown in Figs. 1 and 2 for 900 °C and 1100 °C, respectively. According to the calculations, the products of residue oxidation include liquid slag, spinel Fe_3O_4, $Fe_2(AsO_4)_2$, and gas. Only the spinel does not include arsenic in these phases. Arsenic in the slag and $Fe_2(AsO_4)_2$ will stay in the condensed system. Only the arsenic in gas can be removed from the condensed system.

It can be seen from Fig. 1 that at 900 °C, there is a small window of 45–47 g O_2 per 100 g FeAsS in which only the spinel and gas are present. In ideal situation, all arsenic can be removed as gas. This window is increased significantly when the temperature is increased to 1100 °C as shown in Fig. 2. However, the second series experiments did not achieve the expected results as shown in Fig. 2. It seems that

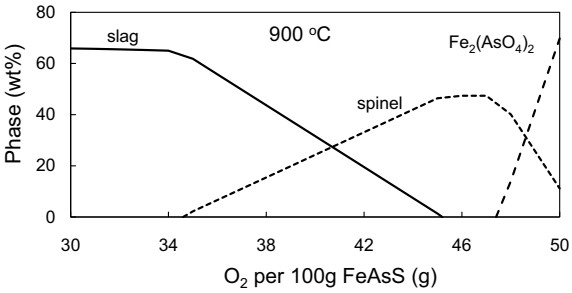

Fig. 1 Percentage of the condensed phases present for oxidation of FeAsS at 900 °C calculated by FactSage 8.1 [18]

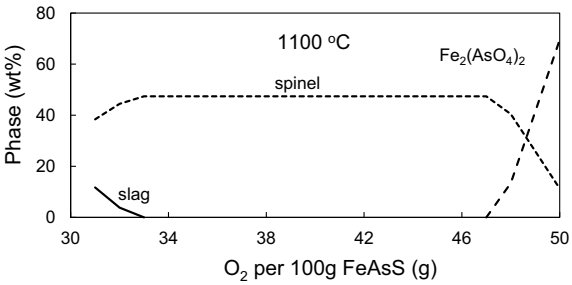

Fig. 2 Percentage of the condensed phases present for oxidation of FeAsS at 1100 °C calculated by FactSage 8.1 [18]

the mixed gas of air and N_2 did not provide enough O_2 for the reactions to reach the window between 33 and 47 g O_2 per 100 g FeAsS as shown in Fig. 2. It is difficult to control the amount of oxygen to react with the multi-phases to attain equilibrium.

In conclusion, in the temperature range 800–1100 °C, the FeAsS in the tungsten leaching residue can react with other components present in the residue. It is difficult to remove arsenic from the condensed system by vaporization.

Removal of Arsenic by Roasting and Leaching

It has been demonstrated that direct leaching or high-temperature vaporization cannot remove arsenic from the leaching residue. A roasting–leaching approach was proposed to produce harmless residue based on the following reactions:

$$FeAsS(s) + Na_2CO_3(s) + O_2(g) \rightarrow Na_3AsO_4(s) + Fe_2O_3(s) + CO_2(g) + SO_2(g) \quad (3)$$

$$FeAsS(s) + K_2CO_3(s) + O_2(g) \rightarrow K_3AsO_4(s) + Fe_2O_3(s) + CO_2(g) + SO_2(g) \quad (4)$$

The roasting products Na_3AsO_4 and K_3AsO_4 can dissolve into water and therefore separate from the residue. Thermodynamic analysis by FactSage 8.1 is shown in

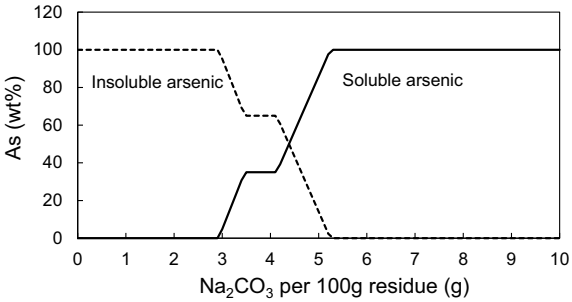

Fig. 3 Percentage of the soluble and insoluble arsenic as a function of sodium carbonate at 800 °C calculated by FactSage 8.1 [18]

Fig. 3. 100 g as-received leaching residue reacts with different amounts of Na_2CO_3 at 800 °C. The insoluble arsenic in the figure represents AsFeS and As-containing slag. The soluble arsenic in the figure represents Na_3AsO_4 and K_3AsO_4 that can be dissolved into water. The Na_2CO_3 can directly react with SO_3, WO_3, Al_2O_3, and SiO_2 at different extents. It seems that Reaction 3 only starts when Na_2CO_3 is higher than 3 g. It can be seen from the figure that the insoluble arsenic decreases and the soluble arsenic increases with increasing Na_2CO_3. When Na_2CO_3 is higher than 5.2 g for 100 g residue, all arsenic is converted to the soluble arsenic. Thermodynamic calculations give only the trend of the reactions. In practice, the Na_2CO_3 consumption is always much higher than the theoretical values.

The conditions and results of the roasting–leaching experiments are presented in Table 3. The new leaching residue is named as second residue to be differentiated from the original leaching residue. Experiments 4–8 describe the effect of Na_2CO_3 on the removal of arsenic. Experiments 6, 9, and 10 describe the effect of temperature on the removal of arsenic. It can be seen from Table 3 that not only arsenic, but also tungsten decreases with increasing Na_2CO_3. The aqueous leachate containing both tungsten and arsenic is similar to the conventional leachate which can be processed in the existing plant to remove arsenic and recover tungsten. The second residue with low arsenic is harmless and can be used for cement production.

Figure 4 shows the remaining arsenic and tungsten in the second residue. It can be seen from the figure that when Na_2CO_3 is higher than 30 g, the As in the second residue is below 0.1 wt% which makes the residue harmless according to the environmental policy. At the same conditions, the WO_3 in the second residue is decreased from 3.8 to 0.4–0.7 wt%. Over 90% tungsten is recovered, and nearly 90% arsenic is removed from the as-received residue in this process.

Figure 5 shows the remaining arsenic and tungsten in the second residue as a function of temperature. It can be seen from the figure that both arsenic and tungsten remained in the second residue decrease with increasing temperature. 800 °C seems to be a minimum temperature to enable the remaining arsenic in second residue to be lower than 0.1 wt%. Increase of temperature from 800 to 900 °C can slightly decrease arsenic in second residue but can significantly decrease tungsten in second residue.

Table 3 Compositions of the second residue after sodium carbonate roasting–water leaching (wt%)

Exp.	Temperature (°C)	Na_2CO_3/residue (wt)	WO_3	Na_2O	Al_2O_3	SiO_2	SO_3	K_2O	CaO	MnO	Fe_2O_3	As
4	800	10	3.4	5.6	5.1	12.2	1.8	0.2	18.1	15.8	37.1	0.7
5	800	20	3.5	8.2	4.6	11.6	1.9	0.3	17.3	15.3	36.7	0.6
6	800	30	0.7	7.9	4.3	11.3	0.7	0.1	18.8	16.2	39.7	0.1
7	800	40	0.5	9.7	4.6	10.2	0.5	0.2	18.9	16.8	38.5	0.1
8	800	50	0.4	10.2	5.0	10.2	0.3	0.1	18.9	16.6	38.0	0.1
9	700	30	1.7	8.1	4.3	11.4	0.9	0.3	18.9	16.2	37.8	0.3
10	900	30	0.3	9.0	4.9	11.6	0.7	0.1	18.0	16.3	39.0	0.1

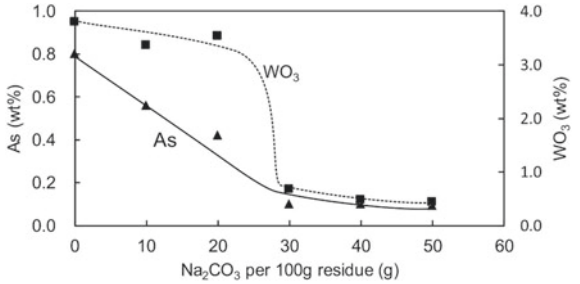

Fig. 4 Effect of sodium carbonate on remaining arsenic and tungsten in the second residue

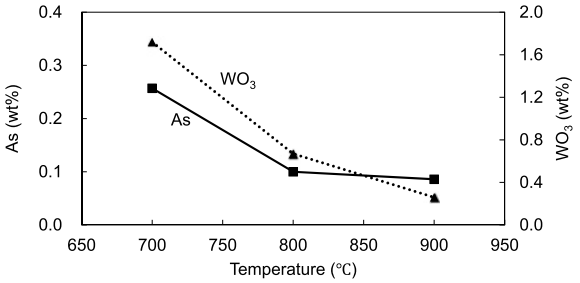

Fig. 5 Effect of temperature on remaining arsenic and tungsten in the second residue

Conclusions

High-temperature experiments have been conducted to evaluate the proposed approaches to remove arsenic from tungsten leaching residue. It is not possible to remove arsenic from the residue by vaporization. Reactions of the arsenic with other components in the residue stopped vaporization of arsenic in the forms of element or oxide.

Roasting–leaching route is an effect process to remove arsenic from the residue. Optimum Na_2CO_3 addition and temperature have been identified from the experiments to obtain harmless residue. At the same conditions, over 90% valuable tungsten can also be recovered. The aqueous leachate containing tungsten and arsenic can be processed in the existing plant to remove arsenic and recover tungsten.

References

1. Pitfield P, Brown T (2011) Tungsten. British Geological Survey, Natural Environment Research Council
2. Premchand (1996) Processing of low grade tungsten ore concentrates by hydrometallurgical route with particular reference to India. Bull Mater Sci 19(2):295
3. Gedgagov EI, Besser AD, Yanakov VYa, Smolyarchuk VP (2009) Analyzing the raw materials market and methods for processing tungsten concentrates to obtain competitive products. Theor Found Chem Eng 43(4):529

4. Zhu X, Liu X, Chen X, Li J, He L, Zhao Z (2019) Comprehensive utilization and development trend of tungsten smelting slag. Conserv Utilization Mineral Resour 39(3):119
5. Dai Y, Zhong H, Zong H (2012) Novel process for preparation of mangano-manganic oxide from tungsten residue. Chin J Nonferrous Metals 22(4):1242
6. Luo X, Liu B, Tang M (2005) Experimental investigation of complex recovery of valuable minerals containing in the residue abandoned in wet-metallurgical process of wolframite. China Tungsten Ind 20(3):24
7. Liu H, Liu H, Nie C, Zhang J, Steenari BM, Ekberg C (2020) Comprehensive treatments of tungsten slags in China: a critical review. J Environ Manage 270:110927. https://doi.org/10.1016/j.jenvman.2020.110927
8. Chen YL, Guo XY, Wang QM, Tian HQ, Huang SB, Zhang JX (2021) Tungsten and arsenic substance flow analysis of a hydrometallurgical process for tungsten extracting from wolframite. Tungsten 3:348–360
9. Xie H, Zhao ZW, Cao CF, Liang Y, Li JT (2012) Behavior of arsenic in process of removing molybdenum by sulfide method. J Cent South Univ 42(2):435–439
10. Duker AA, Carranza EJM, Hale M (2005) Arsenic geochemistry and health. Environ Int 31:631–641
11. Williams PN, Price AH, Raab A, Hossain SA, Feldmann J, Meharg AA (2005) Variation in arsenic speciation and concentration in paddy rice related to dietary exposure. Environ Sci Technol 39:5531–5540
12. Li YL, Zhao ZW (2017) Separation of molybdenum from acidic high-phosphorus tungsten solution by solvent extraction. JOM 69(10):1920–1924
13. Yang Y, Xie BY, Wang RX, Xu SM, Wang JL, Xu ZH (2016) Extraction and separation of tungsten from acidic high-phosphorus solution. Hydrometallurgy 164:97–102
14. Liu CP, Luo CL, Gao Y, Li FB, Lin LW, Wu CA, Li XD (2010) Arsenic contamination and potential health risk implications at an abandoned tungsten mine, Southern China. Environ Pollut 158:820–826
15. Wang X, Ma X, Su K, Liao C, Zhao B (2020) Fundamental studies for high temperature processing of tungsten leaching residues for alloy formation. Tungsten 2(4):362–370
16. Wang X, Ma X, Liao C, Zhao B (2020) High temperature processing of tungsten slag. In: Proceedings of the 11th international symposium on high-temperature metallurgical processing. The Minerals, Metals & Materials Series, San Diego; Springer, Cham, pp 289–294
17. Su K, Ma X, Zhao B (2021) Harmless treatment and valuable metals recovery of tungsten leaching residues: a thermodynamic and experimental study. JOM 73(6):1937–1946. https://doi.org/10.1007/s11837-021-04682-2
18. Bale CW, Bélisle E, Chartrand P, Degterov SA, Eriksson G, Gheribi AE, Hack K, Jung IH, Kang YB, Melançon J, Pelton AD, Petersen S, Robelin C, Sangster J, Spencer P, Van Ende MA (2016) FactSage thermochemical software and databases. Calphad 54:35–53

Experimental Studies on Reduction Mechanisms of Lead-Rich Slag with Different PbO Concentrations

Sui Xie, Chunfa Liao, and Baojun Zhao

Abstract Smelting reduction of lead-rich slag is a clean technology recently developed in China to produce primary lead metal. The technology has the advantages of more efficient capture of SO_2 and lead fugitive emissions and low energy consumption. The extent of the slag reduction was continuously measured by the product gas volume. Effect of PbO concentration on the reduction of lead-rich slag was determined in the temperature range 1073–1473 K. The reduction of lead-rich slag by carbon was found to be chemically controlled at early stage and then diffusion-controlled at late stage. The activation energy for chemically controlled reduction decreases with increasing PbO concentration in lead-rich slag. The reaction mechanism has been discussed by experimental results and FactSage 8.1.

Keywords Lead-rich slag · Reduction · PbO concentration · Kinetics · FactSage

Introduction

Lead is widely used in chemical power sources, metallurgy, and radiation protection due to the characteristics of excellent ductility, corrosion resistance, and low electrical conductivity [1, 2]. The lead-rich slag has been used to replace sinter to produce lead metal [3, 4]. Smelting oxidation and reduction process to produce lead metal simplifies the operation, increases the capture of SO_2 and decreases the energy consumption [5–7].

Kinaev et al. studied the reduction of lead oxide by carbon at high temperature [8]. It was found that the reduction was the chemical-controlled stage at the first stage, mixed controlled at the second stage, and diffusion-controlled at the last stage [8].

S. Xie · B. Zhao (✉)
International Research Institute for Resources, Energy, Environment and Materials, Jiangxi University of Science and Technology, Ganzhou, China
e-mail: bzhao@jxust.edu.cn

S. Xie · C. Liao · B. Zhao
College of Materials, Metallurgy and Chemistry, Jiangxi University of Science and Technology, Ganzhou, China

Z. Peng et al. (eds.), *12th International Symposium on High-Temperature Metallurgical Processing*, The Minerals, Metals & Materials Series,
https://doi.org/10.1007/978-3-030-92388-4_9

Zhao et al. investigated the reduction of synthetic lead slags and industrial lead sinters by CO gas and examined the microstructure and phase compositions of the reduced sample [9]. Liao and Zhao studied the phase equilibria of the system "Fe_2O_3"–ZnO–Al_2O_3–(PbO+CaO+SiO_2) to characterize the lead-rich slag [10]. The softening behaviors of lead-rich slag and sinter were investigated under reducing condition, and the reduced samples were examined by EPMA [11, 12]. Yang et al. reported the effect of CaO/SiO_2 ratio on the reduction of lead-rich slag by carbon [13]. In the present study, the reduction experiments of lead-rich slag with different PbO concentrations were systematically carried out between 1073 and 1473 K. The reduction kinetics are discussed by experimental results and thermodynamic calculations [14–17].

Experimental

Materials

YM1, YM2, and YM3 are the synthetic slags prepared from pure PbO, ZnO, Fe_2O_3, $CaCO_3$, and SiO_2 in air. Table 1 shows the compositions of the YM1, YM2, and YM3. These samples have approximately the same ZnO/Fe_2O_3/CaO/SiO_2 ratios but different PbO concentrations to cover the range of the potential industrial lead-rich slags. The samples contain up to 3.2 wt% Al_2O_3 because they were prepared in alumina crucibles.

Experimental Procedure

The equipment used in the reduction experiments is shown in Fig. 1. The experiments were performed in a 19 mm ID corundum tube. The graphite crucible (18 mm OD, 14 mm ID, and 40 mm high) was placed on a platform consisting of an inverted corundum crucible and supported by a corundum thermocouple sheath in which a R-type thermocouple was inserted. The graphite crucible was introduced into the reaction tube from the bottom of the furnace and held on the hot zone under Ar gas flow. Then, the reaction tube was sealed, and the gas flashing was stopped.

Table 1 Compositions of the lead-rich slags for reduction experiments

Sample	PbO	ZnO	Fe_2O_3	CaO	SiO_2	Al_2O_3
YM1	58.7	9.1	13.1	5.5	10.4	3.2
YM2	51.8	11.4	17.0	6.7	11.9	1.3
YM3	47.3	13.3	19.6	7.4	12.1	0.3

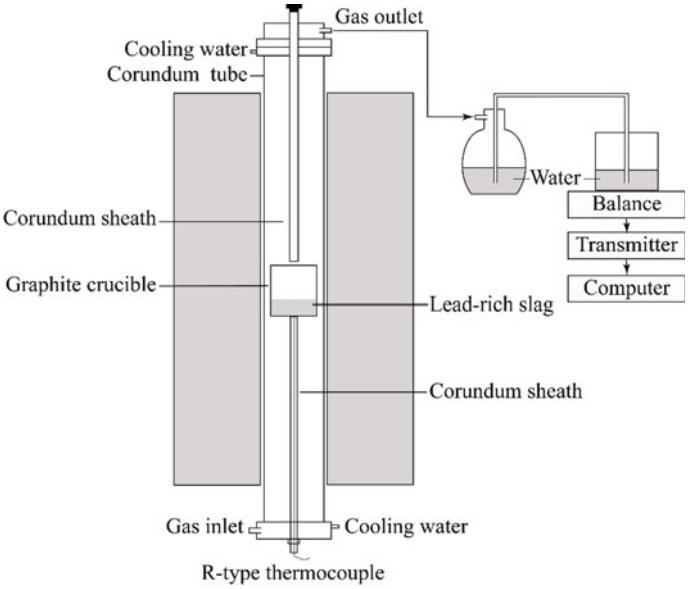

Fig. 1 Assembly of the vertical tube furnace, gas collection, and data record system

5.00 g lead-rich slag (~1 mm diameter size) was added from the top of the furnace into the graphite crucible, and the system was sealed again. As the lead-rich slag touched the hot graphite crucible, the reduction reaction started, and the product gas was released. The gas generated from the reduction included CO and CO_2. However, the gas composition was not determined, and the total gas volume was used to represent the reduction extent. A water-containing pressure device captured the CO/CO_2 gas generated from the reduction reaction. The same volume of water was displaced by the captured gas into a container on a balance. The volume of the CO/CO_2 gas produced from the reduction was determined by continuously measuring the weight of the displaced water every 5 s. The graphite crucible and reduction products were cooled with the furnace to room temperature under Ar gas flow as the reduction reaction finished.

FactSage Calculations

FactSage 8.1 software was used in the thermodynamic calculations [18]. The databases selected in FactSage 8.1 for calculations were "FactPS" and "FToxide". The solution phases selected in the calculations included "FToxid-SLAGA", "FToxid-SPINA", "FToxid-MeO", "FToxid-cPyrA", "FToxid-PyrA",

"FToxid-WOLLA", "FToxid-Bred", "FToxid-bC2SA", "FToxid-aC2SA", "FToxid-Mel", "FToxid-Oliv", "FToxid-Mull", "FToxid-CORU", "FToxid-ZNIT", "FToxid-WILL", "FToxid-PbO", and "FToxid-PCSi".

Results and Discussion

Thermodynamic Analysis

The reactions between the lead-rich slag and carbon include

$$\mathrm{PbO(l) + C(s) = Pb(l) + CO(g)} \tag{1}$$

$$\mathrm{Fe_2O_3(l) + C(s) = 2FeO(s) + CO(g)} \tag{2}$$

$$\mathrm{ZnO(l) + C(s) = Zn(g) + CO(g)} \tag{3}$$

$$\mathrm{FeO(l) + CO = Fe(s) + CO(g)} \tag{4}$$

YM1 is taken as an example to describe the processes of reaction 1 to reaction 4 calculated by FactSage 8.1. It can be seen from Fig. 2 that the reduction of Fe_2O_3 to FeO (reaction 2) started first followed by the reduction of PbO (reaction 1). The reduction of ZnO to Zn (reaction 3) started significantly after reactions 1 and 2 almost completed. Metallic iron was not observed in the reduced samples indicating that reaction 4 did not happen in the temperature range investigated.

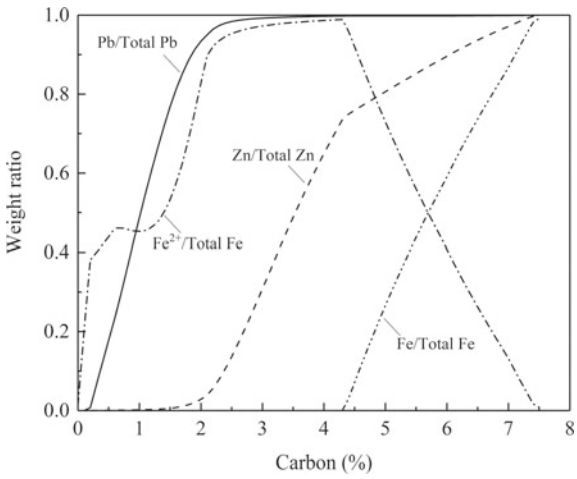

Fig. 2 Equilibrium extents of reactions (1) to (4) at 1473 K calculated by FactSage 8.1

Reduction Experiments

The theoretical volume of the gas generated by Eqs. (1)–(3) can be calculated from the composition and weight of the lead-rich slag. The reduction of FeO(l) to Fe(s) can be neglected because Fe metal was not observed after the reduction. The reducibility is described as follows:

$$\alpha = V_m \times 100\% / V_T \tag{5}$$

where V_m is the volume of the gas measured, V_T is the theoretical volume of the gas produced from Eqs. (1)–(3), and α is the reducibility. The reducibility of YM1 and YM3 is presented in Figs. 3 and 4, respectively. The reducibility of YM2 as a function of reaction time has been reported previously [6].

It can be seen from Figs. 3 and 4 that the reducibility of YM1 and YM3 increases rapidly at the beginning and then slows down with the reaction time. It seems that the reduction of lead-rich slag by carbon is chemical-controlled stage at the first stage and diffusion-controlled at the last stage. The reduction was mixed controlled between the chemical-controlled stage and the diffusion-controlled stage. It is also shown that the reaction between carbon and lead-rich slag was limited at temperatures below 1173 K.

The reducibility of lead-rich slag increases with increasing reaction time and temperature. The reducibility of YM1, YM2, and YM3 at the identical reduction time 100 s and 3600 s are presented in Figs. 5 and 6, respectively. It can be seen from Fig. 5 that in the chemically controlled stage, the reducibility of each slag increases with increasing temperature. At the same temperature, the reducibility of the lead-rich slag increases with increasing the PbO concentration in the slag. Figure 6 shows the same trends for the diffusion-controlled reactions at 3600 s. However, the effect

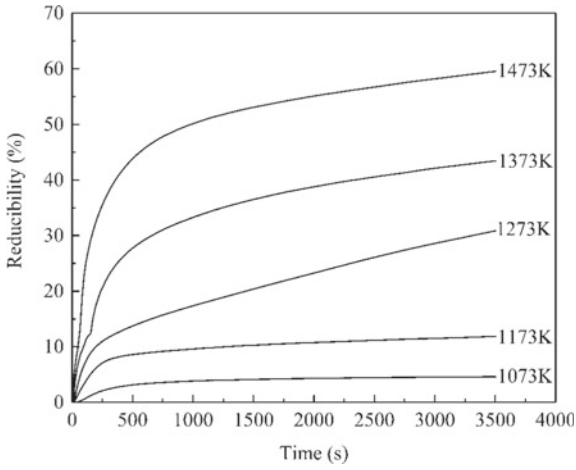

Fig. 3 Reducibility of YM1 in graphite crucible as a function of reaction time

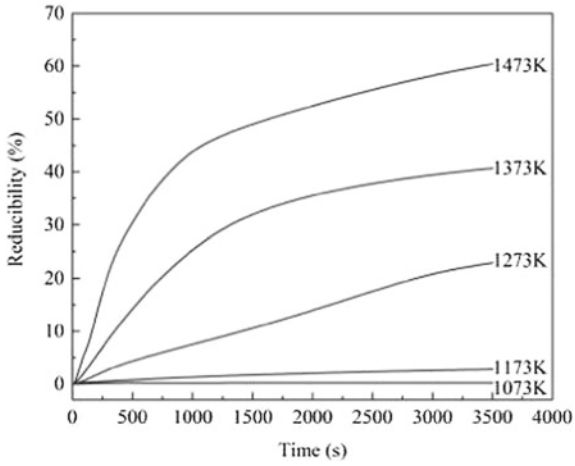

Fig. 4 Reducibility of YM3 in graphite crucible as a function of reaction time

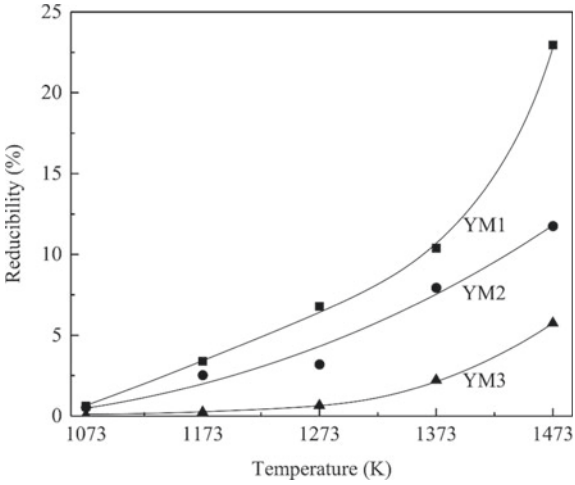

Fig. 5 Comparison of reducibility for slags at 100 s reaction

of PbO concentration on the reducibility is not as significant as that for the chemically controlled reactions.

Reduction Kinetics

The kinetic analysis of the reduction contains two steps:

(1) To calculate the values of the rate constants (k) from the reducibility as a function of reaction time at different temperatures. The reduction reaction was mainly the liquid–solid reaction. The reduction was controlled by the

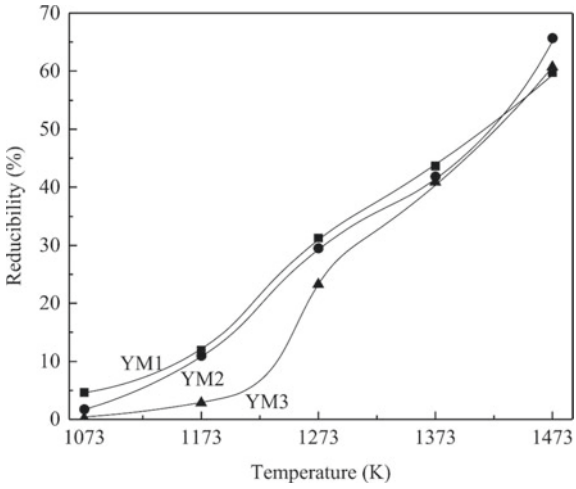

Fig. 6 Comparison of reducibility for slags at 3600 s reaction

chemical reaction at the initial stage, and the shrinking core model is suggested to describe the reduction [14–17]:

$$1 - (1 - \alpha)^{1/3} = kt \tag{6}$$

where α is the reducibility of the reduction, k is the reaction rate constant, and t is the reduction time.

(2) To get activation energy from the fitting of $k - T$ relationship with Arrhenius equation:

$$k = Ae^{-E/RT} \tag{7}$$

where A is the pre-exponential factor (s^{-1}), E is the activation energy (J mol^{-1}), R is the gas constant (8.314 J mol^{-1} K^{-1}), and T is the absolute temperature (K). Figure 7 shows the realtionship between ln(k) and 1/T for the reduction reaction of YM1 at the chemically controlled stage.

The activation energy of YM1 at the chemically controlled stage can be calculated by the slope of ln(k) against 1/T from Fig. 7 which is 94.0 kJ/mol. In the same way, the activation energy of YM2 and YM3 is 94.9 kJ/mol and 139.7 kJ/mol, respectively, at the chemically controlled stage. It looks like that the activation energy does not change significantly when the PbO concentration in the slag decreased from 58.7 wt% (YM1) to 51.8 wt% (YM2). However, further decrease of PbO concentration from 51.8 wt% (YM2) to 47.3 wt% (YM3) increased the activation energy from 94.9 kJ/mol to 139.7 kJ/mol.

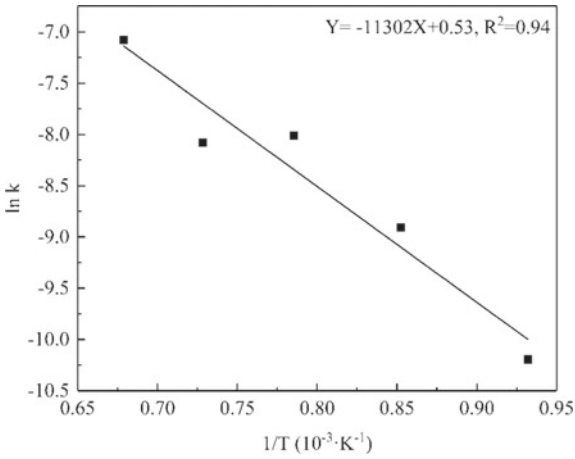

Fig. 7 Realtionship between ln(k) and 1/T for the reduction reaction of YM1 at the chemically controlled stage

Conclusions

Reduction of lead-rich slag in the temperature range of 1073–1473 K has been investigated by accurate measurements of the gas volume generated from the reactions. The activation energy for the reduction has been calculated based on the experimental data. The results showed that.

(1) The reduction of PbO to Pb and Fe_2O_3 to FeO can happen simultaneously followed by the reduction of ZnO to Zn. Under the experimental conditions, FeO cannot be reduced to Fe which was confirmed by the examination of the reduced samples.
(2) The reaction rate of the lead-rich slag containing different PbO concentrations was initially fast but becomes slower as the extent of reaction increases. The reaction rate is limited at temperatures below 1173 K and greatly increases at temperatures above 1173 K.
(3) The reduction of lead-rich slag at the initial stage is chemically controlled. The activation energy of YM1, YM2, and YM3 at the chemically controlled stage is 94.0 kJ/mol, 94.9 kJ/mol, and 139.7 kJ/mol, respectively, which increases with decreasing PbO concentration in the slag.

References

1. Chen HY, Li AJ, Finlow DE (2009) The lead and lead-acid battery industries during 2002 and 2007 in China. J Power Sources 191(1):22–27
2. Zhu XF, Lei L, Sun XJ, Yang DN, Gao LX, Liu JW, Kumar RV, Yang JK (2012) Preparation of basic lead oxide from spent lead acid battery paste via chemical conversion. Hydrometallurgy 117–118:24–31

3. Wu XS (2020) Application of CSC technology in nonferrous metallurgy. Paper presented at the 9th international symposium on lead and zinc processing, United States, San Diego, 23–27 Feb 2020
4. Li WF, Zhan J, Fan YQ, Wei C, Zhang CF, Hang JY (2017) Research and industrial application of a process for direct reduction of molten high-lead smelting slag. JOM 69(4):784–789
5. Matyas AG, Mackey PJ (1976) Metallurgy of the direct smelting of lead. JOM 28(11):10–15
6. Hou XM, Chou KC, Zhao B (2013) Reduction kinetics of lead-rich slag with carbon in the temperature range of 1073 to 1473 K. J Min Metall B 49(2):201–206
7. Errington B, Arthur P, Wang J, Dong Y (2005) The ISA-YMG lead smelting process. Paper presented at proceedings of the international symposium on lead and zinc processing, Japan, Kyoto, 17–19 Oct 2005
8. Kinaev NN, Jak E, Hayes PC (2010) Kinetics of reduction of lead smelting slags with solid carbon. Scand J Metall 34(2):150–157
9. Zhao B, Errington B, Jak E, Peter H (2010) Gaseous reduction of synthetic lead slags and industrial lead sinters. Can Metall Quart 49(3):241–248
10. Liao JF, Zhao B (2021) Phase equilibria study in the system "Fe_2O_3"–ZnO–Al_2O_3–(PbO+CaO+SiO_2) in air. Calphad 74:102282
11. Wang JK, Zhao B, Yang G, Peter H (2004) Properties and reduction mechanism of lead-rich slags. Nonferrous Metals 6:5–8
12. Yang G, Zhao B, Wang JK, Peter H (2006) Study on reduction behaviors between lead-rich slag and sinter. Nonferrous Metals 4:10–13
13. Yang G, Zhao B, Wang JK, Peter H (2008) Study of different behaviors between lead-rich slags and sinter during reduction. Nonferrous Metals 4:5–7
14. Dickinson CF, Heal GR (1999) Solid–liquid diffusion controlled rate equations. Thermochim Acta 340:89–103
15. Bidari E, Aghazadeh V (2015) Investigation of copper ammonia leaching from smelter slags: characterization, leaching and kinetics. Metall Mater Trans B 46:2305–2314
16. Vegliò F, Trifoni M, Pagnanelli F, Toro L (2001) Shrinking core model with variable activation energy: a kinetic model of manganiferous ore leaching with sulphuric acid and lactose. Hydrometallurgy 60(2):167–179
17. Pritzker MD (2003) Model for parallel surface and pore diffusion of an adsorbate in a spherical adsorbent particle. Chem Eng Sci 58(2):473–478
18. Bale CW, Bélisle E, Chartrand P, Degterov SA, Eriksson G, Gheribi AE, Hack K, Jung IH, Kang YB, Melançon J, Pelton AD, Petersen S, Robelin C, Sangster J, Spencer P, Van Ende MA (2016) FactSage thermochemical software and databases. Calphad 54:35–53

Experimental Study on Dephosphorization of High-Phosphorus Mn–Si Alloys

Can Sun, Zizong Zhu, Wanyi Jiao, Chongyuan Zhang, Yingdong Wang, and Jintao Fan

Abstract In an attempt to reduce phosphorus content of the Mn–Si alloys produced by high-phosphorus manganese ores, dephosphorization thermodynamic experiments of high-phosphorus Mn–Si alloys were investigated by using Al-based dephosphorization agent and $CaO–SiO_2–Al_2O_3$ covering slags in silicon molybdenum furnace without protection of gas. This research focused on the transform rule of phosphorus element during the process of its entrance into slag, the effect of CaO/Al_2O_3 (mass ratio of CaO to Al_2O_3) on dephosphorization ratio, and the main phases in dephosphorization slags. The results showed that phosphorus element entered into slag from Mn–Si alloys, respectively, conforming to these two routes: [P] → $Fe_3(PO_4)_2$ → $Ca_3(PO_4)_2$ → 6 . 2CaO . SiO_2–3CaO . P_2O_5 solid solution and [P] → $AlPO_4$. With increase of CaO/Al_2O_3, the dephosphorization ratio increased, and the greatest dephosphorization ratio could reach 79%.

Keywords Manganese-silicon alloys · Al-based dephosphorization agent · Dephosphorization · Dephosphorization slags

Introduction

Extremely rich manganese ores are deposited in Chengkou and Xiushan, two counties of Chongqing city in China. However, those ores are low-quality due to high phosphorus in them, resulting in that Mn-based alloys, produced by them, generally contain high phosphorus around 1 wt.%. Such Mn–Si alloys cannot be used in process of steel-making as deoxidizer and alloy additives, because the excessive phosphorus would cause cold shortness of steel and reduce its quality. Therefore, to improve the utilization of Mn-based alloys produced by such manganese ores in steel-making,

C. Sun · Z. Zhu (✉) · W. Jiao · C. Zhang · Y. Wang · J. Fan
College of Material Science and Engineering, Chongqing University, Chongqing 400044, China
e-mail: Zhuzizong@163.com

C. Sun
e-mail: suncan2230@163.com

Z. Peng et al. (eds.), *12th International Symposium on High-Temperature Metallurgical Processing*, The Minerals, Metals & Materials Series,
https://doi.org/10.1007/978-3-030-92388-4_10

novel dephosphorization method for high-phosphorus Mn-based alloys has to be invented.

Many scholars studied reductive dephosphoriztion of Mn-based alloys, using $CaO–CaF_2$ melt slags [1, 2], metals [3–6] such as Ca, Mg, and Ba, rare-earth metals [7, 8], or alloys such as CaC_2 [9], SiCa [10–12], and Ba alloys [13] to proceed deposition dephosphorization in Argon atmosphere. Unfortunately, some flows exist in those methods. For example, the slags containing CaF_2 are easily pulverized and produce HF gas which is harmful to environment, and Ca metal or Ca alloys contain high carbon content that hinters dephosphorization.

Despite the high efficiency of reductive dephosphorization of Mn-based alloys, it is uneconomical and difficult to obtain strong reductive atmosphere in industrial production. Hence, without protection of argon, this research used $CaO–SiO_2–Al_2O_3$ covering slags and Al-based dephosphorization agent to finish dephosphorization of Mn–Si alloys containing high phosphorus content and studied the transform rule of phosphorus element during the process of its entrance into slag, the effect of CaO/Al_2O_3 (mass ratio of CaO to Al_2O_3) on dephosphorization ratio, and the main phases in dephosphorization slags.

Experimental

Materials

In this experiment, Mn–Si alloys were produced by a certain alloy factory in Chengkou county of Chongqing city in China. The main chemical compositions of the alloy were Mn (60.39 wt.%), Si (25.03 wt.%), Fe (10.57 wt.%), C (1.05 wt.%), P (1.00 wt.%), and S (0.04 wt.%). Al-based dephosphorization agent was used, in which the main component was Al $\geq$ 70.00 wt.%. The covering slag was made of $CaO–Al_2O_3–SiO_2$ slag system, which was composed of pure reagent for chemical analysis of CaO, Al_2O_3, and SiO_2.

Procedure

In this experiment, the slag system composition as shown in Table 1 was used to conduct dephosphorization experiment on Mn–Si alloys with or without Al-based dephosphorization agent. The dosage of alloy was 100 g, the dosage of dephosphorization agent was 5% of the alloy mass, and ratio of the slag to the metal was 0.4.

Given that the Al in the Al-based dephosphorization agent was oxidized to Al_2O_3 in the experimental atmosphere and entered the covering slag, it might lead to the gradual solidification of the covering slag with stirring during the dephosphorization

Table 1 Components of slag system

Number	CaO/wt.%	Al_2O_3/wt.%	SiO_2/wt.%	CaO/Al_2O_3
1	56.0	40.0	4	1.40
2	54.3	41.7	4	1.30
3	51.5	44.5	4	1.16
4	49.3	46.7	4	1.05
5	46.8	49.2	4	0.95

process, and the slag and metal could not be separated finally. Therefore, the following three groups of experiments were carried out under the condition that the slag system component numbered 1 in Table 1 was selected: (a) no Al-based dephosphorization agent was added; (b) the addition of Al-based dephosphorization agent; (c) when the Al-based dephosphorization agent was added, it was assumed that after the Al in the dephosphorization agent had completely removed P from the alloy, the remaining Al was completely oxidized into the slag, and the Al_2O_3 was reduced as formulation $Z = 1.89\ y - 1.65\times$ on the basis of the original slag (y and x are the mass of Al in the Al-based dephosphorization agent and the mass of P in the alloy, respectively). The Al-based dephosphorization agent, Mn–Si alloy particles, and fully mixed CaO–Al_2O_3–SiO_2 covering slag were put into the graphite crucible in turn, and then, we put the graphite crucible into *GM-8-17* silicon molybdenum furnace whose temperature was 1400 °C. After 15 min, the raw materials in the crucible were stirred every 10 min, and then, taking out the crucible quickly after 30 min. In the end, we separated the slag and metal.

The morphologies of dephosphorization slags obtained from the above three groups of experiments are shown in Fig. 1. It was found that when the Al-based dephosphorization agent was added without reducing the Al_2O_3 in the slag, the covering slag gradually solidified from the molten state with agitation, and then, the slag and metal could not be separated. Therefore, when the Al-based dephosphorization agent was added for dephosphorization experiment, the corresponding Al_2O_3 content should be reduced on the basis of the slag system composition shown in Table 1.

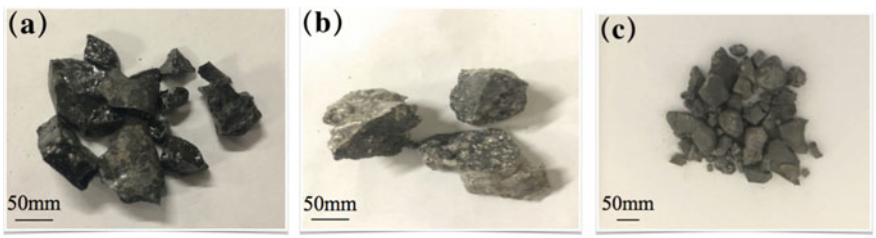

Fig. 1 Dephosphorization slags

Analytical Methods

The alloy samples before and after dephosphorization were ground to the particles whose size is less than 200 mesh, and P, SI, Mn, and Fe contents of alloys were measured by inductively coupled plasma mass spectrometer (ICP-AES, DV-4300). The samples of suitable size were selected from dephosphorization slags and observed under electron probe microanalysis (EPMA, JXA-8530F Plus) after rough grinding, fine grinding, polishing, and carbon spraying, and the distribution of every element was analyzed. The remaining slags were ground to the particle whose size is less than 200 mesh and the phases in them were analyzed by X-ray diffraction (XRD, D/Max 2500pc).

Results and Discussion

The Transformation Law of Phosphorus

X-ray diffraction analysis of dephosphorized slags and Mn–Si alloys after dephosphorization was carried out, and the results are shown in Fig. 2. Without the addition of Al-based dephosphorization agent, P element exists in the form of $6 \cdot 2CaO \cdot SiO_2$–$3CaO \cdot P_2O_5$ solid solution and $3FeO \cdot P_2O_5$ in the dephosphorized slags and alloys, respectively (Fig. 2a, b). This result revealed that in this dephosphorization process, the P in the alloy was first oxidized by FeO to form $3FeO \cdot P_2O_5$. According to the characteristic that the weak alkaline oxide could be replaced by the strong alkaline oxidation in the composite oxide, when the alloy melt and the slag contacted, the more alkaline CaO in the slag replaced the FeO in $3FeO \cdot P_2O_5$ to form $3CaO \cdot P_2O_5$. The phosphoric acid ions in $3CaO \cdot P_2O_5$ in the slag replaced SiO4- 4 in Ca_2SiO_4 in the slag and finally precipitated as $6 \cdot 2CaO \cdot SiO_2$–$3CaO \cdot P_2O_5$ solid solution. Therefore, the transformation mode of phosphorus between slag and metal could be expressed as

$$[Fe] + \frac{1}{2}O_2 = (FeO) \tag{1}$$

$$8(FeO) + 2[P] = (3FeO \cdot P_2O_5) + 5[Fe] \tag{2}$$

$$(3FeO \cdot P_2O_5) + 3(CaO) = (3CaO \cdot P_2O_5) + 3(FeO) \tag{3}$$

$$(3CaO \cdot P_2O_5) + 6(Ca_2SiO_4) = (6 \cdot 2CaO \cdot SiO_2 - 3CaO \cdot P_2O_5) \tag{4}$$

In addition to $6 \cdot 2CaO \cdot SiO_2$–$3CaO \cdot P_2O_5$ solid solution and $3FeO \cdot P_2O_5$, $AlPO_4$ (Fig. 2c, d) was also found to exist in the dephosphorized slag and alloy

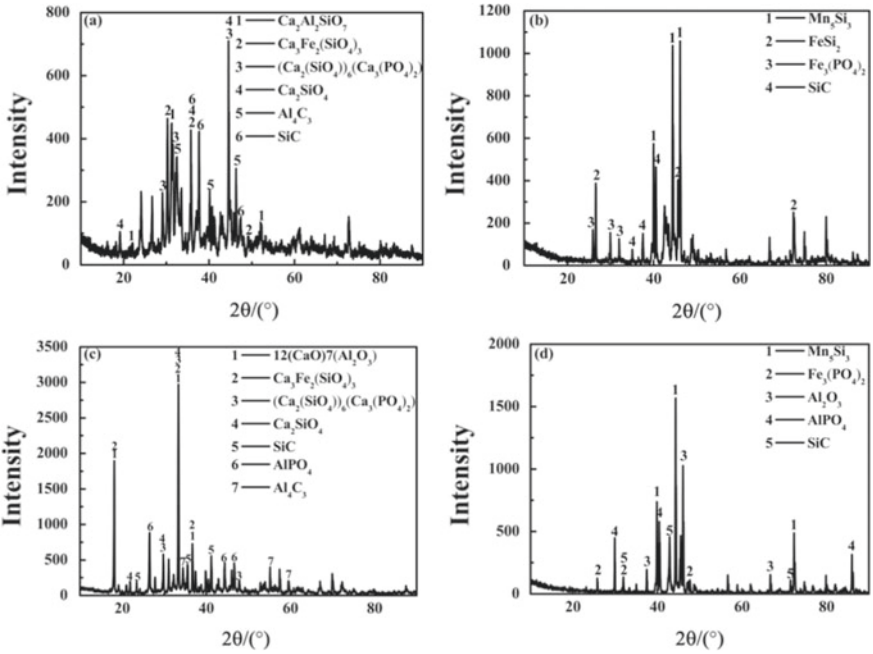

Fig. 2 XRD patterns of dephophorization slags and Mn–Si alloys after dephophorization: without adding Al-based dephophorization agent: **a** slag; **b** alloy; added Al-based dephophorization agent: **c** slag; **d** alloy

with the addition of Al-based dephosphorization agent. In industry, $AlPO_4$ is usually prepared by reacting P_2O_5 with Al_2O_3 at 500–900 °C. However, the alkalinity of Al_2O_3 is lower than that of FeO, so Al_2O_3 cannot replace FeO in $3CaO{\cdot}P_2O_5$ to generate $AlPO_4$, and the P in the alloy could not exist in the form of pure P_2O_5 when the dephosphorization experiment was carried out. Therefore, it was considered in this study that Al in Al-based dephosphorization agent reacted directly with [P] in the alloy to form $AlPO_4$ under oxidizing atmosphere. The melting point of $AlPO_4$ is higher than 1450 °C, and it is stable at the experimental temperature. Moreover, the $AlPO_4$'s density of 2.566 g/cm^3 is lower than that of Mn–Si alloy and slag, and it can float from the alloy melt to the slag with agitation. The reaction between dephosphorization agent and phosphorus is

$$\mathrm{Al(l)} + 2\mathrm{O_2} + [\mathrm{P}] = \mathrm{AlPO_4(s)} \tag{5}$$

Effect of CaO/Al_2O_3 on Dephosphorization Ratio

After the dephosphorization experiment, the content of main elements in Mn–Si alloy was shown in Table 2. Among them, the last five groups of experiments were carried out with the addition of dephosphorization agent. In the slag matching process, the corresponding Al_2O_3 was reduced on the basis of the slag system components shown in Table 1. Theoretically, this part of Al_2O_3 could be supplemented by the oxidation of Al in the dephosphorization agent in the dephosphorization process. Therefore, for convenience of comparison, CaO/Al_2O_3 was not changed.

According to Table 2, in which "DeP" means dephosphorization ratio, the maximum dephosphorization ratio was 19% without adding Al-based dephosphorization agent, which indicated that the slag system did not have high dephosphorization ability under the experimental conditions. The dephosphorization rate increased significantly with the addition of Al-based dephosphorization agent, and the highest dephosphorization rate was 79%. In all cases, the dephosphorization rate increased with the increase of CaO/Al_2O_3.

According to the ionization theory slag, during dephosphorization, a part of PO_4^{3-} in $3CaO \cdot P_2O_5$ will replace SIO_4^{4-} in Ca_2SiO_4, and $Ca_3(PO_4)_2$ and Ca_2SiO_4 will be precipitated together. However, when CaO/Al_2O_3 decreases, Al_2O_3 will continuously absorb O^{2-} to form AlO_4^{5-}. The production of AlO_4^{5-} will also replace the SIO_4^{4-} in Ca_2SiO_4, inhibiting the precipitation of PO_4^{3-} with Ca_2SiO_4, which is not conducive to dephosphorization.

The calculation formulas of phosphorus capacity of slag are as follows:

$$[\mathrm{P}] + \frac{3}{2}\left(\mathrm{O}^{2-}\right) + \frac{5}{4}\mathrm{O}_2 = \left(\mathrm{PO}_4^{3-}\right) \tag{6}$$

Table 2 Contents of main elements in alloys after dephosphorization

Number	CaO/Al_2O_3	Agent/%	Mn/wt.%	Si/wt.%	Fe/wt.%	P/wt.%	DeP/%
1-1	1.40	0	58.72	22.21	10.37	0.81	19
1-2	1.30		58.64	21.95	10.11	0.83	17
1-3	1.16		58.85	22.43	10.18	0.87	13
1-4	1.05		57.21	21.86	10.07	0.89	11
1-5	0.95		58.56	22.15	10.19	0.91	9
2-1	1.40	5	57.90	20.44	9.90	0.21	79
2-2	1.30		57.63	20.52	9.78	0.22	78
2-3	1.16		57.88	20.76	9.90	0.26	74
2-4	1.05		58.24	20.85	9.95	0.29	71
2-5	0.95		57.98	20.70	9.84	0.31	69

$$K = \frac{w\left(PO_4^{3-}\right) \times \gamma\left(PO_4^{3-}\right)}{a_{O^{2-}}^{\frac{3}{2}} \times P_{O_2}^{\frac{5}{4}} \times a_{[P]}} \tag{7}$$

$$C = \frac{w\left(PO_4^{3-}\right)}{P_{O_2}^{\frac{5}{4}} \times a_{[P]}} = \frac{K \times a_{O^{2-}}^{\frac{3}{2}}}{\gamma\left(PO_4^{3-}\right)} \tag{8}$$

where K is the reaction equilibrium constant of Eq. (6); $W(PO_4^{3-})$ is the mass fraction of phosphate ions in the slag; $\gamma(PO_4^{3-})$ is the activity coefficient of phosphate ions in the slag; P_{O_2} is the partial pressure of oxygen in the reaction system; $a_{[P]}$ is the activity of dissolved phosphorus in the alloy; aO_2^- is the activity of oxygen ions in the slag.

According to the calculation of phosphorus capacity of slag, the phosphorus capacity of slag is related to temperature and the activity of oxygen ions in slag. When the temperature is constant, the greater the activity of oxygen ions, the greater the phosphorus capacity of slag. With the increase of CaO/Al_2O_3, the absorption of oxygen ions decreases, and the release of oxygen ions increases. Eventually the activity of oxygen ions in slag increases, and the phosphorus capacity of slag increases, which is conducive to dephosphorization.

The viscosity of the slag determines the difficulty of $AlPO_4$ particles entering the slag from the alloy melt. After the slag system was reconstructed, the covering slag could not be melted at the experimental temperature, and its viscosity could not be measured. Therefore, the change of the slag viscosity with CaO/Al_2O_3 after adding Al-based dephosphorization agent was only analyzed theoretically.

For homogeneous slag, the viscosity obeys the law of Newtonian viscous liquid and depends on the activation energy of moving particles. In the slag system used in the experiment, SiO_2 content is very low, so Al_2O_3 is the main factor affecting the slag viscosity. Al_2O_3 is an amphoteric oxide, which is acidic in alkaline slag and can absorb O^{2-} in alkaline slag to form $Al_xO_y^{z-}$ with network structure. $Al_xO_y^{z-}$ has a large radius, is affected by the surrounding heterogeneous charged ions, and also requires the highest viscous activation energy when moving. With the increase of Al_2O_3 content, the degree of polymerization of $Al_xO_y^{z-}$ increases, as does the viscosity of molten slag. When CaO/Al_2O_3 increases, the viscosity of the slag decreases, and the resistance of $AlPO_4$ into the slag decreases.

Distribution of Elements and Main Phases in Dephosphorization Slag

From Fig. 3a–a7, we can see the main kinds of mineral structures in the slag: gray-white area (position 2) enriched with P element, gray area (position 1) enriched with Al, Ca, and O elements, and gray-black area (position 3) enriched with Si and C elements, bright-white area (position 4) enriched with Mn, Fe elements. Combined

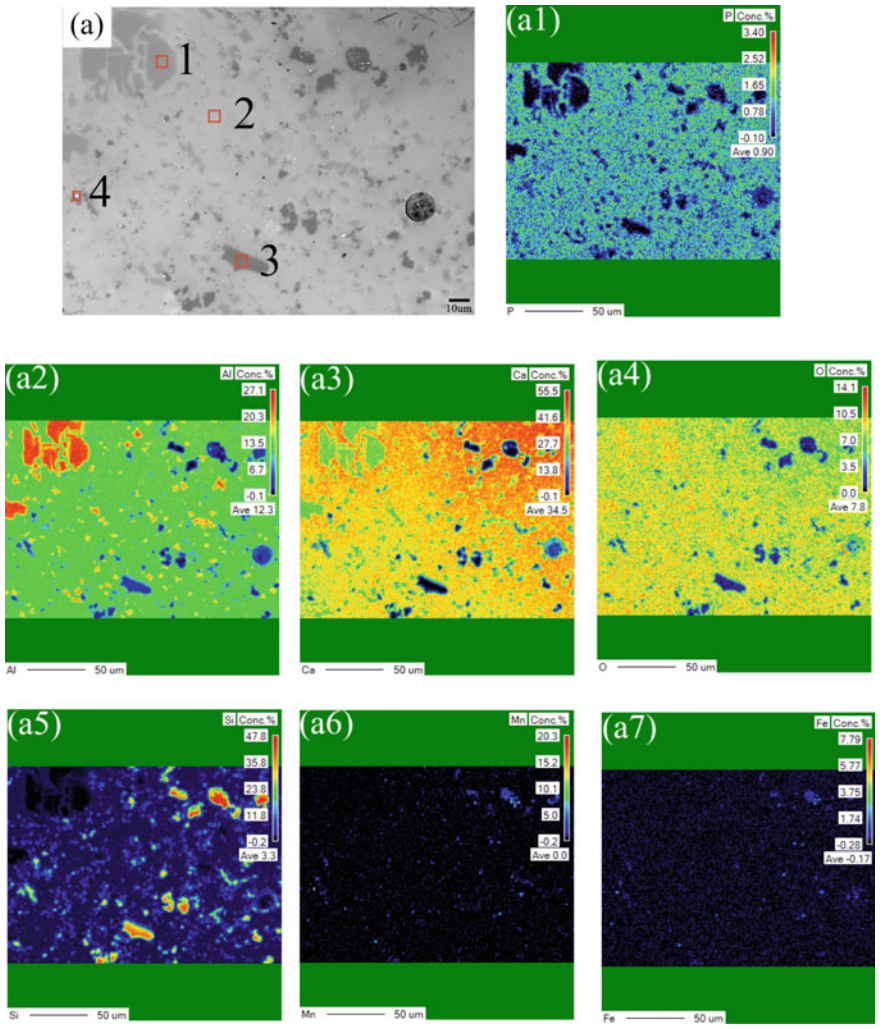

Fig. 3 Backscatter electron component image of dephosphorization slag and the distribution of every element in the slag

with Fig. 2c and Table 3, it can be seen that the main phases in the gray-white area are $6{\cdot}2CaO{\cdot}SiO_2{-}3CaO{\cdot}P_2O_5$ solid solution and $2CaO{\cdot}SiO_2{-}3CaO{\cdot}P_2O_5$ solid solution and $AlPO_4$; the main phase in the gray area is $12CaO{\cdot}7Al_2O_3$; the main phase in the gray-black area is SiC.

At 1400 °C, when Mn–Si–C got ternary melt equilibrium, the solubility of C would decrease with the increase of Si content. When Si content exceeded the critical value of 0.5 mol fraction, C in the melt would not be stable, and at this time, saturated pure substance β-sic existed in the solution stably [14]. The alloy used in this experiment

Table 3 Content of every element in position 1–3

Position	Mn/%	Ca/%	Al/%	Mg/%	P/%	C/%	O/%	Si/%
1	0.014	35.139	25.417	2.127	0.566	2.849	32.147	2.126
2	0.024	41.752	19.067	1.323	1.421	2.448	30.772	2.688
3	0.073	1.686	2.902	0.124	0.091	35.463	1.998	58.198

could be regarded as Mn–Si–Fe–C–P five-binary melt with Mn and Si as the main elements and unchanged content. According to the above research, the experimental graphite crucible carburized in the process of dephosphorization. When the content of C in the alloy exceeded a certain value, the stable existence of β-sic in the alloy would enter the dephosphorization slag through the slag–metal interface.

Conclusions

Without the protection of atmosphere, Al-based dephosphorization agent and CaO–Al_2O_3–SiO_2 slag system were successfully used to dephosphorize high-phosphorus Mn–Si alloy. The main conclusions are summarized: the phosphorus in the alloy finally entered the slag by the transformation law of [P] → $Fe_3(PO_4)_2$ → $Ca_3(PO_4)_2$ → 6·2CaO·SiO_2–3CaO·P_2O_5 solid solution and [P] → $AlPO_4$, respectively; when the dosage of dephosphorization agent was 5%, the ratio of CaO–Al_2O_3–SiO_2 covering slag was 56:44:4 (on the basis of reducing the corresponding amount of Al_2O_3), the temperature was 1400 °C, the slag–metal ratio was 0.4, and the dephosphorization rate was the highest, which was 79%; gray-white area enriched with P element, gray area enriched with Al, Ca, and O elements, and gray-black area enriched with Si and C elements. The main phases in the gray-white area are 6·2CaO·SiO_2–3CaO·P_2O_5 solid solution, 2CaO·SiO_2–3CaO.P_2O_5 solid solution and $AlPO_4$; the main phase in the gray area is 12CaO·7Al_2O_3; the main phase in the gray-black area is SiC.

Acknowledgements The authors greatly acknowledge the financial support provided by The National Natural Science Foundation of China (51774054).

References

1. Ban B, Bai X, Li J (2015) The mechanism of P removal by solvent refining in Al-Si-P system. Metall Mater Trans B 46(6):2430–2437
2. Shimpo T, Yoshikawa T, Morita K (2004) Thermodynamic study of the effect of calcium on removal of phosphorus from silicon by acid leaching treatment. Metall Mater Trans B 35(2):277–284
3. Ni RM, Cheng W, Wei SK (1989) Study on dephosphorization silicon-manganese ferroalloy under reducing stmosphere with metallic calcium. Iron Steel 24(9):49–53

4. Toshiaki A, Tetsuro U, Yoshifumi O (1985) Reducing dephosphorization of molten by metallic calcium. Trans ISIJ 25:326–332
5. Wen XS, Li HY, Sun YY (2011) Application of reduction dephosphorization on low or extra low carbon ferro-manganese-silicon. Ferro-Alloys 42(2):1–3
6. Zeng SL, Chu SJ, Yu HF, Liang ZL (2009) Optimization of technics on precipitation and dephosphorization for ferro-manganese-silicon. Ferro-Alloys 40(6):1–5
7. Meteleva-Fischer Y, Yang Y, Boom R, Kraaijveld B, Kuntzel H (2013) Alloying refining of metallurgical grade silicon with rare earth elements. Paper presented at EPD congress San antonia 201–209 Mar 2013
8. Tang K, Løvvik O, Safarian J (2014) Removal of phosphorus in metallurgical silicon by rare earth elements. Metall Mater Trans B 1(3):257–262
9. Wang DZ, Shao XH (1983) Experimental study on dephosphorization of ferromanganese. Steel 4:14–21
10. Zeng SL, Liu J, Li H (2004) Expriments on outside furnace dephosphorization for ferromanganese-silicon. Ferro-Alloys 1:1–5
11. Lu P (1999) Industrial Experiment on reductive dephosphoriztion of high silicon ferromanganese-silicon. Ferro-Alloys 31(6):6–8
12. Li CD, Wang XL, Tang WH (1992) Experimental study on reductive dephosphoriztion of silicon-manganese alloy. Ferro-Alloys 6:27–29
13. Li Y, Jiang ZH, Liu Y (2006) Deoxidation, desulfurization and reductive dephosphorization of stainless steel using barium bearing Alloys. J Iron Steel Res 18(8):14–18
14. Paek MK, Pak JJ, Kang YB (2014) Phase equilibria and thermodynamics of Mn–C, Mn–Si, Si–C binary systems and Mn–Si–C ternary system by critical evaluation, combined with experiment and thermodynamic modeling. Calphad 46:92–102

Recent Studies on Hot Metal Desulfurization

Ender Keskinkilic

Abstract Hot metal desulfurization station is an indispensable part of a modern integrated iron and steelmaking company. In this plant, roughly speaking, at least ninety percent of sulfur in hot metal is eliminated before basic oxygen steelmaking. In the conventional process, stable sulfide-making additives of various kinds and forms are introduced to the hot metal present in torpedo cars or more commonly in ladles. Together with desulfurization reactions, a slag rich in sulfides is collected at the top, and it is then skimmed out. Other than hot metal treatment stage, further removal of sulfur may be accomplished in secondary steelmaking, depending primarily on suitability of metallurgical conditions in that specific vessel. In this literature work, recent experimental studies related to hot metal desulfurization are reviewed. More emphasis shall be on the works performed after the millennium and specifically in the last decade, including the ones offering new and novel methods.

Keywords Hot metal desulfurization · Integrated iron and steelmaking

Introduction

Desulfurization in iron containing alloy–slag systems can generally be expressed with the following reaction:

$$\underline{S}(\%) + (O^{2-}) = (S^{2-}) + \underline{O}(\%) \tag{1}$$

where underlined ones represent the specie dissolved in the metal while $\left(O^{2-}\right)$ and (S^{2-}) show the oxide and sulfide anions in the slag, respectively. Starting from the equilibrium constant of this reaction, one can easily reach the sulfur slag–metal distribution ratio, $\frac{(\%S)}{\%\underline{S}}$, as follows:

E. Keskinkilic (✉)
Graduate School of Natural and Applied Sciences, Department of Metallurgical and Materials Engineering, Atilim University, Ankara 06830, Turkey
e-mail: ender.keskinkilic@atilim.edu.tr

Z. Peng et al. (eds.), *12th International Symposium on High-Temperature Metallurgical Processing*, The Minerals, Metals & Materials Series,
https://doi.org/10.1007/978-3-030-92388-4_11

$$\frac{(\%S)}{\%\underline{S}} = \frac{K}{\gamma_{S^{2-}}} \cdot f_S \cdot a_{O^{2-}} \cdot \frac{1}{a_O} \tag{2}$$

Therefore, four main parameters govern this partition ratio: (a) K, equilibrium constant, which is temperature-dependent, (b) f_S, activity coefficient of sulfur, so metal composition, (c) $a_{O^{2-}}$, activity of oxide anions in slag (actually related to slag composition or more correctly slag basicity), and (d) a_O, dissolved oxygen activity (oxygen potential of the system). When the two main smelting processes of integrated iron and steelmaking are concerned, unfortunately blast furnace and converter steelmaking are not metallurgically suitable for sulfur removal. Blast furnace, for many reasons, should be operated with acidic slags, which therefore have low $a_{O^{2-}}$. Converter steelmaking systems, on the other hand, are the systems where the oxygen potential (a_O) is very high. These can be regarded as the simple explanation of the main reasons of establishment of external desulfurization process operated between the blast furnace and the converter. Today, desulfurization is an indispensable part of a modern integrated iron and steelmaking company.

Hot metal desulfurization is simply conducted by sending additives, which are capable of forming high stability sulfide compounds, to the hot metal bath kept in torpedo cars or more commonly in ladles. Variation of standard Gibbs free energy change with temperature for some sulfidation reactions is presented in Fig. 1 [1]. Among those given ones, calcium is the most stable sulfide forming element, while nickel sulfide is the least stable sulfide. Sodium is an important and stable sulfide forming element, but due to its corrosive nature, it is not commonly preferred in steelmaking shops. In conventional operations, calcium generally in the form of CaO, named as burnt lime, magnesium (in various forms) is mostly utilized. Elemental Mg share in the desulfurization mix is higher when the target sulfur content is lower. Additionally, fluorspar (CaF_2) is charged in minor amounts to satisfy the fluidity of the slag and to enhance CaO dissolution. CaC_2 is another desulfurizing agent, but its storage necessitates humidity-free bins, so the steelmakers, most of the time, do not hear about it. Desulfurization abilities of various agents were studied and presented in the work conducted by Lindström and Sichen [2].

In this study, recent experimental studies related to hot metal desulfurization are reviewed. More emphasis shall be on the works performed after the millennium and specifically in the last decade, including the ones offering new and novel methods.

Examples to Recent Studies on Hot Metal Desulfurization

Examples to recent studies on hot metal desulfurization can be grouped mainly into four categories as alternative fluxes for desulfurization, ways of addition of desulfurization agents, modeling and simulation of desulfurization, and desulfurization kinetics. In the scope of this work, some examples to the first and the second categories were included.

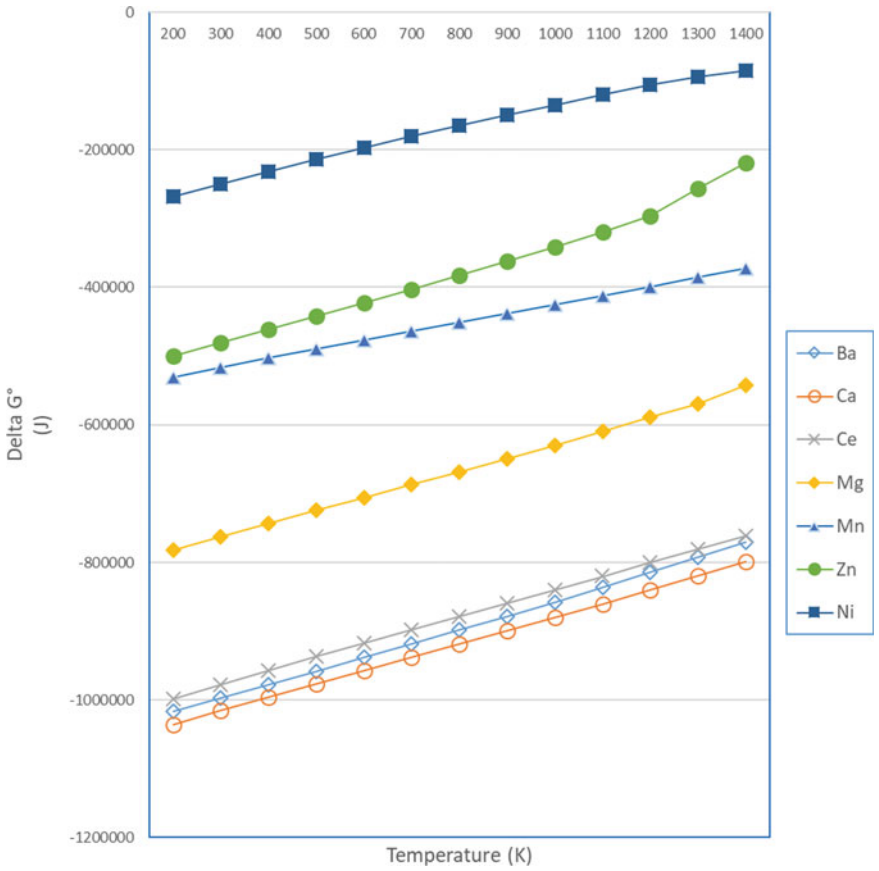

Fig. 1 Variation of ΔG° versus T for various sulfidation reactions: $2X + S_{2(g)} = 2XS$ where X: Ba, Ca, Ce, Mg, Mn, Zn, Ni. *Note* Thermodynamic data was obtained from FactSage 8.1

Alternative Fluxes for Desulfurization

An example to experimental investigation for the use of red mud containing flux in hot metal desulfurization was the work performed by Li and coworkers [3]. The chemical composition of the sintered red mud obtained from Shanxi Xiaoyi aluminum plant was reported as 11.10% Fe_2O_3, 25.12% Al_2O_3, 19.79% CaO, 25.30% SiO_2, 5.42% TiO_2, 0.83% MgO, and 10.08% Na_2O. In lab-scale runs, charges containing molten iron (prepared from chemical reagents, and a composition of 4%C and 0.05–0.1%S) and red mud + CaO mixtures (red mud/CaO ratio: 1.2–4.4) were smelted in the temperature range of 1350–1450 °C. Slag/molten iron ratio was fixed as 0.1 or 0.2. In all experiments, the crucible was kept 30 min at the target temperature. According to the findings of the laboratory runs, the phases having low melting points like $12CaO.7Al_2O_3$, $Ca_{12}Al_{14}O_{33}$, and $Na_4CaSi_3O_9$ were detected in the final slag. Good

slag fluidity was also reported when red mud-based flux was used. Red mud/CaO ratio in between 1.2 and 2.4 was found to give a high %desulfurization (~80%) and a low final S composition (<0.02%). The best results were obtained when red mud/CaO ratio was 2 providing %desulfurization value of ~86% and final sulfur content of 0.016%. Results of the pilot-scale tests were reported to verify the feasibility of red mud usage in hot metal desulfurization.

More recently, Zhang et al. proposed a method aiming to recycle the red mud in hot metal desulfurization [4]. The red mud obtained from a Chinese company was reported to contain 46.91% TFe, 7.90% Al_2O_3, 0.35% CaO, 5.01% SiO_2, 3.92% TiO_2, 0.09% MgO, and 1.73% Na_2O. This iron-rich red mud was first subjected to prereduction with coke. Then, prereduced red mud was mixed with CaO–Al_2O_3 or CaO–Al dross in certain proportions, and then, the mixture was equilibrated with pig iron (4.34%C, 0.431%Si, and 0.070%S) using a vertical tube furnace. The runs were conducted at 1300 °C for 5–60 min. Traditional desulfurization mixture (90% CaO + 10%CaF_2) was used in the experiments where no prereduced red mud was used. The authors concluded that (prereduced red mud–CaO–Al_2O_3) or (prereduced red mud–CaO–Aluminum dross) mixtures showed nearly the same desulfurization efficiency with the traditional flux, and therefore, other than the benefit of iron recovery, they proposed use of prereduced red mud containing mixtures instead of fluorine containing traditional mixtures in hot metal desulfurization. As another recycling proposal, Ayguiar and coworkers investigated the use of marble waste (70%CaO, 20%MgO) in hot metal treatment [5]. According to the results obtained from a lab-scale setup, they concluded that it could be used as a desulfurizer.

Santo et al. investigated the possibility of use of industrial wastes and different fluxes in hot metal desulfurization [6]. They aimed to analyze the possibility of partial replacement of calcitic lime (C) with limestone waste (L) and slag from desulfurization in the Kambara reactor (K). The authors also studied the possible replacement of CaF_2 with B_2O_3 (B), sodalite (S), and aluminum dross (A). Hot metal containing 4.77%C and 0.042%S was equilibrated with traditional flux (95% calcitic lime + 5% CaF_2) and various calcitic lime + alternative fluxes mixtures. According to laboratory-scale experiments conducted at 1350 °C under inert atmosphere, it was concluded that limestone waste could be used to replace part of lime and that use of slag from Kambara reactor was not effective. The authors mentioned that better results were obtained with B_2O_3 compared to fluorspar. The authors also underlined that combined use of agents resulted in better desulfurization efficiencies. The highest efficiency was reported as 92.41% with the mixture abbreviated as $C_{69}L_{15}K_6S_5B_5$ (subscripts indicating weight percentages).

The possibility of use of ZnO in hot metal desulfurization was investigated by Lindström et al. [7]. The authors established a lab-scale setup using a vertical tube furnace. Pig iron containing ~460 ppm sulfur was equilibrated with (ZnO + calcium oxide-based desulfurizing agent) mixture. Stirring was applied at the target temperature (1723 K) for 2–15 min. According to findings of the study, the authors concluded that ZnO could not decrease sulfur concentration and that it was not suitable as an agent in hot metal treatment. This was in contradiction with the previous literature.

The authors indicated that the thermodynamic data obtained in previous studies had calculation mistakes and they also outlined these points.

As mentioned earlier, storage of CaC_2 is critical. Condo et al. investigated the effect of aging on the ability of CaC_2 for hot metal desulfurization [8]. The researchers conducted industrial trials as well as lab-scale experiments to see the effect of the time of storage on its desulfurization power. According to the results of industrials trials, the authors concluded that no significant change was observed. In the laboratory-scale runs, as it is well known, samples exposed to atmosphere caused formation of $Ca(OH)_2$ layer as an outer layer. The thicknesses of the desulfurization product (CaS) layer were compared for the samples subjected to air for different times. No significant difference was reported, as found from industrial tests.

Magnesium is commonly used in hot metal desulfurization in various forms. Its rather low boiling point causes efficiency problems in the hot metal treatment process. Metallic magnesium is also relatively expensive compared to CaO containing fluxes. Therefore, efforts have been made to try magnesium oxide containing fluxes. For example, Nakai and coworkers investigated the use of dolomite flux in lab-scale and industrial-scale experiments as an alternative to Mg or MgO + Al pellet [9]. According to 200 t industrial-scale experiments with charges containing dolomite and aluminum ash, it was reported that Mg efficiency (Mg that became MgS * 100/Mg in flux) for desulfurization was 15–25% with Mg consumption of 1–1.3 kg/ton as MgO. The authors concluded that these efficiency values were similar to the ones obtained from Mg and MgO + Al, so this dolomitic flux could be used in hot metal desulfurization.

Ways of Addition of Desulfurization Agents

Tripathi et al. investigated the effect of lance design on hot metal desulfurization [10]. 0.25 scale plexi-glass model of hundred-ton hot metal ladle was fabricated for the purpose of water model studies. Simulation was based on a system in which CaC_2 sent into the hot metal with nitrogen gas. Seven different lance port configurations including the T-shape port used by the Indian steel company were tried with the water model and simulated using computational fluid dynamics. At the end of plant trials, swirling-type stationary design was reported to yield the best results. The authors also calculated the rate constant obtained from the first-order kinetics. It was found to increase from 0.09 (T-shape) to 0.11 min^{-1} (swirling-type stationary design).

Kikuchi and coworkers studied the effect of reducing gas on hot metal desulfurization with CaO-based agent in mid-scale and commercial-scale experiments [11]. Propane was used as a reducing gas. Its effect was examined from two aspects: 1. Flux injection: Propane was mixed with the nitrogen carrier gas. 2. Mechanical stirring: Top blowing with propane gas was conducted together with mechanical stirring by an impeller. In both ways, the flux efficiency of desulfurization was found to increase. For flux injection, this improvement was explained with a local decrease in oxygen potential as well as an increase in surface area between the hot metal and agent. On

the other hand, for impeller mixing, stirring energy was noted as an additional factor to the oxygen potential and the surface area, so better sulfur slag–metal distribution ratio values were reported. In relation to the top blowing with propane gas, the authors mentioned that due to the absorption of the flame into the hot metal at the cavity created by impeller rotation, H content of the hot metal increased from 1 to 3–8 ppm.

Kumar et al. investigated in situ generation of magnesium in hot metal treatment using porous MgO + Al tablets [12]. Pilot tests were conducted using thirty-kilogram liquid iron bath. At each trial, ~30 kg of metal was melted. The metal was reported to contain 4.5%C and 0.075%S. MgO + Al tablets were placed in a graphite immersion tube—called as reactor—having six openings at the bottom and argon inlet on top. The reactor was used in immersed condition in liquid iron bath allowing in situ production of magnesium vapor from aluminothermic reduction of MgO. Temperatures of trials were reported as in the range of 1233–1401 °C. Better desulfurization results were noted when the flow rate of the carrier gas (Ar) was increased. According to the results of the pilot-scale experiments, the lowest sulfur value at the end of desulfurization was reported as 270 ppm from the starting value of 750 ppm. The authors compared these results with industrial CaC_2 + Mg desulfurization. They further proposed additional items to be fulfilled to reach lower sulfur levels in relation to immersion depth and thickness of the reactor, tablet size, CaO addition to charge mix, etc.

As an alternative to the commercial granular magnesium injection, Su et al. studied magnesium efficiency in hot metal desulfurization with a system where magnesium vapor was sent to the induction furnace from the bottom [13]. Modeling studies were validated with high temperature experiments. According to the results of the induction furnace runs, the authors concluded that magnesium efficiency was inversely proportional with desulfurization temperature, the flow rate of the carrier gas (Ar), and the mass of magnesium injection. In a hot metal bath size of 4.5 kg, the highest magnesium usage efficiency was reported as 83% at the desulfurization temperature of 1573 K, argon flow rate of 3 L/min, and magnesium mass of 1.55 g.

Nakai and coworkers investigated the effect of flux addition method on hot metal desulfurization with both water model tests and seventy-kilogram hot metal tests [14]. Three modes were studied: 1. Batch addition of flux at the beginning of the process, 2. Continuous addition, and 3. Powder blasting (flux was blasted from a lance with nitrogen carrier gas). In all three ways, mechanical stirring was applied with an impeller. In water model tests, teflon particles were used to simulate the flux. Aggregation was highly observed in batch addition, followed by continuous addition. The least aggregation was noted in powder blasting. In hot metal experiments, an induction furnace was used. In each run, 70 kg of hot metal (4–5%C, 0.04%S) was melted in magnesia crucible. Fine CaO particles were added at each test, and its amount was 5 kg/ton. The time for desulfurization was 20 min. In powder blasting experiments, nitrogen carrier gas was sent with a flow rate of 100 and 200 Nl/min. The authors concluded that desulfurization efficiency was improved with the use of powder blasting and this was attributed to 1. Better flux dispersion

and less aggregation, 2. Elimination of desulfurization product aggregation due to mechanical stirring.

Nakai et al. then examined the powder blasting separately in a further study [15]. Plant trials with 300-ton ladle in a Japanese company were performed. The difference of carrier gas flow rates (i.e. 100 and 200 Nl/min) was outlined in more detail. Higher gas flow rate was reported to yield better %desulfurization. Based on these results, blasting conditions for plant trials were determined. Hot metal having initial sulfur content of 0.025–0.030% was subjected to desulfurization tests. The initial temperature of the ladle was in the range of 1523–1663 K. Carrier gas of nitrogen with a flow rate of 6–20 Nm^3/min was used for powder blasting purpose. According to the results of industrial trials of powder blasting, the researchers concluded that CaO-based flux consumption reduced by 19% compared to top-batch addition practice.

Conclusions

Recent experimental studies dealing with hot metal desulfurization were reviewed. In the scope of this work, some investigations related to "alternative fluxes for desulfurization" and "ways of addition of desulfurization agents" were included. In relation to these studies, the following main conclusions can be drawn:

- According to the results of laboratory- and pilot-scale studies, the use of red mud in hot metal desulfurization was reported to be feasible.
- The use of industrial wastes and different fluxes was investigated. From the results of the lab-scale runs, limestone waste was offered to replace part of lime. Combined use of agents was advised for better desulfurization efficiencies.
- The use of ZnO in hot metal desulfurization was found to be unsuccessful. Aging of CaC_2 before hot metal treatment was reported to give nearly the same results with the ones without aging. Use of dolomite was investigated as an alternative to Mg and MgO + Al.
- According to application of different lance designs, the use of swirling-type stationary design was reported to yield higher desulfurization rate constant compared to rotational T-shape port.
- In situ generation of magnesium vapor with the use of MgO + Al tablets was proposed, and the results were compared with industrial CaC_2 + Mg desulfurization. Additional items were reported to be fulfilled to obtain lower final sulfur contents. Sending Mg vapor from the bottom of the vessel was another proposal, and magnesium usage efficiency was found to be 83% from the laboratory-scale experiments.
- Addition alternatives of CaO-based slag were investigated in detail. In mechanically stirred lab-scale and pilot-scale systems, batch addition from the top, continuous addition from the top, and powder blasting with a carrier gas were compared. Powder blasting method was reported to yield the best results, providing better flux dispersion and less aggregation.

References

1. FactSage 8.1, The integrated thermodynamic databank system, reaction module, CRCT—ThermFact Inc. & GTT—Technologies
2. Lindström D, Sichen D (2015) Study on desulfurization abilities of some commonly used desulfurization agents. Steel Res Int 86:73–83
3. Li F, Zhang Y, Guo Z (2017) Experimental study on hot metal desulfurization using sintered red mud-based flux. JOM 69(9):1632–1638
4. Zhang B, Liu C, Jiang M (2020) A new method of red mud recycling in the process of hot metal pretreatment. Metall Res Tech 117:1–7. https://doi.org/10.1051/metal/2020010
5. Aguiar FN, Grillo FF, Tenório JAS, Oliveira JR (2012) Hot metal desulfurization by marble waste and fluorspar. Metall and Mat 65(2):233–239
6. Santo EV, Soares SG, Oliveira HC, Junca E, Grillo FF, Oliveira JR (2021) Influence of industrial wastes and different fluxes on hot metal desulfurization efficiency. JOM 73(6):1909–1918
7. Lindström D, Nortier P, Glaser B, Sichen D (2013) Study on the possibility of using ZnO for hot metal desulfurization. Steel Res Int 84:419–425
8. Condo AFT, Lindström D, Kojola N, Sichen D (2016) Study on the effect of aging on the ability of calcium carbide for hot metal desulfurization. Steel Res Int 87:1137–1143
9. Nakai Y, Kikuchi N, Miki Y, Kishimoto Y, Isawa T, Kawashima T (2013) Hot metal desulfurization behavior with dolomite flux. ISIJ Int 53(6):1020–1027
10. Tripathi P, Kumar DS, Sah R, Sekhar VR (2017) An improved lance design for hot metal de-sulphurisation. Ironmak Steelmak 44(6):421–429
11. Kikuchi N, Nabeshima S, Kishimoto Y (2012) Effect of propane gas on hot metal desulfurization by CaO based flux. ISIJ Int 52(10):1809–1816
12. Kumar A, Chacko ZE, Malathi M, Godiwalla KM, Ajmani SK, Ranganathan S (2014) Desulfurization of hot metal through in situ generation of magnesium in 30-kg molten iron bath-influence of inert gas flow rate. Steel Res Int 85:927–934
13. Su J, Dou Z, Zhang T, Liu Y (2020) Utilization rate of magnesium in hot metal desulfurization by magnesium vapor injection. ISIJ Int 60(5):915–921
14. Nakai Y, Hino Y, Sumi I, Kikuchi N, Uchida Y, Miki Y (2015) Effect of flux addition method on hot metal desulfurization by mechanical stirring process. ISIJ Int 55(7):1398–1407
15. Nakai Y, Sumi I, Kikuchi N, Tanaka K, Miki Y (2017) Powder blasting in hot metal desulfurization by mechanical stirring process. ISIJ Int 57(6):1029–1036

Modification of Basic Oxygen Furnace Slag Using Iron Ore Tailing and Blast Furnace Dust

Liang Wang, Wei Ren, Xiaofang Zhang, Ziwen Han, and Jinlian Li

Abstract Due to the accumulation of solid wastes, more and more attention has been paid to the recycle and reuse of basic oxygen furnace (BOF) slag. However, CaO contained in the slag will cause cracks, which has limited the use of the slag as raw material in architecture to a large extent. In this study, the preparation of cementitious material with BOF slag has been conducted in lab scale and was enlarged in a 50 kg submerged arc furnace to figure out the feasibility of using it. Through reduction and binary basicity modification, effects of C/O (mole), processing time, and metal recovery have been studied. At 1500 °C, the higher the C/O, the greater the reduction of Fe, P, and Mn, and the proper C/O was 1.5. With more and more ore tailings added, the slag reduction deteriorated. The reduction speed was lower, while the binary basicity (mass(CaO)/mass(SiO_2)) climbed up. The vitrification rate of the modified slag was also lower, so the ore tailing should be more than 17.5% considering the limit of vitrification rate (90.3%). Finally, cementitious properties such as flexural and compressive strength can reach 5.2 and 45.3 MPa separately, which fulfills the request of Portland cement.

Keywords BOF slag · Modified slag · Cementitious material · Vitrification rate

L. Wang
Angang Group, Anshan 114021, Liaoning, China

W. Ren (✉) · X. Zhang (✉) · Z. Han · J. Li
Technical Centre, Angang Steel Company Limited, Anshan 114021, Liaoning, China
e-mail: Xfzhang2009@163.com

Z. Han
e-mail: diy00000diy@163.com

J. Li
e-mail: Lijinhao2001@163.com

Z. Peng et al. (eds.), *12th International Symposium on High-Temperature Metallurgical Processing*, The Minerals, Metals & Materials Series,
https://doi.org/10.1007/978-3-030-92388-4_12

Introduction

Great importance has been attached to environmental protection in recent years. China also closely follows this trend and has introduced many policies to protect the environment, thus has brought great burden to steel industries. Therefore, the recycling of iron and steel by-product has attracted people's attention. As a solid by-product, basic oxygen furnace (BOF) slag, which is generated in steel making process (about 80 kg/ton hot metal), has become popular. Most of them were recovered through grinding-magnetic separation-powders. Besides, hot stuffy steel slag technology is also applied. In this process, about 2–5% metal iron can be separated directly, and part of the magnetic iron powder is recycled through second magnetic separation. Totally, about 3% of the iron in the powder is wasted. The existing technology is proficient in dealing with the cold slag, but it cannot help recycle the heat contained in the slag (>1360 °C), which has resulted in a large amount of waste. Moreover, the powder contains some active calcium oxide (f-CaO), which will cause crack trouble if used in road construction.

The treatment of cold BOF slag has been studied for a long time. For the preparation of this kind product mentioned above, carbothermic reduction and slag modification are two important steps; the first step is mainly for the metal recovery and the second is for the valorization of slag. Dankwah et al. [1] and his group have studied the effect of metallurgical coke and waste plastics blends on the reduction of EAF slag, and other researchers used graphite, anthracite, BOF dust, and super graphite [1–13] as reducing agents to recover metal from BOF slag in lab scale. Compared to the carbon-bearing dust (by-product in iron-making), the price of using these reducing agents is higher, thus there is a few pilot studies. Many products, including phosphorous fertilizer, metal recovery, sintering raw material, and cementitious material, have been developed. Morita et al. [14–17] studied the reuse the phosphorus resource. After enriching, the slag can be used as fertilizer. Ye and Liu [2, 3, 17–24] have done the work to recycle the metals in the slag, and Wimmer et al. [5] conducted an overview study on how to apply BOF slag in cement industry. Moreover, he pointed out that the sintering application in which BOF slag was used as raw material was a traditional way in China [15, 19, 25].

In Ansteel, about 1.3 million tons of steel are produced annually. Therefore, in this study, a new method—to recover metal and to prepare cement using modified BOF slag—has been conducted. In addition, the basicity of slag was adjusted by iron tailings from steel works to reduce the melting point of slag and the existence of f-CaO. At the same time, the iron was recovered by carbothermal reduction with blast furnace dust as reducing agent. The converter slag was upgraded to blast furnace slag and used to prepare cement. The effects of C/O ratio, iron tailings ratio, as well as the reduction time in the process were also investigated.

Table 1 Chemical composition of raw materials (%)

Raw material	TFe	FeO	Fe_2O_3	SiO_2	CaO	MgO	Al_2O_3	MnO	C	P_2O_5
BOF slag	17.34	0.72	23.14	12.89	38.38	10.76	9.18	1.47	–	1.16
Ore tailings	11.47	9.36	6.01	69.7	3.23	2.7	1.5	0.23	–	0.044
BF dust	31.04	1.44	42.14	6.09	3.13	0.64	2.26	0.11	35.85	0.082

Experimental Method and Materials

Raw Material

The raw materials were BOF slag, ore tailing, and blast furnace (BF) dust, which all came from Ansteel. The BOF slag has about 17.34% total iron, and the binary basicity (R, same below) was 2.98. As for the ore tailings, it contained about 69.7% silicon dioxide and played a role to modify the R of slag. The BF dust was used to be a reducer which had about 35.85% carbon (for chemical composition, see Table 1). All the raw material mentioned above were grounded and screened before the experiment, and the particle size is lower than 0.075 mm.

Reduction and Melting Procedure

In order to get a reasonable C/O and slag basicity, the reduction was carried out in a high-temperature horizontal resistance furnace. BF dust and BOF slag were mixed evenly according to the C/O = 1.0, 1.5, 2.0, 2.5 before reduction (for detail, see Table 2). Moreover, the reduction temperature was 1500 °C and the constant temperature was 30 min. The whole test process was protected by nitrogen, and the nitrogen flow was 4 L/min.

Reduction and melting procedure were mainly conducted in a 50 kg submerged arc furnace (SAF), and the graphite crucible was used with the inner size φ400 × 600 mm. The mixture of BOF slag, BF dust, and ore tailings was prepared in a fixed proportion based on the C/O (mole) and slag basicity, and part of it were charged into the SAF for a period after preheat of 5 min. Then, add more burden until the last charge was melted. The SAF still worked for 10–30 min even though the whole mixture has been melted.

Test and Characterization

Each slag mixture (4–10 mg) was loaded in an Al_2O_3 crucible to find the suitable reaction temperature and weight loss with thermogravimetric analysis (TGA, Setaram

Table 2 Experimental program

Test	NO	BF dust (%)	BOF dust (%)	Ore tailings (%)	Total mass (g)	C/O (mole)	Temperature (K)	Time (min)
Reduction	A1	16.94	83.06	–	50	1.0	1773	30
	A2	27.32	72.68			1.5		
	A3	39.40	60.60			2.0		
	A4	53.58	46.42			2.5		
TGA	B1	27.32	72.68	0	50	1.5	–	–
	B2	26.70	68.30	5				
	B3	26.08	63.92	10				
	B4	25.48	59.52	15				
	B5	24.84	55.16	20				
Slag modification test	C1	25.48	59.52	15.00	50	1.5	1773	30
	C2	25.15	57.35	17.50				
	C3	24.83	55.17	20.00				
	C4	24.53	52.97	22.50				
	C5	24.22	50.78	25.00				
	C6	23.91	48.59	27.50				
	C7	23.60	46.40	30.00				
SAF	D1	24.83	55.17	20.00	20 k	1.5	–	10
	D2							15
	D3							20
	D4							30

Labsys Evo, 1600 °C). The microstructure of the slag and samples was quantitatively analyzed using field-emission electron probe microanalysis (FEI, Quant400) at fixed accelerating voltage (15 kV) and beam current (4–200 nA). For the wavelength-dispersive spectroscopy (WDS) analysis of the light element Mn and P, the analyzing crystal used was a layered diffracting element 1 at K-α line. Phase identification was achieved via X-ray diffraction (XRD, X'pert Pro), with 2θ ranging from 10 to 80° and Cu Kα radiation at 40 kV and 40 mA.

Results and Discussion

Effect of C/O on BOF Slag Reduction

At 1500 °C, the higher C/O, the greater iron, phosphorus, and manganese reduced, especially the iron recovery can be seen clearly as an iron ball in slag (Table 3).

Table 3 Chemical composition of modified slag (%)

NO	MFe	TFe	SiO_2	CaO	MgO	Al_2O_3	MnO	P_2O_5	MFe/TFe	*R*
A1	18.86	24.74	15.33	37.55	10.99	5.26	1.49	1.11	76.23	2.45
A2	29.45	31.14	14.7	34.28	10.14	5.19	1.33	0.99	94.57	2.33
A3	33.46	35.17	12.66	27.33	8.34	4.33	1.28	0.85	95.14	2.16
A4	38.23	39.76	10.16	19.06	6.15	3.6	1.13	0.66	96.15	1.88

The MFe/TFe can reach over 94%. Through the chemical analyses, it was found that the more BF dust, the higher C/O. Meantime, the iron oxide content in the reduced sample became lower, and the value decreased from 7.96% with C/O = 1.0–2.38%. When C/O = 1.5, the percent of metal iron increase from 18.86 to 29.45%, which was almost the total iron. Moreover, there was no big difference when C/O changed from 1.5 to 2.5. Therefore, the suitable C/O is 1.5. This result was somehow different from the practice of Li's [17], and such a high C/O can attribute to the reducing agent BF dust. The dust had about 35% carbon, which made it difficult to finish the reduction. Also, it had lower opportunity to contact with other ferrous oxide during the reduction. In addition, it was easy to reduce BOF slag when it was modified because the melting point was lower.

For further utilization of iron and slag, the P and Mn separation was studied. Those elements were found in the iron part instead of slag phase. As seen in Fig. 1, after 30 min reduction under the temperature of 1500 °C, most of iron was generated as a style of metal Fe and existed as an iron ball via SEM + EDS. P and Mn were mostly transferred from slag to iron, which was different from the study of Morita et al. The basicity change of slag may play an important role in its transfer. These results were based on the thermo-dynamic theory, which was the same as other researchers likes Qian and Gong [3, 4, 18].

The slag after modification had no active CaO through XRD, and the main phase were $12CaO{\cdot}7Al_2O_3$, MgO, γ-$2CaO{\cdot}SiO_2$ and β-$2CaO{\cdot}SiO_2$ for A1–A3 (Fig. 2). With the addition of $2CaO{\cdot}Al_2O_3{\cdot}SiO_2$, the A4 sample also displayed the same phase. All of them can be directly used as raw materials in construction. In such

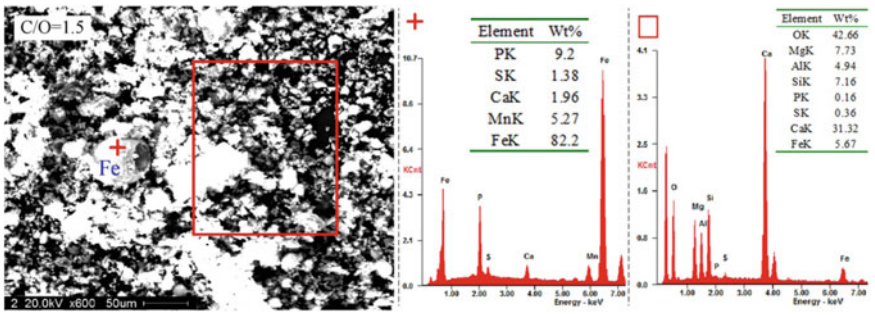

Fig. 1 SEM and EDS for reduced BOF slag

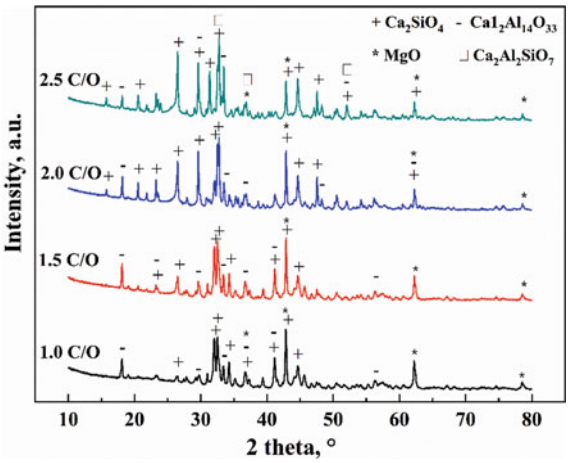

Fig. 2 XRD for sample A1-A4

high basicity modified slag, there was few active CaO. This may be due to Al_2O_3, which was beneficial to the compound of CaO–Al_2O_3 and it has absorbed the extra active CaO compared with the BOF slag.

Effect of Ore Tailing on Modified Slag Reduction

When the C/O ratio is 1.5, ore tailing deteriorated the reduction of mixed sample (mixture of BOF slag and BF dust); the iron ore tailing was within the range of 0–20%; the reduction ratio decreased from 87.10 to 74.15%. The addition of ore tailing was mainly for the modification of slag sample R, and the recycling of metal was also concerned. Therefore, the performance of ore tailing for the reduction should be in test beside of quartz. TG test showed that the weight loss percentage and iron oxide reduction rate decreased with the increase of iron tailings content in the range of 0–20% iron tailings (for detail, see below). The value were 13.265, 12.668, 11.846, 11.237, and 10.27% when the addition of ore tailing was 0, 5%, 10%, 15%, and 20%, respectively (see Fig. 3). Through calculation, the reduction ratio was 87.10, 85.13, 81.47, 79.13, and 74.15%. The ore tailing had a lower total iron and more FeO compared with the other two raw materials. The results suggest that the weight loss should be fewer. Moreover, this condition can be improved with liquid slag (the higher *R*, the higher melting point of slag, and the better C/O contact).

During the test, with an increasing ore tailing, it was interesting to find the unexpected increasing weight loss. Through XRD, the ore tailing contains $CaCO_3$ and other phases (see Fig. 4). The actual weight loss of the mixed sample was calculated by TGA test. It was found that it was the carbonate compound that caused the weight loss of ore tailing. In this condition, the addition of ore tailing may not be economic,

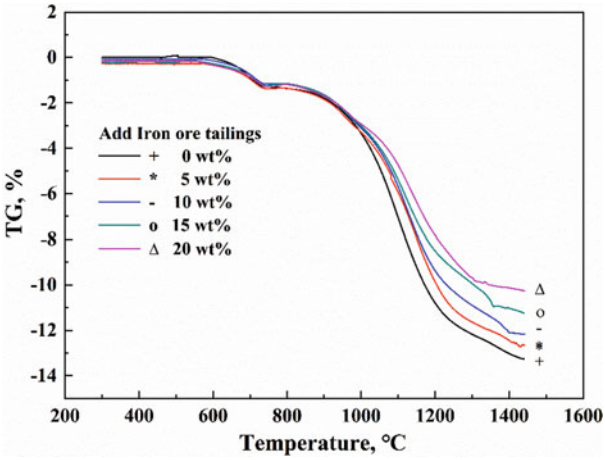

Fig. 3 Weight loss percentage of mixture sample

Fig. 4 XRD of ore tailing

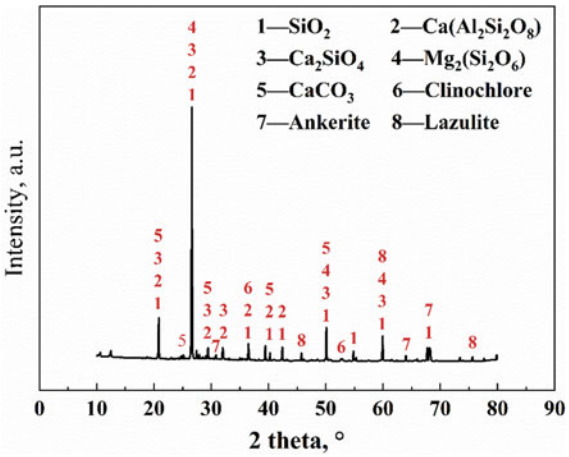

and it led to a further calculation between the recovery of metal and fuel energy exhaustion.

Effect of Ore Tailing on Slag Basicity and Its Vitrification Rate

The basicity of slag has been lowered to 1.0, which was almost the same as BF slag by adding 17.5% ore tailing. The vitrification rate of slag decreased with an increasing basicity. The basicity 0.93 was the key-point in the view point of crystallization compared with BF slag and modified slag. With the high-temperature horizontal

resistance furnace, different levels of basicity in slag were produced with C/O = 1.5. Interestingly, the slag sample cracked in the air cooling period (it may have something to do with the difference in temperature between inner core and outer layer of slag sample, according to the bad conductivity of slag). Moreover, the slag was like glass in some scale as a climbing up ore tailing addition. According to the index of vitrification rate, which was also the main index for cementitious material, the ore tailing should be lower than 17.5%. According to Fig. 5, with 15–30% ore tailing, the non-crystallization ratio is in the range of 75–100%, which suggested that the ore tailing was higher than 17.5% of the BF slag.

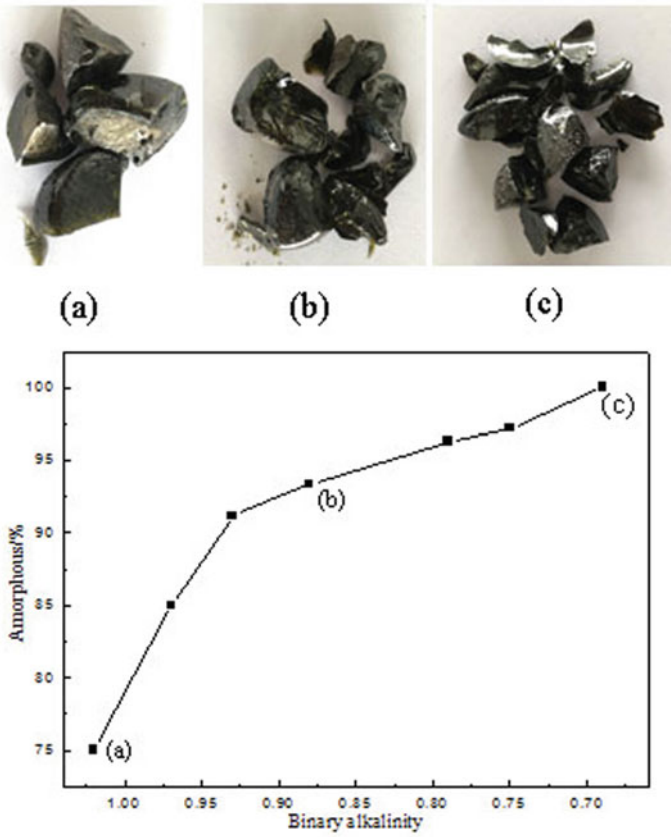

Fig. 5 Vitrification rate of different *R* slag

Preparation Using Submerged Arc Furnace

Separation of Metal and Modified Slag

Via the BF dust and C/O = 1.5, the metal recovery and cement raw material can be prepared with SAF. To enlarge the experiment, SAF was used to prepare different levels of modified slag. As seen in Fig. 6, the metal and slag were separated clearly, and the metal iron was at the bottom due to its heavy weight. However, it was frustrated to find that much more iron oxide in slag compared with the high-temperature horizontal resistance furnace result (for details, see Table 4). 9.52% iron oxide was discovered in slag phase on top. Moreover, more and more gas pore were generated in the reducing process, which can be used to explain the inadequate reaction interface

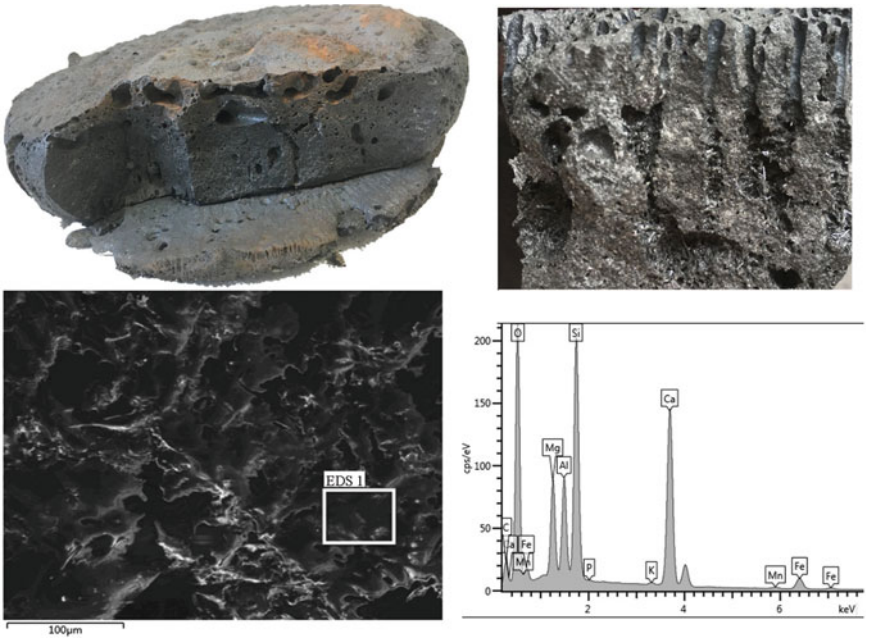

Fig. 6 Modified slag and recovery of metal iron

Table 4 Chemical composition of modified slag (%)

NO	FeO	Fe_2O_3	SiO_2	CaO	MgO	Al_2O_3	MnO	P_2O_5
D1	9.52	3.60	31.01	32.54	9.84	5.47	1.50	0.94
D2	5.48	3.04	33.08	34.89	10.70	5.67	1.62	0.98
D3	5.80	1.74	34.70	35.38	11.34	5.84	1.59	0.95
D4	4.71	0.82	33.54	34.27	10.80	5.71	1.53	0.99

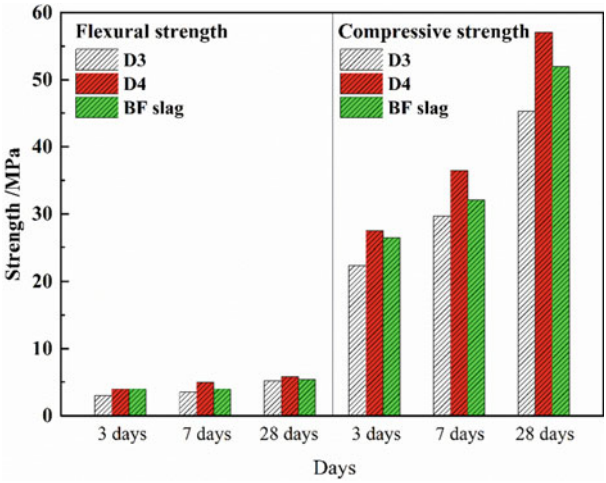

Fig.7 Cementitious properties of samples

between slag and reagent BF dust. During the heating process, BOF slag was melted first and deposited at the bottom, then the BF dust was added as reagent. Thus, it was difficult to reduce the slag even though there was a lot of BF dust.

Cementitious Properties of Modified Slag

Modified slag can be used as cementitious material in the view of compressive and flexural strength, and the value can reach 45.3 and 5.2 MPa (Fig. 7). Modified slag was prepared, and its cementitious properties were tested. The BF slag was analyzed in the same way for comparative evaluation. During this test, the sample was grinded in the size of −0.074 mm and mixed with cement in the ratio of 1:1, and 0.5% additive was used to prepare cement. From the test result, it can be found that the BOF slag sample D4 was better than BF slag, which was thought to be a good raw material for cement production. It is also found that the BOF slag sample D3 was almost the same as BF slag. For 7 days' flexural strength, D3, D4, and BF slag can reach 3.5 Mpa, 5 Mpa, and 4 Mpa, respectively. The value of them increased with time.

Conclusions

Through the experiments and practice in SAF, the conclusions can be outlined as follows:

(1) 1.5 was the reasonable C/O ratio when BF dust was applied to modified BF slag as cementitious material.
(2) Ore tailing deteriorated the reduction of the mixed sample (mixture of BOF slag and BF dust) within range of iron ore tailing addition from 0 to 20%, and the reduction rate decreased from 87.10 to 74.15% when C/O was 1.5.
(3) P, Mn, and metal Fe were separated from slag, and after 30 min of reaction, the contents of Fe_2O_3, MnO, and P_2O_5 in slag decreased to 0.82, 1.53, and 0.99, respectively.
(4) The basicity of slag decreased to 1.0, which was almost the same as BF slag by adding 17.5% ore tailing. The vitrification rate of slag decreased with an increasing basicity, which was the key-point of crystallization compared with BF slag and modified slag.

References

1. Dankwah JR, Koshy P, Saha-Chaudhury NM et al (2011) Reduction of FeO in EAF steelmaking slag by metallurgical coke and waste plastics blends. ISIJ Int 51(3):498–507
2. Liu C, Huang S, Wollants P et al (2017) Valorization of BOF steel slag by reduction and phase modification: metal recovery and slag valorization. Metall Mater Trans B 48(3):1602–1612
3. Ye G, Burstrom E, Kuhn M et al (2003) Reduction of steel-making slags for recovery of valuable metals and oxide materials. Scand J Metall 32(1):7–14
4. Kim T, Lee J (2011) Recovery of Fe and P from CaO-SiO_2-FetO-P_2O_5 slag by microwave treatment. Mater Trans 52(12):2233–2238
5. Wimmer G, Wulfert H, Ludwig HM (2015) A new process for utilization of slags from converter steelmaking in the cement industry METEC of 2nd ESTAD, pp 15–19
6. Min DJ, Han JW, Chung WS (1999) A study of the reduction Rate of FeO in slag by solid carbon. Metall Mater Trans B 30(2):215–221
7. Sarma B, Cramb AW, Fruehan RJ (1996) Reduction of FeO in smelting slags by solid carbon: experimental results. Metall Mater Trans B 27(5):717–730
8. Warczok A, Utigard TA (1998) Fayalite slag reduction by solid graphite. Can Metall Q 37(1):27–39
9. El-Rassi KP, Utigard TA (2000) Rate of slag reduction in a laboratory electric furnace—alternating versus direct current. Metall Mater Trans B 31(6):1187–1194
10. Jouhari AK, Galgali RK, Chattopadhyay P et al (2001) Kinetics of iron oxide reduction in molten slag. Scand J Metall 30(1):14–20
11. Teasdale SL, Hayes PC (2005) Kinetics of reduction of FeO from slag by graphite and coal chars. ISIJ Int 45(5):642–650
12. Miki T, Kaneko S (2015) Separation of FeO and P_2O_5 from steelmaking slag utilizing capillary action. ISIJ Int 55(1):142–148
13. Migas P, Karbowniczek M (2010) Interactions between liquid slag and graphite during the reduction of metallic oxides. Arch Metall Mater 55(4):1147–1157
14. Morita K, Muxing Guo, Oka N et al (2002) Resurrection of the iron and phosphorus resource in steel-making slag. J Mater Cycles Waste Manage 4(2):93–101
15. Du C (2012) A new method of steelmaking slag utilization. Shandong Metall 34(2):51–53
16. Wang Y, Li H, Luo G et al (2017) Macrokinetics of gasification dephosphorization of converter slag by microwave carbon thermal reduction. J Iron Steel Res 29(2):93–97
17. Li G, Zhang F, Zhang L et al (2003) Recycle of converter slag by high temperature carbon thermal reduction. J Mater Metall 2(3):167–172

18. Shen HT, Forssberg E (2003) An overview of recovery of metals from slags. Waste Manage 23(10):933–949
19. Jiang Y (2011) Treatment and complex utilization of steelmaking slag at masteel new atea. Iron Steel 46(5):89–96
20. Ma S, Li Y, Zhang L et al (2017) Effects of EAF slag basicity on its recovery rate of iron components. Iron Steel 52(4):78–83
21. Zhai X, Xu N, Zhang X et al (2011) Recovery of cobalt from converter slag of Chambishi copper using reduction smelting process. Trans Nonferrous Metals Soc China 21(9):2117–2121
22. Hooey L, Jikström JO, Sikström P (2011) The future of blast furnace iron making—nordic perspective. World Iron Steel 11(1):1–5
23. Xue P, He D, Xu A et al (2017) Formation of $MgFe_2O_4$ and recycling of iron from modified BOF slag by magnetic separation. Iron Steel 52(7):104–110
24. Zhang Q, Shi Y (2005) Discussion about clenaning mechanism of mixed slag from Isa furnace and converting furnace. China Nonferrous Metall 5:33–37
25. Umadevi T, Roy P, Mahapatra PC et al (2011) Optimization of steel making slag in iron ore sintering process. World Iron Steel 11(3):22–29

Evaporation of Antimony Trioxide from Antimony Slag by Nitrogen Injection in a Top-Submerged Lance Smelting Set-Up

Hongbin Ling, Annelies Malfliet, Bart Blanpain, and Muxing Guo

Abstract In this work, we studied the evaporation of antimony trioxide (Sb_2O_3) from an antimony slag by bubbling nitrogen gas in the temperature range 1000–1300 °C. Experiments were carried out at gas flow rates of 20–60 l/h for 70 min. The slag evaporation ratio and Sb recovery were evaluated by a gravimetric method. Increasing temperature and gas flow rate resulted in a higher slag evaporation ratio and Sb recovery. The Sb recovery reached around 69% at 1200 °C with a gas flow rate of 40 l/h. The generated Sb_2O_3 product consisted of senarmontite and valentinite. With Sb_2O_3 evaporation, the PbO content in the molten slag gradually increased, resulting in an increase of PbO content in the product. Based on the overall economic benefits, the evaporation process can be optimized to balance the Sb recovery and the purity of the Sb_2O_3 product.

Keywords Evaporation · Antimony trioxide · Antimony slag · Bubbling nitrogen

Introduction

The Sb recovery from industrial residues has attracted more and more attention in recent years due to the increasing scarcity and criticality of Sb [1, 2]. Sb-containing industrial residues can be processed by carbothermic reduction to produce antimony metal or by evaporation to produce antimony trioxide (ATO) [3, 4]. The latter is more attractive because ATO has a diverse application in industry and dominates overall

H. Ling (✉) · A. Malfliet · B. Blanpain · M. Guo
Department of Materials Engineering, KU Leuven, 3001 Leuven, Belgium
e-mail: hongbin.ling@kuleuven.be

A. Malfliet
e-mail: annelies.malfliet@kuleuven.be

B. Blanpain
e-mail: bart.blanpain@kuleuven.be

M. Guo
e-mail: muxing.guo@kuleuven.be

Z. Peng et al. (eds.), *12th International Symposium on High-Temperature Metallurgical Processing*, The Minerals, Metals & Materials Series,
https://doi.org/10.1007/978-3-030-92388-4_13

global Sb end-use [5]. There have been many studies regarding the direct evaporation of ATO from Sb-containing industrial residues. Mendoza et al. reported that the ATO evaporation rate decreases with increasing the slag basicity in a $CaO\text{-}SiO_2\text{–}FeO_{1.5}$ slag at 1300 °C [6]; Itoh et al. confirmed the feasibility to produce ATO by blowing oxygen into the recycled antimony-lead–bismuth alloy at around 800 °C with higher oxygen partial pressure [7]; On the premise of slag conditioning, Binz and Friedrich proposed to produce commercial-grade ATO from lead dross by evaporation at 700–900 °C [8]. However, research work is limited on the ATO production by evaporation of antimony slag (AS), a typical slag generated in industry. AS usually consists of antimony oxide and a fraction of iron oxide, lead oxide, silica, and alumina. It is considered as a significant secondary resource due to its high Sb content (>60 wt%) [9].

In this work, we studied the evaporation of ATO from AS in a top-submerged lance smelting bath with N_2 injection, focusing on the effect of injection parameters on the evaporation ratio and Sb recovery. The behavior of PbO in molten slag during the evaporation was also monitored. Finally, the generated ATO product and the residual slag after evaporation were characterized.

Experimental Method

Experimental Material

The AS samples used in this study were collected from Campine, Belgium. According to our previous study [9], the AS sample is mainly composed of Sb (61.9 wt%) with Al (5.0 wt%), Fe (1.7 wt%), and Pb (1.1 wt%) as minor constituents. The mineral phases in AS include valentinite (Sb_2O_3), antimony (Sb), alumina (Al_2O_3), alumina-chromium oxide solid solution ($(Al, Cr)_2O_3$), and spinels ($(Mg, Fe)(Al, Cr)_2O_4$ and $(Mg, Fe)Sb_2O_4$).

Experimental Set-Up

Figure 1 shows the schematic diagram of the experimental set-up, which consists of a 4000 ml capacity induction furnace (Indutherm TF 4000) and gas injection system. A SiC crucible was placed inside the furnace chamber as induction susceptor. An alumina crucible (OD 64.6 mm, ID 58.8 mm, and H 110 mm) was used for the slag evaporation, and this crucible was placed in another protection alumina crucible. The purpose of using the alumina crucible is to protect the SiC induction susceptor from the slag splashing. The N_2 injection lance (alumina tube with OD 12.1 mm and ID 8.3 mm) was inserted in the slag at 1.5 or 10 mm above the bottom of the reaction crucible, while the Ar lance (the same as the N_2 lance) was positioned above the slag

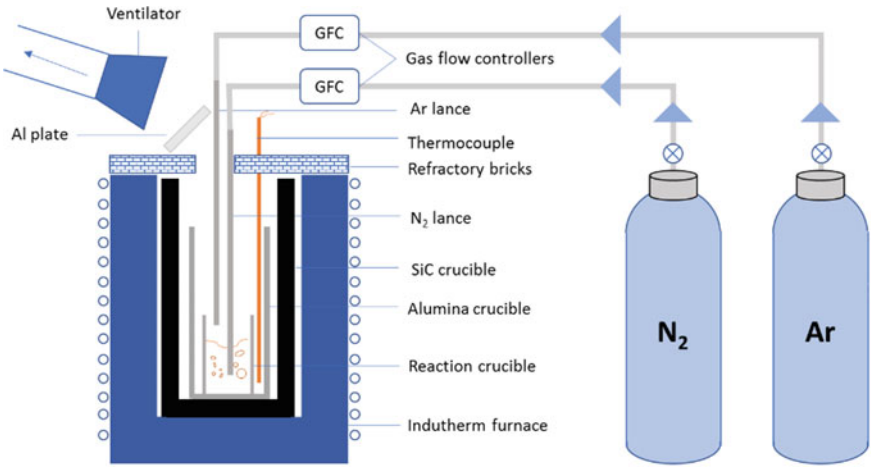

Fig. 1 Schematic diagram of the experimental set-up used for AS slag evaporation test

surface. A thermocouple enclosed inside an alumina sheath was located close to the reaction crucible to monitor the temperature. An Al plate was placed between the top opening of the furnace and the ventilator to collect the generated ATO product.

Slag Evaporation Experimental Procedure

300 g slag sample was added into the reaction crucible, which was covered by a graphite plate during the furnace heating. Ar gas with a flow rate of 100 l/h was blown during the heating to prevent the oxidation of Sb_2O_3 to Sb_2O_4. We stopped Ar injection and removed the graphite plate when the temperature exceeded 1000 °C. At a temperature above 1000 °C, Sb_2O_4 is unstable and would not be formed. When the temperature stabilized at a set value, the slag was stirred with a steel rod, and the first sample was taken by freezing slag on the rod. Subsequently, N_2 with a specified flow rate was injected into the slag bath. Slag samples were taken at intervals of 10 min during the evaporation. The sample was immediately quenched in water, then dried, and ground for chemical analysis. The evaporation continued for 70 min for each test. During evaporation, a part of the fume was deposited on the Al plate, and the rest was evacuated by the ventilator. The detailed experimental conditions are shown in Table 1.

Table 1 Detailed experimental conditions and PbO content of the ATO at different time intervals

Run no	Temperature (°C)	N_2 flow rate (l/h)	Lance inner diameter (mm)	Lance position (mm)	PbO content of ATO (wt%)		
					0–20 min	20–40 min	>40 min
S-1	1000	60	8.2	1.5	0.013	0.035	0.040
S-2	1100	60	8.2	1.5	0.015	0.028	0.100
S-3	1200	60	8.2	1.5	0.004	0.044	–
S-4	1300	60	8.2	1.5	0.061	0.254	1.448
S-5	1200	20	8.2	1.5	–	0.022	0.191
S-6	1200	30	8.2	1.5	0.004	0.007	0.024
S-7	1200	40	8.2	1.5	0.016	0.002	0.082
S-8	1200	50	8.2	1.5	0.010	0.023	0.187
S-9	1200	60	8.2	10	0.020	–	–
S-10	1200	60	5.7	1.5	0.018	0.065	0.101

Analytical Techniques

Inductively Coupled Plasma Optical Emission Spectroscopy (ICP-OES, *Varian 720-ES*) was used in this study to determine the chemical composition of the slag samples. Approximately 0.1 g solid sample was digested with three acids (6 ml HCl + 3 ml HNO_3 + 3 ml HF) in a microwave reactor (*CEM MARS 6 iWAVE*) at 200 °C for 20 min. 1 g boric acid was added to neutralize HF. A *Seifert 3003 TT* X-ray diffractometer with Cu Kα radiation was applied to identify the mineral phases in the samples. The sample was measured in the 2θ-range from 5° to 80° with a step size of 0.03° per second. Scanning Electron Microscopy (SEM, *Philips XL30*) was used to characterize the morphology of the ATO product. A *JXA-8530F* Electron Probe Micro-analyzer with Wavelength Dispersive Spectrometers was used for microstructure and composition analyses of the residual slag after evaporation. The standards used for slag analysis were antimony trioxide for Sb, almandine garnet for Si, Al, Mg, Ca, and Fe, albite for Na, crocoite for Pb, chromium oxide for Cr, and willemite for Zn. The beam current and accelerating voltage were set at 15 nA and 15 kV, respectively. The acquisition time was 10 s on peak and 5 s on the background left and right.

Results and Discussion

Slag Evaporation Ratio and Sb Recovery

The slag evaporation ratio and Sb recovery are defined by Eqs. (1) and (2), respectively. In Eqs. (1) and (2), W_0, W_i, and W_t represent the weight of the original slag, the sample i taken during evaporation, and the residual slag after evaporation,

respectively. M_{Sb} and M_{ATO} refer to the molar mass of Sb and Sb_2O_3, respectively. The value 185.7 in Eq. (2) refers to the weight of Sb (in gram) in the slag before evaporation. The possible oxidation of Sb_2O_3 may affect the slag evaporation ratio in Eq. (1), but this influence is not considered here as the mass increase due to oxidation is much less than the mass loss due to evaporation. For Sb recovery calculation in Eq. (2), we assume that the weight loss of AS was only attributed to ATO evaporation from the slag. The evaporation of PbO is not considered owing to its low content in the slag. The obtained results are shown in Figs. 2 and 3.

$$\text{Evaporation ratio}\,(\%) = \frac{W_0 - \sum_{i=0}^{7} W_i - W_t}{W_0} \times 100\% \tag{1}$$

$$\text{Sb recovery}\,(\%) = \frac{2\mathrm{M_{sb}}(W_0 - \sum_{i=0}^{7} W_i - W_t)}{185.7\,\mathrm{M_{ATO}}} \times 100\% \tag{2}$$

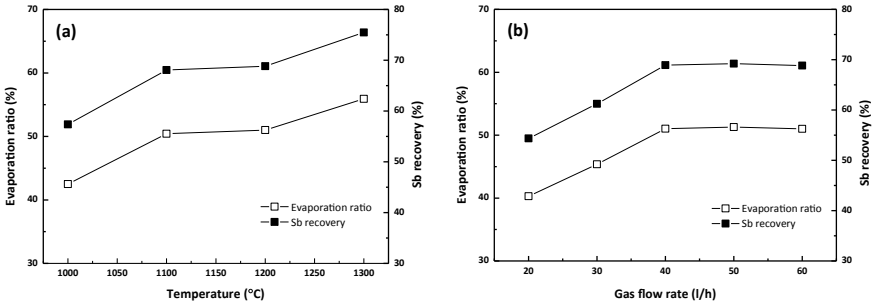

Fig. 2 Effect of temperature **a** and N_2 gas flow rate **b** on the slag evaporation ratio and Sb recovery (under conditions of lance inner diameter of 8.2 mm, and lance position of 1.5 mm and evaporation time of 70 min)

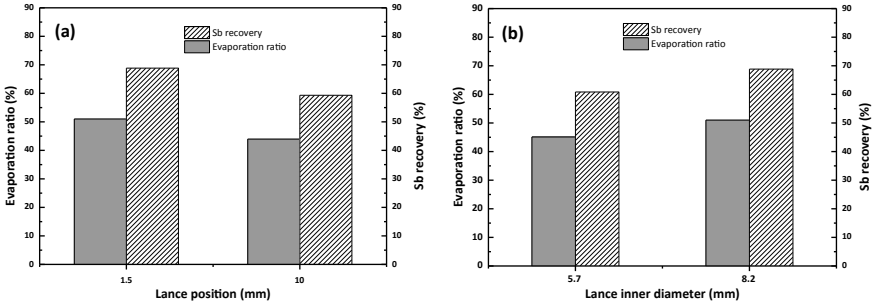

Fig. 3 Effect of lance position **a** and lance inner diameter **b** on the slag evaporation ratio and Sb recovery

With increasing the temperature from 1000 to 1300 °C, the evaporation ratio gradually increased from 42.5 to 55.9% (Fig. 2a). Correspondingly, the Sb recovery increased from 57.4 to 75.5%. This can be understood by the increase in the vapor pressure or volatility of Sb_2O_3 with increasing temperature. In addition, the viscosity of the slag decreases with temperature, enhancing the fluidity in the molten slag and facilitating the mass transfer of Sb_2O_3. At 1300 °C, slag splashing was observed during the experiment, suggesting that the actual evaporation ratio and Sb recovery were somewhat lower than the calculated value.

The slag evaporation ratio gradually increased from 40.3 to 51.0% when increasing the N_2 flow rate from 20 to 40 l/h (Fig. 2b). Correspondingly, the Sb recovery increased from 54.4 to 68.9%. Normally, a higher N_2 flow rate can improve molten slag agitation, facilitating the mass transfer of Sb_2O_3 in the slag. Therefore, increasing the gas injection rate is beneficial to the Sb_2O_3 evaporation from the slag. With further increasing the N_2 flow rate to 50 and 60 l/h, there is no increase of the slag evaporation ratio and/or Sb recovery. The evaporation can be maximized at 40 l/h of N_2 injection.

The slag evaporation ratio increased from 44.0 to 51.0% as the position of the N_2 lance (represented by the distance from the crucible bottom to the lance end) decreased from 10 to 1.5 mm. Correspondingly, the Sb recovery climbed from 59.3 to 68.8% (Fig. 3a). Since the height of the molten slag bath gradually decreased during the test, the extent of slag agitation decreased with time. The deeper the N_2 lance was immersed, the more the slag agitation is intensified in the slag bath, which is favorable to the mass transfer of Sb_2O_3. At a specified N_2 flow rate of 60 l/h, the slag evaporation ratio is 45.1 and 51.0% when using a lance with an inner diameter of 5.7 mm and 8.2 mm, respectively (Fig. 3b). Accordingly, the Sb recovery yields 60.9 and 68.8%, respectively. Apparently, Sb_2O_3 evaporation is more favorable by using a large inner diameter lance. However, using a small diameter lance can increase the gas momentum at a given gas flow rate, increasing the evaporation ratio [10]. This is contradictory with the results obtained in the present work. Further work is needed to clarify this.

PbO Content in the Molten Slag and in the Generated ATO

During the experiment, PbO in molten slag can also be evaporated into the gas phase and co-deposited with ATO. Since commercial-grade ATO has a stringent limit for the PbO content, it is essential to monitor the PbO content in the slag and the ATO product during the evaporation process. As shown in Fig. 4, the PbO content in the molten slag gradually increases with processing time. This increase in PbO content is attributed to the PbO enrichment with ATO evaporation and is larger than the loss due to PbO evaporation. As such, a higher PbO content is expected in the molten slag with more ATO evaporation. In Fig. 4a, the PbO content in the molten slag at 1300 °C is much higher than that at lower temperatures for a given evaporation time.

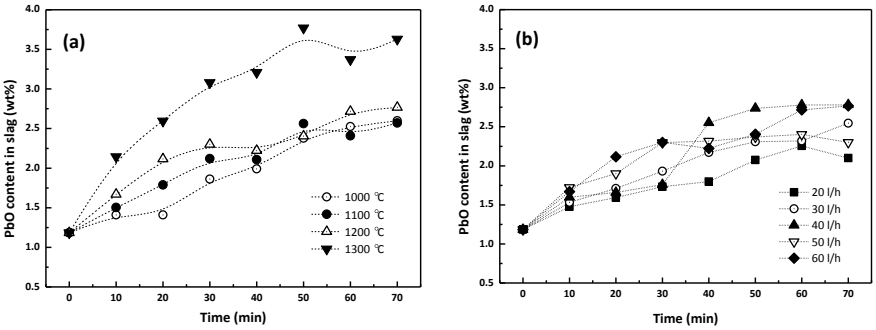

Fig. 4 PbO content in the molten slag as a function of time at different **a** temperatures and **b** N_2 flow rates (under conditions of 1200 °C, 60 l/h N_2 flow, 8.2 mm lance inner diameter, and 1.5 mm lance immersed depth)

The PbO content in the molten slag also increased with increasing temperature and N_2 flow rate (Fig. 4a, b).

Table 1 also shows the PbO content in the evaporated ATO at different times. The PbO content in the ATO increases with time (due to the PbO enrichment in molten slag), leading to a decrease in ATO product purity as the evaporation proceeds. It is difficult to understand the effect of other parameters on the PbO content in the ATO since only a small fraction of ATO was collected in this work. In short, the PbO content is below 0.25 wt% (the upper limit specified by International Antimony Association [8]) in all tests except for S-4, where the evaporation temperature was 1300 °C.

Characterization of the Evaporated ATO and the Residual Slag

The ATO deposited on the Al plate shows a white color (Fig. 5a). As seen in the X-ray diffraction pattern (Fig. 5b), senarmontite (α-Sb_2O_3) and valentinite (β-Sb_2O_3) are the main phases of the ATO. The SEM image exhibits the ATO particles with octahedral, rod-shaped, and spherical morphologies (Fig. 5c). The octahedral and spherical crystals are senarmontite, and the rod-shaped crystals are identified to be valentinite [11, 12]. It should be noted that commercial ATO products prefer senarmontite with octahedral crystals. The crystal structure and morphology of ATO mainly depend on the deposition conditions, especially the temperature [13]. In addition, the ATO contains a small amount of PbO. The ICP-OES analysis confirms that the PbO content in ATO is less than 0.2 wt% when the evaporation temperature is below 1200 °C (Table 1).

The residual slag from test S-7 was characterized using different analytical techniques. Figure 6a shows the main elemental composition of the residual slag analyzed with $LiBO_2$ fusion followed by ICP-OES. The slag sample is mainly composed of

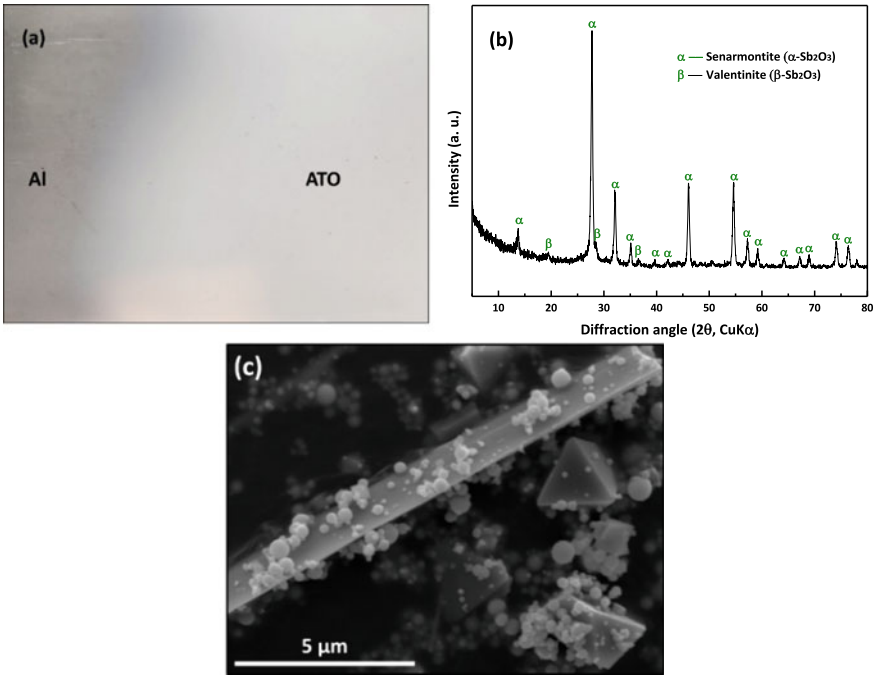

Fig. 5 Characterization of the ATO deposited on the Al plate, **a** white color, **b** phase composition, and **c** morphology

Sb (36.6 wt%), Al (13.0 wt%), Fe (4.1 wt%), Pb (2.4 wt%), Cr (1.6 wt%), and Si (4.3 wt%). As seen in the X-ray diffraction pattern (Fig. 6b), valentinite (β-Sb_2O_3), aluminum oxide (Al_2O_3), and amorphous phase are identified in the residual slag. Figure 6c shows the BSE images of the residual slag sample. According to the EPMA-WDS measurement, spinel and metallic antimony were also present in the residual slag. Phase C in Fig. 6c is rich in CaO (12.0 wt%) and Sb_2O_5 (72.8 wt%) with minor Fe_2O_3, Al_2O_3, and PbO contents. The calculated formula of phase C is $CaSb_2O_6$. The amorphous phase Am1 contains 16.4 wt% SiO_2, 2.3 wt% Na_2O, 10.7 wt% Al_2O_3, 2.2 wt% Fe_2O_3, 5.4 wt% PbO, 1.2 wt% CaO, 0.4 wt% MgO, and 61.3 wt% Sb_2O_5. The amorphous phase Am2 contains more Sb_2O_5 (68.1 wt% on average) and less other oxides than Am1. Sb_2O_5 rather than Sb_2O_3 is present in the amorphous phase because under this assumption, the analyzed total oxide composition is closer to 100%. However, the presence of Sb_2O_5 needs to be further confirmed in our follow-up experiments.

The residual slag contains a considerable amount of Sb (36.6 wt%), indicating the evaporation of Sb_2O_3 was not fully completed. This incomplete Sb_2O_3 evaporation is probably due to (i) the slag viscosity increased with Sb_2O_3 evaporation, impeding the mass transfer in the molten slag; (ii) Sb_2O_3 in the molten slag was oxidized into Sb_2O_4 or Sb_2O_5 (since the experiments were carried out in an open furnace), which

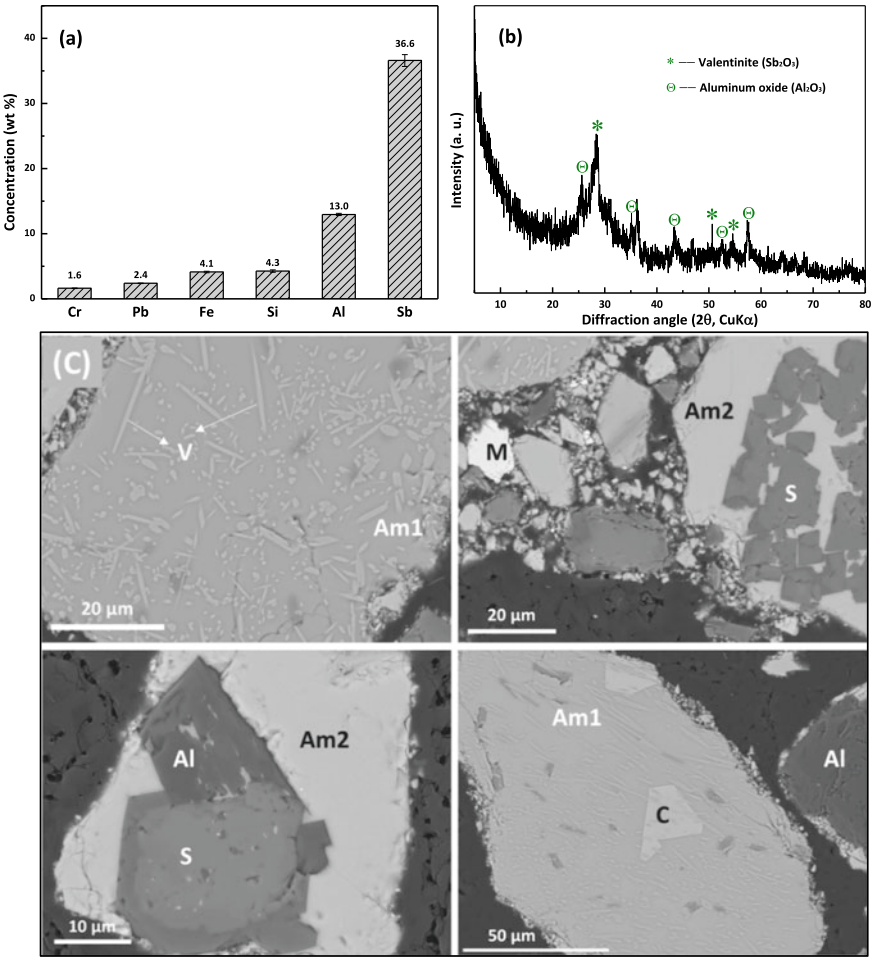

Fig. 6 Characterization of the residual slag of run S-7, **a** chemical composition, **b** mineral phases, and **c** BSE images (V = valentinite, Am = amorphous, M = metallic Sb, S = spinel, Al = Al_2O_3 and $(Al, Cr)_2O_3$, C = $CaSb_2O_6$)

are difficult to be evaporated; (iii) the changes in slag composition decreased the Sb_2O_3 activity in the molten slag. These possible reasons will be further investigated in our future research.

Conclusions

The evaporation of Sb-rich slag was experimentally studied to obtain fundamental knowledge on Sb-rich slag evaporation. The main conclusions of this work can be drawn as follows:

(1) Increasing the temperature, gas flow rate, lance inner diameter, and lance position resulted in a higher slag evaporation ratio and Sb recovery.
(2) The optimum evaporation conditions using the present experimental set-up are 1200 °C and a N_2 flow rate of 40 l/h.
(3) The PbO content in the slag is enriched during evaporation, resulting in an increasing PbO content in the ATO product.
(4) The produced ATO consists of both senarmontite (α-Sb_2O_3) and valentinite (β-Sb_2O_3).
(5) The residual slag after evaporation contains 36.6 wt% Sb, indicating an incomplete evaporation of Sb_2O_3 under the present experimental conditions.

References

1. Henckens MLCM, Driessen PPJ, Worrell E (2016) How can we adapt to geological scarcity of antimony? Investigation of antimony's substitutability and of other measures to achieve a sustainable use. Resour Conserv Recycl 108:54–62
2. Dupont D, Arnout S, Jones PT, Binnemans K (2016) Antimony recovery from end-of-life products and industrial process residues: a critical review. J Sust Metall 2(1):79–103
3. Liu WF, Yang TZ, Zhang DC, Chen L, Liu YF (2014) A new pyrometallurgical process for producing antimony white from by-product of lead smelting. JOM 66(9):1694–1700
4. Ye LG, Tang CB, Liu H, Chen YM (2019) Efficient bath-smelting reduction of antimony oxide in FeO-SiO_2-CaO-Na_2O quaternary slag with low melting point. JOM 71(11):3903–3908
5. Anderson CG (2012) The metallurgy of antimony. Geochemistry 72:3–8
6. Mendoza DG, Hino M, Itagaki K (2001) Volatility and vapor pressure measurements of antimony and arsenic components in CaO-SiO_2-$FeO_{1.5}$ slags at 1573 K by transpiration method. J Min Mater Process Inst Jpn 117:63–68
7. Itoh S, Ono J, Hino M, Nagasaka T (2005) Kinetic study on recovery of antimony in anode slime from used lead batteries utilizing volatile oxide formation. Mater Trans 46(3):658–664
8. Binz F, Friedrich B (2017) Development of secondary antimony oxides from metallurgical slags for the application in plastic products. J Sust Metall 3(4):683–689
9. Ling HB et al (2021) Mineralogical characterization of antimony-containing metallurgical residues. Paper presented at the 7th international slag valorisation symposium, Leuven, Belgium, 27–29 Apr 2021
10. Waladan M, Nilmani M (1995) The effect of injection parameters on slag fuming. Can Metall Quart 34(4):311–318
11. Qiu KQ, Zhang RL (2006) Research on preparation of nanometer antimony trioxide from slag containing antimony by vacuum evaporation method. Vacuum 80(9):1016–1020
12. Biver M, Shotyk W (2013) Stibiconite (Sb_3O_6OH), senarmontite (Sb_2O_3) and valentinite (Sb_2O_3): Dissolution rates at pH 2–11 and isoelectric points. Geochim Cosmochim Acta 109:268–279
13. Orman RG, Holland D (2007) Thermal phase transitions in antimony (III) oxides. J Solid State Chem 180(9):2587–2596

Microstructural Evolution of Thermal Insulation Materials Prepared by Sintering of Ferronickel Slag and Fly Ash Cenosphere

Guangyan Zhu, Zhiwei Peng, Lei Yang, Wenxing Shang, and Mingjun Rao

Abstract The annual output of ferronickel slag in China has increased rapidly in recent years, causing a serious threat to the environment. In this study, the influence of addition of FAC up to 35 wt% on the process of preparing thermal insulation materials from ferronickel slag was investigated, with an emphasis on the microstructural evolution. When the addition of FAC increased from 15 wt% to 35 wt%, along with phase transformations, the microstructure of thermal insulation material varied significantly, featured by conversion from isolated pores to connected pores. The pore size and porosity of the material increased rapidly from 84 μm and 28% to 140 μm and 47%, respectively, improving the thermal insulation performance of the material.

Keywords Ferronickel slag · Fly ash cenosphere · Sintering · Microstructure · Porosity

Introduction

Ferronickel slag is a byproduct generated in the process of production of ferronickel from laterite ores by pyrometallurgical methods, primarily the rotary kiln-electric arc furnace (RKEF) process [1]. The annual output of ferronickel slag in China has exceeded 40 million tons, causing a serious threat to the environment [2]. Due to use of laterite ores, the ferronickel slag discharged often has high magnesium and silicon contents [3]. At present, ferronickel slag is used as a raw material for land-filling, production of cement and concrete, recovery of valuable metals, preparation of refractory materials, etc [4–11]. However, there are still some problems in the utilization of ferronickel slag, such as low utilization percentage of the slag, high production cost, and poor product quality [4].

G. Zhu · Z. Peng (✉) · L. Yang · W. Shang · M. Rao
School of Minerals Processing and Bioengineering, Central South University, Changsha 410083, Hunan, China
e-mail: zwpeng@csu.edu.cn

Z. Peng et al. (eds.), *12th International Symposium on High-Temperature Metallurgical Processing*, The Minerals, Metals & Materials Series,
https://doi.org/10.1007/978-3-030-92388-4_14

Fly ash cenosphere (FAC) is a solid waste generated from coal-fired power plants [12]. Its main chemical components are silica and alumina. Because of its hollow structure, high porosity, and large specific surface area [6], FAC can be used as a pore former for producing thermal insulation materials.

Recently, a facile route has been developed for preparation of high-temperature thermal insulation materials by sintering of ferronickel slag in the presence of FAC [13, 14]. It was demonstrated that at 1200 °C, a good thermal insulation material with thermal conductivity less than 1 W/(m K) and compressive strength greater than 10 MPa could be obtained by adding 25 wt% FAC for sintering of ferronickel slag for 2 h. Both the addition of FAC and sintering temperature affected the preparation of the thermal insulation material [14]. However, a detailed study of the microstructural evolution during the sintering process with different additions of FAC has not been reported. The purpose of this study was to investigate the effect of FAC addition on the microstructure of thermal insulation material derived from ferronickel slag.

Experimental

Raw Materials

The raw materials were mainly ferronickel slag and FAC. Figure 1 shows the XRD patterns of ferronickel slag and FAC. The slag was composed of olivine, while FAC was primarily constituted by mullite and quartz. Figure 2 shows the SEM images of the materials. Evidently, the slag particles were very fine, while the FAC particles were basically spherical with larger sizes. Besides, for briquetting of the mixture of ferronickel slag and FAC before sintering, sodium carboxymethyl cellulose (CMC) was used as binder.

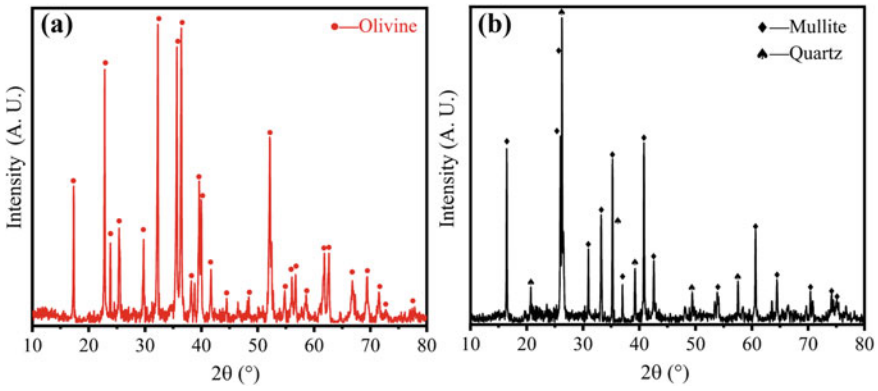

Fig. 1 XRD patterns of **a** ferronickel slag and **b** FAC

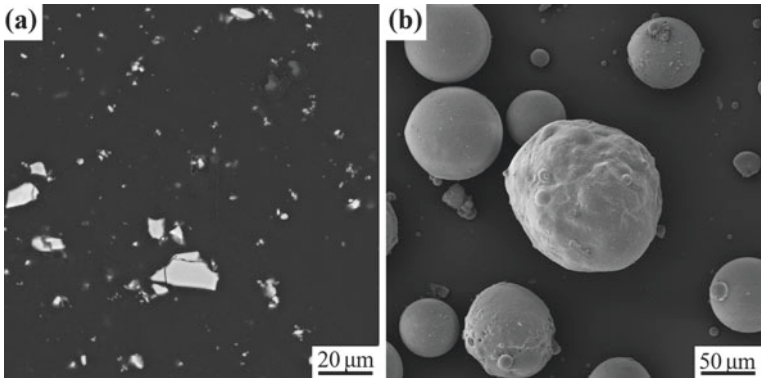

Fig. 2 SEM images of **a** ferronickel slag and **b** FAC

Experimental Procedure

Initially, ferronickel slag and FAC were ground to passing through a 200-mesh (0.074 mm) sieve, and mixed evenly with different FAC additions and 0.5 wt% sodium carboxymethyl cellulose (CMC). Their mixtures were then briquetted by a manual hydraulic press at 6 MPa. The briquettes were dried in an oven at 105 °C for 3 h and sintered in a muffle furnace at 1200 °C for 2 h. The resulting materials were then taken out and cooled as thermal insulation materials for characterizations of properties.

Characterizations

The microstructural evolution of the thermal insulation materials was characterized using an electron scanning electron microscope (SEM, FEI QUANTA 200; FEI, Eindhoven, The Netherlands) equipped with an energy dispersive X-ray spectroscopy (EDS) detector (EDAX, Inc., Mahwah, NJ, USA). The apparent porosities of the materials were determined by the Archimedes method. The pore sizes were measured by using software ImageJ (National Institutes of Health, Bethesda, MD, USA) to analyze SEM images. The BET surface areas of the materials were measured using an automated gas adsorption analyzer (ASAP 2420, Micromeritics, USA).

Results and Discussion

Figure 3 shows the microstructures of thermal insulation materials obtained by sintering of ferronickel slag with the additions of 0 wt%, 15 wt%, 20 wt%, 25 wt%, 30 wt%, and 35 wt% FAC. Without the addition of FAC, the thermal insulation

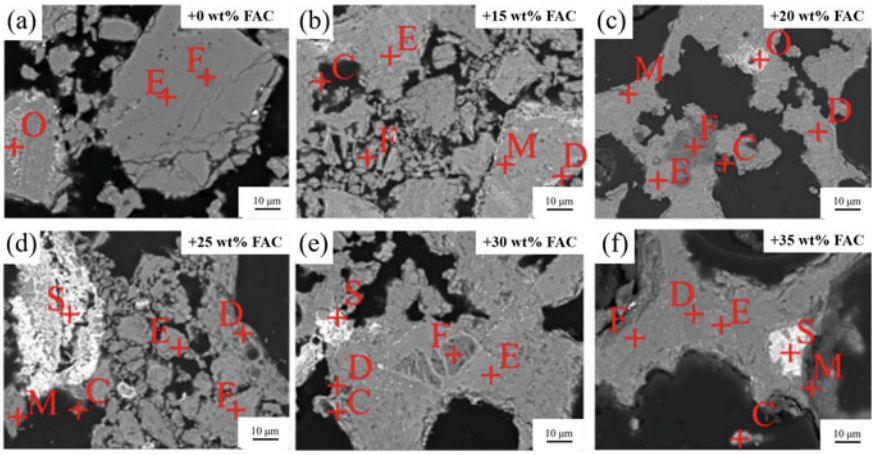

Fig. 3 SEM images of the thermal insulation materials prepared by sintering of ferronickel slag with different additions of FAC showing the phase transformations: C–cristobalite, D–cordierite, E–enstatite, F–forsterite, M–mullite, O–olivine, and S–spinel

material was mainly composed of three phases, namely forsterite (point F), olivine (point O), and enstatite (point E). For the insulation material prepared by sintering with the addition of 15 wt% FAC, mullite (point M), cordierite (point D), and cristobalite (point C) began to appear. It was in association with the decomposition of olivine in ferronickel slag to forsterite which had preferential reaction with SiO_2, producing enstatite. The enstatite would subsequently react with Al_2O_3 and SiO_2 to form cordierite. On the other hand, cristobalite was a result of phase transformation of SiO_2 from the raw materials at high temperature. The main reactions are given as follows.

$$2\left[(\mathrm{Mg}\cdot\mathrm{Fe})\mathrm{O}\cdot\mathrm{SiO_2}\right]+3/2\mathrm{O_2}=\mathrm{Mg_2SiO_4}+\mathrm{Fe_2O_3}+\mathrm{SiO_2} \quad (1)$$

$$\mathrm{Mg_2SiO_4}+\mathrm{SiO_2}=2\mathrm{MgSiO_3} \quad (2)$$

$$14\mathrm{MgO}+2\mathrm{Al_2O_3}+17\mathrm{SiO_2}=12\mathrm{MgSiO_3}+\mathrm{Mg_2Al_4Si_5O_{18}} \quad (3)$$

Except the above main phases, there were also spinel (point S) phases. When the addition of FAC increased to 20 wt%, the reaction between ferronickel slag and FAC was still incomplete, indicated by residual olivine in Fig. 3. After sintering with the addition of 25 wt% FAC, the thermal insulation material had no obvious olivine phase. On the contrary, the large quantity of cordierite (point D) indicated the complete reaction between ferronickel slag and FAC. Meanwhile, more spinel particles were identified. For the insulation materials obtained by sintering with the additions of 30 and 35 wt% FAC, their main phases were enstatite, cordierite, and

forsterite with clear crystal boundaries, in addition to spinel. Note that for brevity, the corresponding EDS spectra for identifying the phases in Fig. 3 were not provided.

As a pore former, FAC was expected to play an important role in preparing the thermal insulation materials by introducing pores with variable morphology. Figure 4 shows the evolution process of pore structure of the insulation materials. When the addition of FAC was below 20 wt%, the materials contained mainly isolated pores. As it increased to 25 wt%, connected pores began to appear. When it continuously increased further to 35 wt%, large connected pores were observed.

Because of the changes of pore structures, the pore size and porosity of the thermal insulation material varied significantly with the addition of FAC. As shown in Fig. 5,

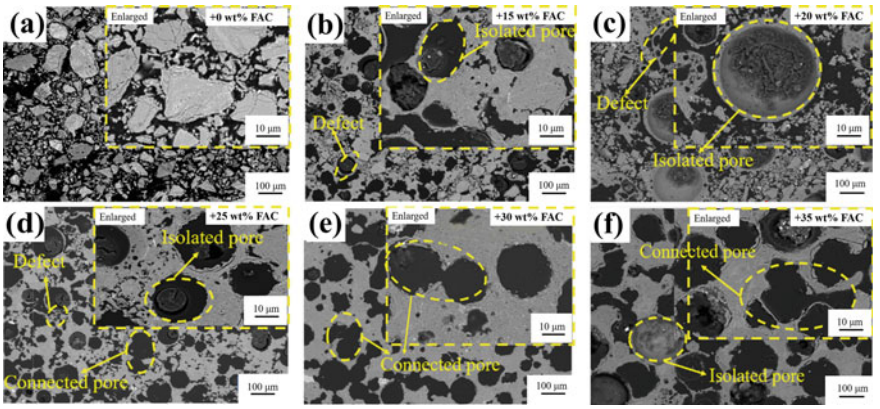

Fig. 4 SEM images of the thermal insulation materials prepared by sintering of ferronickel slag with different additions of FAC showing the pore changes

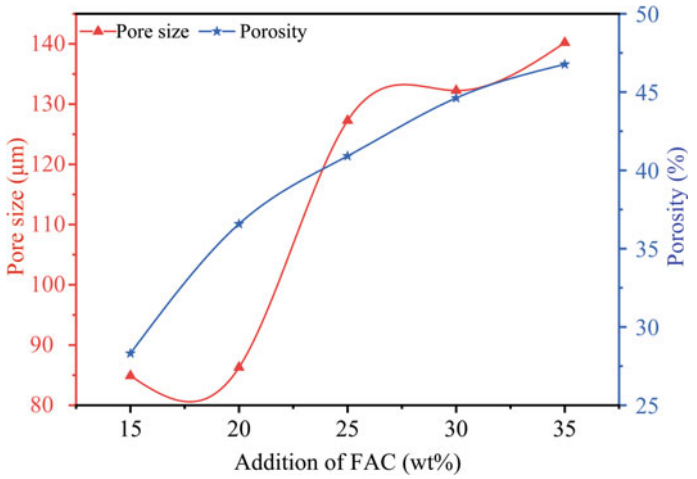

Fig. 5 Variations of pore size and porosity of thermal insulation material with addition of FAC

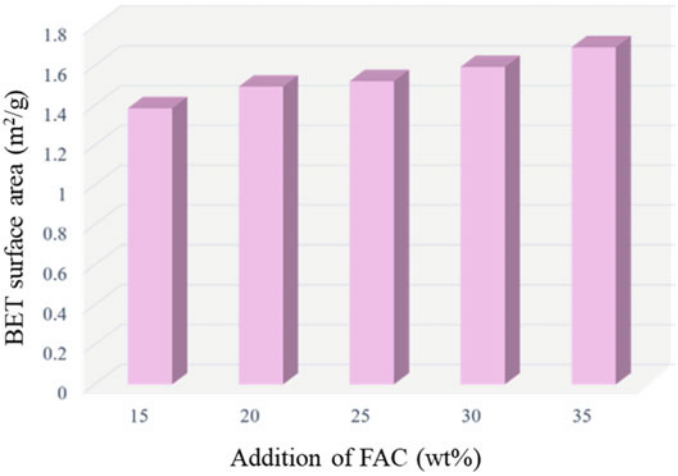

Fig. 6 Variations of BET surface area of thermal insulation material with addition of FAC

when the addition of FAC increased from 15 wt% to 35 wt%, the pore size and porosity of the material increased rapidly from 84 μm and 28% to 140 μm and 47%, respectively. Due to the addition of FAC which had hollow structure, the BET surface area of the material also increased steadily with increasing addition of FAC, as demonstrated in Fig. 6. As expected, these changes would contribute to higher insulation performance of the material, in agreement with the decreasing trend of thermal conductivity reported previously [13].

Conclusions

This study reported the effect of the addition of FAC on producing thermal insulation materials using ferronickel slag as a main raw material. Adding FAC could induce phase transitions with significant changes of microstructure. When the addition of FAC increased from 15 wt% to 35 wt%, along with phase transformations, the microstructure of thermal insulation material varied considerably. There was an evident conversion from isolated pores to connected pores. It was demonstrated that the pore size of the material increased from 84 μm to 140 μm. Meanwhile, the porosity increased rapidly from 28% to 47%, respectively. These changes would improve thermal insulation performance of the material.

Acknowledgements This work was partially supported by the Science and Technology Planning Project of Hunan Province, China under Grant 2019RS2008, the Project of State Key Laboratory Cultivation Base for Nonmetal Composites and Functional Materials under Grant 17kffk11, and the Hunan Provincial Co-Innovation Center for Clean and Efficient Utilization of Strategic Metal Mineral Resources under Grant 2014-405.

References

1. Tiwari A, Singh S, Nagar R (2016) Feasibility assessment for partial replacement of fine aggregate to attain cleaner production perspective in concrete: a review. J Clean Prod 135:490–507
2. Sun J, Feng J, Chen Z (2019) Effect of ferronickel slag as fine aggregate on properties of concrete. Constr Build Mater 206:201–209
3. Chen Y, Ji T, Yang Z, Zhan W, Zhang Y (2020) Sustainable use of ferronickel slag in cementitious composites and the effect on chloride penetration resistance. Constr Build Mater 240:117969
4. Kim H, Lee C, Ann K (2019) Feasibility of ferronickel slag powder for cementitious binder in concrete mix. Constr Build Mater 207:693–705
5. Saha AK, Sarker PK (2016) Expansion due to alkali-silica reaction of ferronickel slag fine aggregate in OPC and blended cement mortars. Constr Build Mater 123:135–142
6. Lemonis N, Tsakiridis P, Katsiotis N, Antiohos S, Papageorgiou D, Katsiotis M, Beazi-Katsioti M (2015) Hydration study of ternary blended cements containing ferronickel slag and natural pozzolan. Constr Build Mater 81:130–139
7. Saha AK, Sarker PK (2017) Sustainable use of ferronickel slag fine aggregate and fly ash in structural concrete: Mechanical properties and leaching study. J Clean Prod 162(20):438–448
8. Maragkos I, Giannopoulou I, Panias D (2009) Synthesis of ferronickel slag-based geopolymers. Miner Eng 22(2):196–203
9. Gu F, Peng Z, Zhang Y, Tang H, Tian W, Lee J, Rao M, Li G, Jiang T (2020) Promoting spinel formation and growth for preparation of refractory materials from ferronickel slag. Int J Appl Ceram Technol 17(4):1701–1712
10. Zhang Z, Zhu Y, Tao Y, Liang F, Li C, Hua Z, Hao W (2017) Conversion of local industrialwastes into greener cement through geopolymer technology: a case study of high-magnesium nickel slag. J Clean Prod 141463–471
11. Deepthi MV, Sharma M, Sailaja RRN, Anantha P, Sampathkumaran P, Seetharamu S (2010) Mechanical and thermal characteristics of high density polyethylene–fly ash cenospheres composites. Mater Des 31(4):2051–2060
12. Sukkae R, Suebthawilkul S, Cherdhirunkorn B (2018) Utilization of coal fly ash as a raw material for refractory production. J Met Mater Miner 28(1):116–123
13. Yang L, Peng Z, Huang Y, Wang L, Zheng L, Rao M, Li G, Jiang T (2020) Preparation of thermal insulation materials from ferronickel slag with addition of fly ash cenosphere. Characterization of Minerals, Metals, and Materials 2020, pp 217–226
14. Yang L, Peng Z, Huang Y, Wang L, Zheng L, Rao M, Li G, Jiang T (2021) Co-utilization of ferronickel slag and fly ash cenosphere for production of superior thermal insulation materials. Ceram Int 47(7):10019–10026

Comparative Study on the Cleanliness of Ultra-Low Carbon Al-Killed Steel by Different Heating Processes

Shen-yang Song, Jing Li, Wei Yan, and Jian-xiao Zhang

Abstract Cleanliness of aluminum-killed ultra-low carbon steel produced through BOF-RH-CC and BOF-LF-RH-CC was comparatively investigated by various test equipment. Three different heating processes were used when the converter tapping temperature was low: reheating by blowing oxygen and Al addition during RH early decarburization stage (Process-A); reheating by blowing oxygen and Al particles addition at the end of RH decarburization (Process-B); and no Al addition at RH decarburization stage but the process was BOF-LF-RH-CC (Process-C). The non-metallic inclusions can be removed obviously in three refining processes. Statistical analysis of inclusion area fraction showed Process-A was substantially less than those in Process-B. Furthermore, the proportion of single inclusion area <8 μm^2 increased from Process-A level 85% to Process-C level 95%. Moreover, this study proposed an XGBoost model based on big data mining methods to investigate the computational simulation and the introduction of the XGBoost model ensured 90% accuracy rate for seeking an optimum refining process.

Keywords Ultra-low carbon aluminum-killed steel · Deoxidation · Desulfurization · Cleanliness · Datamining · XGBoost model

Advanced ultra-low carbon Al-killed steel has been widely used in automobiles, household appliances as well as other products because of its high strength, good plasticity, and excellent formability [1]. Automobile and household appliances have extremely high requirements for the surface quality of cold-rolled panel. On the contrary, amount of large-sized non-deforming inclusions cause the surface defects of cold-rolled panel. Therefore, it is important to reduce the amount of inclusions and control inclusions size during the refining process [2–5].

Ruhrstahl Heraeus (RH) refining is a preferred process for mass production of ultra-clean steel because of its advantages in decarburization, deoxidation, inclusions

S. Song · J. Li (✉) · W. Yan · J. Zhang
State Key Laboratory of Advanced Metallurgy, University of Science and Technology Beijing, Beijing 100083, China
e-mail: lijing@ustb.edu.cn

Z. Peng et al. (eds.), *12th International Symposium on High-Temperature Metallurgical Processing*, The Minerals, Metals & Materials Series,
https://doi.org/10.1007/978-3-030-92388-4_15

removal, alloying, and short processing cycle. So it always associates with converter and continuous casting to achieve most production of ultra-low carbon Al-killed steel. For low carbon aluminum-killed steel, lots of Al_2O_3 inclusions are generated after aluminum alloy being fed into molten steel with a small amount of dissolved oxygen and they are often considered to be harmful to castability and final product quality. Liu studied the relationship between the total oxygen content in the steel, the amount of Al inclusion in the steel, and steel circulation time during RH refining process. In first two minutes after aluminum addition, the inclusions in steel are pure Al_2O_3 cluster; six minutes later, the cluster of Al_2O_3 inclusions disappear, the majority of inclusions in steel are globular and massive Al_2O_3 with size of less than 5 μm [6]. Moreover, the formation mechanism and morphological evolution of Al_2O_3 inclusions during RH refining process was researched. Some researchers have reported that lower slag oxidizability is beneficial for improving the cleanliness of molten steel during the refining process [7].

It is still difficult to achieve stable and satisfactory temperature control under low end carbon content for converter steelmaking despite some plants or researchers having applied methods like dynamic converter automatic steelmaking system [8]. In order to ensure continuous casting regular production, blowing oxygen and adding aluminum are usually carried out in the decarburization stage of the RH-OB refining process to reheat. As a result, the amount of Al and Al_2O_3 inclusion would increase during the RH process. More Al_2O_3 inclusion decreases the cleanliness of liquid steel. At the same time, reheating of RH-OB requires oxygen blowing, which will deteriorate the improvement of RH-OB vacuum degree, and will be also unfavorable for the improvement of the decarburization rate of molten steel [9–11]. In order to ensure the cleanliness of molten steel, a long holding time in the ladle after RH vacuum process is always required for ultra-low carbon Al-killed steel. A reasonable holding time could improve the cleanliness, but prolonging the holding time long will cause significant temperature drop of molten steel, and further accelerate secondary oxidation of molten steel. Cui studied the influence of the holding time after RH process on the total oxygen content and non-metal inclusion content of IF steel. It is suggested that the holding time should be controlled between 30 and 40 min [12]. With the rapid development of information technology, tens of thousands of production data can be tracked and recorded, which results in exponential data growth. This is often called the ‘big data era’ [13]. Wang established a data mining model to investigate the effect of smelting parameters on the inclusion defect of cold sheet and ranked them as: the total oxygen content before deoxidization in RH > BOF endpoint temperature > temperature before deoxidization in RH. However, Wu didn’t propose a better solution to control these parameters and the number of examined samples was quite small, which limited the model’s generalizability [14]. Therefore, the timing of aluminum addition, how to reduce aluminum addition during RH decarburization process under the condition of stable temperature and improve the cleanliness of molten steel are problems need to solve.

In present work, to study influence of different heating processes on the cleanliness of ultra-low carbon Al-killed steel and to determine the appropriate chemical heating process, RH industrial experiments involved three different heating processes. The

Table 1 Main chemical compositions of steel (wt.%)

C	Si	Mn	P	S	Ti	N	Al_s
<0.0020	0.005	0.07–0.15	<0.012	<0.010	0.060–0.070	<0.0030	0.028–0.050

refining effects of the different heating processes were comparatively investigated from the aspects of liquid steel temperature, impurity element content, and inclusions evolution. Moreover, through collecting and analyzing few months of different heating processes test data, this study introduced an innovative data mining XGBoost model to predict the suitable heating process.

Experimental and Research Methods

Production Process

The current production process of ultra-low carbon Al-killed steel in a domestic steel corporation (see Table 1 for main chemical compositions of steel) was basic oxygen furnace (BOF)—RH—continuous casting (CC)—hot rolling. The converter tapping temperature was 1660 °C, RH-OB vacuum treatment included decarburization for 15 min, followed by aluminum deoxidation, then Ti-Fe and Mn alloying, a circulation for 6 min. After RH treatment, the molten steel in the ladle remained unstirred for more than 30 min before casting.

RH-OB industrial experiments involved two different heating projects during the decarburization stage: Process-A was heating by oxygen blowing and Al particle addition in the early decarburization stage of the RH refining (0–5 min); Process-B was blowing oxygen and Al particle addition at the end of RH decarburization (10–15 min). The process was called a normal process if no extra heat was added during RH decarburization stage.

Process-C was BOF-LF-RH-CC, the converter tapping temperature was 1610 °C, when molten steel was taken into LF refining furnace, followed by heating up with blowing argon for 35 min. No slag was made during LF refining process. The RH vacuum treatment included decarburization for 15 min, followed by aluminum deoxidation, then Ti-Fe alloying, and a circulation for 6 min. After RH treatment, the molten steel in the ladle remained unstirred for more than 30 min before casting; the specific process is shown in Fig. 1.

Experimental Methodology

In three different heating processes, steel samples were taken during refining process. Steel samples were taken by a bucket sampling device at the inlet LF station, leaving

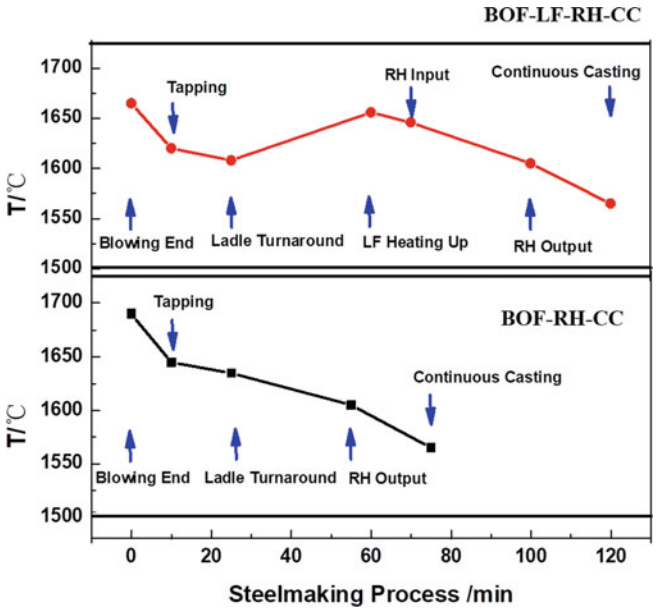

Fig. 1 Ultra-low carbon Al-killed steel time and temperature of steelmaking process

the LF station, at the inlet RH station and leaving the RH station for each process, and the dissolved oxygen content and temperature in RH process were recorded. The sampling process was shown in Fig. 2, and RH refining operation was shown in Fig. 3.

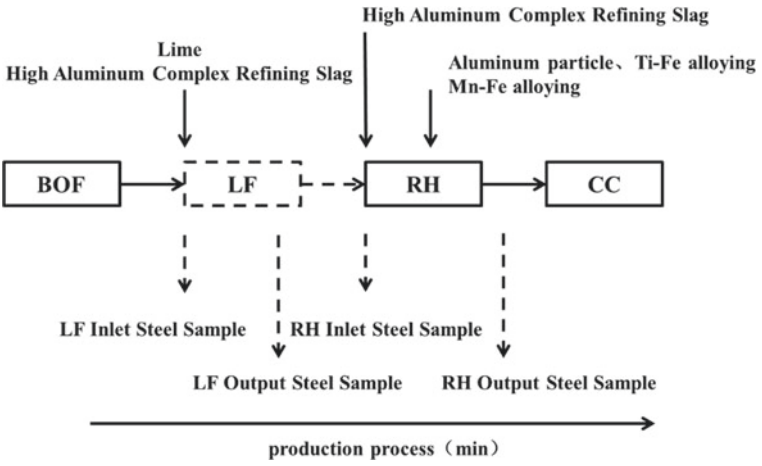

Fig. 2 Secondary refining process sampling

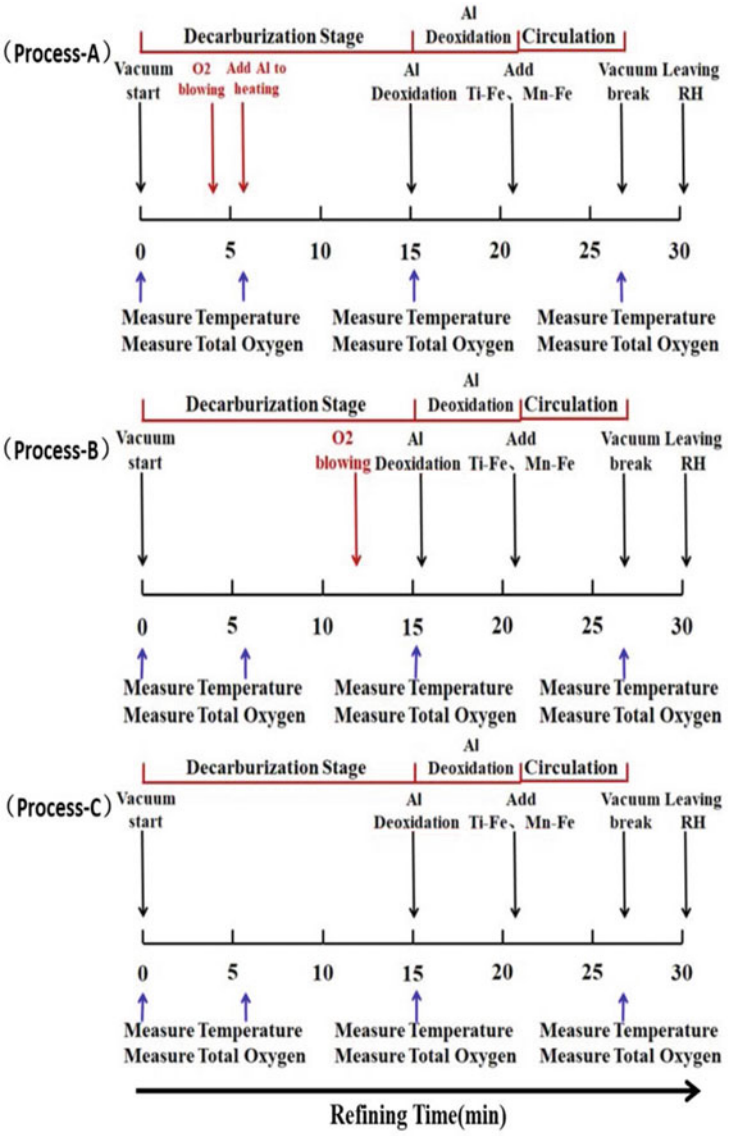

Fig. 3 RH refining operations

Each bucket steel sample took Φ5 × 7 mm sample and 15 mm × 15 mm × 10 mm metallographic sample. The 15 mm × 15 mm × 10 mm metallographic samples were polished by the automatic grinding machine, and the scanning electron microscope (FEI Quanta-250; FEI Corporation, Hillsboro, OR) equipped with EDS (XFlash 5030; Bruker, Germany) examined and analyzed the morphology and chemical composition of non-metallic inclusions. The amount of inclusions and

inclusion size was detected by EVO-INCA steel inclusion automatic scanning system (ZEISS, EVO18 INCASteel, Germany). The Φ5 × 7 mm cylinder samples were polished with 120 mesh sandpaper until the surface was clean, and the total oxygen and nitrogen contents in the samples were measured by an oxygen, nitrogen, and hydrogen analyzer (HORIBA, emga-830, Japan).

Results and Discussion

Temperature Evolution of Different Refining Process

Figure 4 shows the temperature evolution of the different refining processes. In BOF-RH-CC way: normal process, BOF blowing end temperature was 1690 °C; BOF blowing end temperature for Process-A and Process-B was 1680 °C. In Process-C, adopt BOF-LF-RH-CC way, the BOF blowing end temperature was 1650 °C. In RH-OB refining step, at end of decarburization, the temperature of Process-A was 1605 °C the temperature of Process-B was 1600 °C, the normal process and Process-C, the temperature was controlled at 1610 °C; when the vacuum was broken, the temperatures of the molten steel for Process-A and Process-B were controlled close to1600 °C, indicating that two processes achieved the same heating effect. Process-C could control the temperature at 1605 °C, higher than normal process.

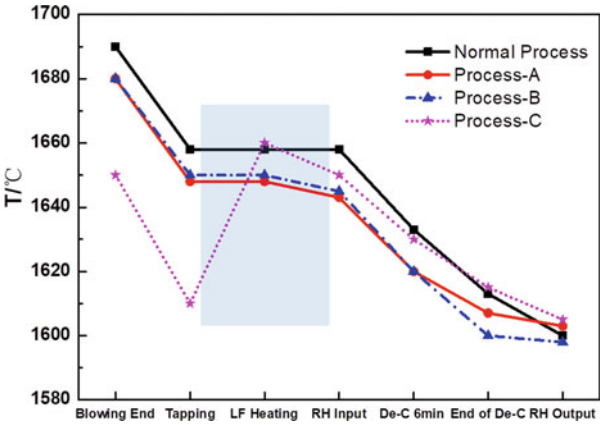

Fig. 4 Temperature evolution of different refining process

Change of Aluminum Adding in RH Refining

Due to that the RH inlet temperature was unstable in the BOF-RH-CC process, the addition of Al particles was needed to increase the temperature during the RH refining process. The function of Al addition in the process of RH refining was temperature-rising, deoxidation, and alloying. Compared with the BOF-RH-CC process, the introduction of the LF furnace made the RH inlet temperature more stable in the BOF-LF-RH-CC process, and therefore the function of Al addition in BOF-LF-RH-CC process changed to deoxidation and alloying.

The decarburization time of the RH refining process was about 15 min. The temperature after decarburization for 5 min determined the amount of Al particles that should be added into the RH decarburization stage. If the temperature after decarburization for 5 min was lower than 1610 °C, Al particles should be added in the furnace. The temperature of the RH refining decarburization process temperature needed to be higher than 1610 °C for 5 min, which was concluded according to the superheat demand of steel continuous casting and the field production data. Figure 5 shows the ratio of oxygen blowing in RH decarburization stage. When the decarburization temperature for 5 min was less than 1610 °C, Al adding rate was up to 86.4%, while when the decarburization temperature for 5 min was more than 1610 °C, Al adding rate was only 11.1%. As can be seen from the above discussion, stabilizing the decarburization temperature for 5 min above 1610 °C can reduce the Al adding ratio at the decarburization stage effectively.

After RH decarburization processing, Al particles were used to deoxidize. According to the condition of 105 tons molten steel and 0.04% content of $[Al]_s$ in steel, the amount of Al added in the RH refining process was shown in Fig. 6. For Process-C, average Al added in RH process was 133.5 kg; for Process-A and Process-B, average Al added in RH process was 175 kg which was significantly higher than the average weight of 140 kg in normal process.

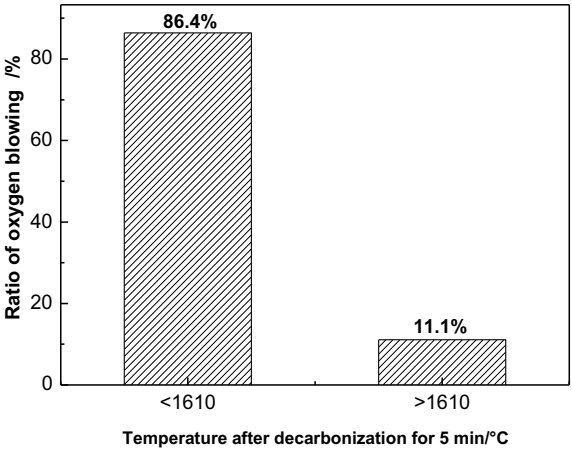

Fig. 5 Ratio of oxygen blowing in RH decarburization stage

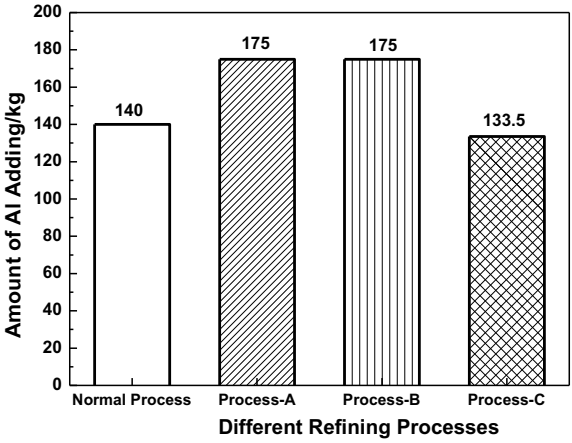

Fig. 6 Amount of aluminum added during refining process

During the RH decarburization stage, the effect of molten reheating through Al addition which was not only controlled by the reasonable amount of aluminum addition, but also by oxygen blowing timing and oxygen blowing intensity. If oxygen blowing was too early, it would damage the refractory material at the bottom of the connecting pipe and delay the improvement of vacuum degree in the vacuum room which could lead to slow down the decarburization. If oxygen blowing was too late, it would not be conducive for timely CO gas release, and the decarburization would be incomplete due to low dissolved oxygen content in molten steel. Through the Process-C, RH furnace temperature was stable, thus reducing the Al addition ratio in the RH refining decarburization stage, which could not only reduce the RH refining cost, but also improve the RH refining effect.

T [O] and Sulfur Content Control in Molten Steel

T [O] Control in Molten Steel

The dissolved oxygen reflected cleanliness of molten steel. Figure 7 shows the variation of dissolved oxygen in different refining processes. It can be seen from Fig. 7, except Process-B blowing oxygen at the end of the decarburization which caused oxygen level raise to 500×10^{-6}, normal process, Process-A, Process-C had a similar oxygen level variation trend in the RH refining stage. By comparing variation of dissolved oxygen in RH refining process, it can be found that:

(1) Compared with the BOF-RH-CC process, Process-C adopted BOF-LF-RH-CC process reduced the RH inlet oxygen level. The average of oxygen level was 300×10^{-6} in Process-C, while the BOF-RH-CC process average oxygen level was 450×10^{-6}.

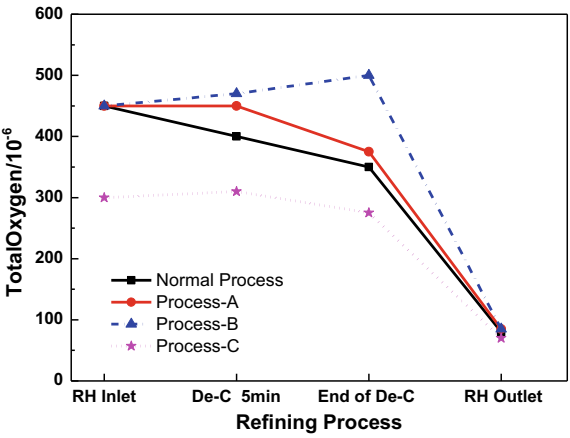

Fig. 7 Variation of dissolved oxygen in RH refining process

Using the Process-C can reduce inlet T [O] about 150 × 10^{-6} compared with the BOF-RH-CC process. The reason was Process-C added high aluminum complex refining slag in the LF refining process which reacted with dissolved oxygen in molten steel. High aluminum complex refining slag can not only reduce the content of dissolved oxygen in molten steel, but also reduce the content of (FeO) and (MnO) in the refining slag.

(2) Normal process, Process-A, and Process-C had similar deoxidation rates which started from the RH decarburization stage for 5 min to the end of decarburization. Within 10 min, the dissolved oxygen level decreased by about 70 × 10^{-6}. After decarburization, the dissolved oxygen content of normal process and Process-A was about 350 × 10^{-6}, while it was about 275 × 10^{-6} for Process-C. The inlet oxygen level of molten steel determined the T [O] at the end of decarburization.

(3) T [O] content at the end of RH decarburization was 500 ppm in Process-B, which is substantially greater than that in other processes.

(4) After the end of decarburization, the vacuum degree was maintained at 1.5 mbar, by adding aluminum particles, different refining ways had same deoxidation rate.

(5) Finally, the normal RH terminal total oxygen content was 80 × 10^{-6}, Process-A was 90 × 10^{-6}, Process-B was 95 × 10^{-6}, and the Process-C was 70 × 10^{-6}. Therefore, the Process-C can reduce the terminal T [O]content effectively.

Sulfur Content Control in Molten Steel

The main chemical compositions of steel during different refining process were listed in Table 2.

Sulfur content changes in the refining process were shown in Fig. 8.

Table 2 Main chemical compositions of steel during different refining process (wt.%)

Process		C	Si	Mn	P	S	Ti	T.O	N	Al
Process-C	LF inlet	0.041	0.004	0.100	0.012	0.010	–	0.0500	–	0.004
	LF outlet	0.044	0.004	0.077	0.008	0.003	–	0.0300	–	0.012
	RH inlet	0.044	0.004	0.077	0.008	0.003	–	0.0300	–	0.012
	RH outlet	0.0015	0.004	0.125	0.008	0.003	0.066	0.0070	0.002	0.04
Normal process	RH inlet	0.028	0.004	0.080	0.008	0.006	–	0.0450	–	0.005
	RH outlet	0.0015	0.004	0.125	0.008	0.006	0.066	0.0080	0.002	0.04
Process-A	RH inlet	0.028	0.004	0.080	0.008	0.006	–	0.0450	–	0.005
	RH outlet	0.0015	0.004	0.125	0.008	0.006	0.066	0.0080	0.002	0.04
Process-B	RH inlet	0.028	0.004	0.080	0.008	0.006	–	0.0450	–	0.005
	RH outlet	0.0015	0.004	0.125	0.008	0.006	0.066	0.0080	0.002	0.04

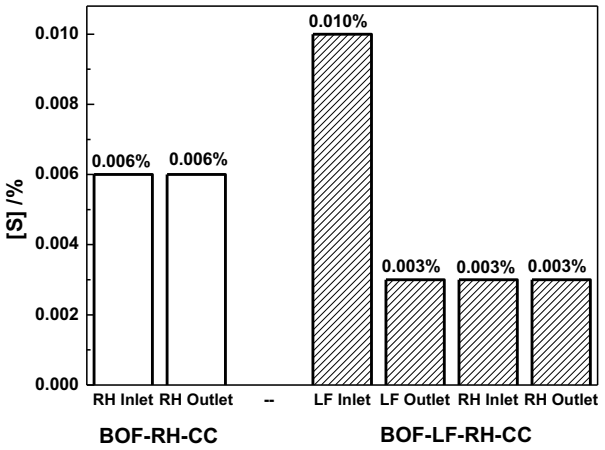

Fig. 8 Sulfur content in molten steel during refining process

In the BOF-RH-CC processing, including Process-A, Process-B, and normal process, the molten steel [S] % was 0.006%. By comparing the RH refining inlet steel compositions and refining terminal steel compositions in Fig. 8, it can be seen that the average [S] % in Process-C was reduced from 0.0100 to 0.0030%.

Change of Inclusion Quantity and Size

Figure 9a shows the average comparison of inclusion area per square millimeter steel sample at the RH refining end under different refining processes.

In Fig. 9a, in normal process had the inclusion control level with inclusion area 220 $\mu m^2/mm^2$; Process-A had the inclusion control level with inclusion area 280 $\mu m^2/mm^2$, whereas Process-B had the worst inclusion control level with and inclusion area of 300 $\mu m^2/mm^2$; Process-C had the best inclusion control level with an inclusion area of 210 $\mu m^2/mm^2$. It can be seen under the condition that the finished product control $[Al]_s$ was 0.04% and the circulation time was 6 min, the Process-B generated more Al_2O_3 inclusions. The normal process RH inlet oxygen level was 450×10^{-6}, adding 140 kg of aluminum in the whole refining process; Process-A and Process-B RH inlet oxygen level was 450×10^{-6}, adding 175 kg of aluminum in the whole refining process; the Process-C RH inlet oxygen level was 300×10^{-6}, adding 133.5 kg of aluminum in the whole refining process.

The RH inlet oxygen level of Process-A and Process-B was almost the same as that of normal process; however, the amount of aluminum added in Process-A and Process-B was 35 kg more than that in normal process. This was because inlet molten steel temperature of Process-A and Process-B was about 1640 °C, and the normal process was 1652 °C Except deoxidation and alloying, the aluminum added in Process-A and Process-B also heated up molten steel temperature during the decarburization stage, which increased the amount of aluminum.

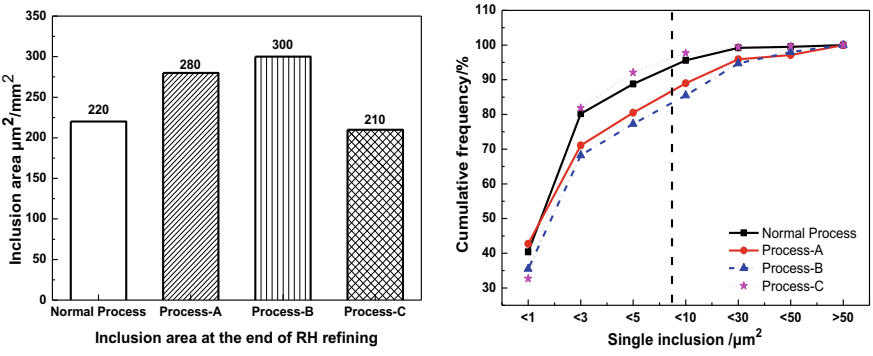

Fig. 9 Inclusion area fraction comparison at the end of RH refining

Figure 9b shows the amount of single inclusion cumulative frequency between different refining processes. The critical area of steel surface inclusion affecting fatigue performance is 8 μm^2, and when the area of a single inclusion was less than 8 μm^2, it was considered that it has no effect on steel quality [15]. In Process-B, the ratio of single inclusion area <8μm^2 proportion was 77.3%; Process-A was 80.5%. As a contrast, the ratio of single inclusion area <8μm^2 proportion was 88.8% in normal process; furthermore, Process-C was 92.1%. Therefore, we can conclude that heating up molten steel temperature during the decarburization stage has a bad effect on steel cleanliness.

Figure 10 shows the large-sized inclusion amount of RH refining end steel samples. The inclusion amount of normal process was 1.5/mm^2, the inclusion amount of Process-A was 2.71/mm^2, and the inclusion amount of Process-B was 3.0/mm^2. In Process-C, inclusion amount was 1.11/mm^2.

Compared with the BOF-RH-CC process, Process-C can lower the RH inlet dissolved oxygen level, reduce the amount of aluminum particles added, stabilize the control level of inclusions, and significantly improve the cleanliness of liquid steel.

Because Al deoxidation was used in this steel, the evolution of Al_2O_3 inclusion size under different refining processes was further studied. The size distribution of Al_2O_3 inclusions in different processes is shown in Fig. 11. According to Fig. 11, the inclusion area of Al_2O_3 in normal process furnaces was evenly distributed, and the of Al_2O_3 inclusions less than 10 μm^2 in molten steel were about 88%, and that of Al_2O_3 inclusions less than 5 μm^2 in molten steel were about 73%; in Process-A, Al_2O_3 inclusions less than 10 μm^2 in molten steel were about 85%, and that of Al_2O_3 inclusions less than 5 μm^2 in molten steel were about 65%; in Process-B, Al_2O_3 inclusions less than 10μm^2 in molten steel were about 79%, and that of Al_2O_3 inclusions less than 5 μm^2 in molten steel were about 40%. According to

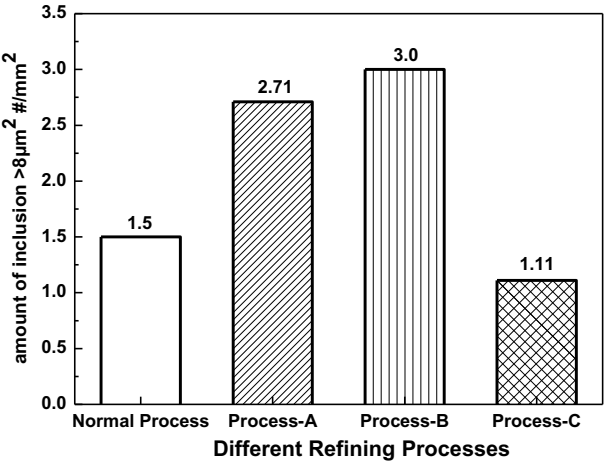

Fig. 10 Large-sized inclusion amount at the end of RH refining #/mm^2

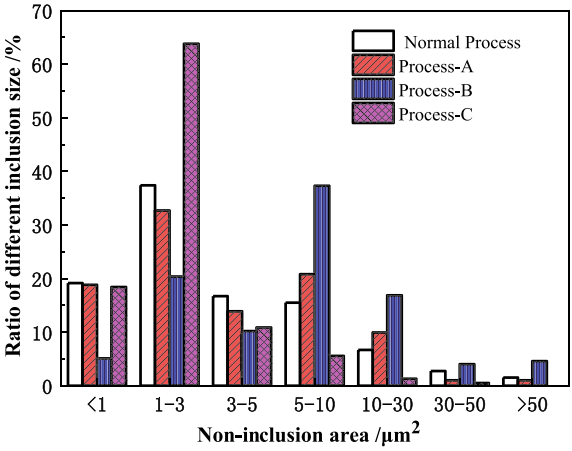

Fig. 11 Al_2O_3 inclusion distribution in different refining process

Fig. 11 which shows the inclusion area of Al_2O_3 in Process-C, the proportion of Al_2O_3 inclusions less than 10 μm^2 in molten steel was about 95%, and that of Al_2O_3 less than 5 μm^2 in molten steel was about 90%. In the Process-C, the proportion of small-size inclusions was higher than that of other processes.

Discussions

Reasons for Improving the Cleanliness of Aluminum-Killed Ultra-Low Carbon Steel

Firstly, in BOF-RH-CC process, the inclusion numbers for Process-A and Process-B were compared. Inclusion numbers for Process-A were substantially lower than those for Process-B at different refining stages.

In Process-A, Al addition was divided into two parts. Part of the Al was added during the decarburization early stage for reheating; at the same time, inclusions produced in the decarburization stage had 10 min to remove; because the dissolved oxygen in the molten steel was reduced, the inclusions produced by final deoxidation were also reduced accordingly.

In Process-A, the inclusion removing time is 10 min in decarburization stage + 6 min in Al deoxidation +6 min in circulation; in Process-B, the inclusion removing time is 6 min in Al deoxidation +6 min in circulation, the oxidizability of molten steel by slag and the inclusion adsorption capacity of slag were similar for Process-A and Process-B; however, the inclusion numbers in molten steel for Process-B were still greater. Therefore, in the case of Process-A, inclusions were remove by longer time, and cleanliness control is more effective.

Secondly, the reason that the Process-C can significantly improve the cleanliness of liquid steel compared Process-A could be attributed to: (1) LF furnace can heat molten steel, so it can avoid heating up of Al adding during the decarburization of RH operation, and (2) LF furnace can blow argon for stirring to promote inclusion rise and better control the cleanliness of liquid steel.

In the ladle argon blowing refining process, liquid steel was in a turbulent state, the rate of inclusion floating and removal consists of two aspects. One was the floating rate of the inclusion itself based on Stokes equation, and the other was the floating rate of the inclusion captured by argon bubbles.

Under laminar flow conditions, the floating velocity of inclusions can be calculated by Stokes Eq. (1)

$$u_s = \frac{g(\rho_{\text{steel}} - \rho_{\text{inclusion}})d_{\text{inclusion}}^2}{18\,\mu_{\text{steel}}} \tag{1}$$

In Eq. (1), g represents the acceleration of gravity, g = 9.8 m/s^2; ρ_{steel}、$\rho_{\text{inclusion}}$ is density of molten steel and inclusions, kg/m^3; μ_{steel} is kinematic viscosity of liquid steel, Pa s; $d_{\text{inclusion}}$ is inclusion diameter, m.

According to Eq. (1), the floating speed of the inclusion Stokes was related to the diameter of the inclusion. With the increase of inclusion's diameter, the Stokes floating speed increases.

Zhang [16] discussed the influence of bubble flotation on the different sizes' inclusion removal rate by establishing a simplified model, but he ignored the influence of turbulence on inclusion removal by bubble flotation. The calculated large-sized inclusions' removal rate was higher than small-sized inclusions. It also explained that turbulence must be considered for the inclusion bubble flotation removal in LF refining process. Duan [17] considered the influence of turbulence on bubble flotation to remove inclusions, he found that in the Ar bubble column, the liquid steel of the turbulent kinetic energy was at around 10^{-1}m^2/s^2, at the same time, utilizing the bubble flotation to remove inclusions mainly concentrated in the Ar bubble column. Under the condition of the turbulent kinetic energy, the catching probability of a single bubble for inclusions of different sizes was basically the same.

The turbulence condition inclusion removal formula is as follows:

$$\frac{\mathrm{d}n_{\text{inclusion}}}{\mathrm{d}t} = -\frac{2u_0}{H} \cdot \frac{\alpha_P}{100} \cdot n_{\text{inclusion}} \tag{2}$$

$$\alpha_P = 2.39 + 573.12 \cdot Q \tag{3}$$

$$u_0 = 0.22 + 3.48 \cdot Q - 158.08 \cdot Q^2 \tag{4}$$

In equation, u_0 is the average rising velocity of molten steel in the plume region, m/s; α_P represents the volume fraction of the plume area of the ladle blowing argon

column, %; $n_{inclusion}$ is the total number of inclusions in the furnace; Q is Argon flow rate of ladle blowing, m^3/s.

The current LF furnace argon flow rate was 220 NL/min; under the condition that the inclusion diameter is 1, 10, 100 μm, Stokes floating speed and inclusion flotation speed were calculated respectively. Figure 12 shows the change of inclusion removal rate with time which the inclusion diameter is 1, 10, 100 μm.

According to Fig. 12a, b, when the inclusion diameter was 1, 10 μm, the inclusion size was small and Stokes floating speed was slow. Compared with Stokes floating removal, bubble flotation was the main inclusion removal method. Under the condition of argon blowing and stirring, almost all 1 μm inclusions were removed by bubble flotation. The ratio of 10 μm inclusion's removal by bubble flotation was about 3 times than Stokes floating removal. It can be seen that ladle argon blowing and stirring can significantly increase the proportion of inclusion removal.

It can be seen from Fig. 12c, when inclusion diameter was 100 μm, Stokes floating speed cannot be ignored due to large size of inclusion, and Stokes floating became the main way to remove inclusions.

In order to further compare the LF refining process in the removal effect of different dimension inclusions, the inclusion removal rate with time was calculated where the inclusion diameter is 1, 10, 100 μm. In this calculation, LF furnace argon gas flow was 220 NL/min; both bubble flotation and Stokes flotation was considered. Figure 13 shows inclusion removal rate for different inclusion diameters.

According to Figs. 12 and 13, when the size of inclusions was 1 and 10 μm, the floating speed of Stokes was relatively small compared with Ar flow field. The main way to remove inclusions was bubble flotation. However, when the inclusion size is 100 μm, the floating speed of Stokes can't be ignored, so Stokes floating removal will be the main way to remove inclusions.

Recently, in the Process-C adopted BOF-LF-RH-CC process, the LF refining time was about 35 min. During this time, the refining furnace can increase the temperature of molten steel effectively, control the composition of molten steel, and reduce molten steel T [O]. In particular, for 100 μm-diameter large-size non-metallic inclusions, the removal rate of LF refining process can reach more than 80%. For 10 μm-diameter size non-metallic inclusions, the removal rate of LF refining process can be close to 15%. Argon blowing and stirring in LF furnace can significantly reduce the amount of inclusions.

Al_2O_3 inclusion has the characteristics of high melting point, poor wettability with steel liquid, and easy to rise to slag for removal. Strong circulating stirring of molten steel under LF refining promoted Al_2O_3 inclusions collision polymerization in molten steel; at the same time, the floating removal of Al_2O_3 inclusions was promoted by molten steel circulation, which reduced the quantity and density of inclusions. After adopting the BOF-LF-RH-CC process, the amount of Al added in RH stage was reduced, the proportion of large-sized Al_2O_3 inclusions in molten steel was reduced, too. For BOF-RH-CC process, it had more addition of Al in decarburization stage and more deoxidation products compared with the BOF-LF-RH-CC process, so it produced more Al_2O_3 inclusions. In the limited RH refining time, the Al_2O_3 inclusions removal efficiency of BOF-RH-CC process was obviously lower than

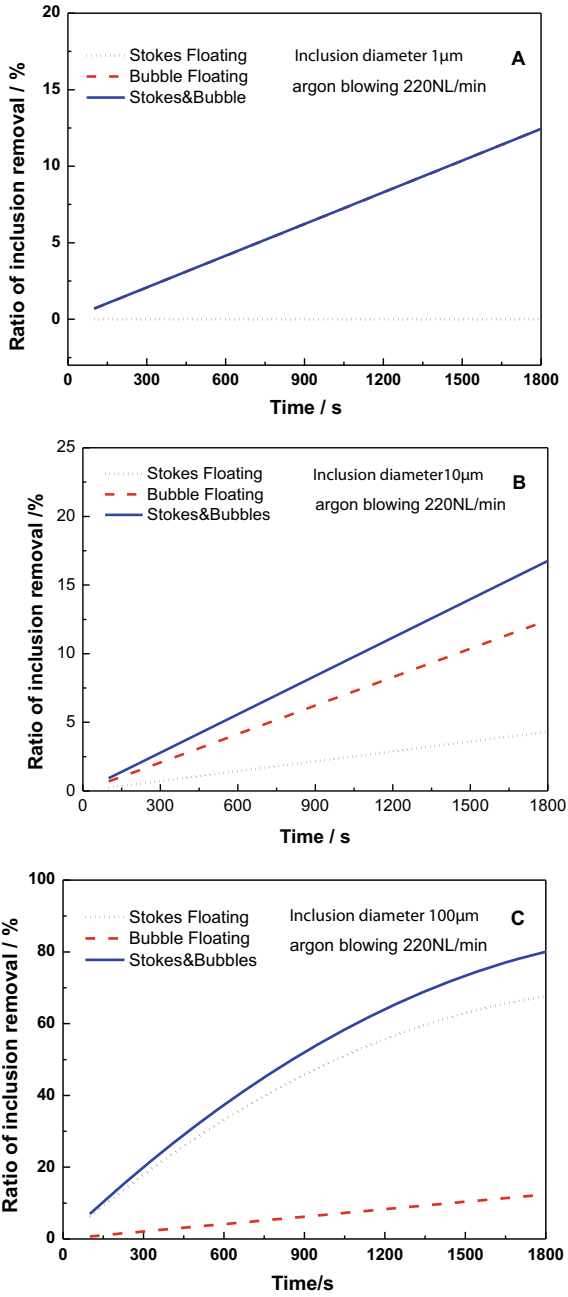

Fig. 12 Inclusion removal fraction as a function of time for different removal conditions with inclusion diameter of 1, 10, 100 μm

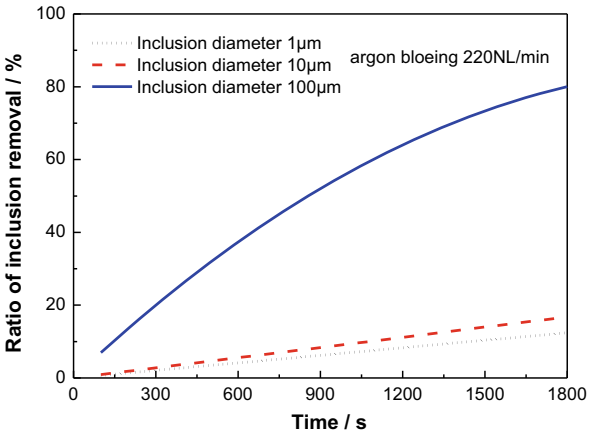

Fig. 13 Inclusion removal rate for different inclusion diameters

that of the BOF-LF-RH-CC process. After RH refining, Al_2O_3 inclusions in the BOF-RH-CC process were larger in size and more in quantity than BOF-LF-RH-CC process.

Selection of Different Heating Process

It could be seen from the above analysis, Process-B was the worst in terms of molten steel T[O] control and inclusion control compared with all heating processes, so Process-B should no longer be used anymore; Process-C had the best performance in molten steel composition and inclusion control, which was conducive to improve product sale price. But it had a disadvantage in long refining time, when the continuous casting production was in a tight pace, as the scheme is not conducive to increase steel production capacity. Process-A was conducive to the acceleration of production pace, but the control of composition and inclusion of liquid steel is worse than Process-C. How to choose the above two heating process under unstable refining inlet temperature situation? Data mining analysis was used to further research.

XGBoost Decision was used in this research. XGBoost Decision belongs to a family of ensemble models. The general idea of boosting trees is to generate a number of simple trees, where each tree is built based on the prediction residuals of the preceding tree. Due to learning from the previous tree, the misclassification can be minimized. On the basis of the traditional boosting tree, the XGBoost algorithm employs a gradient descent algorithm to speed up the convergence [18]. In addition, considering that XGBoost as an ensemble model is more robust than models based on a single algorithm, it can be concluded that the XGBoost model would be the best model for predicting the result with 90% overall accuracy [19].

Data for a total of more than 2000 refining process was obtained. The whole data mining process for XGBoost prediction model is shown in Fig. 14. Python environment was used for data modeling and analysis.

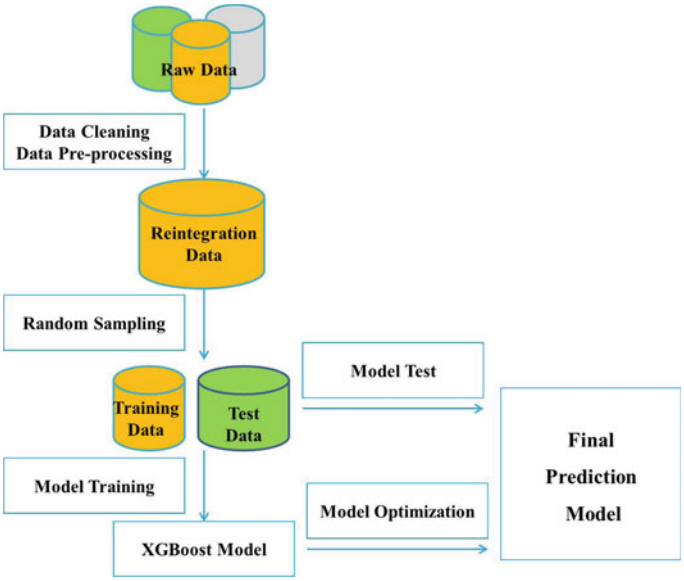

Fig. 14 Logic flows for building final prediction model

Moreover, the robustness of the XGBoost prediction model to the number of decision trees was further investigated. A limited number of decision trees cannot provide enough information, so the prediction accuracy is low. A training decision tree with a very large number may result in overfitting, so XGBoost prediction model decision tree was needed to construct in advance. XGBoost prediction model decision tree is shown in Fig. 15.

XGBoost prediction model decision tree was built by Sklearn module and XGBoost module of Python. The root nodes were selected separately as converter tapping temperature, continuous casting production rhythm tense, and molten steel [S]% ≥0.010. Each decision tree was limited; the max depth was under 5, model

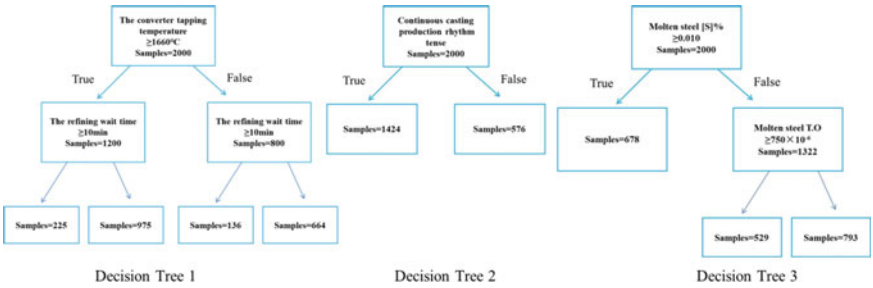

Fig. 15 XGBoost prediction model decision tree

learning rate was under 0.1, and child weight was 1. In the XGBoost model, early stopping rounds were limited as 10 to prevent model overfitting.

Based on the above model establishment process, the prediction accuracy of XGBoost prediction model was 93.4%. It could guide the steel company to adopt different heating processing effectively. When converter tapping temperature was under 1660 °C but waiting time more than 10 min, continuous casting rhythm was fit, the model was recommended to adopt Process-C. Different heating process was needed to consider above variety of conditions.

Conclusions

In view of the problem that RH temperature fluctuates greatly in the production of ultra-low carbon Al-killed steel by BOF -RH-CC, and Al adding heat up of RH process decreases the cleanliness degree of molten steel, this study puts forward the new production process of BOF-LF-RH-CC, and compares the evolution of temperature, aluminum content, sulfur content, oxygen content, and inclusions in the two processes. The main conclusions are as follows:

(1) BOF blowing end temperature for Process-A and Process-B was 1680 °C; in Process-C, the blowing end temperature was 1650 °C. When the RH vacuum was broken, the temperatures of the molten steel for Process-A and Process-B were controlled close to1600°C, indicating that two processes achieved the same heating effect. Process-C could control the temperature at 1605 °C, which was higher than BOF-RH-CC process.

(2) The sulfur content of RH outbound liquid steel in BOF-LF-RH-CC refining process was significantly reduced, from 0.0100 to 0.0030% on average, while the sulfur content of RH outbound is 0.006% in the normal process.

(3) After refining, three heating processes can reduce the total oxygen content of steel. In BOF-RH-CC process, RH-OB has higher inlet oxygen content in the station than BOF-LF-RH-CC. The average aluminum adding in Process-A and Process-B is 175 kg, and the total oxygen content after RH refining is more than 0.0080%. The RH inlet oxygen content in the BOF-LF-RH-CC process was reduced, with the average aluminum adding in the process being 133.5 kg, and the total oxygen mass fraction after RH refining was 0.0070%.

(4) After refining treatment, three processes can reduce the inclusion area fraction and quantity density in the steel effectively. After BOF-LF-RH-CC refining, the average inclusion area fraction after RH treatment decreased from 289.8 to 227.5 $\mu m^2/mm^2$ compared with original process. The proportion of inclusion size less than 8 μm increased from 85 to 95%. The proportion of Al_2O_3 inclusions less than $5\mu m^2$ increased from about 50% to more than 70%. The proportion of which bigger than $5\mu m^2$ was significantly reduced after BOF-LF-RH-CC. BOF-LF-RH-CC process is more beneficial to control the size of

Al_2O_3 inclusions and reduce the impact of inclusions on the cleanliness of liquid steel.

(5) The BOF-LF-RH-CC process has more advantages than BOF-RH-CC process in the aspects of temperature stability of molten steel, control of impurity elements and inclusions, but it had a disadvantage in long refining time. The prediction accuracy of XGBoost prediction model was 93.4%. It could guide the steel company to adopt different heating processing effectively.

Acknowledgements This work was financially supported by National Key R&D Program of China (2017YFB0304000).

References

1. Deng X, Li L, Wang XJ et al (2014) Subsurface macro-inclusions and solidified hook character in aluminum-killed deep-drawing steel slabs. Int J Miner Metall Mater 21(6):531
2. Xiao C, Cui H (2018) Effect of Al content on inclusions in the automobile high strength steel. Chin J Eng S1:26–30
3. Hu Y, Chen W, Wan C et al (2018) Effect of deoxidation process on inclusion and fatigue performance of spring steel for automobile suspension. Metall Mater Trans B 49(2):569
4. Ma H, Wang X, Huang F et al (2016) Effect of deoxidation technology on cleanliness of low carbon aluminum killed steel. Iron Steel 1:19–24 (in Chinese)
5. Yang W, Wang X, Zhang L et al (2013) Cleanliness of Low carbon aluminum-killed steels during secondary refining processes. Steel Res Int 84(5):473–489
6. Qin Y, Wang X, Huang F et al (2015) Influence of reoxidation by slag and air on inclusions in IF steel. Metall Res Technol 112(4):405
7. Shu H, Liu L, Liu X et al (2011) Investigation on variation of inclusions and total oxygen in IF steel after RH deoxidization. J Iron Steel Res 18:S2
8. Rout B K, Brooks G, Akbar Rhamdhani M et al (2018) Dynamic model of basic oxygen steelmaking process based on multizone reaction kinetics: modeling of decarburization. Metall Mater Trans B
9. Li C, Cheng G, Wang X et al (2012) Effect of RH blowing oxygen operation on decarburization rate of treatment for ultra-low carbon steel. Iron Steel 47(3)
10. Li P, Bao Y, Yue F et al (2011) Mechanism of carbon and oxygen reaction in RH decarburization of ultra low oxygen steel. Chin J Eng 33(7):823–827 (in Chinese)
11. Li C, Cheng G, Wang X et al (2011) Mechanism of surface and splash droplet decarburization of RH treatment for ultra low carbon steel. Steelmaking 27(5):35–38 (in Chinese)
12. Cui H, Tian E, Chen B et al (2014) Cleanliness study of IF steel by holding in ladles after RH vacuum process. Chin J Eng S1:32–35 (in Chinese)
13. Provost F, Fawcett T (2013) Data science and its relationship to big data and data-driven decision making. Big Data 1:51–59
14. Wu L, Li S et al (2012) Experimental study on deep desulfurizer in LF process. J Iron Steel Res Int 19(4):17–21
15. Wang H, Investigation of inclusion control and evolution during electroslag remelting for H13 steel. University of Science and Technology Beijing
16. Zhang L, Taniguchi S (2014) Fundamentals of inclusion removal from liquid steel by bubble flotation. Metall Rev 45(2):59–82
17. Duan H, Ren Y, Zhang L (2019) Modeling of turbulent flow around bubbles in molten steel. Steel Res Int 90(6):1–8

18. Chen T, Guestrin C (2016) XGBoost: a scalable tree boosting system. In: The 22nd ACM SIGKDD international conference. ACM
19. Zhang D, Qian L, Mao B et al (2018) A data-driven design for fault detection of wind turbines using random forests and XGBoost. IEEE Access 1–1

Part III
Fundamentals of Metallurgical Processes

Thermal Analysis of Potential High Entropy Alloy Binder Alternatives for Tungsten Carbide

Jannette Chorney, Jerome Downey, K. V. Sudhakar, Morgan Ashbaugh, and Grant Wallace

Abstract Cobalt has been the predominant binder for tungsten carbides for almost one hundred years. However, a suitable substitute is required because cobalt faces supply risks, is in high demand for other applications, and is a known carcinogen. Select high entropy alloys (HEAs) are being investigated as potential alternatives to cobalt. However, published fundamental data are lacking for these alloys. Characterization of the high entropy alloys allows for operating parameter identification and optimization for sintering. Phase transition onset temperatures, the kinetic components of heat flow, and green binder vaporization temperatures have been determined by differential scanning calorimetry (DSC), thermo-gravimetric analysis (TGA), modulated differential scanning calorimetry (MDSC), and thermodynamic modeling for the selected HEAs.

Keywords Tungsten carbide · HEA · Thermodynamics

Introduction

Cemented carbides are composed of hard, wear-resistant, metal carbide particles and a tough, ductile, metal binder phase that combines to form composite materials with high hardness and toughness [1]. While tungsten carbide (WC) is by far the most commercially significant carbide, other important carbides include tantalum carbide (TaC), titanium carbide (TiC), and niobium carbide (NbC) [1, 2]. Cobalt, and to a lesser extent nickel, has traditionally been employed as the metal binder [1, 3].

The search for a satisfactory substitute for cobalt in cemented carbide applications is driven by cobalt's toxic characteristics, susceptibility to supply interruptions (the U.S. is highly import-reliant), and the general desire to replace it with a less expensive

J. Chorney (✉) · J. Downey · K. V. Sudhakar · M. Ashbaugh · G. Wallace
Montana Technological University, Butte, MT 59701, USA
e-mail: jchorney@mtech.edu

J. Downey
e-mail: jdowney@mtech.edu

Z. Peng et al. (eds.), *12th International Symposium on High-Temperature Metallurgical Processing*, The Minerals, Metals & Materials Series,
https://doi.org/10.1007/978-3-030-92388-4_16

metal or alloy [3]. Severe toxicological consequences are associated with both cobalt and nickel [4–8], and notable human health effects identified from human and/or animal studies include respiratory cancer, dermatitis, reproductive effects, and other non-cancerous effects [4–8]. Workplace exposure to cobalt is of primary concern during cemented carbide production and utilization, where cemented carbides may become an inhalation hazard.

A viable alternative to cobalt has proven elusive for most cemented carbide applications. Attempts to substitute other base metals or simple alloys have failed to produce a satisfactory combination of physical properties. Prior research examined the most promising alternatives, nickel and nickel–cobalt [9, 10]. While these alternatives partially mitigate the cost and availability concerns, the human health effects remain. Nickel, while providing excellent corrosion resistance, is lower in hardness and generally lower in strength and presents its own toxicological concerns [4, 5, 7]. Aside from nickel, it is doubtful that any commercially pure metal is a satisfactory substitute for cobalt. Prior research into alloys has not been extensive. Iron-manganese binders have been examined but were found to be unsuitable due to equipment contamination [11].

High entropy alloys (HEAs) are traditionally formed by mixing five or more metals in equimolar proportions. HEAs are a relatively new area of investigation, and research into these alloys has intensified in the last decade because HEAs with higher strength-to-weight ratios, greater tensile strength, and fracture resistance superior to conventional metals and alloys have been identified [12]. This combination of attributes makes HEAs logical binder candidates in cemented carbide applications. To date, most HEAs that have been studied have contained cobalt and or nickel [12].

Materials and Methods

The study examines the use of more complex, high entropy iron-containing alloys. Published thermodynamic data for these novel alloys are lacking; therefore, it is important to experimentally develop these data. Thermodynamic modeling with Thermo-Calc 2021b software was conducted for the alloys of interest, and the phase diagram data generated provided a reference for the temperatures observed with DSC/TGA analyses. Potential sintering temperatures were determined by Differential Scanning Calorimetry and Thermogravimetric Analysis (DSC/TGA) of the HEA alloy/WC mixtures. Decomposition temperatures for the green binders were also identified. Building upon the data derived from these analyses, high temperature X-ray diffraction (XRD) was performed at temperatures determined by DSC/TGA, which allowed the identification of stable and meta-stable compounds formed at these temperatures. The results of these experiments form the foundation for the HEA binder investigation.

Metal powders from US Nano were utilized to prepare all alloys, with the exception of the silver powder, (5–8 micron, 99.9% powder, Sigma Aldrich). The

poly(vinyl butyral-co-vinyl alcohol-co-vinyl acetate) (PVA/PVB, Sigma Aldrich) and polyethylene glycol (PEG, Sigma Aldrich) were used as green binders.

Alloy mixtures were prepared under an argon atmosphere in an INERT I-LAB glovebox. The samples were blended in a Union Process HD-01 Attritor mill with reagent alcohol (anhydrous, Sigma Aldrich) for 72 h to ensure complete mixing. Samples were then dried and crushed under argon in preparation for DSC/TGA characterization and pressing for sintering.

Thermochemical data were collected utilizing a TA Instruments SDT Q650 Simultaneous Thermal Analyzer. All samples were analyzed under an argon atmosphere in a 90 μL alumina crucible. Analyses were conducted utilizing TA Instruments TRIOS software.

A Rigaku IV X-ray Diffractometer with a high temperature furnace attachment (PTC EVO2 temperature controller) was used to conduct XRD analyses. Samples were analyzed under an argon atmosphere at elevated temperatures using PDXL analysis software, and results were quantified. A platinum sample holder was used, and the furnace was ramped at 20 °C per minute to the target temperature, held for five minutes to stabilize before measurement, and held at constant temperature while the measurement was collected. It should be noted that the nature of the furnace attachment, and the scintillation counter used, decreases the peak intensity for the diffractograms.

Results and Discussion

Porosity control is critical in the development and manufacture of sintered tungsten carbide. Therefore, it is important to identify the decomposition temperatures to facilitate the removal of the green binder during sintering of cemented carbides. Through DSC analysis, the decomposition onset temperature for PEG (Fig. 1), PVA/PVB (Fig. 2), and the combined binder (PEG + PVA/PVB) (Fig. 3) was determined to be 236 °C, 384 °C, and 255 °C, respectively. The enthalpies of these decompositions were found to be 103 J/g for PEG, 151 J/g for PVA/PVB, and 98 J/g for the combined binder. A one-hour hold performed at the decomposition onset temperature of each of the green binders when sintering allows the decomposition of the green binder and transport of the gaseous binder products to the surface of the sintered piece.

Onset and peak temperatures for phase transitions of the alloy were identified with DSC, and as seen in Figs. 4 and 5, for HEA A4, the enthalpy of the transitions was calculated using TRIOS software. Due to the small size of the deflections for the DSC analyses, derivatives of the heat flow were often utilized to aid interpretation. In Fig. 6, multiple deflections near 1400 °C in HEA 7A are caused by the formation and decomposition of meta-stable phases.

Table 1 shows the peak temperatures for the transitions for nine HEAs; the first deflection, or transition, at approximately 231 °C for each of the alloys is due to the melting of tin. The peak at 577 °C, for example, corresponds to a liquidus temperature indicated on a Thermo-Calc phase diagram produced for HEA 4.

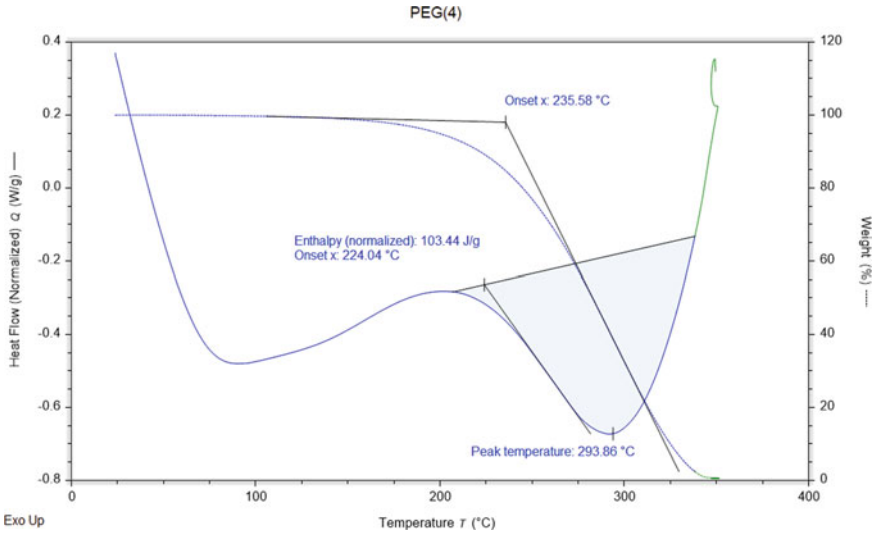

Fig. 1 DSC/TGA of PEG to determine decomposition temperature and enthalpy

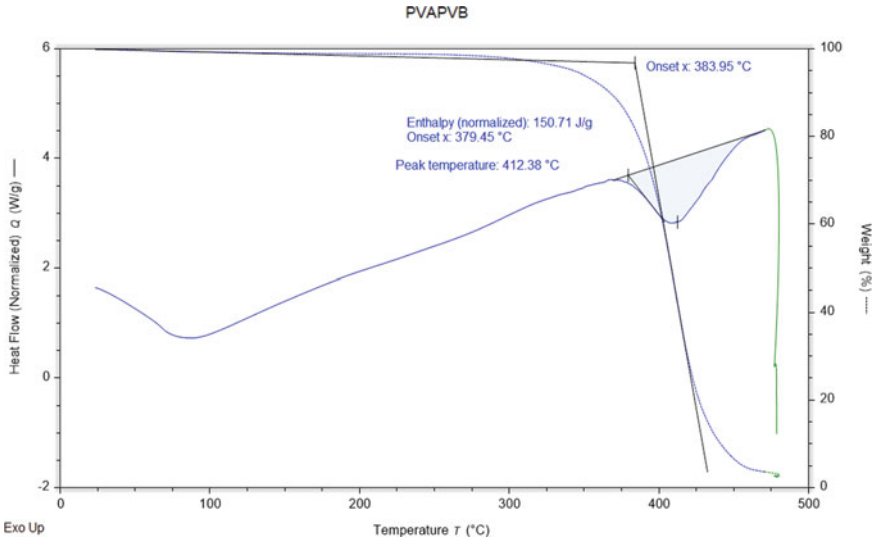

Fig. 2 DSC/TGA of PVA/PVB to determine decomposition temperature and enthalpy

High temperature XRD diffractograms allow identification of the formation of compounds, both stable and meta-stable, at elevated temperatures. In Fig. 7, an overlay of diffractograms obtained at three temperatures allows visualization of the compound formation for HEA 4. The front diffractogram was collected at 25 °C, so the peaks are from the alloy elements and tungsten carbide only, the middle at 990 °C,

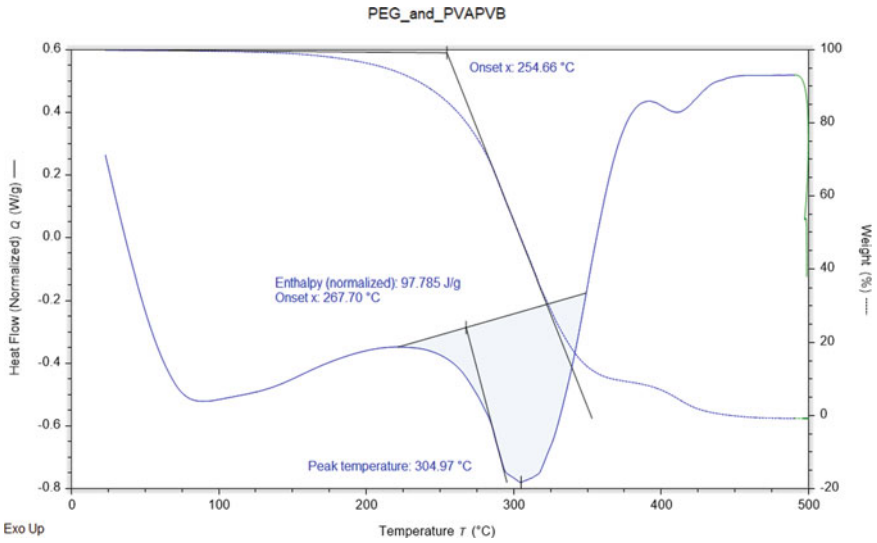

Fig. 3 DSC/TGA scan of green binders, PEG, and PVA/PVB to determine their decomposition temperature

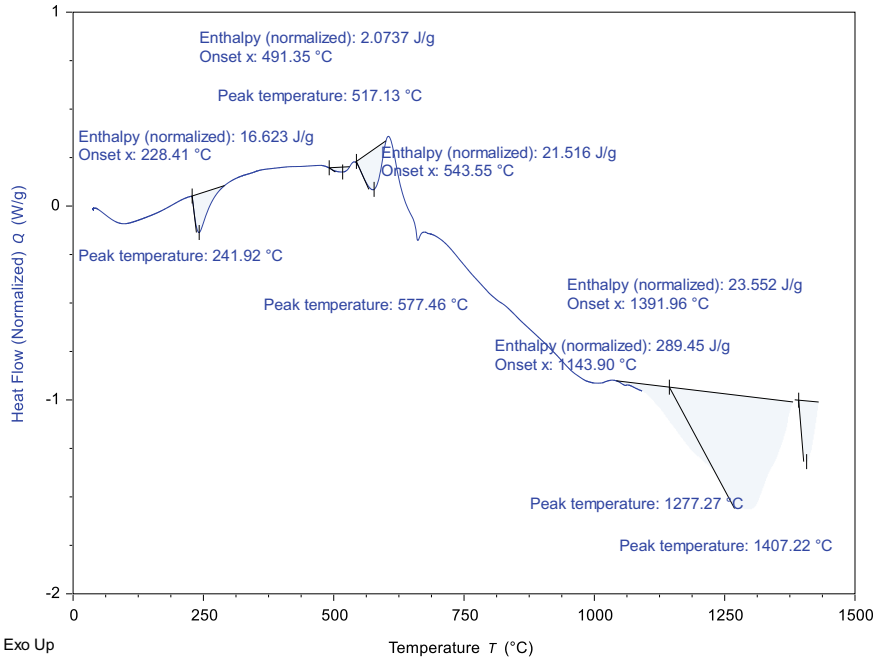

Fig. 4 DSC of alloy HEA A4 which shows the phase transitions and their respective enthalpies

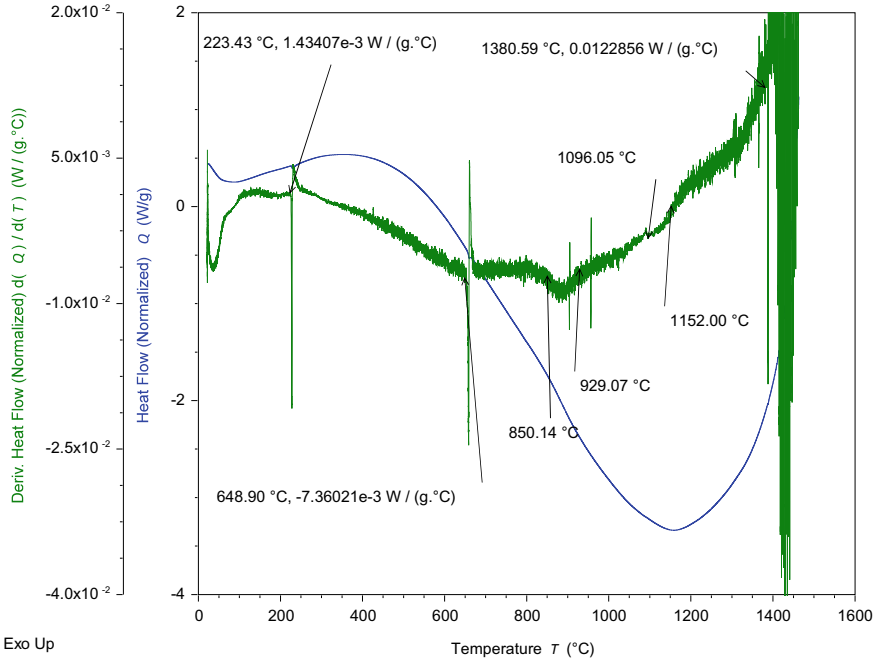

Fig. 5 DSC of WC with HEA 4, which shows the phase transitions. A derivative is used for the alloy with WC, because the deflections are small

and the last diffractogram at 1025 °C. The diffractograms at the elevated temperatures include additional peaks illustrating compounds formed at that temperature. In Fig. 7, at 1025 °C, for example, $CrSn_2$, Cr_3C_2, Fe_3Sn_2, $FeSn_2$, Cu_3Sn, Al_4C_3, W2C, W, and austenite are present, as well as the brittle phase, Fe_3W_3C (η). Detection of the η-phase allows future operating parameter optimization to avoid its formation.

Modulated differential scanning calorimetry (MDSC), as shown in Fig. 8 for HEA 4, provides both reversible heat flow, which is the heat capacity component of the heat flow, and non-reversible heat flow, which is the kinetic, or temperature and time dependent component [13]. The modulated DSC analysis for all of the high entropy alloys investigated showed a high kinetic component.

Conclusions

An alternative to cobalt or nickel as a binder for cemented carbides remains elusive, but HEAs may potentially be a suitable substitute. Determination of the thermodynamic properties is the foundation for an investigation of their suitability. The evaluation of the green binder decomposition temperatures facilitates green binder removal

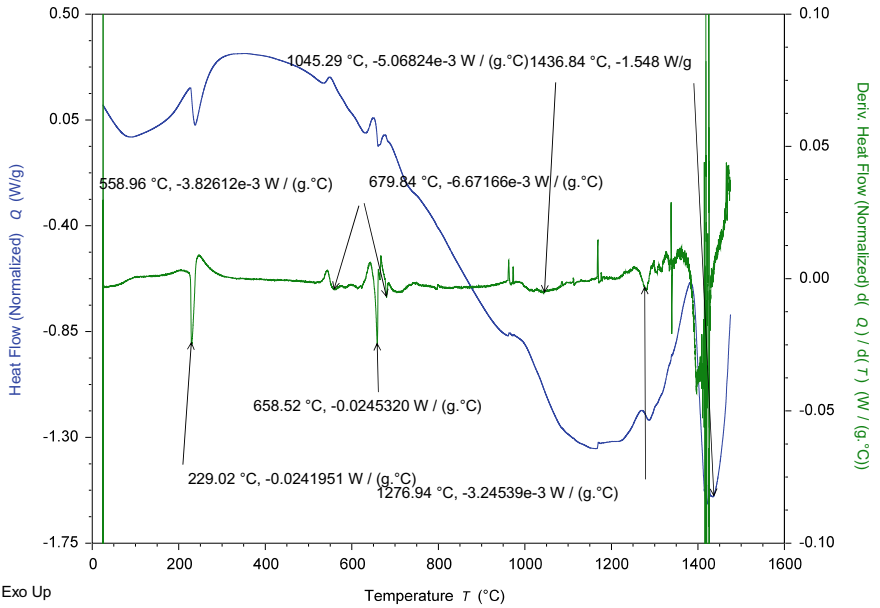

Fig. 6 DSC thermogram of HEA 7 shows the formation and decomposition of meta-stable phases near 1400 °C

Table 1 Transition peak temperatures for nine HEAs

Alloy	1st peak temp (°C)	2nd peak temp (°C)	3rd peak temp (°C)	4th peak temp (°C)	5th peak temp (°C)	6th peak temp (°C)	7th peak temp (°C)
HEA 1	239	581	664	1255	1373	–	–
HEA 2	231	481	1233	1372	–	–	–
HEA 3 (+90 wt.% WC)	228	435	785	882	Not relevant above 906	–	–
HEA 4	243	517	577	1277	1407	–	–
HEA 5	230	475	546	659	1163	1414	–
HEA6 (+90 wt.% WC)	228	414	777	Not relevant above 906	–	–	–
HEA 7	229	559	659	680	1045	1277	1437
HEA 8	230	1073	1213	1291	1410	–	–
HEA 9 (+90 wt.% WC)	227	776	Not relevant above 906	–	–	–	–

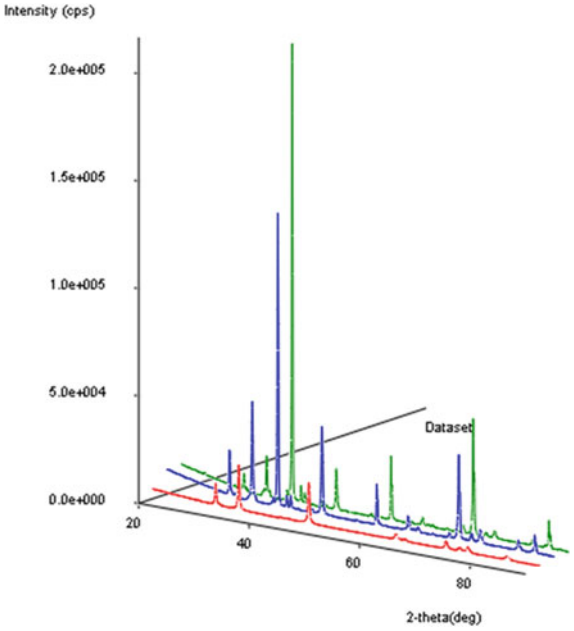

Fig. 7 XRD diffractogram of 25 °C (front), 990 °C (middle), and 1025 °C (back)

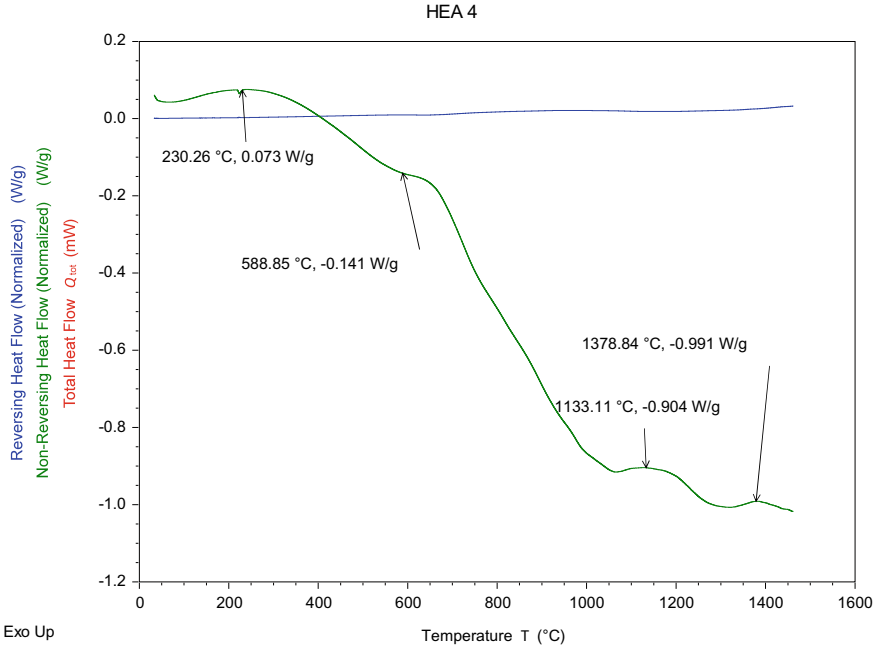

Fig. 8 Modulated DSC for HEA4 shows the strong kinetic component

to reduce porosity in the sintered material. DSC/TGA, thermodynamic modeling software such as Thermo-Calc, and high temperature XRD are invaluable for the determination of phase transitions, and therefore, the determination of potential sintering temperatures for cemented carbides utilizing HEAs as a binder.

Acknowledgements Research was sponsored by the Combat Capabilities Development Command Army Research Laboratory and was accomplished under Cooperative Agreement Number W911NF-20-2-0163. The views and conclusions contained in this document are those of the authors, and should not be interpreted as representing the official policies, either expressed or implied, of the Combat Capabilities Development Command Army Research Laboratory or the U.S. Government. The U.S. Government is authorized to reproduce and distribute reprints for Government purposes notwithstanding any copyright notation herein.

References

1. Lassner E, Schubert WD (1999) Tungsten properties, chemistry, technology of the element, alloys, and chemical compounds. Kluwer Academic/Plenum Publishers, New York, p 321
2. Genga RM, Cornish LA, Akdogan G (2013) Effect of Mo2C additions on the properties of SPS manufactured WC-TiC-Ni cemented carbides. Int J Refract Metal Hard Mater 41:12–21
3. Shedd KB (2021) USGS Mineral commodity summaries, cobalt. https://www.pubs.usgs.gov/periodicals/mcs 2021/mcs2021-cobalt.pdf
4. Das KK, Reddy RC, Bagoji IB, Bagali S, Mullur L, Khodnapur JP, Biradar MS (2018) Primary concept of nickel toxicity—an overview. J Basic Clin Physiol Pharmacol 30(2). https://doi.org/10.1515/jbcpp-2017-0171
5. Buxton S, Garman E, Heim KE, Lyons-Darden T, Schlekat CE, Taylor MD, Oller AR (2019) Concise review of nickel human health toxicology and ecotoxicology. Inorganics 7(7):89. https://doi.org/10.3390/inorganics7070089
6. Lison D et al (1996) Experimental research into the pathogenesis of cobalt/hard metal lung disease. Eur Respir J 9(5):1024–1028
7. Health, Safety and Environmental Department (2020) Alfa Aesar cobalt SDS. https://www.alfa.com/en/msds/?language=EN&subformat=AGHS&sku=10455www.alfa.com
8. Armstead AL, Bingyun L (2016) Nanotoxicity: emerging concerns regarding nanomaterial safety and occupational hard metal (WC-Co) nanoparticle exposure. Int J Nanomed 11:6421
9. Kim HC, Shon IJ, Yoon JK, Doh JM (2006) Comparison of sintering behavior and mechanical properties between WC−8Co and WC−8Ni hard materials produced by high frequency induction heating sintering. Met Mater Int 12(2):141–146
10. Waldorf D, Liu S, Stender M, Norgan D (2008) Alternative binder carbide tools for machining superalloys; MSEC_ICMP2008–72369. In: Proceedings of the international conference on manufacturing science and engineering, p 2
11. Schubert WD, Fugger M, Wittmann B, Useldinger R (2015) Aspects of sintering of cemented carbides with Fe-based binders. Int J Refract Metal Hard Mater 49:110–123
12. Zhang Y, Zuo TT, Tang Z, Gao MC, Dahmen KA, Liaw PK, Ping Lu Z (2014) Microstructures and properties of high-entropy alloys. Progress Mater Sci 61:1–93. ISSN 0079-6425. https://doi.org/10.1016/j.pmatsci.2013.10.001
13. TA Instruments—Thermal Analysis and Rheology (2005) Thermal analysis review, modulated DSC theory. http://www.tainst.com. Accessed on 21 June 2021

Dynamics Behaviors of Droplets Impacting on a Heated Tailings Surface

Yan Zhao, Liangying Wen, Li Su, Bo Liu, JianXin Wang, and Liwen Hu

Abstract Tailings are produced by high-titanium blast furnace slag using "high-temperature carbonization-low-temperature chlorination" technology. In this paper, droplet impact on a heated tailings surface is experimentally investigated over a wide range of Weber numbers and surface temperatures. The spread of droplets into a liquid film on the tailings surface and dynamics behavior of the droplets were observed by a high-speed camera. Five regimes are observed, namely spreading, boiling induced break-up, advancing recoiling, splashing with continuous liquid film, and splashing with broken liquid film. In addition, the effects of Weber number and surface temperature on boiling mode and spread of droplets are examined. The scaling law of maximum spreading ratio with the Weber number is also established, and it agrees well with experimental measurements and the literatures over a range of Weber numbers and high temperature.

Keywords Droplet · Impact · Tailings surface · Maximum spreading ratio

Introduction

The phenomena of liquid droplets impacting on a hot wall have widespread application in diverse industries such as the chemical industry, the metallurgical industry, the aerospace industry, and the manufacturing industry [1–5]. Generally, the movement

Y. Zhao · L. Wen (✉) · L. Su · B. Liu · J. Wang · L. Hu
School of Materials Science and Engineering, Chongqing University, Chongqing 400044, China
e-mail: cquwen@cqu.edu.cn

Y. Zhao
e-mail: zycqu@cqu.edu.cn

Y. Zhao · L. Wen · L. Su · B. Liu · L. Hu
Chongqing Key Laboratory of Vanadium-Titanium Metallurgy and Advanced Materials, Chongqing University, Chongqing 400044, China

J. Wang
Pangang Group Research Institute Co. Ltd., 90 Taoyuan Street, Panzhihua 617000, China

Z. Peng et al. (eds.), *12th International Symposium on High-Temperature Metallurgical Processing*, The Minerals, Metals & Materials Series,
https://doi.org/10.1007/978-3-030-92388-4_17

of droplets impacting on a solid surface is a surface flow phenomenon. Heated solid surfaces are often accompanied with heat and mass transfer processes; the coupling effect of thermodynamics and dynamics influences the movement evolution of the droplet impacting on the wall, which leads to droplets' behaviors; these behaviors depend on important parameters [6] such as the density, viscosity, and surface tension of liquid [7], droplet impact velocity [8], surface temperature, surface wettability [9], and surface roughness [10, 11]. In order to express these factors quantitatively, the dimensionless parameters of droplet impact are [12]: Weber number written as $\mathrm{We} = \rho v_0^2 D_0/\gamma$, and Reynolds number written as $Re = \rho v_0 D_0/\mu$, where ρ, v_0, D_0, γ, and μ are the droplet density, velocity, initial droplet diameter, respectively. The Weber number is used to assess the relative importance of the droplet inertia compared with the surface tension. Moreover, the Reynolds number defines the relative importance of the droplet inertia and the viscous force. During droplet impact process, kinetic energy transformed into inter facial energy; the shrinkage characteristics of droplets depend on the droplet interfacial energy and energy dissipation degree. Investigating the dynamics process of water impacting on a heated surface is essential to understand the nature of multiphase flow on free surface.

Numerical researches show that Weber number and surface temperature have important effects on droplet impact dynamics [5, 13]. Tran et al. [14] experimentally observed the impact process of droplets on a smooth surface at different surface temperatures and explored the relationship between the spreading diameter and the Weber number. The three typical droplet behaviors (contact boiling, gentle film boiling, and spraying film boiling) were obtained based on the Weber number and surface temperatures. Wang et al. [15] found that the critical temperature of dry impact was lower than the Leidenfrost temperature in the case of a high impact Weber number. At high droplet impact velocity, the dry impact happens to the plate surface temperature much lower than the commonly believed Leidenfrost temperature due to the squeeze film effect. Cen et al. [16] studied the jet break-up dynamics of bio-butanol droplet impinging on a hot wall surface at different Weber numbers and found jet break-up phenomenon occurs at Weber number ranging from 14 and 90. Firstly, length of jet break-up increases slowly, then decreases sharply, and then increases with Weber number. Jadidbonab et al. [17] experimentally studied the impact of diesel–fuel droplets on a similarly sized polished spherical heated solid particle and found that the maximum spreading factor increases with impact Weber number but decreases with the particle temperature. Jin et al. [18] investigated the motion of droplet impacting on a low-temperature solid surface at different angles and analyzed the effects of surface temperatures and collision angles on droplet spreading diameter and spreading time. They concluded that droplet spreading time increased with collision angle. Mitra et al. [19] investigated the effect of hot spherical surfaces on the impact process of three different cold droplets (water, isopropanol, acetone) and found a power function relationship between the droplet impact spreading ratio and Weber number.

Droplet impact experiments were mainly performed on metal surfaces. In this paper, we have studied the dynamics behaviors of droplets impingement on a tailings surface C. The tailings used in this experiment were formed by high-titanium blast

furnace slag after extraction of titanium using "high-temperature carbonization-low-temperature chlorination" technology. The tailings were utilized to prepare glass–ceramic foams. However, the tailings containing more than 3% of the chloride ions could not be directed utilized. Based on the fact that droplet has a singular interface reaction effect on the hot surface. It can help reveal the relationship between the behavioral characteristics of water droplets and dechlorination evaporation rate at the interface of hot tailings. The effects of surface temperature, the velocity of droplet, and the size of droplet on the spreading factor during the impact process are explored.

Experiment

Figure 1 schematically illustrates the experimental setup for observing droplet impact process on the tailings surface. The setup consists of a reactor for placing the titanium extraction tailings sample, a syringe pump, different inner diameters needles, a heating platform, a high-speed camera, an LED light source, and a computer to control the visualization purposes. A tailings sample was closely placed on a hot plate with a temperature controller. The cylindrical sample is 30 mm in diameter and 10 mm in height. The main components of tailings sample used in the experiments are shown in Table 1. The surface temperature of the tailings sample was measured with a mobile K-type thermocouple. A syringe pump is utilized to feed water into the needle at room temperature. The size of the needle can be varied to create different sizes droplets. The water droplet is generated by three needles with a tip inner diameter of 0.21, 0.34, and 0.51 mm, respectively. The needle was initially located far

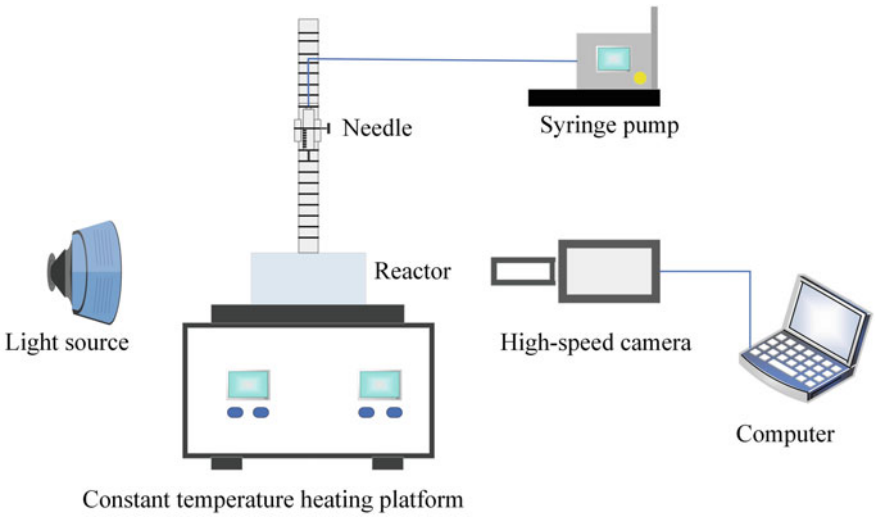

Fig. 1 Schematic of experiment apparatus

Table 1 Components of tailings after extracting titanium

Components	TiC	CaO	MgO	SiO_2	TiO_2	Al_2O_3	MnO	$CaCl_2$	$MgCl_2$	$MnCl_2$	C
Mass fraction/%	3.26	29.08	8.55	27.80	2.25	14.43	0.72	3.86	0.55	0.05	9.45

above the heated surface and then lowed immediately to certain heights, after the surface temperature T_w reached the pre-set value. Water droplets were formed at the tip of a fine needle and driven by gravity before impacting the surface. LED light source provided sufficient backlight to show the profiles of both the surfaces and the droplets. A high-speed camera was employed to record the droplet impact process from the same horizontal height as the tailings surface, at a framerate of 2000 f/s. The spatial resolution of the high-speed camera was 1024 × 786 pixels. The droplet impact experiment was repeated at least three times for each scenario.

The size of droplets is obtained by pixel analysis of the droplet images captured by the high-speed camera. The recorded images of droplet impact were processed through Image-Pro Plus 6.0 (Media Cybernetics) software. Due to the gravity, the shape of the falling droplet was not perfectly spherical. The vertical diameter D_v and the horizontal diameter D_h of the droplet were calculated respectively before impacting the surface, to obtain the equivalent diameter [20] $D_0 = \left(D_v D_h^2\right)^{1/3}$. The impact velocity v_0 was calculated by analyzing the displacements of the droplet in the last three frames.

Distilled water droplets of diameter d_0 = 2.3, 2.9, and 3.4 mm were released from three different inner diameter needles using a syringe pump at a volume rate of 2 μL s^{-1}. The height between the droplets and the surface was from 50 to 100 mm, corresponding to the impact velocity, v_0, from 0.98 to 1.40 ms^{-1}. The droplet conditions, droplet size, droplet velocity, and its corresponding Weber number are summarized in Table 2. The initial conditions and properties of impacting droplet and hot surface used in the present experiments are listed in Table 3.

Table 2 Droplet conditions

d_0 (mm)	v_0(m/s)		
	0.98	1.2	1.4
2.3	We = 31.7	We = 46.9	We = 61.9
2.9	We = 39.3	We = 59.1	We = 78.8
3.4	We = 42.8	We = 67.6	We = 92.7

Table 3 Initial conditions and properties of impacting droplet and hot surface

Impinging droplet	Water
Initial droplet temperature	20 °C
Droplet density	998 kg/m^3
Droplet viscosity	0.001 Pa s
Droplet surface tension	0.0717 kg s^{-2}
Initial droplet velocity	0.98, 1.2, 1.4 m/s
Initial droplet diameter	2.3, 2.9, 3.4 mm
Surface material	Tailings
Solid bulk density	2530 kg/m^3
Surface temperature	100 ± 1–500 ± 1 °C

Results and Discussion

Observations of Different Impact Regimes

Five impact regimes were obtained for droplet impact on the tailings surface for 54 experimental measurement points across the range of droplet impact Weber number and surface temperature conditions. They are spread, boiling induced break-up, advancing recoiling, splash with continuous liquid film, and splash with broken liquid film regimes.

Spread Regime

Figure 2 shows the image sequences of droplets impacting the tailings surface at the temperature of 200 °C and the Weber number of 42.8. After contacting the tailings surface at t = 0 ms, the upper part of droplet remains nearly spherical, while the bottom spreads gradually in all directions. As the spreading diameter increases, the gravitational potential energy of the droplet is gradually transformed into kinetic energy. Due to the porous tailings surface, the spreading of droplets is accompanied by liquid penetration into the surface as time increases. Meanwhile, the liquid film is formed after saturation of the voids at the surface. Owing to the surface tension force, the spreading speed of droplet decays with time. This regime occurs when T_s, which are defined as the Leidenfrost temperature in the Staat et al. Regime map [21].

Fig. 2 Droplet impact behavior on the tailings surface in spread regime. T_s = 200 °C We = 42.8

Fig. 3 Droplet impact behavior on the tailings surface in boiling induced break-up regime. T_s = 300 °C We = 31.7

Boiling Induced Break-Up Regime

Figure 3 shows the image sequences of droplets impacting the tailings surface at the temperature of 300 °C and the Weber number of 39.3. Due to the further increase in the surface temperature, the heat exchange between the droplets and the surface is enhanced. The droplets rapidly enter into the boiling state, and the nucleation density and formation rate of bubbles increase, leading to the violent droplet perturbation. For low Weber numbers, droplets have no enough kinetic energy to overcome surface tension, the central region of the droplets is thick, and the edge of droplet further spreads and reaches the maximum spreading at t = 11 ms. Numerous bubbles are generated at the liquid–solid interfaces during the boiling process, the bubbles break up from the liquid lamella, resulting in the formation of several small secondary droplets. The surface energy is gradually converted into kinetic energy for the upward movement of the droplet at t = 14 ms. At the same time, the vapor pressure between the droplet and the surface produces an upward thrust to prevent the droplet from penetrating into the tailings surface, causing the droplet to roll on the surface at t = 16 ms.

Advancing Recoiling Regime

Figure 4 shows the image sequences of droplets impacting the tailings surface at the temperature of 400 °C and the Weber number of 39.3. The droplets gradually spread under the effect of inertia. After the maximum spreading diameter is reached, the droplet is in a non-equilibrium state, the triple-phase contact line of vapor–liquid-solid converges towards the droplet center, and a vertical liquid column appears, namely "Worthington jet" [22]. It has an upward tendency, eventually overcomes the surface tension under the effect of inertia force, and breaks away from the main

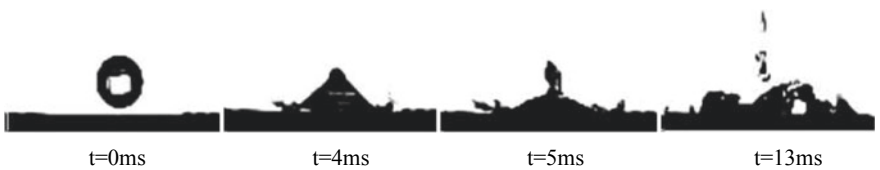

Fig. 4 Droplet impact behavior on the tailings surface in advancing recoiling regime. T_s = 400 °C We = 39.3

Fig. 5 Droplet impact behavior on the tailings surface in splash with continuous liquid film regime. T_s = 450 °C We = 67.6

droplet. The regime here can be identified as advancing recoiling regime. In this regime for low temperature, the kinetic energy dominates over the reaction force from the droplet evaporation process. As surface temperature increases, the evaporation rate relatively rises. The vapor pressure overcomes the downward kinetic energy, leading to the recoil phenomenon. As the temperature further increases, the stable vapor layer beneath the droplet impedes the droplet evaporation and the heat exchange. The downward kinetic energy becomes dominant and suppresses the droplet recoiling due to the vapor pressure reduction.

Splash with Continuous Liquid Film Regime

Figure 5 shows the image sequences of droplets impacting the tailings surface at the temperature of 450 °C and the Weber number of 67.6. Compared with the boiling induced break-up regime, the dropletsC have enough kinetic energy to dominate over the surface tension, and a continuous liquid film forms at the bottom of droplet. The corrugate edge of droplet becomes unstable and breaks into several child droplets at t = 15 ms. Moreover, the central region of liquid film is still continuous. The surface temperature is much higher than the droplet boiling point. After contacting the surface, the droplet boils and vaporizes immediately with a huge disturbance. Some secondary droplets are formed, owing to the Rayleigh-Plateau instability [23] exerted by the interaction of the vapor layer and surface tension.

Splash with Broken Liquid Film Regime

Figure 6 shows the image sequences of droplets impacting the tailings surface at the temperature of 500 °C and the Weber number of 78.8. Increasing the Weber number means an increase in kinetic energy. As a result, the inertia effects dominate to surface tension effects. The higher impact velocity extends the droplet spreading

Fig. 6 Droplet impact behavior on the tailings surface in splash with broken liquid film regime. T_s = 500 °C We = 78.8

to the maximum diameter at $t = 5$ ms, and several child droplets split away from the rim of the liquid film at $t = 15$ ms. Subsequently, the liquid film breaks up and detaches from the surface.

Through the above experimental observations, it was found that surface temperature and impact Weber number had a significant effect on the dynamics behaviors. Furthermore, the dynamics behaviors of droplets impacting on the tailings surface are significantly different from that on the smooth surface. The droplets bounce off the smooth surface for surface temperature higher than the Leidenfrost temperature; it generally considered that this phenomenon represents nucleate boiling transformed into transition boiling. On the other hand, for droplet impacting on the tailings surface, the rebound phenomenon does not occur when the surface temperature is above the Leidenfrost temperature of smooth surface (i.e. iron surface of 280–325 °C). An important factor for this difference is the capillary effect of the rough and undense tailings surface which absorbs a mass of kinetic energy from the spreading liquid film to prevent it rebound off the surface. The droplet impact process is a complex process of multiphase flow and heat and mass transfer, which is accompanied by bubble nucleation, growth, aggregation, and burst.

Spreading Characteristics of Droplets

This section focuses on the effect of Weber number and surface temperature on the spreading ratios of droplets on the tailings surfaces. The droplet spreading ratios β are defined as follows, where D_t is the spreading diameter of droplet impacting on the surface, t is time. $\beta_{\max}$ is the maximum droplet spreading factor.

$$\beta = \frac{D_t}{D_0}$$

Effect of Weber Number

Many previous works have shown that Weber number We is an important parameter that affects the spreading characteristics of droplets impaction on the surface. The droplets maximum spreading ratios β increase with We. Weber number We is defined to represent the ratio of inertia force to surface tension. In the present experimental study, the Weber number We is affected by the droplet diameter and impact velocity.

The spreading ratios β of droplets on the tailings surface with different temperature at various Weber numbers We are shown in Fig. 7. Figure 7a indicates β on the surface temperature of 300 °C. At the lower Weber numbers We, the droplets keep spreading under the effect of inertia force. After reaching maximum spreading diameter, the droplets start to retract due to the surface tension, and the spreading ratios β decrease with time. In Fig. 7b, for the surface temperature of 400 °C and We = 78.8, the kinetic

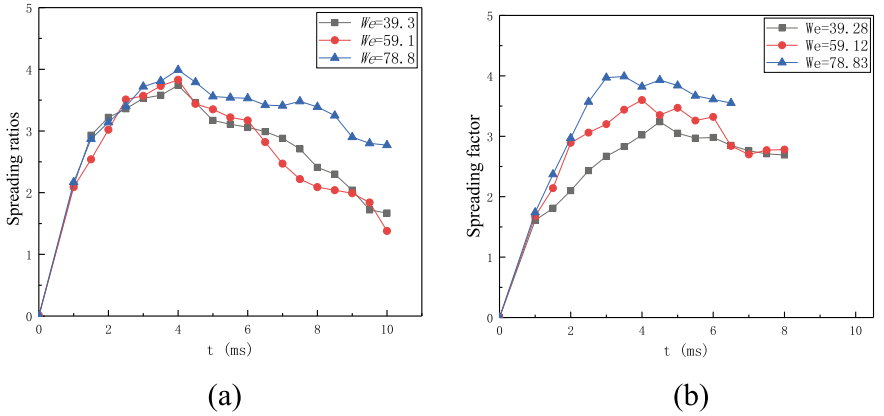

Fig. 7 Variations of the spreading factors on tailings surface with different Weber numbers. **a** Surface temperature $T_s = 300$ °C, **b** surface temperature $T_s = 400$ °C

energy of droplets dominates over the surface tension, and the fact can be shown at $t = 6.5$ ms where the spreading process is stopped. It is clear that droplets spreading rate and maximum spreading ratio $\beta_{\max}$ increase with We. The observed facts indicate that the time for droplets reaching the maximum spreading ratio is around 4 ms, and it is independent of the Weber number.

The droplet spreads horizontally under the effect of inertial force and surface tension. At high Weber number, the droplets have enough inertial force to reach the maximum spreading diameter. After reaching the maximum spreading diameter, the droplets start to contract due to the surface tension and the viscous resistance. Furthermore, as the maximum spreading diameter increases, the surface tension of the droplet also increases, resulting in the droplet retracting faster.

Effect of Surface Temperature

The variation of spreading factors on tailings surface at different surface temperatures is shown in Fig. 8. As the surface temperature increases from 400 to 500 °C, the droplet spreads more rapidly and reaches a larger maximum spreading diameter when $t > 1.6$ ms. It can be concluded that viscosity and surface tension of droplet decrease with the increase of surface temperature. At $T_s = 300$ °C, the droplet spreads to the maximum diameter at $t = 4$ ms, then recoils, and the spreading factor decreases. The droplets are in the nucleate boiling state, and the bubbles form and grow in the droplet.

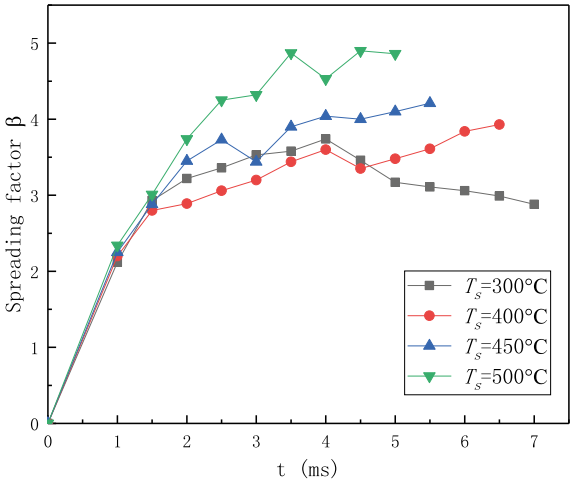

Fig. 8 Effect of surface temperature on droplet spreading factor on tailings surface at We ≈ 61.9

Scaling Analysis of Maximum Spreading Factor

In Fig. 9, the maximum spreading factor is plotted as a function of Weber number. The maximum spreading factor is generally expressed in the form of $\beta_{\max} = c\mathrm{We}^n$, where c and n can be obtained by through regressing experiments data. According to this model, the experimental data for the tailings surface can be fitted by the correction with Weber number:

$$\beta_{\max} = 0.574\mathrm{We}^{0.433} \tag{1}$$

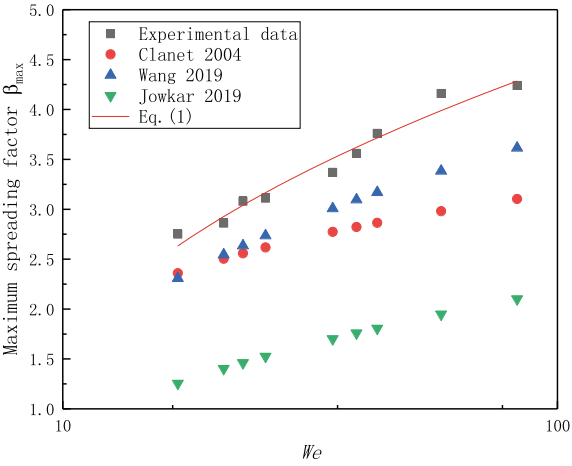

Fig. 9 Effect of Weber number on the droplet maximum spreading factor. (Red solid line represents the prediction of $\beta_{\max} = 0.574\mathrm{We}^{0.433}$ in present study) (Color figure online)

Comparison of present experiments with the results in previous research is also illustrated in Fig. 9. The corrections of maximum spreading factor by Clanet et al. [8], Wang et al. [23], and Jowkar [24] are used for comparison. It is found that the predicted value of Eq. (1) is more consistent with the experimental data. The corrections of Clanet, Wang, and Jowkar are below the maximum spreading diameter in present work.

Conclusions

Dynamic behaviors of droplet impacting on the tailings surface have been investigated in this research. The effects of Weber numbers and the surface temperatures on the maximum spreading diameter are explored. The following conclusions can be drawn:

(1) The droplet impact behaviors are classified into five hydrodynamic regimes in the range of $31.7 < \mathrm{We} < 92.7$ and $T_s < 500$, including spread, boiling induced break-up, advancing recoiling, splash with continuous liquid film, and splash with broken film. Furthermore, no rebound phenomenon occurs under the effect of capillary force on the rough tailings surface.

(2) The surface temperature has negligible effect on the spreading factor at early stage of impact ($t < 1.5$ ms). At $t > 1.5$ ms, the maximum spreading factor and spreading rate increase with increasing the surface temperature. While the time to reach the maximum spreading diameter is found to be insensitive to the surface temperature, it is around 4 ms in this work.

(3) The droplets of larger Weber number can reach a larger maximum spreading diameter and spreads more promptly. The droplet maximum spreading factor can be fitted by the correction with Weber number $\beta_{\max} = 0.574\mathrm{We}^{0.433}$.

Acknowledgements The work is supported by the National Natural Science Foundation Project of China (51974046, 51674052) and by graduate scientific research and innovation foundation of Chongqing, China (Grant No. CYS20003).

References

1. Nayak SK, Mishra PC, Parashar SKS (2016) Influence of spray characteristics on heat flux in dual phase spray impingement cooling of hot surface. Alex Eng J 55:1995–2004
2. Clay MA, Miksis MJ (2004) Effects of surfactant on droplet spreading. Phys Fluids 16(8):3070–3078
3. Aziz SD, Chandra S (2000) Impact recoil and splashing of molten metal droplets. Int J Heat Mass Transf 43:2841–2857
4. Murao Y, Sugimoto J (1981) Correlation of heat-transfer coefficient for saturated film boiling during reflood phase prior to quenching. J Nucl Sci Technol 18:275–284

5. Liang G, Mudawar I (2017) Review of drop impact on heated walls. Int J Heat Mass Transf 106:103–126. https://doi.org/10.1016/j.ijheatmasstransfer.2016.10.031
6. Moon JH, Lee JB, Lee SH (2013) Dynamic behavior of non-newtonian droplets impinging on solid surfaces. Mater Trans 54(2):260–265
7. Wachters LHJ, Smulders L, Vermeulen JR (1966) The heat transfer from a hot wall to impinging water drops in the spheroidal state. Chem Eng Sci 21:1047–1056
8. Clanet C, Beguin C, Richard D, Qur D (2004) Maximal deformation of an impacting drop. J Fluid Mech 517:199–208
9. Borisov VT, Cherepanov AN, Predtechenskii MR, Varlamov YD (2003) Effect of wettability on the behavior of a liquid drop after its collision with a solid substrate. J Appl Mech Tech Phys 44(6):803–808
10. Raman KA, Jaiman RK, Lee TS, Low HT (2016) Lattice Boltzmann simulations of droplet impact onto surfaces with varying wettabilities. Int J Heat Mass Transf 95:336–354
11. Tang CL, Qin MX, Weng XY, Zhang XH, Zhang P, Li JL, Huang ZH (2017) Dynamics of droplet impact on solid surface with different roughness. Int J Multiph Flow 96:56–69
12. Marengo M, Antonini C, Roisman IV, Cameron T (2011) Drop collisions with simple and complex surfaces. Curr Opin Colloid Interface Sci 16(4):292–302
13. Castanet G, Lienart T, Lemoine F (2009) Dynamics and temperature of droplets impacting onto a heated wall. Int J Heat Mass Transf 52(3):670–679
14. Tran T, Staat HJJ, Prosperetti A, Chao S, Lohse D (2012) Drop impact on super heated surfaces. Phys Rev Lett 108(3):036101
15. Wang AB, Lin CH, Cheng CC (2005) Pattern analysis of a single droplet impinging onto a heated plate. Heat Transf Asian Res 34(8):579–594
16. Cen CZ, Wu H, Lee C, Liu FS, Li YK (2018) Experimental investigation on the characteristic of jet break-up for butanol droplet impacting onto a heated surface in the film boiling regime. Int J Heat Mass Transf 123:129–136
17. Jadidbonab H, Mitroglou N, Karathanassis IK, Gavaises M (2018) Experimental study of dieselfuel droplet impact on a similarly sized polished spherical heated solid particle. Langmuir 34:36–49
18. Jinz Y, Zhang HH, Yang ZG (2016) The impact and freezing processes of a water droplet on a cold surface with different inclined angles. Int J Heat Mass Transf 103:886–893
19. Mitra S, Sathe MJ, Doroodchi E, Utikar R, Shah MK, Pareek V, Joshi JB, Evans GM (2013) Droplet impact dynamics on a spherical particle. Chem Eng Sci 100(2):105–119
20. Jinz Y, Suid Y, Yang ZG (2015) The impact, freezing, and melting processes of a water droplet on an inclined cold surface. Int J Heat Mass Transf 90:439–453
21. Staat HJJ, Tran T, Geerdink B, Riboux G, Sun C, Gordillo JM, Lohse D (2015) Phase diagram for droplet impact on superheated surfaces. J Fluid Mech 779
22. Worthington AM (1908) A study of splashes. Longmans, Green, and Company
23. Wang ZF, Xiong J, Yao W, Qu W, Yang Y (2019) Experimental investigation on the Leidenfrost Phenomenon of droplet impact on heated silicon carbide surfaces. Int J Heat Mass Transf 128:1206–1217
24. Jowkar S, Morad MR (2019) Water drop impact on a semi-cylindrical convex hot surface for a diameter ratio of unity. Exp Thermal Fluid Sci 106:68–77

Contact Line Undulation Induced Capillary Interaction Between Micron-Sized Ce_2O_3 Inclusions at the Ar Gas/Liquid Steel Interface

Zilong Qiu, Annelies Malfliet, Bart Blanpain, and Muxing Guo

Abstract The behavior of Ce_2O_3 inclusions was observed in-situ at the argon gas/liquid steel interface. A fast agglomeration of inclusions was frequently observed. It is found that inclusions usually have rough surfaces and surface chemical heterogeneities, suggesting an undulating contact line around the inclusions on the liquid steel surface. In this work, both the undulating contact line induced capillary force and the resistive drag force on inclusions are considered. In calculations, the inclusions are treated as capillary 'charges' or 'multipoles' through the analogy with electrostatics. The results show that the capillary 'quadrupole' assumption best represents the strong pairwise attractive force between inclusions. The resistive drag force is dominant compared to the net (inertial) force on the particles by 5 or 6 orders of magnitude. We can conclude that the contact line undulation provides a sufficient attraction for inclusion agglomeration, even for particles smaller than 10 μm.

Keywords Capillary force · Contact line undulation · Meniscus shape · Drag force

Introduction

The dynamic behavior of non-metallic inclusions at the gas/liquid steel interface or slag/liquid steel interface is of importance for inclusion removal and steel quality control [1]. The agglomeration of Al_2O_3 particles/clusters at the gas/steel interface was studied *in-situ* at high temperature for the first time by Yin and co-workers using high-temperature confocal scanning laser microscopy (CSLM) [2]. An obvious attraction was observed between the floating inclusions, and this attractive force is attributed to the capillary interaction due to the meniscus deformation around the particles. A detailed description of the capillary interaction between floating spheres was analytically derived by Kralchevsky et al. [3], i.e., the so-called K-P model.

Z. Qiu (✉) · A. Malfliet · B. Blanpain · M. Guo
Department of Materials Engineering, KU Leuven, Kasteelpark Arenberg 44 Box 2450, 3001 Leuven, Belgium
e-mail: zilong.qiu@kuleuven.be

Z. Peng et al. (eds.), *12th International Symposium on High-Temperature Metallurgical Processing*, The Minerals, Metals & Materials Series,
https://doi.org/10.1007/978-3-030-92388-4_18

In reality, most of the inclusions are non-spherical. To apply the K-P model to non-spherical particles, these particles are usually simplified as spheres with an equivalent radius [4]. However, the force calculated using the K-P model with an equivalent radius is usually one or two orders smaller than the observed force [4, 5]. Since the capillary force is proportional to particles size, the particle radius is scaled up from the equivalent radius to the effective radius by a shape factor to decrease this discrepancy [6]. In previous studies, the viscous drag force from the liquid steel is usually ignored when particles are sliding on the steel surface. However, the drag force can overwhelm the previously calculated attractive force based on particle accelerations [7]. Therefore, the drag force should be taken into account in this system. It is worth noting that inclusion surfaces are usually rough, and the surface chemical composition may vary at different positions [8]. These topological or chemical heterogeneities can introduce an undulating triple-phase contact line around the particles to satisfy Young's equation [9, 10]. The contact line undulation type ('quadrupolar' or 'hexapolar') and the capillary force resulting from this undulation will be discussed in this paper.

Models for the Capillary Interaction

Interaction Between Capillary 'Charges'

The so-called 'charge' type meniscus shape means the meniscus around an isolated particle is uniform, and the contact line is planar. A schematic configuration of a particle at a fluids' interface is shown in Fig. 1a. We suppose the interface is flat far from the particle, and this flat interface coincides with the xy plane. The meniscus shape is controlled by the Young–Laplace equation, which can be linearized when the particle is small ($qR^2 \ll 1$).

$$\frac{\mathrm{d}^2 h}{\mathrm{d}r^2} + \frac{1}{r}\frac{\mathrm{d}h}{\mathrm{d}r} = q^2 h, \tag{1}$$

where r is the distance from a sphere center in the radial coordinate; q^{-1} is the capillary length $q^2 = (\rho_{\mathrm{I}} - \rho_{\mathrm{II}})/\gamma$ (γ is the surface tension); If the contact line undulation is not considered, the meniscus shape around a capillary 'charge' is analytical given in Eq. (2), and a counter-plot of the meniscus shape calculated from Eq. (2) is demonstrated Fig. 1b.

$$h_{\mathrm{Chrg}}(r) = -Q \ln\left(\frac{\gamma_e q r}{2}\right), \tag{2}$$

where the subscript 'Chrg' is the abbreviation of 'charge'; $\gamma_e = 1.781$ is the constant of Euler-Mascheroni [3]; Q is the so-called capillary 'charge'.

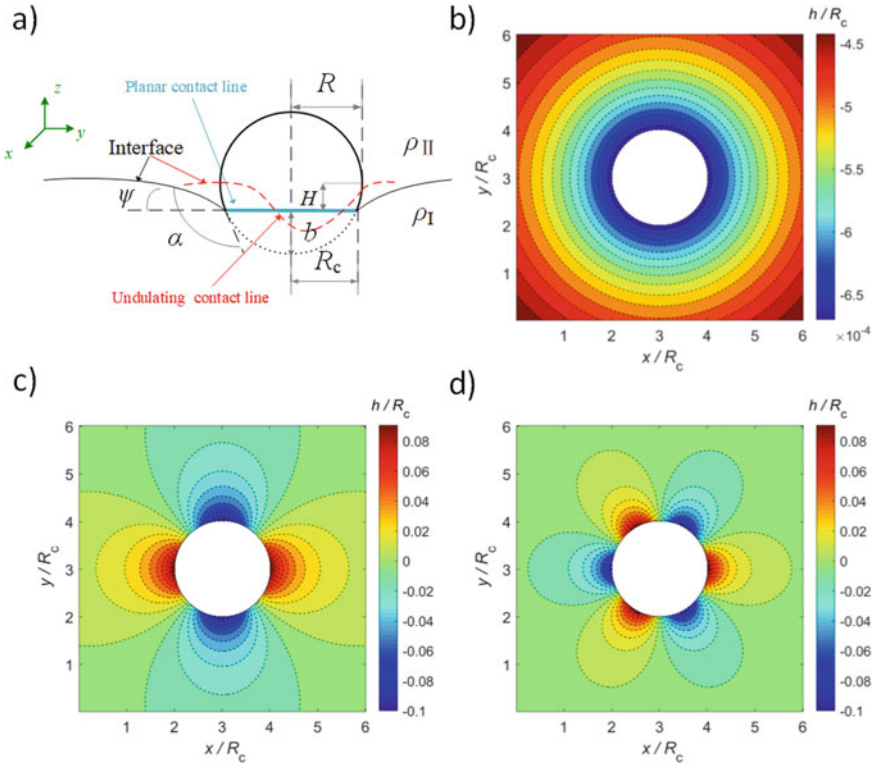

Fig. 1 **a** Schematic of capillary meniscus around a sphere of radius R with contact angles of α, where Rc is the radius of the triple-phase contact lines, b the immersion depth, H the amplitudes of contact line undulations, ψ the meniscus slope at the contact line, ρ_{I} and ρ_{II} the densities of fluids I and II. **b**, **c** and **d** are the contour-plot diagrams of the meniscus shape around a capillary 'charge', 'quadrupole' and 'hexapole', respectively. The x and y coordinates and the height of the meniscus are scaled by the contact radius R_{c}

$$Q = \frac{1}{6} q^2 R^2 \left(2 - 4D + 3\cos\alpha - \cos^3\alpha\right), \tag{3}$$

where D is the density ratio ($D = (\rho - \rho_{\mathrm{II}})/(\rho_{\mathrm{I}} - \rho_{\mathrm{II}})$, and ρ is the particle density).

For two capillary 'charges' with an inter-center distance of L, the respective capillary energy and force are

$$\Delta W_{\mathrm{Chrg-Chrg}} = 2\pi\gamma Q_A Q_B \ln\left(\frac{\gamma_e q L}{2}\right), \quad 2R_c \ll L \tag{4}$$

$$F_{\mathrm{Chrg-Chrg}} = 2\pi\gamma \frac{Q_A Q_B}{L}, \quad 2R_c \ll L \tag{5}$$

where subscripts A and B indicate particle A and particle B; L is the inter-center distance.

Interaction Between Capillary 'Multipoles'

For particles that have rough surfaces and surface chemical heterogeneities, the triple-phase contact line can be undulated [9]. The boundary condition of a capillary 'multipole' is [10]

$$h_{\mathrm{MP}}(r = R_c) = H\cos[n(\varphi - \varphi_0)], \tag{6}$$

where the subscript 'MP' means capillary 'multipole'; n is the 'multipole' order: $n = 2$ for capillary 'quadrupole' abbreviated as 'QP', and $n = 3$ for capillary 'hexapoles' abbreviated as 'HP'; φ_0 is the phase angles and φ is the running azimuthal angle. The meniscus shape around a capillary 'multipole' is

$$h_{\mathrm{MP}}(r) = H\cos[n(\varphi - \varphi_0)]\left(\frac{R_c}{r}\right)^n. \tag{7}$$

The counter-plot diagrams of the meniscus shape around a capillary 'quadrupole' and a capillary 'multipole ' calculated from Eq. (7) are demonstrated in Fig. 1c, d respectively.

For two interacting capillary 'multipoles', the interaction energy and charge are.

$$\Delta W_{\mathrm{MP-MP}} = -\pi\gamma G_0 H_A H_B \cos(n_A\varphi_A + n_B\varphi_B)\frac{R_{c,A}^{n_A} R_{c,B}^{n_B}}{L^{(n_A+n_B)}}, \quad 2R_c \ll L \tag{8}$$

$$F_{\mathrm{MP-MP}} = (n_A + n_B)\pi\gamma G_0 H_A H_B \cos(n_A\varphi_A + n_B\varphi_B)\frac{R_{c,A}^{n_A} R_{c,B}^{n_B}}{L^{(n_A+n_B+1)}}, \quad 2R_c \ll L \tag{9}$$

where n_A and n_B are the multiple orders of particle A and particle B, respectively. G_0 is a constant depending on the 'multipole' orders.

$$G_0 = \sum_{n=1}^{\min(n_A,n_B)} \frac{2(-1)^{n_A+n_B} n_A! n_B!}{(n_A - n)!(n_B - n)! n! (n-1)!}. \tag{10}$$

Results and Discussion

The 20%Cr steel sample containing Ce_2O_3 inclusions was prepared in a vertical tube furnace (GERO HTRV V 100-250/18). The detailed preparation procedure can be found in our previous work [11]. To observe the 3D morphology of inclusions, the particles were electrolytically extracted using a 10% acetic acid solution [12]. The extracted particles were analyzed using scanning electron microscopy with energy dispersive spectroscopy (SEM–EDS, Philips XL 30 FEG). The typical morphologies of the extracted particles are shown in Fig. 2. Analysis of the other 39 particles shows that the surfaces of most particles are rough and 61% of them are not pure Ce_2O_3 but have minor impurities of S or Si (less than 10 mass percent). Compounds such as Ce_2O_2S can be precipitated on the Ce_2O_3 surface when the content of oxygen is low in the liquid steel [13]. These topological and chemical heterogeneities of inclusion surfaces can induce an undulating triple-phase contact line around the inclusions to satisfy Young's equation.

For the CSLM *in-situ* observation, the steel sample was machined into discs (Φ 4 mm × 2 mm) and then melted in a high purity alumina crucible (with 4.5 mm ID and 5.5 mm OD) in the CSLM (1LM21H-SVF17SP) located at the upper focal point of the oval heating chamber under a purified argon atmosphere ($P_{O2} < 10^{-20}$ atm). The observation was carried out at 1823 K, and the images were recorded at a

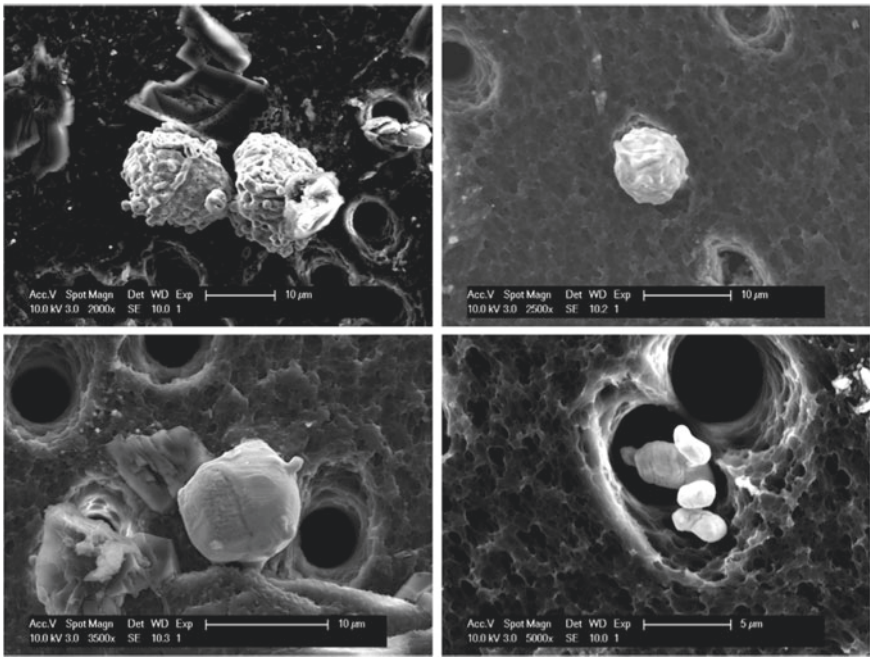

Fig. 2 SEM images of electrically extracted inclusions

rate of 30 fps. The background around the inclusion particles was removed, and the inter-center distances between the particles were measured (see Fig. 3a). The detailed procedure of the background removal and the mass center determination can be found in our previous work [11]. Figure 3b shows the inter-center distance as a function of time (blue rectangles). The top-view inclusion perimeter (l), area (A), and the corresponding equivalent radius ($R_{\mathrm{eq}} = \sqrt{A/\pi}$) and effective radius ($R_{\mathrm{eff}} = l/2\pi$) are listed in Table 1. It should be noted that the inter-center distance cannot be measured very accurately due to the relatively low image resolution (0.7 μm/pixel) [11]. The particle acceleration calculated by Newton's law of motion using the less accurate distance data can be oscillating significantly, leading to unreasonable force output. Fitting the distance data points to a 4th order polynomial function helps to reduce this force oscillation [11]. The inertial force on particles can be derived from the second differentiation of the fitted function after multiplication with the particles'

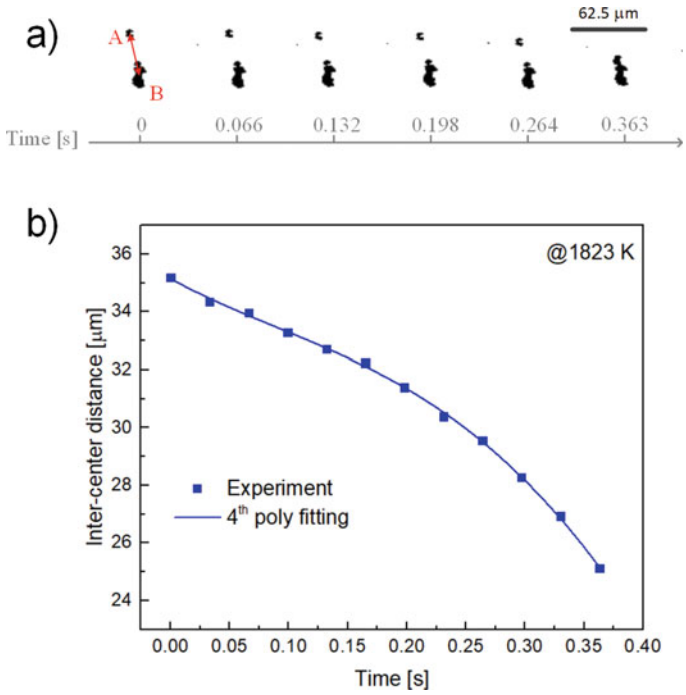

Fig. 3 **a** CSLM image sequence of two inclusions approaching each other, and **b** the inter-center distance vs time, including the experimental distance points and the fitted curve by the 4th order polynomial function

Table 1 Areas and perimeters of the inclusions and the corresponding equivalent and effective radii

	A (μm^2)	l (μm)	R_{eq} (μm)	R_{eff} (μm)	Shape parameter (S)
Particle A	63.7	33.5	4.5	5.3	0.71
Particle B	61.1	34.2	4.4	5.5	0.65

Note The shape parameter $S = 4\pi A/l^2$ and $R_{eff} = R_{eq}/\sqrt{S}$

effective mass [11]. The fitted function of the current distance data points is shown in Eq. (11), and the fitted distance is plotted in Fig. 3b as well (solid curve).

$$L = 1.32 \times 10^{-4}\,t^4 - 2.67 \times 10^{-4}\,t^3 + 6.61 \times 10^{-5}\,t^2 - 2.26 \times 10^{-5}\,t + 3.51 \times 10^{-5} \tag{11}$$

For micron-sized particles moving to each other with a low velocity, the Reynolds number is small. The drag force can be calculated from Stokes' law [14]

$$F_{drag} = 6\pi\mu R f(b/R) v G^{-1}(L/R), \tag{12}$$

where v is the particle velocity; μ is the viscosity that equals 0.0046 (Pa•s) for 20%Cr steel at 1823 K [15]; f is the viscous drag coefficient, which equals 0.43 in the current system [16], where the densities of the Ce_2O_3 and the steel are 6920 kg/m^3 and 6200 kg/m^3, respectively [17, 18], the contact angle between the particle and the steel is 105° [19]; $G^{-1}(L/R)$ accounts for the hydrodynamic resistance

$$G^{-1}(L/R) = \left(1 + \frac{R}{2(L-2R)}\right) \times \left[1 + 0.3766\,\exp\left[-\frac{(\ln(L-2R) - \ln R + 0.6789)^2}{6.297}\right]\right] \tag{13}$$

Studies at room temperature show that the inertial force based on particle acceleration is negligible compared to the drag force [14]. Therefore, the resistive drag force should be almost balanced by the attractive capillary force, and the following equations should hold

$$\frac{dL}{dt} = |v_A| + |v_B| \tag{14}$$

$$6\pi\gamma R_A f_A |v_A| G_A^{-1} = 6\pi\gamma R_B f_B |v_B| G_B^{-1} \tag{15}$$

where v_A and v_B are the velocities of the individual particles.

For inclusion particles attached to the interface of inert gas and liquid steel, the triple-phase contact line around the particles can be undulated when the particles have surfaces of topological or chemical heterogeneities. However, the real meniscus shape is not able to be measured directly due to the high temperature and the non-transparent properties of the liquid steel [20]. Note that the drag force derived from the CSLM images should be almost balanced by the attractive capillary force [14]. To evaluate the performance of the 'quadrupolar' or the 'hexapolar' undulations, we search the undulation amplitudes, which have the minimum sum of squared residuals (SSR) between the measured drag force and the theoretical capillary force at different separation distances. Suppose the contact line is undulated from the ideal planar contact line due the pinning effect and the contact angle hysteresis (CAH) is small. The relationship between the undulation amplitude and the CAH is

$$H = 2R \sin\left(\frac{\mathrm{CAH}}{4}\right) \sin\left(\frac{4\alpha - \mathrm{CAH}}{4}\right) \tag{16}$$

Since the capillary force is very sensitive to the undulation amplitude, we assume the CAH is small from 0° to 2°. The searching step for the minimum SSR is 0.01°. The contour plot of the SSR for capillary 'quadrupoles' and capillary 'hexapoles' is shown in Fig. 4. The CAHs at the minimum SSR are, respectively, 1.72° (particle A) and 0.08° (particle B) for capillary 'quadrupoles', 0.39° (particle A) and 1.38° (particle B) for capillary 'hexapoles'.

The capillary forces calculated from the 'quadrupolar' and 'hexapolar' meniscus shapes are shown in Fig. 5a using the CAHs at minimized SSR values from Fig. 4. The force calculated from the capillary 'quadrupole' shows a better prediction than the capillary 'hexapoles' with coefficients of determination (R^2) of 0.93 and 0.61, respectively. The inertial force can be six orders of magnitude smaller than the drag force (see Fig. 5a). This result confirms that the inertial force is negligibly small compared to the drag force. The attractive force provided by the capillary 'charge'

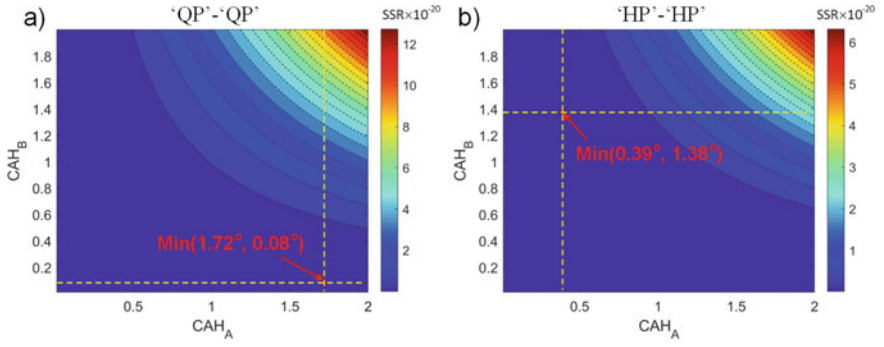

Fig. 4 Contour-plot diagrams of the SSR between the experimentally measured attractive force and the capillary force predicted from **a** capillary 'quadrupoles' and **b** capillary 'hexapoles'. The equivalent radius of particles is adopted here

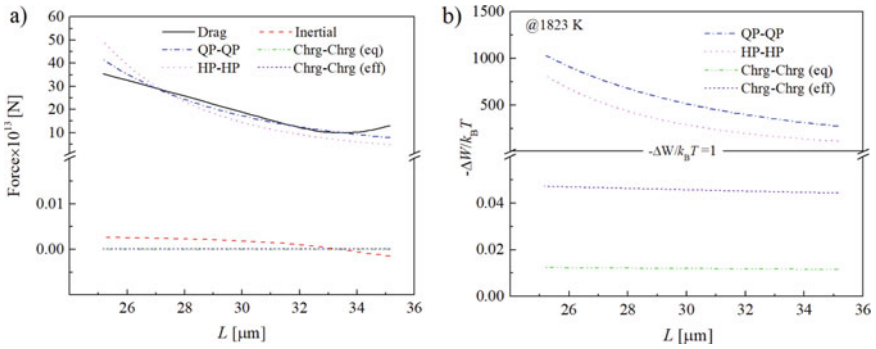

Fig.5 **a** Drag and inertial forces calculated from the CSLM image sequence and the capillary force calculated from capillary models ('charge' and 'multipoles'); **b** interaction energies calculated from capillary models ('charge' and 'multipoles') where the energy is scaled by the thermal energy

with an equivalent radius is even smaller, which is about seven orders of magnitude smaller than the drag force. The calculated capillary attraction force using the effective radius shows a stronger force compared to the equivalent radius, but it is still six orders of magnitude smaller than the drag force. Figure 5b shows the interaction energy between inclusion particles due to the capillary attraction. Theoretically, the interaction energy should exceed the thermal energy to overcome the random thermal motion for a pairwise attraction. Both the capillary 'quadrupole' and 'hexapole' models give sufficient energy for particle agglomeration. However, the capillary 'charge' with the equivalent or effective radius is insufficient to overcome the random thermal motion. Therefore, we can conclude that the meniscus shape without undulation is not able to provide enough attractive force/energy for the inclusion agglomeration when the viscous drag is considered.

Even though the capillary 'multipoles' show a better prediction of the attraction force compared to the capillary 'charge' model, there is always a deviation from the calculated force and the experimental force. This discrepancy is believed to result from the more complex contact line undulation around the inclusions rather than rotational symmetry assumed in the capillary 'multipole' models. In addition, inclusions are simplified as spheres, and this simplification may introduce a certain error. However, the inclusion shape-induced capillary interaction is out of scope for this paper, and it will be investigated in the future.

Conclusions

The Ce_2O_3 inclusion particles usually have topologically and chemically heterogeneous surfaces, which can introduce an undulating triple-phase contact line around the particles on the liquid steel surface. The viscous drag on particles should be counted in the inclusion agglomeration process, and the drag force can be six orders

of magnitude stronger than the inertial force. Comparing to the capillary 'charge' model, the capillary 'multipoles' assumption provides sufficient driving force and energy for inclusion agglomeration on the liquid steel surface.

Acknowledgements The authors thank the China Scholarship Council (CSC) for financial support (File No. 201706080018).

References

1. Vantilt S, Coletti B, Blanpain B, Fransaer J, Wollants P (2004) Observation of inclusions in manganese–silicon killed steels at steel–gas and steel–slag interfaces. ISIJ Int 44(1):1–10
2. Yin H, Shibata H, Emi T, Suzuki M (1997) In-situ observation of collision. Agglomeration and cluster formation of alumina inclusion particles on steel melts. ISIJ Int 37(10):936–945
3. Paunov VN, Kralchevsky PA, Denkov ND, Nagayama K (1993) Lateral capillary forces between floating submillimeter particles. J Collid Interface Sci 157:100–112
4. Shibata H, Yin H, Emi T (1998) The capillary effect promoting collision and agglomeration of inclusion particles at the inert gas-steel interface. Philos Trans R Soc Lond A 356:957–966
5. Kimura S, Nakajima K, Mizoguchi S (2001) Behavior of alumina-magnesia complex inclusions and magnesia inclusions on the surface of molten low-carbon steels. Metall Mater Trans B 32(1):79–85
6. Nakajima K, Mizoguchi S (2001) Capillary interaction between inclusion particles on the 16Cr stainless steel melt surface. Metall Mater Trans B 32(4):629–641
7. Petkov JT, Denkov ND, Danov KD, Velev OD, Aust R, Durst F (1995) Measurement of the drag coefficient of spherical particles attached to fluid interfaces. J Collid Interface Sci 172(1):147–154
8. Mu W, Jönsson PG, Nakajima K (2016) Prediction of intragranular ferrite nucleation from TiO, TiN, and VN inclusions. J Mater Sci 51(4):2168–2180
9. Stamou D, Duschl C (2000) Long-range attraction between colloidal spheres at the air-water interface: the consequence of an irregular meniscus. Phys Rev Lett 62:5263–5272
10. Danov KD, Kralchevsky PA, Naydenov BN, Brenn G (2005) Interactions between particles with an undulated contact line at a fluid interface: capillary multipoles of arbitrary order. J Collid Interface Sci 287(1):121–134
11. Qiu Z, Malfliet A, Guo M, Blanpain B (2021) Inertial force on floating inclusion particles at the interface of liquid steel and inert gas. ISIJ Int 61(9): 2400–2409
12. Janis J, Inoue R, Andrey K, Keiji N, Jonsson P G (2009) Characteristics of Ti-Ce complex deoxidation products in a Fe-20mass %Cr Alloy. Steel Res Int 80(6):450–456
13. Pan F, Zhang J, Chen H-L, Su Y-H, Su Y-H, Hwang W-S (2016) Thermodynamic calculation among cerium, oxygen, and sulfur in liquid iron. Sci Rep 6:35843
14. Dani A, Keiser G, Yeganeh M, Maldarelli C (2015) Hydrodynamics of particles at an oil-water interface. Langmuir 31(49):13290–13302
15. Sterkhova IV, Kamaeva LV, Lad'yanov VI (2014) Study of viscosity of Fe-Cr melts containing 2 to 40 at % of chromium. High Temp 52(6):814–820
16. Pozrikidis C (2007) Particle motion near and inside an interface. J Fluid Mech 575:333–357
17. Lide DR (2003) A ready-reference book of chemical and physical data. In: CRC handbook of chemistry and physics. CRC, Boca Raton, Fla., London, p 4–51
18. Sharan A, Nagasaka T, Cramb AW (1994) Densities of liquid Fe-Ni and Fe-Cr alloys. Metall Mater Trans B 25B:939–942

19. Keene BJ, Mills KC (1995) Contact angle and work of adhesion between ferrous melts and non-metallic solid. In: Slag Atlas. Verlag stahleisen GmbH: Verein Deutsscher Eisenhuttenleute (VDEh), p 530
20. Loudet JC, Yodh AG, Pouligny B (2006) Wetting and contact lines of micrometer-sized ellipsoids. Phys Rev Lett 97(1):18304

Experimental Study on Thermodynamics of $CaO–SiO_2–Ce_2O_3–5wt.\%\ Al_2O_3$ System at 1773 K

Mengchuan Li, Tongsheng Zhang, Wanlin Wang, Hualong Zhang, and Rensheng Li

Abstract The liquidus temperature and relative equilibrium system of Ce containing system have important basic guiding role for comprehensive utilization of rare earth Ce resources, while the lack of thermodynamic information seriously restricts the application of rare earth in steel. The phase equilibrium relationship of $CaO–SiO_2–Ce_2O_3–5wt.\%\ Al_2O_3$ phase diagram system, which was carried out at 1773 K, and was analyzed by X-Ray Diffraction (XRF), X-ray photoelectron spectroscopy (XPS), X-ray diffraction (XRD), Field Emission Scanning Electron Microscopy (FE-SEM), Energy Disperse Spectroscopy (EDS) and Electro-Probe Microanalyzer (EPMA) was studied in this paper. The isotherms and phase relations of $CaO–SiO_2–Ce_2O_3–5wt.\%\ Al_2O_3$ system related to the Ce slag system containing rare earth elements were obtained at 1773 K. And the phase equilibrium data obtained in current work can provide the basis for the control of rare earth inclusions in molten steel and the optimization of relevant thermodynamic database, and provide the theoretical basis for the sustainable utilization of rare earth resources containing cerium.

Keywords Phase equilibrium · Thermodynamic · Ce · Sustainability

Introduction

Thermodynamic behavior of rare earth oxides in calcium silicate system at high temperature is closely related to pyrometallurgical process. In addition, rare earth elements, which are considered as strong deoxidizing and desulfurizing agents and their remarkable effect of purification of molten steel, have a long-term application

M. Li
College of School of Metallurgy and Environment, Central South University, Changsha 410083, People's Republic of China
e-mail: lmc20162176@163.com

T. Zhang (✉) · W. Wang · H. Zhang · R. Li
School of Metallurgy and Environment, Central South University, Changsha 410083, People's Republic of China
e-mail: tongsheng.zhang@csu.edu.cn

Z. Peng et al. (eds.), *12th International Symposium on High-Temperature Metallurgical Processing*, The Minerals, Metals & Materials Series,
https://doi.org/10.1007/978-3-030-92388-4_19

prospect in the production process of ferrous metallurgy. The absolute Gibbs free energy of Ce_2O_3 in molten steel is equivalent to that of CaO, so a series of reactions will occur when Ce is added to molten steel, in which many scholars have done a lot of researches [1–3]. In addition, the thermodynamic data of the system containing rare earth oxides are also necessary to the field of rare earth resource recycling and material processing [4, 5].

In general, the formation characteristics of rare earth mineral phases in metallurgical process can be estimated by systematic phase equilibrium experiments [6]. Jeong et al. [7] confirmed that Ce is stable as Ce_2O_3 in MnO–SiO_2–Al_2O_3–Ce_2O_x system at 1873 K under the conditions of CO, CO_2, SO_2, and Ar mixed atmosphere. Zec et al. [8] studied the phase equilibrium of Ce_2O_3–SiO_2–ZrO_2 system at 1673 K and found the existence of Ce^{4+} in the fired compositions. Tas et al. [9] systematically studied the Ce_2O_3–$Ce_2Si_2O_7$ system from 1423 K and measured a relatively complete phase diagram of the Ce_2O_3–$Ce_2Si_2O_7$ system. Kawamura et al. [10] studied the effect of SiO_2 content in Gd_2O_3–Ce_2O_3–SiO_2 system on the formation of compound $(Gd_{0.9}Ce_{0.1})_2Si_2O_7$. Zhao et al. [11] measured the isothermal phase diagrams of CaO–SiO_2–Ce_2O_3 system at 1873 K and put forward an empirical formula to estimate the activity of Ce_2O_3. However, there is almost no pure CaO–SiO_2–Ce_2O_3 system slag during the resource recycling and material process, and Al_2O_3 is a crucial component. Especially, in steelmaking process of high quality steel, inclusion control is also a major control within CaO–SiO_2–Al_2O_3 system. However, the lack of accurate information on phase diagram of CaO–SiO_2–Ce_2O_3–Al_2O_3 leads to the delay of significant progress in the study of steel containing rare earth.

In this study, the liquid phase isotherm of CaO–SiO_2–Ce_2O_3 system with 5wt.% Al_2O_3 content was accurately determined by high temperature equilibrium experiment, and the phase diagram of the above system was also determined, which provides a theoretical basis for the refining of RE-contained steel and the sustainable utilization of RE-contained minerals.

Experimental

Preparation of Rare Earth Slag Samples

Rapid quenching technology keeps the original phase equilibrium structure state of slag samples at the target temperature. In order to ensure the accuracy of the test results, CaO powder, CeO_2 powder, Al_2O_3 powder, and SiO_2 powder with chemical purity of 99.99% were used in the experiment. Firstly, these powders were placed in muffle furnace (temperature measurement accuracy ± 1 K) and baked at 1273 K for 6 h to evaporate water and remove impurities. According to the predesigned composition ratio, a balance with an accuracy of 0.0001 g was used to accurately weigh. Then the powders were ground in agate mortar for 30 min to make the oxides evenly mixed and served in platinum crucible. A high frequency induction furnace

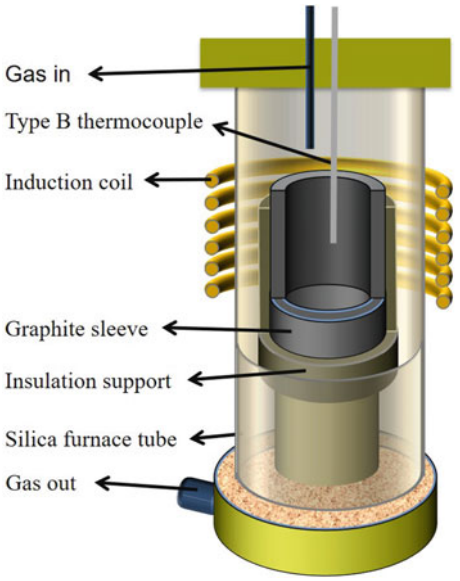

Fig. 1 High frequency induction furnace

adopted in current research is shown in Fig. 1. Mixed powder samples were heated to 1923 K in a reducing atmosphere furnace with Ar + 10% CO, and then the melt kept the temperature for 3 h to get homogeneous liquid slag. Thereafter, the samples were taken out from the high frequency induction furnace and inserted into the ice water for quenching. In order to determine whether CeO_2 could be completely converted into Ce_2O_3 in reducing atmosphere, X-ray photoelectron spectroscopy (XPS) tests were performed on the premelting samples. As shown in Fig. 2, the test results showed that only Ce^{3+} but no Ce^{4+} existed in the premelting samples.

To ensure that there is no crystal precipitation in the slag sample during quenching process, it is necessary to test whether the premelted slag is uniform glass phase.

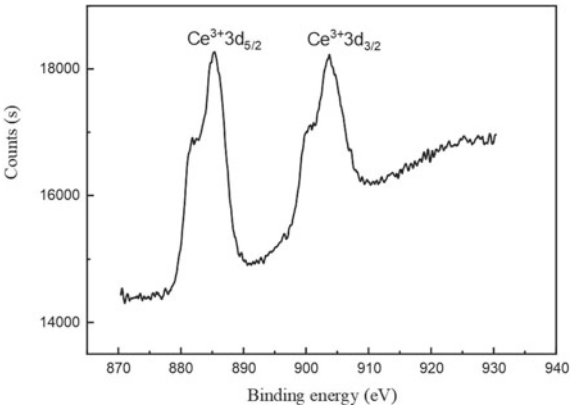

Fig. 2 Test results showing that only Ce^{3+} but no Ce^{4+} existed in the premelting samples

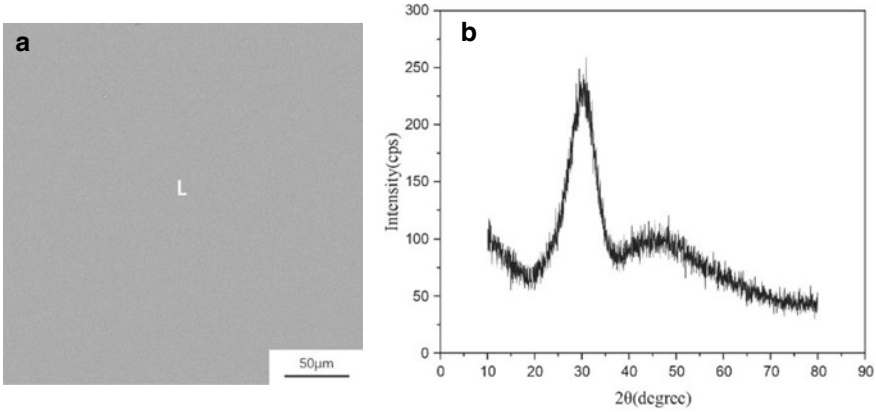

Fig. 3 Microstructure and XRD test results of the premelted slag sample

The premelted slag was ground to below 300 mesh for X-Ray Diffraction (XRD) detection. If crystallization precipitation was detected, the sample was discarded and the content of each oxide was adjusted to carry out the premelting test of the slag sample again. The microstructure and XRD test results of the premelted slag sample are shown in Fig. 3, from which we can determine that the premelted slag sample is glass phase with uniform composition.

The composition of quenching sample was analyzed by X-Ray Diffraction (XRD). It can be seen that the actual measured content of each component shows a small error compared to the design composition from the results listed in Table 1. The actual measured contents of each sample were projected onto the $CaO–SiO_2–Ce_2O_3–5wt.\%$ Al_2O_3 phase diagram, as shown in Fig. 4.

Equilibration Experiments

The premelted slags with uniform composition were adopted to conduct the equilibration experiments. A platinum crucible with the slag samples of different composition was placed in a constant temperature zone in a box-type resistance furnace in which the temperature was measured by a B-type thermocouple with an overall temperature accuracy of ± 1 K as shown in Fig. 5. All samples were heated to 1923 K for 1 h, after which the temperature dropped to 1773 K, and was thermal insulation for 24 h to ensure that the sample reached phase equilibrium state. High purity argon was used as the protective gas to prevent the sample from oxidation in the whole process of the experiment. Thereafter, the sample is also quickly quenched to room temperature.

The quenched samples were put into the resin for grinding and polishing before Energy Disperse Spectroscopy (EDS) was used to detect the composition of the

Table 1 Comparison of design composition and measured composition of quenched molten slag

Number		Composition (wt.%)				
		Al_2O_3	SiO_2	Ce_2O_3	CaO	Total
N1	Designed	5	47.5	33.25	14.25	100
	Measured	5.11	46.24	33.79	14.86	100
N2	Designed	5	57	28.5	9.5	100
	Measured	5.82	53.23	31.21	9.74	100
N3	Designed	5	61.75	19	14.25	100
	Measured	5.24	61.58	19.05	14.13	100
N4	Designed	5	66.5	9.5	19	100
	Measured	4.53	74.3	6.92	14.25	100
N5	Designed	5	38	28.5	28.5	100
	Measured	4.98	38.21	28.64	28.17	100
N6	Designed	5	35	55	5	100
	Measured	5.29	35.38	54.01	5.32	100
N7	Designed	5	38	33.25	23.75	100
	Measured	4.89	38.4	33.21	23.5	100
N8	Designed	5	38	42.75	14.25	100
	Measured	5.04	32.53	43.95	18.48	100
N9	Designed	5	38	47.5	9.5	100
	Measured	6.40	41.26	43.60	8.74	100
N10	Designed	5	42.75	47.5	4.75	100
	Measured	5.55	45.69	44.41	4.35	100
N11	Designed	5	76	4.75	14.25	100
	Measured	5.09	77.96	4.32	12.63	100
N12	Designed	5	52.25	4.75	38	100
	Measured	5.75	54.51	4.76	34.98	100
N13	Designed	5	40.85	23.75	30.4	100
	Measured	5.54	42.70	23.32	28.44	100
N14	Designed	5	66.5	16.625	11.875	100
	Measured	4.95	68.27	16.08	10.70	100
N15	Designed	5	71.25	3.8	19.95	100
	Measured	6.21	72.34	3.54	17.91	100
N16	Designed	5	66.5	23.75	4.75	100
	Measured	4.64	67.09	23.68	4.59	100
N17	Designed	5	38	22.8	34.2	100
	Measured	4.83	38.7	24.01	32.46	100

(continued)

Table 1 (continued)

Number		Composition (wt.%)				
		Al_2O_3	SiO_2	Ce_2O_3	CaO	Total
N18	Designed	5	38	38	19	100
	Measured	5.56	36.69	40.12	17.63	100
N19	Designed	5	36.1	29.45	29.45	100
	Measured	5.44	38.69	17.89	38.43	100
N20	Designed	5	52.25	28.5	14.25	100
	Measured	4.99	50.2	29.6	14.76	100
N21	Designed	5	57	19	19	100
	Measured	5.00	55.49	19.67	19.84	100
N22	Designed	5	38.95	0	56.05	100
	Measured	4.91	40.24	0	54.85	100
N23	Designed	5	57	0	38	100
	Measured	5.17	55.39	0	39.44	100
N24	Designed	5	74.1	0	20.9	100
	Measured	5.08	72.76	0	22.16	100
N25	Designed	5	67.45	0	27.55	100
	Measured	4.97	69.16	0	25.87	100
N26	Designed	5	39.9	2.85	52.25	100
	Measured	5.23	40.54	12.36	41.87	100
N27	Designed	5	38.95	11.4	44.65	100
	Measured	5.45	39.99	13.61	40.95	100
N28	Designed	5	38	52.25	4.75	100
	Measured	4.88	35.56	55.55	4.01	100
N29	Designed	5	39.9	7.6	47.5	100
	Measured	5.27	41.63	9.28	43.82	100
N30	Designed	5	52.25	38	4.75	100
	Measured	6.46	49.05	39.77	4.72	100

coexisting phase in each quenched sample. The current and the electron beam acceleration voltage adopted by EDS tests are 15 mA and 15 kV, respectively. Another portion of the quenched sample was ground into a powder and characterized by XRD to identify the crystalline phase.

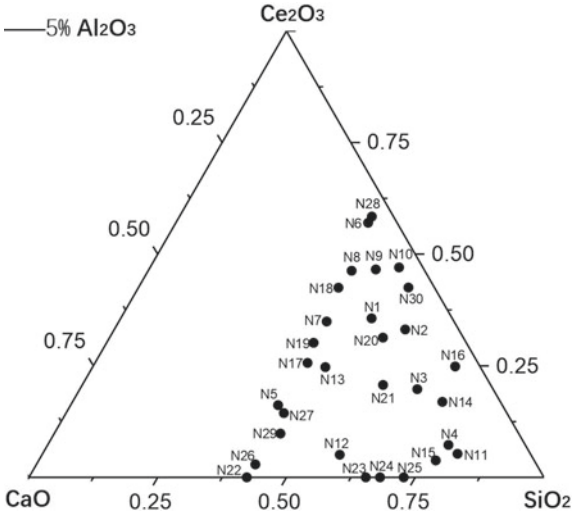

Fig. 4 $CaO–SiO_2–Ce_2O_3–5wt.\%\ Al_2O_3$ phase diagram

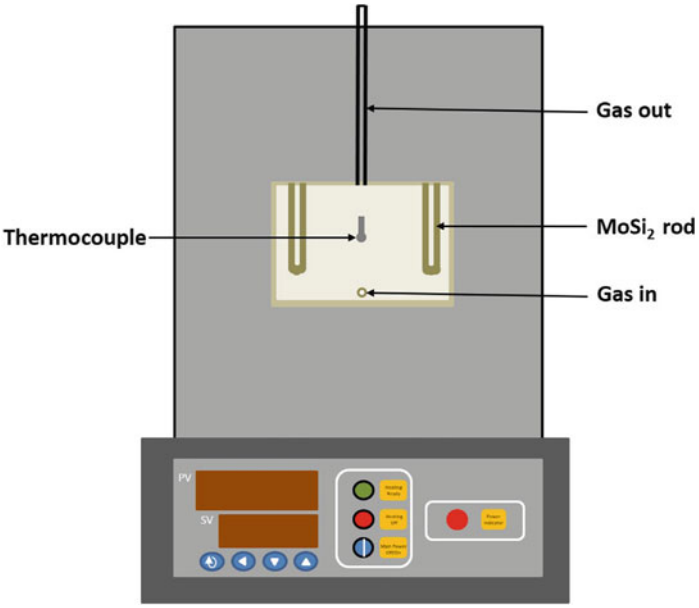

Fig. 5 B-type thermocouple with an overall temperature accuracy of ±1 K

Results and Discussion

Equilibrium Phase Composition of $CaO–SiO_2–Ce_2O_3–5wt.\%$ Al_2O_3 System at 1773 K

In general, the study of phase equilibrium in multi-component systems can be simplified by constructing isothermal pseudo-ternary phase diagrams with fixed typical components [12]. According to the industrial production conditions and common composition of rare earth slag containing trace alumina, the content of Al_2O_3 is fixed at 5wt.% in current research. A large number of secondary precipitates would occur in some samples when quenched to room temperature, resulting in inaccurate liquidus composition. Therefore, the phase equilibrium experiments of some samples in $CaO–SiO_2–Ce_2O_3–5wt.\%$ Al_2O_3 system were selected and studied, and multiple regions in the phase diagram were covered as far as possible. The results of Field Emission Scanning Electron Microscopy (FE-SEM) and XRD of quenched samples show that the samples are composed of amorphous glass and crystalline phase. The crystalline phase is solid precipitated at 1773 K, while the glassy phase is formed by the quenching and supercooling of the liquid in equilibrium with the solid phase.

The chemical composition of glass phase and crystal phase was quantitatively measured by EDS, and the crystal phase was further detected by XRD. It can be found that there are six different equilibrium phases in the samples. Two kinds of solid solutions also appear in $Ce_2O_3–SiO_2–CaO–5wt.\%$ Al_2O_3 system, namely $CaO{\cdot}2Ce_2O_3{\cdot}3SiO_2$ and $Ca_{2-x}Ce_xSiO_{4+\delta}$. Those six different equilibrium phases are: (1) the single liquid phase; (2) the solid–liquid equilibrium phase between SiO_2 and liquid phase; (3) the solid–liquid equilibrium phase between solid solution $Ca_{2-x}Ce_xSiO_{4+\delta}$ and liquid phase; (4) the solid–liquid equilibrium phase between $CaO{\cdot}2Ce_2O_3{\cdot}3SiO_2$ and liquid phase; (5) the solid–liquid equilibrium phase between $Ce_2Si_2O_7$ and liquid phase; and (6) the three-phase equilibrium between SiO_2, $Ce_2Si_2O_7$, and liquid phase. It is remarkable that there is no fixed molar ratio between Ca^{2+} and Ce^{3+} in the $Ca_{2-x}Ce_xSiO_{4+\delta}$ phase in this study. The reason for this phenomenon is probably that Ce3 + can replace part of Ca^{2+} in the compound Ca_2SiO_4, resulting in $Ca_{2-x}Ce_xSiO_{4+\delta}$. Gao [13] studied the reaction behavior of rare earth elements in Bayan Obo minerals during the reduction process, and his research results consistent with those in current paper.

All microstructure and XRD patterns of the equilibrium phase of $CaO\text{-}SiO_2\text{-}Ce_2O_3\text{-}5wt.\%$ Al_2O_3 system are shown in Fig. 6. However, the results indicated by XRD and SEM–EDS cannot reveal its exact chemical composition. Due to the similarity of ion radius and oxygen coordination between Ca^{2+} and REE^{3+}, there was an incomplete occupation relationship between Ca^{2+} and Ce^{3+}, which would change the composition of the equilibrium phase [14]. Therefore, the trace chemical composition of the equilibrium phase was quantitatively analyzed by Electro-Probe Microanalyzer (EPMA) measurement, and the composition of all phases in each investigated sample was summarized in Table 2. The measured compositional data are normalized, which are used to construct phase diagrams.

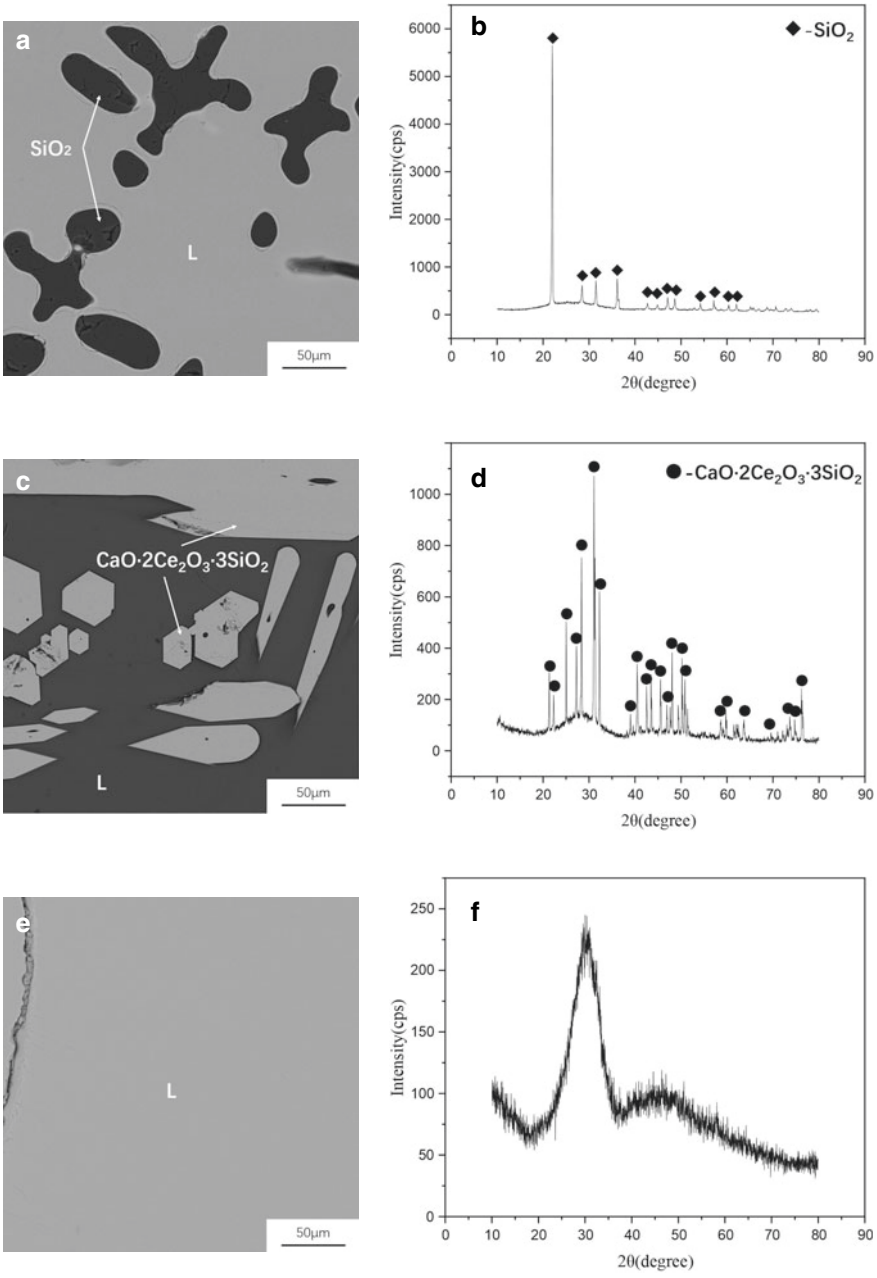

Fig. 6 Microstructure and XRD patterns of the equilibrium phase of $CaO–SiO_2–Ce_2O_3$–5wt.% Al_2O_3 system

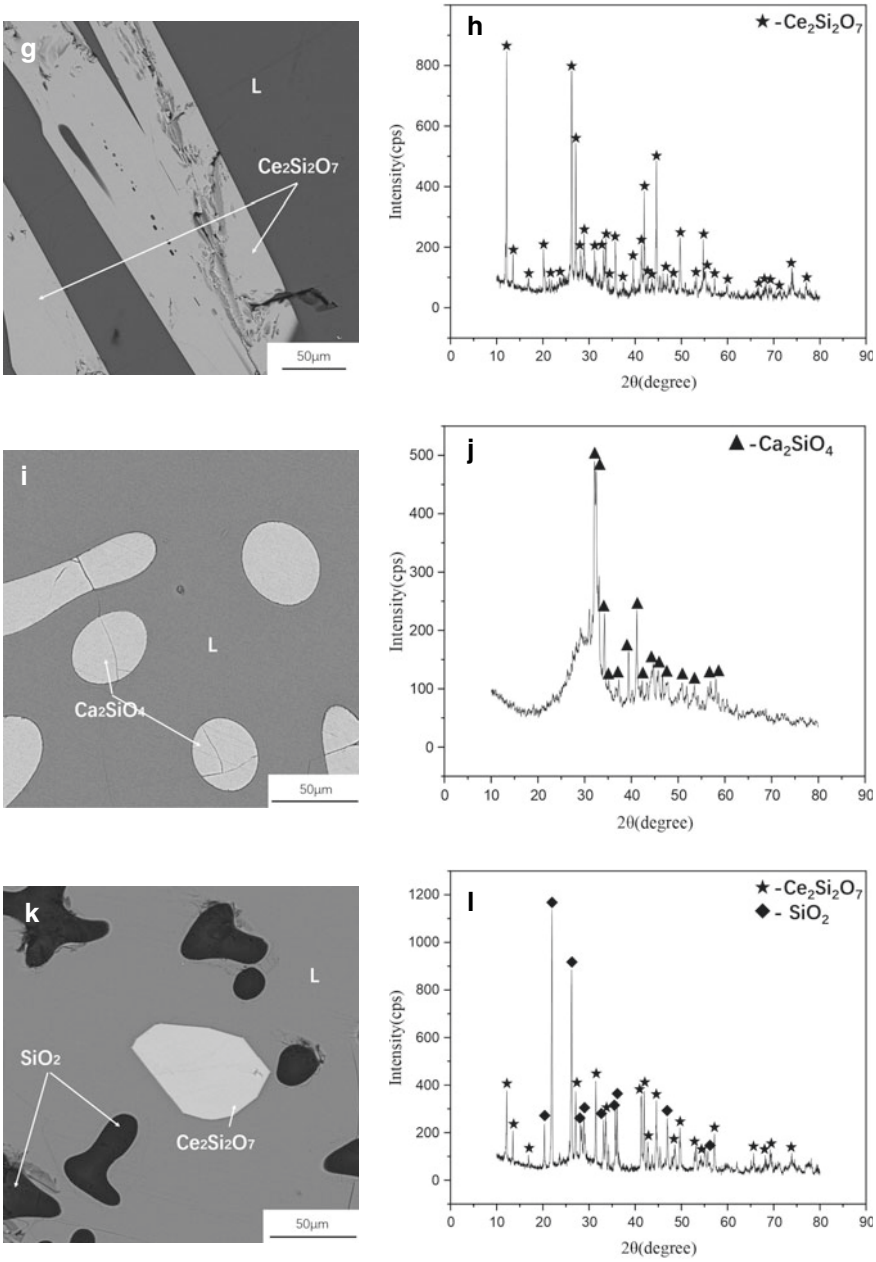

Fig. 6 (continued)

Table 2 Equilibrium phase compositions at 1773 K

Sample No	Phase	Composition (wt.%)			
		Al_2O_3	SiO_2	Ce_2O_3	CaO
N2	L	5.94	56.12	28.71	9.23
	SiO_2	0.35	99.31	0.24	0.1
N3	L	5.36	60.96	19.7	13.98
	SiO_2	0.29	99.17	0.45	0.09
N4	L	5.73	65.5	10.3	18.47
	SiO_2	0.24	99.35	0.22	0.19
N5	L	4.54	37.88	17.01	40.57
	$CaO{\cdot}2Ce_2O_3{\cdot}3SiO_2$	0.16	20.47	73.23	06.14
N6	L	7.21	42.44	41.82	8.53
	$Ce_2Si_2O_7$	0. 21	26.81	72.63	0.35
N7	L	7.23	42.64	25.64	24.49
	$CaO{\cdot}2Ce_2O_3{\cdot}3SiO_2$	0.16	21.13	72.72	5.99
N8	L	10.86	43.84	30.3	15
	$CaO{\cdot}2Ce_2O_3{\cdot}3SiO_2$	0.06	22.47	71.3	6.17
N9	L	7.58	45.68	37.02	9.72
	$CaO{\cdot}2Ce_2O_3{\cdot}3SiO_2$	0.13	21.59	72.07	6.21
N10	L	6.45	48.12	40.52	4.91
	$Ce_2Si_2O_7$	0.22	99.48	0.12	0.18
N11	L	6.23	67.75	7.49	18.53
	SiO_2	0.76	98.1	0.45	0.69
N13	L	5.37	42.72	25.01	26.9
	$CaO{\cdot}2Ce_2O_3{\cdot}3SiO_2$	0. 07	19.93	73.34	6.66
N15	L	5.95	67.37	5.24	21.44
	SiO_2	0.4	98.9	0.52	0.18
N16	L	7.8	53.19	33.48	5.53
	SiO_2	0.35	99.09	0.37	0.19
N17	L	6.43	39.02	21.66	32.89
	$CaO{\cdot}2Ce_2O_3{\cdot}3SiO_2$	0.25	21.79	70.87	7.09
N22	L	6.66	41.01	0.01	52.32
	Ca_2SiO_4	0. 41	64.12	0	35.47
N25	L	8.33	65.8	0.02	25.85
	SiO_2	0.75	98.74	0.3	0.21
N27*	L	8.04	36.55	11.96	43.45
	Ca_2SiO_4	1.14	34.32	12.11	52.43

(continued)

Table 2 (continued)

Sample No	Phase	Composition (wt.%)			
		Al_2O_3	SiO_2	Ce_2O_3	CaO
N28	L	6.39	40.48	47.98	5.15
	$Ce_2Si_2O_7$	0.11	25.46	74.42	0.01
N29*	L	6.82	38.3	8.42	46.46
	Ca_2SiO_4	0.46	31.79	15.45	52.30
N30	L	6.17	50.65	38.61	4.57
	SiO_2	0.33	99.35	0.18	0.14
	$Ce_2Si_2O_7$	0.09	27.87	71.49	0.55

* Represents the results obtained by converting Ce^{3+} into Ca^{2+}

As shown in Fig. 6a, b, the precipitated phase in sample N3 is only SiO_2, the equilibrium result of sample N2, N4, N11, N15, N16, and N25 is the coexistence phase of SiO_2 and liquid phase, also. Sample N7 presents a phase equilibrium state in which $CaO{\cdot}2Ce_2O_3{\cdot}3SiO_2$ coexists with the liquid phase, and the gray phase is $CaO{\cdot}2Ce_2O_3{\cdot}3SiO_2$, as shown in Fig. 6c. A single liquid phase of sample N12 in Fig. 6e is taken as the representative, indicating that its fractional point is within the liquid phase region, while samples N1, N20, and N21 have the same equilibrium results. In the samples N6, N10, and N28, combining with XRD results, it is confirmed that the $Ce_2Si_2O_7$ phase coexists with the liquid phase, as shown in Fig. 6. The dark gray strip is $Ce_2Si_2O_7$ phase, and the matrix phase is coexisting liquid phase. As shown in Fig. 6i, combined with the phase composition and XRD pattern in Table 2, it is confirmed that the light gray precipitated phase of sample N27 is aggregated as Ca_2SiO_4, and the dark gray is liquid phase. It is easy to observe the existence of three equilibrium phase in sample N30 through analyzing Fig.6k. By combining the XRD pattern results and EDS results, it is easy to find that the black phase, light gray phase, and the dark gray phase are SiO_2, $Ce_2Si_2O_7$, and liquid phase, respectively. It should be noted that part of Ca^{2+} was replaced by Ce^{3+} in the sample with '*'. Thus, the precipitated phase Ca_2SiO_4 was obtained by converting Ce^{3+} into Ca^{2+}.

Construction of the Isotherms

In the process of sample preparation, the content of Al_2O_3 was set at 5wt.%. However, due to the crystal precipitation in the slag, the content of Al_2O_3 in the quenching phase cannot be accurately controlled within 5wt.%. Therefore, the composition of the quenched liquid must be standardized so that the phase relationship of CaO–SiO_2–Ce_2O_3–5wt.% Al_2O_3 system can be represented by phase diagram [15, 16]. Based on the above experimental results, the liquid phase isotherms of CaO–SiO_2–Ce_2O_3–5wt.% Al_2O_3 system at 1773 K are shown in Fig. 7. It can be seen that

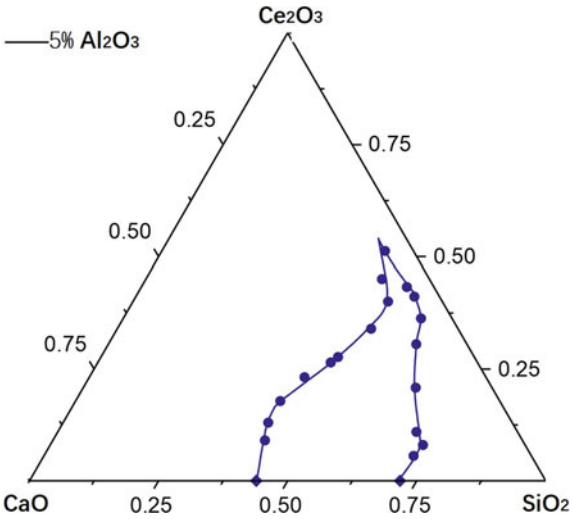

Fig. 7 Liquid phase isotherms of $CaO–SiO_2–Ce_2O_3–5wt.\%$ Al_2O_3 system at 1773 K

when the content of Al_2O_3 is constant, the liquid phase region has a tendency to extend towards the $Ce_2O_3–SiO_2$ boundary. Yet, there is still no liquid region on the $Ce_2O_3–SiO_2$ boundary of the above system, indicating that in the $Ce_2O_3–SiO_2–5wt.\%$ Al_2O_3 system. Therefore, we can speculate that when the temperature of the above equilibrium system increases again, a small part of the liquid phase region may appear on the phase boundary of $Ce_2O_3–SiO_2$, which we will study in the follow-up work. In this study, the range of basicity of the liquid phase increased with the decrease of Ce_2O_3 content. However, the liquidus temperature expands with the increase of Ce_2O_3 content at a fixed basicity.

Phase Diagram of $CaO–SiO_2–Ce_2O_3–5wt.\%$ Al_2O_3 System

Based on all the results of current research, the isotherms and phase relationships of the specific composition associated with the rare earth element Ce are constructed as shown in Fig. 8. The liquid phase data obtained by the experiment in this study is basically consistent with the known data points of $CaO–SiO_2–Al_2O_3$ system, which also proves that this experiment has a high accuracy. According to the law of adjacent phase regions and the trend of phase boundary shown by the experimental results, the phase relations in regions 2, 3, and 4 are deduced, namely the three-phase equilibrium between $Ca_{2-x}Ce_xSiO_{4+\delta}$, $CaO{\cdot}2Ce_2O_3{\cdot}3SiO_2$, and the liquid melt, and the two-phase equilibrium between $Ce_2Si_2O_7$ and the liquid melt. In addition, in Fig. 8, the solid phase area with SiO_2 content less than 20wt% and the area marked by the dotted line have not studied yet in this work.

The variation trend of the primary crystal phase at 1773 K can be summarized as follows. The liquid phase is mainly in the SiO_2 content in the range of 45–70%, in

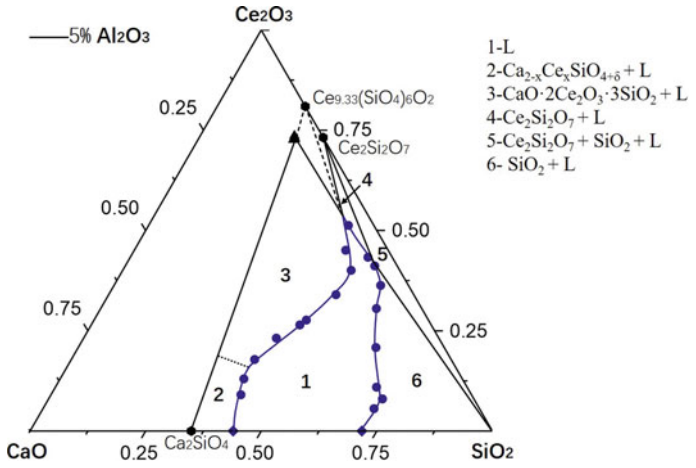

Fig. 8 Solid phase area with SiO_2 content less than 20wt% and the area marked by the dotted line have not been studied

the low cerium oxide content and low basicity region; the primary phase is silica. In the region with high basicity and low cerium oxide content, the precipitated phase is calcium silicate. The main precipitated phase is changed into $CaO{\cdot}2Ce_2O_3{\cdot}3SiO_2$ with the increase of cerium oxide content.

Conclusion

The phase equilibrium relationship of $CaO–SiO_2–Ce_2O_3–5wt.\%\ Al_2O_3$ phase diagram system has been studied in current research. The equilibrium phases at 1773 K are determined by using XRD, XRF, EPMA, FE-SEM, and EDS analysis. The main results can be summarized as follows.

(1) The composition and content of liquid phase (L), $CaO{\cdot}2Ce_2O_3{\cdot}3SiO_2$ solid solution phase, $Ca_{2-x}Ce_xSiO_{4+\delta}$ solid solution phase, and $Ce_2Si_2O_7$ phase were determined by XRD, XRF, EPMA, FE-SEM, and EDS analysis using high temperature equilibrium technology at 1773 K;

(2) The isothermal liquidus of $CaO–SiO_2–Ce_2O_3–5wt.\%\ Al_2O_3$ system at 1773 K was determined by high temperature equilibrium experiments. At the same time, the positions of the primary crystal regions of the four precipitated phases were determined;

(3) According to the experimental results and relevant literature, the phase diagram of $CaO–SiO_2–Ce_2O_3–5wt.\%\ Al_2O_3$ system was obtained.

References

1. Wang H et al (2021) Effect of rare earth CE on the morphology and distribution of Al_2O_3 inclusions in high strength IF steel containing phosphorus during continuous casting and rolling process. ISIJ Int 61(3):657–666
2. Zhou S-C (2013) Study of the clogging of the submersible nozzle in the continuous casting of stainless steel RE-253MA. Metallurgist 57(5–6):510–515
3. Bi Y et al (2014) Three dimensional evaluations of rem clusters in stainless steel. ISIJ Int 54(6):1266–1273
4. Lan X et al (2021) Thermodynamics and kinetics of REEs in $CaO-SiO_2-CaF_2-Ce_2O_3$ system: a theoretical basis toward sustainable utilization of REEs in REE-bearing slag. Ceram Int 47(5):6130–6138
5. Strzelecki AC et al (2020) High-temperature thermodynamics of cerium silicates, A-$Ce_2Si_2O_7$, and Ce-4.67 (SiO4)(3)O. Acs Earth Space Chem 4(11):2129–2143
6. Binnemans K et al (2015) Towards zero-waste valorisation of rare-earth-containing industrial process residues: a critical review. J Clean Prod 99:17–38
7. Jeong SJ et al (2017) Relationship between sulfide capacity and structure of $MnO-SiO_2-Al_2O_3-Ce_2O_3$ system. Metall Mater Trans B 48(1):545–553
8. Zec S et al (2007) Contribution to phase equilibria in the Ce_2O_3 rich part of the $Ce_2O_3-SiO_2-ZrO_2$ system. J Eur Ceram Soc 27(2–3):523–526
9. Tas C et al (1994) Phase relations in the system $Ce_2O_3-Ce_2Si_2O_7$ in the temperature range 1150 °C to 1970 °C in reducing and inert atmospheres. J Am Ceram Soc 77(11):2953–2960
10. Kawamura S et al (2009) Phase relations around the pyrosilicate phase in the $Gd_2O_3-Ce_2O_3-SiO_2$ system. Cryst Growth Des 9(3):1470–1473
11. Zhao Z et al (2019) Experimental study on the thermodynamics of the $CaO-SiO_2-Ce_2O_3$ system at 1873 K. Metall Mater Trans B 50(1):395–406
12. Won KW et al (2006) Thermodynamic methods for pressure relief system design parameters. Fluid Phase Equilib 241(1–2):41–50
13. Gao P et al (2012) Research on the reaction behavior of rare earth elements in reduction. powder technology & applications Iv. S J Dai 454:268–272
14. Elwert T et al (2014) Affinity of rare earth elements to silico-phosphate phases in the system $Al_2O_3-CaO-MgO-P_2O_5-SiO_2$. Chem Ing Tec 86(6):840–847
15. Wang Z et al (2016) Phase equilibria in the TiO_2 rich part of the $TiO_2-CaO-SiO_2$-10wt.% Al_2O_3 system at 1773 K and 1873 K. J Alloy Compd 671:137–143
16. Gran J et al (2011) Experimental determination of the liquidus in the high basicity region in the Al_2O_3(30 mass%)-CaO-MgO-SiO_2 system. Calphad-Comput Coupl Phase Diag Thermochem 35(2):249–254

Investigation of Bubble Penetration Through Interface Between Immiscible Liquids

Xiangfeng Cheng, Baojun Zhao, Fuming Zhang, Gele Qing, and Zhixing Zhao

Abstract As an important source of copper losses to the slag, SO_2 bubbles formed in the quiescent settlement zone of smelting furnace bring matte into slag phase through the immiscible matte-slag interface. The penetration and entrainment mechanisms of large bubbles were studied while the entrainment by micro bubbles was rarely investigated. In this paper, attachment of matte droplets to micro SO_2 bubbles in the industrial smelting slags and laboratory samples have been confirmed by high-temperature experiments. The bubble penetration behaviors through liquid–liquid interface were simulated by the cold model experiments using water and silicone oil. Results showed that fine gas bubbles can pass through the liquid–liquid interface and cause the heavier liquid entrainment. Although the critical bubble penetration size deduced in previous studies is inconsistent with the phenomenon observed in cold model experiments, it is an important parameter to classify the bubble entrainment regimes which is closely associated with the bubble penetration regimes. Greene's theoretical derived values of critical bubble penetration and entrainment sizes are in good agreement but comparatively higher than the experimental results. The Weber numbers based on the critical bubble penetration size, heavier liquid density, and interfacial tension under different experimental conditions are normally between 4 and 4.5.

Keywords Copper loss · Micro bubbles · Liquid–liquid interface · Penetration mechanisms

X. Cheng (✉) · G. Qing · Z. Zhao
Shougang Research Institute of Technology, Beijing 100043, China
e-mail: xiangfeng_2008@126.com

B. Zhao
International Research Institute for Resources, Energy, Environment and Materials, Jiangxi University of Science and Technology, Jiangxi 341099, China
e-mail: bzhao@jxust.edu.cn

F. Zhang
Shougang Group, Beijing 100041, China
e-mail: zhangfuming2018@163.com

Z. Peng et al. (eds.), *12th International Symposium on High-Temperature Metallurgical Processing*, The Minerals, Metals & Materials Series,
https://doi.org/10.1007/978-3-030-92388-4_20

Introduction

The bottom blowing smelting furnace (BBF) and Teniente Converter (TC) are the two important bath copper smelting furnaces used mainly in China and Chile, respectively. BBF injects high pressures gases (high oxygen enrichments: approximately 70%) into the bath using 7° and 22° oxygen lances and is operated at 1160–1200 °C [1]. The gases with low oxygen enrichments (35–42%) were applied in TC and injected horizontally at relatively low pressures [2], and the operating temperature of TC is around 1250 °C. The average copper content in BBF slag is around 3.5 wt%, while the copper content in TC smelting slag is controlled to be around 9 wt%.

In the smelting process, copper concentrate would experience fierce oxidization with oxygen enriched air in the reaction zone, and then two stratified liquid layers would be formed in the relatively quiescent settlement zone. Theoretically, the slag phase (approximately 0.5 m thick) above matte would be discharged cleanly through discharging hole at the end of the smelting furnace. However, the insufficient oxidization of copper concentrate in reaction zone would cause further oxidisation in the settlement zone, leading to numerous microbubbles generation in the matte phase, as shown in Eq. 1.

$$\begin{aligned} &\mathrm{CuFeS_2(s) + O_2(g) + SiO_2(s)(Cu - Fe - S)(l)} \\ &\quad + \mathrm{FeO - SiO_2(l) + SO_2(g) + heat} \end{aligned} \tag{1}$$

Several experimental and numerical studies were carried out on bubble passage through the immiscible liquid–liquid interface by cold model experiments. Some researchers proposed that there exists a critical bubble size that could provide sufficient upward force to overcome the interfacial tension to pass through the interface between superposed liquid layers, and the criterion for the size evaluation depends on liquids surface tensions and densities [1–3]. However, some studies reported that the bubble would be trapped at the interface for milliseconds to minutes if the bubble buoyancy force and inertia force cannot overcome interfacial tension. With the drainage of disjoining film between bubble and interface, the bubble would eventually pass through the interface when the film reaches a critical thickness, which contradicts previous theories [4–6]. Considering the precondition of heavier liquid entrainment by rising gas bubbles is that those bubbles are capable of penetrating the liquid–liquid interface; it is necessary to carry out further studies on fine bubble penetration behaviors and their corresponding entrainment regimes. Meanwhile, quite limited research attached importance to the metal entrainment by bubbles in molten metal-slag systems at high-temperature specifically until now. Therefore, the present study was to clarify the fine bubble penetration behaviors at a liquid–liquid interface in cold model experiments by integrating the analysis of as-received industrial slag samples.

In this work, the industrial slag samples from the bottom-blown furnace (BBF) and side-blown furnace (TC) were analysed by Scanning Electron Microscope (SEM)

to evaluate the SO_2 bubble effects on matte entrainment. Flow regimes of fine and large bubbles at the liquid–liquid interface were observed by high-speed camera, and the suitable equations suitable to predict bubble terminal velocities were compared. Critical bubble sizes to classify the flow regimes were compared.

Experimental

Materials

Liquid–liquid systems in cold model experiments were designed with varying chemical compositions, namely silicone oils (10cP, 50cP, 100cP, 200cP, 500cP, Sigma-Aldrich, USA), SDS (Sodium Dodecyl Sulphate) (99.0%, Sigma-Aldrich, USA), Glycerol (99.0%, Sigma-Aldrich, USA), and $CaCl_2$ (93.0%, Sigma-Aldrich, USA). SDS powder was added into the solution to adjust surface tension without density and viscosity variation. Glycerol solutions of different weight percentages (80, 70, 60, and 40%) were used to change heavier liquid viscosities, and the liquid viscosity could increase from 60 to 3.72cP, while the density and surface tension remained constant by adding SDS powder. The Calcium Chloride of different weight percentages was used to change heavier liquid density due to the high solubility in water. Interfacial tension was determined as the difference between the surface tension of the two liquids. Water, glycerol, $CaCl_2$, and silicone oils were used to create a series of liquid–liquid interface systems. The liquid combinations were chosen to cover a broad range of interfacial tensions, viscosities, and density ratios, as shown in Table 1.

Experimental Apparatus

The system consisted of a transparent glass container (80 mm × 80 mm × 600 mm), in which a single bubble was generated through a glass inlet tube connecting with a syringe pushed by a syringe pump. A high-speed camera was placed at the level of interface between immiscible liquids in front of the glass cube to capture the bubble penetration behaviours at 500 fps; a normal camera was used to make up the high-speed imaging defect of the limited view field. A light source (XGY-II) in the opposite direction of the high-speed camera was used to provide dispersed light through a light shading board to illuminate liquids in the glass cube. Air was injected from a syringe pushed by a syringe pump, and the flow rate was controlled using this syringe pump. The bubble size could be controlled through some specially-made glass nozzles which are replaceable in the notch of the gas injection tube. The experimental apparatus was shown in Fig. 1.

Table 1 Physical properties of liquid–liquid combination systems

Lower phase				Upper phase			
Material	Viscosity/cP	Density/(kg m^{-3})	Surface tension/(mN m^{-1})	Material	Viscosity/cP	Density/(kg m^{-3})	Surface tension/(mN m^{-1})
Glycerol (80%)	60.1	1210	48.06	Silicone oil	10	930	20.1
Glycerol (70%)	22.5	1190	48.26	Silicone oil	50	959	20.7
Glycerol (60%)	10.8	1160	48.11	Silicone oil	100	965	20.9
Glycerol (40%)	3.72	1100	48.66	Silicone oil	200	970	21.1
$CaCl_2$ (40%)	8.48	1420	58.03	Silicone oil	500	970	21.1
$CaCl_2$ (30%)	3.33	1300	58.28				
$CaCl_2$ (20%)	1.81	1190	57.00				

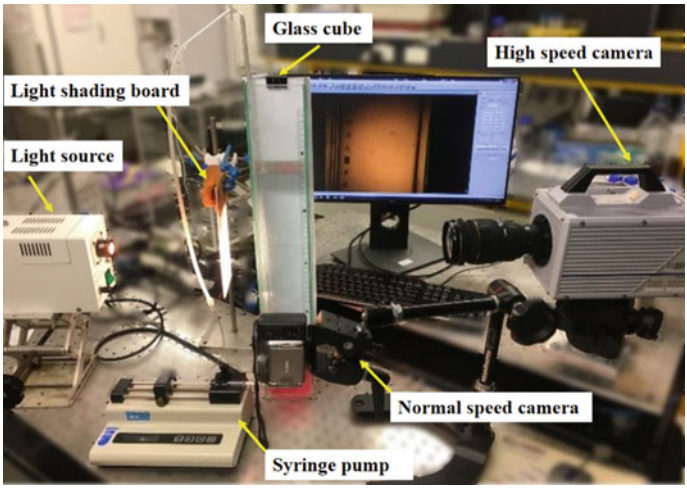

Fig. 1 Cold model experimental apparatus

Four bubble shapes were observed in cold model experiments, i.e. spherical, oblate ellipsoidal, oblate ellipsoidal cap, and spherical cap. Small bubbles tend to present a spherical shape and become elliptical when bubble size grows larger. The bubble size and terminal velocity were processed by ImageJ. Due to the deformation of rising bubbles, the equivalent bubble diameter was defined as

$$d_{\mathrm{eq}} = \left(d_h^2 d_v\right)^{1/3} \tag{2}$$

where d_h and d_v are horizontal and vertical diameters, respectively.

Results and Discussion

Analysis of Industrial Slag Samples

A series of slag samples were collected during slag tappings in commercial BBF and TC and analysed by SEM systematically. The typical microstructures of the BBF and TC slag are shown in Fig. 2a, b, respectively. Quantitative analyses of 368 SEM images of industrial BBF and TC slags show that 14.8% and 11.2% matte droplets are attached to gas bubbles, respectively, compared to 0.2% and 0.4% matte droplets attached to spinel solids. The average bubble size in BBF and TC slags is 130 μm and 168 μm, respectively, with a maximum bubble size of 1800 μm. The attachment between matte and micron bubbles in the industrial slag samples demonstrates the

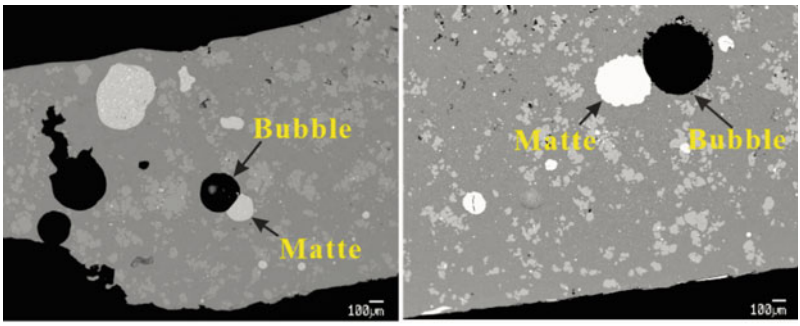

Fig. 2 Attachment between matte droplets and SO_2 bubbles in BBF slags **a** and TC slags **b**

significant effect of micro bubbles on matte entrainment in the matte-slag system at the high temperature.

Small Bubble Penetration Behaviors

In cold model experiments, some small bubbles, usually smaller than 3 mm in diameter, cannot penetrate the interface directly and will dwell for a short period as reported in previous studies [1–3]. To visualize the small bubble penetration and entrainment behaviours at the interface, high-speed imaging techniques were used in cold model experiments.

The sequential photographs of the whole penetrating process of a small bubble (2.5 mm in diameter) through a water-10cP silicone oil interface were shown in Fig. 3. The interfacial force between water and silicone oil tends to prevent the bubble from crossing the interface and makes bubbles dwell at the interface for up to several seconds as shown in Fig. 3a. The thin bubble cap film will drain gradually from the bubble top surface due to the pressure gradient in this period. When bubble cap film is thin enough, the gas bubble will break up the interface and rise to the top at $t = 0.005$ s, as shown in Fig. 3b. The whole heavier liquid peeled off the gas bubble completely within 0.01 s and began to detach from the interface, as shown in Fig. 3c–e. No visible water column is formed in this process due to the insufficient buoyancy force for smaller gas bubbles to penetrate the interface directly and drag denser liquid globules into the upper phase. The formation of water columns behind gas bubbles is associated with the immiscible liquid properties and interfacial tension force [5]. The short denser liquid bridge connecting bubble and interface shown in Fig. 4e breaks eventually, and a small proportion remains stably at the bubble bottom surface. The whole duration time from bubble cap film rupture in Fig. 3a to complete detachment from an interface in Fig. 3f lasts only 0.067 s. It is hypothesized that the denser liquid entrainments by small gas bubbles are mainly in the form of thin

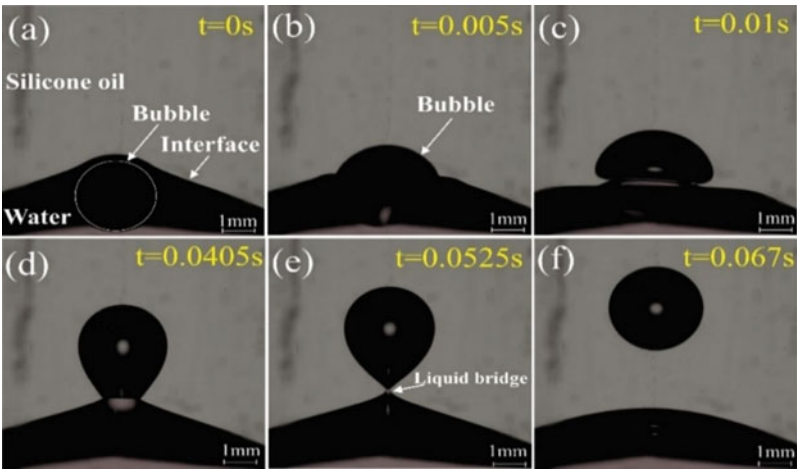

Fig. 3 Small gas bubble transporting behaviouor at interface

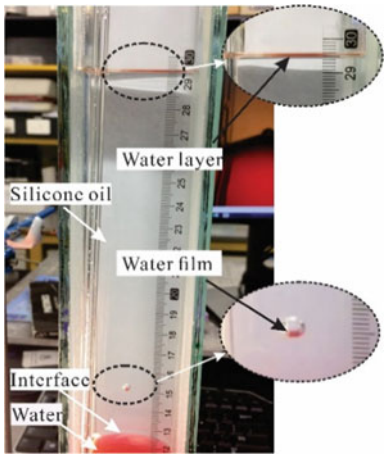

Fig. 4 Water layer accumulation at silicone oil surface after bubble rupture

liquid film accumulated at the bottom of rising bubbles. The surface tension of thin denser liquid film makes it difficult to peel off the bubble bottom surface to form a free denser liquid globule as shown in Fig. 3f. It should be noted that interfacial tension force counteracting bubble buoyancy force and inertia force at the first bubble impact would decrease with the drainage of bubble cap film due to the changing film thickness and interface curve, leading to the force unbalance [7, 8].

Although the thin water film is difficult to be identified directly from a series of photographs due to the limited film thickness and imaging technique limitation by high-speed camera, the water entrainment by a small-sized bubble was confirmed by a normal speed camera. Several gas bubbles with diameters controlled between 0.5 and 3 mm in cold model experiments were observed as shown in Fig. 4. The water

phase is dyed with red ink to provide good contrast between the enveloping water layer and the upper liquid. All fine bubbles passed through the interface eventually despite a short dwelling at the interface, and a thin red water film was found to be floating at the bottom of the rising bubble due to gravity force in front of the white background. With the accumulation of water droplets from the ruptured bubbles at the surface of the silicon oil, a clear thin red water layer was observed at the top of silicon oil as seen in Fig. 4. The observation in cold model experiments was consistent with the SEM analysis of industrial slags samples in Fig. 2, which shows a large number of matte droplets attachment to SO_2 gas bubbles (diameter: 0.016 –1.8 mm) in slag samples.

Medium Bubble Penetration Behaviours

Sequential photographs in Fig. 5a–f illustrate the penetration process of a medium gas bubble (5 mm in diameter) through a water-silicone oil 50 cP interface. The water column forms when a gas bubble attempts to penetrate the water-silicone oil interface at $t = 0.218$ s (Fig. 5b), and a discernible water layer covers the bubble surface at $t = 0.236$ s (Fig. 5c). After the water column breaks at a certain height, the water layer centres beneath the gas bubble due to the higher specific gravity (Fig. 5c). The water layer starts to peel off the gas bubble and forms a spherical water droplet underneath (Fig. 5d, e) which will detach from the bubble when interfacial tension can no longer support the gravity of the water droplet. The water droplet continues to rise due to the bubble wake effect and its original momentum (Fig. 5f) and settles after reaching

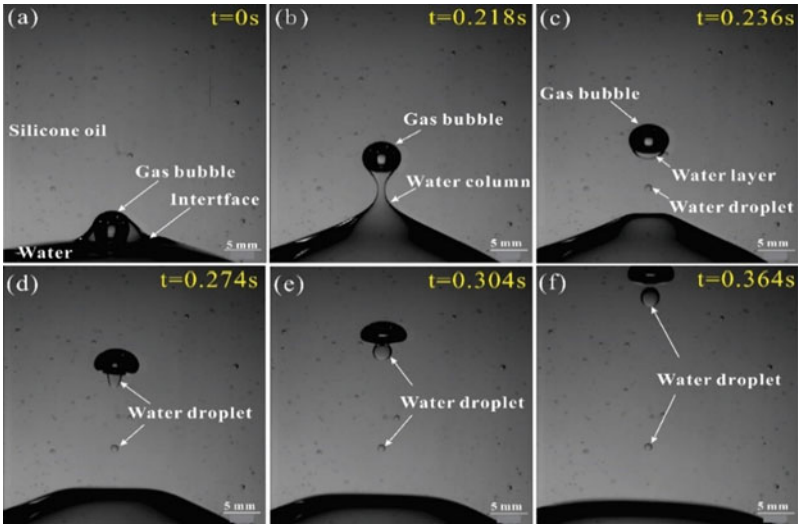

Fig. 5 Medium bubble penetrating behaviour at interface

a certain height in the silicon oil. Previous studies mainly focused on the heavier liquid entrainment by bubbles that can cross the interface directly and carry visible large liquid droplets into the upper phase and ignored the micro bubbles effect in the liquid–liquid system, particularly in metal-slag systems at high temperature [4–6, 9–11].

Bubble Terminal Rising Velocity

As a function of bubble rising velocity, Weber number *We* is an important dimensionless number and parameter in fluid mechanics to analyse an interface between two different fluids, particularly for multiphase flows with strongly curved surfaces. Bubble rising velocity is a complicated function of the bubble geometry, the liquid physical properties, and the physicochemical properties of the gas–liquid interface. A variety of equations were discussed to predict bubble rising velocity in different experimental conditions. The bubble penetration behaviours are essentially the result of the interaction of bubble buoyancy force, bubble inertia force, and interfacial tension force. Weber number *We* relating the inertia forces to the forces resulting from surface tension is indicative of the kinetic energy required to induce the interface deformation necessary for bubble passage, which is related to bubble rising velocity [4, 12]. Therefore, Stokes equation, Hadamard and Rybczynski equation (H-R), Mendelson equation, Davies and Taylor equation, and equation deduced by Travis to predict the rising velocities of bubbles based on previous studies were briefly discussed here [4, 13–15]. A high-speed camera was used to measure the bubble terminal velocity in water, 10 cP silicone oil, 50 cP silicone oil, and 100 cP silicone oil in cold model experiments as shown in Fig. 6a-d, respectively.

As we can see in Fig. 6a–d, Stokes or H-R equations can predict terminal velocity well for small bubbles in micron scale in different silicone oils. However, with the increase of bubble size, the terminal velocity correlation for bubble mobile surface conditions by Travis can well fit the experimental results with bubble size between 1 and 10 mm. Thus, it can be used to predict bubble velocity in cold model experiments considering a similar bubble size range. The terminal velocity correlation for bubble immobile surface conditions can predict bubble terminal velocity more precisely in pure water. Davies and Taylor's correlation and Mendelson's correlation are suitable for bubbles larger than 10 mm in diameter.

Discussion on Weber Number and Critical Bubble Penetration Size

Bubble penetration behaviours through the liquid–liquid interface are essentially the interaction result of bubble buoyancy force, inertial force, and interfacial tension.

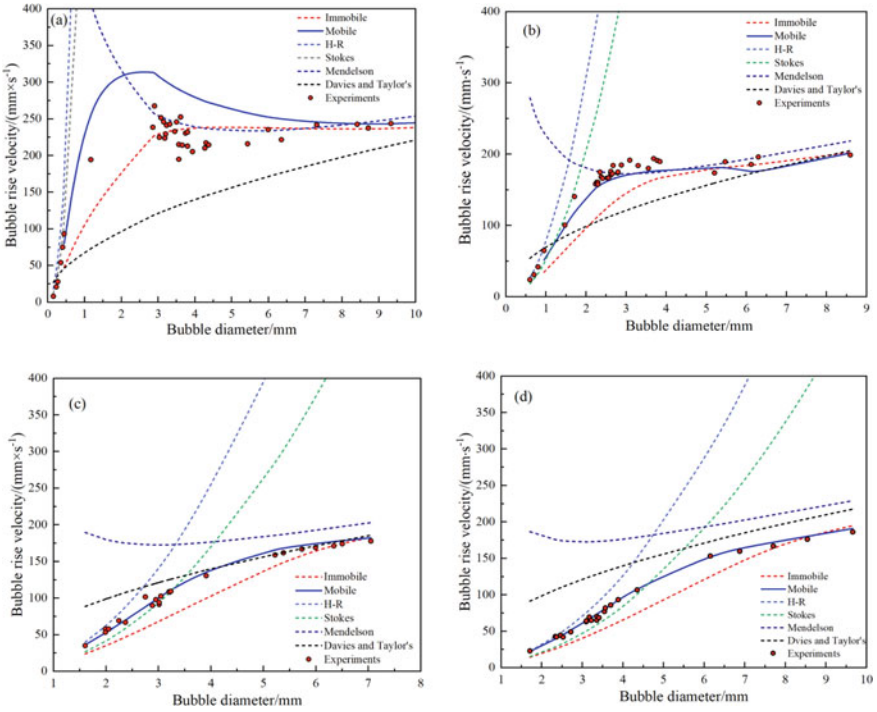

Fig. 6 Comparison of correaltions to predict bubble terminal velocity

As a measure of the relative importance of the fluid's inertia compared to its surface tension, *We* can be used to characterize the kinetic energy of a rising bubble and the interfacial free energy from the interface to counteract this energy, as shown in Eq. 3.

$$We = \left(\frac{8}{C_D}\right)\frac{\left(\frac{\rho v^2}{2} C_D \pi \frac{d^2}{4}\right)}{(\pi d \sigma_I)} = \frac{\rho_2 v^2 d}{\sigma_I} \tag{3}$$

where v is bubble rising velocity, m/s; C_D is the drag coefficient; ρ_2 is the density of heavier liquid, kg/m^3; d is bubble diameter, m; σ_I is interfacial tension, N/m.

As shown in Fig. 3, fine bubbles dwelling at the interface due to the lower bubble buoyancy force and inertia force than interfacial tension can penetrate interface with the drainage of bubble cap film. However, whether bubbles can overcome interfacial tension and cross interface directly at the first impact has a significant influence on heavier liquid entrainment regimes by comparison between Figs. 3 and 4. It should be noted that the volume of visible heavier liquid layer suspending at the bottom of larger bubbles in Fig. 4 is much larger than the indiscernible liquid film enveloping the bubble surface. Thus, previous studies on critical bubble penetration and entrainment sizes make sense in classifying the heavier liquid entrainment methods by

rising bubbles. Greene et al. proposed the theoretical critical bubble penetration and entrainment volumes by balancing a static bubble buoyancy force and interfacial tension and compared with experimental results in cold model experiments [1, 2]. Furthermore, dimensionless number *We* using bottom liquid density and interfacial tension bubbles was analysed in experiments. Different from previous studies based on the static model, *We* can be used to measure the bubble penetration ability to cross interface at the first impact at the interface in dynamic conditions by considering inertia force. In other words, a high *We* number means higher kinetic energy to overcome the constant interfacial energy and could penetrate the interface directly.

As shown in Fig. 7a–d, the critical bubble penetration and entrainment sizes based on Greene's theory are very close but larger than experimental results in different experimental conditions, which is probably because Greene's model was built in static conditions and neglected bubble inertia force. With increasing the interfacial tension, the critical bubble penetration and entrainment size increase, which is in agreement with experimental results. The heavier liquid density has significant effects on bubble entrainment size but a slight influence on bubble penetration size, which also can be confirmed by experimental results. Upper and heavier liquid viscosity have little effect on those two critical bubble sizes, which can be seen from the tiny change of experimental data. It should be noted that the Weber number using

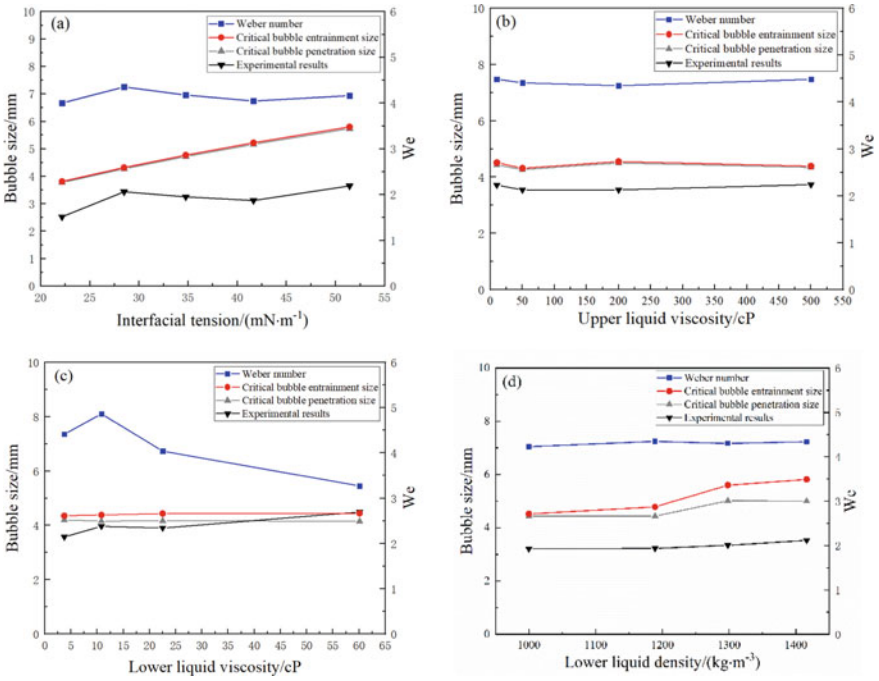

Fig. 7 Comparison of critical bubble size between Greene's theory experimental result and Weber number

bottom liquid density, interfacial tension, and critical bubble penetration size fluctuates around 4.25 between 4 and 4.5 under different experimental conditions, which is of great reference value to determine the heavier liquid entrainment regimes by small bubbles.

Conclusions

In this study, the attachment between micro bubbles and matte droplets in industrial slag samples was confirmed by SEM analysis. In cold model simulation experiments, small bubbles and larger bubbles penetration behaviours through immiscible liquids interface by the high-speed camera were investigated. It was found that fine bubbles stuck at the interface due to interfacial tension managed to cross interface with bubble cap film drainage, and thin indiscernible film enveloping bubbles was observed. Bubbles capable of penetrating interface directly tend to drag a liquid layer at the bottom surface stably, which could lead to heavier liquid entrainment in the upper phase. Greene's hypothesis about critical bubble penetration and entrainment sizes is basically in agreement with experimental results while a little higher. Weber number using bottom liquid density, interfacial tension, and critical bubble penetration size varied between 4 and 4.5, which could provide valuable guidance for industrial operations.

References

1. Greene GA, Chen JC, Conlin MT (1988) Onset of entrainment between immiscible liquid layers due to rising gas bubbles. Int J Heat Mass Transf 31(6):1309–1317
2. Greene GA, Chen JC, Conlin MT (1991) Bubble induced entrainment between stratified liquid layers. Int J Heat Mass Transf 34(1):149–157
3. Mori YH, Komotori K, Higeta K, Inada J (1977) Rising behavior of air bubbles in superposed liquid layers. Can J Chem Eng 55(1):9–12
4. Emery TS, Raghupathi PA, Kandlikar SG (2018) Flow regimes and transition criteria during passage of bubbles through a liquid-liquid interface. Langmuir 34(23):6766–6776
5. Kemiha M, Olmos E, Fei W, Poncin S, Li HZ (2007) Passage of a gas bubble through a liquid-liquid interface. Ind Eng Chem Res 46(19):6099–6104
6. Singh KK, Bart HJ (2015) Passage of a single bubble through a liquid–liquid Interface. Ind Eng Chem Res 54(38):9478–9493
7. Nguyen AV, Schulze HJ, Stechemesser H, Zobel G (1997) Contact time during impact of a spherical particle against a plane gas-liquid interface: theory. Int J Miner Process 50(1):97–111
8. Nguyen AV, Schulze HJ, Stechemesser H, Zobel G (1997) Contact time during impact of a spherical particle against a plane gas-liquid interface: experiment. Int J Miner Process 150(1):113–125
9. Dietrich N, Poncin S, Pheulpin S, Li HZ (2008) Passage of a bubble through a liquid-liquid interface. AIChE J 54(3):594–600
10. Morsi BI, Basha OM (2015) Mass transfer in multiphase systems. In: Solecki M (ed) Mass transfer—advancement in process modelling. IntechOpen, London, pp 189–217

11. Tanno M, Liu J, Gao X, Kim SJ, UEDA S, Kitamura SY (2017) Influence of the physical properties of liquids and diameter of bubble on the formation of liquid column at the interface of two liquid phases by the rising bubble. Metall Mater Trans B 48(6):2913-2921
12. Rapp BE (2017) Chapter 9 - Fluids. In: Rapp BE (ed) Microfluidics: microfluidics: modelling, mechanics and mathematics 2017. Elsevier, Oxford, pp 243–263
13. Talaia M (2007) Terminal velocity of a bubble rise in a liquid. World Acad Sci Eng Technol 1(4):220–224
14. Parkinson L, Sedev R, Fornasiero D, Ralston J (2008) The terminal rise velocity of 10–100 μm diameter bubbles in water. J Colloid Interface Sci 322(1):168–172
15. Celata GP, D'Annibale F, Marco PD, Memoli G, Tomiyama A (2007) Measurements of rising velocity of a small bubble in a stagnant fluid in one- and two-component systems. Exp Therm Fluid Sci 31(6):609–623

Calculation of Heat Loss of Furnace Body in Electric Arc Furnace Steelmaking

Zhihui Li, Lingzhi Yang, Yufeng Guo, Shuai Wang, and Hang Hu

Abstract The heat loss of furnace body in EAF steelmaking process is large and difficult to quantify, which affects the accurate control of smelting end temperature. In this paper, the EAF body is divided into four parts, namely the upper shell, the lower shell, the bottom of the furnace, and the furnace cover. The heat transfer in different regions is studied to explore the characteristics of radiation heat transfer and convection heat transfer between the EAF body and the surrounding environment. A theoretical calculation method of heat loss in EAF steelmaking process is obtained, which provides a theoretical basis for energy saving and emission reduction of EAF steelmaking.

Keywords EAF steelmaking · Heat loss · Furnace division · Heat transfer behavior

Introduction

Electric arc furnace steelmaking (EAF steelmaking) is a steelmaking method with electric energy as the heat source. It is a steelmaking method that converts electric energy into heat energy in arc light. In the process of EAF steelmaking, how heat is transferred has always been the focus of research by metallurgical workers in China and abroad.

Domestic and foreign scholars have carried out a lot of research work on heat transfer analysis in EAF steelmaking process and have made some progress. Chen et al. [1] derived the analytic formula of radiation heat transfer of single electrode arc to molten pool and lining by using radiation heat transfer principle and obtained the law of radiation heat transfer. Guo et al. [2] used a method of numerical model to numerically calculate the velocity field and temperature field of ions, revealing the flow and heat transfer law of arc plasma in DC EAF. Qiao [3] pointed out that during the flat phase of molten pool, only a small part of the heat released from

Z. Li · L. Yang (✉) · Y. Guo · S. Wang · H. Hu
School of Minerals Processing and Bioengineering, Central South University, Changsha 410083, Hunan, China
e-mail: yanglingzhi@163.com

Z. Peng et al. (eds.), *12th International Symposium on High-Temperature Metallurgical Processing*, The Minerals, Metals & Materials Series,
https://doi.org/10.1007/978-3-030-92388-4_21

the ion body surface to the surrounding was put into the molten steel by convection and radiation, and most of it was discharged in the form of furnace gas and lost due to cooling water. Camdali et al. [4] analyzed the heat transfer of AC EAF and determined the convection and radiation heat loss of the outer surface, top, and bottom of the EAF in detail.Zhao et al. [5] analyzed the heat transfer characteristics of DC arc, the heat transfer characteristics of flue gas, and the heat loss of furnace body from the perspective of energy balance, so as to obtain the heat transfer status in the actual operation of EAF. In addition, the analysis of heat transfer has also been widely developed by establishing models. Moghadam et al. [6] established a two-dimensional mathematical model to describe the heat transfer and fluid flow in AC arc zone of heat furnace and calculated the heat transfer from arc to melt surface. Wang et al. [7] established a three-dimensional heat transfer model of tube cooling wall of EAF analyzed the heat transfer, and obtained the heat flux intensity of the cooling wall and the temperature distribution of the key parts. Opitz et al. [8] introduced a radiation heat transfer model of EAF. The model not only considered the radiation exchange between the inner surface of the vessel but also considered the radiation heat transfer between the surface and the participating medium. At the same time, the calculation formula of radiation heat transfer affected by the medium was given. Wang et al. [9] established a three-dimensional mathematical model and studied the basic flow and heat transfer law of DC EAF melt. Contreras-Serna et al. [10] developed a model based on the heat transfer law. The model considered the surface energy balance between different layers of the EAF wall and the heat radiation from the arc and slag surface to the furnace wall and determined the temperature distribution of the tubular plate and calculated the heat transfer.

Through the study of the above heat transfer process, metallurgical researchers can get the internal heat transfer mechanism of the EAF, but a large part of the heat loss in the process of steelmaking is carried out the furnace body. There is little research on the radiation heat transfer and the convective heat transfer between EAF body and external environment. At present, this part of the heat loss cannot be quantified by specific measuring instruments and calculation methods, and it lacks enough attention. Therefore, based on the basic theory of heat transfer, this paper proposes a calculation method for determining the heat loss of the furnace body in the process of EAF steelmaking, to determine the order of magnitude of the radiation heat transfer loss and convection heat transfer loss caused by the large temperature difference between the furnace body and the surrounding building in the process of EAF steelmaking and to understand the size of the heat loss from an intuitive perspective.

Theoretical Analysis of Heat Transfer

This paper mainly analyzes the characteristics and ways of heat transfer in EAF steelmaking process and calculates the heat loss between the furnace body area and the surrounding environment in EAF steelmaking process.

Heat Transfer Behavior in Furnace Body

The heat loss of the furnace body area is analyzed, and the heat dissipation methods of the furnace body area are mainly:

(1) The furnace body area has a high temperature in the smelting process, which will radiate a large amount of heat to the external objects. The radiation heat transfer heat loss caused by temperature difference between the furnace body area with higher temperature and the surrounding building envelope with lower temperature is the radiation heat transfer between the cavity and the inner wall. Radiation heat loss of furnace body mainly includes radiation heat loss of furnace body and radiation heat loss of furnace door.

(2) In the process of EAF smelting, the temperature of the furnace body is high, and the air in the surrounding environment is heated to rise, and the convective heat transfer between the furnace body and the furnace is carried out. The convective heat transfer mode belongs to the natural convective heat transfer in large space.

(3) In order to prevent overheating damage caused by too high temperature in the furnace shell, furnace cover, and other areas, it is often necessary to provide cooling water by means of cooling water pipes circling the relevant areas. Convection heat transfer is carried out between the cooling water and the furnace body, and the heat transfer mode is inter-wall convective heat transfer.

Geometrical Composition and Heat Transfer Characteristics of Furnace Body Area

Based on the division of the furnace body, and according to the temperature characteristics, geometric parameters, and relative positions of different parts of the furnace body area, the furnace body is divided into the upper shell part, the lower shell part, the bottom part, and the furnace cover part. The geometric elements of the furnace body area are shown in Fig. 1.

The heat transfer characteristic of the bottom part of the furnace is the convective heat transfer between the air and the surrounding environment, which is the convective heat transfer of the air heated by the vertical wall and the convective heat transfer of the air heated by the hot surface downward.

The heat transfer characteristic of the lower shell is the convective heat transfer of the air heated on the vertical wall and the convective heat transfer of the air heated up the hot surface when convective heat transfer is carried out between the lower shell and the air in the surrounding environment.

The heat transfer characteristic of the upper furnace shell is that when convective heat transfer is carried out between the upper furnace shell and the air in the surrounding environment, the vertical wall heats the convective heat transfer of the air.

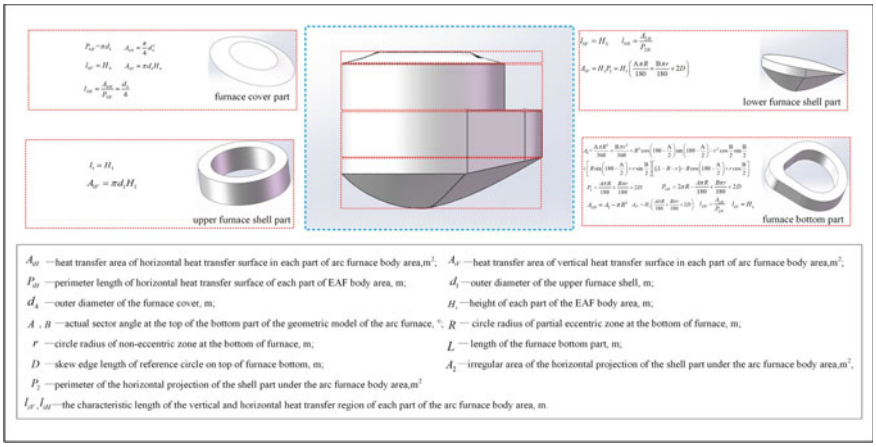

Fig. 1 Geometric composition diagram of furnace body area

The heat transfer characteristic of the furnace cover is the convective heat transfer between the furnace cover and the air in the surrounding environment, which is the convective heat transfer of the air heated on the vertical wall and the convective heat transfer of the air heated up the hot surface.

Modeling and Calculation

Heat Loss Caused by Cooling Water in the Furnace Body Area of the EAF

There are cooling water pipes outside the furnace body area, which are used to cool the various parts of the furnace body area. The heat carried away by the cooling water in each part of the furnace body area in unit time can be calculated by Eq. (1).

$$Q_{iW}=c_i\rho_i V_i(T_{i\text{out}}-T_{i\text{in}}) \tag{1}$$

where Q_{iW} is the heat carried by the cooling water of each part of the furnace body area, W; $T_{i\text{in}}$ and $T_{i\text{out}}$ are the inlet and outlet temperatures of cooling water in each part of the furnace body area, respectively, K; The qualitative temperature $\overline{T_{iW}}$ (K) determined by the average inlet and outlet temperature of cooling water is determined by Eq. (2).c_i is the specific heat capacity of cooling water determined by qualitative temperature $\overline{T_{iW}}$, J/(kg·K); ρ_i is cooling water density determined by qualitative temperature $\overline{T_{iW}}$, kg/m^3; V_i is the volume flow rate of cooling water unit time in each part of the furnace body area, m^3.

$$\overline{T_{iW}} = \frac{T_{i\text{out}} + T_{i\text{in}}}{2} \tag{2}$$

Heat Loss of Convective Heat Transfer in EAF Body

According to the experimental correlation of natural convection in large space:

$$Nu_m = C(Gr \cdot \Pr)_m^n \tag{3}$$

$$Gr = \frac{g\alpha_V \Delta T l^3}{\nu^2} \tag{4}$$

$$\Pr = \frac{\rho c \nu}{\lambda} \tag{5}$$

At the same time, for natural convection heat transfer process, Nu_m can also be calculated by the following formula:

$$Nu_m = \frac{hl}{\lambda} \tag{6}$$

Therefore, from Eqs. (3) and (6), calculation formula of average surface convective heat transfer coefficient of heat transfer wall in EAF can be obtained:

$$h = \frac{\lambda Nu_m}{l} = \frac{\lambda C(Gr \cdot \Pr)_m^n}{l} \tag{7}$$

In this equations, Nu_m is Nusselt number, and it represents the relative size of dimensionless temperature gradient on the furnace wall; Gr is Grashof number, and it characterizes the relative magnitude of natural convection, buoyancy and viscous force; Pr is Prandtl number, and it represents the relative size of momentum diffusion capacity and thermal diffusion capacity; g is acceleration of gravity, m/s^2, the recommended value is 9.81 m/s^2; α_V is the volumetric expansion coefficient of fluid (air) around the furnace body area, for gases conforming to the nature of ideal gas, $\alpha_V = \frac{1}{T}$ in Eq. (4), T is the air qualitative temperature determined by the average temperature of each part of the furnace body area and the surrounding mainstream air temperature by Eq. (8), K; T_A and T_M, respectively, represent the average temperature of each part of the furnace body area and the surrounding mainstream air temperature, K; l is the characteristic length of the heat transfer wall in the furnace body area where the fluid (air) flows through, m;h is the average surface convective heat transfer coefficient of the heat transfer wall in the furnace body area, W/(m^2 · K); α is the thermal diffusion coefficient of fluid (air), m^2/s; ν is the viscous coefficient of fluid (air) motion determined by the qualitative temperature, m^2/s; λ is the

thermal conductivity of fluid (air), W/ (m · K); c is the specific heat capacity of fluid (air) determined by qualitative temperature, J/(kg · K); ρ is the fluid (air) density determined by the qualitative temperature, kg/m^3.

Therefore, it can be concluded that the heat between the heat transfer wall of the furnace body area and the surrounding air due to convective heat transfer:

$$Q = hA\Delta T = \frac{\lambda C(Gr \cdot \mathrm{Pr})_m^n}{l} A\Delta T \tag{8}$$

For the coefficient C and index n, the actual fluid (air) flow pattern around the furnace area can be judged by using the Grash of number and the Prandtl number, so to determine the value of the coefficient and index. The judgment is based on the following Table 1:

According to the above method, calculate convective heat transfer loss of upper shell part by Eq. (9).

$$Q_1 = \frac{C_1 A_{1V} \lambda_{1C}(T_1 - T_{1A})}{l_1} \left[\frac{2g\rho_{1C} c_{1C}(T_1 - T_{1A}) l_1^3}{\nu_{1C} \lambda_{1C}(T_1 + T_{1A})} \right]^{n_1} \tag{9}$$

Similarly, the convective heat transfer loss of the lower shell can be calculated. Since the convective heat transfer loss of the lower shell is composed of two parts, it is:

$$\begin{aligned} Q_2 = Q_{2H} + Q_{2V} = & \frac{C_{2H} A_{2H} \lambda_{2C}(T_2 - T_{2A})}{l_{2H}} \left[\frac{2g\rho_{2C} c_{2C}(T_2 - T_{2A}) l_{2H}^3}{\nu_{2C} \lambda_{2C}(T_2 + T_{2A})} \right]^{n_{2H}} \\ & + \frac{C_{2V} A_{2V} \lambda_{2C}(T_2 - T_{2A})}{l_{2V}} \left[\frac{2g\rho_{2C} c_{2C}(T_2 - T_{2A}) l_{2V}^3}{\nu_{2C} \lambda_{2C}(T_2 + T_{2A})} \right]^{n_{2V}} \end{aligned} \tag{10}$$

The heat loss of convective heat transfer at the bottom and cover of the furnace is calculated by the same method.

Table 1 Value of the coefficient and index

Shape and position of heating surface in body area of EAF	Fluidization state	Coefficient C and index n		Sphere of application
		C	n	
Vertical walls	Laminar flow	0.59	1/4	$1.43 \times 10^4 \le \mathrm{Gr} \le 3 \times 10^9$
	Transition	0.0292	0.39	$3 \times 10^9 < \mathrm{Gr} < 2 \times 10^{10}$
	Turbulent flow	0.11	1/3	$\mathrm{Gr} \ge 2 \times 10^{10}$
Horizontal hot face up		0.54	1/4	$10^4 \le \mathrm{GrPr} \le 10^7$
		0.15	1/4	$10^7 \le \mathrm{GrPr} \le 10^{11}$
Horizontal hot face down		0.27	1/4	$10^5 \le \mathrm{GrPr} \le 10^{10}$

Through the above formula, the heat loss of EAF caused by convective heat transfer is calculated by Eq. (11):

$$Q_C = Q_1 + Q_2 + Q_3 + Q_4 = \sum_{i=2}^{4} \frac{C_{iH} A_{iH} \lambda_{iC} (T_i - T_{iA})}{l_{iH}} \left[\frac{2g\rho_{iC} c_{iC} (T_i - T_{iA}) l_{iH}^3}{\nu_{iC} \lambda_{iC} (T_i + T_{iA})} \right]^{n_{iH}} + \sum_{i=1}^{4} \frac{C_{iV} A_{iV} \lambda_{iC} (T_i - T_{iA})}{l_{iV}} \left[\frac{2g\rho_{iC} c_{iC} (T_i - T_{iA}) l_{iV}^3}{\nu_{iC} \lambda_{iC} (T_i + T_{iA})} \right]^{n_{iV}} \tag{11}$$

Heat Loss of Radiation Heat Transfer in EAF Body

The furnace body in the smelting process temperature is high, and it will radiate a lot of heat to the external object. Radiation heat loss of furnace body mainly includes radiation heat transfer loss of furnace body and radiation heat transfer loss of furnace door.

The EAF is located in a closed workshop and radiates heat with the wall of the workshop, which belongs to the radiation heat transfer between the cavity and the inner wall of the actual object. The net radiation heat exchange per unit time is calculated by Eq. (12):

$$Q_{RW} = \varepsilon_R A_R \sigma \left(T_W^4 - T_A^4 \right) \tag{12}$$

In this equations, Q_{RW} is the net radiation heat exchange per unit time between the surface of furnace body and the surrounding wall, W; ε_R is the emissivity of furnace body, also known as blackness; A_R is the surface area of furnace body, m^2; σ is a Stephen–Boltzmann constant, and it is 5.67×10^{-8} W/($m^2 \cdot K^4$). T_W and T_A, respectively, represent the average temperature of the furnace body area and the surrounding wall surface, K.

The inside of the door of the EAF is high-temperature molten steel, and the outside is low-temperature air. The radiation heat is also large. The molten steel in the EAF can be regarded as blackbody, and the calculation method of blackbody radiation in hemispherical space is adopted. The calculation is carried out according to the following method. The calculation diagram is shown in Fig. 2.

The directional radiation intensity of molten steel in the EAF is obtained by Eq. (13):

$$I_\theta = \frac{E_b}{\pi} = \frac{\sigma T^4}{\pi} \tag{13}$$

where E_b is the radiation energy per unit time per unit radiation area of molten steel, W/m^2; T is the surface temperature of molten steel, K.

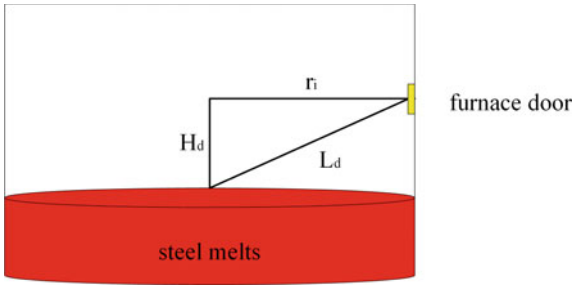

Fig. 2 Schematic diagram of radiation heat transfer between molten steel and furnace gate in EAF

The entrance of the furnace is located above the molten steel level and offsets a certain distance. The internal molten steel input radiation energy to the furnace door can be obtained by Eq. (14):

$$Q_{RD} = I_\theta A \cos\theta \frac{A_d \sin\theta}{H_d^2 + r_i^2} = I_\theta A \cos\theta \frac{A_d \sin\theta}{L_d^2} \tag{14}$$

In this equations, H_d is the height from the center of the furnace door to the center of the molten steel level, m; r_i is the radius of liquid steel, m; L_d is the distance from the center of the furnace door to the center of the liquid steel surface, m; θ is the angle between the height of the furnace door to the liquid steel level and the connection line between the center of the furnace door and the center of the liquid steel level,°; A_d is area of furnace door,m^2.

Results and Discussion

At 100 t EAF smelting site, the geometric size of the EAF was measured, and the continuous temperature measurement was carried out on the external parts of the furnace bottom, furnace wall, furnace cover, and the inlet and outlet of the cooling water in the steelmaking process of the EAF through a portable thermometer (in the middle of smelting, take representative temperature of each part). The measurement results are shown in Table 2.

Table 2 Measurement results form

Measurement area	H/m	d/m	R/m	r/m	L/m	D/m	A/°	B/°	T/°C
Furnace cover	0.50	7.0							371
Upper furnace shell	2.65	7.0							374
Lower furnace shell	2.11		3.5	1.0	10.0	5.0	240	120	376
Furnace bottom	1.50		3.5	1.0	10.0	5.0	240	120	377

Table 3 Heat loss of each part

Name of heat loss	Q_W	Q_1	Q_2	Q_3	Q_4	Q_C	Q_{RW}	Q_{RD}	Q_T
Calculation of heat loss(KW)	4975	138.6	141.15	148	48.5	476.25	1234	370	7055.25

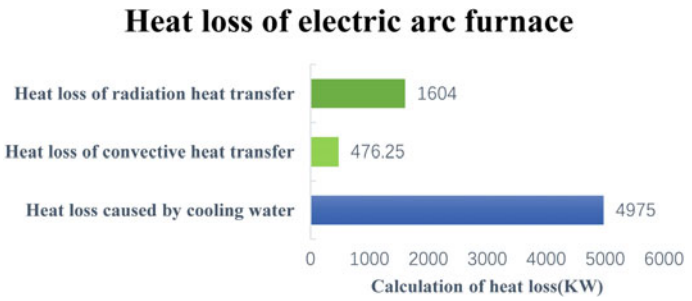

Fig. 3 Heat loss of electric arc furnace

The EAF is regarded as a system. In the system, the cooling water flow is 720 m^3/h, and the inlet temperature of cooling water is 32 °C, and the outlet temperature of cooling water is 38 °C. The heat loss caused by cooling water is obtained by Eq. (1).

The heat loss of each part is calculated according to the above method. The results are shown in Table 3 and Fig. 3.

The average smelting time is one-hour. Therefore, in the smelting process, the heat loss caused by cooling water, convective heat transfer, and radiation heat transfer is calculated by the following equation:

$$W_T = Q_T \times T \tag{15}$$

In this equation, W_T is total heat loss of EAF during smelting, kw·h; Q_T is the heat loss per unit time of EAF, W; Q_T is average smelting time, h.

After the above calculation, $W_T = 7055.25$ kw h; in the smelting process of EAF, the total energy input is 55880 kw h. The percentage of heat loss in the input energy is 12.6% and conforms to the general law of heat loss.

Conclusion

Under the general trend of the development of green EAF, this paper aims at the problem that the heat loss of the EAF is large and has not been well recycled. Based on the basic theory of heat transfer, the following conclusions were obtained: (1) The mathematical model of EAF division is established. (2) A calculation method of the heat loss of the EAF body is proposed. (3) In the smelting process of 100 t

EAF, the percentage of heat loss in the input energy obtained by the calculation formula conforms to the proportion range of heat loss in the actual process, which proves that the calculation formula of heat loss obtained above is roughly accurate. (4) Since the temperature in the calculation formula is a representative temperature, it cannot represent the temperature at each moment in the smelting process. Therefore, the calculated heat loss is not accurate enough. Therefore, in the future, the idea of integration will be used to correct the calculation method of heat loss and obtain more realistic results.

References

1. Chen W, Dong H, Peng H, Hong S, Liu F (1992) The Research of electric-thermal characteristic theory for single electrode direct current arc furnace. J Cent South Univ 23(5):540–545
2. Guo H, Zhang S, Kan W (2003) Numerical calculation of velocity field and temperature field of electrical arc in DC electric arc furnace. J Iron Steel Res 15(001):6–10
3. Qian X (2002) Heat transfer in DC electric arc furnace. HeBei Metall 000(002):13–16
4. Camdali Ü, Tunc M (2005) Heat transfer analysis for industrial AC electric arc furnace. J Iron Steel Res (Int) 04:9–16
5. Zhao P, Meng Y, Yu X (2010) Heat transfer in DC arc plasma melting furnace, doctoral science and technology forum on new energy technology innovation and industrial development
6. Moghadam M, Seyedein S, Aboutalebi M (2010) Fluid flow and heat transfer modeling of AC arc in ferrosilicon submerged arc furnace. J Iron Steel Res 17(009):14–18
7. Wang J, Xu X, Zhang Y (2015) Heat transfer analysis of tubular cooling staves for electric arc furnace. J Anhui Univ Technol (Nat Sci) 32(003):217–221
8. Opitz F, Treffinger P, Wollenstein J (2017) Modeling of radiative heat transfer in an electric arc furnace. Metall Mater Trans B 48:1–15
9. Wang K, Xie Y, Fu J, Ma T, Guo H (1996) Study on three dimensional electromagnetic field numerical simulation in 50T DC eelectric arc furnace (EAF). Min Metall 03:61–66
10. Contreras-Serna J, Rivera-Solorio G, Herrera-García M (2019) Study of heat transfer in a tubular-panel cooling system in the wall of an electric arc furnace. Appl Therm Eng (148):43–56

Comparison of Copper Smelting Slags Between Flash Smelting Furnace and Bottom-Blowing Furnace

Jinfa Liao, Chunfa Liao, and Baojun Zhao

Abstract Flash smelting furnace (FSF) and oxygen bottom-blowing furnace (BBF) are the major technologies used in copper industry to produce matte. Different requirements of copper concentrate, furnace arrangement, and operating parameters result in different slags in FSF and BBF. Quenched slag and matte samples were collected from both FSF and BBF under normal operating conditions. The slag temperatures were measured directly at the tapping hole by a K-type thermocouple. The quenched samples were analysed by XRF and EPMA to obtain slag bulk compositions, microstructures, and phase compositions. It was found that the FSF and BBF are significantly different in operating temperature, slag composition, and copper loss mechanisms. Thermodynamic and viscosity analyses of the FSF and BBF slags have been conducted to understand two technologies. The results will provide detailed information for selection and optimisation of FSF and BBF technologies.

Keywords Bottom-blowing furnace · Flash smelting · Slag · Copper smelting · FactSage

Introduction

Flash smelting and oxygen bottom-blowing smelting are the major processes to produce matte from copper concentrates. The common requirements for copper smelting are large production capacity, energy saving, and environment friendly [1]. As a new technology, oxygen bottom-blowing smelting has the advantages of strong applicability of raw materials, low investment cost, and simple operation. The capital

J. Liao · B. Zhao (✉)
International Research Institute for Resources, Energy, Environment and Materials, Jiangxi University of Science and Technology, Ganzhou, China
e-mail: bzhao@jxust.edu.cn

J. Liao · C. Liao · B. Zhao
College of Materials, Metallurgy and Chemistry, Jiangxi University of Science and Technology, Ganzhou, China

Z. Peng et al. (eds.), *12th International Symposium on High-Temperature Metallurgical Processing*, The Minerals, Metals & Materials Series,
https://doi.org/10.1007/978-3-030-92388-4_22

cost of molten bath smelting equipment is lower than that of flash smelting, and self-heating smelting can be fully realized without adding any fuel, and the production capacity is flexible [2–5].

Flash smelting is a main pyrometallurgical copper smelting technology with large capacity. The fine concentrate particles react in the high-temperature air stream, and the volatile impurities in the raw materials can easily enter the gas phase and be removed from the smelting furnace [6–8]. The flash smelting furnace with high airtightness has little air leakage and uses oxygen-enriched gas to ensure high-concentration of SO_2 in the flue gas and facilitate the production of sulfuric acid [9]. The cost of material preparation is high in the flash smelting as the concentrates must be dry and small size. The dust rate is relatively higher, and the capital cost is also high. Therefore, both BBF and FSF operate in parallel in current copper industry.

The products of BBF and FSF are matte, slag, and SO_2-containing gas. Similar compositions of the matte and gas can be produced by BBF and FSF. Optimal control of the slag chemistry is one of the important issues influencing the efficient and stable operation of the smelting process. The present study aims to understand the difference between BBF and FSF through analyses of the quenched slag samples collected from two furnaces.

Sampling Campaign and Analyses

The sampling campaigns were undertaken during normal productions of the FSF and BBF. The temperatures of the slags on tapping hole were measured directly using a K-type thermocouple. A long cold steel rod was used to dip into the slag flow from the tapping holes, and the slag was stuck on the rod and cooled rapidly. The matte sample was collected at the same time using the steel rod. The bulk compositions of the quenched slag and matte were analysed by XRF. The microstructures of the quenched slags and compositions of the phases present in the samples were determined using a JEOL JXA-8200 electron probe X-ray microanalyser (EPMA) with wavelength dispersive detectors (JEOL is a trademark of Japan Electron Optics Ltd., Tokyo). An accelerating voltage of 15 kV and a probe current of 15 nA were used. The Duncumb-Philibert ZAF correction procedure supplied with JXA-8200 was applied. The average accuracy of the EPMA measurements was estimated to be within 1 weight percent.

Results

Analyses of FSF Slag

Relatively stable temperatures were measured by a K-type thermocouple during the slag taping of the FSF. The measurements showed that the FSF was operated at temperatures 1300–1340 °C at the time of sampling. Typical microstructure of the quenched slag sample is shown in Fig. 1. It can be seen that a large matte droplet and many small matte droplets are present in the slag. It is anticipated that the large matte droplet was present at high temperature, and the small matte droplets were formed during cooling. The area close to the cold steel rod was well quenched and shows a glassy phase. No solid phase was found in the well-quenched area indicating that the slag tapping temperature was higher than its liquidus temperature. The dendrites present in the slow-cooled area were formed during cooling.

The compositions of the liquid and matte phases measured by EPMA and the bulk composition measured by XRF are listed in Table 1. The composition of the liquid phase was measured at the well quenched glassy area which represents the liquid composition at temperature. The Fe/SiO_2 weight ratio of the slag is 1.61 in bulk and 1.47 in liquid. The Fe/SiO_2 ratio of the liquid phase was lower than that of the bulk slag because the matte droplets containing Fe were not included in the liquid composition measured by EPMA. The Al_2O_3 concentration is relatively high (more than 6.0 wt%) in the slag. In addition, the ZnO concentration is around 2.6 wt% and As_2O_3 is 0.5 wt% in the slag. Totally, 3.0 wt% Cu_2O was measured in the slag, and

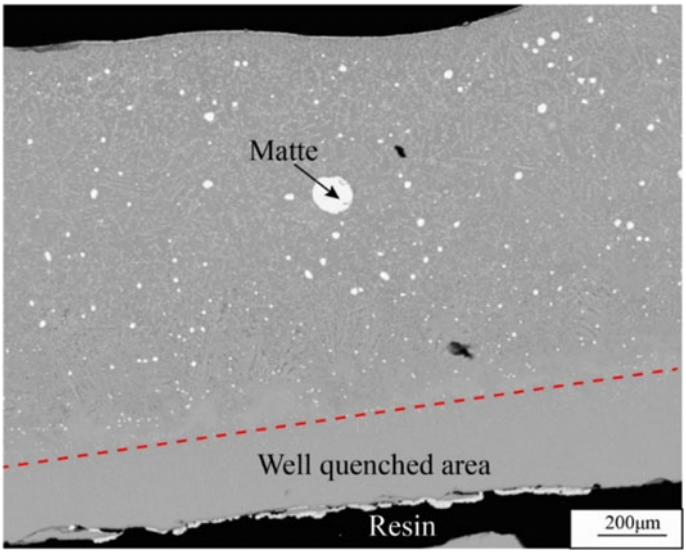

Fig. 1 Typical microstructure of the slag quenched from a FSF

Table 1 Compositions of the bulk, glass, and matte in the FSF slag (wt%)

Phase	"FeO"	SiO_2	Cu_2O	CaO	Al_2O_3	MgO	S	ZnO	As_2O_3	K_2O	MoO_3	PbO	Fe/SiO_2
Bulk	58.0	28.1	3.0	0.8	6.1	0.3	0.6	2.6	0.5				1.61
Glass	55.5	29.3	2.7	0.8	6.4	0.2	0.5	2.6	0.5	1.2	0.2	0	1.47

Phase	Fe	Cu	S	Zn	Pb	As	Mo
Matte in slag	1.9	78.0	19.4	0.1	0.1	0.2	0.2
Bulk matte	5.9	72.3	21.3	0.1	0.2	0.1	0.2

the liquid contains 2.7 wt%. This indicates that most of the copper in the FSF slag was present as chemically dissolved. The matte grade of the entrained matte in the slag is 78 wt% Cu and the bulk matte grade is 72.3 wt% Cu. It is estimated from the compositions shown in Table 1 that the proportion of the liquid is 99.6 wt%, and the proportion of the matte is 0.4 wt%.

Analyses of BBF Slag

The slag tapping temperatures in a BBF were directly measured by a K-type thermocouple during normal operation. It was found that the slag tapping temperatures ranged between 1150 and 1200 °C that are much lower than those of the FSF slags. Figure 2 shows a typical microstructure of the slag quenched from a BBF. It can be seen from Fig. 2 that liquid, spinel, and matte phases are present in the slag. The shape and size of the spinel phase indicate that the spinel was the primary phase presented at high temperature. The slag tapping temperature of the BBF was therefore lower than the liquidus temperature of the slag. The matte droplets in different sizes were also present in the slag.

The compositions of the liquid, spinel, and matte phases measured by EPMA, together with the bulk composition of the slag measured by XRF, are presented in Table 2. The Fe/SiO_2 weight ratio of the slag is 1.88 in bulk and 1.09 in the liquid. The spinel phase contains "FeO" but not SiO_2 resulting in a lower Fe/SiO_2 ratio in the liquid phase. It can be seen from Table 2 that, in addition to the "FeO" and SiO_2,

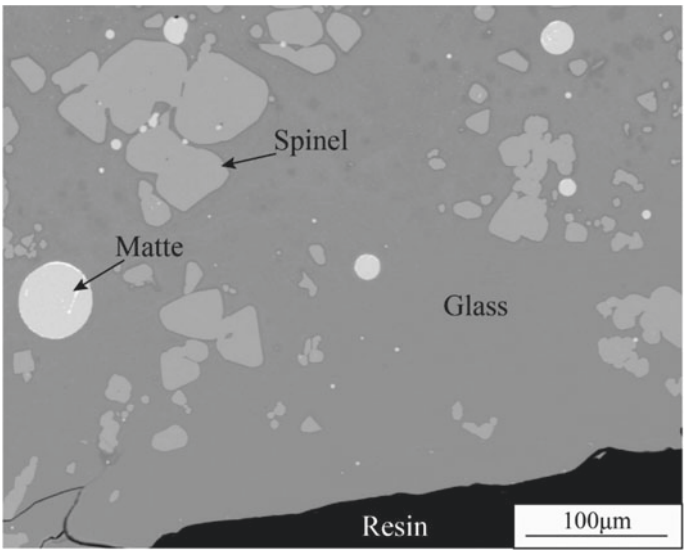

Fig. 2 Typical microstructure of the slag sample quenched from a BBF

Table 2 Compositions of glass, spinel, and matte by EPMA and bulk by XRF for the BBF slag (wt%)

Phases	FeO	Cu_2O	CaO	SiO_2	Al_2O_3	As_2O_3	MgO	S	PbO	ZnO	MoO_3	K_2O	Fe/SiO_2
Bulk	59.8	3.6	1.9	24.7	1.5	0.2	0.7	1.3	0.9	4.9	0.2	0.3	1.88
Glass	50.2	0.6	2.6	35.8	1.6	0.3	0.8	0.6	1.2	5.6	0.1	0.5	1.09
Spinel	94.5	0.0	0.0	0.6	1.4	0.0	0.2	0.0	0.1	2.8	0.2	0.0	

Phase	Fe	Cu	S	Zn	Pb	As	Mo
Matte in slag	5.5	63.6	20.4	0.2	0.1	0.1	0.3
Bulk matte	5.0	62.5	19.4	0.8	2.2	0.1	0

ZnO, Al_2O_3, CaO, MgO, and PbO are also present in the slag. Totally, 3.6 wt% Cu_2O is present in the slag, and the dissolved Cu_2O in the liquid phase is only 0.6 wt%. The matte grade inside the slag is 63.6 wt%, and the bulk matte grade is 62.5 wt%. It is estimated from the compositions showing in Table 2 that the proportions of the liquid, spinel, and matte are 68.5, 28.1, and 4.4 wt%, respectively.

Comparison Between FSF and BBF Slags

It can be seen from the above sections that the slag temperature of the FSF is over 100 °C higher than that of the BBF. The Fe/SiO_2 ratio in bulk FSF slag is lower than that in the BBF slag. It is vital to compare the slag properties of the FSF and BBF systematically. CALculation of PHAse Diagram (CALPHAD) approach has been widely used to predict physiochemical properties of the metallurgical slags [10]. One of the commonly used software, FactSage, has been applied successfully in various areas of high-temperature processes [11]. The liquidus temperatures predicted by FactSage 8.1 as a function of Fe/SiO_2 ratio together with the experimental measurements are shown in Fig. 3. The conditions used in the FactSage predictions are given in Table 3. The oxygen partial pressures for the BBF slag and FSF slag are 10^{-8} atm and 10^{-6} atm, respectively taken from the previous works [3, 12]. It can be seen from Fig. 3 that SiO_2 and spinel are the primary phases in the composition range covering the copper smelting slags. The liquidus temperatures sharply decrease in the SiO_2 primary phase field and slowly increase in the spinel primary phase field with increasing Fe/SiO_2 ratio. According to Fig. 3, both FSF and BBF slag compositions are in the spinel primary phase field. The FSF was operated at the temperature above the slag liquidus so that the slag was completely liquid. On the other hand, the BBF was operated at a temperature lower than the slag liquidus resulting in spinel solid present in the slag. The liquid composition of the BBF slag is located on the isotherm indicating that the FactSage predictions are reasonably accurate.

In copper production, the Cu-loss in the slag is one of the major techno-economic indexes. Reducing the content of Cu in the slag can greatly improve the economic benefits since a large amount of slag is produced in copper smelting process. It is

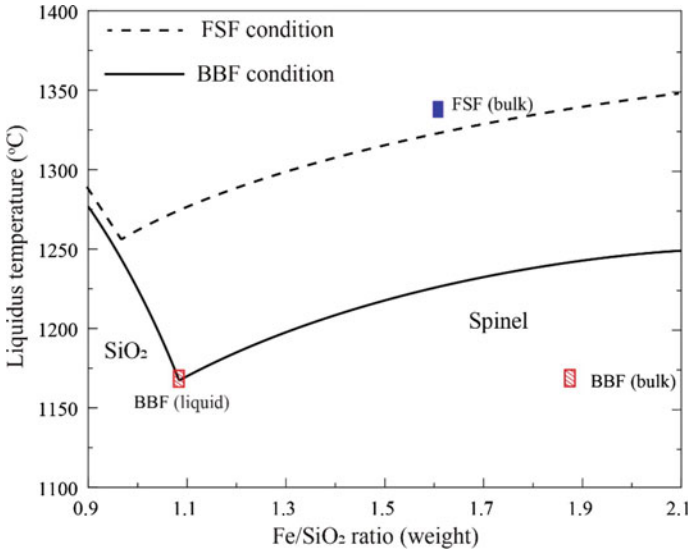

Fig. 3 FactSage [11] predicted liquidus temperatures as a function of Fe/SiO_2 in liquid, using the compositions of BBF slag at $Po_2 = 10^{-8}$ atm and FSF slag at $Po_2 = 10^{-6}$ atm

Table 3 Calculation conditions used in the FactSage predictions

Calculation	Slags	Selected components								Po_2 (atm)
		FeO	SiO_2	CaO	Al_2O_3	MgO	ZnO	Cu_2O	S	
Liquidus	FSF	√	√	√	√	√	√	√	√	10^{*-6}
	BBF	√	√	√	√	√	√	√	√	10^{*-8}
Viscosity	FSF	√	√	√	√	√	√	×	×	–
	BBF	√	√	√	√	√	√	×	×	–
Cu in slag	FSF	√	√	√	√	√	√	√	√	10^{*-6}
	BBF	√	√	√	√	√	√	√	√	10^{*-8}

well known that there are two main copper loss mechanisms in the smelting slag: (1) chemical loss, which is related to the dissolution of copper in the liquid phase, and (2) mechanical or physical loss, which is the entrained matte droplets not completely settled from the slag. The physical loss of the copper in the slag is mainly dependent of slag viscosity. Apparent viscosity of the slag is determined by the liquid viscosity and proportion of solid phase insider the slag. One of the equations to estimate the apparent viscosity of slag is Einstein-Roscoe equation [13]:

$$\eta = \eta_0(1 - f)^{-2.5} \tag{1}$$

where η is apparent viscosity, η_o is liquid viscosity, and f is the solid fraction. When the composition and oxygen partial pressure of the slag are fixed, the solid proportion and apparent viscosity are mainly determined by the operating temperature. As can be seen from Figs. 1 and 2 that the solid phase is only present in the BBF slag not FSF slag. As a result, the proportion of the entrained matte droplets in the BBF slag is much higher than that in the FSF slag. Figures 4 and 5 show the apparent viscosities and solid fractions for FSF and BBF slags predicted by FactSage 8.1. The slag compositions and calculation conditions are from Tables 1, 2 and 3, respectively. It can be seen from Fig. 4 that for the FSF slag, up to 25 wt% solid is present at 1260 °C. The slag viscosities increase slowly if the proportion of the solid is low. However, the apparent viscosities increase dramatically with decreasing temperature when the solid fraction is high. At the current FSF operating temperatures 1300–1340 °C, the solid fraction in the slag is below 5 wt%, and the apparent viscosities are between 0.08 and 0.16 Pa.s.

It can be seen from Fig. 5 that for the BBF slag, the solid phase starts to form at 1230 °C and up to 35 wt% solid is present at 1160 °C. In the current BBF operations, the viscosities of the slag are in the range of 0.2–1.4 Pa.s which is much higher than that of the FSF slags. In conclusion, the high viscosity of the BBF slag resulted in a larger proportion of the physically entrained matter droplets in the slag.

It can be seen from Tables 1 and 2 that liquid in the FSF slag and BBF slag contains different amounts of copper. This can be explained by Fig. 6. Effect of Fe/SiO_2 ratio on the dissolved copper in slag is predicted by FactSage 8.1 and shown in Fig. 6. The calculations are conducted by fixing the matte grade 65 wt% Cu and 1200 °C for the BBF slag, and matte grade 70 wt% Cu and 1350 °C for FSF slag, respectively. It can be seen from the figure that, at the given conditions, the solubility

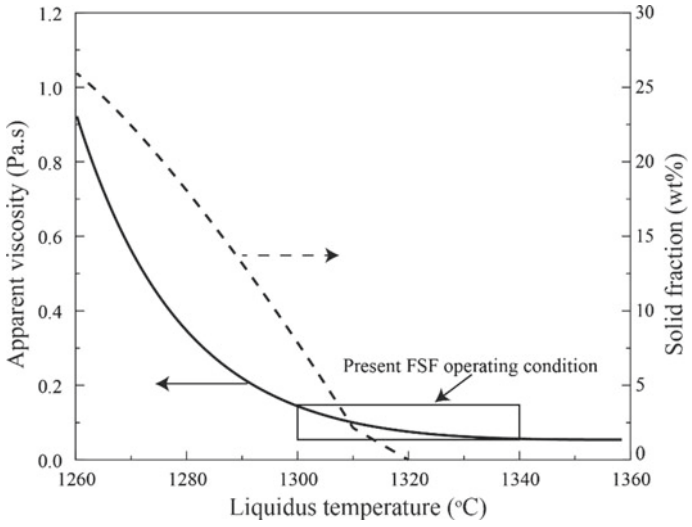

Fig. 4 Apparent viscosity and solid fraction of FSF slag calculated by FactSage 8.1 [11]

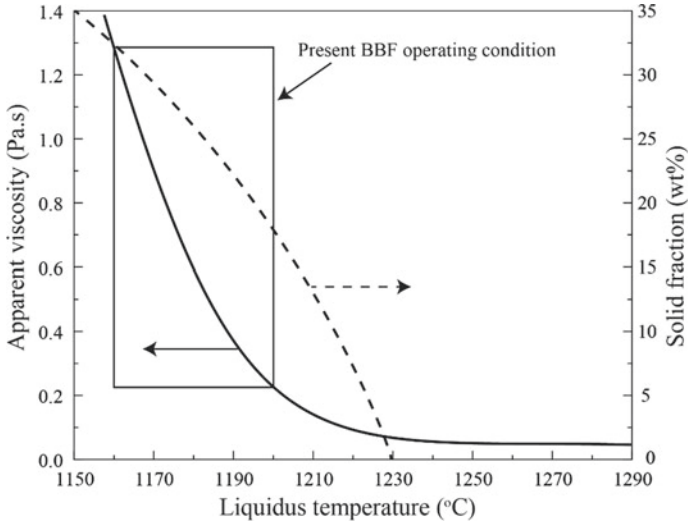

Fig. 5 Apparent viscosity and solid fraction of BBF slag calculated by FactSage 8.1 [11]

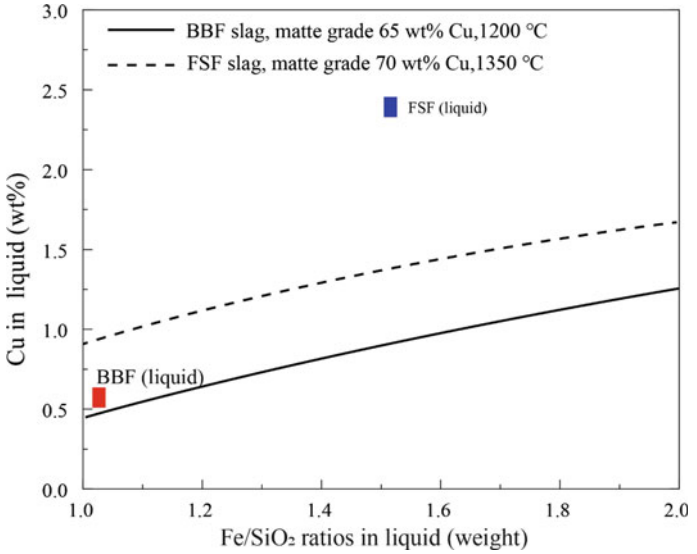

Fig. 6 Solubilities of copper in the liquid phase at fixed matte grade and temperature calculated by FactSage 8.1 [11]; the symbols are the measured solubilities of copper by EPMA

of copper in the slag increases with increasing Fe/SiO_2 ratio. The copper solubility in the FSF slags is higher than that in the BBF slags due to higher matte grade and temperature. It can be seen that the experimentally determined copper solubility in the BBF slag is close to that predicted by FactSage. However, the experimentally determined copper solubility in the FSF slag is much higher than that predicted by FactSage. This indicates that the database of FactSage needs to be improved according to the accurate experimental results.

Conclusions

The quenched slag samples from BBF and FSF were analysed by EPMA and XRF. The slag tapping temperatures were found to be 1150–1200 °C for BBF and 1300–1340 °C for FSF, respectively. The BBF slag tapping temperature was lower than its liquidus and the FSF slag tapping temperature was higher than its liquidus. Copper in the BBF slag is mainly entrained matte droplets due to the high apparent viscosity of the slag caused by lower temperature and solid phase present. Copper in the FSF slag is mainly dissolved copper in the liquid slag due to a higher temperature and Fe/SiO_2 ratio.

References

1. Kapusta JPT (2004) JOM world nonferrous smelters survey, part I: copper. JOM 56(7):21–27
2. Zhao B, Cui Z, Wang Z (2013) A new copper smelting technology-bottom blown oxygen furnace developed at Dongying Fangyuan Nonferrous Metals. In: Jiang T, Hwang JY, Mackey P, Yucel O, Zhou GF (eds) 4th International symposium on high-temperature metallurgical processing. The Minerals, Metals & Materials Society, San Antonio; Springer, New York, pp 3–10
3. Chen M, Cui Z, Zhao B (2015) Slag chemistry of bottom blown copper smelting furnace at Dongying Fangyuan. In: Jiang T, Hwang JY, Gerardo RF, Alvear F, Onuralp Y, Mao XP, Hong Y, Ma NY, Mackey P, Battle T (ed) 6th international symposium on high-temperature metallurgical processing. The Minerals, Metals & Materials Society, Orlando; Springer, New York, pp 257–264
4. Guo XY, Wang QM, Tian QH, Zhao B (2016) Analysis and optimization of oxygen bottom blowing copper smelting process. Chin J Nonferrous Met 26(3):689–698
5. Wang SJ, Davenport W, Yao SP, Walters G, Gonzales T, Siegmund A, George D (2019) Copper smelting: 2019 world copper smelter data. Paper presented at the 10th international copper conference, copper 2019. Vancouver, Canada, 18–21 Aug 2019
6. Liu JJ (2011) Flash furnace smelting process of copper. Copper Eng 03:25–28
7. Jåfs M, Kojo I, Lindgren M, Jyrkönen S, Lahtinen M, Latostenmaa P, Peuraniemi E (2019) The past 70 years of flash smelting. Paper presented at the 10th international copper conference, copper 2019. Vancouver, Canada, 18–21 Aug 2019
8. Dong GG, Ge Z, Zeng QH (2015) The development and self-innovation of flash copper smelting technology. Copper Eng 0:31–35

9. Zhou J, Chen Z, Zhou JM (2019) Mechanism of slag and matte formation in copper flash smelting. Paper presented at the 10th international copper conference, copper 2019. Vancouver, Canada, 18–21 Aug 2019
10. Hack K (2011) Computational thermodynamics: a mature scientific tool for industry and academia. Pure Appl Chem 83(5):1031–1044
11. Bale CW, Bélisle E, Chartrand P, Degterov SA, Eriksson G, Hack K, Jung IH, Kang YB, Melançon J (2016) Reprint of: FactSage thermochemical software and databases, 2010–2016. Calphad 55:1–19
12. Chen M, Contreras L, Zhao B (2016) Comparison of slag chemistry between teniente converter and flash smelting furnace. Paper presented at the 9th International copper conference, copper 2016, Kobe, Japan, 13–16 Nov 2016
13. Roscoe R (1952) The viscosity of suspensions of rigid spheres. J Appl Phys 3(8):267–269

Part IV
High-Temperature Processing

Effect of Ce Content on Non-metallic Inclusions in Si–Mn-Killed Stainless Steels

Lingxiao Cui, Lifeng Zhang, Ying Ren, and Ji Zhang

Abstract The effect of cerium content on inclusions in Si–Mn-killed stainless steels was studied at 1873 K using laboratory experiments. It was found that the addition of Ce had little effect on the removal of oxygen and sulfur. When the total cerium content increased from 0 to 430 ppm, the average diameter, the area fraction, and the number density of inclusions in the steel all increased. With the increase of the total cerium content in the steel, inclusions were modified into Ce-containing ones. The inclusions transformation sequence was: Al–Si–Mn–Ca–O → angular Ce–O–S → irregular Ce–O–S. The experiment result was consistent with the thermodynamic analysis.

Keywords Cerium · Inclusions · Modification mechanism · Thermodynamic analysis

Introduction

The demand for higher performance steels has been increasing year by year, such as toughness, fatigue property, strength, and so on. Thus, more stringent requirements are proposed for steel materials. Non-metallic inclusions in steels have a detrimental effect on the property of steels [1, 2]. Therefore, the control of the dispersion, size distribution, composition, and morphology of inclusions play an important role in controlling the steel quality [3–5]. The application of rare earth elements in steels

L. Cui · Y. Ren · J. Zhang
School of Metallurgical and Ecological Engineering, University of Science and Technology Beijing, Beijing 100083, China

L. Zhang (✉)
State Key Laboratory of Metastable Materials Science and Technology, Yanshan University, Qinhuangdao 066004, Hebei, China
e-mail: zhanglifeng@ysu.edu.cn

L. Cui
State Key Laboratory of Baiyunebo Rare Earth Resource Researches and Comprehensive Utilization, Baotou Research Institute of Rare Earths, Baotou 014030, Inner Mongolia, China

Z. Peng et al. (eds.), *12th International Symposium on High-Temperature Metallurgical Processing*, The Minerals, Metals & Materials Series,
https://doi.org/10.1007/978-3-030-92388-4_23

has received extensive attention due to their strong affinity to oxygen and sulfur. Cai et al. [6] studied the effect of cerium on inclusions in a 205 stainless steel and proposed that the initial Al_2O_3 was modified to $CeAlO_3$ then to $CeAlO_3$–Ce_2O_2S with the increase of cerium content in the steel from 0 to 230 ppm. Kim et al. [7] found that the MnO–SiO_2–Cr_2O_3 inclusions in a duplex stainless steel were modified to SiO_2–Ce_2O_3–Cr_2O_3 with the 32 ppm cerium addition. Shi et al. [8] studied the transformation of inclusions in a stainless steel with different contents of yttrium. It was proposed the transformation sequence of inclusions was Al_2O_3–SiO_2–MnO–CaO → Y_2O_3–Al_2O_3(−SiO_2) → Y_2O_3 → YN. Huang et al. [9] investigated the modification mechanism of inclusions by cerium and proposed the evolution path of inclusions was MgO·Al_2O_3 → $CeAlO_3$ → Ce–O–S with the cerium content in the steel increasing from 0 to 300 ppm.

In the current paper, laboratory experiments were performed to study the effect of the cerium content on inclusions in Si–Mn-killed stainless steels, and thermodynamic analysis was conducted to analyze the transformation of inclusions in the steel.

Laboratory Experiments and Analysis

Approximately, 750 g steel sample was cut from a commercial slab of a Si–Mn-killed stainless steel and was melted in a MgO crucible with a 52 mm inner diameter and 120 mm depth using an electrical resistance furnace with $MoSi_2$ heating bars under argon atmosphere with a flow rate of 2 L/min. The chemical composition of the steel is listed in Table 1. The experimental procedure is shown in Fig. 1. The steel sample was heated to 1873 K at a rate of 10 K/min. After the steel was melted for 5 min, a certain amount of CeFe alloy wrapped in a pure iron bag was added into the molten steel. Samples were taken using a quartz sampler 30 min after the addition of cerium and then quenched in cold water immediately.

After each experiment, the content of the dissolved aluminum ([Al]) and the total cerium (T.Ce) which consist of the cerium dissolved in the steel and the cerium in precipitated particles in the steel was analyzed using inductively coupled plasma mass spectrometry (ICP-MS). The content of the total oxygen (T.O) in the steel

Table 1 Chemical composition of the steel (wt%)

C	Si	Mn	P	Cr	Ni	[Al]	N
0.069	0.37	0.88	0.026	18.2	8.1	0.0017	0.034

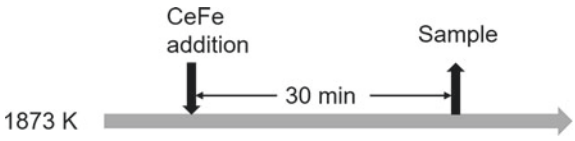

Fig. 1 Schematic of the experimental procedure

Table 2 Chemical composition of steel samples (ppm)

Heat No.	T.Ce	T.O	T.S
1	0	45.8	16.2
2	150	44.5	15.3
3	430	46.9	15.7

was analyzed using a LECO ONH836 analyzer. The content of the total sulfur (T.S) in the steel was analyzed by the infrared absorption method after combustion in an induction furnace using a sulfur analyzer. The steel sample was mounted and polished, and inclusions in steel samples were analyzed using an automatic scanning electron microscope equipped with EDS (SEM–EDS). The minimum detected size of inclusions was 1 μm, and the detected area was approximately 13.5 mm^2.

Chemical Composition of Steel Samples

The content of T.Ce, T.O, and T.S in the steel sample is listed in Table 2. The content of T.O fluctuated around 45 ppm and the content of T.S fluctuated around 15.5 ppm when the content of T.Ce in the steel increased from 0 to 430 ppm. It was indicated that the addition of Ce had little effect on the removal of oxygen and sulfur, because rare earth-containing inclusions had a high density close to the molten steel and were hardly to float from the steel to be removed [10, 11].

Inclusions in Steel Samples

The elemental mapping of typical inclusions in the steel sample is shown in Fig. 2. In the steel without cerium addition, inclusions were mainly small Al–Si–Mn(−Ca)−O and a few larger Al–Si–Ca–O, as shown in Fig. 2a and b. In the steel with 150 ppm cerium, inclusions were mainly angular Ce–O–S. In the steel with 430 ppm cerium, inclusions were mainly irregular Ce–O–S.

The variation of the average composition of inclusions with the T.Ce content in the steel is shown in Fig. 3. With the increase of the T.Ce content in the steel, the content of Al_2O_3, SiO_2, MnO, and CaO in inclusions decreased and approximately disappeared when the content of T.Ce reached 150 ppm. The content of Ce_2O_3 in inclusions first increased to 81% when the content of T.Ce increased from 0 to 150 ppm and then decreased to 71% when the content of T.Ce in the steel increased to 430 ppm. When the content of cerium in the steel was 150 ppm, CeS was generated, and the content of CeS in inclusions increased with the increase of cerium in the steel.

The variation of the area fraction, the number density, and the average diameter of inclusions with the T.Ce content in the steel is shown in Fig. 4. With the increase of the T.Ce content in the steel, the area fraction and number density of inclusions

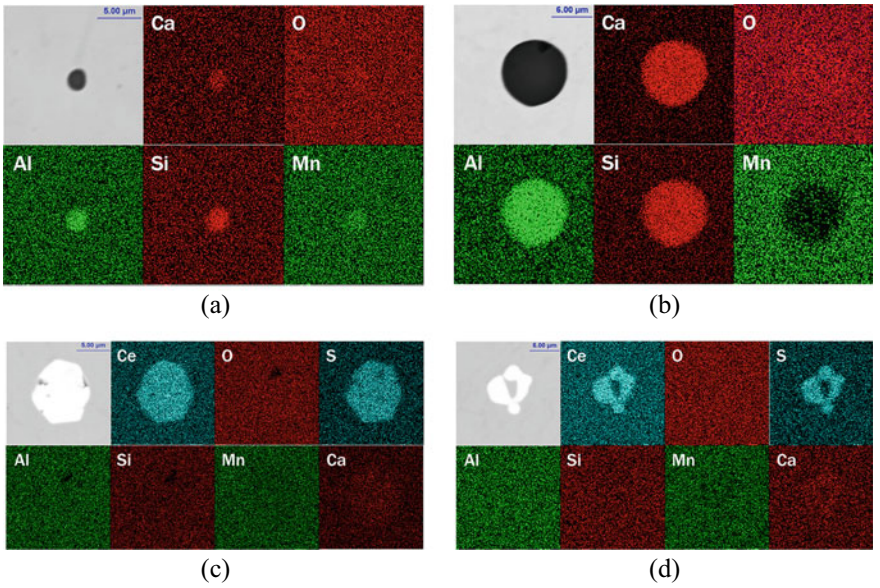

Fig. 2 Elemental mapping of typical inclusions in the steel **a**, **b** without Ce, **c** with 150 ppm Ce, and **d** with 430 ppm Ce

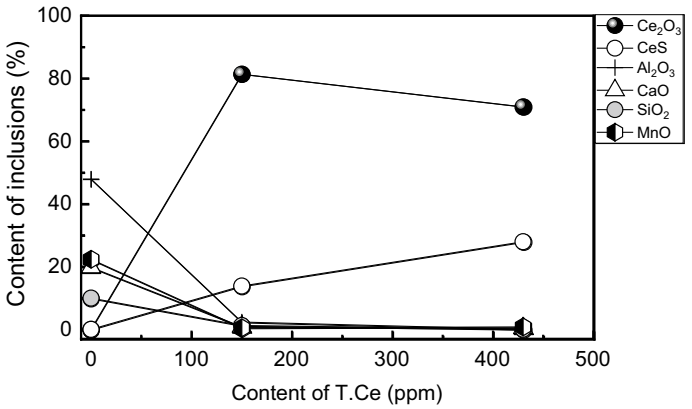

Fig. 3 Variation of the average composition of inclusions with the T.Ce content in the steel

showed an increasing tendency due to the generation of Ce-containing inclusions. The average diameter of inclusions in the steel also showed an increasing tendency with the increase of the T.Ce content in the steel.

Figure 5 shows the schematic of the transformation process of inclusions with the T.Ce content in the steel. In the steel without Ce, inclusions were mainly spherical Al–Si–Mn–Ca–O. When the T.Ce content increased to 150 ppm, inclusions were

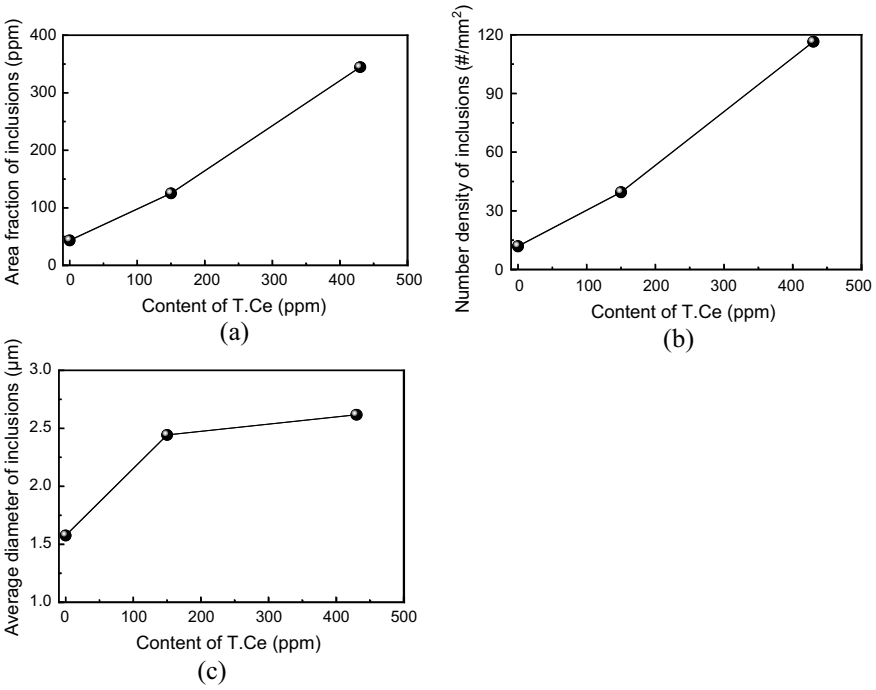

Fig. 4 Variation of **a** the area fraction, **b** the number density, and **c** the average diameter of inclusions with T.Ce content in the steel

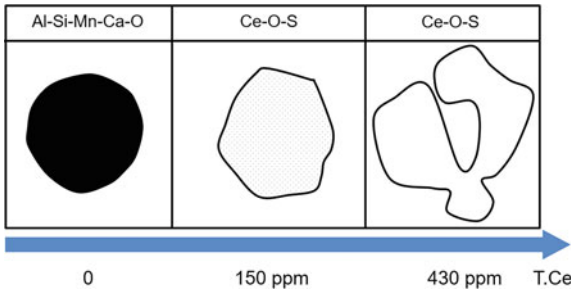

Fig. 5 Schematic of the transformation process of inclusions with the T.Ce content in the steel

completely modified into angular Ce–O–S with larger size. With the T.Ce content in the steel continuously increased to 430 ppm, inclusions were also large-size Ce–O–S ones with irregular shape, and the content of CeS in inclusions was higher.

Table 3 Standard Gibbs free energy of formation and transformation reactions [12–14]

No.	Reaction	Standard Gibbs free energy (J/mol)
1	$[Al] + \frac{3}{2}[O] = \frac{3}{2}(Al_2O_3)$	$-602545 + 193.9\,T$
2	$[Si] + 2[O] = (SiO_2)$	$-580550 + 221\,T$
3	$[Mn] + [O] = (MnO)$	$-284420 + 122.8\,T$
4	$[Ca] + [O] = (CaO)$	$-284420 + 122.8\,T$
5	$[Ce] + [Al] + 3[O] = (CeAlO_3)$	$-1366460 + 364\,T$
6	$[Ce] + \frac{1}{2}[Si] + \frac{5}{2}[O] = \frac{1}{2}(Ce_2SiO_5)$	$-1038915 + 316.3\,T$
7	$[Ce] + \frac{3}{2}[O] = \frac{3}{2}(Ce_2O_3)$	$-1366460 + 364\,T$
8	$[Ce] + [S] = (CeS)$	$-422783 + 120.6\,T$
9	$[Ce] + \frac{3}{2}[S] = \frac{3}{2}(Ce_2S_3)$	$-537290 + 160\,T$
10	$[Ce] + \frac{4}{3}[S] = \frac{1}{3}(Ce_3S_4)$	$-498480 + 146\,T$
11	$[Ce] + (Al_2O_3) = (CeAlO_3) + [Al]$	$-161370 - 23.7\,T$
12	$[Ce] + (SiO_2) + \frac{1}{2}[O] = \frac{1}{2}(Ce_2SiO_5) + \frac{1}{2}[Si]$	$-458365 + 95.3\,T$
13	$[Ce] + (CeAlO_3) = (Ce_2O_3) + [Al]$	$-64630 - 3.9\,T$
14	$[Ce] + \frac{1}{2}(Ce_2SiO_5) + \frac{1}{2}[O] = (Ce_2O_3) + \frac{1}{2}[Si]$	$-392175 + 194.8\,T$

Thermodynamic Analysis

In the steel without cerium addition, Al–Si–Mn–Ca–O was the main inclusion. Since cerium has a strong affinity to O and S, initial Al–Si–Mn–Ca–O inclusions were modified into rare earth-containing inclusions with Ce addition. The possible reaction in the current work could be divided into two types: inclusions formation and transformation reactions. Gibbs free energies of possible formation and transformation reactions can be expressed as Eqs. (1)–(10) and Eqs. (11)–(14), respectively, and were listed in Table 3 [12–14].

Henrian activity coefficients and Henrian activities (1 wt% standard state) of the element in the liquid steel can be calculated by interaction coefficients with Wagner's model. The activity coefficient and activity of each element in the liquid steel were calculated by Eqs. (15) and (16):

$$a_i = f_i[\%i] \tag{15}$$

$$\lg f_i = \sum_{j=1}^{n} e_i^j[\%j] \tag{16}$$

where a_i is the activity of element i, f_i is the activity coefficient of element i, $e_i{}^j$ is the interaction coefficient between element j, and element i in the molten steel. The interaction coefficient of the element is listed in Table 4 [15–17].

Table 4 Interaction coefficients e_i^j of elements in the molten steel at 1873 K [15–17]

e_i^j	C	Si	Mn	P	S	Cr	Ni	Al	Ce	O
Ce	−0.77	–	0.13	1.746	−39.8	–	–	−2.25	−0.003	−5.03
O	−0.45	−0.131	−0.021	−0.07	−0.133	−0.04	0.006	−3.9	−0.57	−0.2
S	0.11	0.063	−0.026	0.029	−0.028	−0.011	0	0.035	−0.231	−0.27
Al	0.091	0.0056	0.012	0.05	0.03	0.025	0.008	0.045	−0.043	−6.6
Si	0.18	0.11	0.002	0.11	0.056	−0.0003	0.005	0.058	−7.7	−0.23

The variation of the change of Gibbs free energy of Eqs. (7)–(10) and Eqs. (11)–(14) with the dissolved Ce content in the steel is shown in Fig. 6. In the steel without Ce addition, reactions in Eqs. (1)–(4) occurred, and the main inclusion in the steel was Al–Si–Mn–Ca–O. The change of Gibbs free energy of Eq. (8) was lower than that of Eqs. (9) and (10), indicating that CeS was more stable in the current study when the content of dissolved cerium in the steel was high enough. The Ce_2O_3 inclusion would precipitate even there was a small amount of dissolved Ce in the molten steel. For transformation reactions, the change of Gibbs free energy of Eq. (11) was lower than that of Eq. (12), and the change of Gibbs free energy of Eq. (13) was lower than that of Eq. (14), indicating that Al_2O_3 was modified to $CeAlO_3$ then to Ce_2O_3 and SiO_2 was modified to Ce_2SiO_5 then to Ce_2O_3 with the increase of the dissolved cerium content in the molten steel. The change of Gibbs free energy of Eqs. (11)–(13) was smaller than zero, indicating that the corresponding reaction occurred in the molten steel. However, the change of Gibbs free energy of Eq. (14) was bigger than zero which was not consistent with the experiment result due to the error caused by the absence of relevant interaction coefficients.

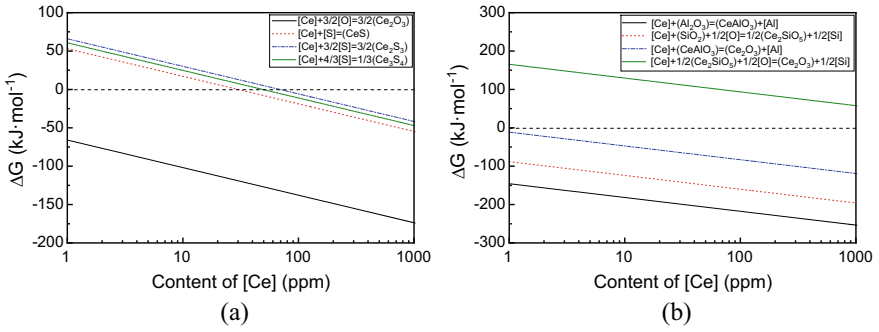

Fig. 6 Variation of change of Gibbs free energy of **a** formation reactions and **b** transformation reactions with the dissolved Ce content in the steel

Conclusions

In the current study, laboratory experiments and thermodynamic calculations were performed to investigate the effect of the cerium content on non-metallic inclusions in Si–Mn-killed stainless steels. The following conclusions were obtained: With the increase of T.Ce content in the steel, inclusions were modified into Ce-containing ones. The transformation sequence was: Al–Si–Mn–Ca–O → angular Ce–O–S → irregular Ce–O–S. With the increase of the T.Ce content in the steel, the average diameter, the area fraction, and the number density of inclusions in the steel, and the addition of Ce had little effect on the removal of oxygen and sulfur. Thermodynamic calculations were performed to analyze the transformation of inclusions in the steel with the cerium addition and the calculated results corresponded with experimental results.

Acknowledgements The authors are grateful for support from the National Natural Science Foundation of China (Grant No. U1860206), the S&T Program of Hebei (Grant No. 20311004D) Baotou Research Institute of Rare Earths, State Key Laboratory of Baiyunobo Rare Earth Resource Researches and Comprehensive Utilization, Baotou Inner Mongolia 014030, China, the High Steel Center (HSC) at Yanshan University, and Beijing International Center of Advanced and Intelligent Manufacturing of High Quality Steel Materials (ICSM) and the High Quality Steel Consortium (HQSC) at University of Science and Technology Beijing, China.

References

1. Zhang L, Thomas BG (2003) State of the art in evaluation and control of steel cleanliness. ISIJ Int 43(3):271–291
2. Zhang L, Thomas BG (2006) State of the art in the control of inclusions during steel ingot casting. Metall Mater Trans B 37(5):733–761
3. Zhang L (2019) Non-metallic inclusions in steels: fundamentals (in Chinese). Metallurgical Industry Press, Beijing
4. Zhang L (2020) Non-metallic inclusions in steels: industrial practice (in Chinese). Metallurgical Industry Press, Beijing
5. Yang W, Zhang L, Wang X, Ren Y, Liu X (2013) Characteristics of inclusions in low carbon Al-killed steel during ladle furnace refining and calcium treatment. ISIJ Int 53(8):1401–1410
6. Cai G, Pang Y, Huang Y (2019) Roles of inclusion, texture and grain boundary in corrosion resistance of low-nickel austenite stainless steel containing Ce. ISIJ Int 59(12):2302–2310
7. Kim S, Jeon S, Lee I, Park Y (2010) Effects of rare earth metals addition on the resistance to pitting corrosion of super duplex stainless steel—Part 1. Corros Sci 52(6):1897–1904
8. Shi W, Yang S, Li J (2018) Correlation between evolution of inclusions and pitting corrosion in 304 stainless steel with yttrium addition. Sci Rep 8(1):4830–4838
9. Huang Y, Cheng G, Li S, Dai W (2018) Effect of cerium on the behavior of inclusions in H13 steel. Steel Res Int 89(12):1800371
10. Ren Q, Zhang L (2020) Effect of cerium content on inclusions in an ultra-low-carbon aluminum-killed steel. Metall Mater Trans B 51(2):589–600
11. Xing L, Zhouhua J, Xin G, Minjun C, Leizhen P (2019) Evolution mechanism of inclusions in H13 steel with rare earth magnesium alloy addition. ISIJ Int 59(9):1552–1561

12. Yue L, Liu Y, Han J, Longmei W (2018) Study on nonmetallic inclusions in clean Cu-P-RE weathering steels. Mater Res Express 5(6):066534
13. Li Y, Liu C, Zhang T, Jiang M, Peng C (2016) Liquid inclusions in heat-resistant steel containing rare earth elements. Metall Mater Trans B 48(2):1–10
14. Suito H, Inoue R (1996) Thermodynamics on control of inclusions composition in ultra-clean steels. Trans Iron Steel Inst Jpn 36(5):528–536
15. Wang L, Liu Y, Wang Q, Chou K (2015) Evolution mechanisms of $MgO{\cdot}Al_2O_3$ inclusions by cerium in spring steel used in fasteners of high-speed railway. ISIJ Int 55(5):970–975
16. Adabavazeh Z, Hwang W, Su Y (2017) Effect of adding cerium on microstructure and morphology of Ce-based inclusions formed in low-carbon steel. Sci Rep 7(46):503–612
17. Jiang M, Yu Y, Li H, Ren X, Wang S (2017) Effect of rare earth cerium addition on microstructures and mechanical properties of low carbon high manganese steels. High Temp Mater Process (Lond) 36(2):145–153

Effect of Ti and Ca Content on the Characteristics of Inclusions in Si–Mn–Al Deoxidized Spring Steel

Rensheng Li, Tongsheng Zhang, Wanlin Wang, Mengchuan Li, and Daoyuan Huang

Abstract The evolution behaviors of nonmetallic inclusions in 55SiCr spring steel were carried out in three melts treated by titanium and calcium in the present study. The composition and morphologies of inclusions were determined by FE-SEM&EDS. The results show that less titanium content more easily modifies the inclusions into the liquid phase ones in Si–Mn–Al deoxidized melt. And more calcium content in steel not only transforms more solid inclusion to liquid inclusions for cleanliness but also avoids the accumulation of titanium oxides in inclusions. The thermodynamic calculations of inclusion formation were performed in Si–Mn–Al–Ti–Ca–O steel system at high temperature and during solidification process by using Factsage 7.2, the thermodynamic calculations consistent with the experimental results, which can predict the formation of the inclusions in Ti-bearing Si–Mn–Al deoxidized steel.

Keywords Spring steel · Calcium treatment · Titanium treatment · Si–Mn–Al deoxidized · Titanium oxides

Introduction

55SiCr spring steel is widely used in automobile suspension and high-speed railway, automobile industry, agricultural machinery, household appliances, and other industries. With the development of light weight and high performance materials in the transportation manufacturing industry, higher requirements are put forward for the fatigue resistance, shock resistance, and elastic attenuation resistance of spring steel [1]. At present, the main means to improve the fatigue property of spring steel is

R. Li · M. Li
College of School of Metallurgy and Environment, Central South University, Changsha 410083, People's Republic of China

T. Zhang (✉) · W. Wang · D. Huang
School of Metallurgy and Environment, Central South University, Changsha 410083, People's Republic of China
e-mail: tongsheng.zhang@csu.edu.cn

Z. Peng et al. (eds.), *12th International Symposium on High-Temperature Metallurgical Processing*, The Minerals, Metals & Materials Series,
https://doi.org/10.1007/978-3-030-92388-4_24

to improve the inclusion control level and microstructure properties. Generally, nonmetallic inclusions in spring steel can cause stress concentrations and hinder the effective improvement of fatigue performance [2].

The addition of titanium can effectively improve the quality of steel. Byun et al. [5] found that titanium oxide inclusions formed by adding titanium to steel could promote the transformation of bainite to acicular ferrite. And Kivio et al. [3, 4] reported that the fine titanium oxide can refine the grain steel. In addition, titanium can partially replace aluminum for deoxidation of molten steel to form relatively stable TiO*x* [6]. However, a large number of studies [6–10] have reported that TiO_x aggregates at the nozzle of continuous casting, which is very harmful to the rhythm of steel production.

Calcium treatment can effectively transform alumina, spinel inclusions, and silicate inclusions into liquid ones in the steel production process, which is not only beneficial to improve the mechanical properties of the steel but also help to reduce nozzle clogging during continuous casting. A large number of previous studies have reported the modification of inclusions and the cleaning effect of calcium treatment on molten steel [11–14]. However, there are few reports on the modification of inclusions in Ti-containing Si–Mn–Al deoxidized steel with calcium treatment. In addition, due to the lack of accurate thermodynamic calculations, the transformation laws of inclusions in Si–Mn–Al–Ti–Ca–O steels are not clear. Therefore, it is a great significance to study the evolution of inclusions in Si–Mn–Al deoxidized steels with different Ti content. The aim in present research is to elucidate the effect of titanium and calcium treatment strength on inclusion characteristics in low aluminum steels.

Methodology

Experimental Procedure

The experiments were carried out in a high-frequency induction tube furnace. The schematic diagram of the furnace is illustrated in Fig. 1. Amounts of 450 g of electrolytic iron, 3 g of electrolytic manganese, 3 g of chromium particles, 6.5 g of high-purity silicon, and 0.32 g of Fe_2O_3 powder were added into a silicon oxide crucible with 53 mm in diameter and 100 mm in depth under a purified argon gas atmosphere. The gas flow rate was maintained at 1L/min with the use of the gas flowmeter. To achieve sufficient homogenization, the melt after becoming fully liquid was held for 20 min at 1823 K (1550 °C). Thereafter, different amounts of deoxidizer aluminum and titanium particles were added to the melt with molybdenum rods. After ten minutes, calcium was added to the melt in the form of Ca-Fe wires for increasing the calcium yield in the molten steel. Before adding Ca-Fe wire for 5 min, the dissolved oxygen content was measured with a probe. Meantime, samples were taken from a quartz glass tube and then quenched in water. The experimental process is shown in Fig. 2.

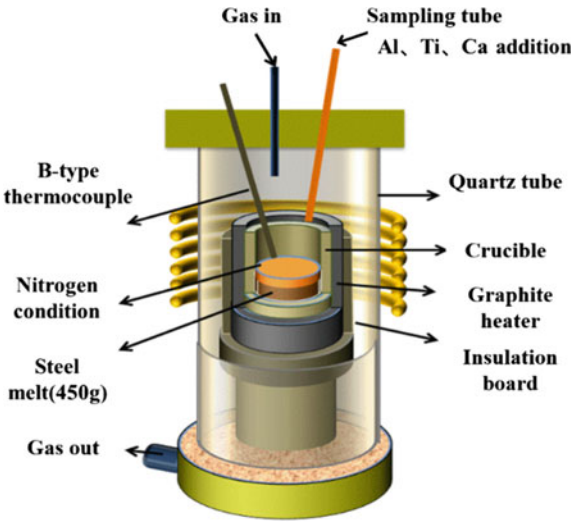

Fig. 1 Schematic diagram of the experimental high-frequency induction furnace

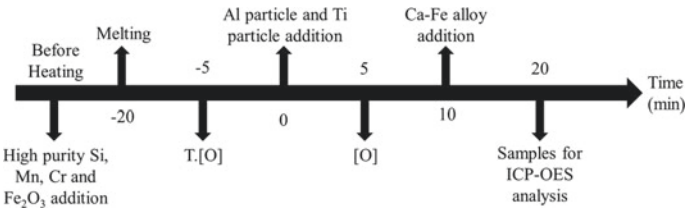

Fig. 2 Melting and sampling process of the present experiments

Chemical Analysis and Inclusion Characterization

Samples were divided into two parts. One half of the steel samples were chemically analyzed by inductively coupled plasma optical emission spectrometry (ICP-OES), with an accuracy of ±0.5 ppm, and the total oxygen content of the sample was detected by inert gas fusion-infrared absorption method with an accuracy of ±1 ppm. The chemical composition of silicon, manganese, chromium, aluminum, titanium, calcium, and oxygen in the melt is shown in Table 1. In order to investigate the effects of titanium and calcium contents on the inclusion types in melt, the addition amount of titanium and calcium was designed and studied in this research. The melts before calcium treatment were divided into two types: low aluminum low titanium melt (Melt 1) and low aluminum high titanium melt (Melt 2, 3). All the melts have different levels of Ca–Fe wires added, which represent different calcium treatment intensities.

Table 1 Chemical compositions of experimental melts (mass percent)

Heat number	Si	Mn	Cr	Al	Ti	Ca	[O]	T.[O]
1	1.41	0.63	0.62	0.0056	0.0052	0.001	0.0015	0.02
2	1.38	0.66	0.64	0.0061	0.153	0.0009	0.0003	0.02
3	1.40	0.65	0.65	0.0058	0.151	0.0024	0.0003	0.021

The other half of the steel sample were characterized by inclusions. The inclusions in steel samples were detected and analyzed by using FE-SEM&EDS at 15 kV acceleration voltage, and the morphology, chemical composition, and size of inclusions were obtained. In consideration of accuracy, the minimum size of inclusion analyzed in this study is 0.5 μm. The plane size distribution of the inclusion particles on the polishing section was evaluated. The total observation area of each sample is 19.46 mm^2, corresponding to the 64 observation areas composed of 8 continuous observation areas in horizontal direction and 8 observation areas in vertical direction under the condition of 500 times magnification of FE-SEM and EDS.

Results and Discussion

Typical Morphologies, Composition, and Size Distribution of the Inclusions

There are three usual valence states of Ti element in oxide: Ti^{2+}, Ti^{3+}, and Ti^{4+}. Several articles have reported in detail that the oxygen potential and the activity of titanium in molten steel determine the existing state of titanium [15–17]. According to the calculation of FACTSAGE 7.2 software and the results of former references, the existence form of titanium oxide in steel is Ti_3O_5. Pseudo-quaternary phase diagrams of Al_2O_3–SiO_2–Ti_3O_5–CaO–10%MnO adopted in this study were calculated by using the FTOxide database in Factsage 7.2, as shown in Fig. 3. Solid phases, such as SiO_2, Al_2O_3, mullite (SiO_2-Al_2O_3), pseudobrookite, manganese aluminate, perovskite, calcium aluminate, and ilmenite, are shown to be in equilibrium with the liquid phase.

To evaluate the transformation behavior of inclusions, the compositions obtained from SEM–EDS were converted into the mass percentages of Ti_3O_5, Al_2O_3, SiO_2, CaO, and MnO, which are plotted on pseudo-quaternary phase diagrams of Al_2O_3–SiO_2–Ti_3O_5–CaO–10%MnO, as shown in Fig. 4. Each dot in the figure represents an inclusion composition, and while the red line is the liquid phase region. As shown in Fig. 4a, the inclusion in Melt 1 mainly located in the liquid phase region, near the side with high SiO_2 content. However, the inclusions in Melt 2 deviated from the liquid phase region, mainly in the coexistence region of pseudobrookite and liquid phase, as shown in Fig. 4b. Moreover, half of the inclusions in Melt 3 are in the liquid

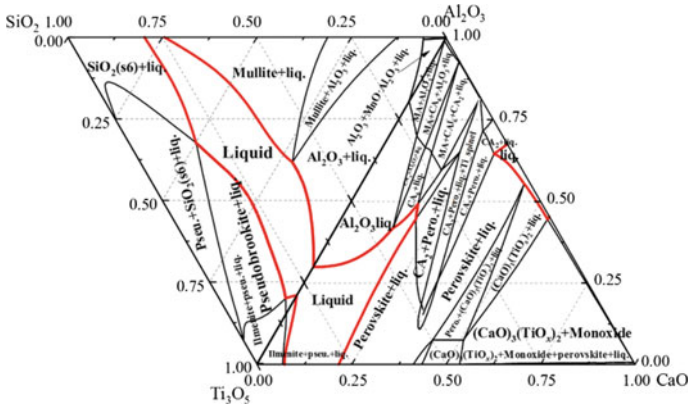

Fig. 3 Pseudo-quaternary phase diagram of Al_2O_3–SiO_2–Ti_3O_5–CaO–10%MnO system and its liquid phase region (T = 1823 K)

phase region, and the other half are in the region of perovskite phase, as shown in Fig. 4c. It is worth noting that the inclusions all appear as white substance in the black matrix. EDS results of the different region in the inclusions in Melt 3 were carried out, as shown in Fig. 5. It is found that the content of Ti element in the white substance is twice that in the black matrix. This indicates that the white substance is closely related to the oxide of titanium.

In order to explore the generation mechanism of white substance, the average composition curve of inclusions was carried out, as shown in Fig. 6. It can be preliminarily found that the content of white substance is related to the ratio of Ti_3O_5.Therefore, a higher Ti_3O_5 ratio leads to an increase in white substance. This means white substance is closely related to the amount of titanium in the liquid steel.

In addition, the increase of calcium content in molten steel can also lead to the decrease of Ti_3O_5 components in the inclusion. This indicates that calcium reduces the titanium oxide in the inclusion. And all the mechanisms was described as following Reactions (1) and (2).

$$3[\mathrm{Ti}] + 5/3(\mathrm{Al_2O_3})_{\mathrm{inc}} = 10/3[\mathrm{Al}] + (\mathrm{Ti_3O_5})_{\mathrm{inc}}$$
$$\Delta G_1^{\theta} = 649,322.67 - 248.63\,\mathrm{T(J/mol)} \quad (1)$$

$$6[\mathrm{Ti}] + 5(\mathrm{SiO_2})_{\mathrm{inc}} = 5[\mathrm{Si}] + 2(\mathrm{Ti_3O_5})_{\mathrm{inc}}$$
$$\Delta G_2^{\theta} = 97,512 - 275.6\,\mathrm{T(J/mol)} \quad (2)$$

Furthermore, comparing Melt 2 with Melt 3, the increase of calcium content in molten steel can greatly reduce the composition of titanium oxide in the inclusion, resulting in the composition of SiO_2 and Al_2O_3 can be increased. It can be described by following Reaction (3).

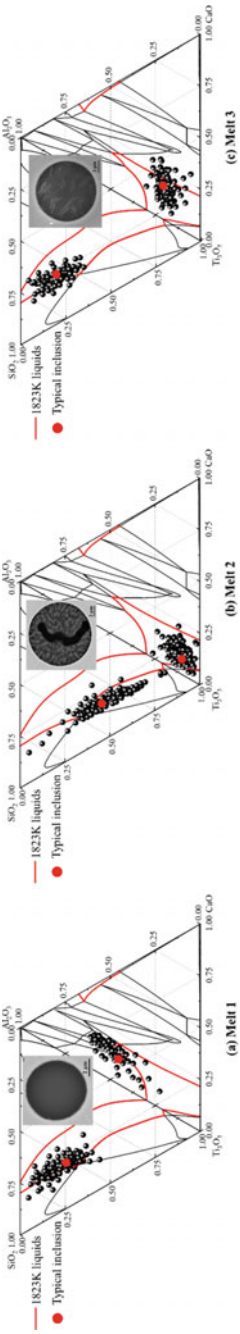

Fig. 4 Composition distribution and morphology of typical inclusions (the red line represents the liquid phase region under 1823 K, the red dots represent the typical inclusion, and **a**, **b**, and **c** represent the Melts 1~3, respectively) (Color figure online)

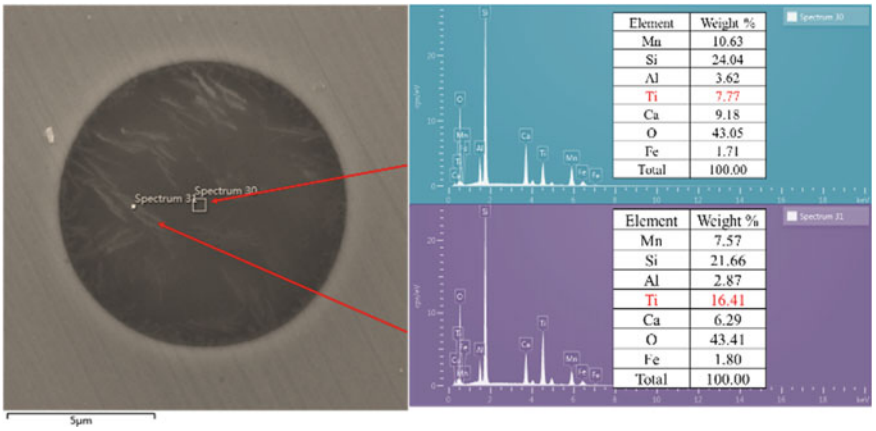

Fig. 5 Composition of the different regions in inclusion in Melt 3

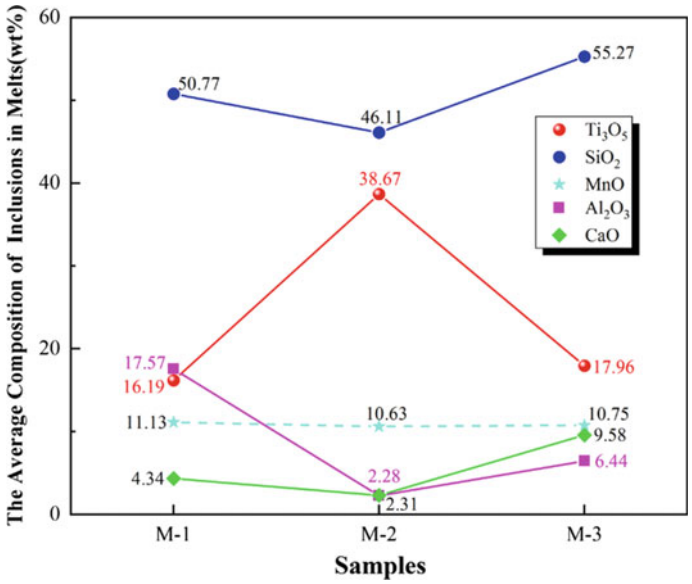

Fig. 6 Average composition curve of inclusions in melts. (M-1, M-2 represent Melt 1 and Melt 2, respectively)

$$5[\mathrm{Ca}] + (\mathrm{Ti_3O_5})_{\mathrm{inc}} = 3[\mathrm{Ti}] + 5(\mathrm{CaO})_{\mathrm{inc}}$$
$$\Delta G_3^{\theta} = 701,144 - 722.7\,\mathrm{T(J/mol)} \tag{3}$$

The standard Gibbs free energy (ΔG^{θ}) of Reactions (1, 2), and (3) can be derived from the equations in Table 2. Moreover, as shown in Tables 1 and 3, the interaction

Table 2 Fundamental equation for the Gibbs free energy calculation

Reactions	ΔG^{θ} (J/mol)	References
[Si] + 2[O] = (SiO_2) (s)	−576,440 + 218.2 T	[18]
[Mn] + [O] = (MnO) (s)	−284,900 + 127.64 T	[18]
2[Al] + 3[O] = (Al_2O_3) (s)	−1,225,000 + 393.8 T	[18]
[Ti] + 2[O] = (TiO_2) (s)	−554,340 + 174.26 T	[17]
2[Ti] + 3[O] = (Ti_2O_3(s)	−845,928 + 248.6 T	[17]
3[Ti] + 5[O] = (Ti_3O_5) (s)	−1,392,344 + 407.7 T	[17]
[Ca] + [O] = (CaO) (s)	−138,240 − 63.0 T	[19]

Table 3 Interaction coefficients used to calculate activity at 1823 K (1550 °C) [20, 21]

e_i^j	Si	Mn	Cr	Al	Ti	Ca	O
Si	0.113	0.002	−0.0003	0.0596	–	−0.0688	−0.236
Mn	0.400	0.00	0.00370	0.0720	0.0195	–	−0.0853
Al	0.00575	0.0123	0.0257	0.0462	0.0720	−0.0483	−6.781
Ti	0.0514	–	0.0565	0.123	0.0133	–	−1.849
Ca	−0.0997	−0.016	0.0205	−0.0740	–	−0.002	−696.60
O	−0.135	−0.0216	−0.0411	−4.00	−0.616	−278.433	−0.205

coefficients and activity of elements with different compositions were calculated. According to the calculation results, it turns out that the Gibbs free energy ($\Delta G = \Delta G^{\theta} + \mathrm{RT} \ln \mathrm{K}$) for Eqs. (1, 2) and (3) is negative.

In addition, to better understand the evolution behavior of inclusions in Si–Mn–Al deoxidized steel under different Ti and Ca treatments, elemental mapping analyses were adopted by FE-SEM and EDS, and the results are shown in Fig. 7. As for low aluminum low titanium melt, the composition of the inclusion core in Melt 1

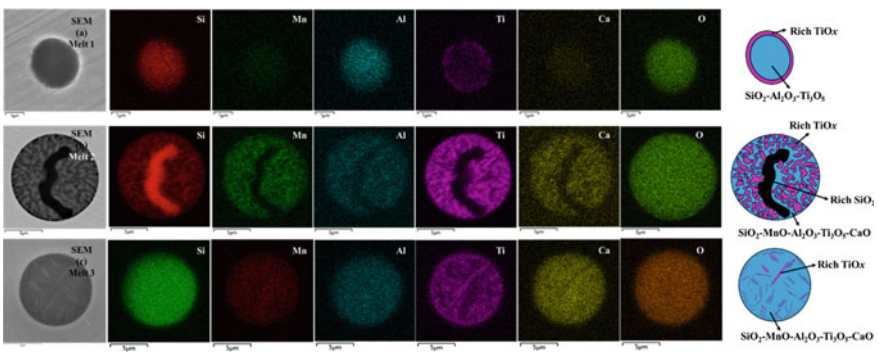

Fig. 7 Elemental mapping of typical inclusions: **a** Melt 1, **b** Melt 2, and **c** Melt 3

is mainly SiO_2–Al_2O_3–Ti_3O_5, and there is Ti aggregation phenomenon at the outer edge after calcium treatment, as shown in Fig. 7a. Wang et al. [10] reported that irreversible transient TiO_x was formed when Ti/Al increase to 1 in molten steel, even though no stable phase of TiO_x was found in thermodynamic calculation. In fact, with the increase of titanium content, the aggregation phenomenon of titanium element is more obvious in the inclusion, and there is more titanium in the inner of the inclusion, as shown in Fig. 7b. However, compared with Melt 2, with the increase of calcium treatment intensity, the accumulation of titanium element in Melt 3 is obviously weakened. This indicates that the accumulation of titanium in the inclusion increases with the increase of Ti/Al ratio, and the accumulation of titanium can be reduced by calcium treatment. The increase of Ti_3O_5 content in the inclusion is in good agreement with this conclusion, as shown in Fig. 6.

To better evaluate the influence of inclusions in steel properties, the number and size distribution of inclusions in 64 areas of 19.46 mm^2 were statistically analyzed for each sample, and the results are shown in Fig. 8. As shown in Fig. 8a, with the increase of titanium content, the content of inclusions in the range of 2–5 μm in Melt 2 is higher than that in Melt 1, and the size of inclusions in the range of 5–10 μm has a similar trend. For Melt 2 and Melt 3, the size distribution of inclusions is only slightly different in the range of 5–10 μm and >10 μm with increase of calcium content.

Moreover, the number density and average size of inclusions in present study were also statistically analyzed, and the results were shown in Fig. 8b. The number density of three melts is above 250/mm^2, and the average size is >2 μm. Compared with Melt 1, with the increased of titanium content, the average size of inclusions showed an upward trend. After increase calcium content in molten steel, the average size and density of inclusions in Melt 3 are higher than Melt 1 and Melt 2. It is probably due to the fact that the calcium oxides formed by calcium elements aggregate with inclusions and increase in size, and some of the calcium oxides are dispersed in the molten steel.

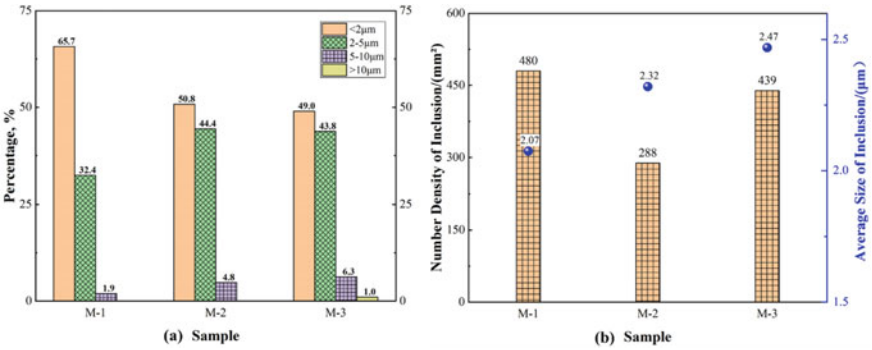

Fig. 8 Size distribution, number density, and average size of inclusions (M-1 and M-2 represent Melt 1 and Melt 2, respectively)

Thermodynamic Analysis of Si–Mn–Al–Ca–Ti–O System Complex Inclusions

Thermodynamic calculations were carried out to get stability region diagram of Fe–1.4Si–0.65Mn–0.006Al–*x*Ti–*y*Ca–0.02O systems by using Factsage 7.2 with the FToxid, FactPS, and FSstel databases, as shown in Fig. 9. The points in the equilibrium diagram represent the experimental melt in this study, respectively. As presented in Fig. 9, with the increase of titanium, the inclusions in the melt changed from liquid inclusion to pseudobrookite inclusion. When [Ti] = 0.15%, with the increase of calcium treatment intensity, the inclusion began to change from pseudobrookite and liquid inclusion to liquid inclusion.

For the actual situation of Ti–bearing Si–Mn–Al deoxidized spring steel, the behavior of typical inclusions in steel during solidification procedure was analyzed, as shown in Fig. 10. When [Al] = 0.006%, [Ti] = 0.005%, [Ca] = 0.0015, the liquid phase exists above 1623 K (1350 °C) in steel. During the solidification process of the steel, the transformed path of oxide inclusions is as follows: Liquid inclusion → Mullite + SiO_2 → Mullite + SiO_2 + $CaO{\cdot}Al_2O_3{\cdot}2SiO_2$ + Ti_2O_3, as shown in Fig. 10a. When the titanium content in the steel increases to 0.15%, the liquid phase and pseudobrookite phase always co-exist at 1723 K (1500 °C), as shown in Fig. 10b. Furthermore, the addition of calcium leads to the formation of calcium titanate, Al_2O_3 and Ti_2O_3 during solidification, as shown in Fig. 10c.

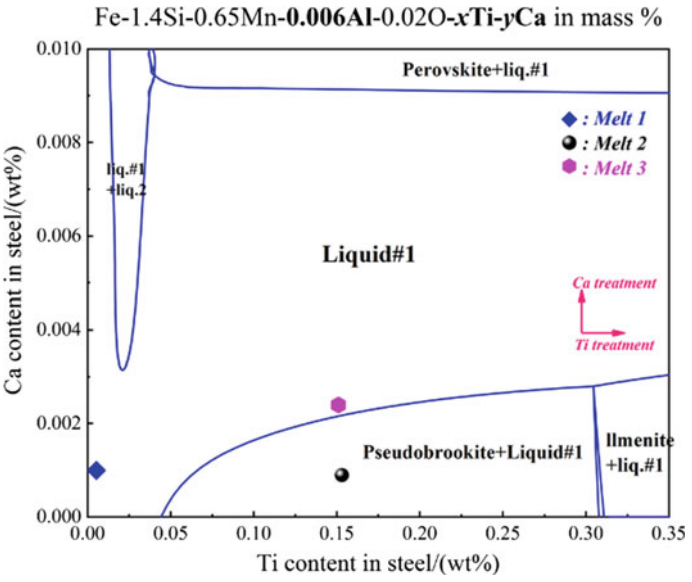

Fig. 9 Thermodynamic equilibrium phase diagram of the precipitation of inclusions under different calcium and titanium treatments: Fe–1.4Si–0.65Mn–0.006Al–*x*Ti–*y*Ca–0.02O in mass percent (Temperature = 1823 K)

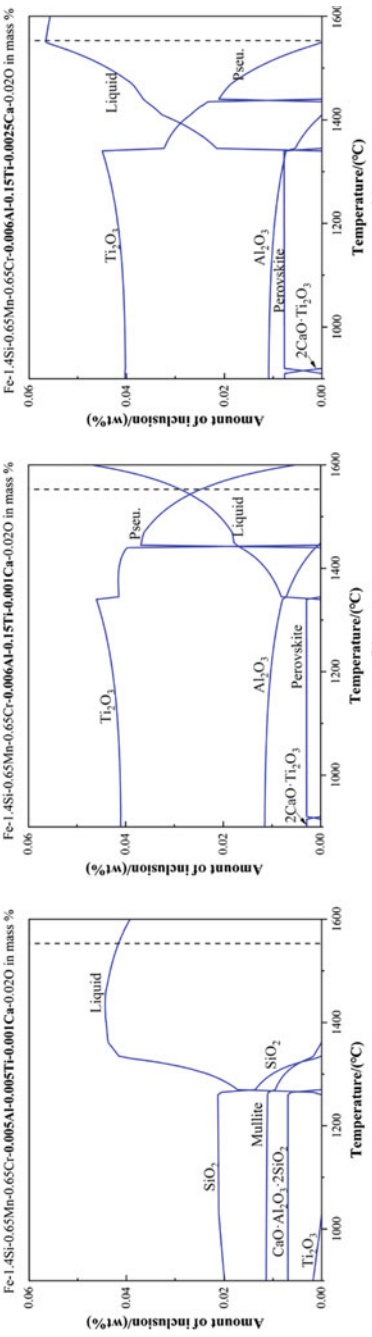

Fig. 10 Equilibria precipitation diagram of melt inclusions in Fe–1.4Si–0.65Mn–0.006Al–Ti–Ca–0.02O (wt%) system under different calcium and titanium treatments during solidification. (Perovskite: $(CaO)_2 \cdot (TiOx)_2$, $x = 2/1.5$; Pseudobrookite: main phase is Ti_3O_5; Mullite: main phase is Al_2O_3–SiO_2)

Considering the observed complex Si-Mn-Al-Ca-Ti–O inclusions and thermodynamic calculations, it can be summarized that appropriate titanium content and the strength of calcium treatment contributes to modify inclusions to liquid ones in the molten steel. To sum up, less titanium content more easily modifies the inclusions into the liquid ones in low aluminum steel. Moreover, more calcium content in steel not only transforms more solid inclusions to liquid inclusions for cleanliness but also helps to avoid the accumulation of titanium oxides in inclusions. It is because that the higher titanium content can lead to the accumulation of titanium oxides in inclusions.

Conclusion

Inclusion evolution after calcium addition in Si-Mn-Al deoxidized spring steel with different titanium contents has been carried out by using chemical experiments and thermodynamic calculations at 1823 K (1550 °C). The main findings can be summarized as follows.

The morphology, composition, and size distribution of inclusions in Si–Mn–Al deoxidized steel are significantly influenced by titanium and calcium treatment. It can be summarized that appropriate titanium and calcium content could modify inclusions into liquid ones in the molten steel. A less titanium content more easily modifies the inclusions into the liquid phase ones in low aluminum content steel. Also, higher calcium content can effectively reduce the accumulation phenomenon of titanium oxides in inclusions. The formation of Si–Mn–Al–Ti–Ca–O system inclusions in spring steel at high temperature and during the solidification process were comprehensively calculated, taking all types of inclusions such as titanium oxide, aluminum oxide, silicon oxide, manganese oxide, calcium titanate, mullite, pseudobrookite, and liquid inclusion into account. The thermodynamic calculations agree well with the experimental results, which can predict the formation of the inclusions in Ti-bearing Si–Mn–Al deoxidized steel.

References

1. Cai X, Bao Y, Lin L, Gu C (2016) Effect of Al content on the evolution of non-metallic inclusions in Si–Mn deoxidized steel. Steel Res Int 87(9):1168–1178
2. Chen L, Chen W, Hu Y, Chen Z, Xu Y, Yan W (2017) Investigation on the origin of Al_2O_3-rich inclusions in valve spring steel under vacuum condition. Steel Res Int 88(7):1600376
3. Kivio M, Holappa L, Iung T (2010) Addition of dispersoid titanium oxide inclusions in steel and their influence on grain refinement. Metall Mater Trans B 41(6):1194–1204
4. Kivio M, Holappa L (2012) Addition of titanium oxide inclusions into liquid steel to control nonmetallic inclusions. Metall Mater Trans B 43(2):233–240
5. Byun J, Shim J, Cho YW, Lee D (2003) Non-metallic inclusion and intragranular nucleation of ferrite in Ti-killed C–Mn steel. Acta Mater 51(6):1593–1606

6. Wang C, Nuhfer N, Sridhar S (2009) Transient behavior of inclusion chemistry, shape, and structure in Fe–Al–Ti–O melts: effect of titanium source and laboratory deoxidation simulation. Metall Mater Trans B 40(6):1005–1021
7. Zhang L, Wang Y, Zuo X (2008) Flow transport and inclusion motion in steel continuous-casting mold under submerged entry nozzle clogging condition. Metall Mater Trans B 39(4):534–550
8. Gao Y, Sorimachi K (1993) Formation of clogging materials in an immersed nozzle during continuous casting of titanium stabilized stainless steel. ISIJ Int 33(2):291–297
9. Davidson X, Lowe A (2000) Flow transitions in vacuum arc remelting. Mater Sci Technol 16(6):699–711
10. Wang C, Nuhfer N, Sridhar S (2009) Transient behavior of inclusion chemistry, shape, and structure in Fe–Al–Ti–O melts: effect of titanium/aluminum ratio. Metall Mater Trans B 40(6):1022–1034
11. Higuchl Y, Numata M, Fukagawa S, Shinm K (1996) Inclusion modification by calcium treatment. ISIJ Int 36(2):151–154
12. Zheng W, Wu Z-H, Li G-Q, Zhang Z, Zhu C-Y (2014) Effect of Al content on the characteristics of inclusions in Al–Ti complex deoxidized steel with calcium treatment. ISIJ Int 54(8):1755–1764
13. Park S, Jung I, Oh K, Lee H (2004) Effect of al on the evolution of non-metallic inclusions in the Mn–Si–Ti–Mg deoxidized steel during solidification: experiments and thermodynamic calculations. ISIJ Int 44(6):1016–1023
14. Yang W, Zhang L, Wang X, Ren Y, Liu X, Shan Q (2013) Characteristics of inclusions in low carbon Al-killed steel during ladle furnace refining and calcium treatment. ISIJ Int 53(8):1401–1410
15. Seok S-H, Miki T, Hino M (2011) Equilibrium between Ti and O in molten Fe–Ni, Fe–Cr and Fe–Cr–Ni alloys equilibrated with 'Ti_3O_5' solid solution. ISIJ Int 51(4):566–572
16. Cha W-Y, Nagasaka T, Miki T, Sasaki Y, Hino M (2006) Equilibrium between titanium and oxygen in liquid Fe–Ti alloy coexisted with titanium oxides at 1873 K. ISIJ Int 46(7):996–1005
17. Pak J-J, Jo J-O, Kim S-I, Kim W-Y, Chung T-I, Seo S-M (2007) Thermodynamics of titanium and oxygen dissolved in liquid iron equilibrated with titanium oxides. ISIJ Int 47(1):16–24
18. The Japan Society for the Promotion of Science (1988) The 19th committee on steelmaking. Gordon and Breach Science Publishers, New York, Steelmaking Data Sourcebook
19. Itoh H, Hino M, Ban-yaS (1997) Solute iron Ca deacidification equilibrium. Tetsu-to-Hagane 83(11):695–700
20. Chen J (2010) Manual of data and charts used in steelmaking, 2nd edn. Metallurgical Industry Press, Beijing, pp 758–761
21. Park J, Todoroki H (2010) Control of $MgO{\cdot}Al_2O_3$ spinel inclusions in stainless steels. ISIJ Int 50(10):1333–1346

Effect of Coarse Coke Breeze Addition on Magnetite Concentrate Sintering

Huaiying Ma, Chunlai Wang, Yue Xin, Yapeng Zhang, Wen Pan, and Wang Zhu

Abstract Coarse coke breeze can cause delayed combustion and increase the permeability of the sintering bed. In order to increase the efficiency of magnetite concentrate sintering, the effect of coarse coke breeze addition was investigated in an experimental-scale sintering pot. The results indicated that under a basicity of 2.15, the increase of coke breeze addition improved sintering speed, productivity, and reduction disintegration index ($RDI_{+3.15}$) of sinter. However, sinter tumbler index and mean diameter were significantly decreased. With increasing coke breeze addition, the maximum temperature increased, while the holding time of high temperature over 1100 °C initially increased and then declined. The mineral analysis of sinter showed that as the coke breeze proportion increased, the amount of silico-ferrite of calcium and aluminum (SFCA) decreased, while the amount of magnetite increased and became the main mineral in sinter.

Keywords Coarse coke breeze · Sintering · Magnetite concentrate · Sintering speed

Introduction

High grade magnetite concentrates are used as a major feed for sintering in many sinter plants in China. Due to its dense particles and high assimilation temperature, magnetite concentrate sintering usually needs higher temperature to ensure adequate sinter strength. Besides, sinter bed formed from blends containing high level of magnetite concentrate are more deformable [1], which reduces the green bed

H. Ma (✉) · Y. Zhang · W. Pan
Research Institute of Technology, Shougang Group Corporation, Beijing, China
e-mail: captainma@163.com

Beijing Key Laboratory of Green Recyclable Process for Iron & Steel Production Technology, Beijing, China

C. Wang · Y. Xin · W. Zhu
Beijing Shougang Corporation Limited, Beijing, China

Z. Peng et al. (eds.), *12th International Symposium on High-Temperature Metallurgical Processing*, The Minerals, Metals & Materials Series,
https://doi.org/10.1007/978-3-030-92388-4_25

permeability during sintering and causes reducing atmosphere. A low productivity is usually encountered in the sintering of blends containing high ratio of magnetite concentrate.

Solid fuel, including coke and coal, supplies mainly 70–80% of sintering total energy and strongly influences the sintering permeability and sinter quality [2, 3]. Thus, it is of great significance to access the suitable properties of the solid fuel such as the total addition and the size distribution. In common, fine coke breeze with −3 mm proportion over 80% is recommended to get the best sintering performance [4, 5]. However, larger fuel particles burn slowly and form larger pores in sinter, thereby increasing the maximum temperature and permeability in sinter bed. As about 20% magnetite concentrate is mixed in sintering blends in Beijing Shougang Corporation Limited, coarse coke breeze is used to improve the sintering permeability. This work focuses on the influences of coarse coke breeze addition towards sintering process and sinter quality under high level of magnetite concentrate and high basicity. The work would provide fundamental understanding of magnetite concentrate sintering with coarse coke breeze.

Experimental

Materials for Sintering Pot Test

Table 1 shows the main chemical composition of raw material used in the tests. Concentrate A is a Chinese magnetite concentrate with a −0.074mm fraction of 60%. Ores B, C, and D are Australian limonite ores. Ore E is a Brazilian hematite ore. The size distributions of coke breeze and anthracite are presented in Table 2. The proportion of coke breeze above 5 mm is 23.1%, which is higher than that of general coke breeze.

Table 1 Chemical composition of raw materials (mass %)

Materials	TFe	SiO_2	Al_2O_3	CaO	MgO	FeO	LOI	C
Concentrate A	66.49	5.53	0.46	0.42	0.49	28.85	−2.54	
Ore B	60.22	4.55	2.32	0.28	0.10	0.19	6.31	
Ore C	61.20	4.47	1.90	0.18	0.06	0.22	5.37	
Ore D	56.31	7.40	1.52	0.12	0.08	0.18	9.99	
Ore E	64.66	1.74	1.27	0.09	0.05	0.30	3.79	
Return fines	55.5	5.32	1.78	11.71	1.75	9.6	−0.15	
Limestone		3.12	0.76	46.17	6.41		42.25	
Quick lime		3.62	0.93	62.87	11.27		20.19	
Coke breeze	0.29	6.83	5.52	0.20	0.14			84.91
Anthracite	0.5	10.39	3.33	1.63	0.40			77.48

Table 2 Size analysis of coke breeze and anthracite (mass %)

Size, mm	−1	1–3	3–5	5–8	+8
Coke breeze	32.6	35.5	8.8	16.9	6.2
Anthracite	17.4	47.6	11.2	18.3	5.5

Sintering Pot Test

Table 3 shows the blending ratio of sintering materials. The basicity of each mix was controlled at a level of 2.15. Besides coke breeze, anthracite was also added to keep the same with the industrial production. The total fuel addition varied from 4.26 to 6.65% by adjusting the coke breeze amount. A schematic diagram of laboratory sinter pot is shown in Fig. 1. The blends were mixed manually and then granulated

Table 3 Blending ratio of sintering materials (mass %)

Materials	Mix 1	Mix 2	Mix 3	Mix 4
Ore A	17.02	16.88	16.74	16.60
Ore B	4.26	4.22	4.18	4.15
Ore C	25.54	25.32	25.11	24.90
Ore D	8.51	8.44	8.37	8.30
Ore E	4.26	4.22	4.18	4.15
Return fines	19.58	19.41	19.25	19.09
Limestone	11.47	11.38	11.28	11.19
Quick lime	5.11	5.06	5.02	4.98
Coke breeze	3.00	3.80	4.60	5.40
Anthracite	1.26	1.26	1.26	1.26

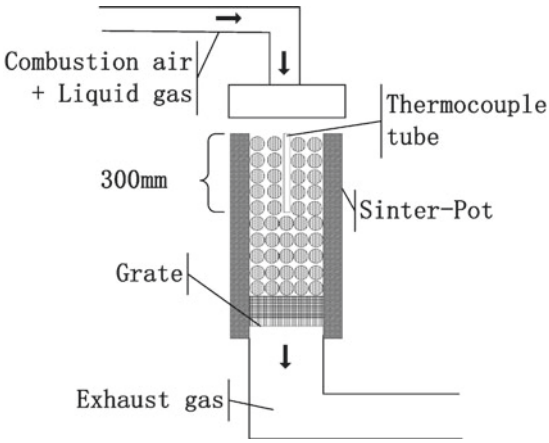

Fig. 1 Schematic diagram of laboratory sinter pot

in a 1000 mm diameter laboratory mixing drum. A hearth layer of 4 kg sinter was placed onto the bottom grate of sinter pot. Subsequently, the prepared sinter mix was put into the sinter pot (300 mm diameter × 760 mm height). After a 300 mm height thermocouple tube was placed in the center of the pot, the bed was ignited by LNG at 1150 °C for 210 s. Once the ignition finished, a K-type thermocouple was placed into the tube to measure the bed temperature. The suction pressure of ignition and sintering was controlled at constant level of 8 and 16 kPa separately. The sintering was completed as the exhaust gas was cooled down to 200 °C from the maximum temperature. Then the thermocouple was taken out, and the sinter was crushed and evaluated for chemical, physical, and metallurgical properties. Also, microstructural test was conducted by a Leica DMRX microscope.

Results and Discussion

Effects of Coke Addition on Sinter Chemistry and Sintering Indexes

Table 4 shows the influence of coke breeze addition on sinter chemistry. It was found that FeO increased from 7.28 to 16.62% with increasing coke breeze addition from 3.00 to 5.40%.

Figure 2d shows that with an increase in coke breeze addition, the sintering speed increased by nearly 20% from 20 to 23.88 mm/min, which was contrary to tests using fine coke breeze [6]. Figure 2c shows that the sinter yield decreased when coke breeze addition was increased. Figure 2b shows when the coke breeze addition increased from 3.00% to 4.6%, the productivity increased from 1.37 t/(m^2.h) to 1.50 t/(m^2.h). However, as the coke addition further increased to 5.4%, the productivity began to decrease. These results indicated that excessive coke breeze had a negative effect on productivity. As both the sintering speed and sinter yield increased, the decreased bulk density would be the main reason for the decrease in productivity as shown in Fig. 2a.

Figure 3 shows results of the maximum temperature and high temperature holding time in the middle sinter bed. As the coke breeze addition increased, the maximum temperature increased. However, the high temperature holding time of >1100 °C and

Table 4 Chemical composition of sinter for different fuel addition (mass %)

Coke breeze	Total fuel	TFe	FeO	CaO	SiO_2	MgO	R
3.00	4.26	55.20	7.28	12.11	5.55	1.81	2.18
3.80	5.06	55.18	9.86	11.83	5.51	1.68	2.15
4.60	5.86	55.83	10.47	11.78	5.5	1.68	2.14
5.40	6.66	55.43	16.62	12.06	5.7	1.71	2.12

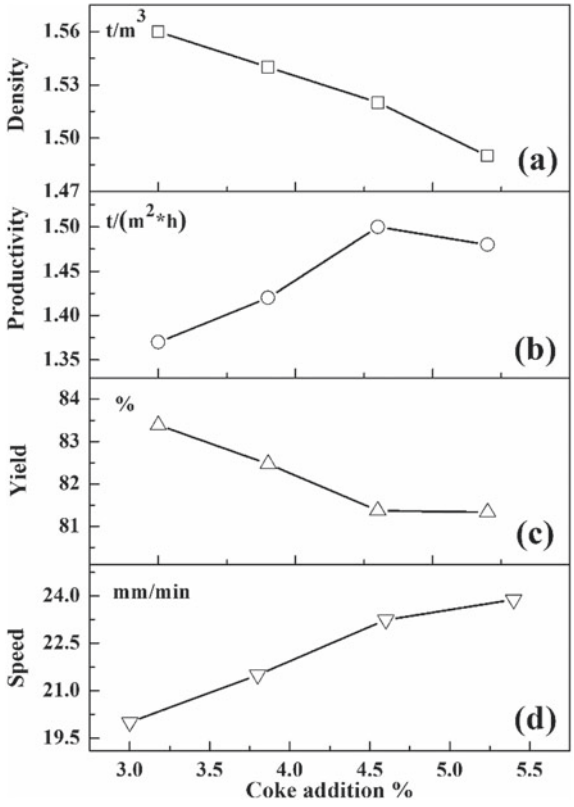

Fig. 2 Effect of coke addition on sintering indexes

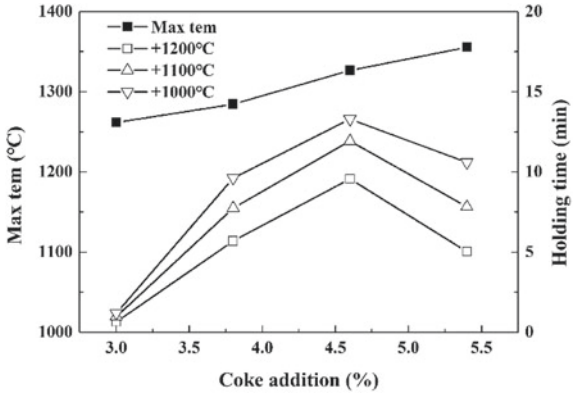

Fig. 3 Effect of coke addition on maximum temperature and high temperature holding time

>1200 °C increased and reached maximum at coke breeze addition of 4.6% and then declined. With increasing the coarse coke breeze addition, the temperature inside the sinter bed increases. However, the permeability of the sinter bed also increases, which would accelerate the cooling process and decrease the high temperature holding time.

Effects of Coke Addition on Strength and Size of Sinter

Sinter with large particle size and high cold strength is usually preferred by large blast furnaces to keep a high permeability. The cold strength of sinter is represented by the tumble strength (TI) which is the percentage of +6.3 mm fraction remaining after the tumbling test. Figure 4 shows the influences of coke breeze addition on sinter TI and mean diameter. As the coke addition increased, both the TI and the mean diameter decreased.

Effects of Coke Addition on Reduction Properties of Sinter

Figure 5 shows reduction properties of sinters. The $RDI_{+3.15}$ increased from 70.22 to 82.10% with increasing coke breeze addition from 3.00 to 5.40%. The reduction degradation of sinter is associated with a volume increase due to the transformation of hematite to magnetite. With the increase of coke breeze addition, the sinter FeO increases, and the amount of hematite in sinter decreases. Reducing the hematite content in the sinter reduces the sinter degradation at lower temperature. RI decreased with increasing coke breeze addition. These results indicate that sinter produced by high coke addition is hard to be reduced and deteriorates the permeability in the blast furnace.

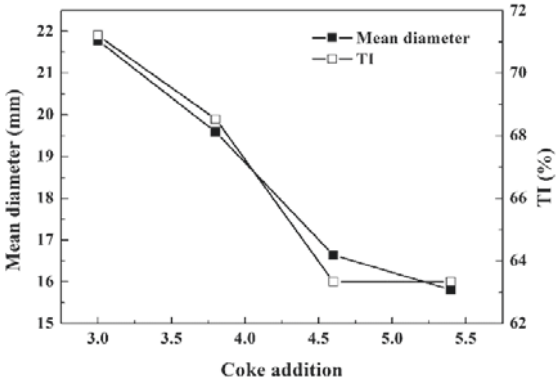

Fig. 4 Effect of coke addition on TI and mean diameter of sinter

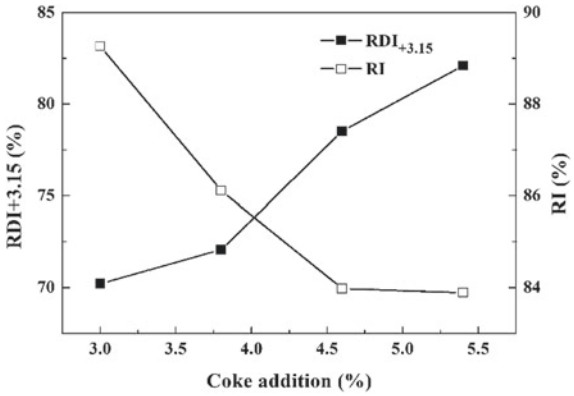

Fig. 5 Effect of coke addition on reduction properties of sinter

Effects of Coke Addition on Minerals Constituent and Microstructure of Sinter

Minerals constituent of sinter were tested and quantified by XRD. Figure 6 shows the results. As the coke breeze addition increased, the content of hematite and SFCA decreased. Meanwhile, the magnetite content increased from 21 to 43% and became the main mineral in sinter when the coke breeze ratio was 5.4%. Low-temperature sintering (T < 1300 °C) is beneficial to the formation of SFCA. With the coke breeze addition increases, the maximum temperature increases and forms more Fe_3O_4 [7].

The sinter microstructures are shown in Fig. 7. When coke breeze addition was below 3.8%, magnetite, hematite, and SFCA were the main minerals. When coke breeze addition increased to 4.6% (Fig. 7c), secondary hematite was observed around the pores. With increasing coke addition, the number of pores in sinter increased, and small pores merged into large pores, which decreased the sinter strength. Meanwhile, secondary hematite formed due to the increasing high temperature and cooling rate.

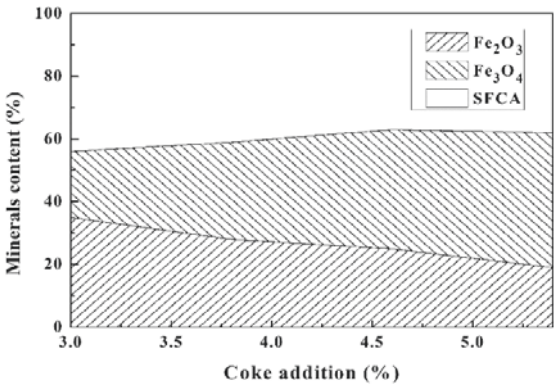

Fig. 6 Effect of coke addition on mineralogy of sinter

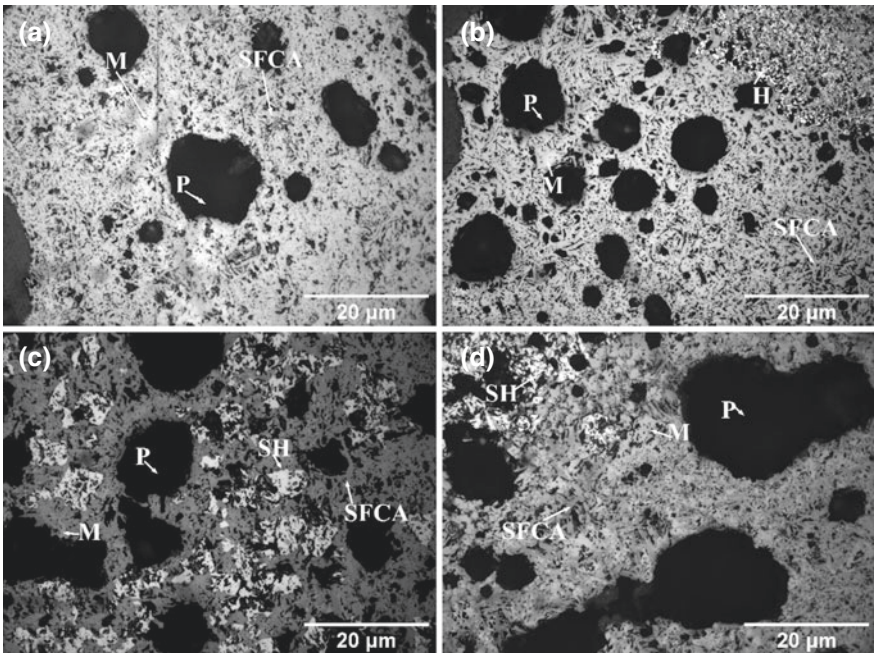

Fig. 7 Microstructure of sinter with different coke breeze additions. **a** 3.0%; **b** 3.8%; **c** 4.6%; **d** 5.4%. H—Hematite; SH—Secondary Hematite; M—Magnetite; P—Pore

Conclusions

In this work, magnetite concentrate sintering with coarse coke breeze has been investigated. The experimental results show that with increasing coke breeze addition, the sintering speed and the productivity increase while the sinter strength and mean diameter have a significant decrease. The holding time of high temperature over 1100 °C initially increases and reaches maximum at coke addition of 4.6% and then declines. Magnetite in sinter increases gradually to be the main mineral with increasing coke addition, while SFCA and hematite decrease. As large amount of coke breeze is added into the sintering mixture, merged pores, which would deteriorate the sinter strength, begin to form.

References

1. Kasai E, Omori Y (1993) Subjects on the evaluation of process and products in the sintering of iron ore. Tetsu-to-Hagané 79(11):1217–1223
2. Yang LX (2005) Sintering fundamentals of magnetite alone and blended with hematite and hematite/goethite ores. ISIJ Int 45(4):469–476

3. Hida Y, Sasaki M, Enokido T (1982) Effect of the existing state of coke breeze in quasi-particles of raw mix on coke combustion in the sintering process. Tetsu-to-Hagané 68(3):400–409
4. Arikata Y, Yamamoto K, Sassa Y (2013) Effect of coke breeze addition timing on sintering operation. ISIJ Int 53(9):1523–1528
5. Liu S, Bai K, Ni G (2019) Study on influence of fuel size on iron ore sintering. Sinter Pelletizing 44(6):17–22
6. Umadevi T, Deodhar AV, Kumar S (2008) Influence of coke breeze particle size on quality of sinter. Ironmak Steelmak 35(8):567–574
7. Umadevi T, Karthik P, Mahapatra PC (2012) Optimisation of FeO in iron ore sinter at JSW steel limited. Ironmak Steelmak 39(3):180–189

Effect of the Injection Angle of Reducing Gas on Coal Flow and Combustion in a 50% Oxygen Blast Furnace

Xing Peng, Jingsong Wang, Zhiyao Li, Haibin Zuo, Xuefeng She, Guang Wang, and Qingguo Xue

Abstract Medium oxygen-enriched blast furnace that utilizes reducing gas injections is a feasible new ironmaking process that can significantly reduce the coke ratio and carbon dioxide emissions. In this study, a three-dimensional numerical model of lance–blowpipe–tuyere–raceway zone was established, which was used to study the influence of the reducing gas injection angle (30–70°) on the flow and combustion of pulverized coal in a new tuyere of the 50% oxygen blast furnace. As the injection angle increases, the tuyere kinetic energy first decreases and then increases, and the pulverized coal combustion efficiency increases. Compared with the injection at 30°, the coal particle temperature under the injection conditions of 70° at the raceway outlet increased by 326 K, and the char conversion ratio and the burnout increased by 27.4% and 22.4%, respectively. However, it is worth noting that under the high injection angle, local high temperature appears on the tuyere wall, which requires cooling to avoid damage to the tuyere in the actual blast furnace.

Keywords Reducing gas injection · Coal combustion · Oxygen-enriched · Blast furnace · Tuyere

X. Peng · J. Wang (✉) · Z. Li · H. Zuo · X. She · G. Wang · Q. Xue
State Key Laboratory of Advanced Metallurgy, University of Science and Technology Beijing, Beijing 100083, People's Republic of China
e-mail: wangjingsong@ustb.edu.cn

X. Peng
e-mail: pengxing_hunan@sina.com

H. Zuo
e-mail: zuohaibin@ustb.edu.cn

X. She
e-mail: shexuefeng@ustb.edu.cn

G. Wang
e-mail: wangguang@ustb.edu.cn

Q. Xue
e-mail: xueqingguo@ustb.edu.cn

Z. Peng et al. (eds.), *12th International Symposium on High-Temperature Metallurgical Processing*, The Minerals, Metals & Materials Series,
https://doi.org/10.1007/978-3-030-92388-4_26

Introduction

Blast furnace is the main reactor for pig iron production, which has the advantages of low cost, high efficiency, and stable operation [1]. Therefore, the blast furnace-converter process accounts for approximately 70% of ironmaking for the steel industry [2]. The blast furnace ironmaking process consumes a large amount of carbon-containing energy and is the sector with the largest CO_2 emission [3]. To overcome this dilemma, some emerging low-carbon technologies for blast furnaces have been developed, such as recycling of metallurgical by-product gas, CO_2 capture, oxygen blast furnaces, and hydrogen-rich gas injection [4–8]. Among them, the technology of top gas circulating oxygen blast furnace combined with CO_2 capture is considered to greatly reduce CO_2 emissions [9]. Owing to the harsh process conditions and equipment limitations, this technology has not yet been used in commercial blast furnaces at this stage. The technology of injecting reducing gas and pulverized coal into a medium oxygen-enriched blast furnace is regarded as a feasible transitional technology [10, 11]. Reducing gas, mainly carbon monoxide and hydrogen, has a wide range of sources and flexible production in industry [12–15].

Pulverized coal injection technology can effectively reduce coke consumption and CO_2 emissions, which is beneficial to economy, environment, and operation. However, the low burnout of pulverized coal in the tuyere and raceway zone will deteriorate the gas permeability of the burden layer, which is not conducive to the stability of the blast furnace[16]. The flow and combustion behavior of pulverized coal have been extensively investigated through experiments and numerical analysis. Babich et al. [17] established a small injection device and studied the combustion behavior of co-injection of oxygen, carbon monoxide, and pulverized coal under a sleeve spray lance. Kim et al. [18] used a laminar flow reactor to study the flame structure, coal particle temperature, and gas phase composition of pulverized coal injection. The influence of the catalysts on the combustion reactivity of coal, including different grades of coal and its char, was investigated using a thermo-gravimetric analyzer [19, 20]. The experimental equipment for pulverized coal combustion provides a good method for pulverized coal combustion, but it is still very different from the physical and chemical environment of the blast furnace tuyere. Numerical simulation is an efficient and low-cost method in engineering applications. Shen et al. [21, 22] established a three-dimensional numerical model with computational fluid dynamic (CFD), investigated the flow and combustion behavior of pulverized coal under various blast and operating conditions, and verified it with a pilot scale test bench. Zhou et al. [23, 24] studied the combustion characteristics of pulverized coal by CFD method in a top gas recycling oxygen blast furnace. CFD modeling of pulverized coal combustion has proven to be a reliable and efficient method.

In this study, a three-dimensional lance–blowpipe–tuyere–raceway model was developed. The effect of the angle of injection reduction on pulverized coal combustion was investigated in a new tuyere of 50% oxygen blast furnace.

Table 1 Governing equations for the gas phase

Mass $\nabla \cdot (\rho U) = \sum_{n_p} \dot{m}$
Momentum $\nabla \cdot (\rho UU) - \mu \cdot [(\mu + \mu_t)(\nabla U + (\nabla U)^T)] = -\nabla \cdot \left(P + \frac{2}{3}\rho k\right) + \sum_{n_p} f_D$
Energy $\nabla \cdot \left[\rho UH - \left(\frac{\lambda}{C_P} + \frac{\mu_t}{\sigma_H}\right)\right] = \sum_{nP} q$
Gas Species $\nabla \cdot \left[\rho UY_i - \left(\Gamma_i + \frac{\mu_t}{\sigma_{Yi}}\right)\right] = W_i$
Turbulent Kinetic Energy $\nabla \cdot \left[\rho Uk - \left(\mu + \frac{\mu_t}{\sigma_k}\right)\nabla k\right] = P_k - \rho\varepsilon$
Turbulent Dissipation Rate $\nabla \cdot \left[\rho U\varepsilon - \left(\mu + \frac{\mu_t}{\sigma_\varepsilon}\right)\nabla \varepsilon\right] = \frac{\varepsilon}{k}(C_1 P_k - C_2 \rho\varepsilon)$

Mathematical Model

In this model, for the sake of simplicity, the flow and reaction of coke, molten slag, and iron in the lower part of the blast furnace were not considered; instead, the focus was on the flow and reaction of the injected fuel. The calculation domains of this model include the lance, blowpipe, tuyere, and raceway, and the following processes: (1) gas-particle flow, (2) heat transfers, and the combustion of (3) coal and (4) the reducing gas.

Governing Equations

The gas phase flow is described using the steady-state Reynolds time-averaged Navier–Stokes equation with a standard k–ε double equation closure. The combined mass conservation equation, momentum equation, and standard k–ε double equation are used to solve the pressure, velocity, turbulent flow energy, and turbulent dissipation rate, among other properties. The gas phase governing equations are summarized in Table 1 [11, 21].

Pulverized coal particles are described by the Lagrangian method, but only the drag force between gas and particles is considered, and the collision between particles is not considered. The particle governing equations are shown in Table 2 [11, 21].

Chemical Reactions

The combustion process of pulverized coal includes preheating, devolatilization, combustion of volatiles ($C_\alpha H_\beta O_\gamma N_\delta$), and conversion (oxidation/gasification) of residual char [11, 22]. The devolatilization process is described by a two-reaction

Table 2 Governing equations for the particle phase

Mass $\frac{\mathrm{dm_P}}{\mathrm{dt}} = -\dot{m}$
Momentum $m_P \frac{\mathrm{du_p}}{\mathrm{dt}} = -f_D, -f_D = \frac{1}{8}\pi d_p^2 \rho C_D \left\|U - U_p\right\| (U - U_p)$
Energy $m_P C_p \frac{\mathrm{dT_p}}{\mathrm{dt}} = h_{i,\mathrm{conv}} A_p \left(T_g - T_p\right) + \sum \frac{\mathrm{d}m_p}{\mathrm{d}t} H_{\mathrm{reac}} + A_p \varepsilon_p \sigma_B \left(T_{\mathrm{rad}}^4 - T_p^4\right)$

Table 3 Reactions of pulverized coal combustion process

	Reaction equations
Homogeneous reactions	$C_\alpha H_\beta O_\gamma N_\delta + O_2 \rightarrow CO + H_2O + N_2$
	$CO + 0.5\,O_2 \rightarrow CO_2$
	$H_2 + 0.5\,O_2 \rightarrow H_2O$
Heterogeneous reactions	$C + CO_2 \rightarrow 2CO$
	$C + H_2O \rightarrow CO + H_2$
	$C + 0.5\,O_2 \rightarrow CO$

competition model. The release of volatiles is as follows:

$$\text{coal} \rightarrow^{k_1} \alpha_1 V M_1 + (1 - \alpha_1) C_1 \quad \text{(low temperature)} \tag{1}$$

$$\text{coal} \rightarrow^{k_2} \alpha_2 V M_2 + (1 - \alpha_2) C_2 \quad \text{(high temperature)} \tag{2}$$

The homogeneous and heterogeneous reactions involved in the combustion process of pulverized coal are shown in Table 3. Homogeneous reaction is simulated by finite rate/eddy dissipation model, while the heterogeneous reaction of the char is described by heterogeneous surface reactions model.

The devolatilization and char conversion ratios, as well as the burnout of particles, are important indicators of the combustion characteristics of pulverized coal. These indicators were calculated based on the ash balance, as follows:

$$\text{Devolatilization Ratio} = 1 - \frac{M m_v}{M_0 m_{v,0}} = 1 - \frac{m_v m_{a,0}}{m_{v,0} m_a} \tag{3}$$

$$\text{Char Conversion Ratio} = 1 - \frac{M m_c}{M_0 m_{c,0}} = 1 - \frac{m_c m_{a,0}}{m_{c,0} m_a} \tag{4}$$

$$\text{Burnout} = 1 - \frac{M(1 - m_a)}{M_0\left(1 - m_{a,0}\right)} = \frac{1 - m_{a,0}/m_a}{1 - m_{a,0}} \tag{5}$$

where M_0 and M are the initial and current mass of the coal particles, respectively; $m_{v,0}$, $m_{c,0}$, and $m_{a,0}$ are the initial volatile, char, and ash contents in the coal particles,

respectively; and m_v, m_c, and m_a represent the current contents of volatile, char, and ash in the coal particles, respectively.

Geometry and Operation Conditions

In this study, based on the heat and material balances of a blast furnace, oxygen contents of 50% in the reducing gas injection process are utilized. In the iron and steel industry, metallurgical by-product gas contains a large amount of hydrogen and carbon monoxide. After removing CO_2 and injecting them into a blast furnace, their chemical energy can be effectively used to reduce coke consumption. Pulverized coal properties and blast furnace operating conditions are listed in Table 4 [11].

The geometric model was based on the lance–blowpipe–tuyere–raceway zone of a 430 m^3 blast furnace. Figure 1 shows the reducing gas injected into the tuyere through the delivery pipe. The diameter of the tuyere is 100 mm, and the depth of the raceway is 780 mm. The injection angles of reducing gas are 30°, 40°, 50°, 60°, and 70°, respectively.

Results and Discussion

Flows and Temperature Distribution

Figure 2 shows the gas velocity and temperature distribution when reducing gas is injected under 50% oxygen blast conditions. As the injection angle increases, the reducing gas has a greater impact on the mainstream hot blast, and its diffusion is better, as shown in Fig. 2a. After the reducing gas is injected, it quickly reacts with the oxygen in the hot blast, leading to the gas temperature to rise rapidly, as shown in Fig. 2b. When the injection angle is 50–70°, the combustion of the reducing gas causes a high temperature zone near the tuyere wall, which may affect the service life of the tuyere in the actual blast furnace.

Figure 3a shows the effect of the reducing gas injection angle on the velocity of coal particles. The mainstream is strongly squeezed under the larger injection angle, which increases the velocity of the mixed gas, thereby increasing the velocity of pulverized coal. The fluctuation of particle velocity in the raceway zone is caused by the whirling motion of the particles. The tuyere kinetic energy (E) has a strong correlation with the activity of the blast furnace hearth, and its formula is:

$$E = \frac{1}{2}mv^2 \tag{4}$$

Table 4 Pulverized coal properties and blast furnace operating conditions

Pulverized coal											
Proximate analysis (wt%)				Ultimate analysis (daf, wt%)				Particle size distribution (μm)			
Moisture	Volatile matter	Ash	Fixed carbon	C	H	O	N	150	80	45	20
1.2	19.02	8.41	71.37	89.16	4.52	4.48	1.84	17%	46%	34%	3%

Reducing gas					
Temperature	H_2 (%)	CO (%)	N_2 (%)	CO_2 (%)	H_2O (%)
298 K	15.3	65.9	16.6	1	1.1

Blast furnace parameters					
Volume	Productivity	Operating pressure	Blast temperature	Coal ratio	Tuyere number
430 m^3	2.5 t/(m^3 d)	303,975 Pa	1473 K	150 kg/tHM	14

Simulation conditions in single tuyere		
Coal flow	Carrier gas (N_2)	Carrier gas temperature
480 kg/h	22 Nm^3/h	360 K
Oxygen content	Blast volume (Nm^3/h)	Reducing gas (Nm^3/h)
50%	1843	1523

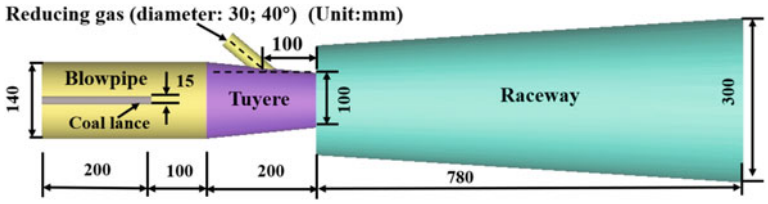

Fig. 1 Geometric dimensions of the three-dimensional numerical model

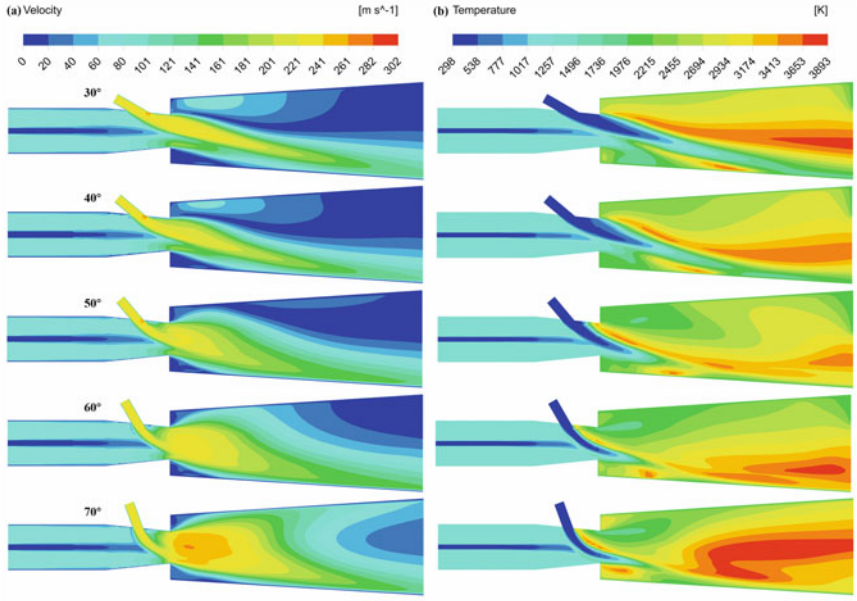

Fig. 2 Computational domain symmetry plane: **a** gas velocity distribution; **b** gas temperature distribution

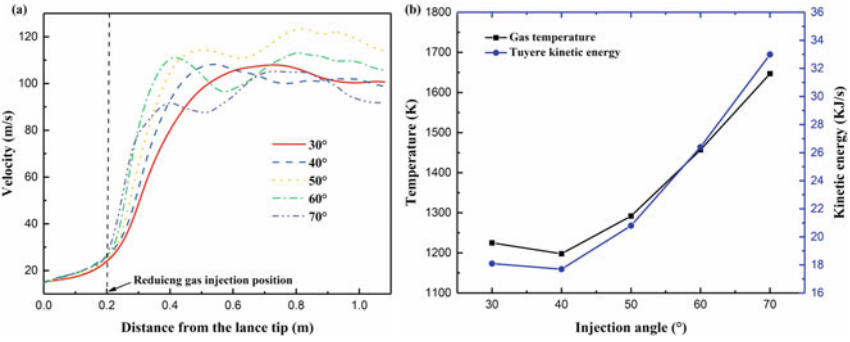

Fig. 3 **a** Average velocity of coal particles at different positions; **b** gas temperature and kinetic energy at the tuyere outlet

m and *v* are the mass flow and velocity of the tuyere outlet, respectively. As shown in Fig. 3b, compared with the injection angle of 30°, the gas temperature and the tuyere kinetic energy under the 40° of injection have a slight decrease in tuyere outlet. This is because the combustion velocity of reducing gas is lower than its diffusion velocity and makes the heat of combustion spread to the raceway, not in the tuyere. However, when injected at 50–70°, the combustion heat of the reducing gas will accumulate in the tuyere, which increases the gas temperature and the tuyere kinetic energy.

Coal Combustion Characteristics

With the increase of the injection angle, the reducing gas is fully mixed and combusted with the main stream of hot gas, which promotes the heating and combustion of the pulverized coal particles. As shown in Fig. 4, when the injection angle is 30°, the temperature of the coal particles at the raceway outlet is 2185 K; and when the injection angle is 70°, the temperature of the coal particles is 2511 K, with an increase of 326 K.

As shown in Fig. 5, under the injection conditions of 30–70°, the pulverized coal devolatilization ratio is more than 94%; at the 50° injection, the devolatilization ratio drops slightly because the 150 μm coal particles diffuse and heat up slowly; as the reducing gas injection angle increases, the char conversion ratio and the coal burnout increase. When the injection angle is 70°, the devolatilization ratio, char conversion ratio, and burnout of pulverized coal reached 100%, 85.3%, and 88.5%, respectively, which will help replace the consumption of coke in the blast furnace.

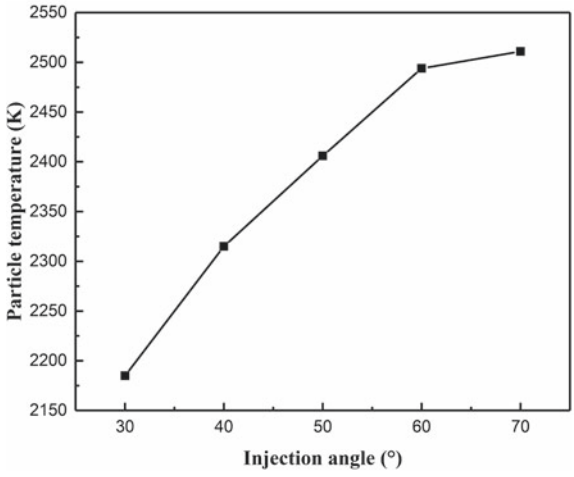

Fig. 4 Average temperature of coal particles at the raceway outlet

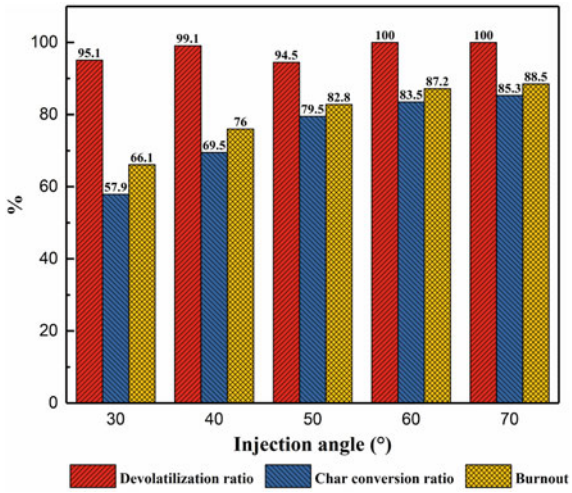

Fig. 5 Devolatilization ratio, carbon conversion ratio, and burnout of pulverized coal at the raceway outlet

Conclusion

In a 50% oxygen blast furnace, the injection of reducing gas through a new tuyere was investigated using a three-dimensional numerical model. As the injection angle of the reducing gas increases, the mixed combustion of coal gas and hot blast is promoted, and the diffusion of pulverized coal is also enhanced, which improves the efficiency of pulverized coal combustion. Compared with the injection at 30°, the tuyere kinetic energy is greatly increased during the injection at 70°, and the coal burnout is also increased by 22.4%, which is conducive to the operation of the blast furnace and reduces the coke ratio. However, the combustion of the reducing gas increases the gas temperature near the tuyere wall, which requires enhanced cooling to prevent damage to the tuyere.

Acknowledgements The authors gratefully acknowledge the financial support of the National Natural Science Foundation of China (No. U1960205) and State Key Laboratory of Advanced Metallurgy (No. 41618029), University of Science and Technology Beijing.

Conflict of Interest The authors declare that they have no conflict of interest.

References

1. Kuang S, Li Z, Yu A (2018) Review on modelling and simulation of blast furnace. Steel Res Int 89(1):1700071
2. Tatsuro A, Michitaka S, Taihei N, Koichi T (2016) Evolution of blast furnace process toward reductant flexibility and carbon dioxide mitigation in steel works. ISIJ Int 56(10):1681–1696

3. Zhang Q, Xu J, Wang Y, Hasanbeigi A, Zhang W, Lu H (2018) Comprehensive assessment of energy conservation and CO_2 emissions mitigation in China's iron and steel industry based on dynamic material flows. Appl Energ 209(JAN.1):251–265
4. Nogami H, Yagi J, Kitamura S (2006) Analysis on material and energy balances of ironmaking systems on blast furnace operations with metallic charging, top gas recycling and natural gas injection. ISIJ Int 46(12):1759–1766
5. Ziebik A, Lampert K, Szega M (2008) Energy analysis of a blast-furnace system operating with the COREX process and CO_2 removal. Energy 33(2):199–205
6. Kuramochi T, Ramírez A, Turkenburg W, Faaij A (2012) Comparative assessment of CO_2 capture technologies for carbon-intensive industrial processes. Prog Energy Combust Sci 38(1):87–112
7. Zhang W, Zhang J, Xue Z (2017) Exergy analyses of the oxygen blast furnace with top gas recycling process. Energy 121(FEB.15):135–146
8. Yilmaz C, Wendelstorf J, Turek T (2017) Modeling and simulation of hydrogen injection into a blast furnace to reduce carbon dioxide emissions. J Clean Prod 154(JUN.15):488–501
9. Jin P, Jiang Z, Bao C, Hao S, Zhang X (2015) The energy consumption and carbon emission of the integrated steel mill with oxygen blast furnace. Resour Conserv Recycl 561–574
10. Zhang W, Xue Z, Zhang J, Wang W, Cheng C, Zou Z (2017) Medium oxygen enriched blast furnace with top gas recycling strategy. J Iron Steel Res Int 24(8):778–786
11. Peng X, Wang J, Li C, Zuo H, Wang G, She X, Xue Q (2021) Influence of reducing gas injection methods on pulverized coal combustion in a medium oxygen-enriched blast furnace. JOM 73(10):2929–2937
12. Song X, Guo Z (2005) A new process for synthesis gas by co-gasifying coal and natural gas. Fuel 84(5):525–531
13. Ouyang Z, Guo Z, Duan D, Song X, Yu X (2005) Experimental study of coal gasification coupling with natural gas autothermal re-forming for synthesis gas production. Ind Eng Chem Res 44(2):279–284
14. Song X, Guo Z (2006) Technologies for direct production of flexible h2/co synthesis gas. Energ Convers Manage 47(5):560–569
15. Wang M, Wang Z, Guo Z (2010) Water electrolysis enhanced by super gravity field for hydrogen production. Int J Hydrogen Energ 35(8):3198–3205
16. Dong X, Zhang S, Pinson D, Yu A, Zulli P (2004) Gas-powder flow and powder accumulation in a packed bed ii: numerical study. Powder Technol 149(1):10–22
17. Babich A, Senk D, Born S (2014) Interaction between co-injected substances with pulverized coal into the blast furnace. ISIJ Int 54(12):2704–2712
18. Kim J, Kim R, Kim G, Jeon C (2016) Effect of coal fragmentation on PCI combustion zone in blast furnace. Exp Thermal Fluid Sci 79:266–274
19. Gong X, Guo Z, Wang Z (2009) Variation of char structure during anthracite pyrolysis catalyzed by Fe_2O_3 and its influence on char combustion reactivity. Energ Fuels 23(9):4547–4552
20. Gong X, Guo Z, Wang Z (2010) Reactivity of pulverized coals during combustion catalyzed by CeO_2 and Fe_2O_3. Combust Flame 157(2):351–356
21. Shen Y, Guo B, Yu A, Zulli P (2009) A three-dimensional numerical study of the combustion of coal blends in blast furnace. Fuel 88(2):255–263
22. Shen Y, Yu A, Austin P, Zulli P (2012) CFD study of in-furnace phenomena of pulverised coal injection in blast furnace: effects of operating conditions. Powder Technol 223:27–38
23. Zhou Z, Xue Q, Tang H, Wang G, Wang J (2017) Coal combustion behavior in new ironmaking process of top gas recycling oxygen blast furnace. JOM 69(10):1790–1794
24. Zhou Z, Yi Q, Wang R, Wang G, Ma C (2020) Numerical investigation on coal combustion in ultralow CO_2 blast furnace: effect of oxygen temperature. Processes 8(7):877

Removal of Arsenic from Molten Bearing Steel by Adding Rare Earth Lanthanum

Peng Yu, Hongpo Wang, Xiaoqing Zhou, Yu Wang, and Xuewei Lv

Abstract Adding rare earth elements is a potential control method to remove residual elements from molten steel. Influence factors of adding lanthanum to remove arsenic from the molten GCr15 bearing steel have been experimentally studied. The results show that lanthanum addition, the melting temperature, and the initial sulfur content significantly affected the removal of arsenic from molten steel. The reaction of lanthanum with sulfur and arsenic occurred within 4 min after its addition. Reactions between lanthanum and the crucible inhibited the arsenic removal. Increasing the amount of lanthanum and lowering the temperature both are beneficial to arsenic removal from molten steel. Fierce competitions existed among the lanthanum's arsenic removal reaction, the desulfurization reaction, and the lanthanum-crucible reactions. For arsenic removal, the initial sulfur content in molten steel must be controlled within an appropriate range.

Keywords Rare earth · Bearing steel · Residual element · Cleanliness

Introduction

The continuous recycling of scrap steel increases the content of copper, tin, arsenic, and other residual elements in steel. These elements seriously endanger the quality and performance of steel products, such as the hot workability and the temper brittleness [1]. The control methods of residual elements in steel can be divided into two categories: reducing their absolute content [2, 3] and change their existing forms to minimize their segregation [4, 5]. Except for the enrichment caused by scrap steel recycling, the utilization of low-grade iron ore is also an essential factor in increasing

P. Yu · H. Wang (✉) · X. Zhou · Y. Wang
College of Materials Science and Engineering, Chongqing University, Chongqing 400044, China
e-mail: wanghp@cqu.edu.cn

X. Lv
The State Key Laboratory of Mechanical Transmissions, Chongqing University, Chongqing 400044, China

Z. Peng et al. (eds.), *12th International Symposium on High-Temperature Metallurgical Processing*, The Minerals, Metals & Materials Series,
https://doi.org/10.1007/978-3-030-92388-4_27

the content of residual elements in steel. China has plenty of arsenic-containing iron ore, and the accumulation of arsenic is particularly prominent.

As the quality requirements for steel products increase, the content of residual elements has become an indicator that must be seriously considered. For example, high-carbon chromium-bearing steels require that the total content of arsenic, tin, and antimony cannot be higher than 0.075%, and the arsenic content cannot be higher than 0.040%. Advanced international manufacturers generally control the arsenic content in bearing steel below 0.0050%. The quality control of bearing steel has been focused on reducing the oxygen content, modifying the size and uniformity of inclusions and carbides, as well as their impact on the performances of products. Research on the hazards of residual elements is rarely mentioned [6–8]. Improving cleanliness is undoubtedly one of the effective means to improve the quality and performance of bearing steel, but it is very hard during the current steelmaking process. The addition of rare earth elements (REEs) to steel plays a vital role in purifying molten steel [9, 10], modifying inclusions [8, 11], and microalloying [12, 13]. Our research team proved that the addition of lanthanum could modify the existing state of residual element arsenic in steel and has great potential for arsenic removal from molten steel [14, 15].

The purpose of this research is to take GCr15 bearing steel as the research object to explore the influence of lanthanum addition, initial sulfur content, and melting temperature on the removal of arsenic from the molten bearing steel.

Materials and Methods

This study used GCr15 bearing steel rods taken from a Chinese iron and steel company as raw materials. Table 1 shows the chemical compositions of the rods. The initial components of molten steel were controlled by adding arsenic particles, FeS powders, and metal lanthanum. A 15 kW intermediate frequency induction furnace was used for steelmaking under argon protection, and the mass of molten steel for each furnace was about 600 g. The raw bearing steel rods were placed in an alumina crucible. When the temperature was raised to the target temperature, the arsenic particles and FeS were added after the rods were melted entirely. Then the metal lanthanum was added after another 10 min. Then, quartz tubes with an inner diameter of 4 mm were used to extract samples from molten steel, followed by water quenching. About 0.75 g of each sample was cut and dissolved in a mixed solution of

Table 1 Chemical compositions of the raw material (mass%)

Elements	C	Si	Mn	P	S	Cr	Al	O	As
Content	0.96	0.23	0.33	0.014	0.002	1.49	0.007	0.0009	0.002

hydrochloric acid and nitric acid; then, the solution was diluted volume to 50 ml. An inductively coupled plasma optical emission spectrometer (Optima 8000, Waltham, MA, USA) was used to detect the content of lanthanum and arsenic in the sample solution.

Results

Effect of Lanthanum Addition on Arsenic Removal

Figure 1 shows the change of arsenic content in molten steel with an initial sulfur content of 0.01% and different lanthanum additions at 1550 °C. As shown in the figure, with the addition of 0.10 and 0.15% La, the arsenic content in the molten steel decreased first and then increased, while the addition of 0.05% La had a more negligible effect on the arsenic content. Previous work showed that lanthanum would react with arsenic and sulfur to form La–S–As compounds after consuming most oxygen in the molten steel, and most La–S–As would float up to the surface of the molten steel or be captured by the crucible wall, thereby reducing the arsenic content [3, 14]. In this work, samples were firstly taken 1 min after adding lanthanum to molten steel. The arsenic content reached a minimum 3 to 4 min after lanthanum was added. It can be predicted that if the lanthanum in the molten steel did not react with the alumina crucible, the removal velocity of arsenic would be faster, and the time for the arsenic content to reach the lowest value would be shortened.

Figure 2 shows the changes of lanthanum and aluminum in molten steel with different lanthanum additions and initial sulfur content of 0.01% under 1550 °C. The lanthanum content in the molten steel decreased gradually due to the reaction between lanthanum and the crucible, which broke the reaction equilibrium of lanthanum, sulfur, and arsenic to generate La–S–As, resulting in the increase of arsenic content.

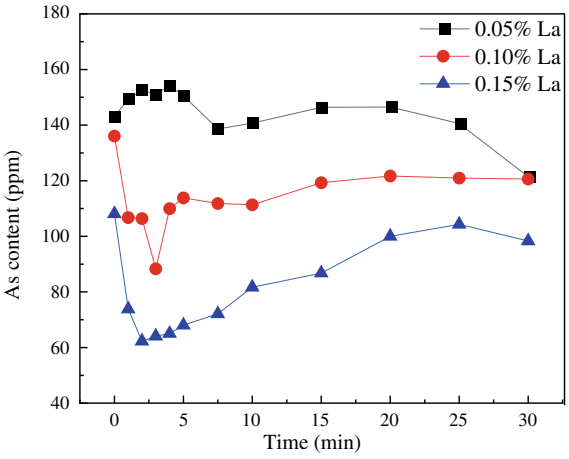

Fig. 1 Arsenic content changes in molten steel with initial 0.01% S and different La additions during smelting at 1550 °C

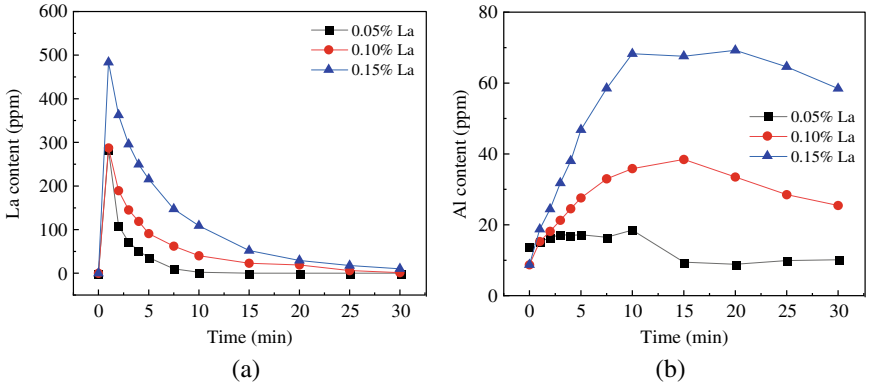

Fig. 2 Component concentrations in molten steel with initial 0.01% S and different La additions at 1550 °C: **a** La content and **b** Al content

Further, the lanthanum was almost exhausted 30 min after its addition. At the same time, the aluminum content first increased and then decreased, and its inflection point was about 10 to 15 min after the lanthanum addition, which is significantly behind the inflection point where the arsenic content first reduced and then increased (3–4 min after the lanthanum addition). It was noted that the initial acid-soluble content of Al in the raw bearing steel rod was around 50 ppm, while it was less than 20 ppm in the molten steel before the lanthanum addition. This is because part of the aluminum was consumed by oxygen pollution caused by re-melting during the smelting period before adding lanthanum. After lanthanum was added to molten steel, the significant increase in Al content was attributed to the lanthanum-crucible reactions. A fierce competition occurred between the reaction of La, S, and As to form La–S–As and the lanthanum-crucible reactions.

Effect of Melting Temperature on Arsenic Removal

Figure 3 shows the change of arsenic content in molten steel with an initial sulfur content of 0.01% and different lanthanum additions at different temperatures. As shown in the figure, compared to smelting at 1550 °C, lowering the temperature to 1500 °C improved the effect of lanthanum on removing arsenic from molten steel. Even adding 0.05% La can remove part of arsenic from molten steel in the first 5 min. The potential maximum of arsenic removal rate calculated according to the arsenic content in the molten steel before adding lanthanum and the lowest arsenic content after adding lanthanum is shown in Fig. 4. The results show that the arsenic removal rate reached the maximum of 56.6% with 0.15% La addition. It can be predicted that if lanthanum did not react with the crucible, the arsenic removal rate would increase further.

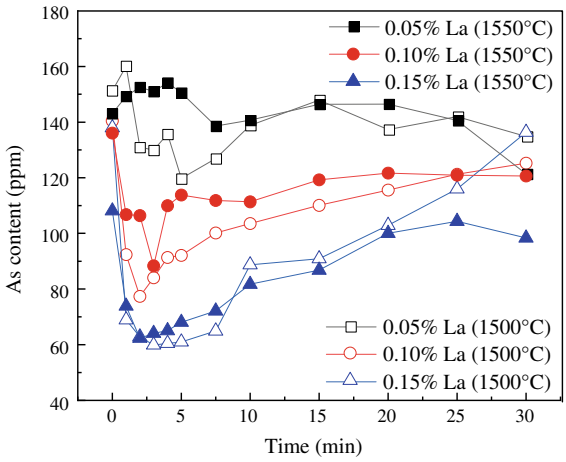

Fig. 3 Arsenic content changes in molten steel with initial 0.01% S and different La additions during smelting at different temperatures

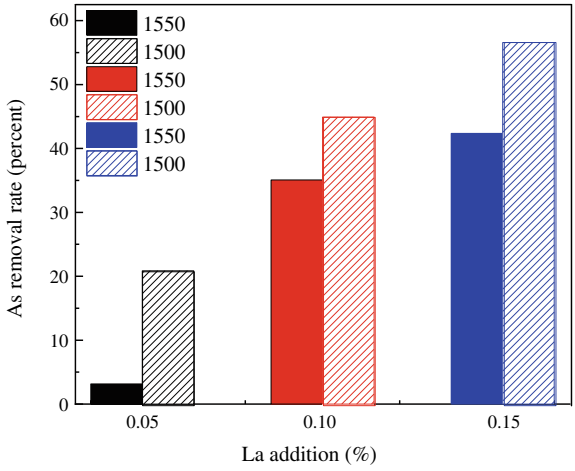

Fig. 4 Effect of lanthanum addition on the potential maximum of arsenic removal rate at different melting temperatures

Effect of Initial Sulfur Content on Arsenic Removal

Figure 5 shows the change of arsenic content in molten steel with 0.15% La addition and different initial sulfur content at 1500 °C. As shown in the figure, when the initial sulfur content was 0.010 and 0.015%, the arsenic removal effect of lanthanum was significantly higher than that of molten steel with an initial sulfur content of 0.005%. However, it does not show a significant monotonic increasing relationship with the initial sulfur content. The literature indicated that La and As could not react to generate LaAs compounds before solidification, which were generally generated during solidification and could not remove arsenic from molten steel [5]. In this work, the potential maximum of arsenic removal rates at the initial sulfur content of 0.010 and 0.015% were close, indicating that the concentration of La and S in the molten

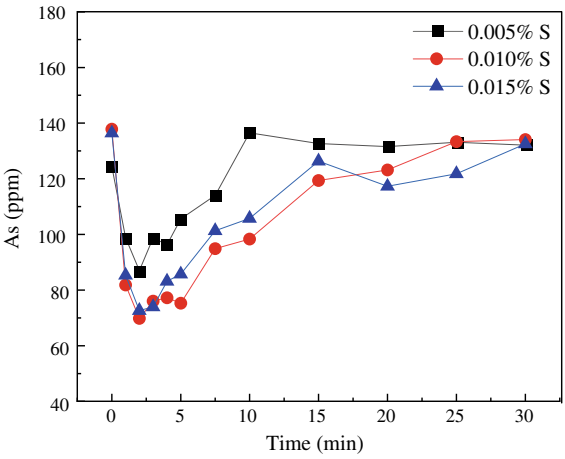

Fig. 5 Arsenic content changes in molten steel with different initial S and 0.15% La addition during smelting at 1500 °C

steel has a proper combination, and it needs to be further studied in combination with accurate thermodynamic data.

Discussion

The mechanism of arsenic removal by adding La is that La reacts with S and As to form La–S–As compounds that float up to the surface of the molten steel or are captured by the wall of the smelting vessel, so as to reduce the As content in the molten steel. The reaction formula can be expressed as Eq. (1). The removal of As is affected by the amount of La-added and the initial S content. Since La and S can react to generate LaS, as shown in Eq. (2), a competition exists between reaction Eqs. (1) and (2), which significantly affects the effective La content for the arsenic removal, indicating that increasing the initial S content does not necessarily increase the arsenic removal effect of La. On the one hand, to remove arsenic, a certain amount of S is necessary; on the other hand, to reduce the formation of LaS, the S content must be controlled within a specific range.

$$x[\mathrm{La}] + y[\mathrm{S}] + z[\mathrm{As}] = \mathrm{La}_x\mathrm{S}_y\mathrm{As}_z \tag{1}$$

$$[\mathrm{La}] + [\mathrm{S}] = \mathrm{LaS} \tag{2}$$

It is worth noting that rare earth elements will react with refractory materials such as alumina and magnesia [16, 17]. The lanthanum-crucible reactions can be shown in Eqs. (3)–(5). These reactions will consume La and reduce its arsenic removal effect.

$$[\mathrm{La}] + (\mathrm{Al_2O_3})_{\mathrm{crucible}} = (\mathrm{LaAlO_3})_{\mathrm{inclusion}} + [\mathrm{Al}] \tag{3}$$

$$2[La] + (Al_2O_3)_{crucible} = (La_2O_3)_{inclusion} + 2[Al] \quad (4)$$

$$2[La] + 3(MgO)_{crucible} = (La_2O_3)_{inclusion} + 3[Mg] \quad (5)$$

The measurement that can avoid the reactions between rare earth elements in the molten steel and the refractory material is to use the corresponding rare earth oxide as the refractory material, which is unrealistic in industrial production. It is also not easy to achieve even on a laboratory scale because it is challenging to prepare crucibles with nearly pure rare earth oxides as raw materials. The good news is that, in industrial production, the contact area between per unit mass of molten steel and the refractory material is significantly smaller than the value during the laboratory-scale steelmaking. When the melting scale is tens or hundreds of tons, the REE-refractory reactions are less fierce. It is expected to be prominent for arsenic removal from molten steel by adding REEs. Related research results will be published in future work.

Conclusions

The lanthanum addition, melting temperature, and initial sulfur content significantly affected the removal of arsenic from molten steel. The reaction of La–S–As formation mainly occurred 3 to 4 min after La addition. Avoiding the reaction between lanthanum and the crucible will increase the arsenic removal rate. Increasing La addition and decreasing steelmaking temperature are beneficial to arsenic removal from molten steel. Fierce competitions exist among the lanthanum's arsenic removal reaction, the desulfurization reaction, and the lanthanum-crucible reactions. For arsenic removal, the initial sulfur content in molten steel must be controlled within an appropriate range.

Acknowledgements The authors acknowledge the financial support from the National Natural Science Foundation of China (Project No. 51704051).

References

1. Garcia CI, Ratz GA, Burke MG, DeArdo AJ (1985) Reducing temper embrittlement by lanthanide additions. JOM 37(9):22–28
2. Wang H, Jiang S, Yu P, Bai B, Sun L, Wang Y (2020) Distribution of arsenic inclusions in rare earth steel ingots. Metals 10(1):146
3. Wang H, Yu P, Jiang S, Bai B, Sun L, Wang Y (2020) Evolution of inclusions in steelmaking process of rare earth steels containing arsenic with alumina crucibles. Metals 10(2):275

4. Xin W, Song B, Huang C, Song M, Song G (2015) Effect of arsenic content and quenching temperature on solidification microstructure and arsenic distribution in iron-arsenic alloys. Int J Miner Metall Mater 22(7):704–713
5. Xin W, Song B, Song M, Song G (2015) Effect of cerium on characteristic of inclusions and grain boundary segregation of arsenic in iron melts. Steel Res Int 86(12):1430–1438
6. Ma W, Bao Y, Wang M, Zhao L (2014) Effect of Mg and Ca treatment on behavior and particle size of inclusions in bearing steels. ISIJ Int 54(3):536–542
7. Yang C, Luan Y, Li D, Li Y (2019) Effects of rare earth elements on inclusions and impact toughness of high-carbon chromium bearing steel. J Mater Sci Technol 35(7):1298–1308
8. Wang X, Li G, Liu Y, Wang F, Wang Q (2021) Cerium addition effect on modification of inclusions, primary carbides and microstructure refinement of H13 die steel. ISIJ Int 61(5):1506–1513
9. Chen L, Ma X, Jin M, Wang J, Long H, Mao T (2015) Beneficial effect of microalloyed rare earth on S segregation in high-purity duplex stainless steel. Metall Mater Trans A 47(1):33–38
10. Wang H, Bao Y, Zhao M, Wang M, Yuan X, Gao S (2019) Effect of Ce on the cleanliness, microstructure and mechanical properties of high strength low alloy steel Q690E in industrial production process. Int J Miner Metall Mater 26(11):1372–1384
11. Wang Y, Liu C (2021) Agglomeration characteristics of various oxide inclusions in molten steel containing rare earth element under different deoxidation conditions. ISIJ Int 61(5):1396–1403
12. Liu H, Huang J, Wang C, Xia S, Ge W, Liu Q, Su Y, Gao Z, Zhao S, Du C (2021) Effects of grain boundaries and nano-precipitates on helium bubble behaviors in lanthanum-doped nanocrystalline steel. Scr Mater 200:113900
13. Dong F, Venezuela J, Li H, Shi Z, Zhou Q, Chen L, Chen J, Du L, Atrens A (2021) Effect of vanadium and rare earth microalloying on the hydrogen embrittlement susceptibility of a Fe–18Mn–0.6C TWIP steel studied using the linearly increasing stress test. Corros Sci 185:109440
14. Wang H, Jiang S, Yu P, Sun L, Wang Y (2020) Effect of steel-refractory reactions on removal of arsenic from molten steel with lanthanum additions. ISIJ Int 60(11):2316–2324
15. Wang H, Xiong L, Zhang L, Wang Y, Shu Y, Zhou Y (2017) Investigation of RE-O-S-As inclusions in high carbon steels. Metall Mater Trans B 48(6):2849–2858
16. Kwon SK, Park JS, Park JH (2015) Influence of refractory-steel interfacial reaction on the formation behavior of inclusions in Ce-containing stainless steel. ISIJ Int 55(12):2589–2596
17. Kwon SK, Kong YM, Park JH (2014) Effect of Al deoxidation on the formation behavior of inclusions in Ce-added stainless steel melts. Met Mater Int 20(5):959–966

Observation on Clogging Behavior of Submerged Entry Nozzle of Al–Killed Steels

Fenggang Liu, Qiuyue Zhou, Lifeng Zhang, and Ying Ren

Abstract To better understand the clogging mechanism of the submerged entry nozzle, clogging materials were analyzed using scanning electron microscopy and energy dispersive spectrometer. The clogging material was divided into several layers, including the alumina inclusion layer, solidified steel layer, and nozzle matrix layer. Due to the difference in the morphology and composition of oxides, observed clogging materials presented different morphologies. Steel droplets were observed at the interface between the nozzle and the clogging materials, indicating that insufficient preheating may lead to the solidification of the molten steel. Alumina inclusions were easy to adhere to the solidified steel layer, which was the starting of the nozzle clogging behavior. The alumina inclusions continuously collided and sintered, resulting in the formation of the alumina inclusion layer. Besides, the reoxidation might also lead to the clogging of the submerged entry nozzle of Al-killed steels.

Keywords Clogging · Submerged entry nozzle · Al-killed steels

Introduction

The nozzle clogging is a very common phenomenon during the continuous casting process of Al–killed steels. During the submerged entry nozzle (SEN) baking process, the oxidation and decarbonization of the inner surface of nozzles generated gaps, which were conducive to the nozzle/steel reaction and the liquid inclusion formation. Meanwhile, it promoted the adhesion of Al_2O_3, inclusions. The lower preheating

F. Liu · Q. Zhou · Y. Ren
School of Metallurgical and Ecological Engineering, University of Science and Technology Beijing, Beijing 100083, China

L. Zhang (✉)
State Key Laboratory of Metastable Materials Science and Technology, Yanshan University, Qinhuangda 066004, Hebei, China
e-mail: zhanglifeng@ysu.edu.cn

Z. Peng et al. (eds.), *12th International Symposium on High-Temperature Metallurgical Processing*, The Minerals, Metals & Materials Series,
https://doi.org/10.1007/978-3-030-92388-4_28

temperature of nozzles was conducive to the solidification of steel droplets. Inclusions in the molten steel continuously adhered, sintered, and matured in the high-temperature molten steel, leading to the nozzle clogging. The Al–Ti–O inclusion was common inclusions in the Ti–Al-killed steel [1–9]. Due to the better wettability of the Al–Ti–O inclusion with the liquid steel, it was more difficult to enter the slag from the liquid steel. The better wettability of the Al–Ti–O inclusion with refractory promoted the adhesion of inclusions on the inner wall of the nozzle during the steel flowing through the nozzle [7, 9–11]. Solid clogging materials were mainly formed from the oxide inclusions such as Al_2O_3 and Al–Ti–O in liquid steel [12]. When the molten steel in the nozzle was oxidized, elements of Ti, Fe, and Al in the steel were oxidized to form FetO–Al_2O_3–TiO_x liquid oxides, which exhibited good wettability to both steel and refractory materials. Liquid oxides of Fe_tO–Al_2O_3–TiO_x were easy to adhere to the inner wall of the nozzle as well as steel droplets [9, 13]. The density of Al–Ti–O clusters was much higher than that of loose Al_2O_3 clusters [14]. Lee et al. [15] proposed that the reoxidation process of the molten steel leading to the generation of oxide clogging materials on the surface of the nozzle wall. The FeO-rich liquid layer first formed on the wall, and then FeO and SiO_2 in the liquid layer were reduced by [Al] in the liquid steel to form a solid inclusion layer rich in Al_2O_3. As the temperature decreased, the steel droplet changed from liquid to solid state and sintered with the surrounding clogging material. Lee et al. [13] reported CaO-containing nozzle increased the clogging during the continuous casting process. The formed Al_2O_3 was produced by the deoxidation in the molten steel and is the cause of the nozzle clogging [16–18]. In the turbulent flow, smaller inclusions were easier to adhered on the inner wall of the nozzle [19]. When the diameter of the inclusion was less than 15 μm, the probability of the clogging material formation on the nozzle inner wall increased significantly [20]. Inclusions generated by the reoxidation of the molten steel were one of the main sources of clogging materials.

Experimental

The Al-killed steel without calcium treatment was teemed from a ladle into a tundish and then poured into two strands continuous mold. Slag powders were added to the tundish to cover the surface of the molten steel at cast start. The composition of the Al-killed steel is listed in Table 1. An used SEN as shown in Fig. 1 was analyzed to investigate the clogging behavior. To investigate the clogging mechanism of the SEN of Al–killed steels. The clogging material was taken from the inwall of the SEM.

Table 1 Main chemical composition of Al-killed steels

C	Si	Mn	P	S	T.Al	[Al]	T.Ti	T.N	T.O
0.0016	0.004	0.14	0.01	0.005	0.047	0.045	0.066	0.0023	0.0021

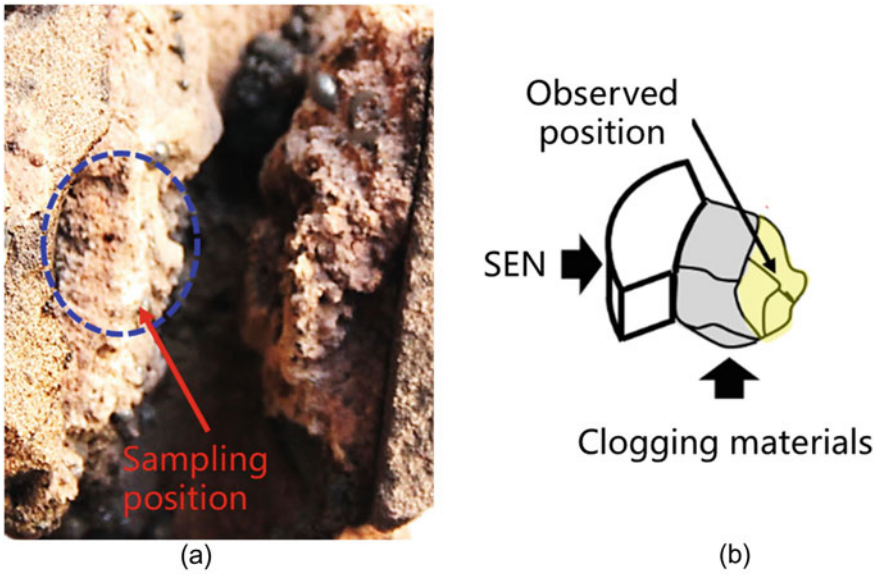

Fig. 1 Image and schematic of the clogging materials on the SEN

The SEM–EDX was applied to the identification of inclusions and phases in nozzle clogging materials.

The Observation of Clogging Materials on the SEN

The local three-dimensional morphology o clogging materials is shown in Fig. 2. Figure 2a and b shows clogging materials containing the molten steel and the nozzle wall. There was an obvious bonding phenomenon between clogging materials in the solidified steel layer. Black Al_2O_3 particles bonded each other, and white FeO_x–Al_2O_3 particles adhered black Al_2O_3. The structure of clogging materials was relatively dense. A small piece of white angular FeO_x–Al_2O_3 sticked on the inner surface of clogging materials. There was a complex inclusion with black and white phases, indicating that FeO_x–Al_2O_3, acted as a binder, bonded Al_2O_3 particles or Al_2O_3 clusters together to form larger inclusion clusters. According to the difference of two-dimensional morphology and composition of clogging materials, clogging materials from the nozzle side to the steel side were divided into the following sequence: smaller steel droplets and the Al_2O_3 complex layer. The slender Al_2O_3 and large size solidified steel complex network layer, the middle layer of single Al_2O_3 particles distributed in large size solidified steel, and the layer containing large size solidified steel and FeO_x–Al_2O_3 in plate shape. There was a thin layer of FeO_x–Al_2O_3 at the edge of the solidified steel.

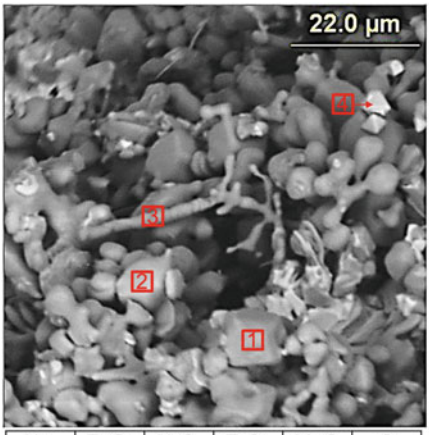

No.	FeO_x	Al_2O_3	ZrO_2	MgO	C
1	0.58	97.60	1.52	0	0.30
2	0.88	96.14	1.45	0	1.53
3	1.16	96.42	1.51	0	0.91
4	23.85	66.86	0	5.97	3.32

(a)

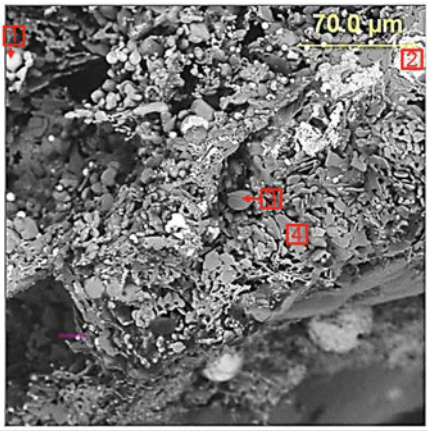

No.	FeO_x	ZrO_2	Al_2O_3	CaO	TiO_x	C
1	0	1.46	95.59	0	0.24	2.70
2	85.94	0	2.01	0	0	11.50
3	8.06	0	10.46	0	0	81.48
4	1.68	1.18	78.95	6.41	1.02	10.76

(b)

Fig. 2 Original morphology and composition of clogging materials: **a** contacting the molten steel and **b** contacting the nozzle wall

Figure 3 shows that there was a thin FeO_x–Al_2O_3 layer at the edge of the steel, containing several layers. Clogging materials closed to the solidified steel and away from the solidified steel layer were in dark and lighter colors. In Fig. 3a and b, the dark color phase was mainly Al_2O_3, while the light one was mainly FeO_x-containing

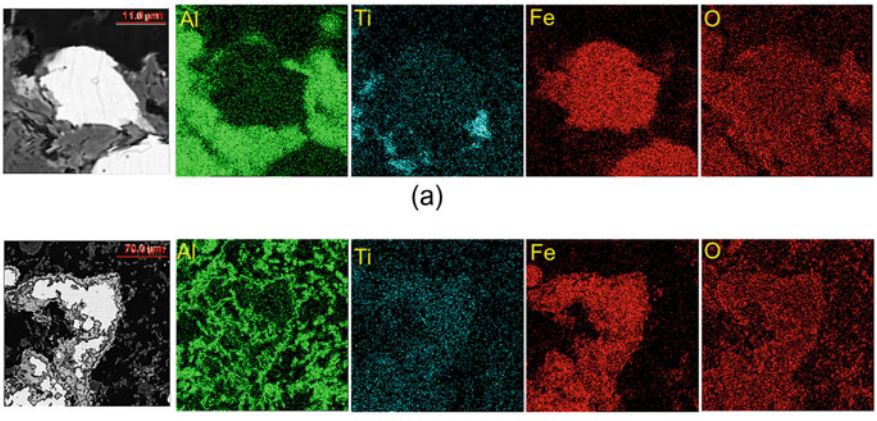

Fig. 3 Elemental mapping results of clogging materials on SEN

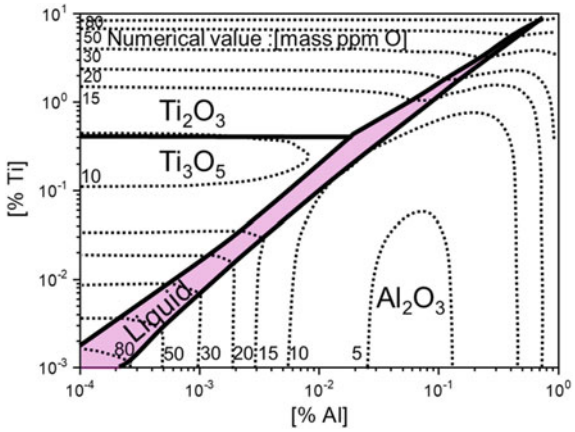

Fig. 4 Stability diagram of inclusions in Fe–O–Al–Ti melts

oxides. The FeO_x–Al_2O_3 thin layer on the edge grew and sintered together with a small distance between the condensed steels. There were Al_2O_3 inclusions adhered on the outside of the FeO_x–Al_2O_3 thin layer.

Thermodynamic Calculation

The stability diagram of Al–Ti–O inclusions at 1823 K was calculated using FactSage with FactPS, FToxid, and FTmisc databases, as shown in Fig. 4. The typical inclusion in equilibrium was Al_2O_3 in the current molten steel, while Al–Ti–O inclusions generated in steel during the reoxidation process. Effects of interfacial tension and melt composition on the oxide nucleation in Fe–O–Al system at 1809 K are shown in Fig. 5 [21]. The interfacial tension (σ) between oxide and melt was 10^3 ergs cm^{-2}. When the dissolved aluminum in steel was 0.04%, formed inclusions were mainly $FeO{\cdot}Al_2O_3$ in the molten steel with 10–10,000 ppm oxygen, while there were FeO_x inclusions generated in steel with 1000–10,000 ppm oxygen.

Conclusions

(1) There was a complex inclusion with black and white phases, indicating that FeO_x–Al_2O_3, acted as a binder, bonded Al_2O_3 particles or Al_2O_3 clusters together to form larger inclusion clusters.
(2) There was a thin FeO_x–Al_2O_3 layer at the edge of the steel, containing several layers. Clogging materials closed to the solidified steel and away from the solidified steel layer were in dark and lighter colors.

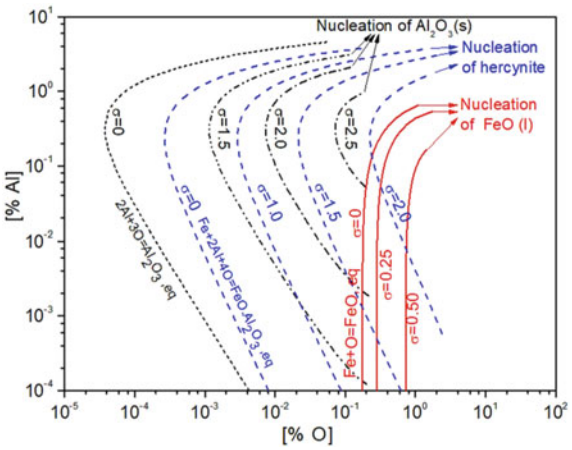

Fig. 5 Effects of interfacial tension and melt composition on the inclusion nucleation in Fe–O–Al melts [21]

(3) The typical inclusion in equilibrium was Al_2O_3 in the current molten steel, while Al–Ti–O inclusions generated in steel during the reoxidation process.

Acknowledgements The authors are grateful for support from the National Nature Science Foundation of China (Grant No. U1860206, No. 51725402), the S&T Program of Hebei (Grant No. 20311004D, 20591001D), the High Steel Center (HSC) at Yanshan University, and Beijing International Center of Advanced and Intelligent Manufacturing of High Quality Steel Materials (ICSM) and the High Quality Steel Consortium (HQSC) at University of Science and Technology Beijing (USTB), China.

References

1. Sun MK, Jung IH, Lee HG (2008) Morphology and chemistry of cxide Inclusions after Al and Ti complex deoxidation. Met Mater Int 14(6):791
2. Lee JH, Kim SK, Kang MH, Kang YB (2018) Interfacial reaction between ultra low C steel and gas generated from refractory material used for submerged entry nozzle for continuous casting. BHM Berg Hüttenmänn Monatsh 163(1):18–22
3. 唐树平 (2014) Ti-IF 钢水口堵塞分析. 炼钢. 30(3):20–23
4. Kaushik P, Kruse D, Ozgu M (2008) Assessment of castability issues in interstitial-free (IF) steels. Rev de Métallurgie 105(2):92–101
5. Matsuura H, Wang C, Wen G, Sridhar S (2007) The transient stages of snclusion svolution during Al and/or Ti additions to molten iron. ISIJ Int 47(9):1265–1274
6. Wang C, Matsuura H, Kikuchi N, Wen G, Sridhart S (2008) Experimental simulation of the role of Ti on transient reactions in Al–killed Fe-melts. Rev De Métallurgie 105(1):22–32
7. Basu S, Choudhary SK, Girase NU (2004) Nozzle clogging behaviour of Ti-bearing Al–killed ultra low carbon steel. ISIJ Int 44(10):1653–1660
8. Cui H, Bao Y, Wang M, Wu W (2010) Clogging behavior of submerged entry nozzles for Ti-bearing IF steel. Int J Miner Metall Mater 17(2):154–158
9. Lee JH, Kang MH, Kim SK, Kang YB (2018) Oxidation of Ti added ulc steel by CO gas simulating interfacial reaction between the steel and sen during continuous casting. ISIJ Int 58(7):1257–1266

10. Ogibayashi S (1995) Mechanism and countermeasure of alumina buildup on submerged nozzle in continuous casting. Taikabutsu Overseas 15(3):3–14
11. Sasai K, Mizukami Y (2002) Mechanism of inclusion buildup on submerged entry nozzle during continuous casting of calcium-treated molten steel. Refractories 54:504–514
12. 李朋欢 (2011) IF钢冶炼关键技术及碳、氧和夹杂物行为研究. 北京科技大学
13. Lee JH, Kang MH, Kim SK, Kim J, Kim MS, Kang YB (2019) Influence of Al/Ti ratio in Ti-ulc steel and refractory components of submerged entry nozzle on formation of clogging deposits. ISIJ Int 59:749–758
14. Wang D, Jiang M, Matsuura H, Tsukihashi F (2014) Dynamic evolution of inclusions in Ti-bearing Al-deoxidized molten irons at 1873 K. Steel Res Int 85(1):16–25
15. Lee YS, Jung SM, Min DJ (2014) Interfacial reaction between Al_2O_3–C refractory and Al killed steel. Ironmak Steelmak 41(4):286–291
16. 张立峰 (2016) 连铸过程夹杂物控制. 连铸. 41(1)
17. Tehovnik F, Burja J, Arh B, Knap M (2015) Submerged entry nozzle clogging during continuous casting of Al-killed steel. Metalurgija -Sisak then Zagreb- 54(2):371–374
18. Deng Z, Zhu M, Zhou Y, Du S (2016) Attachment of alumina on the wall of submerged entry nozzle during continuous casting of Al–killed steel. Metall Mater Trans B 47(3):2015–2025
19. Wilson FG, Heesom MJ, Nicholson A, Hills AWD (1987) Effect of fluid flow characteristics on nozzle blockage in aluminium-killed steels. Ironmak Steelmak 14(6):296–309
20. Long M, Zuo X, Zhang L, Chen D (2010) Kinetic modeling on nozzle clogging during steel billet continuous casting. ISIJ Int 50(5):712–720
21. Turpin ML, Elliott JF (1966) Nucleation of oxide inclusions in iron melts. J Iron Steel Inst 204:217–225

Effect of Lanthanum on Inclusions in a High Sulfur Steel

Sha Ji, Lifeng Zhang, Ying Ren, and Xindong Wang

Abstract Laboratory experiments were performed to study the evolution of inclusions in a high sulfur steel with additions of 40, 200, and 800 ppm lanthanum. With the increase of lanthanum content in the steel, evolution paths of inclusions were Al–Ca–O → Al–Ca–(La)–O, Al–Ca–O → La–O–S and La–S → La–S, Al–Ca–O → La–O–S and La–S. Thermodynamic calculation results show that the evolution path of inclusions with lanthanum additions was Al_2O_3 → $La_2O_3{\cdot}Al_2O_3$ → La_2O_2S → $La_2O_2S + LaS$, which were in good agreement with experimental results. Lanthanum additions promoted the generation and collision of La-rich inclusions and inhibited the precipitation of MnS inclusions in the solid steel with the number density and area fraction of MnS inclusions decreased obviously. An appropriate amount of lanthanum was beneficial to improve the distribution of sulfide and promoted the formation of type I sulfide in the high sulfur steel.

Keywords Lanthanum · Inclusions · Thermodynamic calculation · High sulfur steel

Introduction

The non-quenched and tempered steel is widely used in the automobile manufacturing, machine tool assembly, instrument production, and other fields due to its high strength and good machinability [1, 2] with the development of the low energy consumption and green development of ironmaking and steelmaking industry [3, 4]. Generally, a certain amount of free-cutting element like sulfur is added to promote the

S. Ji · Y. Ren · X. Wang (✉)
School of Metallurgical and Ecological Engineering, University of Science and Technology Beijing, Beijing 100083, China
e-mail: echem@ustb.edu.cn

L. Zhang (✉)
State Key Laboratory of Metastable Materials Science and Technology, Yanshan University, Qinhuangdao 066004, China
e-mail: zhanglifeng@ysu.edu.cn

Z. Peng et al. (eds.), *12th International Symposium on High-Temperature Metallurgical Processing*, The Minerals, Metals & Materials Series,
https://doi.org/10.1007/978-3-030-92388-4_29

precipitation of manganese sulfide (MnS) and improve the machinability of steel [5]. Since the machinability and mechanical properties of steels are significantly affected by the morphology and distribution of MnS inclusions [6–8], numerous studies have focused on the formation mechanism and shape control of MnS inclusions [9–12]. Recently, rare earth elements were widely used in modifying inclusions, deep purifying steel, and alloying due to their unique electronic layer structure. Torkamani et al. [13] found that elongated inclusions of MnS were transformed to spherical or near spherical ones of (RE, Al)(S, O) and RE(S) with the addition of 200 ppm La and Ce in the micro-alloyed steel. Huang et al. [14] reported the evolution path of $MgAl_2O_4 \rightarrow CeAlO_3 \rightarrow$ Ce–O and Ce–O–S with Ce content increased from 0 to 300 ppm in the H13 stainless steel. Comprehensive analysis was conducted by Ren et al. [15–17] to study the inclusions evolution by cerium treatment both in industrial trials and laboratory experiments of a Al-killed non-oriented electrical steel. In the current work, laboratory experiment and thermodynamic calculations were performed to study the effect of lanthanum treatment on inclusions in a high sulfur steel (HSS). The composition, number, size, and distribution of inclusions in both the molten and the solid HSS after additions of 40, 200, and 800 ppm lanthanum were comprehensively analyzed.

Laboratory Experiment and Analysis

A commercial HSS bloom with the composition shown in Table 1 was used as the base material in the experiment. Approximately, 650 g bloom samples after grinding were melted in an alumina crucible with an inner diameter of 48 mm and a height of 115 mm, and the alumina crucible was placed in a graphite protection crucible using $MoSi_2$ heating bars under the argon atmosphere at a flow rate of 2.0 L/min. The steel was heated to 1873 K at the rate of 10 K/min and kept for 5 min, and then the first sample was taken by the quartz sampler and water-cooled immediately. One minute after sampling, a certain amount of La-Fe alloy (20 wt% La) packed in an iron foil was added to the molten steel. At 1, 3, 5, and 10 min after the lanthanum addition, samples were taken with quartz samplers and water-cooled immediately. During the sampling process, the insertion depth of samplers was fixed to ensure the same sampling position. The schematic of the experimental procedure, quartz sampler, and sample processing diagram was shown in Fig. 1. After holding for 10 min at 1873 K, samples with the alumina crucible were furnace-cooled to 1400 °C and then quenched in water.

Table 1 Chemical composition of the bulk HSS (wt%)

C	Si	Mn	P	S	Cr	[Al]	T.Al
0.242	0.245	2.004	0.018	0.04	0.463	0.010	0.013

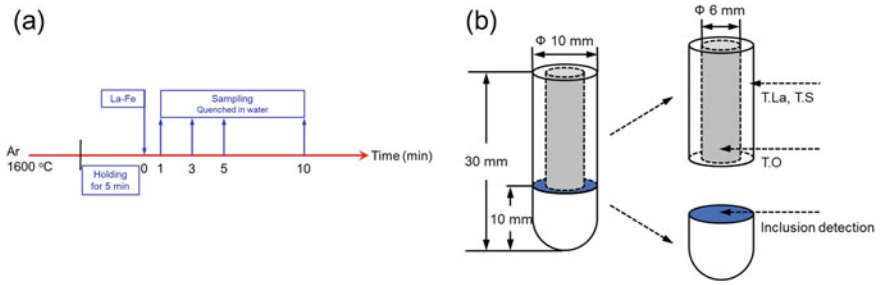

Fig. 1 Schematic of **a** the experimental procedure and **b** the sample processing diagram

The content of the total lanthanum (T.La) in the steel was analyzed using the inductively coupled plasma emission spectrometry (ICP-ES). The total oxygen (T.O) and total sulfur (T.S) were analyzed using the Leco analyzer. Other elements of the bulk steel were analyzed using a spark direct reading spectrometer. The chemical composition of steel samples is listed in Table 2. The morphology, size, and chemical composition of inclusions were detected using an automated Scanning Electron Microscope-Energy Dispersive Spectrometer (SEM–EDS) inclusion analysis system, operated at an acceleration voltage of 15 kV and 35% spot size. The working distance of the BSED detector was 16.0–17.0 mm. The minimum diameter of inclusions was set as 1.0 μm, and the maximum diameter of inclusions was chosen as the size of inclusions in the current work.

Evolution of Inclusions in the Molten Steel with Lanthanum Addition

The element mapping and composition of typical incluisons in the molten steel before the lanthanum addition are shown in Fig. 2. Inclusions were spherical or nearly spherical homogeneous Al_2O_3–CaO–MgO type. The homogeneous distribution of elements indicated that inclusions were liquid in the molten steel before the lanthanum addition.

The ternary phase diagram distribution of non-metallic inclusions in the molten HSS before and after the addition of 40 ppm lanthanum is shown in Fig. 3, where the mole fraction of each component in inclusions was analyzed. According to the composition of non-metallic inclusions, inclusions were put into the Al–La–O and La–O–S ternary phase diagrams, respectively. The Al–La–O ternary phase diagram mainly focused on the transformation of oxide inclusions, and the other mainly focused on the transformation of La-containing oxy-sulfide and sulfide inclusions. The scanning area of each sample was more than 7.5 mm^2 to obtain enough inclusions for the accuracy of experiment results, and inclusion types indicated by red arrows were shown in the ternary phase diagram. The scanning area, number, maximum

Table 2 Chemical composition of steel samples (wt%)

No	T.La addition (ppm)	Time (min)	T.La (ppm)	T.S (ppm)	T.O (ppm)	No	T.La addition (ppm)	Time (min)	T.La (ppm)	T.S (ppm)	T.O (ppm)
1	40	0	NA[a]	NA	6.75	2	200	0	NA	NA	4.41
		1	NA	NA	12.42			1	NA	NA	8.58
		10	20	382	15.74			10	140	363	12.40
3	800	0	NA	NA	7.81						
		1	NA	NA	10.27						
		10	610	362	13.22						

[a] *NA* Not analyzed

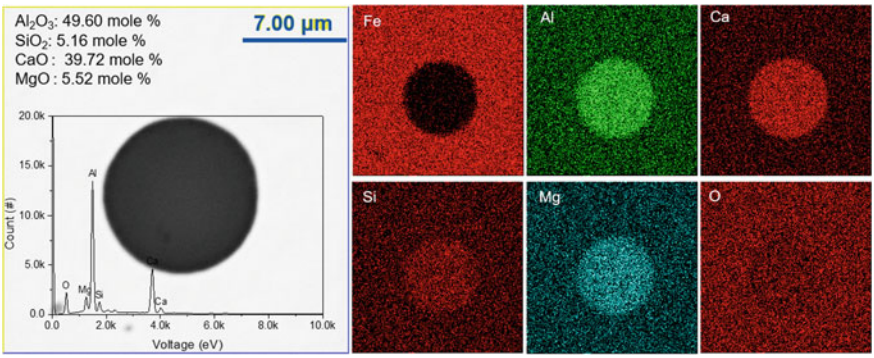

Fig. 2 Typical morphology and composition of inclusions in the molten HSS before the lanthanum addition

diameter (D_{max}), average diameter (D_{ave}), number density (ND), and area fraciton (AF) of inclusions detected in samples were also shown in the diagram. Inclusions in the molten steel before the addition of lanthanum were mainly Al_2O_3 type. After the addition of lanthanum of 40 ppm, part of initial inclusions of Al_2O_3 were modified to Al–(La)–O type. Inclusions in the molten steel were mainly Al_2O_3 type and Al–La–O type. With the increase of holding time, more inclusions of Al_2O_3 in the steel were gradually modified to Al–(La)–O ones.

The ternary phase diagram distribution of non-metallic inclusions in the HSS before and after additions of lanthanum of 200 ppm and 800 ppm is shown in Figs. 4 and 5. When 200 ppm lanthanum was added into the molten steel, the content of aluminium in inclusions decreased rapidly. Transient inclusions of La–S were first formed at 1 min after the addition of 200 ppm lanthanum and then dissoluted with the holding time. Inclusions were mainly La–O–S type at 10 min after the addition of lanthanum. After the addition of 800 ppm lanthanum, inclusions were modified to La–O–S and La–S rapidly, which was stable with the holding time.

Typical morphology, composition and element mapping of inclusions in the molten HSS with 40, 200, and 800 ppm lanthanum additions were shown in Figs. 6, 7, and 8. Inclusions were modified into spherical small-size Al–Ca–La–O type 1 min after the addition of 40 ppm lanthanum with the content of lanthanum in inclusions lower than 1.0 mol%, and there was no obvious transformation of inclusions composition with the holding time. After the addition of 200 ppm lanthanum, inclusions were modified into spherical or near spherical ones of La–O–S and La–S rapidly. The content of lanthanum of La–O–S inclusions was about 40.00 mol%, and that of La–S was about 50.00 mol%. After 10 min the addition of lanthanum, transient inclusions of La–S disappeared, and the main type of inclusions was La–O–S with the average content of lanthanum about 45.0–48.0 mol%. Inclusions were modified into spherical or near spherical La–O–S and La–Sinclusions at 1 min after the addition of 800 ppm lanthanum, and La–S type inclusions acted as stable products with the holding time.

The transformation of the average composition of inclusions at different holding times with the addition of 40 ppm lanthanum is shown in Fig. 9a. After the addi-

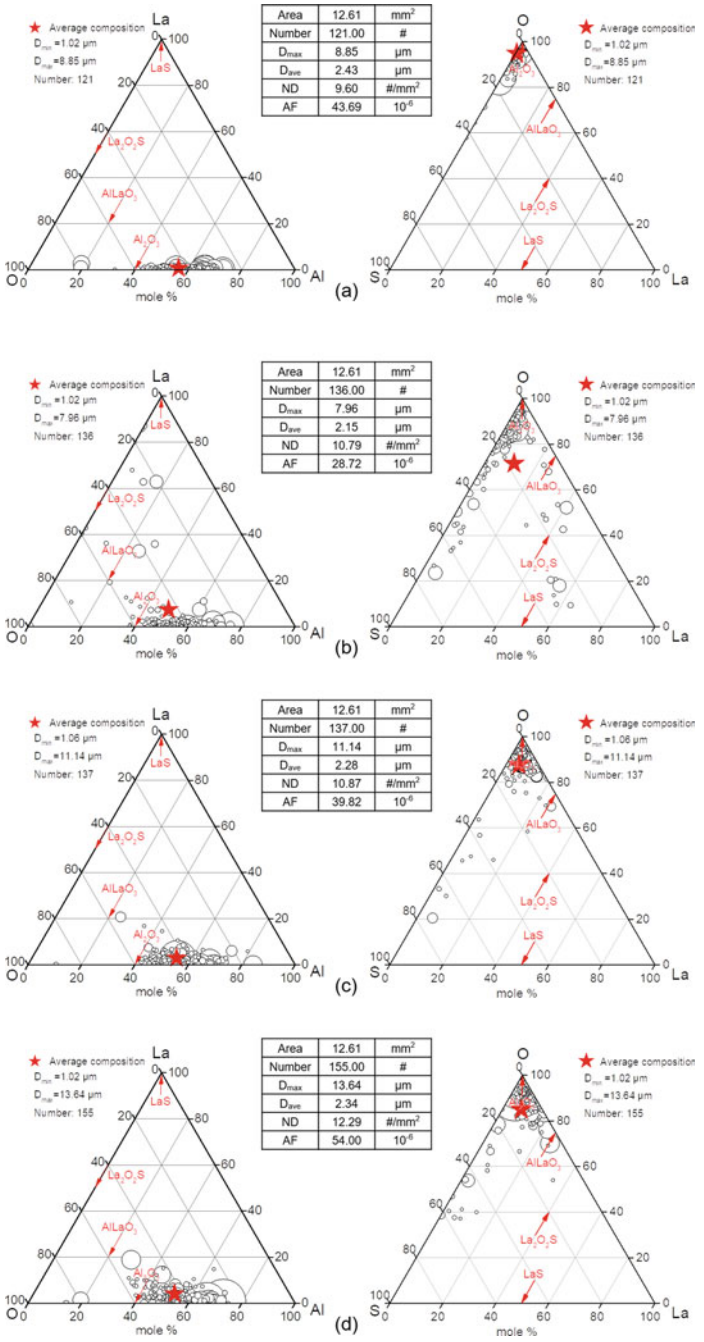

Fig. 3 Distribution of non-metallic inclusions in the molten HSS before (**a**), 1 min (**b**), 5 min (**c**), and 10 min (**d**) after the addition of 40 ppm lanthanum

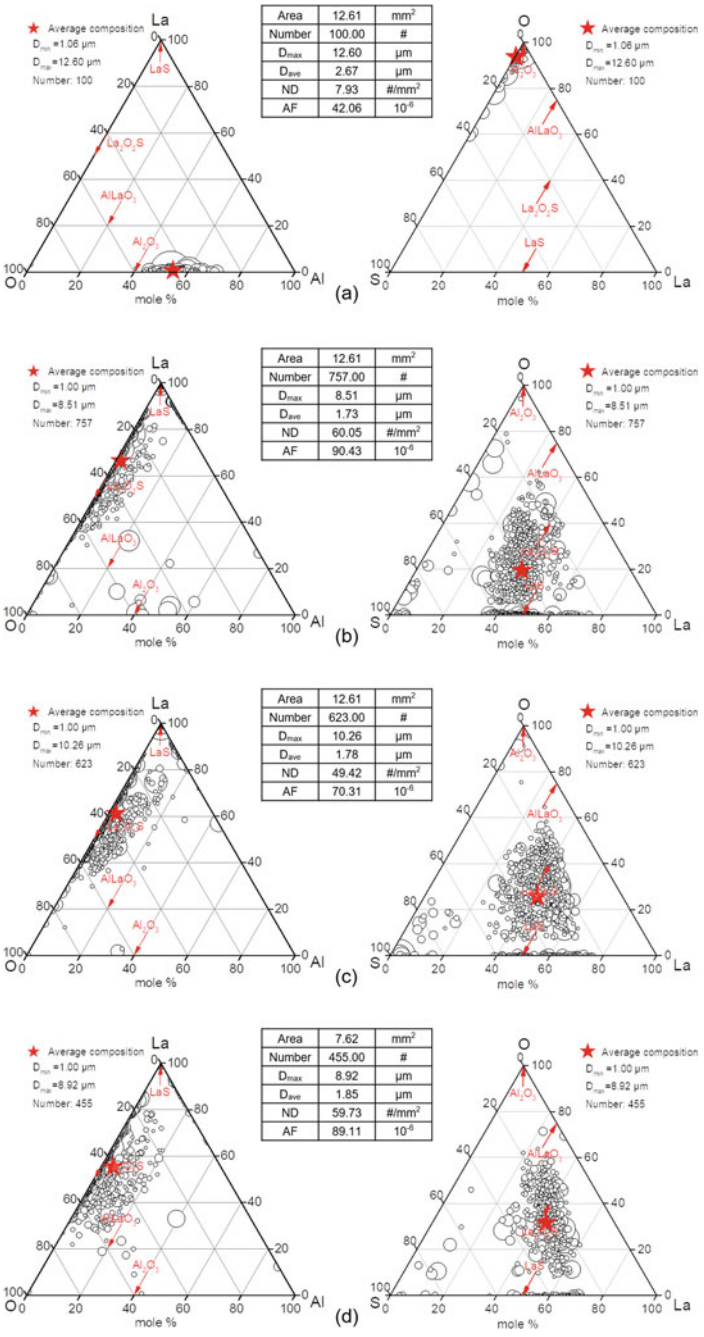

Fig. 4 Distribution of non-metallic inclusions in the molten HSS before (**a**), 1 min (**b**), 5 min (**c**), and 10 min (**d**) after the addition of 200 ppm lanthanum

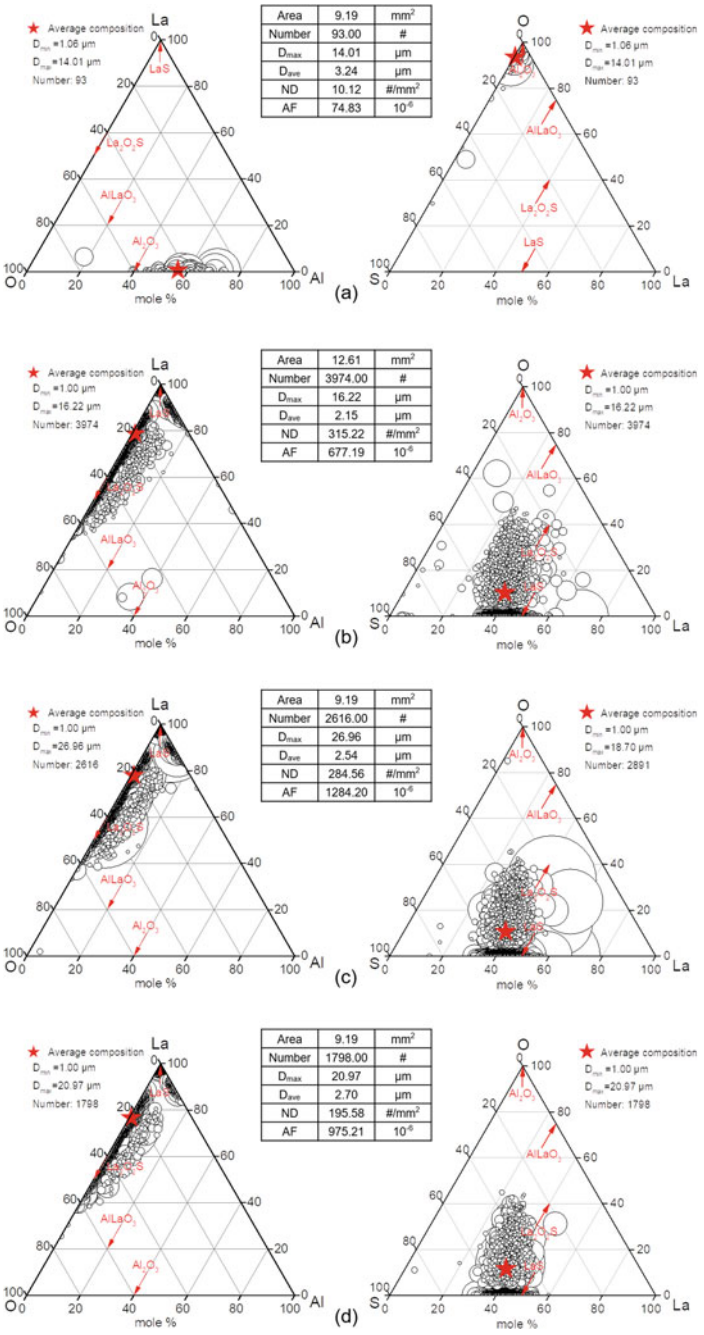

Fig. 5 Distribution of non-metallic inclusions in the molten HSS before (**a**), 1 min (**b**), 5 min (**c**), and 10 min (**d**) after the addition of 800 ppm lanthanum

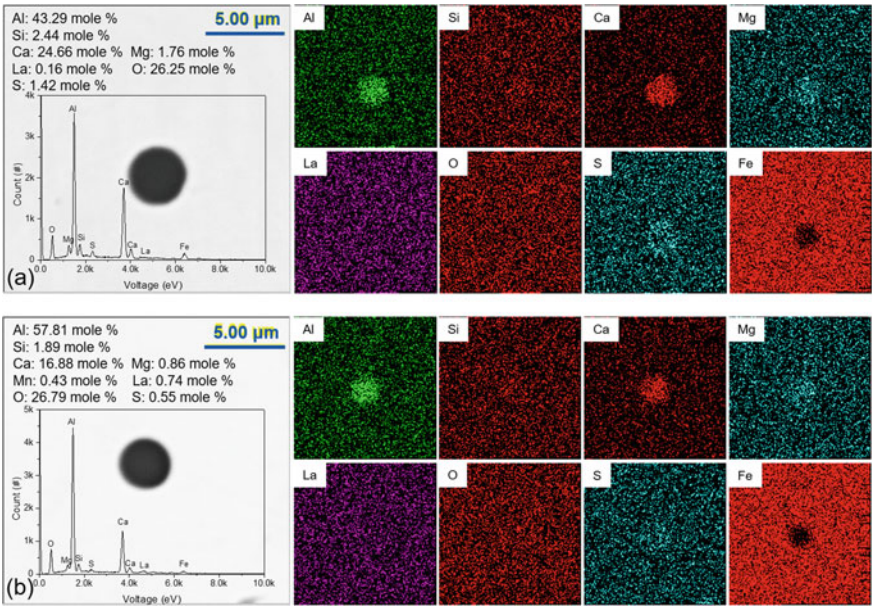

Fig. 6 Typical morphology, composition, and element mapping results of inclusions in the molten HSS: **a** 1 min and **b** 10 min after the addition of 40 ppm lanthanum

tion of lanthanum, the content of lanthanum in inclusions increased rapidly and then decreased gradually. The composition of inclusions fluctuated and the average content of lanthanum in inclusions were less than 5.0 mol% 3 min after the lanthanum addition. The evolution path of inclusions in the molten HSS with the 40 ppm lanthanum addition was Al–Ca–O → Al–Ca–La–O. The composition of inclusions at different holding times with additions of 200 and 800 ppm lanthanum was shown in Fig. 9b and c. After the addition of 200 ppm lanthanum, contents of Al and Ca in inclusions disappeared rapidly while that of La and S in inclusions increased to 35.57 mol% and 36.32 mol%, respectively. The transient product of La–S disappeared with the holding time, and inclusions of the molten steel were mainly La–O–S 10 min after the addition of lanthanum. The evolution path of inclusions with the 200 ppm lanthanum addition was Al–Ca–O → La–O–S and La–S → La–O–S. Inclusions transformed into stable phases of La–O–S and La–S rapidly after the addition of 800 ppm lanthanum. The content of La and S in inclusions increased to 36.74 mol% and 49.25 mol%, respectively. The composition of inclusions in the molten steel hardly changed 3 min after the lanthanum addition. The evolution path of inclusions with the addition of 800 ppm lanthanum in the molten HSS was Al–Ca–O → La–O–S and La–S.

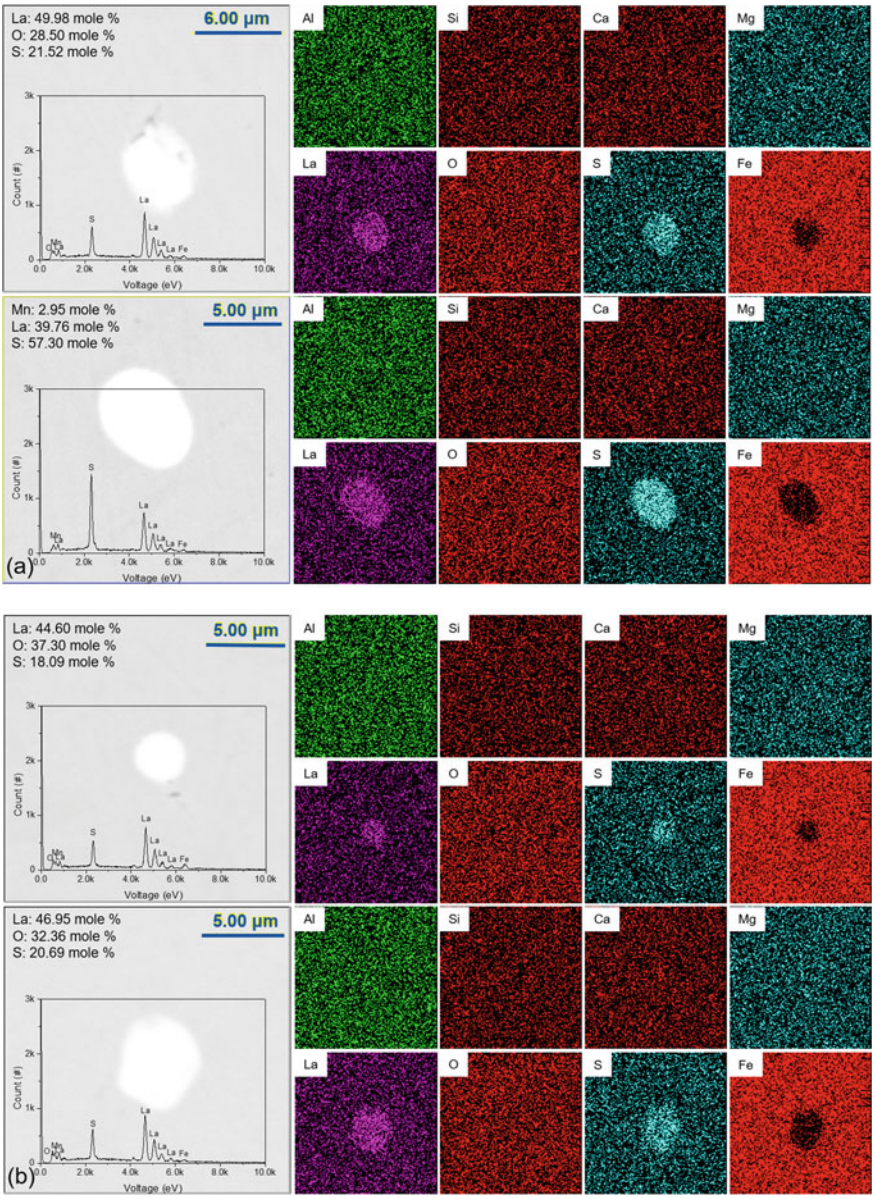

Fig. 7 Typical morphology, composition, and element mapping results of inclusions in the molten HSS: **a** 1 min and **b**10 min after the addition of 200 ppm lanthanum

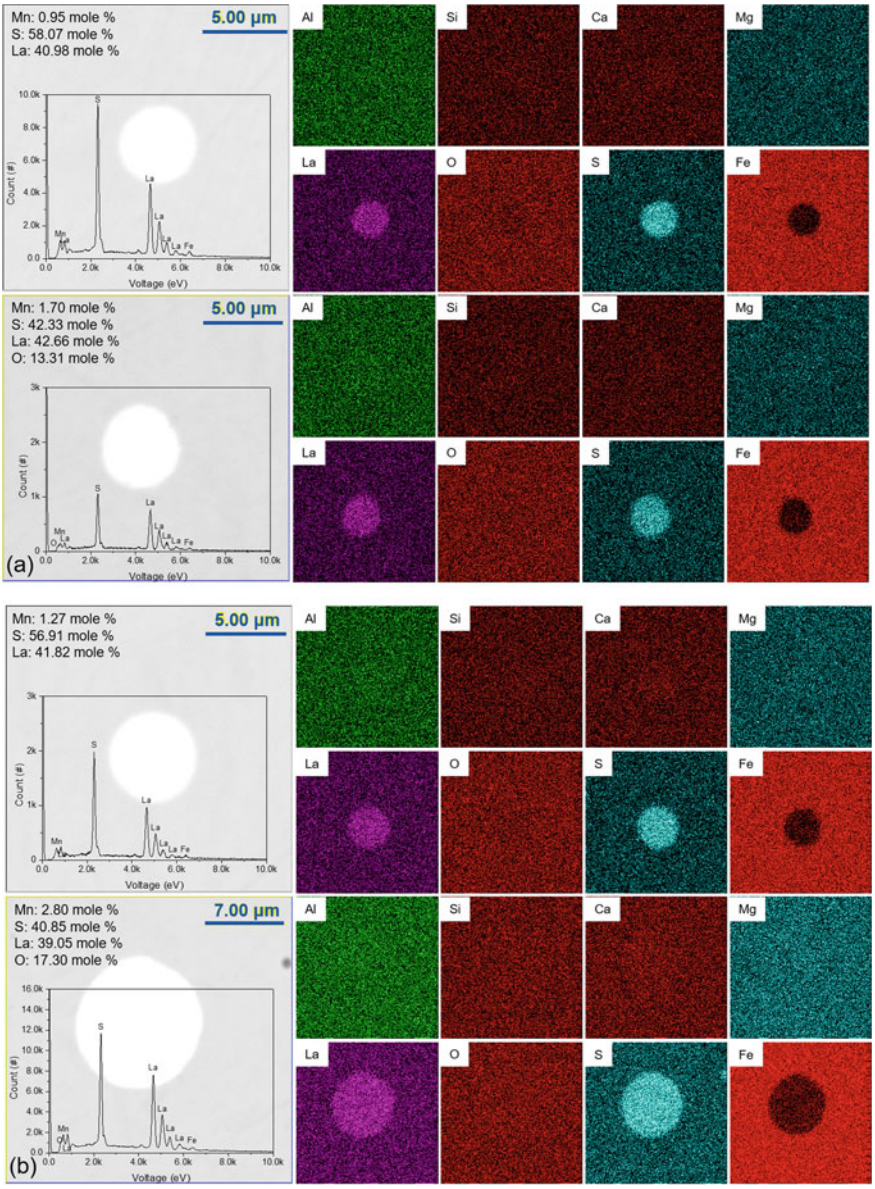

Fig. 8 Typical morphology, composition, and element mapping results of inclusions in the molten HSS: **a** 1 min and **b** 10 min after the addition of 800 ppm lanthanum

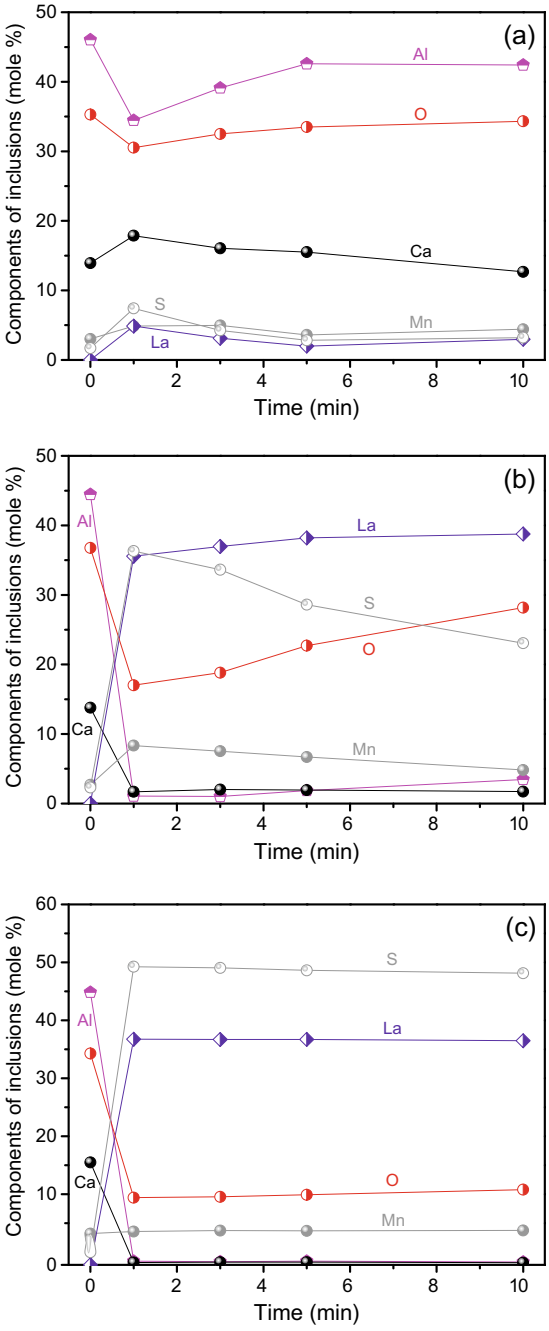

Fig. 9 Average composition of inclusions with additions of **a** 40 ppm, **b** 200 ppm, and **c** 800 ppm lanthanum

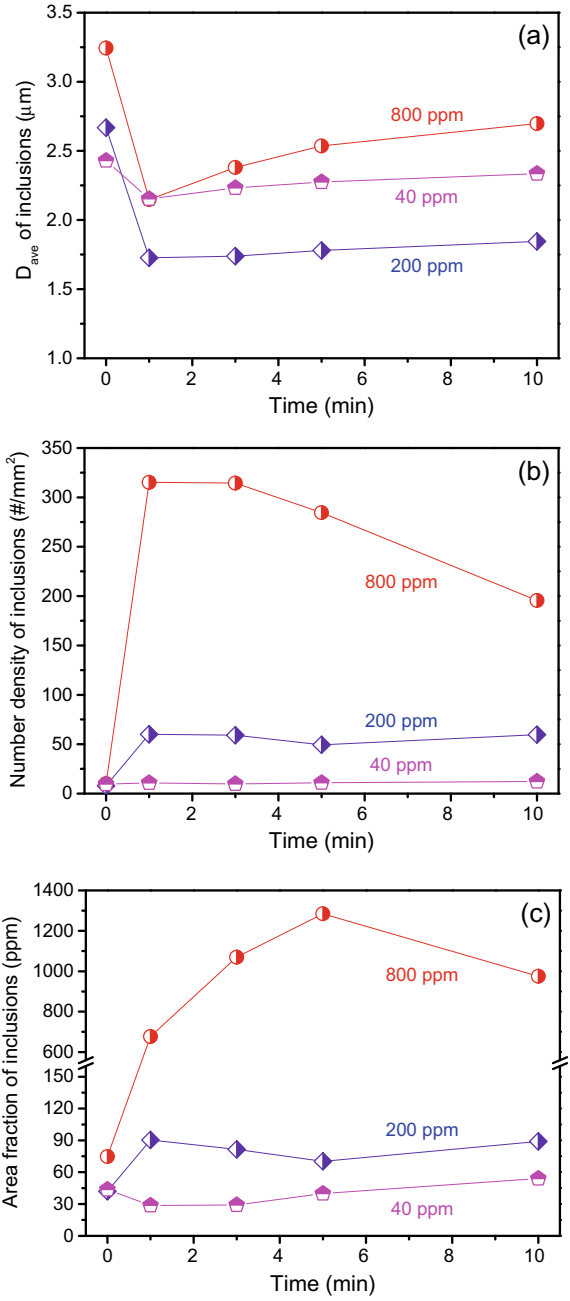

Fig. 10 Comparison of **a** the average diameter **b** the number density and **c** the area fraction of inclusions in the HSS after lanthanum additions

Figure 10 shows comparisons of the average diameter, number density, and area fraction of inclusions with different lanthanum additions. After the addition of lanthanum, the average size of inclusions in the molten steel first decreased and then rose up, which was due to the generation of small-size La-containing inclusions and the collision of La-rich inclusions. With the increase of the addition of lanthanum, the average diameter of inclusions first decreased then rose up with the holding time, indicating that an appropriate addition of lanthanum could refine the size of inclusions of the molten HSS. The higher lanthanum content in the molten steel promoted the formation of inclusions, the number density and area fraction of inclusions increased with the addition of lanthanum. However, the number density and area fraction of inclusions showed an obvious increase with 800 ppm lanthanum addition. With the addition of 200 ppm lanthanum, the aggregation and growth of inclusions were relatively weak with the holding time. That is to say, an appropriate amount of lanthanum addition can refine the size of inclusions in the HSS.

Fifty fields of views at a size scale of 100 microns were randomly measured to evaluate the number and proportion of different types of sulfide inclusions; quantitatively analysis was conducted to further study the distribution of different kinds of

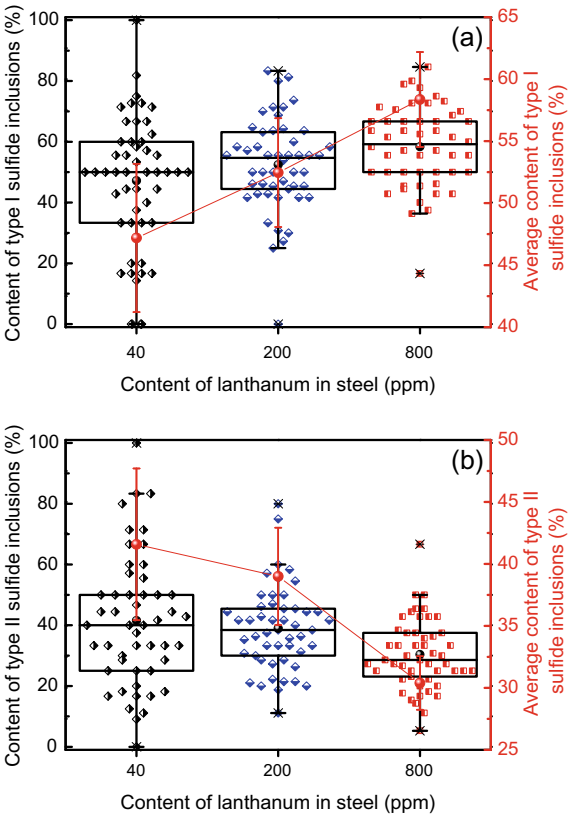

Fig. 11 Distribution of different types of sulfide inclusions in the solid HSS after lanthanum additions: **a** type I **b** type II

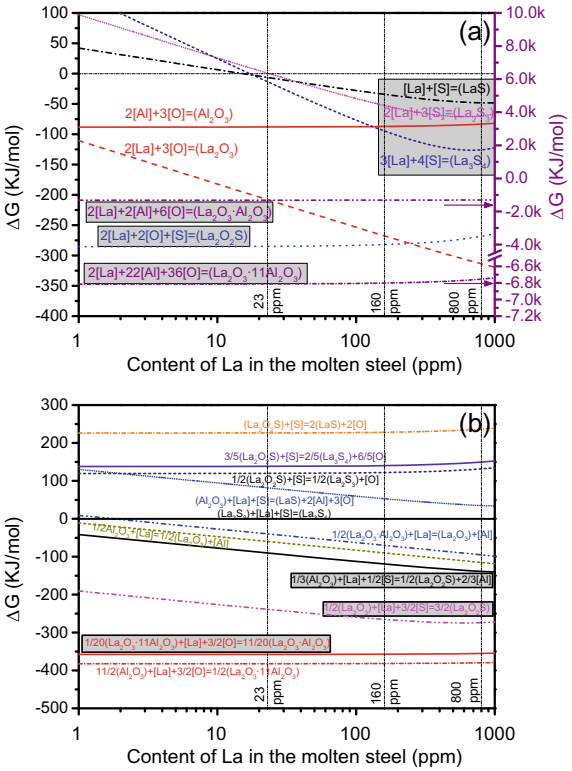

Fig. 12 Gibbs free energy of inclusions formation (**a**) and transformation (**b**) in the HSS with lanthanum additions

sulfide inclusions in the HSS with lanthanum additions in Fig. 11. The proportion of type I sulfide inclusions increased from 47.19 to 58.36% with the lanthanum addition, and the distribution of sulfide inclusions was more concentrated. While the sulfide inclusions of type II decreased from 41.58 to 30.39%, indicating that an appropriate addition of lanthanum could promoted the generation of type I sulfide inclusions. An appropriate amount of the lanthanum addition improved the distribution of sulfide and promoted the formation of type I sulfide in the solid HSS.

Thermodynamic Calculation of Lanthanum Modification of Inclusions

Possible reactions and standard Gibbs free energy [18–20] were considered, and the Henry activity was taken as the standard state in the current work due to the trace content of each element in the molten HSS. The Henry activity coefficient and Henry activity of elements could calculated by the Wagner model and first-order interaction coefficient of elements [18, 21]. The Gibbs free energy of inclusion

formation with lanthanum additions was shown in Fig. 12. With the increase of the lanthanum content in the HSS, La_2O_3, La_2O_2S, $La_2O_3{\cdot}Al_2O_3$, and $La_2O_3{\cdot}11Al_2O_3$ type inclusions formed in the HSS at 1873 K. La-containing oxide inclusions and oxy-sulfide inclusions were more stable than Al_2O_3, which could be detected in the molten steel. With the further increase of lanthanum content in the HSS, La-containing sulfide inclusions were formed. Inclusions were predicated to be La-containing oxide inclusions with 40 ppm lanthanum addition, and that with 200 and 800 ppm lanthanum should be La-containing sulfide and oxy-sulfide inclusions. The higher content of lanthanum, the more stable La-containing sulfide inclusions were formed. Figure 12b shows the effect of lanthanum on the transformation of inclusions at 1873 K. Combined with Fig. 12a, the evolution path of inclusions with lanthanum additions was $Al_2O_3 \rightarrow La_2O_3{\cdot}Al_2O_3 \rightarrow La_2O_2S \rightarrow La_2O_2S + LaS$, which was in good agreement with experimental results. At the same time, thermodynamic calculation results show that under current calculation conditions, inclusions of La_2O_2S acted as a stably phase in the steel which could not be transformed into inclusions of La-containing sulfide.

Conclusions

(1) After additions of 40, 200 and 800 ppm lanthanum in the HSS, the evolution path of inclusions was Al–Ca–O → Al–Ca–(La)–O, Al–Ca–O → La–O–S and La–S → La–O–S, and Al–Ca–O → La–O–S and La–S, respectively, which were in good agreement with thermodynamic calculation results.

(2) When 40 ppm lanthanum was added, the initial liquid Al–Ca–O inclusions were modified to small-size liquid inclusions of Al–Ca–(La)–O. Inclusions of La–O–S and transient La–S were detected in the molten steel with 200 ppm lanthanum addition. After the addition of 800 ppm lanthanum into the steel, a large number of stable La–O–S and La-S inclusions generated.

(3) When the lanthanum addition in steel increased from 40 to 800 ppm, the proportion of type I sulfide in steel increased from 47.19 to 58.36%, and that of type II sulfide decreased from 41.58 to 30.39%. An appropriate amount of 200 ppm lanthanum in the HSS was beneficial to improve the distribution of sulfide inclusions, promote the formation of type I sulfide, and improve the properties of the HSS.

Acknowledgements The authors are grateful for support from the National Nature Science Foundation of China (Grant No. U1860206, No. 51725402), the S&T Program of Hebei (Grant No. 20311005D), the High Steel Center (HSC) at Yanshan University, and Beijing International Center of Advanced and Intelligent Manufacturing of High Quality Steel Materials (ICSM) and the High Quality Steel Consortium (HQSC) at University of Science and Technology Beijing (USTB), China.

References

1. Sun H, Wu LP, Xie JB, Ai KN, Zeng ZQ, Shen P, Fu JX (2020) Inclusions modification and improvement of machinability in a Non-quenched and tempered steel with Mg treatment. Metall Res Technol 117(208):1–9
2. Li M, Wang F, Li C, Yang Z, Meng Q, Sufen T (2015) Effects of cooling rate and Al on MnS formation in medium-carbon non-quenched and tempered steels. Int J Miner Metall Mater 22(6):589–597
3. Wang K, Yu T, Song Y, Li H, Liu M, Luo R, Zhang J, Fang F, Lin X (2019) Effects of MnS inclusions on the banded microstructure in non-quenched and tempered steel. Metall Mater Trans B 50(3):1213–1224
4. Zhang LF (2019) Non-metallic inclusions in steels: industrial practice (in Chinese). Metallurgical Industry Press, Beijing
5. Zeng J, Zhu C, Wang W, Li X (2020) In situ observation of the MnS precipitation behavior in high-sulfur microalloyed steel under different cooling rates. Metall Mater Trans B 51(6):2522–2531
6. Luyckx L, Bell JR, Mclean A, Korchynsky M (1970) Sulfide shape control in high strength low alloy steels. Metall Trans B 1(12):3341–3350
7. Liu H, Chen W (2012) Effect of total oxygen content on the machinability of low carbon resulfurized free cutting steel. Steel Res Int 83(12):1172–1179
8. Yang W, Yang X, Zhang LF, Liu X (2013) Review of control of MnS inclusions in steel. Steelmaking 29(6):71–78
9. Sanbongi K (1978) Controlling sulfide shape with rare earth or calcium during the processing of molten steel. Tetsu Hagane 64(1):145–154
10. Yoichi I, Noriyuki M, Kaichi M (1980) Formation of MnS-type inclusion in steel. Tetsu-to-Hagane 66(6):647–656
11. Diederichs R, Bleck W (2006) Modelling of manganese sulphide formation during solidification, Part I: description of MnS formation parameters. Steel Res Int 77(3):202–209
12. Zhang X, Yang C, Chai F, Luo X, Zhang LF, Dong Y (2019) Precipitation and control of MnS inclusions by thermodynamic analysis. Iron and steel 54(12):27–34
13. Torkamani H, Raygan S, Mateo CG, Rassizadehghani J, San-Martin D (2018) Contributions of rare earth element (La, Ce) addition to the impact toughness of low carbon cast niobium microalloyed steels. Met Mater Int 24(3):1–16
14. Huang Y, Cheng G, Li S, Dai W (2018) Effect of cerium on the behavior of inclusions in H13 steel. Steel Res Int 89(12):1800371–1800377
15. Ren Q, Zhang LF, Hu Z, Cheng L (2021) Transient influence of cerium on inclusions in an Al-killed non-oriented electrical steel. Ironmak Steelmak 48(2):191–199
16. Ren Q, Zhang LF (2020) Effect of cerium content on inclusions in an ultra-low-carbon aluminum-killed steel. Metall Mater Trans B 51(2):589–600
17. Ren Q, Zhang LF, Liu Y, Cui L, Yang W (2020) Transformation of cerium-containing inclusions in ultra-low-carbon aluminum-killed steels during solidification and cooling. J Market Res 9(4):8197–8206
18. Mikhailov GG, Makrovets LA, Smirnov LA (2016) Thermodynamic modelling of rare-earth elements—Oxygen interaction. Mater Sci Forum 843:39–45
19. Vahed A, Kay DAR (1976) Thermodynamics of rare earths in steelmaking. Metall Trans B 7B(3):375–383
20. He Y, Liu J, Qiu S, Deng Z, Yang Y, Mclean A (2018) Thermodynamic analysis of inclusion characteristics in As-cast FeCrAl-(La) alloys. Iron Steelmak 47(1):13–21
21. Wei S (1980) Thermodynamics of the metallurgical process. Shanghai Scientific and Technical Literature Publishing House, Shanghai

Part V
Process Optimization

Effect of Calcium Treatment on Non-metallic Inclusions in Steel During Refining Process

Weijian Wang, Lifeng Zhang, Ying Ren, Yan Luo, and Xiaohui Sun

Abstract Different amounts of calcium wire were added to the molten steel during the refining process in industrial trials to study the effect of calcium contents on the size distribution, content, and morphology of inclusions. Thermodynamic calculations were also conducted to study the effect of calcium contents on inclusions. It was found that with the increase of calcium content in steel, Al_2O_3 content in inclusions decreased while CaS content increased. However, when calcium content was bigger than 30 ppm, the CaO content decreased slightly and the CaS content increased more. As the calcium content in steel increased, the average size and area fraction of inclusions decreased, which means that appropriate calcium treatment technology will not reduce the cleanliness of molten steel as well as will not increase the proportion of large-sized inclusions in the steel.

Keywords Calcium treatment · Inclusions · Calcium content · Refining process

Introduction

As a strong deoxidizer, aluminum is widely used in the steelmaking process. However, after the addition of aluminum to the liquid steel, a large number of Al_2O_3 inclusions were generated, causing nozzle clogging and product defects [1–4]. Calcium treatment was used to modify Al_2O_3 into liquid calcium aluminate inclusions at steelmaking temperature. However, there was a reasonable calcium content range during the calcium treatment process. If the calcium content in the molten steel

W. Wang · L. Zhang (✉) · Y. Ren · Y. Luo · X. Sun
School of Metallurgical and Ecological Engineering, University of Science and Technology Beijing, Beijing 100083, China
e-mail: zhanglifeng@ysu.edu.cn

L. Zhang
State Key Laboratory of Metastable Materials Science and Technology, Yanshan University, Qinhuangdao 066004, Hebei, China

X. Sun
Shanghai Meishan Iron and Steel Co. Ltd, Nanjing 210039, China

Z. Peng et al. (eds.), *12th International Symposium on High-Temperature Metallurgical Processing*, The Minerals, Metals & Materials Series,
https://doi.org/10.1007/978-3-030-92388-4_30

is too low, inclusions were hardly fully modified to liquid state. But solid CaS–CaO would be generated after the excessive calcium was added to the molten steel, which also cause nozzle clogging [5–8]. On the one hand, the dissolved calcium reacts with Al_2O_3 inclusions directly to generate calcium aluminates [6, 9–11]. On the other hand, it was also reported that the added calcium transiently reacted with sulfur to form CaS inclusions [5, 12–15]. Then Al_2O_3 inclusions can be modified by CaS to calcium aluminates. Additionally, it was found that Al_2O_3–CaS inclusions were observed with a higher T.S/T.O ratio in the steel [16]. The relationship between the solid ratio of inclusions and the calcium content in the steel was also reported [17].

In the current study, industrial trials were performed to study the effect of calcium treatment on inclusions. Different amounts of calcium wire were added into the molten steel to study the effect of calcium contents on the size, composition, and morphology of inclusions. The effect of calcium content on the composition, solidus, and liquidus of inclusions was also calculated by Factsage.

Methodology

The production route of the Al–killed steel was BOF → LF → calcium treatment → continuous casting. During the calcium treatment process, CaFe alloy wire was inserted into the molten steel to modify alumina-based inclusions in ladles. Steel samples were taken 3 min before calcium treatment and 3 min after calcium treatment. Contents of T.Al (total aluminum), T.Ca (total calcium), and T.S (total sulfur) in steel samples were analyzed using the Optical Emission Spectrometer. The T.Al, T.Ca, and T.S contents included the dissolved elements in the steel matrix and the oxide or sulfide in inclusions. The total oxygen content was analyzed using a LECO OHN836 analyzer. The size, composition, and morphology of inclusions were analyzed using an automatic Scanning Electron Microscope-Energy Dispersive Spectrometer analysis system.

Evolution of Inclusions in the Steel with Calcium Treatment

The variation of composition in different steel samples is shown in Table 1. The T.O and T.S in samples with different T.Ca contents changed little, and the total aluminum content of the sample with the 28 ppm T.Ca was higher. Figure 1 shows the composition distribution of inclusions in different samples. With less than 3 ppm T.Ca, inclusions in the steel were mainly Al_2O_3. As the calcium content in the steel increased, the contents of CaO and CaS in the steel increased. When the calcium content in the steel was 19 ppm, the inclusions were mainly Al_2O_3–CaO–CaS compound inclusions, and the Al_2O_3 content was higher than 50%. In steel samples with T.Ca contents of 28 ppm and 35 ppm, inclusions were mainly Al_2O_3–CaS. The change of inclusions composition with different T.Ca contents is shown in Fig. 2. The Al_2O_3 content decreased

Table 1 Compositions of steel samples

Number	T.O. (ppm)	T.Ca (ppm)	T.S. (ppm)	T.Al (ppm)
1	17	2	37	276
2	17	5	58	357
3	23	7	55	340
4	19	19	51	316
5	36	28	28	381
6	15	35	44	294

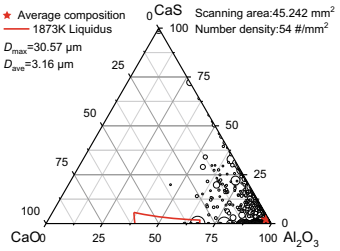

(a) T.Ca = 2 ppm

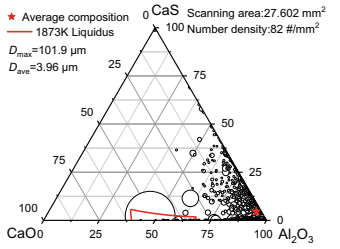

(b) T.Ca = 5 ppm

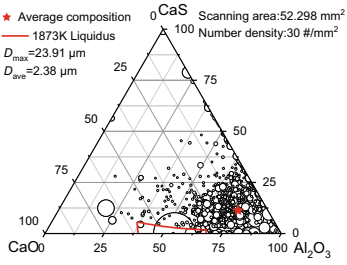

(c) T.Ca = 7 ppm

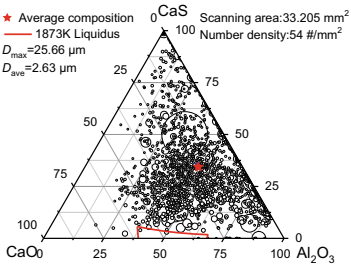

(d) T.Ca = 19 ppm

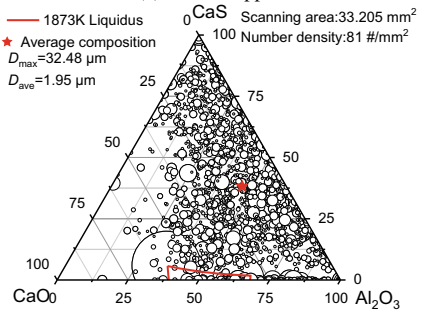

(e) T.Ca = 28 ppm

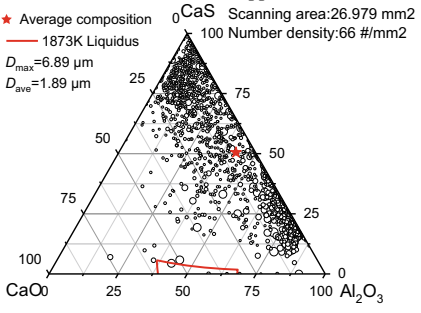

(f) T.Ca = 35 ppm

Fig. 1 Composition distribution of inclusions with various T.Ca contents

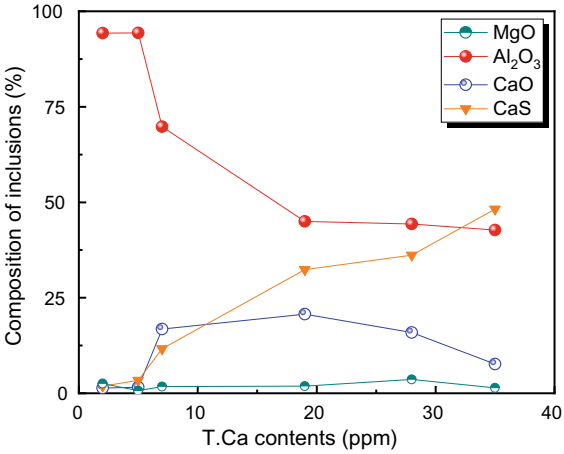

Fig. 2 Variation of inclusions composition with different T.Ca contents

with the increase of T.Ca content while CaO and CaS contents increased. However, the CaO inclusions decreased slightly and CaS inclusions increased obviously in steel with higher than 19 ppm T.Ca.

A large amount of small CaS inclusions were generated after calcium addition, as shown in Fig. 3. The number density was calculated to describe the number of inclusions in the steel, as shown in Eq. (1).

$$ND = \frac{n}{A_{\text{total}}} \tag{1}$$

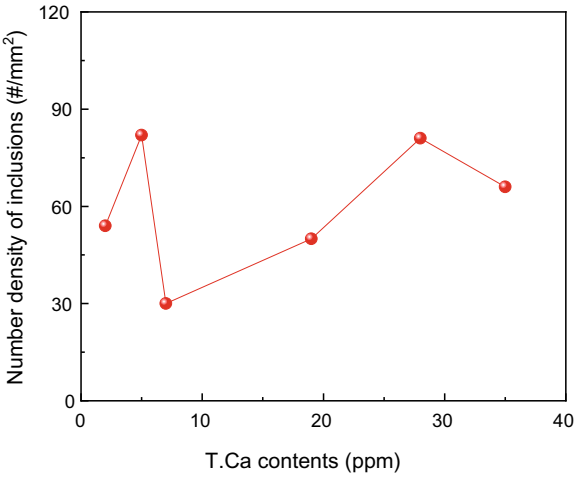

Fig. 3 Number density of inclusions with different T.Ca contents

where *ND* is the number density of inclusions, per mm^2, n is the number of detected inclusions on the scanning area of A_{total}.

With the increase of T.Ca content in the steel, the number density of inclusions increased. The average and maximum diameter of inclusions with different T.Ca contents are shown in Fig. 4. With the increase of T.Ca content, the variation of the average diameter and maximum diameter of inclusions decreased slightly due to the generation of small CaS inclusions. The maximum diameter of inclusions reached 101 μm in the steel with 5 ppm T.Ca, which might be caused by slag entrainments.

Figure 5 shows the morphology of inclusions with various Ca additions. Before calcium treatment, inclusions were mainly Al_2O_3 and Al_2O_3–MgO. After calcium treatment, contents of CaS and CaO in inclusions increased. The shape of inclusions was irregular, and inclusions were transformed into Al_2O_3–CaS–CaO compound inclusions.

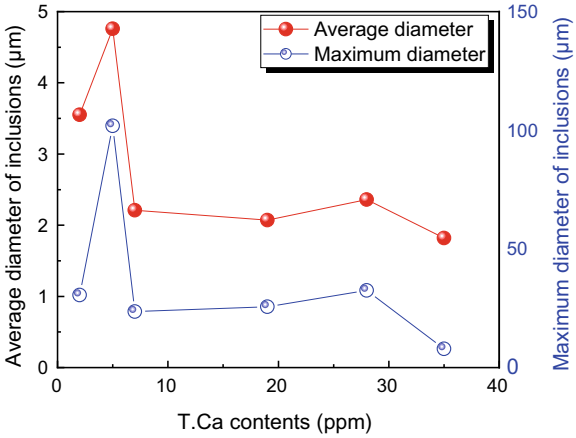

Fig. 4 Diameter of inclusions with different T.Ca contents

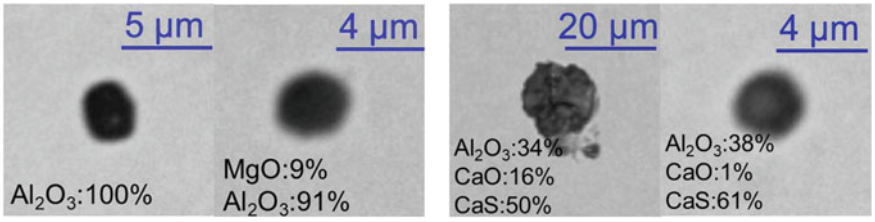

(a) Lower T.Ca content (b) Higher T.Ca content

Fig. 5 Morphology of inclusions with different T.Ca contents

Thermodynamic Calculation

Composition changes of inclusions with different T.Ca contents calculated using Factsage 7.0 are shown in Fig. 6. With the increase of T.Ca content in steel, the evolution path of inclusions was Al_2O_3 → $CaO{\cdot}6Al_2O_3$ → $CaO{\cdot}2Al_2O_3$ → Liquid inclusions → CaS. The CaO content in the liquid phase increased while the Al_2O_3 content decreased with the increase of T.Ca content in the steel. The 'liquid window' of inclusions was 12–24 ppm. The CaS inclusions were formed when T.Ca content is higher than 24 ppm.

The liquidus and solidus temperature of inclusions was calculated using Factsage 7.0. Figure 7 shows the effect of T.Ca contents on the liquidus and solidus temperature of inclusions. The liquidus as well as the solidus temperature of inclusions firstly decreased with the increase of T.Ca content in the steel and then rose after T.Ca

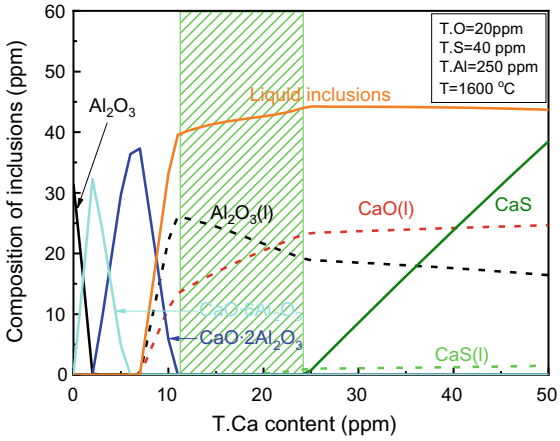

Fig. 6 Composition change of inclusions with different T.Ca content calculated by Factsage

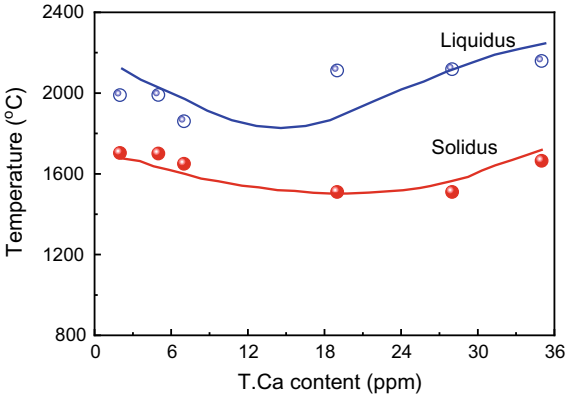

Fig. 7 Effect of T.Ca in steel on liquidus and solidus temperature of inclusions

content reaching 7 ppm. The solidus was lower than 1873 K in steel with T.Ca contents of 19 and 28 ppm, which was beneficial to the continuous casting process.

Conclusions

With the increase of T.Ca content, the Al_2O_3 content of inclusions decreased while CaS and CaO contents increased. A large amount of small CaS inclusions were generated when excessive calcium was added to the molten steel. The average diameter decreased slightly and the number density of inclusions increased with the increase of T.Ca content. The evolution path of inclusions was $Al_2O_3 \rightarrow CaO{\cdot}6Al_2O_3 \rightarrow CaO{\cdot}2Al_2O_3 \rightarrow$ Liquid inclusions $\rightarrow$ CaS with the increase of T.Ca content in the steel. The 'liquid window' of inclusions was 12–24 ppm. The liquidus as well as the solidus temperature of inclusions firstly decreased with the increase of T.Ca content in the steel and then rose after T.Ca content reaching 7 ppm. The solidus was lower than 1873 K in steel with T.Ca contents of 19 and 28 ppm, which was beneficial to the continuous casting process.

Acknowledgements The authors are grateful for the support from S&T Program of Hebei (Grant No. 20311004D, 20311005D, 20311006D, 20591001D), the High Steel Center (HSC) at Yanshan University, Hebei Innovation Center of the Development and Application of High Quality Steel Materials, Hebei International Research Center of Advanced and Intelligent Manufacturing of High Quality Steel Materials (ICSM) and the High Quality Steel Consortium (HQSC) at University of Science and Technology Beijing, China.

References

1. Choudhary SK, Ghosh A (2008) Thermodynamic evaluation of formation of oxide-sulfide duplex inclusions in steel. ISIJ Int 48(11):1552–1559
2. Zhang L, Thomas BG (2006) State of the art in the control of inclusions during steel ingot casting. Metall Trans B 37(5):733–761
3. Wang QY, Bathias C, Kawagoishi N, Chen Q (2002) Effect of inclusion on subsurface crack initiation and gigacycle fatigue strength. Int J Fatigue 24(12):1269–1274
4. Larsson M, Melander A, Nordgren A (1993) Effect of inclusions on fatigue behaviour of hardened spring steel. Mater Sci Technol 9(3):235–245
5. Zhang L, Liu Y, Zhang Y, Yang W, Chen W (2018) Transient evolution of nonmetallic inclusions during calcium treatment of molten steel. Metall Trans B 49(4):1841–1859
6. Yang W, Zhang L, Wang X, Ren Y, Liu X, Shan Q (2013) Characteristics of inclusions in low carbon Al-killed steel during ladle furnace refining and calcium treatment. ISIJ Int 53(8):1401–1410
7. Zhang L (2019) Non-metallic Inclusions in Steels: fundamentals (in Chinese). Metallurgical Industry Press, Beijing
8. Zhang L (2020) Non-metallic inclusions in steels: industrial practice (in Chinese). Metallurgical Industry Press, Beijing
9. Ito YI, Suda M, Kato Y, Nakato H, Sorimachi KI (1996) Kinetics of shape control of alumina inclusions with calcium treatment in line pipe steel for sour service. ISIJ Int 36(S1):S148–S150

10. Cicutti CE, Madias J, Gonzalez JC (1997) Control of microinclusions in calcium treated aluminium killed steels. Ironmak Steelmak 24(2):155–159
11. Ye G, Jönsson P, Lund T (1996) Thermodynamics and kinetics of the modification of Al_2O_3 inclusions. ISIJ Int 36(S1):S105–S108
12. Verma N, Pistorius PC, Fruehan RJ, Potter M, Lind M, Story S (2011) Transient inclusion evolution during modification of alumina inclusions by calcium in liquid steel: part I. Background, experimental techniques and analysis methods. Metall Trans B 42(4):711–719
13. Verma N, Pistorius PC, Fruehan RJ, Potter M, Lind M, Story S (2011) Transient inclusion evolution during modification of alumina inclusions by calcium in liquid steel: part II. Results and discussion. Metall Trans B 42(4):720–729
14. Verma N, Pistorius PC, Fruehan RJ, Potter MS, Oltmann HG, Pretorius EB (2012) Calcium modification of spinel inclusions in aluminum-killed steel: reaction steps. Metall Trans B 43(4):830–840
15. Higuchi Y, Numata M, Fujagawa S, Shinme K (1996) Inclusion modification by calcium treatment. ISIJ Int 36(Suppl):S151–S154
16. Xu J, Huang F, Wang X (2016) Formation mechanism of CaS–Al_2O_3 inclusions in low sulfur Al-killed steel after calcium treatment. Metall Trans B 47(2):1217–1227
17. Yuan F, Wang X, Yang X (2006) Influence of calcium content on solid ratio of inclusions in ca-treated liquid steel. J Univ Sci Technol Beijing 13(6):486–489

Improvement of Iron Coke Strength by Adding Coal Tar During Coking

Chen Yin, Mingxuan Song, and Shengfu Zhang

Abstract This paper aims to provide useful knowledge on the use of coal tar as binder for the production of iron coke. The components of coal tar were investigated by gas chromatography-mass spectrometer (GC–MS); consequently, the effects of coal tar on strength and structure of iron coke were analyzed. The results show that the main components of coal tar are benzene and aliphatic compounds, and its pyrolysis resultants are similar to the metaplast (fluid phase) components, which is helpful to improve the strength of iron coke. The addition of coal tar increases the degree of graphitization, aromaticity, and crystallite size of iron coke and reduces the specific surface area and reactivity of iron coke, thereby increasing the mechanical strength and the index of coke strength after reaction (CSR) of iron coke. 3% coal tar addition amount was determined as the optimal binder for strength optimization, and the iron coke with 40.21% CRI and 55.86% CSR was prepared.

Keywords Iron coke · Strength improvement · Coal tar · GC–MS · Metaplast

Introduction

As the current main ironmaking process, blast furnace with high energy consumption and carbon dioxide emissions is difficult to fulfil ever stricter environmental regulations [1, 2]. According to the Rist line and many previous studies [3], iron coke, as a new type of burden, is considered to have the effect of reducing the fuel ratio and CO_2 emissions of blast furnace ironmaking.

C. Yin · M. Song · S. Zhang (✉)
College of Materials Science and Engineering, Chongqing University, Chongqing 400044, China
e-mail: zhangsf@cqu.edu.cn

C. Yin
e-mail: yinchen@cqu.edu.cn

S. Zhang
Chongqing Key Laboratory of Vanadium-Titanium Metallurgy and Advanced Materials, Chongqing University, Chongqing 400044, China

Z. Peng et al. (eds.), *12th International Symposium on High-Temperature Metallurgical Processing*, The Minerals, Metals & Materials Series,
https://doi.org/10.1007/978-3-030-92388-4_31

Iron coke is produced by co-pyrolysis of iron-containing minerals and coal at high temperature and has higher index of reactivity [4–6]. However, compared with the ordinary coke used in blast furnace, the iron coke has lower index of CSR, which is unfavorable to the blast furnace [7–9]. Therefore, the strength of iron coke should be optimized to realize the industrial application of iron coke. As we known, the coke strength is closely related to the thermoplasticity of coal during coking process. Generally, the larger the fluidity and the thermoplastic range, the higher the coke strength after reaction. At present, according to the thermoplasticity change of coal in coking process, the method of coal blending or adding binder to improve coke strength has been studied. Chang et al. [10] studied the effect of the addition of phenolic oil extract of weakly-bonded coal during coking and found that the thermoplasticity of coal was improved during coking, and the strength of obtained coke increases, indicating that coal extract is an effective binder in coal coking. Tsubouchi et al. [11] have co-coked the pyridine extract of HPC (hyper-coal) with low-quality coal in thermoplastic stage and found that coal samples containing HPC pyridine extract component are more capable of producing high-strength coke than raw coal or coal samples containing extract component. Coal extracts are converted into gaseous and liquid products during coal pyrolysis, thereby stabilizing free radical fragments and forming coke in the pore structure of the coal matrix. Collin et al. [12] have added tar and pitch as a binder to coal for coking and found that the cohesiveness of coal and the index of CSR have been greatly improved. Polycyclic aromatic hydrocarbons (PAHs) is the main component of pitch. Hayashizaki et al. [13] added PAHs to coal and found that when PAHs with molecular weight between 178.23 and 378.47 Da are added to the coal, the maximum expansion of coal and the strength of the resulting coke increases significantly. Although many researchers have done some research on the enhancement of iron coke strength, and some results have been achieved, none of the above studies gives the mechanism of the binder in the coking process. Therefore, there are certain limitations on the choice and use of the binder, which leads to defects in the optimization of the iron coke strength.

Our previous research [14, 15] has confirmed that the main reason for the strength decrease of iron coke is that the addition of Fe_2O_3 reduces the formation of liquid phase in the coking process, resulting in the reduction of the aromaticity and the average accumulation height of iron coke. As a by-product of coal coking, the composition of coal tar is very similar to that of the fluid phase produced during coking. In this study, it was selected as a binder to optimize the strength of iron coke, and the influence of coal tar on the properties and structure of iron coke were obtained by analyzing the thermoplastic changes before and after the addition of coal tar.

Table 1 Proximate and ultimate analyses of the coals (wt%)

Samples	Proximate analyses (wt%)				Ultimate analyses (wt%)					R_0 (%)	H/C
	M_{ad}	V_{daf}	FC_d	A_d	C_{daf}	H_{daf}	O_{daf}	N_d	S_d		
Coal-A	2.30	22.25	71.90	7.52	87.97	4.95	5.11	1.45	0.37	1.228	0.056
Coal-B	1.74	31.72	61.72	9.61	85.49	5.10	6.28	1.36	1.47	1.008	0.060
Coal-C	2.34	34.40	60.94	7.12	84.30	5.66	8.87	0.94	0.15	0.85	0.067
Coal-D	1.70	18.34	70.30	13.92	88.80	4.51	5.23	1.25	1.06	1.713	0.051

M moisture, *V* volatile matter, *FC* fixed carbon, *A* ash, *ad* air dry, *d* dry, *daf* dry and ash-free, R_0 the maximum reflectance of vitrinite, *H/C* the ratio of element H to C

Experiment

Sample Preparation

Four coals, Coal-A, Coal-B, Coal-C, and Coal-D from a steel corporation located in Northeast of China, with 1–3 mm particle size distribution were used in this work and the basic properties of the coals were described in Table 1. A standard mixed coal is composed of Coal-A (30 wt%), Coal-B (20 wt%), Coal-C (40 wt%), and Coal-D (10 wt%), and Fe_2O_3 (Purity > 99.9%, particle size < 50 nm) was used as the iron-containing mineral. The coals and Fe_2O_3 were dried under vacuum at 100 °C for 12 h before used.

Coal Tar Collection and Analyses

A sample of 2 kg of standard mixed coal was loaded into a laboratory coke oven that was fitted with a condenser at gas outlet. Thermal extraction was performed under nitrogen atmosphere and extracting at temperatures of 1050 °C for 2 h. The coal tar obtained is used as binder [16].

The chemical composition of the tar was identified by GC–MS system (QP 2010 Ultra, Shimadzu). 1 mL tar (with butyl acetate as solvent) was injected into the inlet in split injection mode at a split ratio of 30: 1 under a voltage of 70 eV. The temperature in the oven was maintained at 80 °C for 3 min, then raised to 300 °C at a heating rate of 10 °C/min, and held at this temperature for 5 min. Helium (purity > 99.999%) was used as a carrier gas at a current speed of 1 mL/min in the experiment. The chemical composition of the tar was identified using NIST 11 library data, and their quantitative analyses were conducted using the area normalization method in GC–MS solution 4.11 (software developed by Shimadzu). Further, the peak of butyl acetate was removed after treatment.

Iron Coke Preparation

Coking experiments were carried in a 2 kg laboratory coke oven. Approximately, 2 kg of standard mixed coal, 200 g distilled water, 600 g Fe_2O_3, and a certain amount of coal tar (1 wt%, 3 wt%, 5 wt%, 7 wt% of coal mass respectively) were mixed homogeneously. Then they were loaded into a coking tank with an inner diameter of 100 mm and a height of 500 mm with the bulk density of 0.85 t/m^3. The coking tank was quickly placed into the coke oven with preheating temperature of 800 °C. After the temperature of the coal cake center was raised to 800 °C, rising the temperature of the coal cake center to 1050 °C at a heating rate of 10 °C/min, and then keeping the coke temperature constant for 6 h. Finally, stopped heating, so that the coal sample was cooled to room temperature with the furnace under a nitrogen atmosphere to obtain the iron coke sample we excepted.

Coke Characterization

The cold mechanical strength of the resultant cokes was assessed by the Chinese Industrial Standard method (GB/T 2006–2008), while the reactivity towards carbon dioxide at 1100 °C (CRI) and the index of coke strength after reaction (CSR) were recorded using the SAC method (GB/T 4000–2017).

The carbon structure of iron coke was analyzed by an X-ray diffractometer (MAX2500PC X, Nippon koji co. LTD). All samples were pulverized in the laboratory and screened to below 0.074 mm. The X-ray source was generated by a copper $K\alpha$ radiation (40 kV, 150 mA). The scanning angular started from 15° to 90° at a rate of 4°/min, 0.02°/step. The broad peak of 2θ ranging from 15° to 32° was fitted by two Gaussian peaks around 21° and 26°, representing the γ-band, π-band (002), respectively. In this work, f_a was obtained from the following equation [17].

$$f_a = A_{C_{ar}} / \left(A_{C_{al}} + A_{C_{ar}}\right) = A_{\pi} / \left(A_{\pi} + A_{\gamma}\right) \tag{1}$$

where A is the diffraction peak area, Cal is aliphatic carbon, and Car is aromatic carbon.

Furthermore, d_{002}, L_c, and L_a were calculated using the classical Scherrer equations [18, 19].

The specific surface area (S_g) of iron coke is obtained through an automatic multi-station ratio surface and aperture analyzer (Max-II, McGee bayer, Japan). Samples with particle size of 3–5 mm were selected for isothermal nitrogen adsorption/ desorption at 77 K, and calculate the specific surface area of the sample by the BET adsorption isotherm equation and specific surface area calculation formula [20].

$$S_g = A_m \times N_A \times \frac{V_m}{22414} \times 10^{-18} \quad (2)$$

where A_m is the average cross-sectional area of the nitrogen molecule (nm^2), N_A is 6.02×10^{23}, and V_m is the single-layer saturated nitrogen adsorption.

Results and Discussion

Compositional Analyses of Coal Tar

Figure 1 is the GC–MS chromatogram of the tar of the standard mixed coal. It can be seen that coal tar contains a variety of substances, and the molecular weight of the compounds detected in coal tar increases gradually with the extension of residence time. As shown in Table 2, there are 38 kinds of compounds with a relative content of more than 1% in coal tar, mainly complex polycyclic compounds, such as naphthene, and some aliphatic compounds and phenolic substances. In fact, after treatment by GCMS solution 4.11, it was found that coal tar contained about 200 kinds of organic compounds, indicating the complexity of coal tar composition. At the same time, it should be noted that the relative content of sulfur and nitrogen compounds in coal tar is generally low, so it is not shown in Table 2.

The 38 compounds in coal tar are divided into three categories: (1) benzene compounds, including monocyclic benzene compounds and complex polycyclic compounds, such as o-xylene, naphthalene, anthracene, and phenanthrene; (2) aliphatic compounds such as n-butyl ester, Butyl butyrate, tridecane, tetradecane, undecane, and docosane. It is worth noting that the presence of alcohols and acids

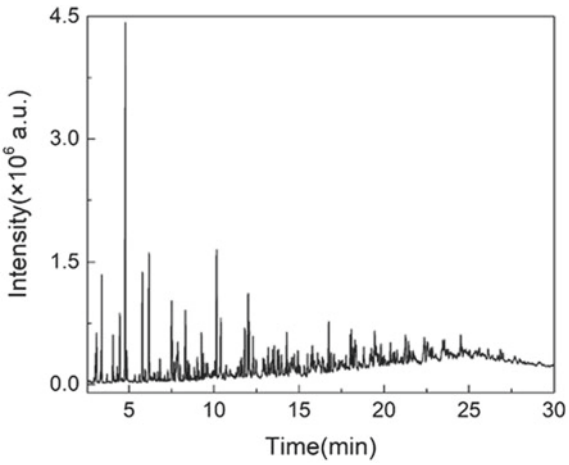

Fig. 1 GC–MS chromatogram of standard mixed coal tar

Table 2 Chemical compounds in coal tar (%)

Time (min)	Components	Relative amount (%)	Time (min)	Components	Relative amount (%)
3.03	o-Xylene	1.04	13.19	1,4,6-trimethylnaphthalene	1.17
3.10	N-butyl ester	1.08	13.67	Pentadecane	1.29
3.39	Butyl propionate	2.76	14.28	Fluorene	1.71
4.05	2-methyl propionate	2.28	14.37	Nonadecane	1.14
4.47	phenol	1.17	16.67	Tricosane	1.08
4.78	Butyl Butyrate	3.22	16.75	Anthracene	1.77
4.87	1,2,4-trimethylbenzene	7.58	18.01	Tetracosane	1.19
5.79	2-methylphenol	2.59	18.08	1-methylanthracene	1.62
6.18	3-methylphenol	1.28	18.28	5-methylanthracene	1.43
7.50	2,4-dimethylphenol	2.74	18.81	2-methylanthracene	1.47
7.87	3,5-dimethylphenol	1.17	19.45	2,5-dimethylphenanthrene	2.21
8.32	2,3-dimethylhydroquinone	1.25	20.37	Pyrene	1.21
9.27	2-ethyl-5-methylphenol	3.93	20.79	Pentacosane	1.34
9.35	Tridecane	1.36	21.27	benzofluorene	1.12
10.15	Naphthalene	2.24	22.38	O-terphenyl	1.63
10.39	2-methylnaphthalene	1.81	23.55	chrysene	1.39
11.56	Tetradecane	1.42	24.24	Hexacosane	1.09
11.80	1,2-dimethylnaphthalene	1.45	24.51	1-methylchrysene	1.08
11.99	1,7-dimethylnaphthalene	2.76	Others [a]	–	30.51
12.29	1,3-dimethylnaphthalene	1.42			

[a]Component content < 1.00%

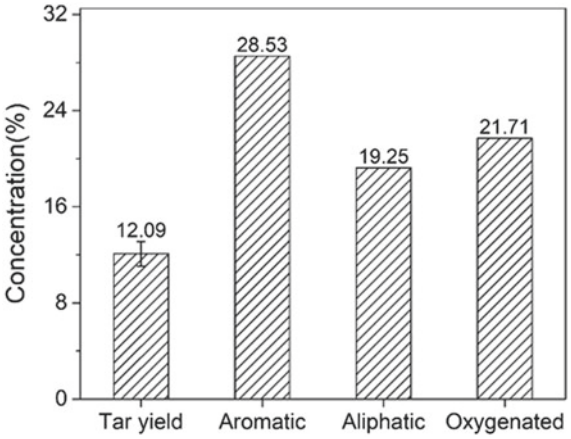

Fig. 2 Classification and amount of coal tar

can greatly promote the fluidity of metaplast in the thermoplastic stage [14]. Therefore, in this section, esters are classified as aliphatic substances; (3) oxygenated compounds, mainly phenolic substances.

It is well known that the strength of coke is closely related to the metaplast (fluid phase) in coal coking [21, 22]. Qiu et al. [14] found that the composition of metaplast is mainly monocyclic benzene compounds, such as methylbenzene, ethylbenzene and o-xylene, and long-chain unbranched alkanes with 19 to 26 carbon atoms. The addition of Fe_2O_3 inhibits the formation of ethylbenzene, o-xylene, and long-chain unbranched alkanes with 24–26 carbon atoms in the thermoplastic stage of coal, which reduces the amount of metaplast produced, which in turn leads to a decrease in iron coke strength.

It can be seen from Fig. 2 that the proportion of benzene compounds in the tar of mixed coal is as high as 28.53%, and the content of aliphatic compounds mainly composed of alkanes is as high as 19.25%. These substances all contribute to the formation of metaplast in the thermoplastic stage of the coal coking process. Therefore, coal tar can be used as a binder to optimize the strength of iron coke.

Effects of Coal Tar on the Properties of Iron Coke

Figure 3 shows the mechanical properties of iron coke obtained by adding coal tar with different amounts. With the increase of coal tar content (0 wt%, 1 wt%, 3 wt%, 5 wt%, and 7 wt%), the crushing strength of iron coke increases by 0.78%, 1.19%, 1.14%, and 1.09%, respectively, while the wear resistance index decreases by 0.42%, 1.70%, 1.64%, and 1.66%, respectively. From the perspective of the overall trend, the cold performance of iron coke is enhanced with the increase of the amount of coal tar. When the amount of coal tar is increased from 1 to 3%, the strength indexes of iron coke increase more obviously. When the added amount is increased to 5%

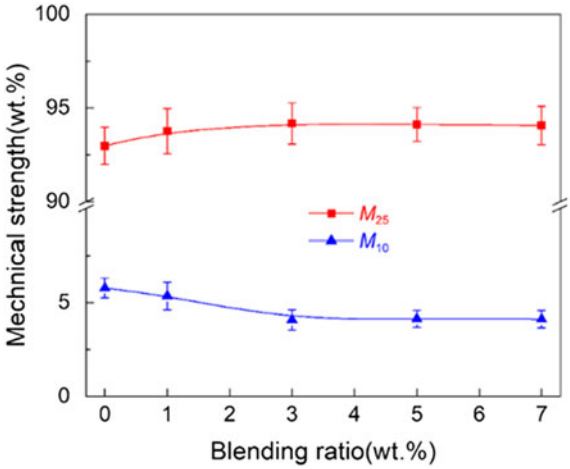

Fig. 3 Mechanical strength of iron coke with different blending ratio of coal tar

and 7%, the intensity change is not obvious, but there is a slight downward trend. It shows that reasonable addition of coal tar is beneficial to improve the cold strength of iron coke.

Figure 4 shows the thermal property and the particle size distribution of iron coke obtained by adding coal tar with different contents. When coal tar is not added, the iron coke has a CRI of 41.57% due to the addition of 3% Fe_2O_3 during the previous preparation. As the amount of coal tar added increases, the CRI of iron coke gradually decreases, but when the amount of coal tar reaches 3%, the CRI of iron coke is still above 40%. When the amount of coal tar is within 3%, the index of CSR of iron coke gradually increases as the amount of tar added increases, and when the addition of coal tar is 3%, the index of CSR reaches a maximum of 55.86% which meets

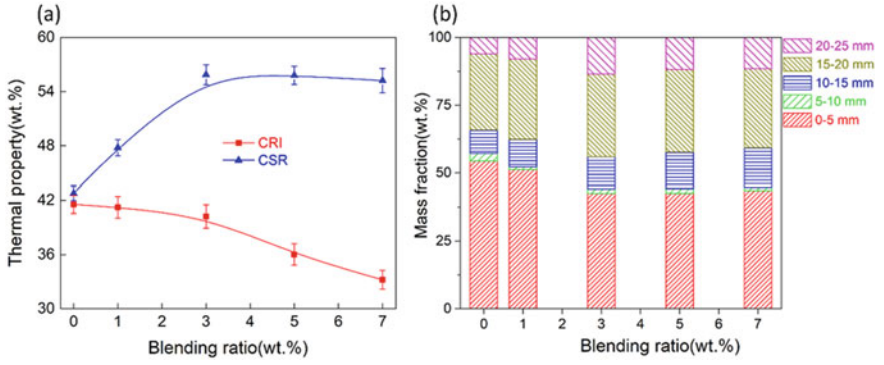

Fig. 4 Thermal property and particle size distribution after of iron coke with different blending ratio of coal tar: **a** thermal property and **b** particle size distribution

the national secondary coke strength standard. However, there was a slight decrease when tar was added at 5% and 7%. With the increase of the addition of coal tar, the content of iron coke with particle sizes in the range of 15 ~ 20 mm and 20 ~ 25 mm first increased and then decreased, and the pulverization rate decreased first and then increased slightly.

Effect of Coal Tar on the Structure of Iron Coke

Figure 5 shows the XRD spectrum of iron coke after adding coal tar with different contents (10–50°). It can be seen that XRD patterns of samples have strong diffraction peaks around the diffraction angle 26. This diffraction peak is a mixture of γ and π peaks, indicating that iron coke is between graphite and amorphous carbon after adding coal tar [23]. However, after adding coal tar, the peak intensity of the diffraction peak increases, indicating that adding coal tar can increase the degree of graphitization of iron coke. Further, the diffraction pattern is subjected to Gaussian peak processing to obtain the carbon structure characteristics of iron coke after adding coal tar with different contents.

When the amount of coal tar is added within 3%, the aromaticity of iron coke gradually increases, and the interlayer spacing of the carbon microcrystalline structure gradually decreases, indicating that the degree of graphitization of coke at this time gradually increases with the increase of the amount of coal tar added. The average stacking height and lateral size also gradually increase with the increase of the addition of coal tar, indicating that the crystallite size of the coke gradually increases at this time. However, when the addition of coal tar is 5 and 7%, the aromaticity, average stacking height, and lateral size of coke are reduced to a certain extent, and the interlayer distance is slightly increased. Combining the influence of coal tar addition on the mechanical strength and thermal properties of iron coke, (Figs. 3 and 4), it can be found that coal tar can gradually increase the graphitization degree

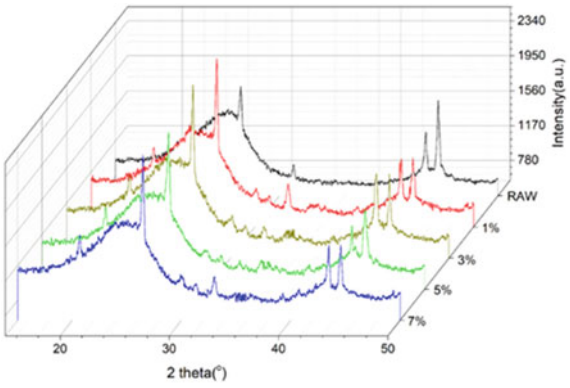

Fig. 5 XRD spectra of iron coke with different blending ratio of coal tar

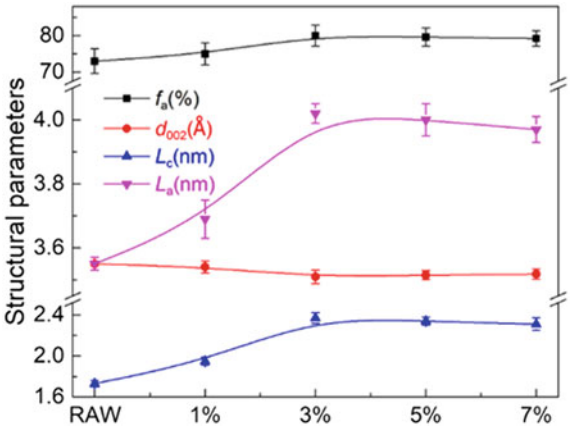

Fig. 6 Carbon structural parameters of iron coke with different addition of coal tar

and grain size of iron coke within 3%, thereby gradually increasing the mechanical strength and CSR index of iron coke. However, when the addition amount is 5 and 7%, due to the limited effect of coal tar on the structure and properties of iron coke, the microcrystalline structure parameters of iron coke slightly decrease, which in turn leads to a slight decrease in coke strength (Fig. 6).

Effects of Coal Tar on Specific Surface Area of Iron Coke

The specific surface area of iron coke after adding different amounts of coal tar is displayed in Fig. 7. It can be seen that the specific surface area of the raw iron

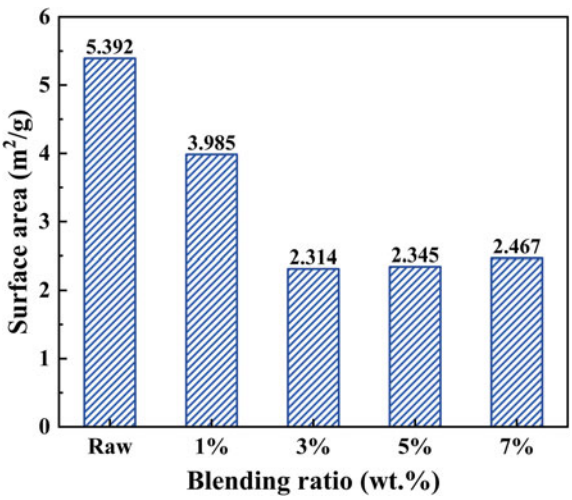

Fig. 7 Surface area of iron coke with different addition content of coal tar

coke is 5.392 m^2/g. With the addition of coal tar, the specific surface area of iron coke decreases and reaches a minimum value of 2.314 m^2/g when the amount of coal tar is 3%. It shows that the addition of coal tar can reduce the specific surface area of iron coke and then reduce the amount of contact between the surface of the iron coke and CO_2, which is conducive to improving the strength of the iron coke. Considering the influence characteristics of coal tar on the reactivity, strength, and structure (microcrystalline structure and specific surface area) of iron coke, the coal tar content of 3% was selected to optimize the strength of iron coke, and the iron coke with a reactivity of 40.21% and a strength of 55.86% after the reaction was prepared.

Conclusion

In this study, the composition of coal tar was analyzed using GC–MS, and compared with the composition of metaplast, coal tar was determined as an additive to optimize the strength of iron coke. Then the influence of coal tar on the properties and structure of iron coke was analyzed by XRD and BET. The components of coal tar are mainly complex polycyclic compounds, aliphatic compounds, and phenolic substances. The pyrolysis products of complex polycyclic compounds and aliphatic compounds are similar to the components of metaplast, so coal tar can be selected as the strength optimization additive of iron coke. The addition of coal tar can increase the cold performance and post-reaction strength of iron coke and reach the optimal value when the addition amount is 3%, but the reactivity of iron coke decreases slightly after the addition of coal tar. It is due to the fact that the added coal tar can increase graphitization degree, aromatic degree, and microcrystalline size of coke and reduce specific surface area of coke. After comprehensively considering the influence characteristics of coal tar on the mechanical strength, CRI, CSR, the carbon structure, and the specific surface area of iron coke, the 3% (based on coal mass) coal tar addition amount was selected as the optimal binder addition amount to prepare iron coke with 40.21% CRI and 55.86% CSR.

References

1. Srishilan C, Shukla AK (2017) Static thermochemical model of COREX melter gasifier. Metall Mater Trans B 49:388–398
2. Zhang X, Yee SA, Yee ZL (2019) Three-terminal heterojunction bipolar transistor solar cells with non-ideal effects: efficiency limit and parametric optimum selection. Energy Convers Manage 188:112–119
3. Nomura S, Terashima H, Sato E (2007) Some fundamental aspects of highly reactive iron coke production. ISIJ Int 47(6):823–830
4. Price JD, Mador ME (1958) Coal carbonization research—a world-wide problem. Indus Eng Chem 50(1):17–20
5. Nok PS (1959) Production of pig iron with the use of coke iron. Metallurgist 3(6):237–239

6. Michitaka S, Hidetoshi M, Kunihiko I (2015) Recent development of mid-and long-term CO_2 mitigation technology at JFE Steel. In: Paper presented at Asia steel international conference, Yokohama, Japan
7. Nomura S, Naito M, Yamaguchi K (2007) Post-reaction strength of catalyst-added highly reactive coke. ISIJ Int 47(6):831–839
8. Xu RS, Dai BW, Wang W (2018) Effect of iron ore type on the thermal behavior and kinetics of coal-iron ore briquettes during coking. Fuel Process Technol 173:11–20
9. Xu RS, Zheng H, Wang W (2018) Influence of iron minerals on the volume, strength, and CO_2 gasification of ferro-coke. Energy Fuel 32(12):12118–12127
10. Chang CM, Whang TJ, Huang DS (2014) Thermoplasticity and strength improvement of coking coal by addition of coal extracts. Fuel 117:364–371
11. Tsubouchi N, Naganuma R, Mochizuki Y (2019) Production of high-strength coke from low-quality coals chemically modified with thermoplastic components. ISIJ Int 59(8):1396–1403
12. Collin G, Bujnowska B (1994) Co-carbonization of pitches with coal mixtures for the production of metallurgical cokes. Carbon 32(4):547–552
13. Hayashizaki H, Kanehashi K, Uebo K (2019) Effects of hydrocarbon addition on increase in dilatation of coal. Isij Int 59(8):1404–1412
14. Qiu S, Zhang S, Sou G (2020) Effecvts of Fe_2O_3 addition on the thermoplasticity and structure of coking coal matrix during thermoplastic stage of pyrolysis. Fuel 260:374–383
15. Zhou H, Wu CF, Onwudili JA (2015) Effect of interactions of PVC and biomass components on the formation of polycyclic aromatic hydrocarbons (PAH) during fast co-pyrolysis. RSC Adv 5(15):11371–11377
16. Qiu S, Zhang S, Fang Y (2019) Effects of poplar addition on tar formation during the co-pyrolysis of fat coal and poplar at high temperature. RSC Adv 9:28053–28060
17. Qiu S, Zhang S, Zhu R (2018) Influence of TiO_2 addition on the structure and metallurgical properties of coke. Int J Coal Prep Util. https://doi.org/10.1080/19392699.2018.1496913
18. Gupta S, French D, Sakurovs R (2008) Minerals and ironmaking reactions in blast furnaces. Prog Energy Combust 34:155–197
19. Gupta S, Sahajwalla V, Burgo J (2005) Carbon structure of coke at high temperatures and its influence on coke fines in blast furnace dust. Metall Mater Trans B 36(3):385–394
20. Barrett EP, Joyner LG, Halenda PP (1951) The Determination of pore volume and area distributions in porous substances. Computations from nitrogen isotherms. J Am Chem Soc 73(1):373–380
21. Alvarez R, Diez MA, Barriocanal C (2017) An approach to blast furnace coke quality prediction. Fuel 86(14):2159–2166
22. Gayo F, Garcia R, Diez MA (2016) Modelling the Gieseler fluidity of coking coals modified by multicomponent plastic wastes. Fuel 165:134–144
23. Sonibare O, Haeger T, Foley SF (2010) Structural characterization of Nigerian coals by X-ray diffraction Raman and FTIR spectroscopy. Energy 35(12):5347–5353

Pelletizing of Iron Ore with High Iron Grade and Low Silicon Content

Yan Zhang, Gele Qing, Yunqing Tian, Zhixing Zhao, Guoyou Liu, Kai Wang, Wenwang Liu, Ming Li, Dawei Sun, Luyao Zhao, Li Ma, and Tao Yang

Abstract In this paper, an iron ore with high iron grade and low silicon content was used in pelletizing experiments. Specific surface areas were tested, and it would increase slowly and then have a rapid increase with the increasing of particle sizes. Thirty percentage of the high iron grade ore could be used when −200 meshes content of the ore reached to 89% or the ore was grinded by high pressure roller. Compression strength of firing pellet would decrease, higher than 2500 N/P yet, when the ore was added. SiO_2 content of firing pellets would decrease from 4.22 to 3.36%, a 20.38% decline, while 30% of the high iron grade ore was added.

Keywords Pelletizing · Specific surface area · High pressure roller · SiO_2 content

Introduction

Sinters and pellets are the main raw materials for blast furnace smelting. Pellets have the advantages of higher grade, lower energy consumption, and pollutant emission compared with sinters [1, 2]. The smelting process of blast furnace is to reduce iron oxide to iron, and the acidic impurities in iron ores will form slag with alkaline flux meanwhile [3]. Too much slag will take away a large amount of heat and increase the fuel consumption of blast furnace, which is not conductive to the realization of low-carbon ironmaking. Therefore, the higher the grade of iron ore was into the blast furnace, the better on the premise of ensuring the quality.

Y. Zhang (✉) · G. Qing · Y. Tian · Z. Zhao · L. Zhao · L. Ma · T. Yang
Research Institute of Technology of Shougang Group Co., Ltd, Beijing, China
e-mail: yanzhang@shougang.com.cn

Y. Zhang · G. Qing · Y. Tian · Z. Zhao
Beijing Key Laboratory of Green Recyclable Process for Iron & Steel Production Technology, Beijing, China

G. Liu · K. Wang · W. Liu · M. Li · D. Sun
Shougang Jingtang United Iron and Steel Co., Ltd, Tangshan, Hebei, China

Z. Peng et al. (eds.), *12th International Symposium on High-Temperature Metallurgical Processing*, The Minerals, Metals & Materials Series,
https://doi.org/10.1007/978-3-030-92388-4_32

In this paper, study on an iron ore with high iron grade and low silicon content (HILS) used in pelletizing was carried out. Specific surface areas (SSA) of the iron ores with different particle sizes were measured. Experiments of pelletizing were conducted, and ballabilities of the iron ores with different ratios and particle sizes were tested. Proportions of the iron ores could be used in pellets were determined.

Materials and Experimental Methods

Chemical Compositions of Materials

Chemical compositions of two major iron ores used in one Shougang pelletizing plant were listed in Table 1. Iron grades of Iron ores A and B were 68.20% and 69.32%, respectively. SiO_2 content of Iron ore B was less than 2.0%. The particle sizes of Iron ores A and B were small with percentages of −200 meshes less than 80%. Iron ore A had a better pelletizing performance than Iron ore B from the production practice. Iron ore A could be used up to 100%, while maximum using proportion of Iron ore B was 30%.

Chemical compositions and physical properties of the bentonite used in the experiments were shown in Tables 2 and 3. This bentonite was a kind of sodium bentonite with the 2-h water absorption 364%.

Chemical compositions of the iron ore with high iron grade and low silicon content used in the experiments were listed in Table 4. Iron grade of HILS was higher than 70% with the silicon content less than 1.0%.

Table 1 Chemical compositions of two iron ores used in Shougang

Content (%)	TFe	FeO	SiO_2	Al_2O_3	CaO	MgO	−200 meshes
Iron ore A	68.70	28.59	3.58	0.49	0.38	0.49	83.47
Iron ore B	69.32	28.92	1.95	0.34	0.45	0.66	88.48

Table 2 Chemical compositions of the bentonite

Content (%)	SiO_2	Al_2O_3	CaO	MgO	K_2O	Na_2O	LOI
Bentonite	63.30	14.20	3.10	2.98	1.31	2.63	9.37

Table 3 Physical properties of the bentonite

Physical properties	2-h water absorption %	Methylene blue adsorbed g/100 g	Swelling index ml/2 g
Bentonite	364	29.3	17

Table 4 Chemical compositions of HILS

Content (%)	TFe	FeO	SiO_2	Al_2O_3	CaO	MgO
HILS	70.57	27.91	0.61	0.30	0.11	0.58

Table 5 SSAs of Iron ores A and B

Name	−200 meshes %	SSA cm^2/g
Iron ore A	83.47	1206
Iron ore B	88.48	1062

Table 6 SSAs of HILS with different particle sizes

Name	−200 meshes %	SSA cm^2/g
HILS-1	72.95	687
HILS-2	75.66	698
HILS-3	83.07	726
HILS-4	84.15	757
HILS-5	85.89	815
HILS-6	89.05	1034

Specific Surface Areas of Iron Ores

Specific surface area is referred to the total area of materials per unit mass [4]. In this paper, SSAs of different iron ores were measured by Blaine method [5].

SSAs of Iron ores A and B were shown in Table 5. Although Iron ore A had a coarser particle distribution than Iron ore B, SSA of Iron ore A was much higher than Iron ore B that meant SSA was not proportional to particle size for different iron ores. SSAs of HILS with different particle sizes were tested, and the results were shown in Table 6 and Fig. 1.

As shown in Fig. 1, SSA of HILS would increase slowly when the −200 meshes increased from 72.95 to 83.07% and then it would have a rapid increase, from 726 to 1034 cm^2/g, as the −200 meshes increased from 83.07 to 89.05%. The results signified that there was a positive correlation between SSA and particle size for the same iron ore.

Particle Morphology of HILS with Different Particle Sizes

Particle morphology had an important influence on the ballability of green pellet. Therefore, particle morphologies of HILS with different particle sizes were observed by scanning electron microscope. As presented in Fig. 2, distribution of the powder

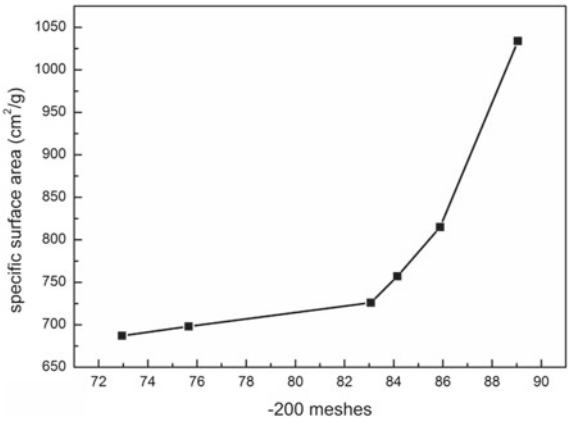

Fig. 1 SSA of HILS with different particle sizes

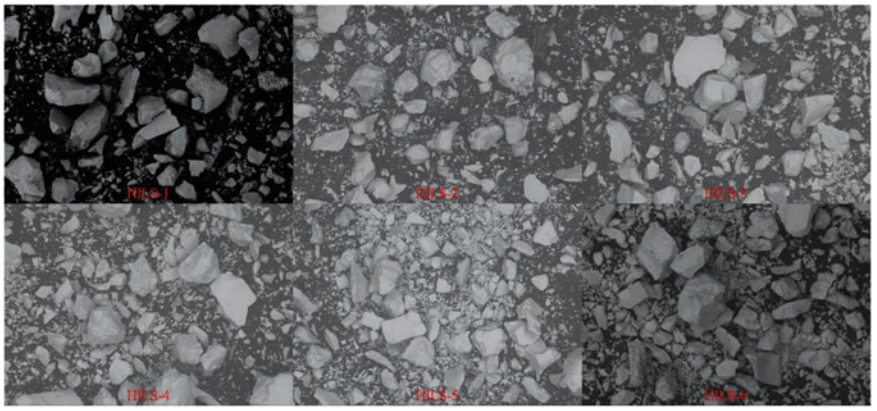

Fig. 2 Particle morphology of HILS with different particle sizes (×200)

particle was uniform and surface of the powder was smooth especially when the content of −200 meshes was little.

Results and Discussion

Influence of Single Iron Ores on Green Pellets Quality

Six kinds of HILS with different particle sizes and SSAs together with Iron ores A and B were prepared in a pelletizing disc with diameter of 800mm. Falling strength greater than 4 times and compression strength bigger than 8 N/P were considered to

meet the requirements of green pellets. The pelletizing schemes of single iron ore were listed in Table 7.

Figures 3 and 4 showed the falling strength and compression strength of green pellets by using single iron ore. As results showed, falling strength would be more than 5 times and less than 4 times, respectively, when Iron ores A and B were used alone. Iron ore A had the better pelletizing performance than other ores. Falling strength and compression strength of the green pellets would increase when HILS with higher content of −200 meshes was added.

Table 7 Pelletizing schemes of single iron ore

Proportion (%)	Iron ore A	Iron ore B	HILS-1	HILS-2	HILS-3	HILS-4	HILS-5	HILS-6	Bentonite
1	100								1.8
2		100							1.8
3			100						1.8
4				100					1.8
5					100				1.8
6						100			1.8
7							100		1.8
8								100	1.8

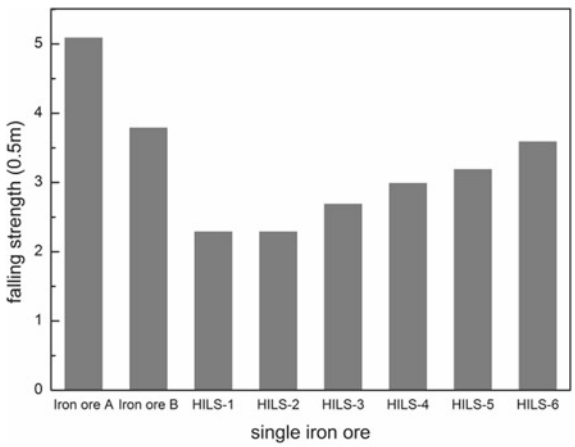

Fig. 3 Falling strength of green pellets

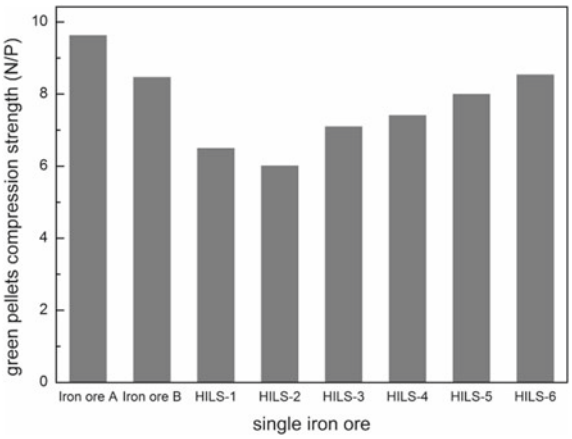

Fig. 4 Compression strength of green pellets

Influence of Mixed Iron Ores on Green Pellets Quality

Proportions of Iron ore A and Iron ore B used in one Shougang pelletizing plant were 80 and 20%. In order to reduce the silicon content of pellet, HILS with different particle sizes was used to replace up to 30% of Iron ore A which the silicon content was 3.98%. Pelletizing schemes using mixed iron ores were listed in Table 8.

As shown in Table 8, falling strength, less than 4 times, of green pellets could not satisfy the quality demand when HILS-1, HILS-2, HILS-3, and HILS-4 were used. Falling strength would reach to 4.0 times, and compression strength would be 8.51 N/P when 10% of Iron ore A was replaced by HILS-5. HILS-6 could be added up to 30%, and quality of green pellets could meet the requirements.

Influence of HILS After High Pressure Roller Grinding

Due to the poor balling performance of HILS, high pressure roller was used. Table 9 illustrated the content of −200 meshes and SSAs after high pressure roller grinding (AHPRG). There were little change of content of −200 meshes and a great improvement of SSA when HILS-5 was grinded by high pressure roller.

Pelletizing experiments were also carried out by using HILS-5 and HILS-5 (AHPRG), and the results were shown in Table 10. HILS-5 could be used 30% to replace Iron ore A after high pressure roller grinding.

Table 8 Pelletizing schemes of mixed iron ores

Proportion (%)	Iron ore A	Iron ore B	HILS-1	HILS-2	HILS-3	HILS-4	HILS-5	HILS-6	Bentonite	Green pellets falling strength (0.5 m)	Green pellets compression strength (N/P)
1	80	20							1.8	4.8	9.02
2	50	20	30						1.8	2.5	6.72
3	60	20	20						1.8	2.7	7.05
4	70	20	10						1.8	3.0	6.95
5	50	20		30					1.8	2.4	6.82
6	60	20		20					1.8	2.7	6.85
7	70	20		10					1.8	3.1	7.56
8	50	20			30				1.8	2.9	7.25
9	60	20			20				1.8	3.2	7.28
10	70	20			10				1.8	3.3	7.59
11	50	20				30			1.8	3.1	7.46
12	60	20				20			1.8	3.3	8.15
13	70	20				10			1.8	3.5	8.08
14	50	20					30		1.8	3.5	8.15
15	60	20					20		1.8	3.7	8.37
16	70	20					10		1.8	4.0	8.51
17	50	20						30	1.8	4.5	8.55
18	60	20						20	1.8	4.4	8.86
19	70	20						10	1.8	4.5	8.83

Table 9 Content of −200 meshes and SSAs after high pressure roller grinding

name	−200 meshes %	SSA cm^2/g
HILS-5	85.89	815
HILS-5 (AHPRG)	86.30	1038

Firing Experiments with HILS

Tubular electric furnace was used to fire the green pellets with a maximum temperature of 1260°C. Compression strength should be higher than 2500 N/P for large blast furnace.

As presented in Table 11, compression strength would be higher than 3000 N/P when the firing pellets with the proportion of 80% of Iron ore A and 20% of Iron ore B. Compression strength decreased when HILS-5 was added. Compression strength would be higher than 2800 N/P when HILS-5 (AHPRG) and HILS-6 were added to replace Iron ore A.

Table 12 illustrated the decline ratio of SiO_2 content while using HILS. SiO_2 content of firing pellets would decrease from 4.22 to 3.36%, a 20.38% decline, while 30% of the HILS was added.

Conclusions

Specific surface areas of HILS with different particle sizes were tested; SSA would increase slowly and then has a rapid increase with the increasing of particle sizes. Falling strength and compression strength of the green pellets would increase when HILS with higher content of −200 meshes was added. HILS could be used up to 30% if the content of −200 meshes reached to 89.05%. Proportion of HILS could be increased after high pressure roller grinding. Compression pressure of firing pellets could meet the requirements of large blast furnace when 30% of HILS was added. SiO_2 content of firing pellets would decrease from 4.22 to 3.36%, a 20.38% decline, while 30% of the HILS was added.

Table 10 Pelletizing schemes of mixed iron ores

Proportion (%)	Iron ore A	Iron ore B	HILS-5 (AHPRG)	Bentonite	Green pellets falling strength (0.5 m)	Green pellets compression strength (N/P)
1			100	1.8	3.6	8.75
2	50	20	30	1.8	4.4	8.85
3	60	20	20	1.8	4.8	9.05
4	70	20	10	1.8	4.6	9.32

Table 11 Schemes of firing experiments

Proportion (%)	Iron ore A	Iron ore B	HILS-5	HILS-5 (AHPRG)	HILS-6	Bentonite	Compression strength of firing pellets (N/P)
1	80	20				1.8	3038
2	50	20	30			1.8	2527
3	60	20	20			1.8	2652
4	70	20	10			1.8	2665
5	50	20		30		1.8	2838
6	60	20		20		1.8	3018
7	70	20		10		1.8	2987
8	50	20			30	1.8	2859
9	60	20			20	1.8	2957
10	70	20			10	1.8	3056

Table 12 Decline ratio of SiO_2 content while using HILS

Proportion (%)	Iron ore A	Iron ore B	HILS	Bentonite	SiO_2 content of firing pellets (%)	Proportion of decline of SiO_2 content (%)
1	80	20		1.8	4.22	
2	70	20	10	1.8	3.93	6.87%
3	60	20	20	1.8	3.65	13.51%
4	50	20	30	1.8	3.36	20.38%

References

1. Zhu D, Huang W et al (2017) Technical progress in iron ore pelletization. Sinter Pelletizing 42:42–49
2. Xu M, Zhan Y et al (2017) Analysis of pellet technology and production of China in 21st century. Sinter Pelletizing 42:25–30
3. Spirin NA, Lavrov VV, Burykin AA et al (2011) Complex of model systems for supporting decisions made in managing blast-furnace smelting technology. Metallurgist 54:566–569
4. Carter DL, Mortland MM, Kemper WD (1986) Methods of soil analysis: part 1 physical and mineralogical methods. American Society of Agronomy, Madison
5. Moisés F, de Rojas S, Isabel M et al (1991) Determination of specific surface area by the laser diffraction technique. Comparison with the blaine permeability method. Cem Concr Res 5:709–717

Influence of Aluminum on the Hot Ductility of a High-Strength Steel

Pei Zhu, Lifeng Zhang, and Ying Ren

Abstract The influence of Al contents (0.035, 0.5, and 0.8%) on hot ductility of high-strength steel was studied by experimental hot tensile tests in the temperature range of 600–1300 °C and under the strain rate of 0.001 s^{-1} by a Gleeble-1500 thermal simulation machine. According to the tensile results, the true stress–strain curve was obtained and the reduction of area was calculated. The results showed that when the Al content was 0.035%, the reduction of area of steel was less than 40% at 600, 700, 750, and 850 °C, and when the Al content was 0.5%, the reduction of area was less than 40% at 600–1000 °C and more than 40% at 1000–1300 °C; when the Al content was 0.8%, the reduction of area was less than 40% at 650–1050 °C. Overall, the hot ductility was the worst when the Al content was 0.5%. In addition, the fracture morphology of the samples was observed by the scanning electron microscope.

Keywords Hot deformation · Microstructural evolution · High-strength steel

Introduction

Fe–Mn–Al–C series low-density high-strength steel is a kind of advanced automobile steel (3G- AHSS), which is a new type of structural material that has lower density and higher strong plastic. A research pointed out that for every 1% of Al added to steel, the density decreases by 0.101 g/cm^3, and that the weight can be reduced by about 1.3% [1]. At present, the research on reducing the cracks of the cast slab has attracted more and more attention. The causes of billet cracks are complex and affected by the type of equipment, solidification conditions, and process operations. However, the mechanical behavior of steel at high temperatures is still the most

P. Zhu · Y. Ren
School of Metallurgical and Ecological Engineering, University of Science and Technology Beijing, Beijing 100083, China

L. Zhang (✉)
State Key Laboratory of Metastable Materials Science and Technology, Yanshan University, Qinhuangdao City 066004, Hebei Province, China
e-mail: zhanglifeng@ysu.edu.cn

Z. Peng et al. (eds.), *12th International Symposium on High-Temperature Metallurgical Processing*, The Minerals, Metals & Materials Series,
https://doi.org/10.1007/978-3-030-92388-4_33

intrinsic factor. Under laboratory conditions, it is particularly important to simulate the continuous casting process with experimental methods to determine the high-temperature mechanical properties of steel [2, 3]. Hamada and Karijalainen [4] studied the thermal plasticity of four high-manganese TWIP steels in the range of 700–1300 °C. When the contents of Al and Si both reached 3%, the first generation of Fe–Mn-Si-Al TWIP steel, the ferrite was precipitated along the grain boundary during high-temperature deformation, which seriously affected its hot ductility. Kang et al. [5] conducted an experimental study on the thermal plasticity of high-Al TWIP steel containing Nb/V at 650–1150 °C. It was found that the addition of Nb and V would make the thermal plasticity of TWIP steel worse, which was due to the fact that a large amount of Nb (C, N) and VN were precipitated nearby the grain boundary. However, if the temperature increased further, the carbonitride precipitated near the grain boundary gradually decomposed and the plasticity increased. Kang and Mintz [6] experimentally analyzed the high-temperature hot ductility of three high-Al TWIP steels with different S contents, and the relationship between the reduction of area and the S contents was also studied. Liu [7] studied the effect of Mn (14.94, 18.21, and 23.6 wt%) and Al (0.002, 0.75, and 1.47 wt%) contents on hot ductility of five high-alloy Fe-xMn-C-yAl austenitic twinning-induced plasticity (TWIP) steels which were investigated by the Gleeble-3500 thermo-mechanical simulator in the temperature range of 700–1200 °C under a constant strain rate of 3×10^{-3} s^{-1}. Zambrano [8] studied the mechanical properties of Fe–Mn–Al–C steel which were significantly enhanced after κ-carbide precipitation via aging; however, most aging treatments are energy demanding because they require relatively high temperatures and extended holding times. Xu [9] studied the hot deformation behavior of Fe-26Mn-6.2Al-0.05C steel by experimental hot compression tests in the temperature range of 800–1050 °C and strain rate range of 0.01–30 s^{-1} on a Gleeble-3500 thermal simulation machine. Zhang [9] studied the influences of steel composition and cooling rate on the steel hot ductility comprehensively. It was pointed out that the sampling position had much influence on the hot ductility behavior and the specimens extracted from the columnar zone performing the best hot ductility. Therefore, in the current study, the influence of Al contents (0.035, 0.5, and 0.8%) on hot ductility of high-strength steel was studied by experimental hot tensile tests in the temperature range of 600–1300 °C and under the strain rate of 0.001 s^{-1} by a Gleeble-1500 thermal simulation machine.

Hot Tensile Test of High-Strength Steel

The continuous casting billet of high-strength steel (0.035%Al, 0.5%Al, and 0.8%Al) was processed into a sample of ϕ10 mm × 110 mm, and the sample was tested in a Gleeble-1500 thermal simulation machine at the temperature range of 600–1300 °C and strain rate of 0.001 s^{-1} as shown as Fig. 1. The sample was heated to 1350 °C at 10 °C/s and held for 5 min. The continuous casting slab at the exit of the mold is simulated at this stage. After that, the sample was lowered to the tensile temperature

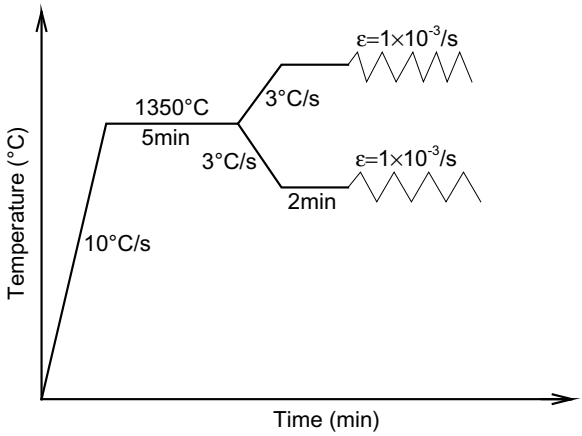

Fig. 1 Temperature control of hot tensile strength test

Table 1 Tensile temperature

600 °C	650 °C	700 °C	750 °C	800 °C	850 °C	900 °C	950 °C
1000 °C	1050 °C	1100 °C	1150 °C	1200 °C	1250 °C	1300 °C	

listed in Table 1 at a cooling rate of 3 °C/s. This stage simulates the temperature drop of the continuous casting slab after it is far from the mold outlet. When the sample reached the tensile temperature, it was held for 2 min, and then the sample was tensile loaded at a strain rate of 1×10^{-3} until it was broken, and the fractured sample was water quenched to room temperature. This stage simulates the high-temperature mechanical conditions of continuous casting billet in the bending and straightening section.

The stress–strain curve of hot tensile can effectively obtain the hot tensile strength and hot ductility of the sample at high temperature. Figure 2 shows the stress–strain curve of the samples after the hot tensile using the Gleeble-1500. Figure 2a shows the stress–strain curve of the sample with 0.035%Al, and it can be concluded that the tensile strength of sample decreased with the tensile temperature increased. And, it could be figured out that when the temperature is 600, 700, 750 °C, the hot ductility of the sample was bad. Figure 2b shows the stress–strain curve of the sample with 0.5Al. It shows that the ductility of the sample was worse than that with 0.035%Al.

Figure 3c shows the stress–strain curve of the sample with 0.8Al. It can be concluded that the tensile strength of the sample gradually decreased with the increase of the tensile temperature. When the tensile temperature increased from 600 to 950 °C, the tensile strength of the sample decreased greatly. After the sample was tensed until it was broken, the degree of deformation of the sample can reflect the ductility of the material at high temperature. It is concluded that with tensile temperature increasing from 600 to 950 °C, the degree of deformation of the sample gradually decreases, indicating that the high-temperature ductility of the sample is continuously decreasing. In the process of increasing the tensile temperature from

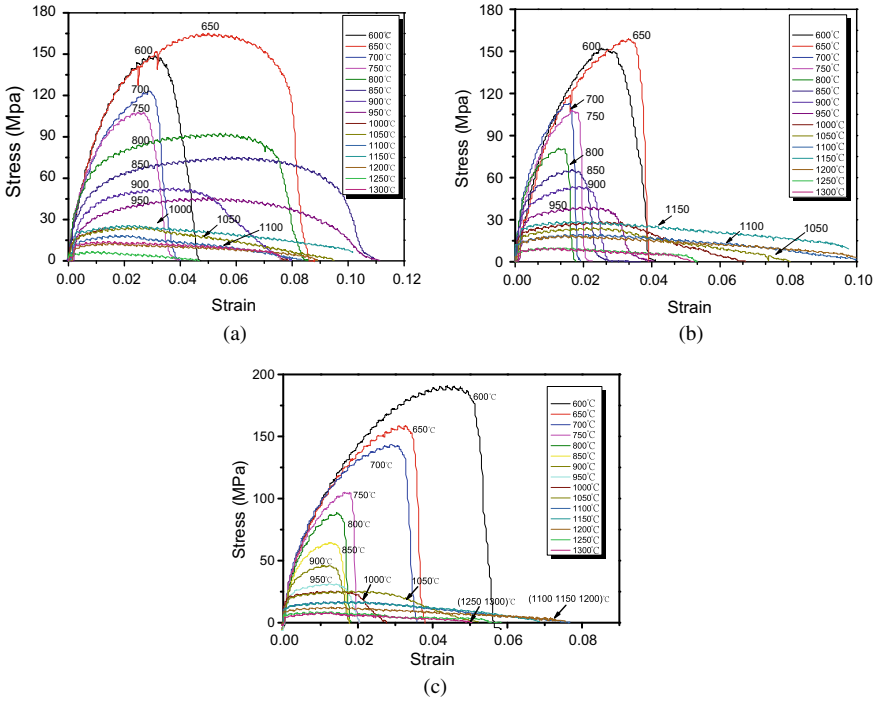

Fig. 2 Stress–strain curve of the steel with **a** 0.035Al, **b** 0.5Al, **c** 0.8Al

950 to 1300 °C, the degree of deformation of the sample before fracture continued to increase, indicating that the high-temperature hot ductility of the sample was continuously increasing. The good hot ductility of the continuous casting billet during the continuous casting process will reduce the occurrence of crack defects, thereby improving the quality of the steel.

Hot Ductility of High-Strength Steel

The reduction of area is an index to measure the deformation ability of a material. Test uses standard tensile specimens. The reduction of area can be calculated by Eq. (1),

$$\mathrm{RA} = \frac{A_0 - A_1}{A_0} \times 100\% \tag{1}$$

where A_0 is the cross-sectional area of sample before hot tensile test, A_1 is the cross-section area of sample after hot tensile test, RA is the reduction of area.

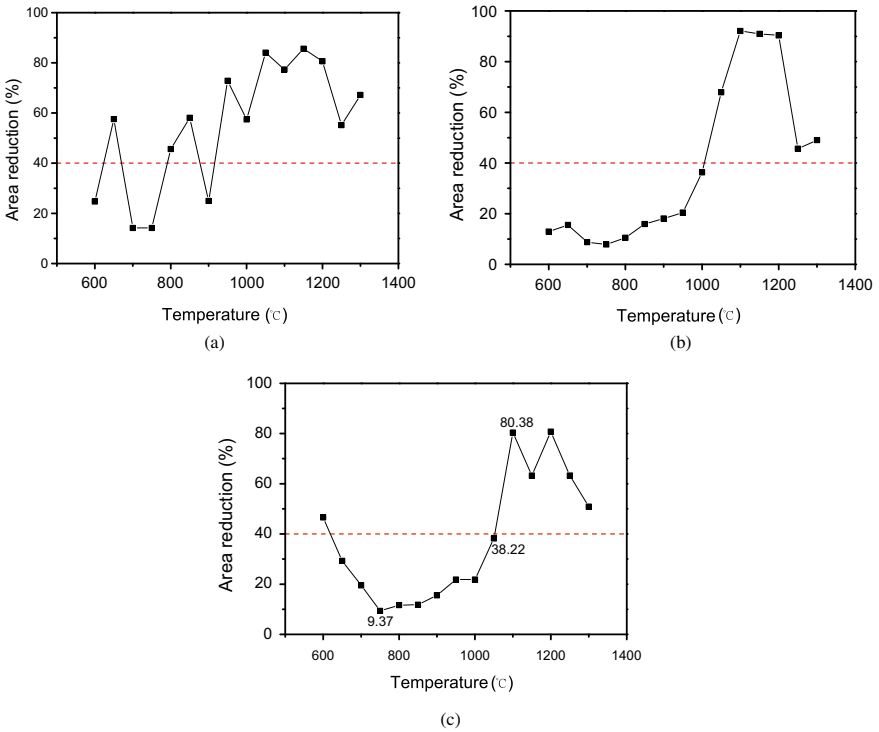

Fig. 3 Reduction of area of the steel with **a** 0.035%Al, **b** 0.5%Al, **c** 0.8%Al

Figure 3 shows the reduction of area of the sample after hot tensile. Figure 3a shows the RA of sample with 0.035Al, and it can be seen that the sample's hot ductility is best among these three samples. Figure 3b shows the RA value with 0.5%Al, when temperature during 600–1000 °C, the RA is less than 40%. Figure 3c shows the RA value with 0.8%Al. With the tensile temperature increasing from 600 to 750 °C, the reduction of area of the sample continued to decrease. During the process of increasing the tensile temperature from 750 to 1100 °C, the reduction of area continued to increase. The lowest RA is 9.37%.

When RA is more than 40%, the hot ductility of steel performs well. Overall, the hot ductility with 0.5%Al was the worst, and this result corresponds to the result of stress–strain curve as well as actual production situation.

Fracture of the Steel Sample After Tensile Test

When the material undergoes brittle fracture, the fracture is perpendicular to the tensile direction, the fracture morphology is stepped, and the fracture form is epitaxial fracture, and the extension of the crack extension to the grain boundary can be clearly observed.

Figure 4 shows the fracture morphology of steel sample with 0.035%Al. According to fracture morphology, it can be figured out that it was a kind of plastic fracture when the temperature was 650, 800, 850, 900 °C, the dimples are small. It shows that the sample at these temperatures has high ductility. In the next stage, finding the precipitates in dimples is much important, which can explain the mechanism of the appearance of voids.

Figure 5 shows the microscopic analysis of the fracture morphology of sample with 0.8%Al. Figure 5a–d are the typical brittle fracture morphology of the sample after the brittle fracture. The fracture morphology of the specimens tensed at 650, 750, and 950 °C can be clearly distinguished as rock sugar-like, with obvious characteristics of epitaxial fracture. Under the tensile condition of 1000 °C, smaller cleavage-like fractures appeared in the fracture morphology. The SEM microscopic analysis of the fracture morphology is consistent with the plastic change trend of the reduction of area.

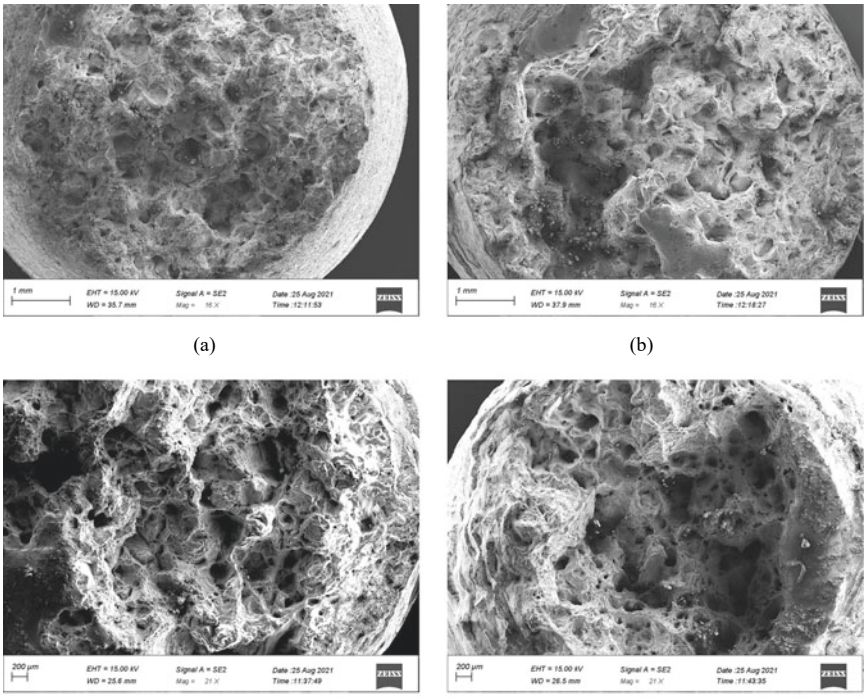

(a) (b)

(c) (d)

Fig. 4 Fracture of samples containing 0.035%Al, **a** 650 °C, **b** 800 °C, **c** 850 °C, and **d** 900 °C

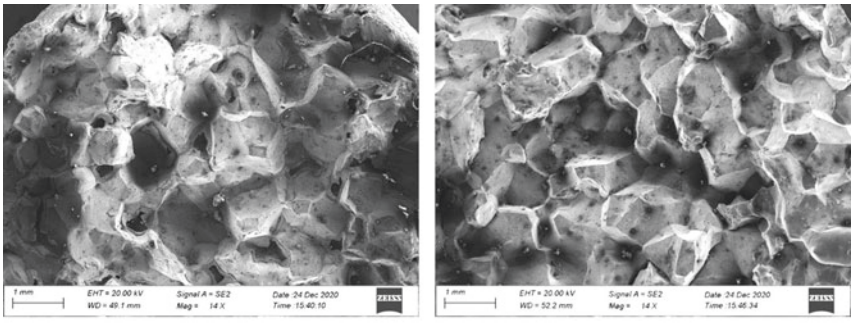

(e) (f)

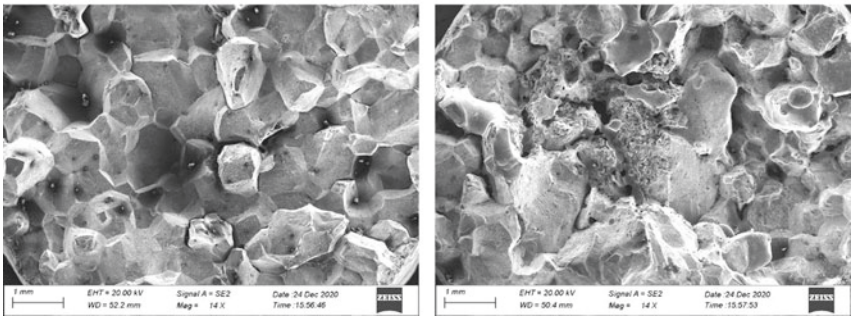

(g) (h)

Fig. 5 Fracture of samples containing 0.8Al, **a** 650 °C, **b** 750 °C, **c** 950 °C, and **d** 1000 °C

Conclusions

(1) According to the results of stress–strain curve and reduction in area, the hot ductility of sample with 0.5%Al was the worst, and the hot ductility of sample with 0.035%Al was the best, which corresponds well to the actual production situation.

(2) The fracture of morphology obtained by SEM showed that when Al content is 0.035%, the third brittle zone is 600–900 °C; when Al content is 0.5%, the third brittle zone is 600–1000 °C; when Al content is 0.8%, the third brittle zone is 650–1050 °C.

Acknowledgements The authors are grateful for support from the National Nature Science Foundation of China (Grant No. U1860206, No. 51725402), the S&T Program of Hebei (Grant No. 20311004D), the High Steel Center (HSC) at Yanshan University, and Beijing International Center of Advanced and Intelligent Manufacturing of High Quality Steel Materials (ICSM) and the High Quality Steel Consortium (HQSC) at University of Science and Technology Beijing (USTB), China.

References

1. Frommeyer G, Brüx U (2006) Microstructures and mechanical properties of high-strength Fe-Mn-AI-C light-weight TRIPLEX steels. Steel Res 77:9–10
2. Suzuki HG, Nishimura S, Yamaguchi S (1979) Characteristics of embrittlement in steels above 600 °C. Testu-To-Hagane 65:2038–2043
3. Mintz B, Arrowsmith JM (2013) Hot-ductility behaviour of C-Mn-Nb-AI steels and its relationship to crack propagation during the straightening of continuously cast strand. Metals Technol 6:24–32
4. Hamada AS, Karjalainen LP (2011) Hot ductility behaviour of high-Mn TWIP steels. Mater Sci Eng, A 528:1819–1827
5. Kang SE, Tuling A, Lau I, Banerjee JR, Mintz B (2013) The hot ductility of Nb/V containing high Al, TWIP steels. Mater Sci Technol 27:909–915
6. Kang SE, Banerjee JR, Mintz B (2013) Influence of S and AlN on hot ductility of high Al, TWIP steels. Mater Sci Technol 28:589–596
7. Liua H (2017) Effect of Mn and Al contents on hot ductility of high alloy Fe-xMn-C-yAl austenite TWIP steels. Mater Sci Eng, A 708:360–374
8. Zambranoa BA (2017) Hot deformation of a Fe-Mn-Al-C steel susceptible of κ-carbide precipitation. Mater Sci Eng A 689:269–285
9. Xu LX, Wu HB, Wang XT (2017) Influence of microstructural evolution on the hot deformation behavior of an Fe–Mn–Al Duplex lightweight steel. Acta Metall Sin (Engl Lett) 31:389–400
10. Zhang HJ, Zhang LF, Wang YD (2018) Effect of sampling locations on hot ductility of low carbon alloyed steel. Steel Res 1–11

Separation and Recovery of Iron from Low-Grade Refractory Iron Ore by Magnetizing Roasting

Luxing Feng, Jiandong Chen, Xiao Zhang, Hongchuan Zuo, and Hanjie Guo

Abstract In this study, a process of magnetizing roasting followed by low-intensity magnetic separation, which is used to separate and recover iron from low-grade refractory iron ore, was investigated. In addition, the ore is crushed and divided into different sizes and put into the electric rotary kiln at different times to participate in reduction reaction. The optimum magnetizing roasting conditions were obtained as the following: roasting at 800 °C for 30 min, mass ratio of lignite to iron ore of 5/1000, and grinding 12 min of roasted samples. Under the optimum roasting conditions, the two main parameters of the recovery process of magnetically separated concentration were obtained as the following: the grade of magnetic concentrate of 61.6 mass% Fe and iron minerals recovery rate of 87.5%. The results could be useful for comprehensive utilization of low-grade refractory iron ore by magnetizing roasting process.

Keywords Magnetizing roasting · Magnetic separation · Low-grade iron ore · Iron recovery

Introduction

China is rich in iron ore resources, with proven reserves of more than 80 billion tons. However, China's iron ore endowment is poor, which is mainly reflected in the fine crystal size and complex composition of minerals, especially the low iron grade.

L. Feng · J. Chen
Jidong Development Group Co., Ltd., East of Linyin Road, Fengrun District, Tangshan 063000, China

X. Zhang · H. Zuo
Tangshan Jidong Equipment Engineering Co., Ltd, Tangshan Caofeidian District Equipment Manufacturing Industrial Park, Tangshan 063200, China

H. Guo (✉)
School of Metallurgical and Ecological Engineering, University of Science and Technology Beijing, 30 Xueyuan Road, Beijing 100083, China
e-mail: guohanjie@ustb.edu.cn

Z. Peng et al. (eds.), *12th International Symposium on High-Temperature Metallurgical Processing*, The Minerals, Metals & Materials Series,
https://doi.org/10.1007/978-3-030-92388-4_34

More than 97% of iron ores need to be processed before they can be sent to blast furnace for smelting [1, 2]. Magnetization roasting followed by the low-intensity magnetic separation technology is one of the effective ways to deal with complex refractory iron ores. Magnetization roasting can transform the weakly magnetic iron oxides (hematite, siderite, limonite, etc.) to ferromagnetic minerals such as magnetite (Fe_3O_4) or maghemite (γ-Fe_2O_3) which are suitable for magnetic separation, so as to increase the separability of iron ores [3–7].

Structural deterioration of iron ore particles during thermal processing has been investigated [8, 9]. Previous research results show that the dehydroxylation of limonite occurs at 250–350 °C, the decomposition of siderite occurs at 490–630 °C, and the conversion of hematite to magnetite occurs at about 850 °C.

Based on the previous works, the present study mainly described experiments on the separation and recovery of iron from a low-grade iron ore by means of magnetizing roasting and magnetic separation processes. The influence of ore powder particle size on ore reduction process is mainly considered. Especially in the range of 0.3–0.9 mass% of reductant, the behavior of magnetization roasting and magnetic separation was studied.

Experimental

Experimental Mechanism

According to the difference of ore property, magnetizing roasting process for the recovery of iron minerals includes reducing roasting, oxidizing roasting, and neutral roasting. In this study, the main purpose of magnetizing roasting is reducing hematite and limonite to magnetite. According to the reduction roasting theory, high volatile lignite particles were added into the roasting section as reducing agent. The volatile matter of lignite is violently pyrolyzed at about 600 °C, resulting in a large amount of reduced gas and solid carbon. The content of H_2 in the reduced gas is the highest, followed by the content of CO. The rapid reduction of iron oxide by H_2 was realized by controlling the material temperature in the roasting section at about 700–850 °C. Due to its small molecular radius, H_2 has stronger diffusion capacity than CO and has faster internal and external diffusion speed of iron oxide, which can realize rapid reduction and greatly improve the roasting efficiency of rotary kiln system. The reaction theory can be expressed with the following equations:

$$3Fe_2O_3 + H_2 \rightarrow 2Fe_3O_4 + H_2O \quad \Delta_r G^\theta = -15,547 - 74.40T \quad J \cdot mol^{-1} \tag{1}$$

$$3Fe_2O_3 + CO \rightarrow 2Fe_3O_4 + CO_2 \quad \Delta_r G^\theta = -52,130 - 41.0T \quad J \cdot mol^{-1} \tag{2}$$

$$H_2O + C \rightarrow H_2 + CO \quad \Delta_r G^\theta = 13,104 - 146.31T \quad J \cdot mol^{-1} \tag{3}$$

$$CO_2 + C \rightarrow 2CO \quad \Delta_r G^\theta = 170,460 - 174.43T \quad J \cdot mol^{-1} \tag{4}$$

$$Fe_3O_4 + H_2 \rightarrow 3FeO + H_2O \quad \Delta_r G^\theta = 71,940 - 73.62T \quad J \cdot mol^{-1} \tag{5}$$

$$Fe_3O_4 + CO \rightarrow 3FeO + CO_2 \quad \Delta_r G^\theta = 35,380 - 40.16T \quad J \cdot mol^{-1} \tag{6}$$

During the roasting process, the H_2O generated in the reduction reaction of Fe_2O_3 subsequently reacts with the solid carbon to produce more H_2 and CO. What's more, the CO_2 produced during reduction reaction further reacts with solid carbon to produce more CO. Then, H_2 and CO continually react Fe_2O_3 to magnetite. However, the formed magnetite may be over-reduced to be wustite by Eqs. (5) and (6) if the reduction gas concentration is too high.

In this study, iron ore is classified into coarse, medium, and fine grains to avoid over-reduction of coarse-grained iron ore on surface and under-reduction of core, while over-reduction of fine-grained iron ore on the whole. According to the characteristics of slow temperature rise and long reduction time of coarse-grained iron ore, on the contrary, fine-grained iron ore has the fast temperature rise and short reduction time. The heating time of coarse-grained iron ore is longer, that of medium-grained iron ore is next, and that of fine-grained iron ore is the shortest. That is to say, the reduction roasting process of coarse-grained iron ore requires the highest temperature and the longest time, followed by medium-grained iron ore and fine-grained iron ore.

Materials

The iron ore sample used for this investigation was obtained from Xiaohebian Iron Mine in Yunnan Province of China. The chemical multi-element analysis for the compositions and the phase analysis of iron are given in Tables 1 and 2, respectively. The results of multi-element analysis demonstrated that the main valuable metal in the sample was Fe, with a content of 22.35 mass%. The amounts of impurities like P and S were very low by 0.026 mass% and 0.299 mass%, respectively.

From Table 2, the iron elements were mainly found to exist in the form of magnetite, hematite, and limonite in the low-grade iron ore sample, and hematite and limonite occupied about 22.37 mass% of the total iron, which should be reduced to magnetite first.

Table 1 Multi-element analysis of the iron ore sample

Compositions	Fe	FeO	Al_2O_3	SiO_2	CaO	MgO	P	S
Mass fraction (mass%)	22.35	12.38	3.04	31.82	16.19	1.89	0.026	0.299

Table 2 Phase analysis of iron for sample

Phase name	Fe in magnetite	Fe in siderite	Fe in hematite and limonite	Fe in pyrite	Fe in silicate	Total
Content (mass%)	12.08	1.21	5.00	0.426	3.64	22.35
Percentage (%)	54.04	5.41	22.37	1.90	16.28	100

The lignite, obtained from Xinjiang Province of China, was used as a reducing agent. It had a controlled particle size distribution from 5 to 10 mm and was assayed to have 41.05 mass% volatile matters, 43.60 mass% fixed carbon, and 10.74 mass% ash.

Magnetizing Roasting and Magnetic Separation

The low-grade iron ore fines contain weakly magnetic iron minerals such as hematite and siderite, which could not be separated effectively by low-intensity magnetic separation. Therefore, the ore fines were magnetized by magnetization roasting, then low-intensity magnetic separation was used to enrich magnetic iron minerals. In this work, the experimental process is schematically represented in Fig. 1. First, the amount of low-grade ore used in each experiment was 1000 g, then broken and screened into three particle sizes of 5–10 mm, 1–5 mm, and 0–1 mm, of which the weights were 220, 480, and 300 g. What's more, the particle size with 0–1 mm ore was mixed well-distributed with a given amount of lignite, which particle size was 5–10 mm. Secondly, the particle size with 5–10 mm ore was put into a laboratory-scale electric rotary kiln after the temperature was raised to a given value. After that, the rotary kiln started to rotate at a speed of 60 s/r. Then, 5 min later, put 1–5 mm raw ore into the electric rotary kiln. Then, divide the mixture of 0–1 mm ore and lignite into ten parts on average and put them into the rotary kiln, respectively. After a given time, roasted samples were taken out when cooling down to 100 °C in the airtight kiln. Next, the cooled roasted sample was ground with a ball grinding mill to a given particle size. Finally, the ground material was separated with the Davis magnetic tube at an optimized intensity of 0.15 T. The non-magnetic product was the tailing, while the magnetic product was iron concentrate. The grades of magnetic concentrate were analyzed by chemistry method. Then, the recovery rates of iron (the ratio of the amount of iron minerals in magnetic concentrate to those of in iron ore raw material) were deduced according to mass balance in magnetic separation process.

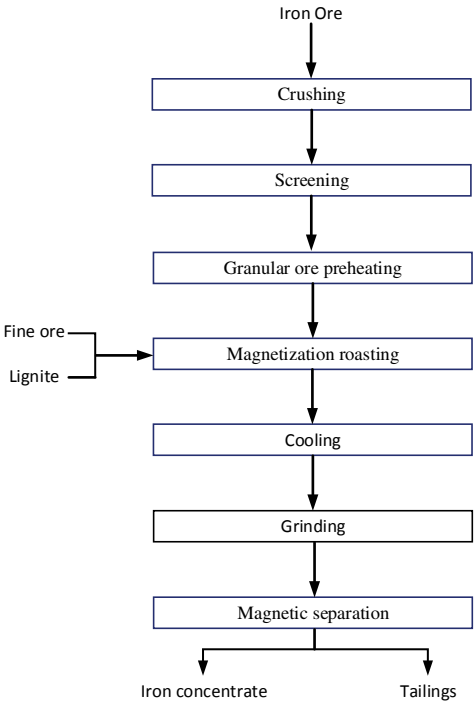

Fig. 1 Schematic diagram of magnetization roasting and magnetic separation process

Results and Discussion

The effects of main process parameters, which included roasting temperature, mass ratio of lignite to iron ore, roasting time, and grinding fineness, on the separation and recovery of iron were examined.

Effects of Roasting Temperature on Iron Recovery

Roasting temperature is the main factor that impacts the reaction. In this experiment, roasting temperature was selected as 700, 750, 800, and 850 °C, mass ratio of lignite to iron ore of 5/1000, roasted 30 min, with the milling time of 15 min. Results were shown in Fig. 2.

From Fig. 2, with the roasting temperature increasing, the iron recovery of iron concentrate increased until it reached the maximum at 800 °C, and then decreased slightly with the further increase of temperature. The maximum recovery of iron is about 87.5%, and the iron grade is 61.6 mass% Fe. At the same time, the grade of iron concentrate decreases with the increase of roasting temperature. This result might be due to the fact that when the temperature was low, and the reaction was

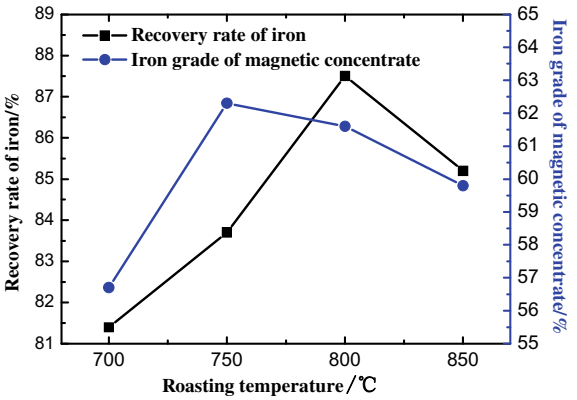

Fig. 2 Effects of roasting temperature on iron recovery (mass ratio of lignite to iron ore: 5/1000, roasting time: 30 min, grinding time: 12 min)

incomplete due to the limited reaction rate. At high temperatures, the pyrolyzation of lignite and the gasification of solid carbon are accelerated, which speed up the conversion of hematite or limonite to magnetite. But if the temperature was too high (850 °C), the product (Fe_3O_4) may be over-reduced to generate wustite [10], which is weakly magnetic and difficult to recycle in magnetic separation process.

Effects of Mass Ratio of Lignite to Iron Ore on Iron Recovery

In order to investigate the optimum content of lignite, different mass ratios of lignite to iron ore were studied, respectively. Under the conditions of roasting temperature 800 °C, roasting time 30 min, and grinding time 12 min, the effect of lignite ratio on the separation and recovery of iron was studied, and the mass ratio of lignite to iron ore was selected as 3/1000, 5/1000, 7/1000, and 9/1000. Results were shown in Fig. 3.

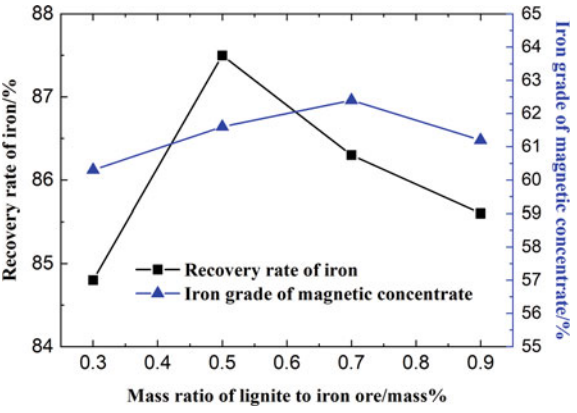

Fig. 3 Effects of the mass ratio of lignite to iron ore on iron recovery (roasting temperature: 800 °C, roasting time: 30 min, grinding time: 12 min)

As shown in Fig. 3, the grades of magnetic concentrate were all over 60 mass% Fe. With the lignite ratio increasing, the grade of iron concentrate increased slowly until it reached the maximum value and then decreased gradually, and the maximum was 62.4 mass%. When the mass ratio of lignite to iron ore was 5/1000, the recovery rate of iron was achieving a peak, where the maximum value was 87.5%. The results might indicate that adding too much lignite would produce excessive reducing gas, which made the formed magnetite to be over-reduced, and converted into wustite by Eqs. (5) and (6). Wustite is weakly magnetic, leading to the decrease of iron recovery. As a result, the mass ratio of lignite to iron ore of 5/1000 was recommended for the optimal condition.

Effects of Roasting Time on Iron Recovery

Samples were roasted at the temperature of 800 °C for different roasting time, with the mass ratio of lignite to iron ore of 5/1000 and milling time 12 min. The effect of roasting time on the recovery of iron is shown in Fig. 4.

As shown in Fig. 4, both of the iron recovery rate and grade of magnetic concentrate increased continuously with the prolonging of roasting time until reaching the maximum values and then declined quickly. When roasting time was about 30 min, the recovery rate of iron was achieving a peak, with the grade of magnetic concentrate 61.6 mass% Fe. It was inferred that when the roasting temperature was 800 °C, the optimum roasting time was about 30 min, during which magnetic roasting was mostly completed.

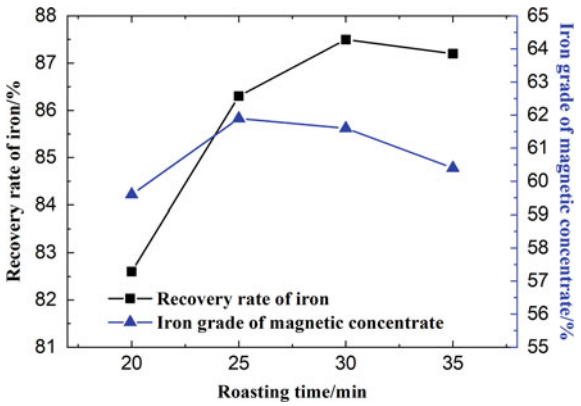

Fig. 4 Effects of roasting time on iron recovery (roasting temperature: 800 °C, mass ratio of lignite to iron ore: 5/1000, grinding time: 12 min)

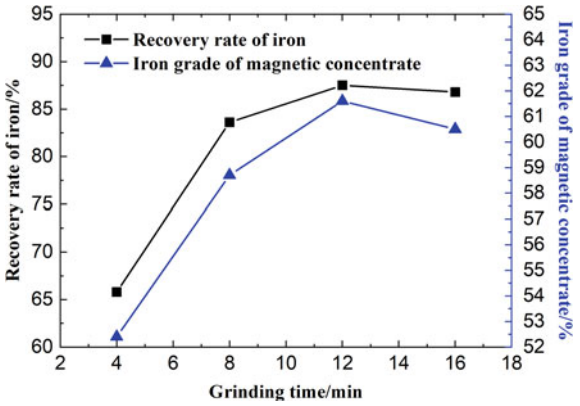

Fig. 5 Effects of grinding time on iron recovery (roasting temperature: 800 °C, roasting time: 30 min, mass ratio of lignite to iron ore: 5/1000)

Table 3 Particle sizes after different milling time

Grinding time (min)	4	8	12	16
Minus 74 μm (mass%)	64.6	83.7	100	100

Effects of Grinding Time on Iron Recovery

Due to the complex dispersion characteristics of roasted samples, magnetic separation was difficult, and grinding was needed before magnetic separation. In this work, the effect of grinding time of the roasted samples on the recovery of iron was tested. The conditions of magnetic roasting were as the following: the roasting temperature of 800 °C for 30 min, with the mass ratio of lignite to iron ore of 5/1000. The results were shown in Fig. 5, and the particle sizes of roasted samples with different grinding times were shown in Table 3 and screened through a 74 micron sieve.

From Fig. 5, as the increase of the grinding time, both of the recovery and grade of iron concentrate increased continuously until peaking and then declined slowly. When grinding 12 min, the percentage of minus 74 μm was 100 mass%, the maximum value of the recovery and grade of iron concentrate was 87.5% and 61.6 mass%. However, if the roasted samples were ground too fine (16 min), the particles were agglomerate easily and difficult to be separated in magnetic separator, so the grade was only 60.5 mass% Fe. At the same time, the decrease of recovery rate was due to that it was difficult to capture fine magnetite particles by magnetic separation [11, 12].

Conclusion

Major chemical compositions of the low-grade iron ore were SiO_2, Fe_3O_4, Fe_2O_3, CaO, and Al_2O_3. Quartz, magnetite, hematite, limonite, calcite, mica, and kaolinite existed in the iron ore samples as main phases, and most of iron and quartz were

fine-disseminated complexly together, which was hard to be separated. Effective utilization of low-grade iron ore by lignite pyrolysis was proposed to reduction roasting and iron recovery. The roasting temperature, ratio of lignite to iron ore, roasting time, and grinding time of roasted samples were four main factors which had effects on the recovery and grade of iron concentrate. Through corresponding four groups of experiments, optimum magnetic roasting conditions were obtained as the following: roasting at 800 °C for 30 min, mass ratio of lignite to iron ore of 5/1000, and grinding 12 min of roasted samples. Under the optimum roasting conditions, of the total iron present in this low-grade ore, 87.5 mass% were recovered in the form of iron concentrate (grade: 61.6 mass%), after the roasted product was treated by a magnetic separation process. The results demonstrated that it is feasible to separate and recover iron from low-grade iron ore by magnetization roasting and magnetic separation process.

References

1. Liu J, Zhou MS, Zhai LW, Liu JT, Cao YJ (2011) Present status of China's complex refractory iron ore study. China Min Mag 20(5):63–66
2. Zhang ZW, Li J, Li Y, Pan CC (2012) The development and utilization status of China's refractory ore. Nonferrous Met Sci Eng 3(1):72–77
3. Yu JW, Han YX, Li YJ, Gao P (2018) Experimental study on utilization of crude concentrate from an Anshan-type hematite ore by suspension magnetization roasting-magnetic separation. J Cent South Univ Sci Technol 49(4):771–778
4. Gao P, Yu JW, Zhang SM, Han YX (2016) Experimental study on suspension roasting-low intensity magnetic separation of magnetic mixed concentrate from Donganshan. Metal Mine 45(12):18–21
5. Chen YX, Bai JL, Zhao B (2013) Suspened state magnetization roasting beneficiation test of poor hematite from gold tailings. J Iron Steel Res 25(6):24–28
6. Zhang HQ, Wang FL (2014) Regulation of mineral composition and phase transformation in hematite and limonite magnetic roasting process. J Iron Steel Res 26(7):8–11
7. Li C, Sun HH, Bai J, Li LT (2010) Innovative methodology for comprehensive utilization of iron ore tailings. Part 1. The recovery of iron from iron ore tailings using magnetic separation after magnetizing roasting. J Hazard Mater 174:71–77
8. Gialanella S, Girardi F, Ischia G, Lonardelli I, Mattarelli M, Montagna M (2010) On the goethite to hematite phase transformation. J Therm Anal Calorim 102:867–873
9. Strezov V, Evans TJ, Zymla V, Strezov L (2011) Structural deterioration of iron ore particles during thermal processing. Int J Miner Process 100:27–32
10. Uwadiale G, Whewell RJ (1988) Effect of temperature on magnetizing reduction of agbaja iron ore. Metall Mater Trans B 19(5):731–735
11. Yu JW, Han YX, Li YJ, Gao P, Sun YS (2017) Separation and recovery of iron from a low-grade carbonate-bearing iron ore using magnetizing roasting followed by magnetic separation. Sep Sci Technol 52(10):1768–1774
12. Chen LZ (2011) Effect of magnetic field orientation on high gradient magnetic separation performance. Miner Eng 24:88–90

Part VI
Preparation of Alloys and Materials

Evaluation of Processing Parameters for the Production of Tungsten Carbide in a Fluidized Bed Reactor

Maureen P. Chorney, Jerome P. Downey, and K. V. Sudhakar

Abstract Synthesis of submicron tungsten carbide (WC) particles has been achieved utilizing fluidized reactor technology at temperatures lower than those used in current commercial production. Fluidized bed technology provides improved gas–solid contact in a controlled reaction atmosphere to increase conversion efficiency. A tungsten-bearing activated carbon precursor was prepared and utilized in all experiments to evaluate the effect of time, temperature, and reaction atmosphere on tungsten carbide synthesis. The experimental products were analyzed with a variety of characterization tools including X-ray diffraction (XRD), scanning electron microscopy (SEM), and energy dispersive X-ray spectroscopy (EDS). The analytical results indicate uniform submicron tungsten carbide particles were successfully produced at greater than 90% total carbide conversion.

Keywords Tungsten carbide · Synthesis · Fluidization

Introduction

Tungsten carbide (WC) has many desirable properties. Its strength, high hardness, high melting point, good electrical and thermal conductivity, and high corrosion resistance make it a versatile, sought-after material. Tungsten carbide is widely used for cutting and machining tools, drill bits, structural materials, and military applications. Commercial production processes require extremely high temperatures and highly reactive gas atmospheres to produce tungsten carbide powders that range from submicron up to 50 μ [1].

In conventional tungsten carbide production, tungsten powder is blended with carbon in preparation for carburization, which is effected in a hydrogen atmosphere

M. P. Chorney (✉) · J. P. Downey · K. V. Sudhakar
Montana Technological University, Butte, MT 59701, USA
e-mail: mchorney@mtech.edu

J. P. Downey
e-mail: jdowney@mtech.edu

Z. Peng et al. (eds.), *12th International Symposium on High-Temperature Metallurgical Processing*, The Minerals, Metals & Materials Series,
https://doi.org/10.1007/978-3-030-92388-4_35

at temperatures ranging from 1300 to 1700 °C [1]. High-temperature carburization may be utilized with the same initial mixture of tungsten powder and carbon, with reaction temperatures as high as 1800–2000 °C in a hydrogen atmosphere, held under vacuum [1]. With both methods, particle size is determined by input tungsten particle size, and it should be noted that agglomeration and sintering of tungsten carbide occur [1].

Tungsten carbide formation is defined by many different reaction mechanisms, depending on the selection of the starting material. In many commercial processes, the reaction (Eq. 1) is relatively simple because tungsten metal powder serves as the tungsten source. The hydrogen in the furnace atmosphere may react with the carbon to produce methane, which then reacts with tungsten metal to form tungsten carbide (Eq. 2).

$$\mathrm{W} + \mathrm{C} \rightarrow \mathrm{WC} \tag{1}$$

$$\mathrm{W} + \mathrm{CH_4} \rightarrow \mathrm{WC} + \mathrm{H_2} \tag{2}$$

A commercial process developed in Japan consistently produces submicron tungsten carbide from tungsten oxide. Pellets composed of tungstic oxide (WO_3) and carbon are fed to a dual rotary furnace configuration that operates with a nitrogen atmosphere (1350–1600 °C) during the reduction stage and with a hydrogen atmosphere (1650–2000 °C) during the carburization stage [1]. The reaction sequence (Eq. 3) comprises several steps to accomplish the reduction and carburization [1].

$$\mathrm{WO_3} \rightarrow \mathrm{WO_{2.9}} \rightarrow \mathrm{WO_{2.72}} \rightarrow \mathrm{WO_2} \rightarrow \mathrm{W} \rightarrow \mathrm{W_2C} \rightarrow \mathrm{WC} \tag{3}$$

Previous research on the tungsten carbide synthesis was primarily performed in static tube furnaces, where uniform isothermal conditions are difficult to achieve and where the reactive gases do not evenly contact all particles [2–10]. Recent research employed rotary tube furnaces akin to those used for commercial production in an effort to improve gas–solid contact and realize higher reaction yields [11–13].

Fluidization technology provides the superior gas–solid contact needed for efficient synthesis. Fluidized bed technology is recognized for its superior heat and mass transfer characteristics that improve solid–gas reactions. Fluidized bed reactors also provide a more uniform reaction temperature and atmosphere, and they are easily scaled to the desired throughput requirements [14, 15]. In this study, utilization of a fluidized bed reactor has proved to be an important step towards consistent production of tungsten carbide.

Materials and Methods

The tungsten oxide precursor material consists of tungstate anions (WO_4^{2-}) adsorbed on an activated carbon substrate. Precursor was prepared using an aqueous solution containing 18,000 ppm tungsten and 5,844 ppm sodium chloride (Sigma Aldrich, anhydrous, ReagentPlus®, ≥99%). Tungsten was sourced from sodium tungstate dihydrate ($Na_2WO_4 \cdot 2H_2O$, Sigma Aldrich, Emplura®). The solution pH was adjusted to 2.0 using concentrated hydrochloric acid. Activated carbon, 50.0 g, (Sigma Aldrich, untreated, 100–400 mesh) was added to the solution, which was then agitated for two hours. Vacuum filtration of the solution was immediately followed, and the solid precursor material was left in a drying oven for several days. The finished precursor contains approximately 0.35 g W/g C; this precursor loading technique was optimized in previous research [11].

A vertical MTI 1200X fluidized bed furnace was used for all high-temperature fluidization experiments. The experiments were performed in a quartz tube with a 22-mm inner diameter bed region and a 44-mm freeboard. A maximum of approximately two grams of tungsten precursor material is processed for each fluidization experiment, so that fluidization could be achieved.

Cold flow fluidization experiments were performed to evaluate the precursor fluidization characteristics. At ambient laboratory temperature, a flow rate of 0.5–0.6 LPM was determined to provide good fluidization with minimal entrained particle loss through the freeboard. The flow rates were scaled for higher temperature experimentation. A series of scoping experiments was completed to narrow the range of parameters for further investigation through a design of experiments matrix.

Experiments were performed predominantly in a methane (CH_4) atmosphere at temperatures within the range of 700–975 °C. The furnace was programmed with a 5.3 °C/min ramp rate to attain the desired bed temperature, which was held for the desired time. The cool down commenced at a −3 °C/min ramp to 400 °C, after which the furnace cooled naturally to room temperature. Argon gas flowed through the furnace during the heat-up and cool-down periods to provide an inert atmosphere to prevent particle agglomeration or sintering in the reactor bed. Reaction times were varied from 1.0 to 7.0 h, during which either methane or argon was the sole gas present. An afterburner was installed to safely oxidize the combustible species in the fluidized bed discharge gases.

The experimental products were characterized using a Rigaku Ultima IV X-ray diffractometer (XRD) and JADE analysis software to determine WPPF values. Additional characterization was performed using a MIRA3 TESCAN scanning electron microscope (SEM), with energy dispersive X-ray spectroscopy (EDS) attachments.

Results and Discussion

In preparation for the scoping experiments, thermodynamic modeling was performed with HSC Chemistry 7 software to evaluate the potential products produced given the known input chemistry (Fig. 1). The input parameters included tungsten, as tungsten oxide (WO_3), and an excess of carbon. Gas atmosphere was also included in the input parameters and was selected as either argon or methane.

The free energy minimization diagrams illustrate the reaction product (kilomoles, in logarithmic space) as a function of temperature (°C). In the calculations performed to examine the influence of an argon atmosphere, tungsten carbide is predicted to be the predominant tungsten-bearing product; other products are ditungsten carbide (W_2C) carbon (C), carbon monoxide (CO), and carbon dioxide (CO_2). A similar suite of potential reaction products is predicted in the methane atmosphere diagram as well as hydrogen (H_2), methane (CH_4), and water vapor ($H_2O(g)$). The formation of tungsten carbide and ditungsten carbide behaves similarly in thermodynamic terms for both reaction atmospheres, with the relative amount of ditungsten carbide increasing with increasing reaction temperatures. In both cases, tungsten carbide is the predominant tungsten-bearing species across the temperature range.

Seven scoping experiments were performed at reaction temperatures between 700 and 975 °C. Reaction times of one, five, and seven hours were examined. The experimental products were analyzed by XRD, and the results are illustrated in Fig. 2 and consolidated in Table 1. As predicted by the thermodynamic analysis, tungsten carbide was the predominant reaction product in most of the experiments; the exceptions are the two experiments performed at 700 °C, the lowest temperature evaluated.

Total carbide production (WC + W_2C) exceeded 95.0% in four of the seven scoping experiments. The highest total carbide conversion (97.2% WC + W_2C) was realized in the experiment performed for 7 h at 900 °C in a methane atmosphere. This

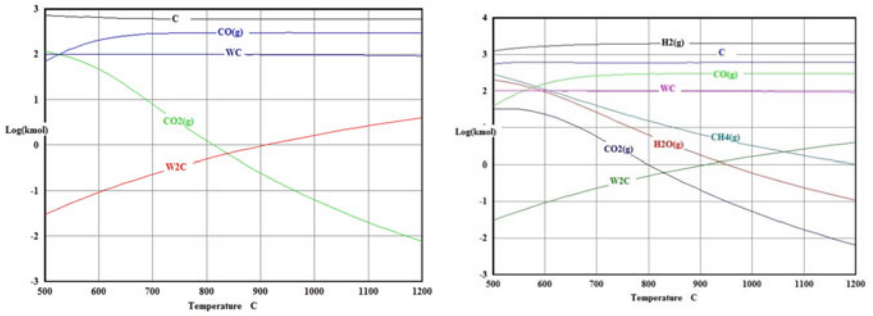

Fig. 1 Gibbs free energy minimization diagrams, produced in HSC Chemistry 7, to evaluate formation of tungsten carbide in an argon atmosphere (left: input of 10,000 kmol Ar, 1000 kmol C, and 100 kmol WO_3) and methane atmosphere (right: input of 10,000 kmol Ar, 1000 kmol C, 1000 kmol CH_4, and 100 kmol WO_3) given initial quantities of tungsten oxide and an excess of carbon

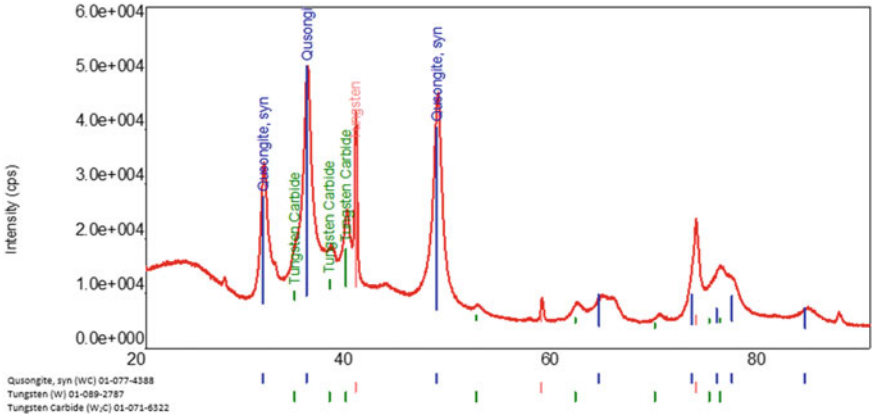

Fig. 2 XRD diffractogram of tungsten carbide produced in methane atmosphere at 875 °C, with a reaction time of 7 h

Table 1 Fluidized bed tungsten carbide synthesis scoping experiment XRD results

Run parameters			WPPF analysis (%) average					
Temp. (°C)	Time (h)	CH_4 (%)	WC	W_2C	W	WO_2	$WO_{2.83}$	$WO_{2.92}$
850	1	100	72.7	19.1	8.2	–	–	–
850	5	100	77.8	18.4	3.8	–	–	–
975	7	100	68.4	27.5	4.0	–	–	–
700	5	Argon	–	–	–	12.3	34.8	52.9
700	5	100	0.6	0.6	2.2	10.7	40.6	45.3
900	5	100	83.9	13.3	3.0	–	–	–
875	7	100	76.8	18.6	4.5	–	–	–

experiment also resulted in the highest monotungsten carbide conversion (83.9% WC). Experiments conducted at the lower temperatures showed poor conversion efficiencies. Experiments performed under methane at temperatures above 850 °C consistently produced high conversion to carbide (WC + W_2C).

The scoping series confirmed temperature is an important reaction parameter. Contrary to the thermodynamic model predictions, tungsten carbide was not successfully synthesized in experiments performed at the lower reaction temperatures. Instead, the experiments performed at 700 °C in methane or in argon atmospheres produced similar quantities of reduced tungsten oxides ($WO_{2.92}$, $WO_{2.83}$, and WO_2). The highest reaction temperature analyzed, 975 °C, resulted in deleterious effects on WC synthesis due to carbon–carbon interactions that formed carbon sheets in the fluidized bed.

Bed residence time at temperature did not appear to be a significant variable within the range evaluated in the scoping experiments. High percentages of tungsten carbide were synthesized, even at the shortest (1.0 h) reaction time. Increasing the

reaction time may promote further reaction of carbon with the reduced tungsten (W), as shown by lesser amounts of W found in the products from experiments performed for longer reaction times.

The diffractogram in Fig. 2 illustrates that the predominant peaks are those of qusongite (WC). The diffractograms generally have a fairly pronounced amorphous component, likely due to carbonaceous matter produced by methane cracking in the reactor bed. For the purpose of this analysis, the amorphous regions were relegated as part of the background in order to semi-quantitatively determine WPPF values. SEM and EDS were employed to further characterize the WC samples. The SEM images in Fig. 3 depict morphological changes that occurred as a function of reaction atmosphere and temperature.

In Fig. 3, the SEM images of the low temperature experiments corroborate the XRD results by indicating little to no formation of tungsten carbide and primarily show small tungsten oxide particles at the sites of anion loading on the activated carbon. Thin sheets of tungsten oxide, as well as needle-like structures of reduced

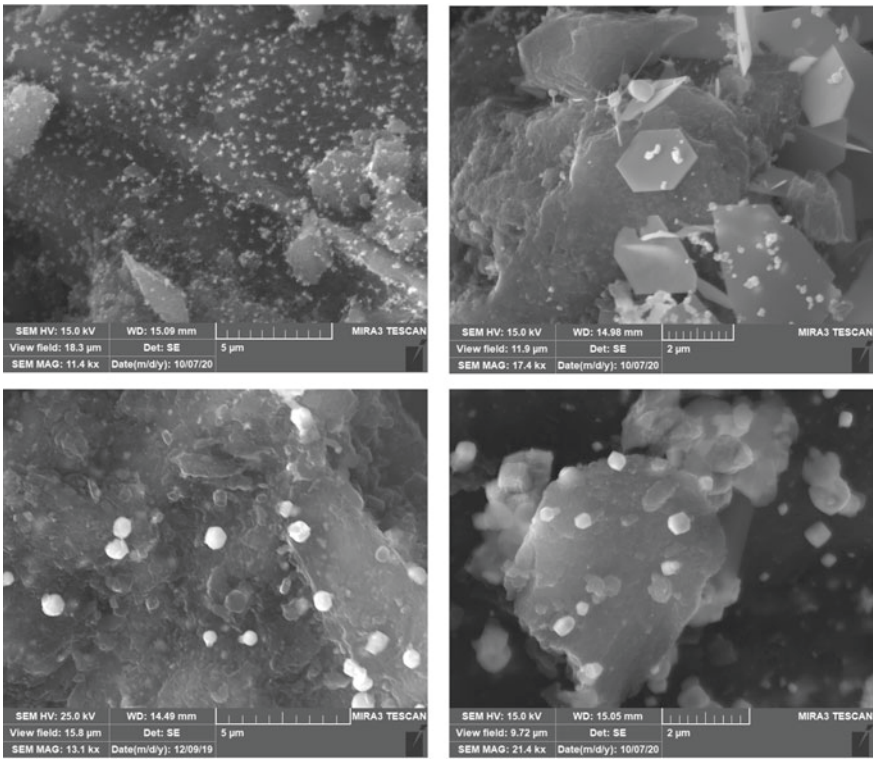

Fig. 3 SEM image of reaction product after a 5 h, 700 °C, methane atmosphere fluidization experiment (top left), and the reaction product after a 5 h, 700 °C, argon atmosphere fluidization experiment (top right). The methane atmosphere experiments—5 h, 850 °C (bottom left); 7 h, 875 °C (bottom right)—showcase marked differences in morphology and structure of the tungsten constituents

tungsten oxide, are apparent in the SEM image of the reaction product from the argon atmosphere experiment. The synthesis of tungsten carbide at high temperatures is further substantiated by the morphological changes in the tungsten particles in the bottom row of SEM images. Several particles exhibit a distinct hexagonal structure, the crystal structure of tungsten carbide, and the particles are a relatively uniform submicron size. EDS was used to evaluate the elements, and their quantities, at selected locations. The resultant data are presented in Figs. 4 and 5.

The EDS spectra collected from Spot 3, in Fig. 4, were found to contain significant percentage of oxygen, indicating that this particular location is potentially an oxide or another oxygen-bearing compound. Conversely, the defined particles analyzed, in Fig. 5, were found to contain 79 wt% tungsten and 19 wt% carbon. Higher carbon percentages than what would be calculated are to be expected with such small, submicron particle sizes and the nature of the collection of the characteristics X-rays, which come from beneath the sample surface. Depending on the height of the particles extending above the carbon surface, some additional carbon could potentially be detected. The large weight percent of tungsten that was detected signifies that this particle is most likely tungsten carbide.

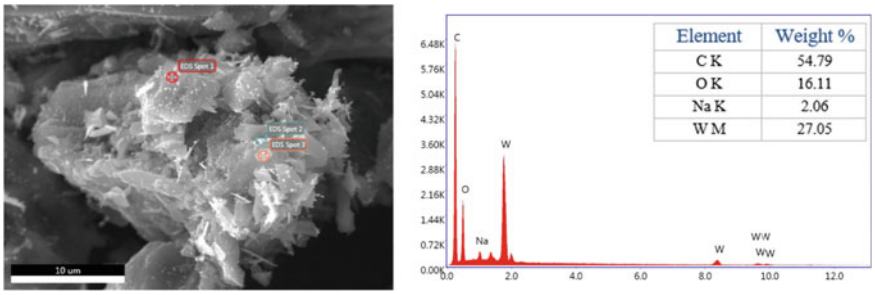

Fig. 4 SEM image (left) of the reaction product from the 700 °C, 5 h, argon atmosphere fluidized bed experiment, indicating locations of EDS spot analyses, and EDS spectra of Spot 3 (right)

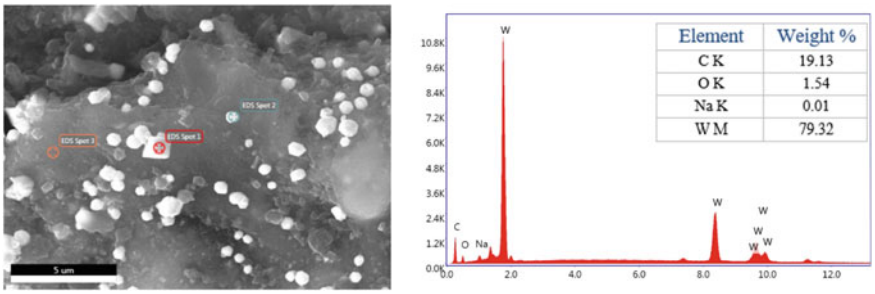

Fig. 5 SEM image (left) of the reaction product from the 850 °C, 5 h, methane atmosphere fluidized bed experiment, indicating locations of EDS spot analyses, and EDS spectra of Spot 1 (right)

Conclusions

Tungsten carbide (WC + W_2C) was synthesized at greater than 95% conversion efficiency at operating temperatures that are less than half of those used in commercial WC production. The near uniform temperature and superior gas–solid contact within the fluidized bed reactor resulted in the production of discrete, uniformly sized, submicron particles. The reaction atmosphere could be enhanced to further promote the reduction of tungsten oxides to tungsten and the carburization of tungsten to tungsten carbide. Temperatures in the 800–875 °C range consistently produced high percentages of WC. Temperature is a key variable, which will be further evaluated in future work to potentially optimize the synthesis of tungsten carbide in a fluidized bed reactor.

Acknowledgements Research was sponsored by the Combat Capabilities Development Command Army Research Laboratory and was accomplished under Cooperative Agreement Number W911NF-20-2-0163. The views and conclusions contained in this document are those of the authors and should not be interpreted as representing the official policies, either expressed or implied, of the Combat Capabilities Development Command Army Research Laboratory or the U.S. Government. The U.S. Government is authorized to reproduce and distribute reprints for government purposes notwithstanding any copyright notation herein.

References

1. Lassner E, Schubert W-D (1999) Tungsten in hardmetals. In: Tungsten: properties, chemistry, technology of the element, alloys, and chemcial compounds. Kluwer Academic/Plenum Publishers, New York, pp 321–363
2. Koc R, Kodambaka SK (2000) Tungsten carbide synthesis from novel precursors. J Eur Ceram Soc 20:1859–1869
3. Wang KF, Sun GD, Wu YD, Zhang GH, Chou KC (2019) Size-controlled synthesis of high-purity tungsten carbide powder via a carbothermic reduciton-carburization process. Int J Refract Metal Hard Mater 84:1–9
4. Polini R, Palmieri E, Marcheselli G (2015) Nanostructure tungsten carbide synthesis by carbothermic reduction of scheelite: a comprehensive study. Int J Refract Metal Hard Mater 51:289–300
5. Mitran RA, Radulescu MC, Buhalteanu L, Tanase LC, Dumitrescu DG, Matei C (2016) Formation of pure-phase W2C nanoparticles through carbothermal reduciton in the presence of Pd(0) nanoparticles. J Alloy Compd 682:679–685
6. Cetinkaya S, Eroglu S (2011) Comparative kinetic and structural analyses of nanocrystalline WC powder synthesis from pre-reduced W under pure and diluted CH4 atmosphere. Int J Refract Metal Hard Mater 29:214–220
7. Islam M, Martinez-Duarte R (2017) A sustainable approach for tungsten carbide synthesis using renewable biopolymers. Ceram Int 43:10546–10553
8. Lukovic J, Babic B, Bucevac D, Prekajski M, Pantic J, Bascarevic Z, Matovic B (2015) Synthesis and characterization of tungsten carbide fine powders. Ceram Int 41:1271–1277
9. Jin Y, Liu D, Li X, Yang R (2011) Synthesis of WC nanopowders from novel precursors. Int J Refract Metal Hard Mater 29:372–375
10. Lin H, Tao B, Xiong J, Li Q, Li Y (2013) Tungsten carbide (WC) nanopowders synthesized via novel core-shell structured precursors. Ceram Int 39:2877–2881

11. Wallace GC, Downey JP, Chorney J, Mallard A, Hutchins D (2017) Synthesis of carbide ceramics via reduction of adsorbed anions on an activated carbon matrix. In: 8th International symposium on high-temperature metallurgical processing. Springer, Cham, pp 49–57
12. Wallace GC, Downey JP, Chorney J, Schumacher K, Mallard A (2018) Synthesis of nanocrystalline carbide ceramics via reduction of anion-loaded activated carbon percursors. In: 9th International symposium on high-temperature metallurgical processing. Springer, Cham, pp 125–134
13. Wallace GC, Downey JP, Chorney J, Schumacher K, Bayless T (2019) Statistical optimization of tungsten carbide synthesis parameters. In: 10th International symposium on high-temperature metallurgical processing. Springer, Cham, pp 371–378
14. Kunii D, Levenspiel O (1991) Fluidization engineering, 2nd edn. Butterworth-Heinemann, Oxford
15. Cheremisinoff NP, Cheremisinoff PN (1984) Hydrodynamics in fluidization. In: Hydrodynamics of gas-solids fluidization. Gulf Publishing Company, Houston, pp 137–206

Effect of Austenitizing and Cooling Process on Microstructure Transformation of Low-Carbon Bainite Steel

Xiaoqing Zhou, Hongpo Wang, Mingjian Chen, Li Shi, and Yu Wang

Abstract Microstructure and grain size are important factors affecting the mechanical properties of low-carbon bainite steels. The influence of austenitization and cooling rate on the phase transformation of low-carbon bainite steel was investigated. The results show that the continuous cooling microstructure of low-carbon bainite steel was determined by pre-deformation, austenitization temperature, and cooling rate. The austenitizing process significantly affected the phase transformation of low-carbon bainite steel. When samples were heated in the range of 830–930 °C, their austenite grain sizes were relatively small with a maximum of 12.3 μm; when they were cooled at the cooling rate range of 1–30 °C/s, the microstructures consisted of mainly a large amount of ferrite and a small amount of retained austenite. When the austenitizing temperature increased to 1220 °C, the austenite grain size increased to 71.2 μm. The structure was mainly proeutectoid ferrite and granular bainite at the cooling rate of 1 °C/s. As the cooling rate increased, the amount of proeutectoid ferrite reduced, and the amount of bainite increased, resulting in a higher hardness. When the cooling rate was 10 °C/s, the proeutectoid ferrite disappeared completely, and the bainite was further refined.

Keywords Low-carbon bainite steel · Bainite transformation · Austenitization · Cooling rate

X. Zhou · H. Wang (✉) · M. Chen · Y. Wang
College of Materials Science and Engineering, Chongqing University, Chongqing 400044, China

Y. Wang
e-mail: wanghp@cqu.edu.cn

L. Shi
Wuyang Iron and Steel Co., Ltd, Wuyang 462599, China

Z. Peng et al. (eds.), *12th International Symposium on High-Temperature Metallurgical Processing*, The Minerals, Metals & Materials Series,
https://doi.org/10.1007/978-3-030-92388-4_36

Introduction

Low-carbon bainite steels have been widely used and developed recently owing to their high strength and good welding performance [1–3]. This kind of steel can be directly produced by the rolling and cooling controlled process that is more productive than the quenching and tempering process. Therefore, these steels are an essential direction of high strength and toughness and low-price structural steel. However, many problems have not been resolved, such as accurate microstructure control and bainite refinement. Segregation of slabs and poor deformability at the center of steel plates usually result in coarse microstructure, especially when their thickness is large, significantly reducing the low-temperature impact toughness of low-carbon bainite steel.

The impact toughness is mainly determined by the composition and microstructure of the steel plate and is significantly affected by factors such as the austenitization process [4–7], the rolling process, and the cooling process [8–11]. Non-metallic inclusions and precipitates are also important factors affecting the toughness of steel plates [12]. The higher the cleanliness of the steel, the fewer non-metallic inclusions, and the smaller their size, the higher the impact toughness. Due to chemical segregation, there is usually a part of niobium carbide with a larger size in the core of the cast slab, which will further grow during the heat treatment process of the slabs. Niobium carbide is hard and brittle, that is not easily deformed during the rolling process, resulting in stress concentration that significantly reduces the impact toughness of the steel plate. In addition, the heredity of the microstructure is also one of the critical factors affecting the impact toughness. The impact toughness of the steel plates produced by steel sheets with severe porosity and central segregation is usually not high. Therefore, it is necessary to carry out comprehensive control from refining, continuous casting, rolling, heat treatment, and other processes to obtain suitable bainite microstructure; and to control inclusions and precipitates fine to improve the impact properties of low-carbon bainite steel [13, 14].

This work intended to study the influence of the austenitizing and cooling process on the continuous cooling structure of austenitic steel from the perspective of austenitizing and cooling processes.

Experimental Materials and Methods

The experimental raw material is the rolled 07MnNiMoDR low-carbon bainite steel sheet manufactured in an iron and steel company in China. A pie-shaped sample with a diameter of 5 mm and a thickness of 3 mm was cut at one-fourth of the thickness of the steel plate. A muffle furnace was used to austenitize the sample. The samples were kept at 830, 850, 870, 890, 910, 930 °C for 360 s, followed by water quenching. After polishing, they were corroded by a picric acid solution. The metallographic structure and statistical austenite crystals size were observed with a metallurgical microscope.

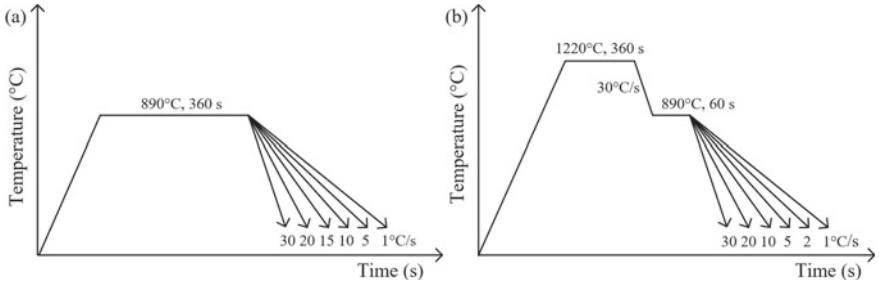

Fig. 1 Austenitization and cooling process: **a** Low-temperature austenization; **b** High-temperature austenization

A confocal laser scanning microscope was used to austenitize another sample at 1220 °C, and the video was recorded at 15 frames per minute. Screenshots of the sample surface under different constant temperature times were taken to count the austenite grain size. The statistical method of grain size is the straight-line intercept method specified by the national standard GB/T 6394-2017.

A confocal laser scanning microscope was also used to carry out the continuous cooling process after the samples were austenitized at 890 °C and 1220 °C, respectively, and the cooling rate was set to 1–30 °C/s, as shown in Fig. 1. After grinding and polishing, the samples were corroded with a nitric acid alcohol solution with a volume fraction of 4%, and the metallographic microstructure was observed. A Vickers hardness tester was used to test the hardness of the sample.

Results

Austenitized Microstructure

Figure 2 shows the quenched microstructure of the samples after being austenitized for 360 s at different temperatures. It can be seen that when the sample was austenitized at 830 °C, the recovery process mainly occurred, and only part of the austenite began to grow; when the temperature increased to 850 °C, relatively complete austenite grains began to appear. As the temperature increased, the degree of austenitization gradually increased, and the grain size increased slowly. It is worth noting that the grain size did not grow significantly during the austenitization in the entire range of 830–930 °C. When the temperature increased to 930 °C, the austenite grain size was only 12.3 μm. When the austenitizing temperature increased to 1220 °C, some grains grew significantly by merging small grains nearby (Fig. 3), and the austenite grains reached 71.2 μm. The statistical results of austenitizing grain size at different temperatures are shown in Fig. 4.

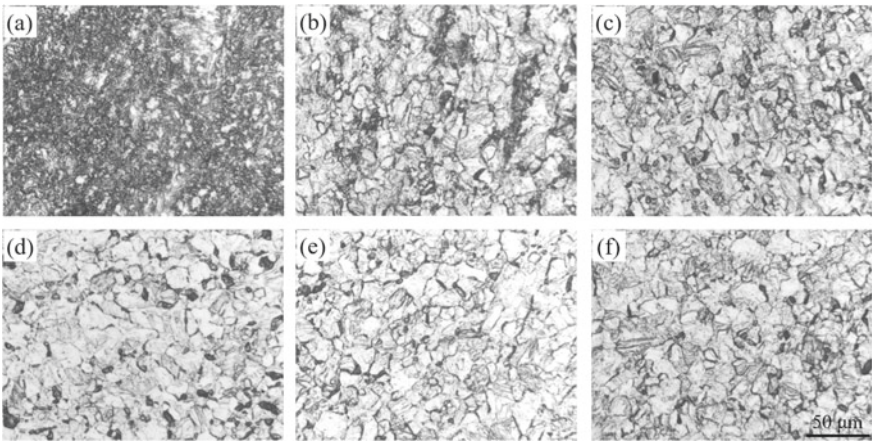

Fig. 2 Austenitized microstructure of samples after holding at different temperatures for 360 s: **a** 830 °C; **b** 850 °C; **c** 870 °C; **d** 890 °C; **e** 910 °C; **f** 930 °C

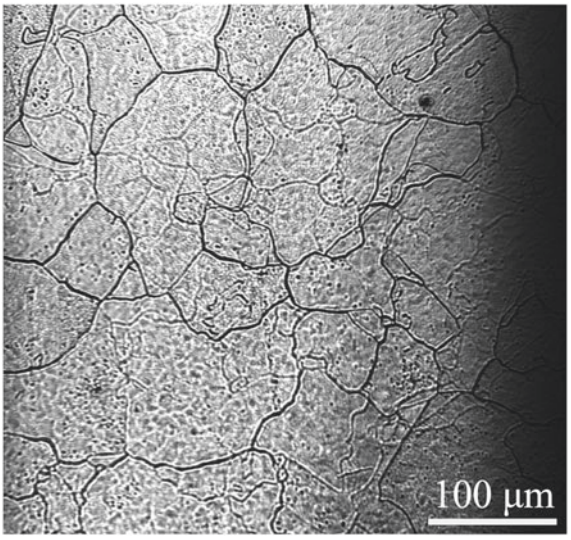

Fig. 3 Austenitized microstructure of a sample after holding at 1220 °C for 360 s

Microstructure After Continuous Cooling

Figure 5 shows the microstructure of samples after being austenitized at 890 °C and cooled at different cooling rates. It can be seen that when the cooling rate was 1 °C/s, the sample structure was almost all proeutectoid ferrite (PF), and it had grown significantly; when the cooling rate was 5 °C/s, except for the proeutectoid ferrite, some retained austenite (RA) was also discovered. After that, as the cooling rate increased, the sample microstructure was composed of proeutectoid ferrite and

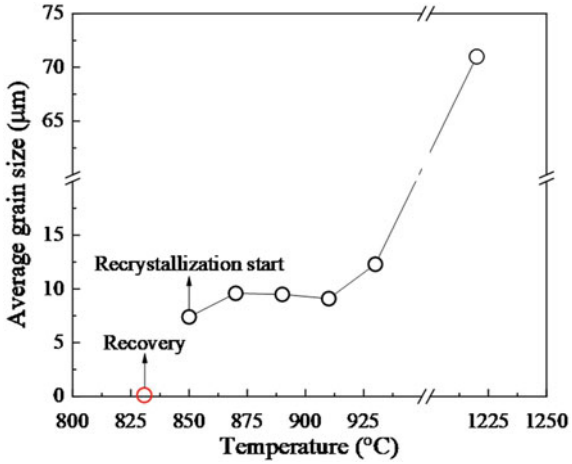

Fig. 4 Austenite grain size of samples after holding at different temperatures

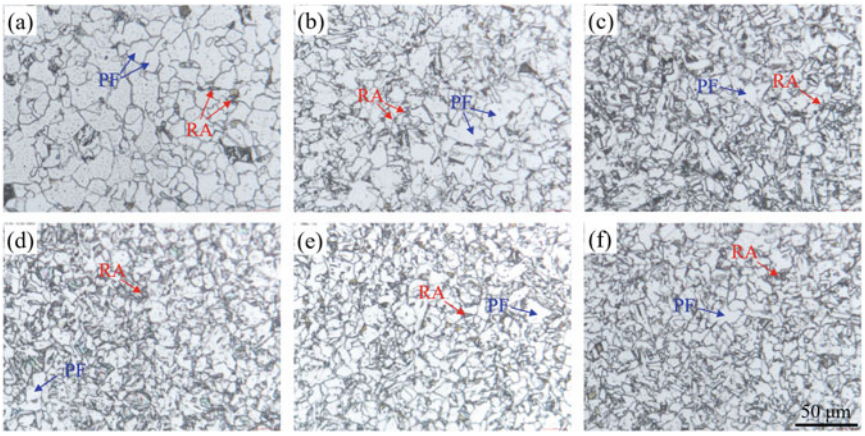

Fig. 5 Microstructure of samples after being austenitized at 890 °C and cooling at different cooling rates: **a** 1 °C/s; **b** 5 °C/s; **c** 10 °C/s; **d** 15 °C/s; **e** 20 °C/s; **f** 30 °C/s

retained austenite. The grain size of proeutectoid ferrite gradually decreased, and the proportion of retained austenite increased.

Figure 6 shows the microstructures of the austenitized samples at 1220 °C after cooling at different cooling rates. It can be seen that when the cooling rate was 1 °C/s, the sample microstructure was mainly proeutectoid ferrite (PF) and a small amount of granular bainite (GB). When the cooling rate was 2 °C/s, bainite became the primary microstructure, and proeutectoid ferrite was significantly reduced. When the cooling rate was 5 °C/s, the proportion of bainite continued to increase, while proeutectoid ferrite decreased. After the cooling rate was greater than 10 °C/s, no proeutectoid

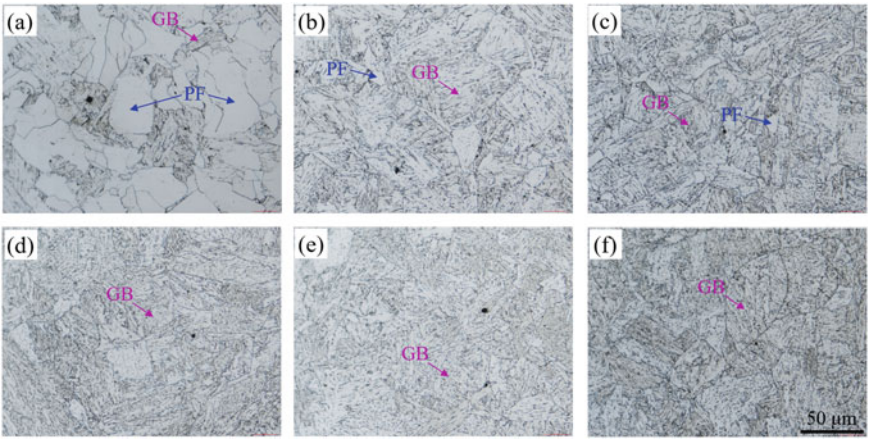

Fig. 6 Microstructure of samples after holding at 1220 °C and cooling at different cooling rates: **a** 1 °C/s; **b** 2 °C/s; **c** 5 °C/s; **d** 10 °C/s; **e** 20 °C/s; (f) 30 °C/s

ferrite was found in the sample. In general, as the cooling rate increased, the amount of proeutectoid ferrite gradually decreased, the amount of bainite increased correspondingly, and the sizes of bainite ferrite and martensite-austenite islands decreased progressively.

In Situ Observation of Austenitization

Figure 7 shows the evolution of samples' microstructure during austenitization at 1220 °C. As shown in the figure, when the temperature increased to 1220 °C, the sample was still in the recovery stage and did not recrystallize. The austenite grains began to appear after holding for 30 s, and the austenite recrystallization process was completed after 60 s. As the holding time increased, part of the crystal grains grew up by merging nearby tiny crystals. Compared with the sample austenitized in the range of 830–930 °C (Fig. 2), the sample had a more thorough austenitization process at 1220 °C, and the average grain size dramatically increased.

Hardness of the Microstructure

Figure 8 shows the hardness of the microstructure of samples after austenitizing at 890 and 1220 °C and cooled at different cooling rates. As shown in the figure, the hardness of the samples increased with the increasing cooling rate. Two points are worth noting: first, the hardness of the samples after austenitization at 1220 °C at all cooling rates was higher than the hardness of the samples after austenitization at

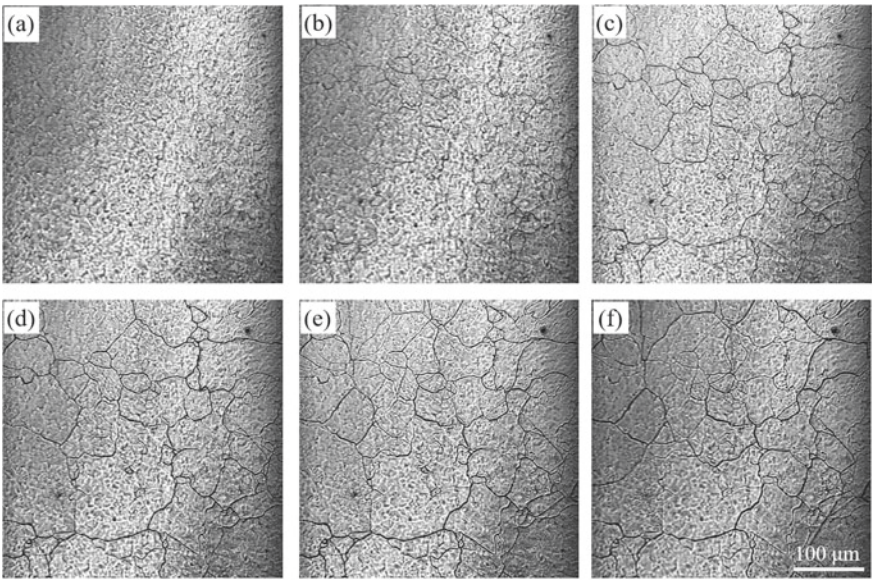

Fig. 7 Microstructure evolution of a sample holding at 1220 °C for different times: **a** 0 s; **b** 30 s; **c** 60 s; **d** 120 s; **e** 180 s; **f** 300 s

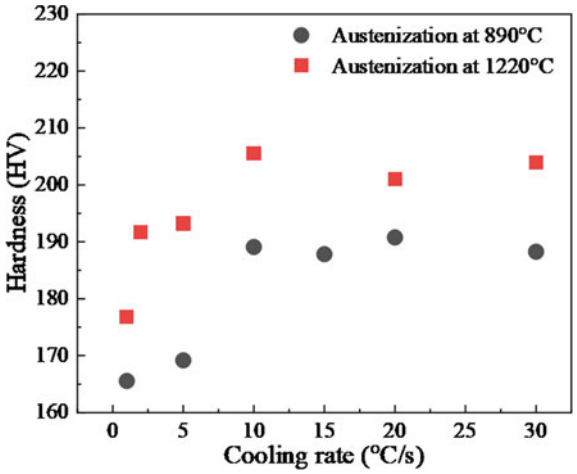

Fig. 8 Hardness of samples under different cooling rates after holding at 890 °C and 1220 °C, respectively

890 °C; second, when the cooling rate was greater than 10 °C/s, the hardness of the two austenitized samples after cooling did not increase with the increasing cooling rate.

The following two factors may account for this. On the one hand, there is a limit to the phase change driving force contributed by increasing the cooling rate. When the cooling rate exceeded the critical value, it had little effect on the phase change

driving force. On the other hand, the cooling capacity of the confocal laser scanning microscope is weak in the low-temperature section, failing to achieve the set cooling rate. Based on the fact that martensite is generally formed when the cooling rate is large, it can be inferred that the latter may be the reason why the hardness did not change significantly when the cooling rate was larger than 10 °C/s.

Discussion

Bainite transformation is a process of nucleation and growth. Its essence is the decomposition and transformation of supercooled austenite into ferrite, cementite, and other carbides. At the same time, part of the austenite will remain at room temperature together with a small amount of martensite. This phase transition process is jointly determined by nucleation and growth. The significant difference in the heat treatment process of the two types of samples in this work is the austenitizing temperature; some were austenitized in the range of 830–930 °C (low temperature), and the others were austenitized at 1220 °C (high temperature).

After low-temperature austenitization, the austenite grains were fine, and many interfaces existed that were conducive to nucleation, but the driving force for phase transformation was small. After high-temperature austenitization, the austenite grains were coarse, and a few interfaces existed that were not conducive to nucleation, but the driving force for phase transformation was large. The experimental results show that the driving force of the phase transformation plays a decisive role in the bainite transformation in this work. The continuous cooling method is generally used to cool the steel plate after rolling in industrial production. The temperature before cooling is generally around 900 °C. The microstructure of the steel plate cooled to room temperature is mainly bainite. The slower the cooling rate, the more proeutectoid ferrite and the larger the size of bainite ferrite. The faster the cooling rate, the less proeutectoid ferrite and the smaller the bainitic ferrite size. When the cooling rate exceeds a specific value, martensite will appear.

In this work, the austenitization temperature before continuous cooling was 890 °C, similar to the temperature used in industrial production, but no bainite was discovered in the samples after being cooled at all cooling rates. The reason is that the sample did not undergo thermal deformation before continuous cooling, and its deformation storage energy was significantly lower than that of steel plates in industrial production. Therefore, there was not enough driving force to promote the bainite transformation during the cooling process, and only proeutectoid ferrite was formed, and part of austenite remained. For the samples that undergo continuous cooling after austenitization at 1220 °C, although the grain size was coarse and the nucleation points were relatively few, the driving force for phase transformation was significantly increased, promoting the bainite transformation of these samples.

Conclusions

The influence of the austenitization and cooling process of low-carbon bainite steel on microstructure transformation was investigated. The following conclusions were obtained.

(1) The continuous cooling microstructure of low-carbon bainite steel was jointly determined by pre-deformation, austenitizing temperature, and cooling rate.
(2) The heating temperature had a significant effect on the austenitization process of low-carbon bainite steel. When the sample was heated in the range of 830–930 °C, the austenite grain size was relatively small, with a maximum value of 12.3 μm. When the subsequent cooling rate was in the range of 1–30 °C/s, the structure was mainly composed of a large amount of ferrite and a small amount of retained austenite.
(3) As the heating temperature increased to 1220 °C, the austenite grain size increased to 71.2 μm. When the cooling rate was 1 °C/s, the structure was mainly proeutectoid ferrite and bainite. As the cooling rate increased, the amount of proeutectoid ferrite reduced and bainite increased, resulting in the increase of its hardness. When the cooling rate was 10 °C/s, the proeutectoid ferrite completely disappeared, and the granular bainite structure was further refined.

References

1. Garcia-Mateo C, Caballero FG (2005) Ultra-high-strength bainitic steels. ISIJ Int 45(11):1736–1740
2. Caballero FG, Roelofs H, Hasler S, Capdevila C, Chao J, Cornide J, Garcia-Mateo C (2012) Influence of bainite morphology on impact toughness of continuously cooled cementite free bainitic steels. Mater Sci Technol 28(1):95–102
3. Xi X, Wang J, Chen L, Wang Z (2020) On the microstructural strengthening and toughening of heat-affected zone in a low-carbon high-strength Cu-bearing steel. Acta Metall Sin (English Letters) 34(5):617–627
4. Liu M, Xu G, Tian J, Yuan Q, Chen X (2020) Effect of austempering time on microstructure and properties of a low-carbon bainite steel. Int J Miner Metall Mater 27(3):340–346
5. Chen G, Hu H, Xu G, Tian J, Wan X, Wang X (2020) Optimizing microstructure and property by ausforming in a medium-carbon bainitic steel. ISIJ Int 60(9):2007–2014
6. Guo H, Feng X, Zhao A, Li Q, Chai M (2020) Effects of ausforming temperature on bainite transformation kinetics, microstructures and mechanical properties in ultra-fine bainitic steel. J Mater Res Technol 9(2):1593–1605
7. Yao C, Lan H, Tao Z, Misra RDK, Du L (2021) Enhanced strength and toughness of low-carbon bainitic steel by refining prior austenite grains and austempering below Ms. Steel Res Int 92:2100263
8. Caballero FG, Bhadeshia HKDH, Mawella KJA, Jones DG, Brown P (2001) Design of novel high strength bainitic steels: part 1. Mater Sci Technol 17(5):512–516
9. Caballero FG, Bhadeshia HKDH, Mawella KJA, Jones DG, Brown P (2001) Design of novel high strength bainitic steels: part 2. Mater Sci Technol 17(5):517–522

10. Sung HK, Shin SY, Hwang B, Lee CG, Lee S (2012) Effects of B and Cu addition and cooling rate on microstructure and mechanical properties in low-carbon, high-strength bainitic steels. Metall Mater Trans A 43A(10):3703–3714
11. Ravi AM, Kumar A, Herbig M, Sietsma J, Santofimia MJ (2020) Impact of austenite grain boundaries and ferrite nucleation on bainite formation in steels. Acta Mater 188:424–434
12. Zong Y, Liu CM (2021) Microstructure, mechanical properties, and corrosion behavior of ultra-low carbon bainite steel with different niobium content. Materials 14(2):311
13. Garcia-Mateo C, Caballero FG (2007) Design of carbide-free low-temperature ultra high strength bainitic steels. Int J Mater Res 98(2):137–143
14. Zhu W, Cui J, Chen Z, Feng Y, Zhao Y, Chen L (2021) Design and performance of 690 MPa grade low-carbon microalloyed construction structural steel with high strength and toughness. Acta Metall Sin 57(3):340–352

Evaluation of Aluminum White Dross

İlayda Elif Öner, Buse Tuğçe Polat, Selçuk Kan, Kağan Benzeşik, and Onuralp Yücel

Abstract Aluminum secondary production demand is significantly risen due to high energy consumption and waste production of primary aluminum production. On the other hand, it is inevitable to have several harmful by-products during secondary aluminum production such as dross. In this study, the aim is to obtain high-purity alumina by pyrometallurgical methods in order to use it in ceramic and refractory industry. Within the scope, non-metallic residue of aluminum white dross (NMR of AWD) has been subjected three sets of experiments. In the first set, calcination experiments were done for elimination of nitrogen and fine metallic aluminum content of NMR. The effects of temperature and duration on the elimination were investigated at 1000, 1100, and 1150 °C for from 15 min to 2 h in a rotary furnace. It was determined that at 1150 °C and 2 h of duration, 5.21 wt% N was eliminated, and metallic aluminum content was decreased; thus, alumina purity has reached 94.67 wt%.

Keywords Waste minimization · Dross recycling · Recovery · Calcination

Introduction

Aluminum is the third most common element in the earth's crust after oxygen and silicon. Aluminum is the most commonly produced and used non-ferrous metal due to its superior properties such as lightweight, high corrosion resistance, and high strength values. For this reason, the application areas of aluminum are expanding day by day. The main uses of aluminum can be listed as construction, electronics, automotive, aviation, railways, and packaging industry.

Although aluminum is a common material in terms of availability, energy consumption is high in production processes. Increasing demand and high energy consumption make secondary aluminum production and recycling a necessity [1]. Since 2000, global aluminum production has increased by 260%, reaching 63.7

İ. E. Öner · B. T. Polat · S. Kan · K. Benzeşik · O. Yücel (✉)
Department of Metallurgical and Materials Engineering, Istanbul Technical University, Sarıyer, 34469 Istanbul, Turkey
e-mail: yucel@itu.edu.tr

Z. Peng et al. (eds.), *12th International Symposium on High-Temperature Metallurgical Processing*, The Minerals, Metals & Materials Series,
https://doi.org/10.1007/978-3-030-92388-4_37

million tons in 2019, largely due to growth in China. By 2040, global aluminum demand is expected to grow steadily. The size of this forecast is such that 90 million tons of primary production will meet demand with 70 million tons of secondary aluminum from recycling [2, 3].

Aluminum production is divided into two sub-categories: primary aluminum production and secondary aluminum production. In primary production, aluminum is extracted from its ores (mostly bauxite) by pyrometallurgical or hydrometallurgical methods. Primary aluminum production is an energy intensive industry that uses about 174–186 GJ per ton aluminum produced. On the other hand, aluminum process scraps (dross, salt cake, etc.) and used aluminum products (cans, etc.) are used as raw materials in secondary production. Therefore, energy consumption of secondary production is considerably less than primary production with 10–20 MJ per ton Al. In addition to the much higher energy consumption, water consumption is 57 kg/ton in primary production, while it is only 1.6 kg/ton in secondary production. Also, primary Al production releases significant atmospheric emissions (21.81 tons CO_2/ton Al) and solid wastes compared to secondary Al production [2–5]. Aluminum can be recycled many times without losing its mechanical properties. In addition to this feature, secondary aluminum production not only reduces energy consumption, but also minimizes environmental concerns. Overall, secondary aluminum production requires 5% less energy and emits 5% less greenhouse gases than primary production [2].

The most commonly used method for secondary production is the melting process with salt slag containing low amounts of fluoride, sodium, and potassium in reverber or rotary furnaces. These slags have two main functions: to minimize oxidation losses during the process and to facilitate the separation of aluminum from non-metallic impurities.

Recycling methods may differ depending on the metallic aluminum or alumina concentration of the waste product. Wastes from primary aluminum production are called white dross (AWD). It consists of a high proportion of aluminum oxide and can contain 15–70% recyclable metallic aluminum. Wastes from secondary aluminum production are called black dross and typically contain aluminum oxide and oxides of aluminum alloys and often contain between 12 and 18% recyclable aluminum [6]. The worldwide secondary aluminum industry produces nearly five million tonnes of furnace waste each year.

Most common treatment practice for such non-metallic products is landfilling. This old-fashioned disposal method of black and white dross costs the industry an estimated £50 million [7]. In addition, tighter environmental regulations and spiraling costs are forcing the industry to consider alternatives.

Recycling these non-metallic residues (NMR) instead of landfilling not only helps preserve raw material reserves but also provides many economic and environmental benefits.

Smelting and mechanical sorting processes take place during Al recycling. During smelting process, N and Al reactions occur. Products of these reactions during smelting and mechanical sorting processes which contain N, stay in non-metallic residue. Therefore, this material is used in landfilling. AlN, in aluminum dross, turns

into alumina and ammonium gas in contact with humidity as shown in Reaction 1, and it is harmful to the environment when landfilled. This situation prevents the formation of ammonium gas in the atmosphere when moisture is removed by reaching high temperatures in an oxidizing environment as seen in Reaction 2 [8].

$$2AlN + 3H_2O \rightarrow NH_3 + Al(OH)_3 \quad (1)$$

$$2AlN + 3/2\,O_2 \rightarrow Al_2O_3 + N_2 \quad (2)$$

In this study, the FactSage program was used to determine the temperatures at which the experiments will be performed for the removal of salts from the NMR of Al white slag in the rotary kiln and the impurity removal of other impurities. Evaporation temperatures of NaCl and KCl salts under atmospheric pressure have been calculated as approximately 1400 °C.

The acquisition of aluminum from white and black dross and salt cakes has recently begun to attract the attention of researchers. These current researches are concentrated on obtaining high-purity aluminum oxide by hydro- and pyrometallurgical methods from NMRs. In this study, it is aimed to recover high-purity alumina from white dross by pyrometallurgical method.

Experimental

As it can be seen from Fig. 1, firstly, Al white dross (AWD) is crushed and milled prior to sieving process as current method of dross handling in the secondary aluminum production facilities. The pieces coarse enough to remain on the sieve are rich in metallic aluminum and are melted again with the addition of flux and sold as ingots. The fine-grained part under the screen is rich in oxide, and this is the part (NMR) used in this study as a raw material.

Raw Materials

After metallic aluminum content is separated, white dross (AWD) is used as raw material of this work. Separation is done by crushing and milling, and lastly collecting the NMR part from vacuumed bag filters. Prior to calcination experiments, raw materials are characterized by using sieving analysis, X-ray diffraction, and chemical analysis. The results are given as Tables 1 and 2 and Fig. 2.

Sieve analysis details are summarized in Table 2, and related graphic is given for non-metallic residue (NMR) in Fig. 2.

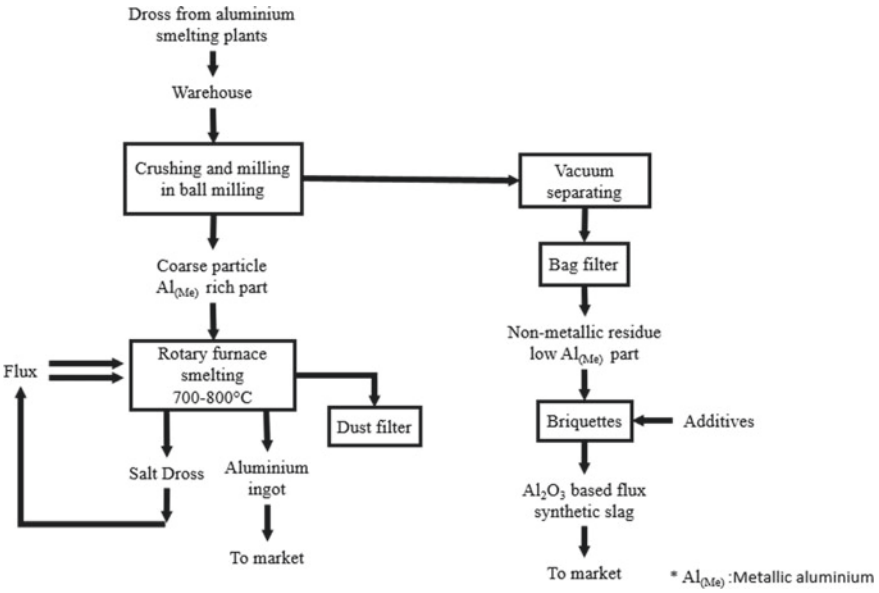

Fig. 1 Flow diagram of dross processing [9]

Table 1 Raw material chemical analysis results

	Al dross (wt%)
Al_2O_3	68.83
$Al_{(Me)}$	9.27
N	5.47
K_2O	2.49
SiO_2	1.11
Na_2O	0.66
Fe_2O_3	0.54
MgO	0.15

Table 2 Particle size of NMR

Mesh size (μm)	Weight (g)
−45	6.38
45	52.02
106	32.2
250	9.4
Total	100

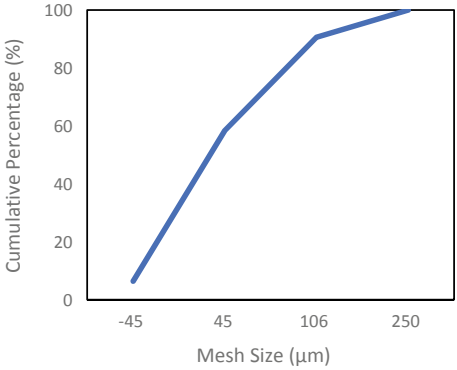

Fig. 2 Cumulative sieving analysis of NMR

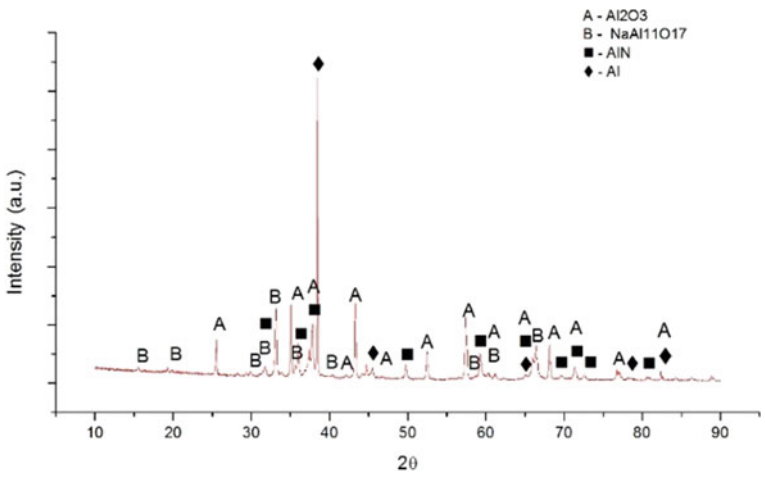

Fig. 3 XRD pattern of NMR

According to characterization results of NMR, it can be clearly seen in Table 1 that metallic aluminum and N which has harmful effects contents are high. Additionally, these phases can be seen from XRD results as shown in Fig. 3.

Procedure

After raw material analysis, calcination experiments were designed in a rotary furnace. It is a both open-end laboratory scale rotary furnace. Reaction zone is in a tube which is designed to hold the temperature stable during experiment. The tube can easily be changed with using hand-operated pump which is connected to hydraulic

mechanism. The maximum temperature that can be heated up to is 1400 °C utilizing via SiC resistances. The rotation is applied by the gears on side, and rotation speed can be adjusted between 0 and 10 rot/min. In this study, speed is set to 1 rot/min. The furnace schematic and a picture from an experiment are given in Fig. 4.

Three calcination experiments aimed to find out optimum temperature and duration for calcining non-metallic residue of aluminum white dross (NMR) were conducted. The furnace was heated up to 1000 °C which was named as Rotary Furnace I (RFI), second experiment at 1100 °C named as Rotary Furnace II (RFII), and lastly third experiment at 1150 °C named as Rotary Furnace III (RFIII) and charged with 1000 g of non-metallic residue. In the first hour, 4 samples were taken out every 15 min, and in the second hour, 4 samples were taken out every 30 min by using the scoop. Therefore, 8 samples were taken out in total and weight. Pictures of NMR before and after calcination are given in Fig. 5.

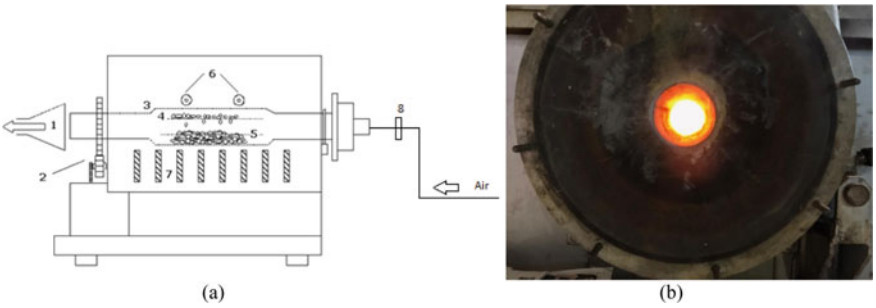

Fig. 4 **a** Rotary kiln (1—gas and powder collector, 2—gear, 3—stainless steel reaction tube, 4—mixing wing, 5—charge materials, 6—thermocouples, 7—SiC resistances, 8—flowmeter). **b** View of inside of the rotary kiln during the experiment

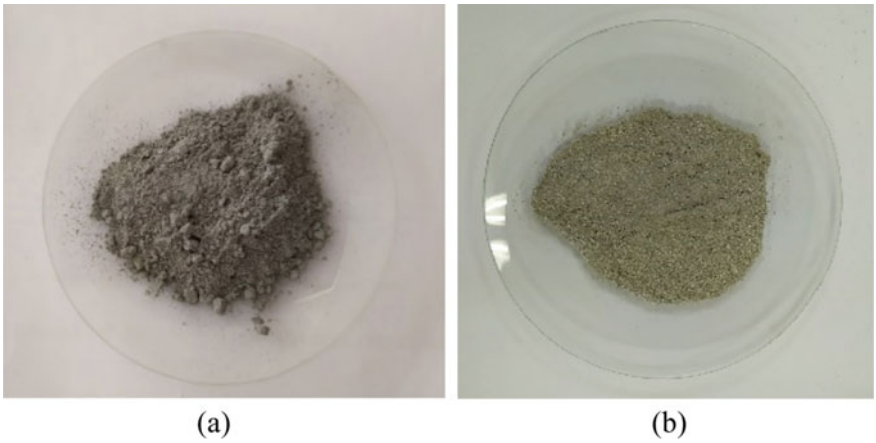

Fig. 5 **a** Raw and calcined (NMR). **b** At 1000 °C for two hours

Results and Discussion

After experiments are done, related results were obtained through chemical analysis and X-ray diffraction (XRD) analysis. The aim is to obtain desired chemical composition which was eliminated from impurities as well as unwanted different phases. According to results from RF I experiment which are shown in Tables 3 and 4 and Fig. 6, N elimination is achieved with decreasing metallic aluminum content, but it is not sufficient enough after at 1000°C for 2 hours of calcination. Additionally, the phases such as $NaAl_7O_{11}$ and $NaAl_{11}O_{17}$ still exist.

Results of RF II experiment with similar conditions at 1100 °C are given in Fig. 7 and Table 5. Similarly to RF I results, the $NaAl_7O_{11}$ and $NaAl_{11}O_{17}$ still exist as seen on XRD results.

The calcination experiments continued at 1150 °C as the obtained results showed that the increasing temperature was very effective in removal of N and increasing alumina content. The obtained results are given at Tables 6 and 7 and Fig. 8.

From the result of the experiments, it is seen that with increasing temperatures and holding time, decreasing amount of N content from 5.47 to 0.25% and decreasing amount of metallic aluminum (Al_{Me}) from 9.27 to 0.73% are possible. Additionally, analyses results show that optimum temperature and duration parameters for removing impurities like K, Na, Cl are at 1150 °C and 2 h.

Table 3 Chemical analysis results of NMR (Al dross residue) and calcined white dross at 1000 °C, 2 h

	Al dross	RFI 120
Al_2O_3	68.83	88.17
$Al_{(Me)}$	9.27	2.2
N	5.47	0.84
K_2O	2.49	1.29
SiO_2	1.11	1.17
Na_2O	0.66	0.27
Fe_2O_3	0.54	1.37
MgO	0.15	0.10

Table 4 Existing phases of calcined NMR at 1000° for 30, 60, and 180 min

Sample	Al_2O_3	$NaAl_7O_{11}$	$NaAl_{11}O_{17}$
RF I 30	+	+	+
RF I 60	+	+	+
RF I 180	+	+	+

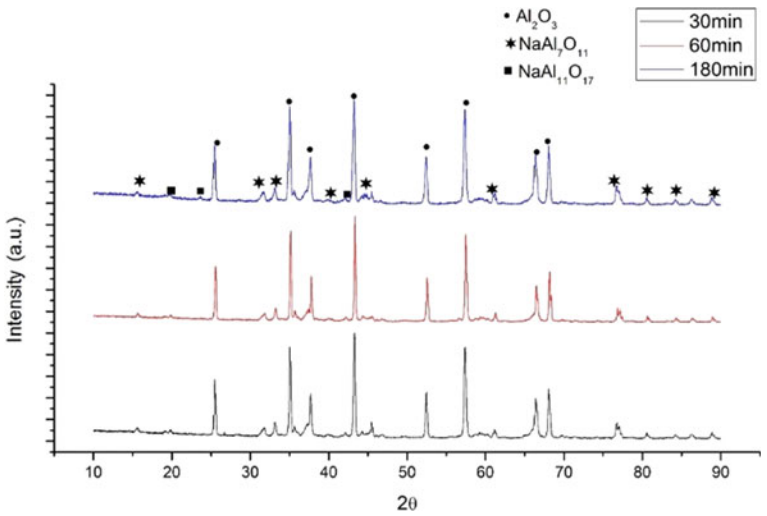

Fig. 6 XRD patterns of 30, 60, and 180 min of calcined NMR at 1000 °C

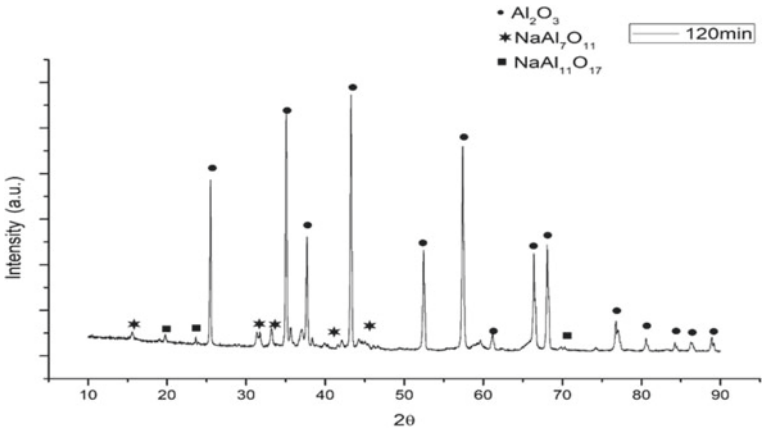

Fig. 7 XRD analyses patterns of calcined NMR at 1100 °C for 120 min

Table 5 Existing phases of calcined NMR residue at 1100 °C for 120 min

Sample	Al_2O_3	$NaAl_7O_{11}$	$NaAl_{11}O_{17}$
RF II 120	+	+	+

Table 6 Chemical analysis of calcined NMR at 1150 °C for 2 h

	Al dross	RFIII 120
Al_2O_3	68.83	94.67
$Al_{(Me)}$	9.27	0.73
N	5.47	0.25
K_2O	2.49	0.83
SiO_2	1.11	0.96
Na_2O	0.66	0.22
Fe_2O_3	0.54	0.59
MgO	0.15	0.23

Table 7 Existing phases of calcined NMR at 1150 °C

Sample	Al_2O_3	$NaAl_{11}O_{17}$
RF III 30'	+	+
RF III 90'	+	+
RF III 180'	+	+

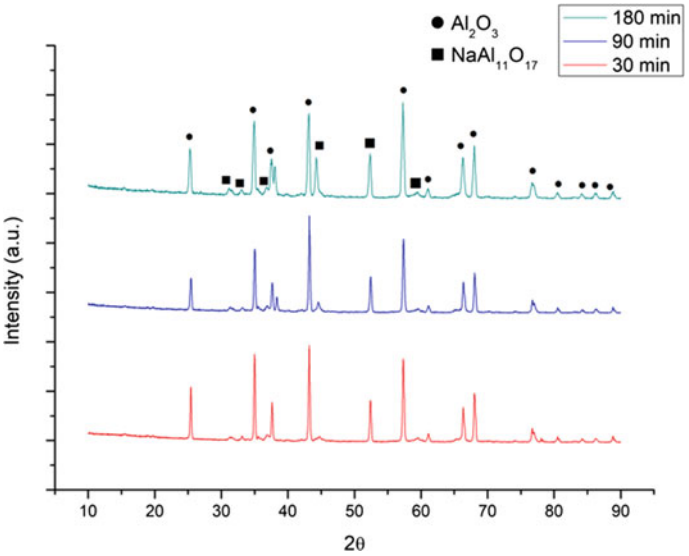

Fig. 8 XRD analyses patterns of calcined NMR at 1150 °C for 30, 90, and 180 min

Conclusion

In this study, effects of calcination temperature and duration on decreasing of harmful aspects, that occur during recycling process and landfilling, of NMR were investigated. Optimum calcination parameters were determined as at 1150 °C for 2 h on

eliminating N from non-metallic residue. High-purity Al_2O_3 (approximately 95%) was obtained. Thus, the risks that may arise due to the chemical content of the material are eliminated when it is stored for disposal or reuse. Products are resistant to high temperature, and they can be used as fire or building bricks and pavers.

References

1. Eminoğlu S, Aytaş S, Ayhan S, Varır A (2011) Alüminyum Isil Metalürjisi Atik Yönetimi (Alüminyum Sektörü) Rehber Dokümani
2. Wong DS, Lavoie P (2019) Aluminum: recycling and environmental footprint. JOM 71(9):2019. https://doi.org/10.1007/s11837-019-03656-9
3. International Aluminium Institute, Primary Aluminium Production (2019) http://www.world-aluminium.org/statistics/primary-aluminium-production/. Accessed 19 May 2020
4. Tsakiridis P (2012) Aluminium salt slag characterization and utilization—a review. J Hazard Mater 217–218:1–10
5. Jafari NH, Stark TD, Roper R (2014) Classification and reactivity of secondary aluminum production waste. J Hazard Toxic Radioact Waste 18(4):04014018
6. Kulik GJ, Daley JC (1990) Aluminum dross processing in the 90's. In: van Linden JHL, Stewart DL Jr, Sahai Y (eds) Second international symposium—recycling of metals and engineered materials, Warrendale PA, TMS, p 427
7. Rankin J (2012) Energy use in metal production. In: High temperature processing symposium 2012. Swinburne University of Technology
8. Breault R et al (1995) Process for the preparation of calcium aluminates from aluminium dross resources. 5,407,459
9. Shinzato MC, Hypolito R (2005) Solid waste from aluminum recycling process: characterization and reuse of its economically valuable constituents. Waste Manag 25:37–46

Investigation of Microstructure and Mechanical Properties of Ferritic Stainless Steels Joined by Laser Welding

Günseli Güç and Onuralp Yücel

Abstract Laser welding is widely used in the joining of materials due to the advantages it provides. This study aims to investigate the suitability of different ferritic stainless steels to laser welding method. Within the scope, ferritic stainless steel sheets with a thickness of 0.5 mm of different grades (430, 430Ti and 441) were welded by solid-state disk laser, and welding parameters were determined as 1300 W power, 6 m/min welding speed in continuous wave mode. As a shielding gas, argon was used. Metallographic examinations, SEM–EDS analysis, microhardness measurement were performed, and tensile, cupping tests, and bending tests were carried out with welded and unwelded samples. Thus, the structure and property relationships of ferritic stainless steels joined by laser welding were examined and compared. As a result, adequate welding quality could not be achieved in 430 samples, and it was observed that the welding ability was insufficient compared to 430Ti and 441 samples.

Keywords Stainless steels · Laser welding · Joining steels

Introduction

Especially in the white goods sector, automation-appropriate joining methods are required in terms of production efficiency and high-strength joints. Due to this necessity, mechanical joining methods leave their place to automation-friendly joining methods such as laser welding. Stainless steel sheets are generally used in parts where corrosion resistance is required in addition to strength in the white goods sector and can be conveniently joined by all welding methods, with some limitations. Different stainless steel grades (different chemical compositions and characteristics) affect the welding process depending on its grade and classification. Some important characteristics of welding different stainless steels can be listed as grain growth, carbide formation, low heat conduction coefficient, high electrical conductivity and

G. Güç (✉) · O. Yücel
Metallurgical and Materials Engineering Department, Faculty of Chemical and Metallurgical Engineering, Istanbul Technical University, 34469, Maslak Istanbul, Turkey

Z. Peng et al. (eds.), *12th International Symposium on High-Temperature Metallurgical Processing*, The Minerals, Metals & Materials Series,
https://doi.org/10.1007/978-3-030-92388-4_38

coefficient of thermal expansion, sensitivity to cold forming, intergranular and stress corrosion cracking corrosion, and structural changes such as sigma phase and delta ferrite [1]. In terms of low heat conduction and high expansion properties, the heat input should be low during the welding process to prevent distortion [2]. Ferritic stainless steels are preferred due to their strength, corrosion resistance, toughness, and intermediate welding ability, which are also widely used in household appliances, automobile, and machinery industries. Moreover, the use of ferritic stainless steel offers a more economical alternative compared to austenitic stainless steel [3, 4].

The weldability of ferritic stainless steel is quite better than that of martensitic stainless steel. However, certain problems may be encountered in the welding process of ferritic stainless steel. One of the major problems is their excessive tendency to grain growth in a heat-affected zone (HAZ) at temperatures above 1150 °C. Since austenite-ferrite transformation does not occur in ferritic stainless steels, the grains cannot be reduced by a heat treatment. Ferritic stainless steels, which generally have a fine-grained and ductile structure, become brittle when they become coarse-grained, and as a result, their strength of impact decreases. As a solution, nitrogen can be added to their composition to prevent grain growth [2, 5].

Another problem is the sensitivity to intergranular corrosion occurring during the high-speed cooling at temperatures above 900 °C in a HAZ. In regions adjacent to the weld seam, they are more susceptible to intergranular corrosion due to higher rates of chromium carbide precipitation in the ferritic structure compared to the austenitic structure. They are, for this reason, susceptible to intergranular corrosion in areas adjacent to the weld seam. If they are annealed at 750 °C immediately after welding, welded joints made with stabilized 17% chromium ferritic stainless steels can be made resistant to intergranular corrosion. Moreover, welded joints are resistant to intergranular corrosion without heat treatment if they are stabilized with titanium or niobium alloy elements. In addition, martensite formation is not expected in the heat-affected zone since there is no austenite-ferrite transformation. However, martensite formation can be seen at grain boundaries in some ferritic stainless steels according to chemical composition, and it causes brittleness [2, 5, 6].

Compared to other welding methods, laser welding has many advantages. These are little or no distortion owing to low heat input in weld seam, high-speed manufacturing reaching high welding speeds above 10 m/min, unaffected base metal, narrow weld seam, and HAZ region via high-speed cooling, easy and flexible process, compliance with automation, possibility to weld different materials, and in places where it cannot be welded with conventional methods and high depth/width ratio [7]. According to the active material used to create laser beam, lasers can be classified as gas, solid-state, liquid, and semiconductor diode lasers. Industrial uses of solid-state lasers have increased significantly with the developed neodymium (Nd): yttrium aluminum garnet [YAG ($Y_3Al_5O_{12}$)] lasers. Generally, the cylindrical rod-shaped crystal is fixed in a metal container after being polished at both ends and coated with anti-reflective material in solid-state laser systems. Considering the method to be used as a stimulator, special flash lamps and reflective mirrors are placed inside this container. The most important problem of this type of laser is formation of thermal stresses by the heat differences between the excited crystal's inner and outer surfaces.

The quantity and quality of the laser beam that the crystalline structure can emit are affected by these thermal stresses. As a solution to this problem, in recent studies, it has been evaluated that the crystalline form used in the production of laser beams is a thin disk or a long and thin fiber instead of a cylindrical form, and as a consequence, fiber and disk lasers with much higher beam quality and efficiency have been developed. In such crystals, unlike the rod form, no significant thermal stress occurs in the crystal since the distance between the excited surface and the inner parts of the crystal is less than a few hundred microns. This enables the crystal to be used more efficiently [8].

Although conventional welding methods and different laser techniques such as laser spot welding are frequently seen in the literature, studies on continuous wave solid-state disc laser welding are less common. Despite its advantages, the material and process parameters to be used should be investigated because of the use of laser welding in mass production to be applicable in practice [9]. Therefore, it was aimed to investigate the suitability of different ferritic stainless steels to be joined by a solid-state disk laser with certain welding parameters. To determine if 430, 430Ti, and 441 ferritic stainless steel were weldable, the sheets were joined by solid-state disk laser welding in continuous wave mode, and chemical analysis, metallographic examinations, microhardness measurement, SEM–EDS analysis, tensile tests, bending tests, and cupping tests were carried out.

Experimental Procedure

To determine the influence of different grades of ferritic stainless steel sheets joined by laser welding, metallographic examinations, SEM–EDS analysis, microhardness measurement, tensile, cupping tests, and bending tests were carried out. In order to evaluate and compare the mechanical properties after laser welding, unwelded ferritic stainless steel sheets were also subjected to tensile and cupping tests. In this study, unstabilized 430 grade and stabilized 430Ti and 441 ferritic stainless steel grades with a thickness of 0.5 mm were joined using a solid-state disc laser, and the welded properties of the samples were investigated by keeping the welding parameters constant.

The stainless steel sheets used in the studies were obtained from stainless steel manufacturers, and the laser welding of the sheets was carried out in Weil Technology, a German origin automation company. Chemical analysis, determination of mechanical properties, and microstructure characterization of stainless steel sheets joined by laser welding process are carried out in Arcelik and Istanbul Technical University laboratories.

Firstly, the supplied sheet samples were cut to a width of approximately 200 mm and a length of 150 mm for the butt-welding process. Ferritic stainless sheets with the same grade were placed and fixed on the manual clamping device shown in Fig. 1 and welded together with Trudisk solid-state laser. Parameters of laser welding with Trudisk solid-state laser of AISI 430, 430Ti, and 441 stainless steel with a thickness

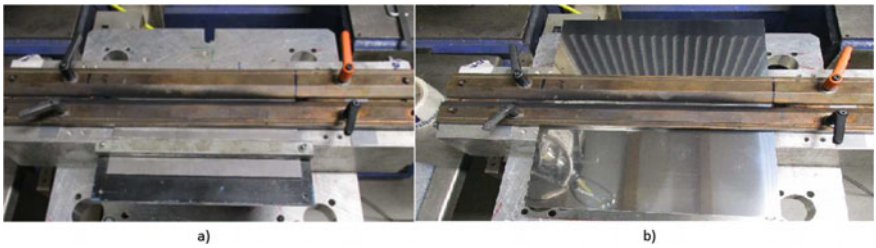

Fig. 1 **a** Sample fixing device. **b** Image of the fixed samples used in the welding process

of 0.5 mm are welding speed of 6 m/min, an output power of 1300 W, and heat input of 13 J/mm. Other parameters include that welding was performed with a focus diameter of 400 μm in focus, beam incidence angle was vertical from above on the top surface of samples, and argon gas was used as a shielding gas.

To compare the mechanical properties of the welded plates, different test samples were prepared from the same welded plates. In the same way, samples were prepared from unwelded sheet plates for comparison purposes.

Chemical analysis of the stainless steel sheet samples was carried out at the optical emission spectrometer. For microstructural investigations of the fusion zone, heat-affected zone, and base metal, the samples extracted in suitable dimensions are cold molded along their large surfaces. Sanding and polishing processes were performed, respectively, by standard metallographic methods. After polishing, the electrolytic etching process was carried out at 12 V DC using 10% $H_2C_2O_4$ (oxalic acid) solution in 30 s.

In the tensile tests, the test specimens were prepared so that the weld seam remains in the middle and perpendicular to the tensile direction. The change in strength and elongation values of stainless steel sheets before and after welding and the location of rupture of welded samples were investigated.

The bending test of the samples was performed with a 3-point bending apparatus. In the bending tests, test specimens were prepared with a length of 50 mm and a width of 20 mm, and the distance between supports was measured as 25 mm where the support and mandrel diameters are 5 mm.

Samples polished by standard metallographic methods were used in the micro-hardness measurement. In the experiments using a standard Vickers tip and 500 g load, microhardness measurements were carried out at regular intervals in the fusion zone and in the region up to approximately 2 mm on both sides of the fusion zone. The results regarding the formability of unwelded and welded samples were compared by performing cupping tests. The samples were prepared with a width of 95 mm with the weld seam in the center.

Zeiss Supra 55VP scanning electron microscope was used for the SEM–EDS analysis. SEM images were taken from the weld zones of 430, 430Ti, and 441 welded samples, and elemental Cr, Ti, Nb, C, N ratios were investigated by EDS analysis. The samples were first made into tangible by bakelite mounting, and then the surfaces were prepared with 320, 500, 800, 1200, and 2500 sandpapers, respectively, and

polished with 3- and 1-micron polishing felts. The microstructures were revealed by etching in the reagent composed of 15 ml of HCl, 6 ml of HNO_3, and 100 ml of H_2O solution. After that, since the bakelite is an insulator, the surfaces were coated with gold and for imaging, and the mounted sample was placed in the electron device chamber for imaging.

Results and Discussion

In Table 1, the results of the chemical analysis of the different grades of stainless steel samples used in the study are given. For the 430Ti stabilized grade, the titanium ratio (wt% Ti) should be at least 0.15, more than four times the carbon content. According to the amount of carbon in the sample used, the Ti ratio should be higher than 0.198%. This rate was measured as 0.38% and found appropriate. For the 441 stabilized grade, the Ti ratio should be at least 0.1%, and the niobium (Nb) ratio should be at least 0.30, more than three times the carbon content. The ratio of Ti in the used sample was measured as 0.164% and found appropriate. According to the carbon content, the ratio of Nb should be higher than 0.328%. This rate was also measured as 0.37% and found appropriate.

Observations of the micrographs in the region up to approximately 200 μm on both sides of the fusion zone reveal that the width of the heat-affected zone is negligible, and the interface between fusion zone and base metal is flat for 430Ti and 441 samples. On the contrary, approximately 100 μm in width heat-affected zone on both sides of the fusion zone consisting of elongated grains was observed in sample 430 as can be seen in Fig. 2.

Tensile testing of the samples prepared from welded and unwelded plates was carried out to determine the location of rupture and measure the tensile properties of weldments. As can be seen in Table 2, all the welded samples were ruptured in the base metal, away from the weld zone, except welded samples of 430 grade. In the welded samples of 430 grade ferritic stainless steel, rupture was observed in the weld zone. This reveals that welded samples of 430 grade have poor welding quality compared to other samples. In the samples of 430Ti and 441, the rupture was observed in the base metal region. In the study of Kökey et al. with pulsed laser welded 430 stainless steel, the situation in which the rupture occurred in the weld zone in sample 430 was also associated with poor weld quality [10].

Table 1 Chemical analysis of 430, 430Ti, and 441 (wt%)

Grade	Chemical composition (wt%)										
	C	Mn	P	S	Si	Cr	Mo	Cu	Ti	Nb	W
430	0.039	0.54	0.001	<0.0005	0.31	17	<0.005	0.004	0.001	0.004	0.12
430Ti	0.012	0.33	0.001	<0.0005	0.34	16.8	0.021	0.103	0.38	0.01	0.16
441	0.009	0.31	<0.001	<0.0005	0.51	18.3	0.021	0.09	0.164	0.373	0.15

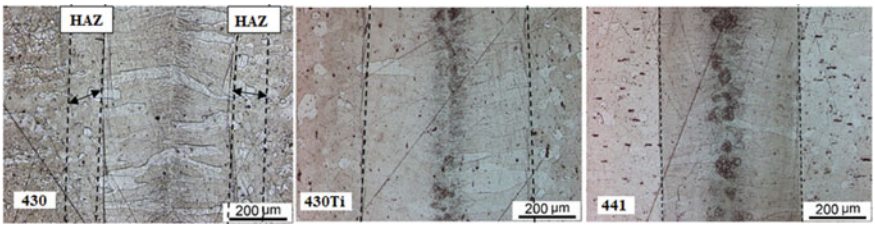

Fig. 2 Microstructures of the butt joints on 430, 430Ti, and 441 ferritic stainless steels with a thickness of 0.5 mm produced at the heat input 13 J/mm

Table 2 Tensile test results of 430, 430Ti, and 441

Sample		Yield strength (N/mm^2)	Tensile strength (N/mm^2)	Elongation %	Rupture location
430	Welded	479.92	333.16	18.40	Weld zone
	Unwelded	476.28	314.99	26.28	
430Ti	Welded	433.09	315.97	27.73	Base metal
	Unwelded	446.61	312.87	30.57	
441	Welded	471.98	301.36	30.85	Base metal
	Unwelded	480.70	313.72	29.79	

The mechanical properties of all samples except samples of 430 grade are acceptable according to the AISI standard (tensile strength in the range of 450–650 N/mm^2, 420–600 N/mm^2, and 430–630 N/mm^2; minimum yield strength of 260 N/mm^2, 230 N/mm^2, and 230 N/mm^2; and a minimum elongation of 23%, 23%, and 18% for 430, 430Ti, and 441, respectively). The decrease in elongation at break in the 430 ferritic stainless steel sample was associated with the fracture being from the weld zone. As can be seen, the yield strengths of welded and unwelded 430, 430Ti, and 441 samples were examined, and 6% of increase, 1% of increase, and 4% of decrease were determined in the welded samples compared to unwelded ones, respectively. Moreover, the tensile strength of the 430 welded samples increased by 1% compared to the original unwelded sample. The tensile strengths of 430Ti and 441 sheets, on the other hand, decreased by 3% and 2%, respectively, compared to their original unwelded condition. However, the strength values are within acceptable ranges according to the standard. In the study of Niklas Somer et al., according to the tensile test results of welded samples, an increase (5.09%) was also observed in the tensile strength of 430 sheets, while a decrease (2.62%) was observed in 430Ti samples [11].

In the bending tests, no damage in the form of cracking was observed in the weld zone of the 430, 430Ti, and 441 ferritic stainless steel samples. Average bending strengths were determined as 9.8, 10.8, and 9.6 MPa for 430, 430Ti, and 441, respectively. The highest bending strength was measured as 11 MPa in the 430Ti samples.

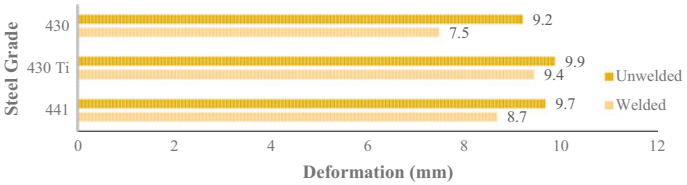

Fig. 3 Cupping test results

In microhardness measurements throughout the weld zone, hardness values of 430, 430Ti, and 441 samples were determined in the range of 157–187 HV, 160–211 HV, and 169–223 HV, respectively. In the study of Niklas Sommer et al. with laser welded 430 and 430Ti sheets, high hardness values in the range of 290–325 HV were determined in the weld zone of 430 sample as a result of the formation of martensite observed in the grain boundaries. Like the results we obtained in the weld seam of the 430Ti sample, the hardness values of 430Ti samples were measured in the range of 200–210 HV, and it was determined that it decreased towards the base metal [11]. On the other hand, in this study, martensite formation was not observed in the microstructure of the 430 welded samples, as well as in the 430Ti and 441 welded sheet samples. As a result of this, high hardness changes were not observed.

Cupping testing of the samples prepared from welded and unwelded plates was carried out in Erichsen cupping device to determine the location of tearing and compare the amount of deformation of weldments. In the comparison of welded and unwelded samples, the least change was observed in 430Ti samples with a decrease rate of 4% as shown in Fig. 3. In the 430 and 441 welded samples, deformation values decreased by 19% and 10%, respectively. At the end of the test, it was determined that the tearing zones of all the samples were not along the weld seam.

Various EDS scans, including point, line, and mapping, were performed on the samples prepared for SEM examination in the weld zone. Thin and long structures were observed in SEM image and EDS line analysis of the weld zone of 430 ferritic stainless steel samples. In the EDS line scan, it was seen that the carbon ratio increased in these structures and was interpreted as carbide. Moreover, chromium carbide precipitates are observed in the EDS spectrum that is given by multipoint analysis in the weld zone, as shown in Fig. 4. In the study of Sarkari et al., EDS analyzes were performed in the HAZ of 430 ferritic stainless steels, and similar intragranular carbide precipitates were observed [12]. SEM image and EDS line analysis of the weld zone of 430Ti samples were also carried out. As shown in Fig. 5, precipitation was observed in the grains in the weld zone. According to the line scan and point analyzes performed on the precipitate, the main composition of the precipitate consists of Ti, N, and C elements that was interpreted as Ti(C,N) precipitate. It was observed that the investigated precipitate morphology was similar to the particle morphologies in the study of Michelic et al. on the characterization of TiN, TiC, and Ti(C,N) in Ti-alloyed ferritic chromium steels [13]. No chromium carbide precipitate was observed in the examinations made in the weld area. Transgranular precipitation was also observed in the weld zone of 441 samples, as shown in Fig. 6. According to

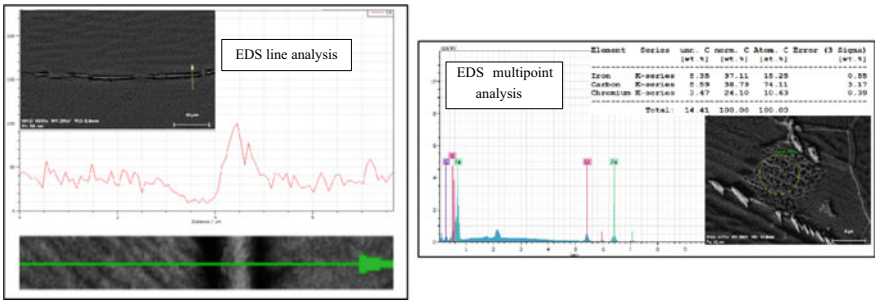

Fig. 4 SEM–EDS analysis of precipitates in 430 sample

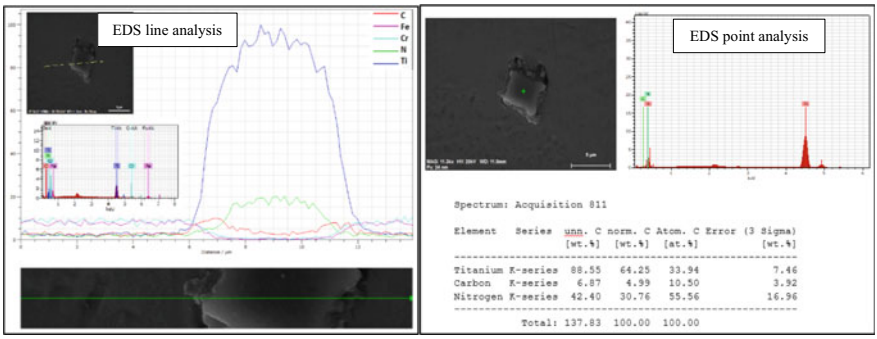

Fig. 5 SEM–EDS analysis of precipitates in 430Ti sample

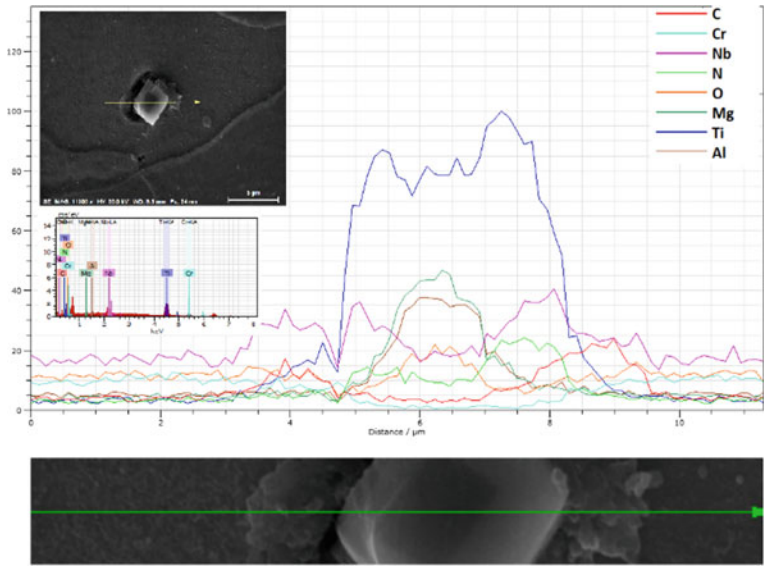

Fig. 6 SEM–EDS analysis of precipitate in 441 sample

its main composition, the precipitate was interpreted as (Ti, Nb) (N, C) composite precipitate. In addition, Al, Mg, and O elements were also detected in the core of the precipitate. It reveals that there may be aluminum and magnesium oxide inclusions. A similar precipitate structure was also observed in Junwei Fu et al.'s study, where they examined the effect of Nb element on the microstructure of ferritic stainless steel [14]. No chromium carbide precipitate was observed in the weld zone. Since 441 grade ferritic stainless steels contain titanium and niobium and 430Ti grade ferritic stainless steels contain titanium as a stabilized element, excess carbon and nitrogen in the composition tended to precipitate with these elements instead of chromium.

Conclusion

This study investigated the structure and property relationships of ferritic stainless steels joined by the laser welding method. In this scope, 430Ti, 441 grades containing stabilizer elements (Ti, Nb, etc.) in order to improve weldability and 430 grade ferritic stainless steel sheet samples were used in the experiments. The laser welding process was carried out under argon gas using Trudisk device in continuous wave mode with a heat input of 13 J/mm (output power of 1300 W power and welding speed of 6 m/min) by keeping welding parameters constant.

In microstructural examinations, except for the 430 grade sample, interface between fusion zone and base metal was flat in samples 430Ti and 441, and no significant heat-affected zone was observed. In the 430 stainless steel sample, approximately 100 μm in width heat-affected zone on both sides of the fusion zone was observed. In the tensile tests, it was determined that all of the welded samples were ruptured in the base metal, away from the weld zone except for welded samples of 430 grade which the rupture observed in the weld zone that reveals the weld quality of 430 grade samples was not sufficient. In the bending test, the highest bending strength was measured as 11 MPa in the 430Ti sample. In the cupping tests, the least change was detected in the 430Ti welded samples with a 4% of decrease rate when compared to the original samples without welds. The highest deformation value after welding was observed in the 430Ti samples with an average value of 9.4 mm. On the other hand, the deformation values of 430 and 441 samples decreased by 19% and 10%, respectively. SEM and EDS analyzes were also performed, and thin and long precipitate structures were observed in the weld zone of 430 sample. EDS line and mapping analyzes show that the C ratio increased in these structures and the precipitates were interpreted as carbides. Multipoint analysis was performed in the weld area, and precipitates predicted to be chromium carbide were observed in the structure. In the weld zone of the 430Ti sample, the precipitate was also observed in the grain. As a result of EDS line and point analyzes, the precipitate was interpreted as titanium carbonitride precipitate. In the weld zone of 441 sample, a similar precipitate was observed in the grain. As a result of the line and mapping analyzes, the precipitate whose main composition consists of Ti, N, C, and Nb elements was interpreted as (Ti, Nb) (N, C) composite precipitate. Al, Mg, and O elements were also detected in the core of the precipitate.

Considering all the examinations, it has been concluded that the welding quality of 430 ferritic stainless steel, which does not contain stabilized elements, is not

suitable, and 430Ti ferritic stainless steel is a more suitable option for laser welding in consideration of its formability.

References

1. Baylan O (2003) Elektrik ark kaynak yöntemiyle birleştirilen östenitik- martenzitik farklı paslanmaz çeliklerin kaynaklı bağlantılarında, mikroyapı ile özellikler arasında ilişkinin araştırılması. Postgraduate Thesis, Z.K.U. Karabük Faculty of Technical Education, Zonguldak, pp 3–33
2. Aran A, Temel M (2004) Paslanmaz çeliklerin üretimi, kullanımı, standartları. Sarıtaş Teknik Yayın No: 1, Acar Matbaacılık A.Ş., Istanbul, pp 54–65
3. Shao Y, Li X, Ma J, Liu C, Yan Z (2019) Microstructure formation of low-carbon ferritic stainless steel during high temperature plastic deformation. Metals 9(4):463
4. Mohandas T, Reddya GM, Naveed M (1999) A comparative evaluation of gas tungsten and shielded metal arc welds of a “ferritic” stainless. J Mater Process Technol 94:133–140
5. Kaluç E, Tülbentçi K (1998) Paslanmaz çelikler ve kaynaklanabilirliği. Seminar Notes, Kocaeli University Welding Technology Research Education and Application Center
6. Lippold JC, Kotecki DJ (2005) Welding metallurgy and weldability of stainless steels. Wiley, New Jersey
7. Çelen S (2006) Paslanmaz çeliklerin lazer kaynağında kaynak parametrelerinin bağlantının dayanım ve korozyon özelliklerine etkisinin incelenmesi. Postgraduate Thesis, Dokuz Eylül University, Institute of Science and Technology, Izmir
8. Koechner W, Bass M (2003) Solid-state lasers. Springer, New York
9. Lisiecki A, Kurc-Lisiecka A (2018) Automated laser welding of AISI 304 stainless steel by disc laser. Arch Metall Mater 63(4):1663–1672
10. Kökey C, Sezgin S, Çavuşoğlu N, Gençalp-İrizalp S, Saklakoğlu İE (2016) İnce paslanmaz çelik sacların fiber lazer ile kaynak edilebilirliğinin incelenmesi. Mühendis ve Makina 57(674):65–72
11. Sommer N, Kryukov I, Wolf C, Wiegand M, Kahlmeyer M, Böhm S (2020) On the intergranular corrosion properties of thin ferritic stainless steel sheets welded by fiber-laser. Metals 10(8):1088
12. Khorrami MS, Mostafaei MA, Pouraliakbar H, Kokabi AH (2014) Study on microstructure and mechanical characteristics of low-carbon steel and ferritic stainless steel joints. Mater Sci Eng A 608:35–45
13. Michelic SK, Loder D, Reip T, Ardehali BA, Bernhard C (2015) Characterization of TiN, TiC and Ti(C, N) in titanium-alloyed ferritic chromium steels focusing on the significance of different particle morphologies. Mater Charact 100:61–67
14. Fu J, Wang J, Li F, Cul K, Du X, Wu Y (2020) Effect of Nb addition on the microstructure and corrosion resistance of ferritic stainless steel. Appl Phys A 126:194. https://doi.org/10.1007/s00339-020-3383-1

Structural and Magnetic Properties of Rare Earth Lanthanum-Doped Cobalt Ferrites

Xijun Zhang, Guoqian Wang, Xin Peng, Sujun Lu, Dalin Chen, Yutian Ma, and Ailiang Chen

Abstract Cobalt ferrite($CoFe_2O_4$) nanoparticles exhibit high magnetocrystalline anisotropy, high coercivity, and medium saturation magnetization. It shows great potential in various fields. So it is an active research topic to synthesize $CoFe_2O_4$ with controllable size, different shapes, and magnetic properties. In this study, $CoFe_{2-2x}La_{2x}O_4$ was synthesized by cobalt ferrite and rare earth La^{3+} with the route of sol–gel auto combustion. The results show that rare earth La^{3+} doping can refine the crystalline grain and change the magnetic properties of $CoFe_2O_4$. When the content of La^{3+} doping is less than 10%, it can refine the grain and make the grain size tends to homogeneous. Otherwise, it will appear heterogeneous phase $La(FeO_3)$. The excessive doping even makes most of the crystal shapes are destroyed and tends to disappear. When the content of La^{3+} doping is not less than 15%, the coercivity of $CoFe_{2-2x}La_{2x}O_4$ increased and saturation magnetization decreased. This is expected to control the magnetism of cobalt ferrite by doping rare earth ions.

Keywords Rare earth · $CoFe_2O_4$ · Sol–gel auto combustion · $CoFe_{2-2x}La_{2x}O_4$ · Magnetic properties

Introduction

Currently, magnetic nanomaterials have a wide range of applications as a functional material in the fields of magneto-optical storage materials, magnetic fluid materials, shadow body materials, and biological materials [1]. And spinel oxide (AB_2O_4) is one of the important functional materials in recent years. There are many kinds of transition metal ferrite (M = Co, Zn, Cd, Ni, Mn). Among them, researchers have great interest in the study of $CoFe_2O_4$ nanomaterials because of their special

X. Zhang · S. Lu · D. Chen · Y. Ma · A. Chen (✉)
State Key Laboratory of Nickel and Cobalt Resources Comprehensive Utilization, Jinchang 737100, China

G. Wang · X. Peng
School of Metallurgy and Environment, Central South University, Changsha 410083, China

Z. Peng et al. (eds.), *12th International Symposium on High-Temperature Metallurgical Processing*, The Minerals, Metals & Materials Series,
https://doi.org/10.1007/978-3-030-92388-4_39

characters, like large magnetocrystalline anisotropy, high Curie temperature (793 °C), high coercivity (Hc), moderate saturation magnetization strength (Ms), low cost and chemical stability, and so on [2]. Based on these excellent properties, $CoFe_2O_4$ is used in high-frequency magnets, microwave absorbers, magnetic catalysis, and drug delivery [3–5]. Therefore, it is necessary to study the magnetic properties of cobalt ferrite from different perspectives.

Doping with rare earth ions is one of the common means to regulate the magnetic properties of cobalt ferrite materials. Rare earth elements are mostly magnetic at low temperatures due to unfilled 4f electron layers generating uncanceled magnetic moments. But the Curie temperature is generally lower than room temperature. They cannot be magnetic materials for practical applications. $CoFe_2O_4$ is magnetic at room temperature and has a higher Curie temperature. Therefore, the structure and magnetic properties of cobalt ferrite can be controlled by doping appropriate amount of rare earth in cobalt ferrite materials. [6–8]. The common preparation methods are solid phase, co-precipitation, hydrothermal, self-combustion and sol–gel method, etc. [9]. It is known that the sol–gel method has the advantages of simple operation, low reaction temperature, small particle size, and high purity. But this has a long reaction time and easy agglomeration during sintering. The self-combustion method reaches a certain temperature that can be burned at a certain temperature. It greatly shortens the preparation time and reduces energy consumption. This also improves the agglomeration phenomenon of sintering to a certain extent [10–12]. Therefore, in this paper, in order to prepare cobalt ferrite with high purity, regular shape and small particle size, the sol–gel method was combined with the self-combustion method to synthesize $CoFe_{2-2x}La_{2x}O_4$ ($x = 0, 0.05, 0.10, 0.15, 0.20, 0.25$). The influence of different La^{3+} doping amounts on the structure and magnetic properties of cobalt ferrite was studied by the analysis of XRD, SEM, and VSM. The experimental and analytical results can also provide basic data and theoretical basis for further research on cobalt ferrite with rare earth doping.

Experiment

Experimental Materials

Cobalt nitrate ($Co(NO_3)_2 \cdot 6H_2O$), iron nitrate ($Fe(NO_3)_3 \cdot 9H_2O$, Guanghua Chemical Plant Co.-Ltd.), citric acid ($C_6H_8O_7$–H_2O, Tianjin Chemical Reagent Factory), and sodium hydroxide (NaOH, Guangzhou Chemical Reagent Factory) were used as raw materials. All reagents were analytically pure. and water was deionized water.

Experimental Methods

La-doped $CoFe_2O_4$ of composition $CoFe_{2-2x}La_{2x}O_4$ ($x = 0, 0.05, 0.10, 0.15, 0.20, 0.25$) was prepared using sol–gel self-combustion technique.

The 1.46 g $Co(NO_3)_2 \cdot 6H_2O$, 4.04 g $Fe(NO_3)_3 \cdot 9H_2O$ and lanthanum nitrate (the amount is determined by replacing 5, 10, 15, 20, and 25% of the substance of Fe^{3+} with La^{3+}) were weighed and dissolved in minimum amount of deionized water. Then, the solutions were placed in a stirring pot at 60 °C for 1 h. Citric acid as a complexing agent was added, and sodium hydroxide was added to adjust the pH to 7. The obtained suspension was further stirred at 70 °C for 2 h. Next, the suspension was dried at 120 °C until it turned into a gel. Finally, the dry gel was calcined at 650 °C for 2.5 h to obtain a black powder.

Sample Characterization

The crystal and phase composition of the synthesized powder samples were tested and analyzed using an Empyrean 2 X-ray diffractometer from PANalytical, Netherlands using Cu Kα radiation ($\lambda = 1.5414$ Å) in 2θ range from 20° to 90°. Scanning Electron Microscope (SEM) analyses for all the samples were carried out using a high and low vacuum electron microscope JSM-6360LV of JEO LTD, Japan, which observe the morphological distribution of the sample; magnetic properties were measured at room temperature using a Lake Shore (Model 7404) vibrating sample magnetometer (VSM). The maximum field used was 1.5 T.

Results and Discussion

Structural Analysis

Figure 1 shows the XRD results of the synthesized $CoFe_{2-2x}La_{2x}O_4$ ($x = 0, 0.05, 0.10, 0.15, 0.20, 0.25$). It can be seen that the diffraction peaks correspond to planes (220), (311), (400), (440), and (511) when the lanthanum doping $x(La^{3+})$ is less than 10%. The peaks are in line with the main crystalline peaks corresponding to the cobalt ferrite standard card. No other heterogeneous peaks appear. It illustrates that it has a space group of Fd-3 m structure (with cubic spinel structure). This indicates that the $x(La^{3+}) < 10\%$, the doping of La^{3+}, does not bias the heterogeneous phase of the $CoFe_2O_4$ sample and changes the face-squared riser structure of the cobalt ferrite. When the $x(La^{3+}) \geq 10\%$, the heterogeneous phase $La(FeO_3)$ appears until the doping reaches 20%. Its half-height width reaches its maximum. At this point, the sample has a poor peak shape and poor crystallinity with a large number of amorphous

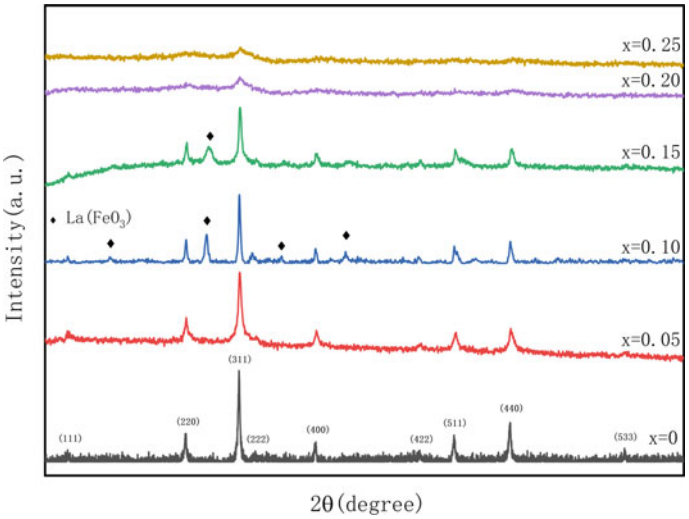

Fig. 1 X-ray diffraction patterns of $CoFe_{2-2x}La_{2x}O_4$ ($x = 0, 0.05, 0.10, 0.15, 0.20, 0.25$)

regions. And, the diffraction peaks of the main spinel structure becoming weak (not prominent).

Table 1 shows the XRD parameters of synthesized samples. It can be seen that the average grain size of the doped samples is significantly smaller than undoped samples. This indicates that La^{3+} has a certain effect of refining the grains. At the same time, with the increase of the doping amount, the diffraction peaks are shifted to the right, and the peak shape is broadened.

It fully illustrates that the doping of La^{3+} changes the lattice constants, half-peak widths, and grain sizes of nanoparticles. Figure 2 shows the trends of lattice constants and half-height widths with different amounts of La^{3+}. They show a nonlinear variation with the amount of lanthanum doping. The main reasons for the analysis are as follows:

(1) It can be seen that the lattice constant increases gradually with the increase of La^{3+} doping. This is because the radius of La^{3+} ion (0.106 nm) is larger

Table 1 XRD parameters of La^{3+}-doped cobalt ferrite samples

La^{3+}doping amount(x) (%)	a	2θ (°)	FWHM (B)	D (nm)	d	Density (c)
0	8.360	35.428	0.265	34	2.5315	5.300
5	8.360	35.507	0.419	20	2.5271	5.300
10	8.396	35.467	0.242	30	2.5289	5.239
15	8.392	35.546	0.379	22	2.5235	5.304
20	8.390	35.558	0.681	12	2.5226	5.3
25	8.377	35.547	0.596	14	2.5234	5.3

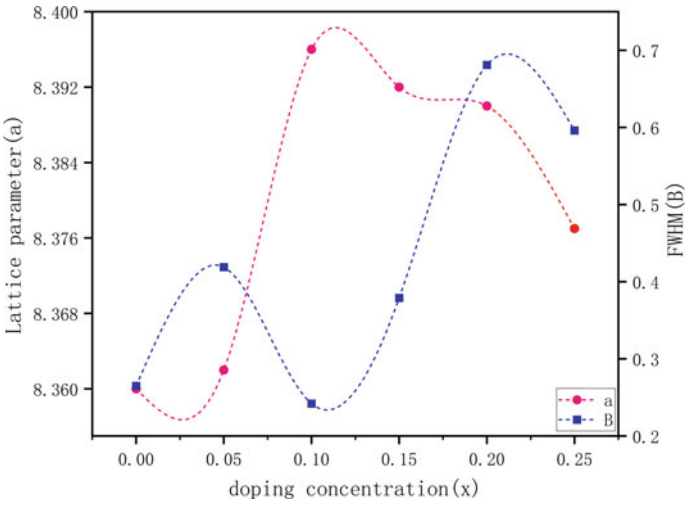

Fig. 2 Variation of lattice parameter(a) and FWHM(B) with $CoFe_{2-2x}La_{2x}O_4$ ($x = 0$, 0.05, 0.10, 0.15, 0.20, 0.25)

than Fe^{3+} ion (0.067 nm). The gap space of tetrahedron is smaller than that of octahedron. According to the volume effect, the possibility of La^{3+} entering the tetrahedral position is very small, and it will definitely enter the octahedral position to occupy the B-site [13]. When the La^{3+} replaces the Fe^{3+} at the B-site, this causes the lattice was expanded, and the lattice constant was increased. While the cell occurred distortion, internal stress was generated, and the grain size was reduced.

(2) When the $x(La^{3+}) > 10\%$, the synthesized nanoparticles start to show the second phase $La(FeO_3)$. It has the structure of chalcogenide orthorhombic crystal system. This suggests that La^{3+} cannot be fully doped into the lattice of octahedra when the doping amount reaches a certain amount. A part of La^{3+} may aggregate on the grain boundaries to form heterogeneous phases [14]. In addition, the bonding energy of La^{3+}-O^{2-} is greater than Fe^{3+}-O^{2-}. The ions need more energy to enter the lattice (more energy is needed for crystallization and grain growth). So, the internal grain size can exert a certain pressure, which inhibits grain growth and causes shrinkage distortion of the lattice. Thus, the lattice constant makes smaller [13].

(3) When the $x(La^{3+}) > 20\%$, the samples show only one characteristic peak of a broadened peak shape and poor crystallinity. The lattice constant is reduced. It is likely that the La^{3+} makes the intensification of lattice distortion, the orderly arrangement of Fe^{3+} is affected, and the complete growth of grains is inhibited. The spinel structure is unstable or damaged and amorphous regions may be formed and so on.

Morphological Analysis

Figure 3 exhibits the SEM comparison of the cobalt ferrite powders calcined at 650 °C with different La^{3+} doping amounts. It can be seen that most of the undoped sample particles gather together to form irregular aggregates. Figure 3a, b–f shows that the samples' agglomeration phenomenon is improved to some extent. The particle size decreases compared with undoped ones. When the content of La^{3+} reaches 10%, most of particles are spherical and tend to be homogeneous. After that, the sample particles aggregate again in large numbers with the increase of La^{3+} content. On the one hand, the particles are attracted to each other due to the ferromagnetism. On the other hand, the sample particles are easily agglomerated due to the small size of the grains (its surface energy becomes increased) [11]. This indicates that the appropriate amount of La^{3+} can slow down the agglomeration and inhibit the growth of grains. It is beneficial to the uniformity and integrity of the grains.

Magnetic Property Analysis

Figure 4 shows the magnetic hysteresis loop of $CoFe_{2-2x}La_{2x}O_4$ ($x = 0, 0.05, 0.10, 0.15, 0.20, 0.25$) sintered at 650 °C and naturally cooled to room temperature. Table 2 shows the magnetic parameters of saturation magnetization strength (Ms), remanence (Mr), and coercivity (Hc).

As shown in Fig. 5 and Table 2, the saturation magnetization intensity of the doped samples shows a nonlinear variation. It has a minimal value of 4.30 emu/g. This indicates that the $x(La^{3+}) < 15\%$, the doping of La^{3+}, makes the saturation magnetization intensity decrease. Because the radius of La^{3+} is larger than that of Fe^{3+} ion, and it will preferentially enter the octahedral position to occupy the B-position [13].

While the magnetic superexchange effect strongly depends on the distribution of cations in tetrahedral and octahedral sites, the magnetization intensity mainly comes from Fe^{3+} ions in octahedral sites. Total magnetic moment: $M = M_A - M_B = \left[5\mu_B \times (1-x) + 3\mu_B + m\mu_B \times x\right] - 5\mu_B = [3 + (m-5)x] \times \mu_B$. With the increases of La^{3+} content, the Fe^{3+} content of the B-site is decreased accordingly. The magnetic moment of La^{3+} is zero due to the absence of electrons in the 4f electronic layer of La^{3+}. Thus, the total magnetic moment is decreased. Its saturation magnetic strengthening intensity is also decreased with the increase of La^{3+} content, decreasing to 4.30 emu/g. However, when the $x(La^{3+}) > 15\%$, La^{3+} ions do not completely replace the iron on the lattice point, a part of one resides in the grain boundary to form a heterogeneous phase [14]. It will produce a certain pressure on the grain boundary, and this pressure will increase the A-O-B superexchange effect. So, the saturation magnetization intensity is increased.

Meanwhile, Fig. 6 shows that the coercivity of the doped sample is increased firstly and then decreased. It has a great value of 2371.21Oe. When the $x(La^{3+}) >$

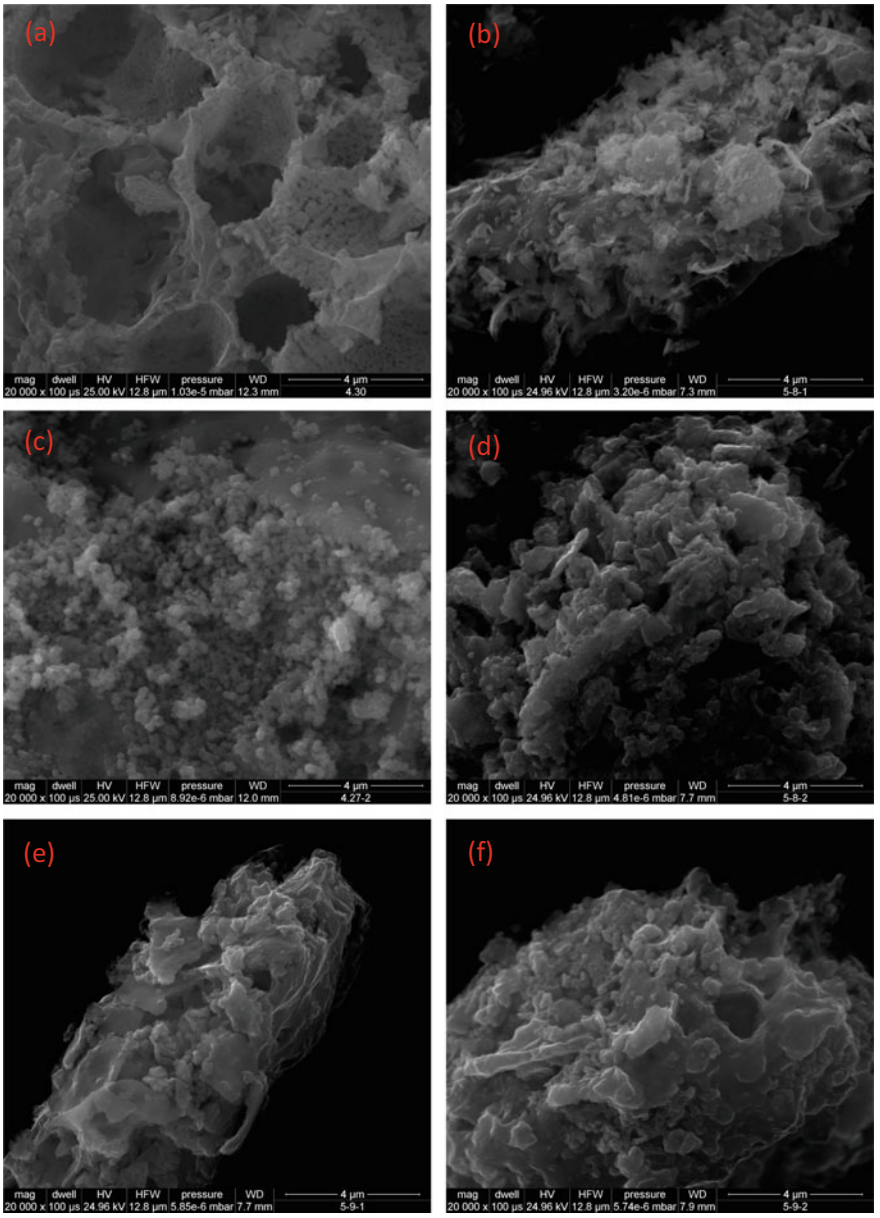

Fig. 3 SEM images of $CoFe_{2-2x}La_{2x}O_4$ where **a** $x = 0.0$, **b** $x = 0.05$, **c** $x = 0.10$, **d** $x = 0.15$ and **e** $x = 0.2$, **f** $x = 0.25$

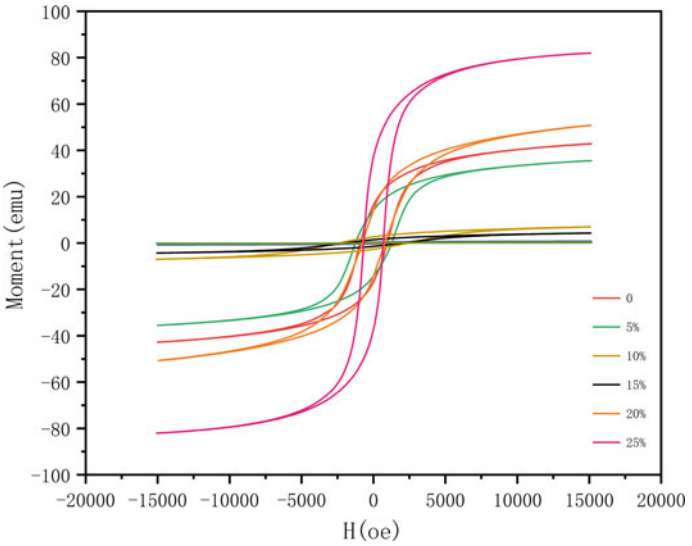

Fig. 4 Magnetic hysteresis loop of $CoFe_{2-2x}La_{2x}O_4$

Table 2 Magnetic properties parameters for different La^{3+} doping amounts

La^{3+}doping amount(x)	Ms(emu/g)	Mr(emu/g)	Hc(Oe)
0	42.73	16.83	942.36
5%	35.50	14.09	1262.19
10%	6.99	2.67	2371.21
15%	4.30	1.43	1999.47
20%	50.79	14.20	764.80
25%	81.94	37.08	691.447

10%, the coercivity starts to decrease significantly, even it is less than the undoped sample. On the one hand, the rare earth has strong s-l coupling and weak crystal field effects. The crystal symmetry of the sample makes reduced. And the crystal with low symmetry has strong magnetocrystalline anisotropy. Thus, the coercivity increases with La^{3+} doping [15]. On the other hand, the ferromagnetic behavior of the subferromagnetic oxides is mainly controlled by Fe^{3+}-Fe^{3+} interactions (spin coupling of 3d electrons). The RE^{3+}-Fe^{3+} interactions (3d-4f coupling) and weak RE^{3+}-RE^{3+} interactions are appeared by introducing rare earth into the spinel lattice. This affects the magnetocrystalline anisotropy and coercivity of the system.

In addition, the coercivity is also related to the particle size. Usually, the magnetic single domain size of cobalt ferrite is about 42 nm. The larger the particle size of nanoparticles, the higher the coercivity [16]. Figure 6 depicts that the coercivity of the doped sample is positively correlated with its grain size. It increases as the grain size of the doped sample increases. The coercivity then reaches a very high value

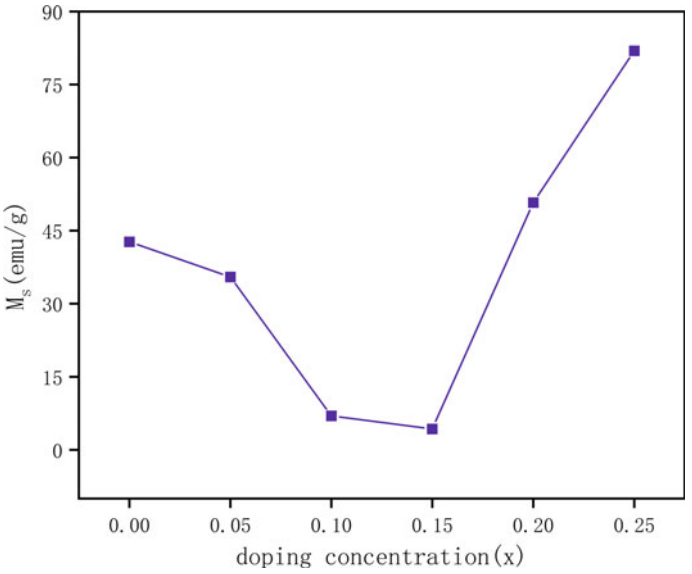

Fig. 5 Variation of saturation magnetization (Ms) with La^{3+} concentration(x)

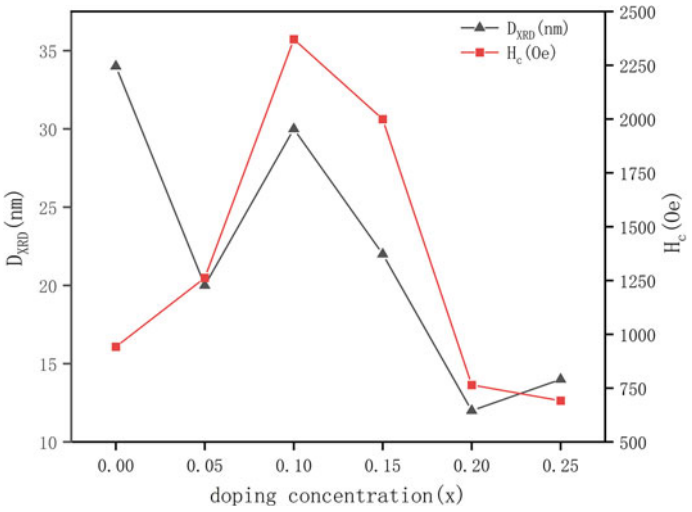

Fig. 6 Variation of lattice diameter (D_{XRD}) and coercivity (Hc) with La^{3+} concentration(x)

of 2371.21Oe when the particle size is 30 nm. However, when the x(La^{3+}) > 10%, the B sub-lattice magnetic moment MB is decreased. This makes the dominant A-B exchange weaker, and its grain size decreased. So coercivity is a decreasing trend.

Conclusions

In summary, cobalt ferrite samples of different La^{3+} concentration are prepared easily and successfully by sol–gel self-combustion method. The results show that: When the $x(La^{3+}) < 10\%$, the synthesized samples show cubic spinel structure with Fd-3 m space group. There are not other heterogeneous peaks. The lattice constant is increased. The samples tend to be uniform spherical nanoparticles, and the agglomeration is reduced to some extent. When the $x(La^{3+}) > 10\%$, the second phase $La(FeO_3)$ starts to appear. The peak pattern and its crystallinity become worse. Most of the peaks gradually disappear after the doping reaches 20%. The saturation magnetization and coercivity of the doped sample demonstrate a nonlinear trend with increasing La^{3+} content. $CoFe_{1.7}La_{0.3}O_4$ has the minimum saturation magnetization of 4.30 emu/g. $CoFe_{1.8}La_{0.2}O_4$ has the maximum coercivity of 2371.21Oe.

References

1. Narang SB, Pubby K (2021) Nickel spinel ferrites: a review. J Magn Magn Mater 519:167163
2. Sundararajan M, Kennedy LJ, Aruldoss U, Pasha SK, Vijaya JJ, Dunn S (2015) Microwave combustion synthesis of zinc substituted nanocrystalline spinel cobalt ferrite: structural and magnetic studies. Mater Sci Semicond Process 40:1–10
3. Amiri S, Shokrollahi H (2013) The role of cobalt ferrite magnetic nanoparticles in medical science. Mater Sci Eng C 33:1–8
4. Psimadas D, Baldi G, Ravagli C, Comes Franchini M, Locatelli E, Innocenti C, Sangregorio C, Loudos G (2014) Comparison of the magnetic, radiolabeling, hyperthermic and biodistribution properties of hybrid nanoparticles bearing $CoFe_2O_4$ and Fe_3O_4 metal cores. Nanotechnology 25:025101
5. Demirci E, Manna PK, Wroczynskyj Y, Aktürk S, van Lierop J (2018) Lanthanum ion substituted cobalt ferrite nanoparticles and their hyperthermia efficiency. J Magn Magn Mater 458:253–260
6. Akhtar MN, Khan MA (2018) Effect of rare earth doping on the structural and magnetic features of nanocrystalline spinel ferrites prepared via sol gel route. J Magn Magn Mater 460:268–277
7. Hashim M, Raghasudha M, Meena SS, Shah J, Shirsath SE, Kumar S, Ravinder D, Bhatt P, Alimuddin R, Kumar RKK (2018) Influence of rare earth ion doping (Ce and Dy) on electrical and magnetic properties of cobalt ferrites. J Magn Magn Mater 449:319–327
8. Yadav RS, Kuˇritka I, Vilcakova J, Havlica J, Kalina L, Urbanek P, Machovsky M, Skoda D, Masaˇr M, Holek M (2018) Sonochemical synthesis of Gd^{3+}doped $CoFe_2O_4$ spinel ferrite nanoparticles and its physical properties. Ultrason Sonochem 40:773–783
9. Kefeni KK, Msagati TAM, BhekieB M (2017) Ferrite nanoparticles: synthesis, characterisation and applications in electronic device. Mater Sci Eng B 215:37–55
10. Al Yaqoob K, Bououdina M, Akhter MS, Al Najar B, Judith Vijaya J (2019) Selectivity and efficient Pb and Cd ions removal by magnetic MFe_2O_4 (M=Co, Ni, Cu and Zn) nanoparticles. Mater Chem Phys 232:254–264
11. Ateia EE, Ahmed MA, Salah LM, El-Gamal AA (2014) Effect of rare earth oxides and La^{3+} ion concentration on some properties of Ni–Zn ferrites. Physica B 445:60–67
12. Boda N, Gopal Boda K, Naidu CB, Srinivas M, Batoo KM, Ravinder D, Panasa Reddy A (2019) Effect of rare earth elements on low temperature magnetic properties of Ni and Co-ferrite nanoparticles. J Magn Magn Mater 473:228–323

13. Kahn ML, Zhang ZJ (2001) Synthesis and magnetic properties of $CoFe_2O_4$ spinel ferrite nanoparticles doped with lanthanide ions. Appl Phys Lett 78:3651–3653
14. Gubbala S, Nathani H, Koizol K, Misra RDK (2004) Magnetic properties of nanocrystalline Ni–Zn, Zn–Mn, and Ni–Mn ferrites synthesized by reverse micelle technique. J Phys Rev B Condens Matter 348:317–328
15. Roy PK, Bera J (2008) Characterization of nanocrystalline NiCuZn ferrite powders synthesized by sol-gel auto-combustion method. J Mater Process Technol 197(1):279–283
16. Tijerina-Rosa A, Greneche JM, Fuentes AF, Rodriguez-Hernandez J, Menéndez JL, Rodríguez-González FJ, Montemayor SM (2019) Partial substitution of cobalt by rare-earths (Gd or Sm) in cobalt ferrite: effect on its microstructure and magnetic properties. Ceram Int 45:22920–22929

Optimization of VD Refining Slag and Control of Non-metallic Inclusions for 55SiCrA Spring Steel

Chen Wang, Qing Liu, Jiangshan Zhang, Jun Chen, Dan Lin, Xuji Wang, and Jiancheng Zhu

Abstract Non-metallic inclusions with high melting points can easily be crack sources and reduce the service life of spring wire. Refining slag can adjust the composition and melting point of inclusion through the reaction with molten steel. Therefore, studying the optimization of refining slag systems and controlling the low melting point of inclusions have great significance. Before the optimization, the basicity (1.1–1.3) and Al_2O_3 content (>8%) of refining slag in VD (vacuum degassing) are high. By optimizing the composition of the slag, the basicity is controlled at 0.8–1.0, and the content of Al_2O_3 is less than 6%. After optimization, the results of the plant trials show that the content of dissolved Al in steel is less than 0.0020%, the inclusion ratio with a melting point less than 1400 °C increased from 8.33 to 25.58%, and the ratio with the melting point less than 1550 °C increased from 61.11 to 84.88%.

Keywords Refining slag · Basicity · Spring steel · Non-metallic inclusions

Introduction

Spring steel is an important manufacturing material widely used in many fields [1–4], and its working environment is diverse, some of which are even very bad [5, 6]. It is inevitable to have inclusions in the steel. However, with the development of society and economy, stricter requirements have gradually been put forward for the permissible stress of spring steel [7], so that it can bear the periodic load without fracture. At this time, inclusions in steel have become an important factor restricting the quality of spring [8, 9]. Relevant studies [10–13] show that the melting point of the inclusion affects its deformation ability, and the oxide inclusion with a low

C. Wang · Q. Liu (✉) · J. Zhang
State Key Laboratory of Advanced Metallurgy, University of Science and Technology Beijing (USTB), Beijing, People's Republic of China
e-mail: qliu@ustb.edu.cn

J. Chen · D. Lin · X. Wang · J. Zhu
Xiangtan Branch, Hunan Valin Iron & Steel Co., Ltd, Xiangtan, People's Republic of China

Z. Peng et al. (eds.), *12th International Symposium on High-Temperature Metallurgical Processing*, The Minerals, Metals & Materials Series,
https://doi.org/10.1007/978-3-030-92388-4_40

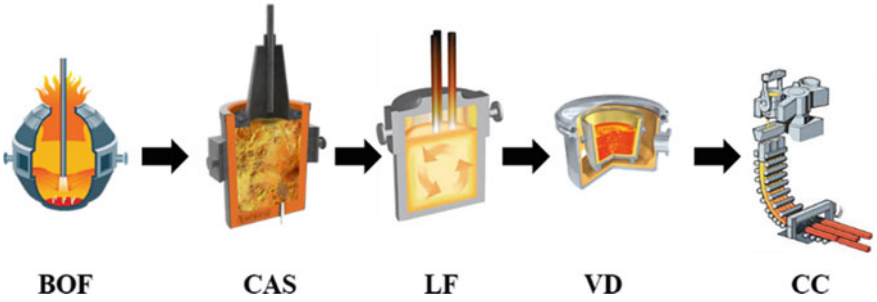

Fig. 1 Production process flow chart

melting point has better deformation ability. Slag refining [14, 15] is a method to control the melting point of inclusions.

The thermodynamic calculation and industrial trials were carried out for the problems of poor plasticity and the high melting point of spring steel inclusions in a domestic plant. By optimizing the composition of refining slag in the VD refining process, the content of [Al]s in molten steel is reduced, the melting point of inclusions is reduced, and the plasticity of inclusion is improved.

Production Process

As spring steel has requirements for oxide inclusions and sulfide inclusions in steel, the process flow of producing spring steel 55SiCrA in a domestic steel plant is shown in Fig. 1. During converter tapping, Fe-Si, metallic Mn, and Fe–Cr were added to the ladle to deoxidize and alloy the molten steel. Composition adjustment by sealed argon bubbling (CAS) station only does argon blowing. When the ladle arrived at ladle furnace (LF) station, the slag materials were added to the ladle to make desulfurization slag for desulfurization operation. When the ladle left the LF station, slag materials were added again to reduce the basicity of refining slag and modify the inclusions (Refining slag adjustment).

Industrial Trials Before Optimization

Refining Slag Before Optimization

The main components of refining slag used for 55SiCrA spring steel are shown in Table 1. The basicity of the LF refining slag is generally higher than 1.4. The refining slag with high basicity is conducive to the desulfurization of molten steel, but it is unfavorable to the control of inclusion plasticity. Therefore, the basicity of refining

Table 1 Main components of refining slag before optimization

Number	Station	CaO	SiO_2	Al_2O_3	MgO	R
Heat A	LF	44.13	29.61	8.79	17.47	1.49
	VD	39.24	34.12	8.42	18.22	1.15
Heat B	LF	43.88	27.95	9.23	18.95	1.57
	VD	39.27	32.45	8.90	19.39	1.21
Heat C	LF	29.72	42.20	9.59	18.49	1.42
	VD	31.50	39.70	9.08	19.72	1.26

slag is reduced in the VD refining process. The basicity of refining slag is between 1.1–1.3, and the content of Al_2O_3 in refining slag is greater than 8%.

Changes of T.O and [Al]s in Steel Before Optimization

The changes of T.O and [Al]s contents in the whole process of 55SiCrA spring steel before optimization are shown in Figs. 2 and 3. It can be seen from Fig. 2 that during the LF and the VD refining, the T.O content in steel decreases significantly, and the deoxidation effect is just. At the end of VD, the T.O content in steel is between 0.0007 and 0.0009%. In the process of continuous casting, the T.O content in steel increases slightly, and it is between 0.0010 and 0.0012% in the billet, which indicates that there is an absorb gas phenomenon in molten steel during continuous casting.

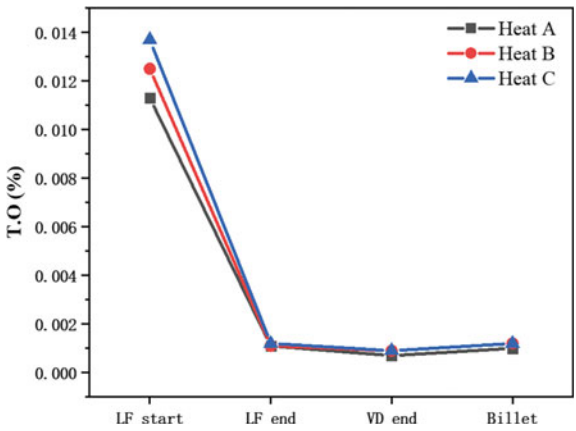

Fig. 2 Change of T.O in steel of the process

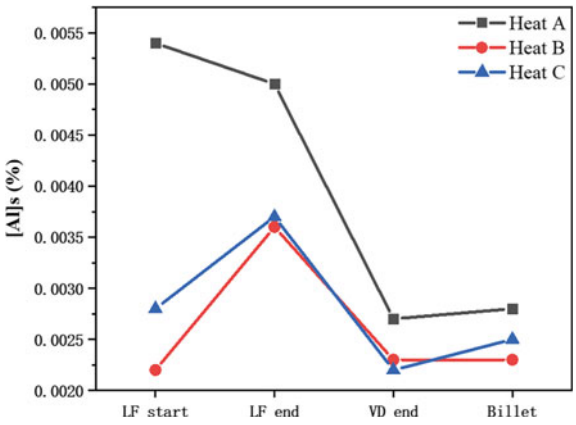

Fig. 3 Change of [Al]s in steel of the process

Inclusion in Steel Before Optimization

The main components of micro inclusions in the billet are projected onto the ternary phase diagram of $CaO–Al_2O_3–SiO_2$, as shown in Fig. 4. The annular line in the figure is the isotherm of the inclusions melting point, and different colors represent different melting temperatures. It can be seen from Fig. 4 that most of the inclusions in the steel deviate from the low melting point region. Statistics show that the proportion of inclusions with a melting point less than 1400 °C in the billet is 8.33%, and the proportion of inclusions with a melting point less than 1550 °C is 25.58%. The

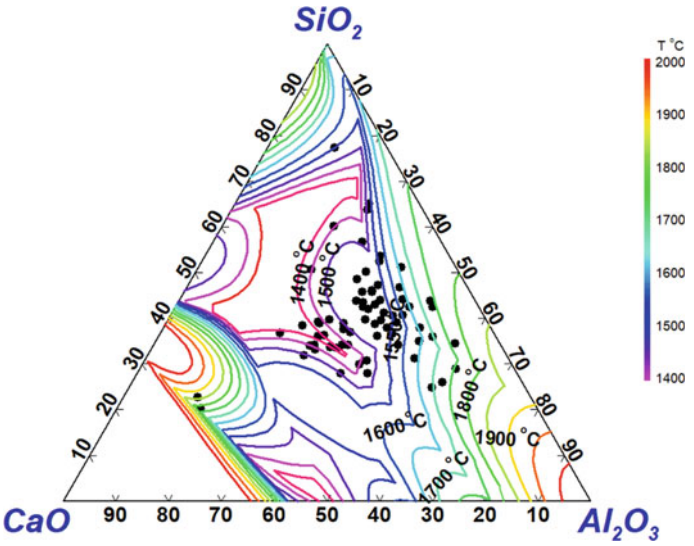

Fig. 4 Distribution of inclusions in billet before optimization

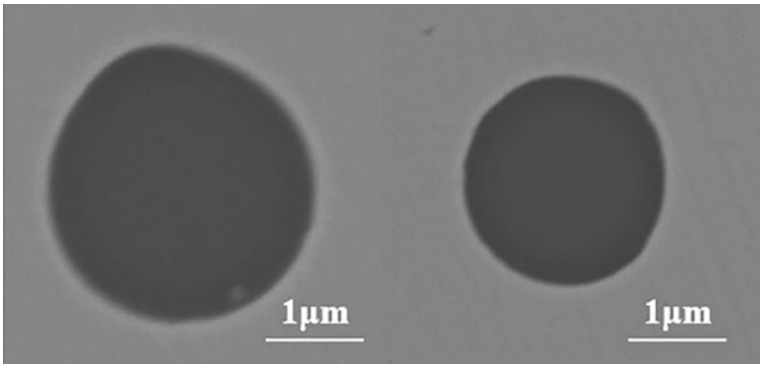

Fig. 5 Morphology of typical inclusions in billet

plasticity of inclusions is poor. Figure 5 shows the morphology of typical inclusions in the billet. It can be seen that the inclusions in the billet are spherical, which proves that the inclusions exist in liquid form in molten steel.

Thermodynamic Calculation of Refining Slag Optimization

The main components of refining slag are MgO, Al_2O_3, SiO_2, and CaO. Therefore, the Factage 7.2 software is used to calculate the iso-activity lines of SiO_2, Al_2O_3, and, CaO in the 10% MgO-Al_2O_3-SiO_2-CaO refining slag system. The iso-activity lines of SiO_2 are shown in Fig. 6. It is shown that the increase of SiO_2 content in refining slag will lead to the increase of SiO_2 activity. The change of SiO_2 activity in refining slag will affect the change of dissolved oxygen content in the steel, as shown in Eq. (1).

$$\begin{gathered}[\mathrm{Si}] + 2[\mathrm{O}] = \mathrm{SiO_2}(s) \\ \Delta G^0 = -581900 + 221.8T \text{ J/mol}\end{gathered} \tag{1}$$

The iso-activity lines of Al_2O_3 in the 10% MgO-Al_2O_3-SiO_2-CaO refining slag system are shown in Fig. 7. It can be seen that the activity of Al_2O_3 in refining slag decreases with the reduction of Al_2O_3 content. According to Eq. (2), the increase of Al_2O_3 activity will lead to the growth of [Al] element content in steel, which is not conducive to control of inclusions plasticity.

$$\begin{gathered}2/3\ \mathrm{Al_2O_3}(s) + [Si] = \mathrm{SiO_2}(s) + 4/3\ [\mathrm{Al}] \\ \Delta \mathrm{G}^0 = 219{,}400 - 35.7T \text{ J/mol}\end{gathered} \tag{2}$$

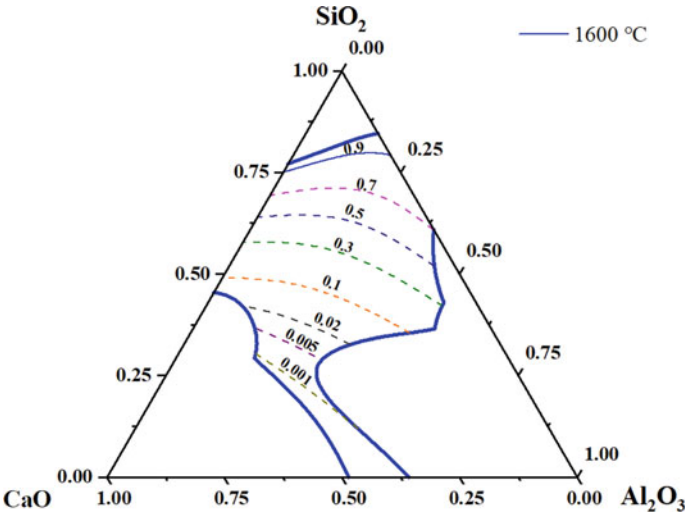

Fig. 6 Iso-activity lines of SiO_2 in the 10% MgO-Al_2O_3-SiO_2-CaO refining slag

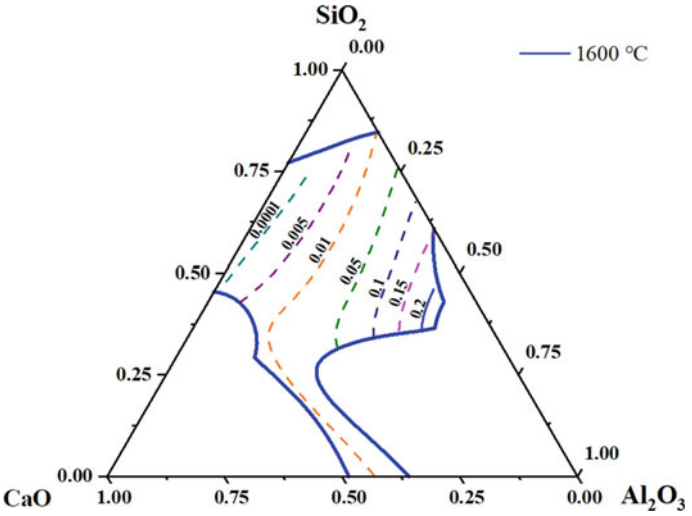

Fig. 7 Iso-activity lines of Al_2O_3 in the 10% MgO–Al_2O_3–SiO_2–CaO refining slag

The iso-activity lines of CaO in the 10% MgO–Al_2O_3–SiO_2–CaO refining slag system are shown in Fig. 8. It can be seen that the activity of CaO in refining slag decreases with the reduction of CaO content in refining slag.

The iso-[Al] lines of molten steel with the 10% MgO–Al_2O_3–SiO_2–CaO refining slag system are shown in Fig. 9. It can be seen that with the increase of basicity and Al_2O_3 content, the content of [Al] element in molten steel increases, which will

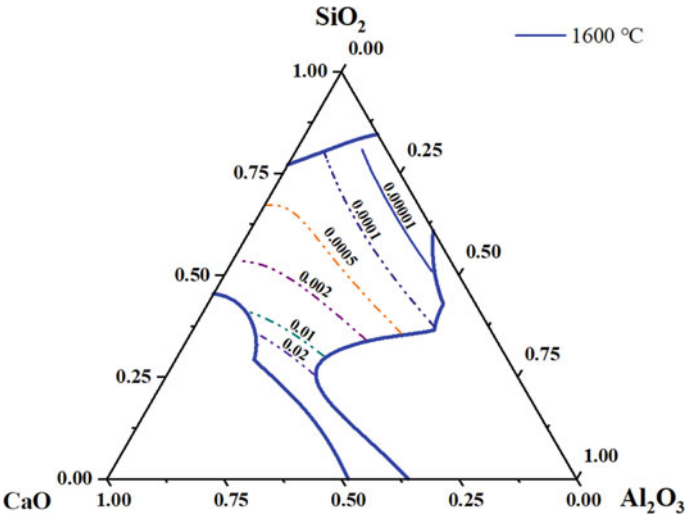

Fig. 8 Iso-activity lines of CaO in the 10% MgO–Al_2O_3–SiO_2–CaO refining slag

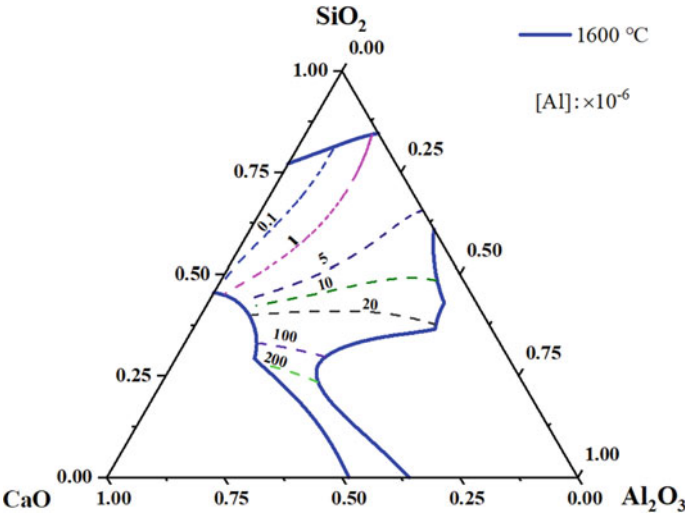

Fig. 9 Iso-[Al] lines of molten steel with the 10% MgO–Al_2O_3–SiO_2–CaO refining slag system

increase the Al_2O_3 content in inclusions, and which is unfavorable to controlling the inclusion plasticity. The influence of basicity and Al_2O_3 content on [Al] in molten steel is shown in Fig. 10.

It can be seen from Fig. 10 that the basicity and the Al_2O_3 content of refining slag have obvious effects on the activity of Al_2O_3. In the range of basicity 0.8–1.25 and Al_2O_3 content 3–20%, the [Al] content in molten steel increases with the

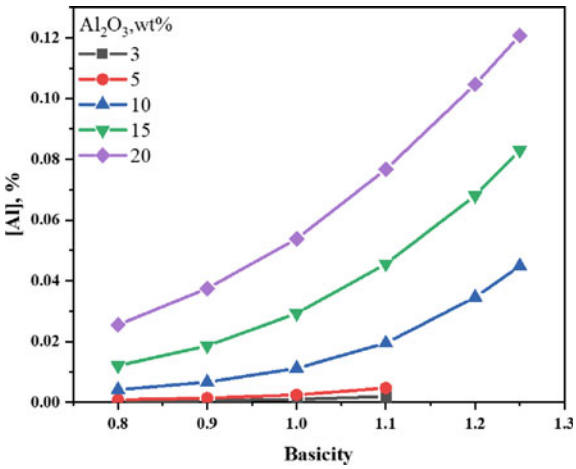

Fig. 10 Influence of [Al] element content in molten steel on the basicity of refining slag and Al_2O_3 content in the slag

growth of basicity and Al_2O_3 content. When the basicity increases from 0.8 to 1.25, the equilibrium [Al] content in liquid steel maximum increases 10 times. When the Al_2O_3 content increases from 3 to 20%, the equilibrium [Al] content in liquid steel maximum increases 70 times.

Industrial Trials After Optimization

Refining Slag After Optimization

According to the above industrial trials and thermodynamic calculations, in order to reduce the melting point of inclusions, it is necessary to reduce the basicity of refining slag and the content of Al_2O_3. Therefore, by adjusting the additional amount of slag material, the basicity of VD refining slag is controlled between 0.8–1.0, and the content of Al_2O_3 is less than 6%. The main components of refining slag after optimization are shown in Table 2.

Table 2 Main components of refining slag after optimization

Number	Station	CaO	SiO_2	Al_2O_3	MgO	R
Heat D	LF	55.89	30.83	4.99	8.29	1.81
	VD	37.91	42.76	5.02	14.30	0.89
Heat E	LF	61.28	27.79	5.48	5.46	2.21
	VD	40.46	40.69	5.33	13.52	0.81
Heat F	LF	52.04	33.78	5.73	8.45	1.54
	VD	40.28	41.64	4.24	13.83	0.91

Changes of T.O and [Al]s in Steel After Optimization

The changes of T.O and [Al]s contents in the whole process of 55SiCrA spring steel produced after optimization are shown in Figs. 11 and 12. After optimization, the T.O content in steel decreased during LF and VD refining and increased slightly during continuous casting, about 0.0002–0.0003% in the billet. This proves that there is still have an absorb gas phenomenon during continuous casting. The content of [Al]s in molten steel increases during LF refining, which may be related to the composition of ladle refractory. It decreases during VD refining, and the content of [Al]s in molten steel changes little during continuous casting.

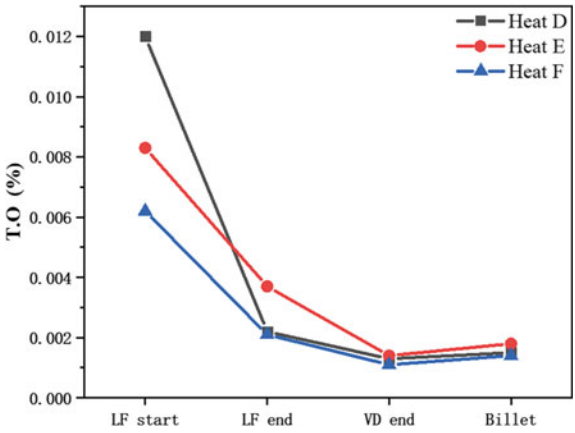

Fig. 11 Change of T.O in steel of the process

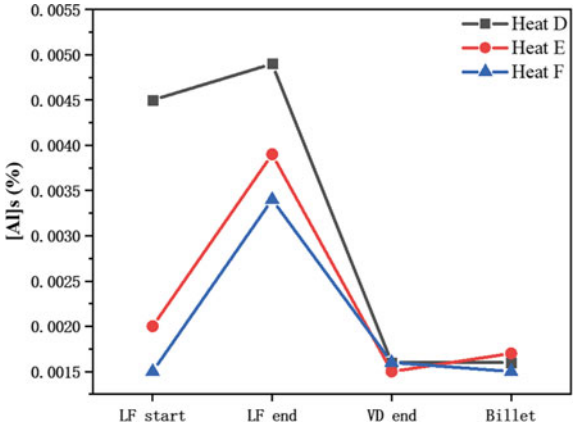

Fig. 12 Change of [Al]s in steel of the process

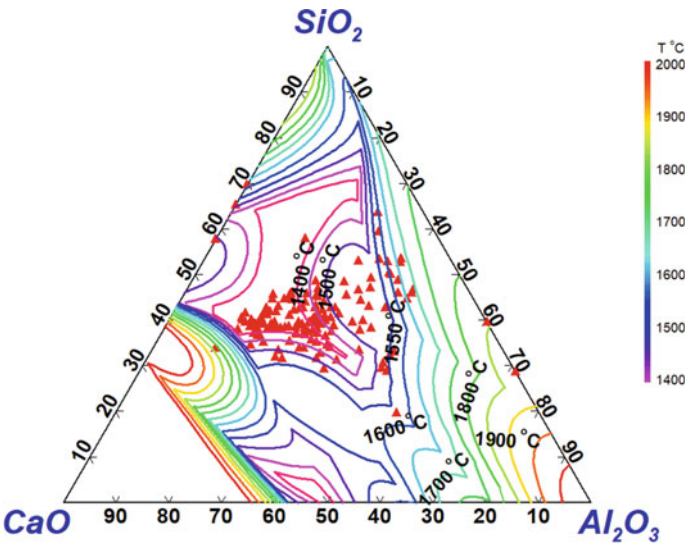

Fig. 13 Distribution of inclusions in billet after optimization

Inclusion in Steel After Optimization

The main components of micro inclusions in the billet are projected onto the ternary phase diagram of $CaO–Al_2O_3–SiO_2$, as shown in Fig. 13. Compared with before optimization, the inclusions are close to the low melting point area. The proportion of inclusions with a melting point less than 1400 °C is 25.58%, and the proportion of inclusions with it less than 1550 °C is 84.88%.

Conclusions

Before the process optimization, the [Al]s content in the steel is greater than 0.0020%, and the inclusions in the steel are far away from the low melting point region. The inclusions with a melting point lower than 1400 °C account for 8.33%, and with it lower than 1550 °C account for 61.11%. Thermodynamic calculation shows that increasing the slag basicity and Al_2O_3 content in slag will significantly improve the equilibrium [Al] content in the steel. Therefore, the optimized VD refining slag is basicity 0.8–1.0, and Al_2O_3 content is less than 6%. After process optimization, the content of [Al]s in the steel is less than 0.0020%, and the inclusions are close to the low melting point zone. The proportion of inclusions with a melting point lower than 1400 °C is 25.58%, and the with it lower than 1550 °C is 84.88%.

References

1. Wang C, Han YS, Zhang JS, Xiao D, Yang J, Chen J, Liu Q (2021) Behaviour of oxide inclusions and Sulphur in "two-stage basicity control" refining method of Si-killed spring steel. Ironmaking Steelmaking 48(4):466–476
2. Tang W, Yang J, Liu Q, Wang C (2020) Control of oxide inclusions in high quality spring steel during refining process. Chin Metall 30(5):17–22
3. Lyu S, Ma XD, Huang Z, Yao Z, Lee HG, Jiang ZH, Wang G, Zou J, Zhao BJ (2019) Inclusion characterization and formation mechanisms in spring steel deoxidized by silicon. Metall Mater Trans B 50(2):732–747
4. Cai XF, Bao YP, Lin L, Gu C (2016) Effect of Al content on the evolution of non-metallic inclusions in Si-Mn deoxidized steel. Steel Res Int 87(9):1168–1178
5. McClaflin D, Fatemi A (2004) Torsional deformation and fatigue of hardened steel including mean stress and stress gradient effects. Int J Fatigue 26(7):773–784
6. Farrahi GH, Lebrijn JL, Couratin D (1995) Effect of shot peening on residual stress and fatigue life of a spring steel. Fatigue Fract Eng Mater Struct 18(2):211–220
7. Prawoto Y, Ikeda M, Manville SK, Nishikawa A (2008) Design and failure modes of automotive suspension springs. Eng Failure Ana. 15(8):1155–1174
8. Tang H, Wang Y, Wu GH, Peng L, Zhang JQ (2017) Inclusion evolution in 50CrVA spring steel by optimization of refining slag. J Iron Steel Res Int 24(9):879–887
9. Wang Y, Tang H, Wu T, Wu GH, Li JS (2017) Effect of acid-soluble aluminum on the evolution of non-metallic inclusions in spring steel. Metall Mater Trans B 48(2):943–955
10. Malkiewicz T, Rudnik S (1963) Deformation of non-metallic inclusions during rolling of steel. J Iron Steel Inst Jpn 201(1):33–38
11. Xue ZL, Li ZB, Zhang JW, Yang W, Gan CF, Wang Y (2003) Theory and practice of oxide inclusion composition and morphology control in spring steel production. J Iron Steel Res Int 10(2):38–44
12. Kawahara J, Tanabe K, Banno T, Yoshida M (1992) Advance of valve spring steel. Wire J Int 25(11):55–61
13. Bertrand C, Molinero J, Landa S, Elvira R, Wild M, Barthold G, Valentin P, Schifferl H (2003) Metallurgy of plastic inclusions to improve fatigue life of engineering steels. Ironmaking Steelmaking 30(2):165–169
14. Steneholm K, Andersson N, Tilliander A, Jönsson PG (2018) The role of process control on the steel cleanliness. Ironmaking Steelmaking 45(2):114–124
15. Guo C, Ling H, Zhang L, Yang W (2017) Effect of slag basicity adjusting on inclusions in tire cord steels during ladle furnace refining process. Metall Res Technol 114(6):602

Part VII
Poster Session

Changes of SO_2, NO_x Emission, and Production of Iron Ore Sintering with Steam Injection at the Surface of Sintering Bed

Yapeng Zhang, Wen Pan, Shaoguo Chen, Huaiying Ma, Jingjun Zhao, Zhixing Zhao, and Huayang Liu

Abstract The effect of steam injection on emission reduction and the quality index of sintering were studied. The sintering cup test showed that steam injection on the sintering bed surface has the effect of reducing NO_x. It was also beneficial to reduce fuel consumption and the emission of SO_2. After steam injection, the sinter drum index is slightly increased, the solid fuel consumption in sintering reduced by 1.64 kg/t, and the ratio of 5–10 mm sintered is reduced by 0.8%. The steam injection improved the sinter quality and reduced the solid fuel consumption. Furthermore, the effect of steam injection in the middle part of sintering process was the most significant.

Keywords Steam injection · SO_2 · NO_x · Solid fuel consumption

Introduction

At present, the national environmental protection policy is becoming more and more strict in China, and the iron and steel industry is facing more and more stringent pollutant discharge requirements [1]. The ultra-low emission standard for air pollutants in iron and steel industry (DB 13/2169-2018) issued by Hebei province has been implemented. As one of the main sources of sulfur dioxide and nitrogen oxide emissions, the sintering process still faces severe challenges in energy conservation and emission reduction. In recent years, iron and steel enterprises have made great progress in sintering process control [2, 3] and flue gas terminal treatment [2–5],

Y. Zhang (✉) · W. Pan · S. Chen · H. Ma · Z. Zhao
Shougang Group Co., LTD Research Institute of Technology, Beijing 100043, People's Republic of China

Beijing Key Laboratory of Green Recyclable Process for Iron & Steel Production Technology, Beijing 100043, People's Republic of China

J. Zhao · H. Liu
Ironmaking Department, Shougang Jingtang United Iron &Steel Co., Ltd, Tangshan 063200, People's Republic of China

Z. Peng et al. (eds.), *12th International Symposium on High-Temperature Metallurgical Processing*, The Minerals, Metals & Materials Series,
https://doi.org/10.1007/978-3-030-92388-4_41

and desulfurization and denitration facilities have been gradually improved [6–9]. Shougang group has also made significant progress in energy saving and emission reduction in sintering process [10]. In particular, the effect of steam spraying on sintering surface to improve fuel combustion efficiency has been confirmed in 550 m^2 sintering machine. Through sintering waste gas composition test, it has been verified that proper amount of steam injection on sintering surface can improve the proportion of fuel complete combustion. $CO_2/(CO + CO_2)$ increases from 80 to 85%, which is conducive to energy saving and pollutant emission reduction in sintering [11, 12]. This paper focuses on the emission reduction effect of sulfur dioxide, nitrogen oxide, and other pollutants and the impact on sintering production and quality indexes after steam injection.

Materials and Methods

In order to study the effect of steam injection on emission reduction of sulfur dioxide, nitrogen oxide, and other pollutants and the influence on sintering production and quality indexes, sinter cup tests and industrial tests were carried out, respectively. The sinter cup tests with steam injection were carried out in accordance with the test method and scheme given in reference [11]. During the sinter cup tests, a flue gas analyzer was used to test the composition of sintering flue gas.

The industrial test of steam injection on sinter surface was carried out on the Jingtang sintering machine, as shown in Fig. 1. In order to analyze the effect of steam injection, one week was selected in which the iron ore matching mode and technical parameters remained stable to carry out industrial steam injection experiments. The early four days were as a benchmark with no steam injection, and the other three days were as a trial period in which the steam injection volumes were 2.0–3.0 t/h. After industrial tests, sintering process parameters before and after steam injection and the sinter quality index were analyzed and compared.

Results and Discussion

Effect of Surface Steam Injection on NO_x Emission

Wetting technology during combustion has been reported to reduce NO_x emissions in other industries. As there are many factors affecting NO_x emission in the sintering process, the NO_x content in the exhaust gas was analyzed in the sinter cup tests, as shown in Figs. 2 and 3. The effect of steam injection on NO_x reduction was observed: there were more cases for the peak value of NO_x in flue gas to be diminished after steam injection; The NO_x content was in the range of 100–140 ppm without steam

Fig. 1 Schematic diagram of steam injection on sinter surface in Jingtang

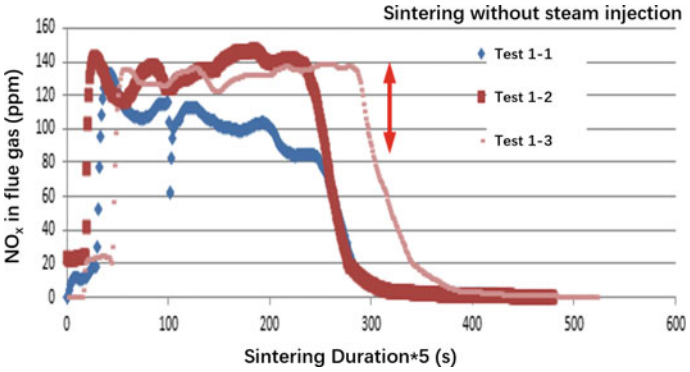

Fig. 2 Change of NO_x content in exhaust gas without steam injection

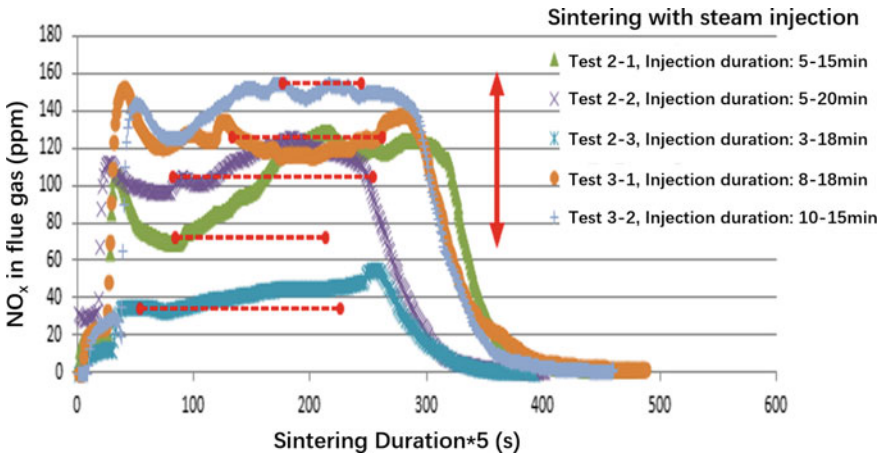

Fig. 3 Change of NO_x content in exhaust gas with steam injection

injection and 40–160 ppm after injection. Furthermore, it is noted that the earlier the steam injection was in the sintering process, the more peak value of NO_x decreased.

Figure 4 shows the change of NO_x in the sintering exhaust gas after the sintering fuel ratio is reduced by 5%. It can be seen that the peak content of NO_x in the exhaust gas is reduced by about 20 ppm after steam injection. Compared with the NO_x in the exhaust gas before reducing the fuel ratio, the NO_x peak content could be reduced by about 10 ppm. In general, reducing the fuel ratio is beneficial to reducing NO_x content in sintering exhaust gas, and steam injection can further strengthen the effect.

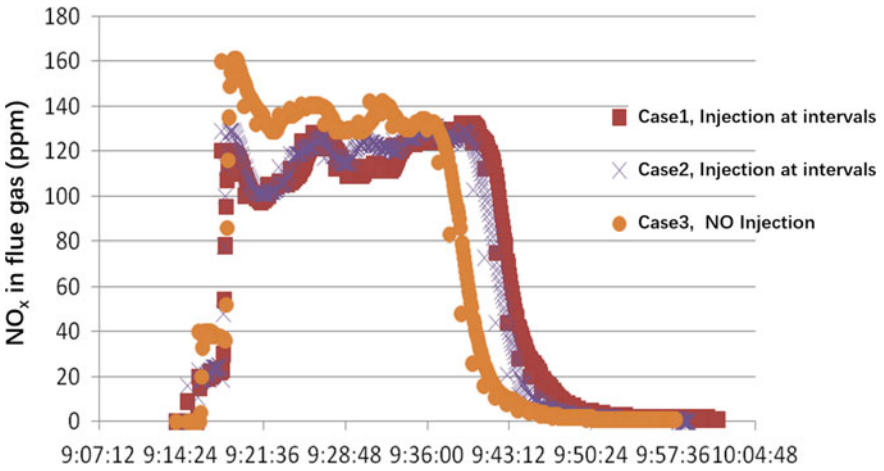

Fig. 4 Change of NO_x content in exhaust gas by interval steam injection

In terms of the mechanism of reducing NO_x in the process of steam sintering, the decrease of solid fuel consumptionC after steam injection directly contributes to the reduction of fuel type NO_x. The endothermic reaction of water vapor in the high temperate zone reduces the maximum temperature of the sintering bed, which is also conducive to reducing the generation of high temperature NO_x.

There were many factors affecting NO_x emission in sintering process. For example, steam injection is beneficial to the generation of sillico-ferrite of calcium and aluminum (SFCA) in sinter; SFCA is beneficial to catalytic reduction of NO_x. The reduction of solid fuel consumption after steam injection is also helpful to reduce the generation of fuel type NO_x. However, steam injection improves sintering machine output and is not conducive to NO_x concentration. Therefore, the effect of NO_x reduction by steam injection should be comprehensively analyzed based on the changes of sintering process parameters.

Figure 5 shows the influence of steam injection on NO_x content in sintered exhaust gas during the second industrial test. It can be seen from Fig. 5a that, compared with

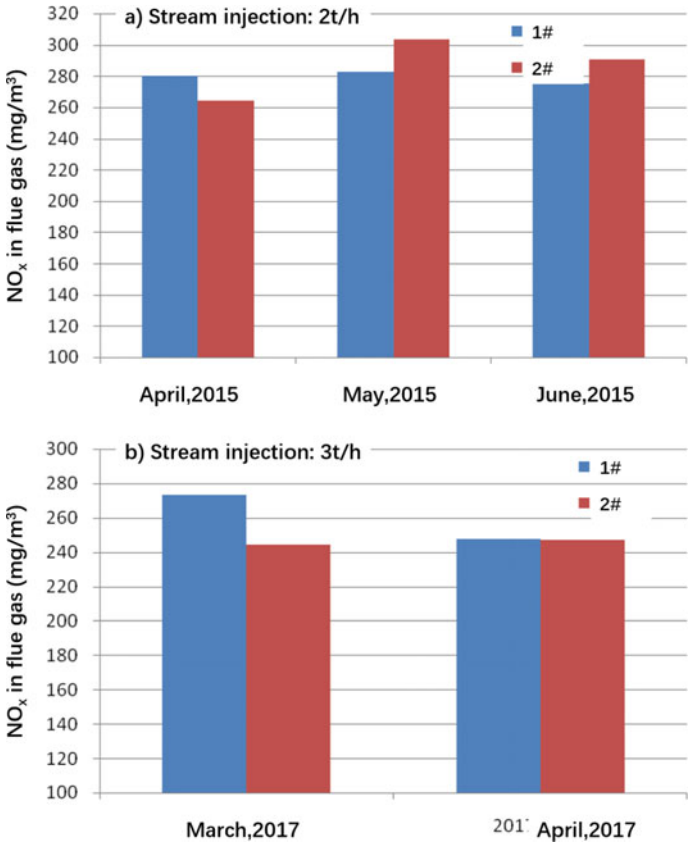

Fig. 5 Change of NO_x content in sintering exhaust gas of two machines

no steam injection, the NO_x content of No. 1 machine did not change much after steam injection, but the increase of NO_x in exhaust gas of No. 2 machine (No. 2 machine applied with steam injection, and the charging structure is the same with No. 1 machine) in the same period indicated that steam injection of No. 1 machine inhibited NO_x generation. Compared with No. 1 machine, after steam injection by 2 t/h, it helped to reduce NO_x content by 12 mg/Nm^3, decreasing by 4.4%; Similarly, the comparison in Fig. 5b shows that after steam injection by 3 t/h, No. 1 machine reduced NO_x content by 29 mg/Nm^3, a reduction of 10.4%.

On the basis of the industrial tests, it is concluded that the effect of steam injection on NO_x reduction is by 12–29 mg/Nm^3, with an average reduction of 7.4%.

Effects of Surface Steam Injection on SO_2 Emission

According to the previous research results, it is beneficial to reduce fuel consumption after spraying steam on sintering surface. As the solid fuel is the main source contributing to SO_2 emission from sintering, reducing solid fuel consumption will be beneficial to the reduction of SO_{2C} emission.

According to the analysis of the 5% reduction and improvement of combustion efficiency of steam injection, the solid fuel consumption is reduced by 2–2.5 kg/t (average 2.25 kg/t). The sulfur content of solid fuel is 0.8%, and then it is reduced by 2.25 kg/t. 90% of sulfur enters into the exhaust gas, and the single consumption of exhaust gas is 2000 Nm^3/t. Then, the content of SO_2 in flue gas would decrease by 16.2 mg/Nm^3 (2.7%) after the decrease of solid fuel consumption.

Figure 6 shows the influence of steam injection on SO_2 content in sintered exhaust gas during the second industrial test. It can be seen from Fig. 6a that, compared with no steam injection sintering, the SO_2 content in No. 1 machine has little change after steam injection, but the comparison of the increase in the same period from No. 2 machine (No. 2 machine applied with steam injection, and the charging structure is the same with No. 1 machine) shows that the effect of steam injection in No. 1 machine on reducing fuel consumption can be shown. After steam injection by 2 t/h, it is helpful to reduce the content of SO_2 by 88 mg/Nm^3. Similarly, No. 1 machine reduces SO_2 content by 101 mg/Nm^3 after spraying steam by 3 t/h. It is believed that the effect of steam spraying on SO_2 reduction in sintering is 2.7%.

Effect of Steam Injection on Sintering Yield and Quality Index

As shown in Table 1, during the steam injection test, the negative pressure of sintering is reduced by about 0.5 kPa, the temperature of main exhaust gas is increased by 5–7 °C, and the BRP and BTP positions are advanced by 1 m and 0.4 m, respectively.

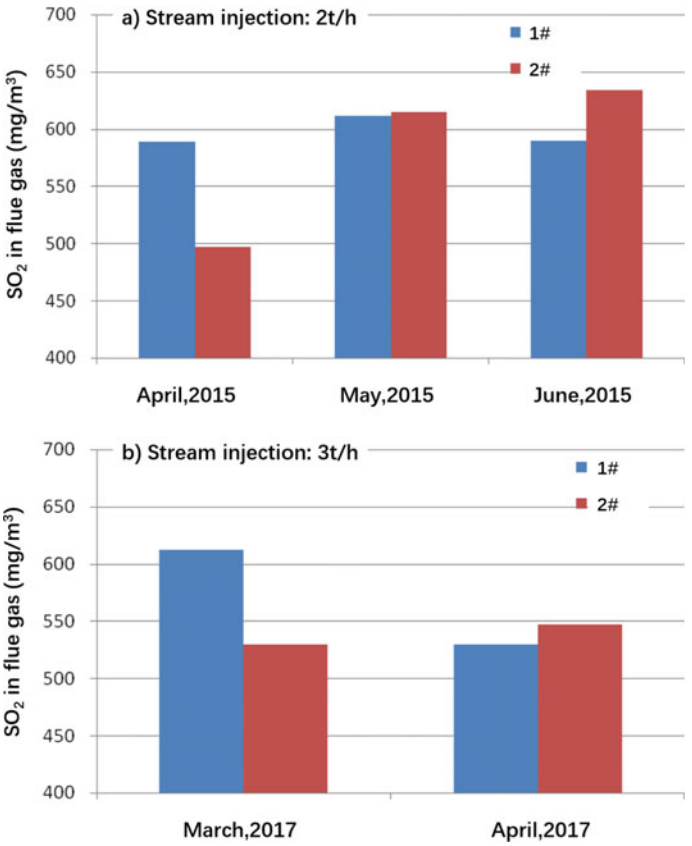

Fig. 6 Effect of steam injection on SO_2 content in exhaust gas

Table 1 Sintering negative pressure and temperature change

Item	Index	Unit	Base period	Test period	Comparison
1# exhaust fan	Rate of flow	m^3/min	21,271	22,120	848
	Negative pressure	kPa	−15.15	−14.68	0.5
	Temperature	°C	158	165	7
2# exhaust fan	Rate of flow	m^3/min	17,546	17,268	−278
	Negative pressure	Kpa	−13.56	−13.15	0.4
	Temperature	°C	158	163	5
BRP		m	64.7	63.7	−1
BTP		m	91.3	90.8	−0.4

Table 2 Index of sinter quality

Item		Base period	Test period	Comparison
TI/%		82.59	82.74	0.15
Sinter return ratio/%		25.82	25.44	−0.38
solid fuel consumption (kg/t)		50.21	48.57	−1.64
Size distribution of sinter	>40 mm	7.87	7.54	−0.3
	40–25 mm	17.9	17.81	−0.1
	25–16 mm	35.6	36.43	0.8
	16–10 mm	20.47	20.86	0.4
	10–5 mm	15.85	15.1	−0.8

The analysis shows that the heat transfer rate of air and sintering bed is accelerated after the steam is sprayed on the sintering bed surface. And the sintering rate is improved, which is manifested in the improvement of air permeability, increase of exhaust gas temperature, decrease of negative pressure, and advance of terminal position. The rate of output with steam injection is higher than that of no steam injection, which indicates that steam injection is beneficial to improve sintering and increase production.

As shown in Table 2, after steam injection, the sinter drum index is slightly improved, the ore return rate is slightly decreased by 0.38%, and solid fuel consumption decreased by 1.64 kg/t. The particle size of sinter also showed an improvement trend, and the ratio of 5–10 mm decreased by 0.8%. It can be seen that steam injection is conducive to the improvement of sinter quality and the reduction of solid fuel consumption. Steam injection can not only improve the permeability of sintering and sintering machine speed but also improve the quality of sinter and reduce the solid fuel consumption by 1.64 kg/t.

Conclusions

(1) Sinter cup tests showed that steam injection on sinter surface has the effect of reducing NO_x. The peak content of NO_x in exhaust gas was reduced by 10–20 ppm, so as to achieve the effect of energy saving and emission reduction. On the basis of the industrial tests, it is concluded that the effect of steam injection on NO_x reduction is by 12–29 mg/Nm^3, with an average reduction of 7.4%. Considering the 6.6% reduction of the total exhaust emission, the total NO_x emission reduction is 7.9%.

(2) After spraying steam on the sintering surface, it is beneficial to reduce fuel consumption. Therefore, reducing solid fuel consumption will be beneficial to reduce SO_2 emission. Reduction of 2.7% of SO_2 in exhaust gas was achieved by steam injection and reducing solid fuel consumption.

(3) After steam injection, the sinter drum index slightly increases, and the ore return rate slightly decreases by 0.38%. The sintering solid fuel consumption decreased by 1.64 kg/t, and the ratio of 5–10 mm decreased by 0.8%. The steam injection contributed to the improvement of sinter quality and the reduction of solid fuel consumption.

Acknowledgements The authors are grateful to the financial support of National Key R&D Program of China (2017YFB0304300&2017YFB0304302).

References

1. The Chinese Society for Metals (2018) Investigation report on ultra-low emission of sintering and coking flue gas in iron and steel enterprises. Chin Metall 28(11):84–87
2. Lv H, Yang J, Wang W (2012) Energy saving and emission reduction practice of 2×265m2 sintering machine in Laigang. Shandong Metall 34(03):46–48
3. Wei H, Wang W, Liu W et al (2012) Energy saving and emission reduction production practice of 400m^2 sintering machine in iron making department of Handan iron & steel co. South Met (03):24–29
4. Yu H (2016) Synergistic optimization of SO_2 and NO_x process control and energy saving and emission reduction in iron ore sintering flue gas circulation. Northeastern University (China)
5. Wang Y, Wu S, Zhang Y et al (2014) Review and discussion on energy saving and emission reduction technology of sintering in Baosteel. Sint Pell 39(06):54–57.
6. Li P (2017) Present situation and development trend of sintering flue gas desulfurization and denitrification technology. Worldmetals 2017–11–28 (B12)
7. Fan Y, Zheng P, Wang B et al (2017) Discussion on desulfurization and denitrification technology of sintering flue gas in steel works. Chem Eng Des Com 43(08):198–202
8. Zou L, Sun P (2016) Comparative analysis of sintering flue gas desulfurization and denitrification treatment technology. Shanxi Metall 39(04):57–59
9. Li S, Du X (2016) Comparison of sintering flue gas combined desulfurization and denitrification technology. Chem Ent Man 27:111
10. Zhao Z (2017) A new process of sintering high temperature flue gas circulation for quality improvement, energy saving and emission reduction of Shougang. The Chinese society for metals. In: Proceedings of the 11th China iron and steel annual conference—S01, 7
11. Pei Y, Ou S, Ma H et al (2018) Effect of steam injection on sinter quality and CO emission. Sint Pell 43(01):35–39
12. Pei Y, Shi F, Wu S et al (2016) Study on improving fuel combustion efficiency by spraying steam on sintering surface. Sint Pell 41(06):16–20

Comprehensive Recovery of Multisource Metallurgical Solid Wastes: Coupling Modification and Carbothermal Reduction of Converter Slag and Copper Slag

Bowen Cao, Nan Wang, and Min Chen

Abstract The recovery of valuable metals in multisource metallurgical slag is conducive to achieve resource recycling and slag utilization. The method of coupling modification and carbothermal reduction of converter slag and copper slag as well as the migration of elements and changes in mineral phases in the process were studied. Based on the element mapping of modified slag, under the interaction of converter and copper slags, Fe_2O_3 and 'FeO' could be separated from the relevant structures of the two slags. The reduced metal phase of the modified slag was Fe-Cu-Mn-P crude alloy, and XRD detection of the reduced slags indicated a complex characterization. The factors of the reduction temperature, the modified basicity, and the C/O ratio on the recovery degree of Fe, Cu, Mn, and P were studied, and the optimal technical parameter was determined as 1773 K, 1.0, and 1.0, respectively.

Keywords Converter slag · Copper slag · Coupling modification · Recycling

Introduction

Metallurgical slag refers to the solid waste discharged after metal extraction by primary ore or artificial rich ore, such as converter slag and copper slag. Converter slag is a by-product of steelmaking; according to statistics, China's annual production of converter slag exceeds 100 million tons, but its utilization rate is less than 30% [1, 2]. Copper slag is a solid waste from the copper smelting industry, every production of 1 ton of copper will produce 2.2–3 tons of copper slag, and the world has accumulated more than one hundred million tons of copper slag every year thus far [3, 4]. However, only a small part of slag is returned to the smelting process for recycling, while the rest is directly discharged into the heaps, resulting in resource waste and environmental problems. Therefore, it is significant to investigate the effective methods of large-scale and low-cost disposal of metallurgical slag.

B. Cao · N. Wang (✉) · M. Chen
School of Metallurgy, Northeastern University, Shenyang, Liaoning Province, China
e-mail: wangn@smm.neu.edu.cn

Z. Peng et al. (eds.), *12th International Symposium on High-Temperature Metallurgical Processing*, The Minerals, Metals & Materials Series,
https://doi.org/10.1007/978-3-030-92388-4_42

The valuable resources are usually recovered by reducing or oxidizing magnetic separation after adding modifiers to metallurgical slag. Ma et al. [5] found that adding SiO_2 as modifier to converter slag can improve the stability of slag, which is conducive to the reduction of iron oxide and slag iron separation. The metallization and metal recovery rates after reduction can reach 87.30% and 96.45%, respectively. Liu et al. [6] studied the influence of adding SiO_2 on reduction of converter slag and found that adding SiO_2 can effectively eliminate the influence of free CaO, which is conducive to improving recovery rate. Wang et al. [7] added 15% CaO to copper slag as modifier and obtained alloy with copper content of about 3% after reduction. Li et al. [8] added Na_2CO_3 and CaO as modifiers to copper slag; when the basicity of the pellets was 0.5 and the addition amount of Na_2CO_3 was 8%, the recovery of iron and copper after reduction magnetic separation could reach 94.3% and 86.5%, respectively.

So far, most of the research work has focused on the reuse of solid waste by adding modifiers to metallurgical slag. Based on the above research, this paper proposes to realize the coupling modification between converter slag and copper slag without adding modifier by utilizing the characteristics of high calcium and high silicon, meanwhile to recover valuable resources in the modified slag through carbothermal reduction. The element migration and mineral phase transformation in the coupling modification and reduction process were studied. Moreover, the effects of basicity reduction temperature and C/O ratio on metal recovery were discussed to determine the optimal technological parameters.

Experimental

Raw Materials

Converter slag and copper slag were collected from a domestic steel enterprise and a copper smelting company, respectively. The chemical composition of the two kinds of metallurgical slag is shown in Tables 1 and 2. TFe content in converter and copper slags is 22.02% and 44.73%, respectively. Figure 1 shows the characterization of two slags. In Fig. 1a, the main phase composition of converter slag was dicalcium

Table 1 Chemical compositions of the converter slag (wt%)

TFe	CaO	SiO_2	MgO	Al_2O_3	MnO	P_2O_5
22.02	41.74	11.96	8.73	1.04	2.09	1.98

Table 2 Chemical compositions of the copper slag (wt%)

TFe	FeO	MFe	CaO	SiO_2	MgO	Al_2O_3	Cu	Zn	Pb	S
44.73	37.31	1.13	1.63	23.98	1.21	2.56	4.48	2.54	0.29	1.38

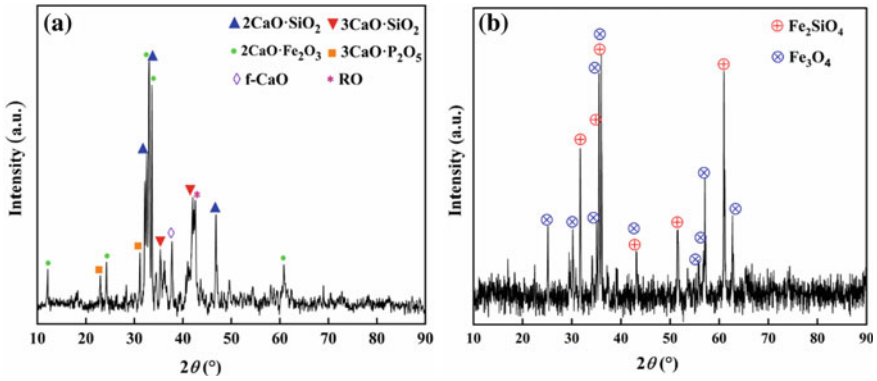

Fig. 1 XRD patterns of converter and copper slags

silicate, tricalcium silicate, dicalcium ferrite, calcium phosphate, free CaO, and RO phase. As shown in Fig. 1b, it could be observed that minerals in copper slag were fayalite and magnetite.

Thermodynamic Analysis

Figure 2 shows the relationship between standard Gibbs free energy and temperature for calculating related reactions in the modification process by the thermodynamic software Factsage 7.0. As shown in Fig. 2a, it can be seen that free CaO, calcium silicate, dicalcium ferrite, and other calcium-containing phases in converter slag can interact with fayalite in copper slag without additional modifier, releasing Fe_2O_3 and 'FeO', realizing the coupling modification between converter and copper slags, which is conducive to the recovery of iron resources.

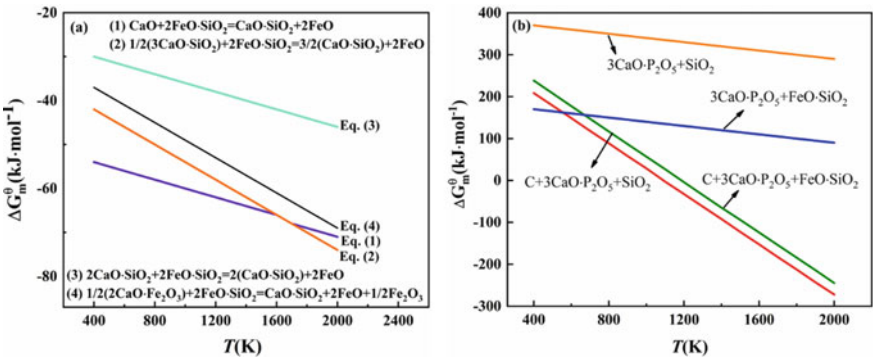

Fig. 2 Relationship between the standard Gibbs free energy and temperature

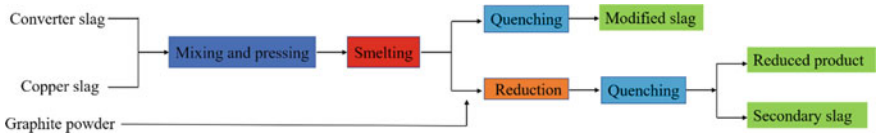

Fig. 3 Flowsheet of the modified and reduction process

As shown in Fig. 2b, the calcium phosphate phase can interact with the fayalite only under the condition of carbothermal reduction, and the fayalite can promote the dissociation of the calcium phosphate phase.

Experimental Procedure

Figure 3 shows the flowsheet of the experiment. Modification experiment was carried out firstly. The converter slag and copper slag were mixed in mortar with different modified basicity ($R = 0.75$–2.0) and pressed into tablet, then put them into corundum crucibles (diameter: 30 mm, height: 40 mm), respectively. The crucible was placed in a high temperature furnace and heated to the required temperature ($T = 1773$ K). The modified slag was held for 60 min, and high-purity argon gas was injected throughout the experiment. After the experiment, the crucible was taken out quickly and placed in liquid nitrogen for quenching; samples are used for X-ray diffraction and elemental mapping. For the reduction experiment, technological procedure was similar. Firstly, the converter slag is added to the required temperature ($T = 1773$–1873 K), and then the tablet made of copper slag and graphite powder is put into the crucible with quartz tubes under different modification basicity ($R = 0.75$–2.0) and C/O ratio (1.0, 1.2, and 1.4). After quenching, the samples are examined by chemical analysis measuring.

Results and Discussion

Element Mapping and Phase Composition of Coupled Modified Slag

In order to study the element migration of converter slag and copper slag during the coupling modification process, element mapping analysis is carried out on the initial slag and modified slag. The results are shown in Fig. 4. Figure 4a [9] shows the distribution of main elements in converter slag, in which elements of Ca and Si have the same distribution and the overlapping distribution of P and Ca elements. As shown in Fig. 4b, the distribution of elemental Fe, Si, and O exists in the form

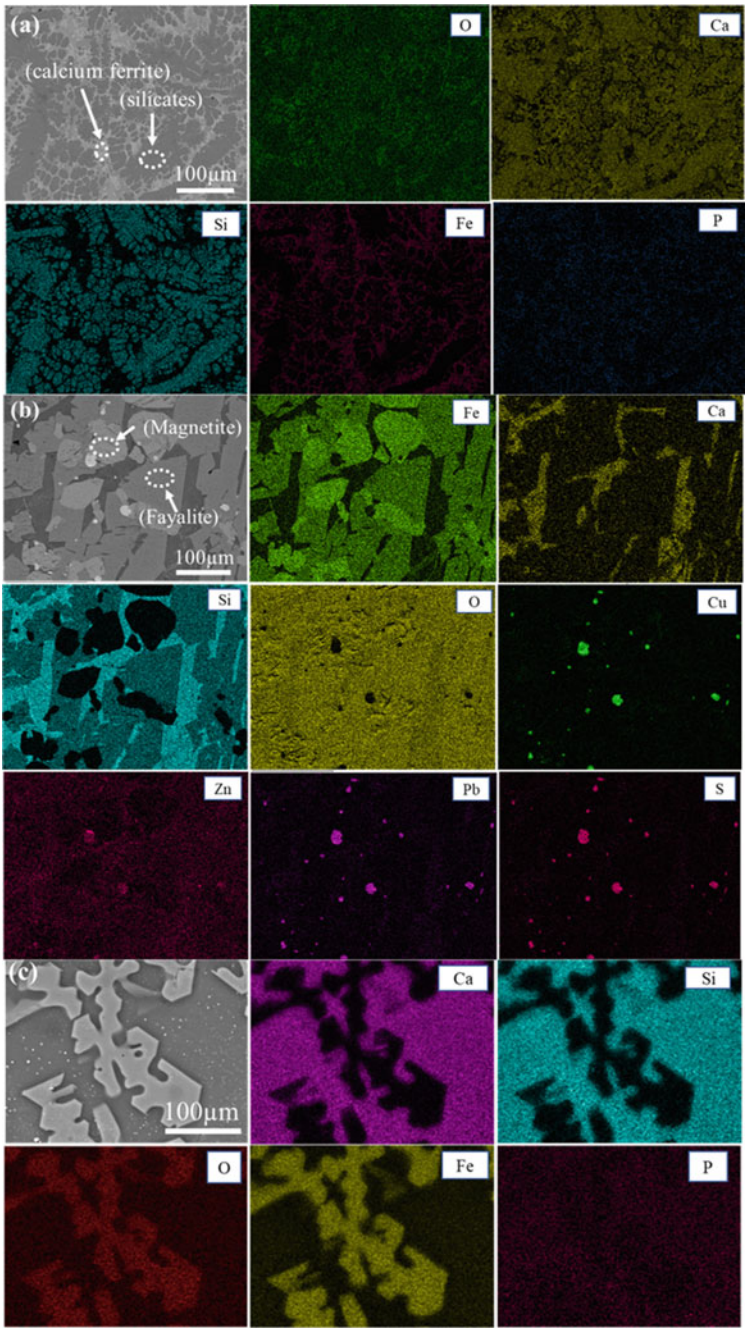

Fig. 4 Element mapping of original slag and modified slag

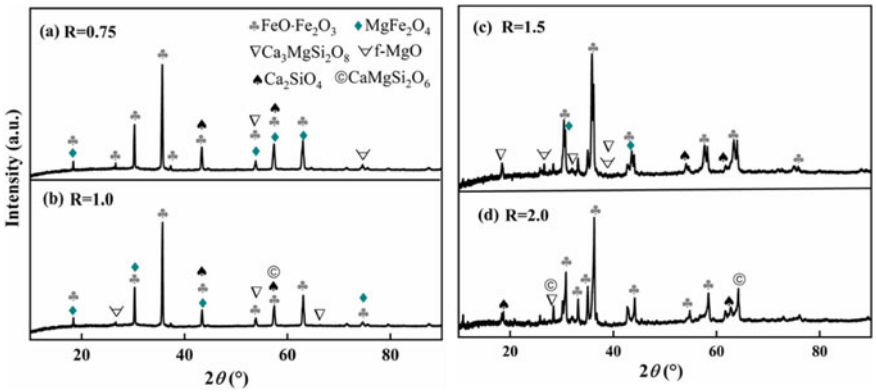

Fig. 5 XRD patterns of different basicity modified slags at 1773 K

of polymer in the copper slag. Combined with the XRD pattern of the copper slag, phases are fayalite and magnetite.

As shown in Fig. 4c, compared with the original slag, the distribution of elements in the modified slag changed significantly. The elemental of Ca and Fe is separated in converter slag, and the elemental of Fe and Si is separated in copper slag.

Figure 5 shows the phase composition of the modified slag under different basicity. It can be seen that Fe_2O_3 and FeO are dissociated from calcium ferrite and fayalite, respectively, during the coupling modification process of converter slag and copper slag, realizing the coupling modification between the two slags and improving the activity of iron oxide. Due to the strong binding ability of CaO and SiO_2, Ca_2SiO_4 will appear in the modified slag. Meanwhile, the converter slag contains a small amount of MgO (8.73 wt%); as the basicity of the modification increases, $Ca_3MgSi_2O_8$ and $CaMgSi_2O_6$ will also appear in the slag. After modification, the basicity of the converter slag decreases, which causes the RO phase in the slag to dissociate, and the released MgO exists in the form of free MgO or combined with Fe_2O_3 to form $MgFe_2O_4$. In the process of basicity increasing from 0.75 to 2.0, more phases with high melting point are generated in the modified slag, which increases the liquidus temperature of the slag and is not conducive to subsequent reduction experiments. Therefore, the appropriate modified basicity is 1.0.

Element Mapping of Modified Slag After Carbothermic Reduction

Figure 6 shows the element mapping after the reduction of modified slag. It can be seen that elements of Fe and Cu dissolve each other, and the contents of elemental P and Mn are inevitably reduced during the process. The reduced metal phase is

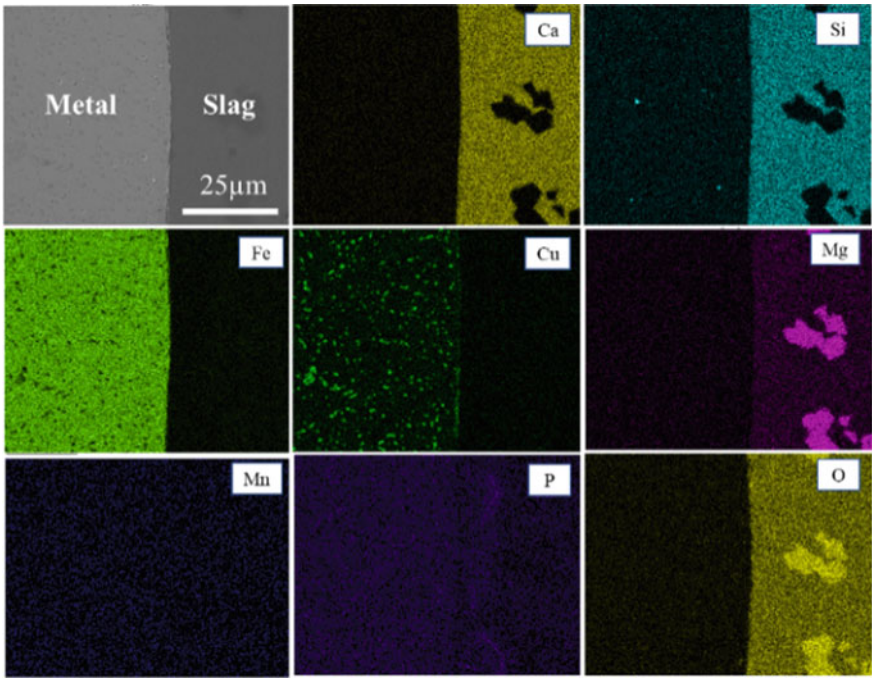

Fig. 6 Element mapping of modified slag after carbothermic reduction

Fe-Cu-Mn-P alloy, and the secondary slag contains elements of Ca, Si, Mg, and O with complicated phases.

Influence on Basicity of Modified Slag

Figure 7 shows the reduced picture of the modified slag with different basicity at the reduction temperature of 1773 K and C/O ratio of 1.0. It can be seen that with the increase of basicity, the size of the metallic phase gradually decreases, and the

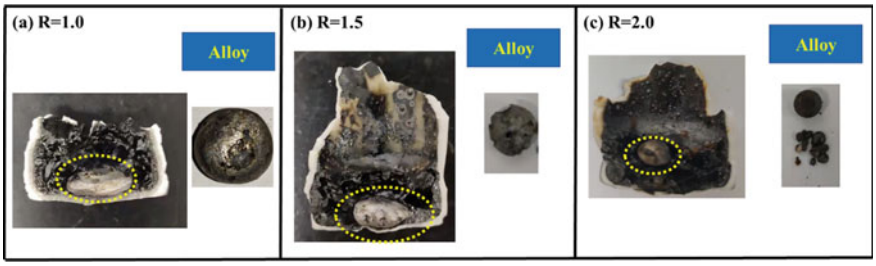

Fig. 7 Photographs of modified slag after reduction at different basicities

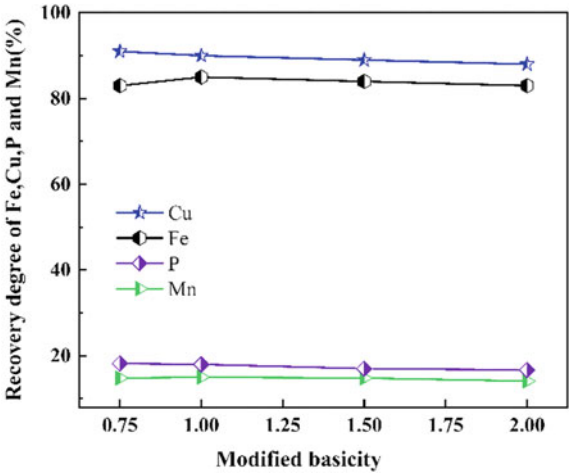

Fig. 8 Effect of modified basicity on recovery of Fe, Cu, P, and Mn

aggregation is incomplete. As shown in Fig. 8, the effects of different modified basicity on reduction rate are studied. The recovery rate of Cu, P, and Mn gradually decreases with the increase of basicity, and the reduction rate of Fe reached the maximum at basicity of 1.0, indicating that calcium ferrite and fayalite had the best dissociation effect and the maximum activity of iron oxide at 1.0 basicity. With the increase of basicity, phases with high melting point will appear in the modified slag, which increases the liquidus temperature of the slag and affects the recovery of Cu.

Influence of Reduction Temperature

Figure 9 shows the photos of the reduced slag at different reduction temperatures with basicity of 1.0 and C/O ratio of 1.0. It can be seen that the metal phase precipitated at the bottom of the crucible and was well separated from the slag phase within the temperature range of 1773–1873 K, indicating that the kinetic conditions of the

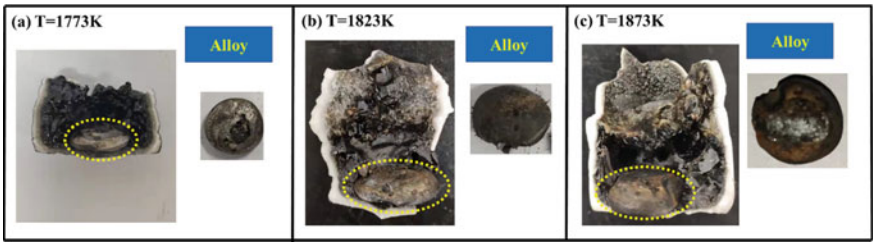

Fig. 9 Photographs of modified slag after reduction at different reduction temperatures

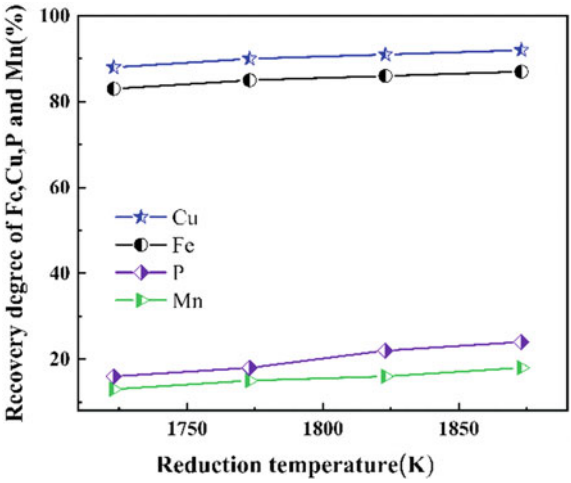

Fig. 10 Effect of reduction temperature on recovery of Fe, Cu, P, and Mn

reaction were good. Figure 10 shows the dependence of the recovery degree on the reduction temperature; with the increase of reduction temperature, the reaction rate and mass-transfer rate were accelerated; meanwhile, the recovery rate of Fe, Cu, P, and Mn monotonically increased. The change of recovery rate was related to the viscosity of slag. However, when the temperature rises further, the influence of viscosity change on recovery rate is negligible, and the recovery rate has no obvious change, so the appropriate reduction temperature is 1773 K.

Influence of C/O Ratio

Figure 11 shows the reduced photos of the modified slag with different C/O ratios at reduction temperature of 1773 K and modified basicity of 1.0. It can be observed that the metal phase is completely consolidated and settled, and the metal phase can be well separated from slag phase. The relationship between C/O ratio and recovery

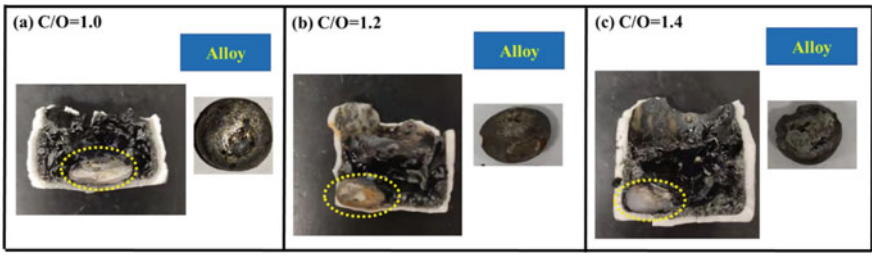

Fig. 11 Photographs of modified slag after reduction at different C/O ratios

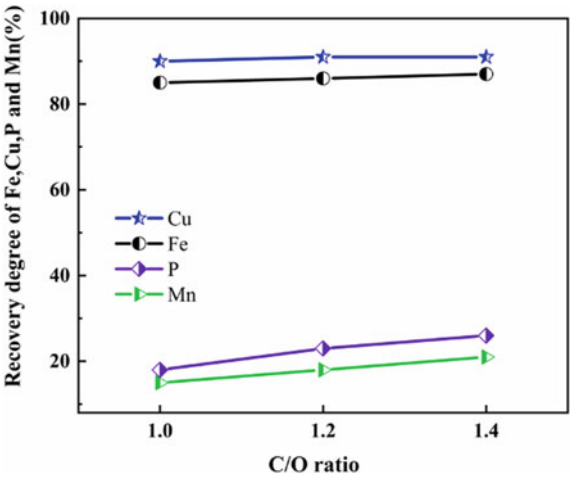

Fig. 12 Effect of C/O ratio on recovery of Fe, Cu, P, and Mn

rate was studied, and the results are shown in Fig. 12. With the increase of C/O ratio, the recovery rates of Fe, Cu, P, and Mn gradually increase. When the C/O ratio is greater than 1.0, the recoveries of Fe and Cu lead to a slight ascension, while the recoveries of P and Mn increase significantly, indicating that the reduction order of Fe and Cu is higher than that of P and Mn. Considering that the excessively high C/O ratio will affect the reduction kinetic conditions, the appropriate C/O ratio is determined to be 1.0.

Conclusions

In this paper, element migration and mineral phase transformation of converter and copper slags in the process of coupled transformation and carbothermic reduction have been studied. Moreover, the effects of basicity, reduction temperature, and C/O ratio on recovery are discussed to determine the optimal technical parameter. The following conclusions can be drawn: (1) Thermodynamic analysis shows that the calcium-containing phase in converter slag can interact with the fayalite in copper slag to dissociate Fe_2O_3 and 'FeO', while the calcium phosphate phase in converter slag can interact with quartz or fayalite only under the condition of reduction. (2) Element mapping and X-ray diffraction indicate that the distribution of elemental Ca, Fe, and Si is separated; Fe_2O_3 and 'FeO' are dissociated from calcium ferrite and fayalite, respectively, realizing the coupling modification between the two slags. Moreover, the RO phase in the converter slag is dissociated, and the released MgO exists in the form of free MgO or $MgFe_2O_4$. With the increase of basicity, Ca_2SiO_4, $Ca_3MgSi_2O_8$, and $CaMgSi_2O_6$ also appear in the modified slag. (3) The reduced product is Fe-Cu-P-Mn alloy, and the optimum technical parameter is modified basicity of 1.0, reduction temperature of 1773 K, and C/O ratio of 1.0, respectively.

Acknowledgements The authors gratefully acknowledge the National Natural Science Foundation of China [Grant numbers: 51974080, 52074077 and 52174301]; the Fundamental Research Funds for the Central Universities was supported by Chinese Education Ministry [Grant number. N2125018].

References

1. Hu SY, Dai XT, Na XZ (2019) Treatment technology and comprehensive utilization of steel slag. Foundry Technol 40(2):220–224
2. Tong S, Li CX, Wang SH, Zhao DG, Xue YK, Liu JM (2020) Analysis of steel slag treatment technology and comprehensive utilization. Energy Metall Ind 39(6):3–7
3. Gorai B, Jana RK, Premchand (2003) Characteristics and utilization of copper slag-a review .Resour Conserv Recycl 39(4):299–313
4. Tian HY, Guo ZQ, Pan J, Zhu DQ, Yang CC, Xue YX, Li SW, Wang DZ (2021) Comprehensive review on metallurgical recycling and cleaning of copper slag. Resour Conserv Recycl 168:105366
5. Ma J, Zhang YB, Hu TQ, Sun SS (2018) Utilization of converter steel slag by remelting and reducing treatment. Mater Sci Eng. https://doi.org/10.1088/1757-899X/382/2/022088
6. Liu CW, Huang SG, Wollants P, Blanpain B, Guo MX (2017) Valorization of BOF steel slag by reduction and phase modification: metal recovery and slag valorization. Metal Mater Trans B 48(3):1602–1612
7. Wang JP, Erdenebold U (2020) A study on reduction of copper smelting slag by carbon for recycling into metal values and cement raw material. Sustainability 12(4):1421
8. Li SW, Pan J, Zhu DQ, Guo ZQ, Xu JW, Chou JL (2019) A novel process to upgrade the copper slag by direct reduction-magnetic separation with the addition of Na_2CO_3 and CaO. Powder Technol 347:159–169
9. Zhang GZ, Wang N, Chen M, Cheng YQ (2020) Comprehensive recovery of multisource metallurgical wastes: recycling nickel slag by aluminum dross with converter-slag addition: fundamentals of high temperature processes. ISIJ Int 60(9):1863–1871

Disintegration Behavior of Vanadium–Titanium Magnetite Pellets in $CO–H_2–CO_2–N_2$ Gas Mixtures

Yue Wang, Jianbo Zhao, Qingqing Hu, Donglai Ma, Yongjie Liu, and Zhixiong You

Abstract As a polymetallic symbiotic mineral, vanadium–titanium magnetite (VTM) primarily contains iron, vanadium, titanium, and other valuable elements such as chromium, cobalt, nickel, etc. On the other hand, VTM is generally sintered or pelletized for iron making process. Under the worldwide trend of low-carbon metallurgy, hydrogen (H_2) is a potential option for the further reduction of CO_2 emission in both blast furnace (BF) and non-blast furnace ironmaking process. Also, H_2 promotes the reduction of iron-bearing burden, while its influences on reduction disintegration behavior deserves research in details, especially for VTM burden. In this study, the disintegration behavior of VTM pellets in gas mixtures of $CO–H_2–CO_2–N_2$ was investigated. The effects of gas composition, reduction temperature as well as reduction time on disintegration index were explored. The reduction samples were observed by an optical-microscope for the evaluation of reaction mode.

Keywords Reduction disintegration · Hydrogen · Ironmaking · Vanadium-titanium magnetite

Introduction

Vanadium (V) and titanium (Ti) are widely used in military and civilian manufacturing industry, and they are the strategic resources that countries all over the world compete for. More than 90% of V and Ti resources in the world were found in composite minerals of vanadium–titanium magnetite (VTM) [1, 2]. Therefore, efficient and green utilization of VTM resources has become an inevitable requirement for extracting V and Ti. In China, VTM is mainly smelted in blast furnace [3], with large production scale and mature technology, while the recovery ratio of V and Ti is low. Carbonaceous is used as reduction agent in blast furnace, which leads to a large amount of CO_2 emission [4]. In order to reduce CO_2 emission, it has been proved that the method of partly replacing carbon with H_2 is efficient [5–7].

Y. Wang · J. Zhao · Q. Hu · D. Ma · Y. Liu · Z. You (✉)
College of Materials Science and Engineering, Chongqing University, Chongqing 400044, China
e-mail: youzx@cqu.edu.cn

Z. Peng et al. (eds.), *12th International Symposium on High-Temperature Metallurgical Processing*, The Minerals, Metals & Materials Series,
https://doi.org/10.1007/978-3-030-92388-4_43

VTM can also be used by direct reduction process [8, 9]. H_2 and CO are always used as reduction agents in gas-based direct reduction method, and VTM is reduced into sponge iron in shaft furnace. It can be seen that H_2 plays a vital role in the reduction of VTM by blast furnace method or non-blast furnace method. The reduction ability of H_2 at high temperature is stronger than that of CO [10], so H_2 can promote the reduction of iron-bearing burden. However, the effects of H_2 on the disintegration behavior at low temperatures deserve to be extensively investigated, especially for the VTM burden. At present, there are few literatures [11, 12] that systematically study the disintegration behavior of VTM pellets in H_2 and CO gas mixture. Therefore, it is of great significance to explore the disintegration behavior characteristics of VTM pellets in gas mixtures of CO–H_2–CO_2–N_2. In this study, the effects of gas composition, reduction temperature as well as reduction time on disintegration index, phase transformation, and microstructure were systematically investigated.

Experimental

Materials

The samples of VTM pellets used in this study were obtained from a domestic steel company, and the chemical composition of the samples was displayed in Table 1. The pellets were sieved to grain size range between 12.0 and 18.0 mm. Samples with the total weight of 500 ± 1 g were randomly picked up and prepared for reduction degradation experiments.

Methods

The reduction degradation index (RDI) of VTM pellets was examined based on the national standard of China (GB/T 13242–2017). All samples were heated in a N_2 gas stream with a flow rate of 5NL/min. When the temperature reached the reduction temperature, the N_2 gas flow rate was increased to 15NL/min and kept for 30 min. Then, N_2 was replaced by gas mixture listed in Table 2 with the same flow rate and continuously reduced for 15, 30, 45, and 60 min, respectively. After the reduction, the gas was changed to N_2, and the samples were cooled to below 100 °C. The reduction index (RI) was calculated from weight change during the reduction process.

Table 1 Main chemical composition of VTM pellets (mass %)

TFe	FeO	SiO_2	CaO	Al_2O_3	MgO	TiO_2	V_2O_5	S	R_2
54.40	2.30	5.69	1.35	3.66	1.62	8.78	0.54	0.004	0.23

Table 2 Reducing gas composition applied in this study (vol. %)

Case	$H_2/(H_2 + CO)$	H_2	CO	CO_2	N_2
1	0	0	57.0	5.0	8.0
2	0.2	11.4	45.6	35.0	8.0
3	0.26	15.0	42.0	35.0	8.0
4	0.5	28.5	28.5	35.0	8.0
5	0.8	45.6	11.4	35.0	8.0
6	1	57.0	0	35.0	8.0

Disintegration tests were conducted using a tumbling drum at a rotation speed of 30 rpm for 10 min. Subsequently, the samples were sieved with 6.3, 3.15, and 0.5 mm to determine the weight of samples with different grain sizes. RDI was expressed by weight fraction and calculated on the basis of the following equation:

$$\mathrm{RDI}_{+6.3\ \mathrm{mm}} = \frac{m_1}{m_0} \times 100\% \tag{1}$$

$$\mathrm{RDI}_{+3.15\ \mathrm{mm}} = \frac{m_1 + m_2}{m_0} \times 100\% \tag{2}$$

$$\mathrm{RDI}_{-0.5\ \mathrm{mm}} = \frac{m_0 - (m_1 + m_2 + m_3)}{m_0} \times 100\% \tag{3}$$

where m_0 is a weight of the sample after the reduction experiment, m_1 refers to a weight of sample left on the 6.3 mm mesh, m_2 means a weight of sample left on the 3.15 mm mesh, and m_3 represents a weight of sample left on the 0.5 mm mesh. $\mathrm{RDI}_{+3.15\ \mathrm{mm}}$ is taken as the evaluation index for the disintegration degree.

Results and Discussion

Effects of Reducing Temperature

The composition of the reducing gas is shown as Case 3 in Table 2, and the reduction time is 30 min. Figure 1 displays the relationships between reduction temperature and reduction degradation index. As the temperature increases from 400 to 550 °C, $\mathrm{RDI}_{+3.15\ \mathrm{mm}}$ decreases from 98.5 to 55.4%. With the further increase of temperature from 550 to 700 °C, $\mathrm{RDI}_{+3.15\ \mathrm{mm}}$ increases from 55.4 to 82.9%. $\mathrm{RDI}_{+3.15\ \mathrm{mm}}$ is the lowest at 550 °C, which indicates that the sample disintegrates seriously at this temperature. Similarly, most of the iron-bearing burden disintegrates obviously at 500–600 °C [13, 14]. $\mathrm{RDI}_{+3.15\ \mathrm{mm}}$ and $\mathrm{RDI}_{+6.3\ \mathrm{mm}}$ are close to each other, and

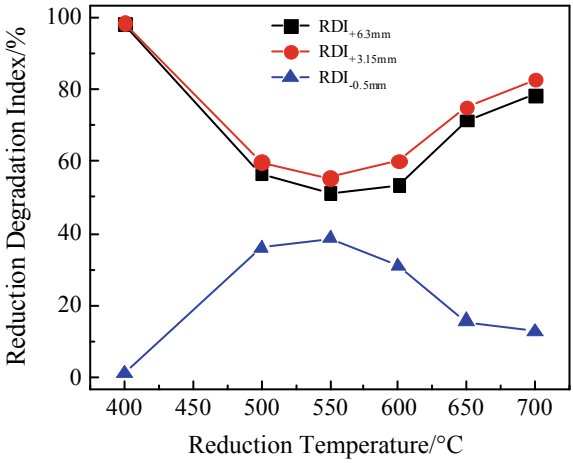

Fig. 1 Influences of reduction temperature on RDI

$RDI_{-0.5\ mm}$ reaches in the range of 30.8–38.6% at 500–600 °C, which suggests that pellets mainly disintegrate in the form of producing fine powder.

The XRD patterns of samples reduced at different temperatures are shown in Fig. 2. The main phases in the reduction samples are hematite and magnetite. With the increase of reduction temperature, the content of hematite decreases, while the content of magnetite increases. The experimental results reveal that the increase of the temperature is beneficial to the reduction of VTM pellets. It should be noted

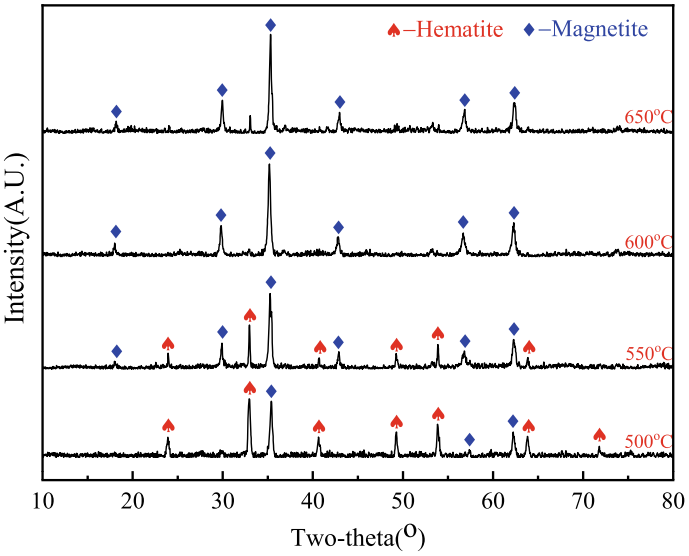

Fig. 2 XRD patterns of samples reduced at different temperatures

that hematite in this study is actually titanium hematite, while magnetite is titanium magnetite.

Figure 3 illustrates the microstructure of samples that reduce at different temperatures. After reducing at 400 and 500 °C, the morphology of samples is relatively integrated, and there are few cracks. Many cracks are formed at 550 °C, and the structure of samples is seriously damaged. When the temperature is higher than 550 °C,

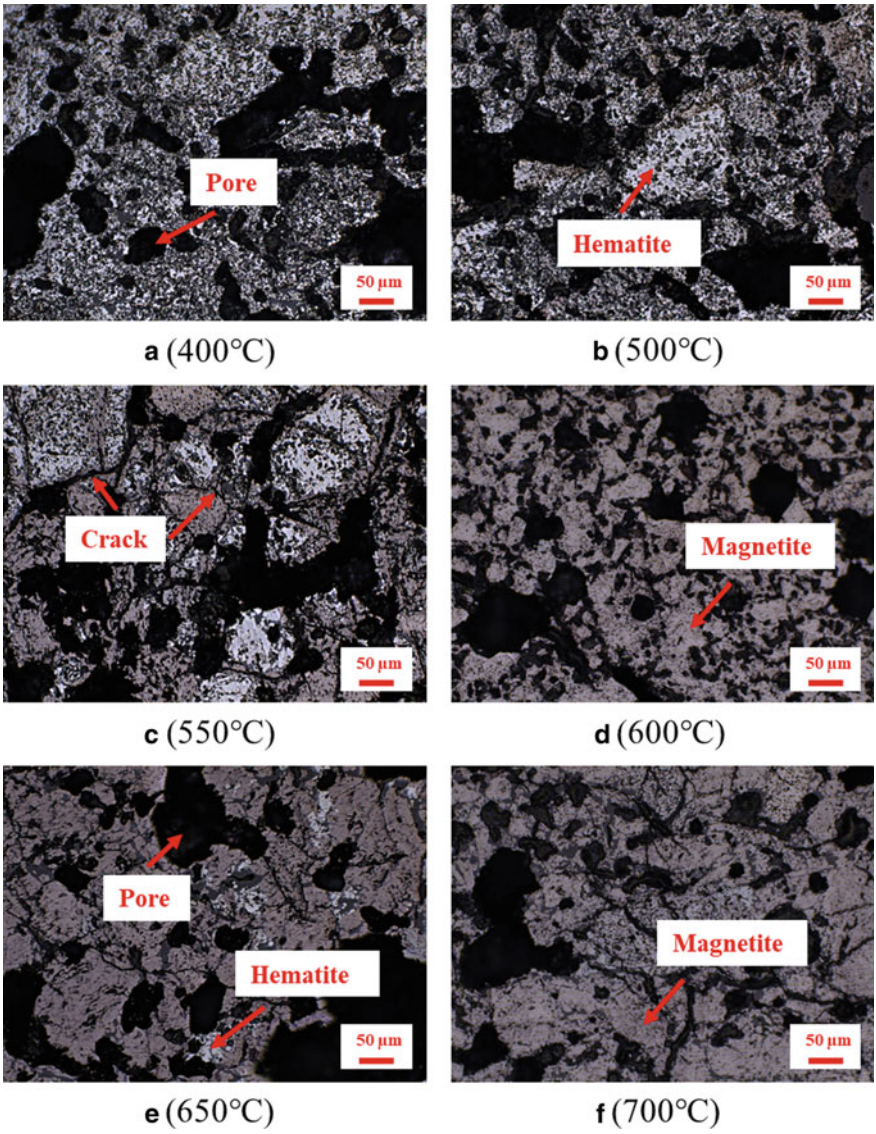

Fig. 3 Microstructure of samples reduced at different temperatures

the main phase of the sample is magnetite, which implies that the disintegration of the sample mainly occurs in the stage of hematite reduction to magnetite. As the temperature increases to above 600 °C, magnetite grains gradually grow and connect into pieces, and the number of pores in the sample also tends to decrease.

According to the results in Figs. 2 and 3, it can be concluded that increasing the reduction temperature could promote the reduction of hematite to magnetite and lead to the expansion of VTM pellets, which further aggravates the disintegration of pellets. However, when hematite is completely reduced to magnetite, the disintegration of VTM pellets is inhibited.

Effects of Reduction Time

The composition of the reducing gas is also shown as Case 3 in Table 2, and the reduction temperature is 550 °C. Figure 4 exhibits the relationship between reduction time and reduction degradation index. With the increase of reduction time, $RDI_{+3.15\ mm}$ tends to decrease. The $RDI_{+3.15\ mm}$ decreases fastest from 15 to 30 min, whose value decreases from 91.6 to 55.4%. The $RDI_{+3.15\ mm}$ is stable from 30 to 45 min, but it decreases slightly from 45 to 60 min.

Figure 5 displays the XRD patterns of samples obtained at different reduction time. With the increase of reduction time, the content of hematite decreases, while the content of magnetite increases. At the initial stage of the reduction reaction, the reduction gas has a good contact with the surface of the sample, which results in the rapid reduction of hematite to magnetite, so the VTM pellets are easy to disintegrate. With the progress of reduction reaction, it is difficult for reduction gas to pass through

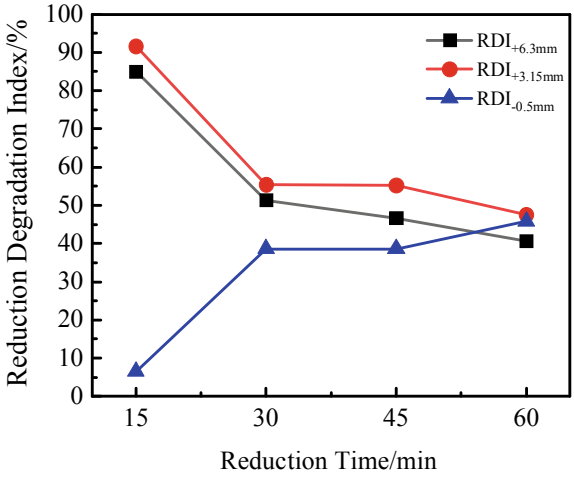

Fig. 4 Influence of reducing time on RDI

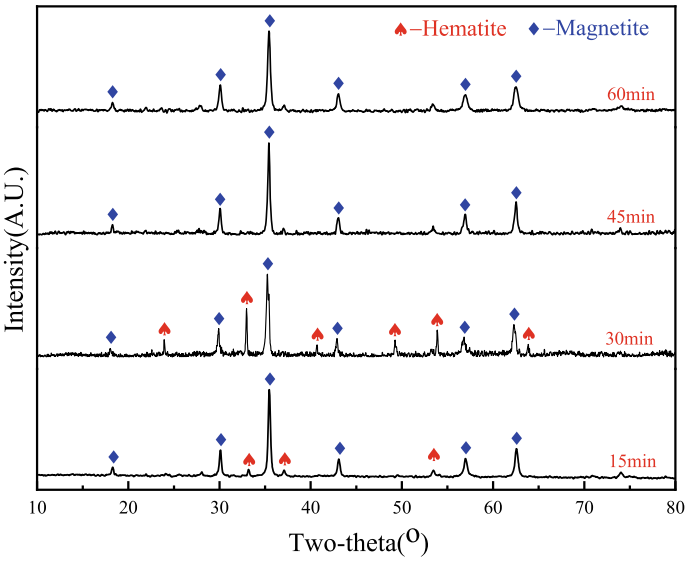

Fig. 5 XRD patterns of samples obtained at different reducing time

magnetite in the outer layer of the sample. The speed of reduction reaction slows down, and the disintegration index also decreases slowly, as illustrated in Fig. 4.

Figure 6 demonstrates the microstructure of samples obtained at different reduction time. At the initial stage of reduction, hematite is still observed and magnetite is formed around hematite. With the increase of reduction time, the structure of pellets is gradually destroyed. When the reduction time is 60 min, almost only magnetite is contained in the sample, and there are coarse cracks.

Effects of Gas Composition

The reduction time is 30 min, and the reduction temperature is 550 °C. Figure 7 shows the relationship between $H_2/(H_2 + CO)$ and reduction degradation index. $RDI_{+3.15\ mm}$ in gas mixture of H_2-CO is always lower than that obtained by CO or H_2. When $H_2/(H_2 + CO)$ is 0.20%, the disintegration of pellets is the most serious. The disintegration of VTM pellets is improved by further increasing the H_2 content.

Figure 8 displays the XRD patterns of samples reduced at different H_2 content. Under different gas composition, the phases obtained by reduction of pellets are almost the same, including hematite and magnetite.

The microstructure of samples reduced at different gas mixtures is plotted in Fig. 9. It is obvious that magnetite is obviously observed, but its content is different from each other. Large area of magnetite and cracks can be seen at $H_2/(H_2 + CO)$ of 0.26. The $RDI_{+3.15\ mm}$ is also the lowest in the range of 0.20–0.26. The content of

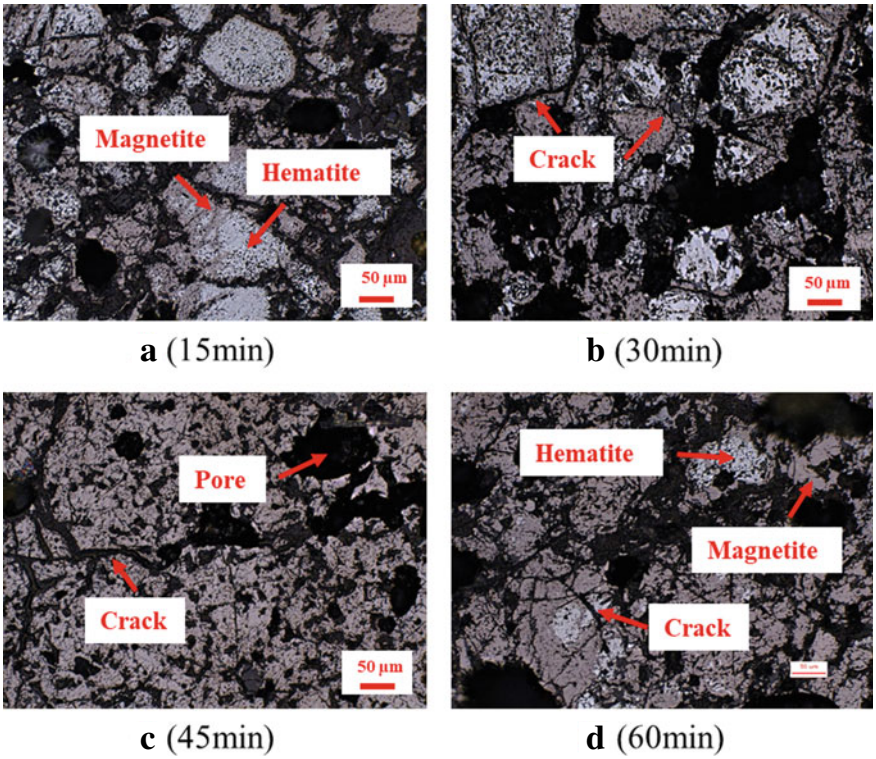

Fig. 6 Microstructure of samples reduced at different time

Fig. 7 Influence of $H_2/(H_2 + CO)$ on RDI

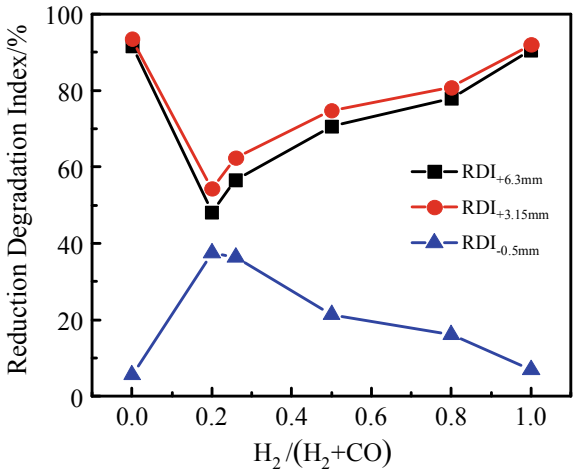

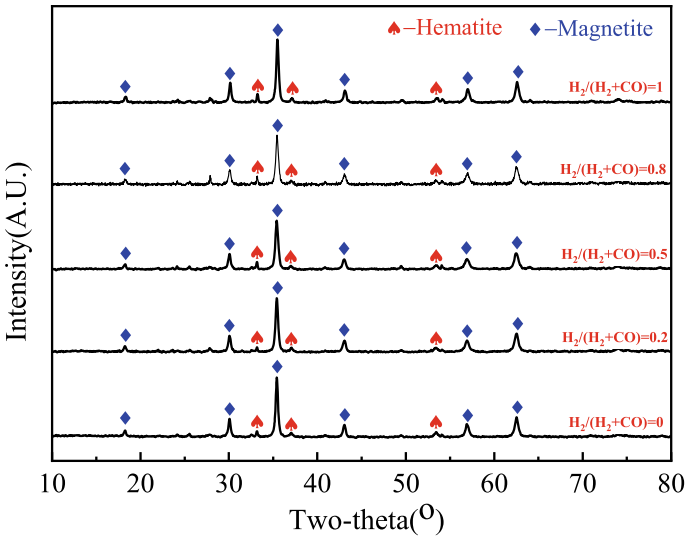

Fig. 8 XRD patterns of samples reduced at different H_2 content

magnetite is observed to decrease as the ratio of $H_2/(H_2 + CO)$ increases to above 0.50, which is consistent with the results of RDI, because the reduction ability of H_2 is lower than that of CO at low temperature (<810 °C). The reduction of VTM pellets is inhibited when the hydrogen content increases.

Reduction Degradation Index and Reduction Index

Figure 10 illustrates the relationship between $RDI_{+3.15\ mm}$ and RI obtained under different reduction conditions. With the increase of RI, $RDI_{+3.15\ mm}$ first decreases and then increases. When RI is about 13%, $RDI_{+3.15\ mm}$ has the lowest value. According to the composition of unreduced VTM pellets, if hematite is completely reduced to magnetite, the theoretical RI is 12.11%, which indicates that the disintegration of VTM pellets mainly occurs in the process of hematite reduction to magnetite.

Conclusions

With the temperature increased from 400 to 700 °C, $RDI_{+3.15\ mm}$ of VTM pellets first decreased and then increased, while disintegration behavior was the most serious at 550 °C. Increasing the reduction time reduced the $RDI_{+3.15\ mm}$. With the increase of H_2 content in the gas mixture, the $RDI_{+3.15\ mm}$ of VTM pellets first decreased and then increased. The microstructure analysis of the reduced VTM pellets indicated

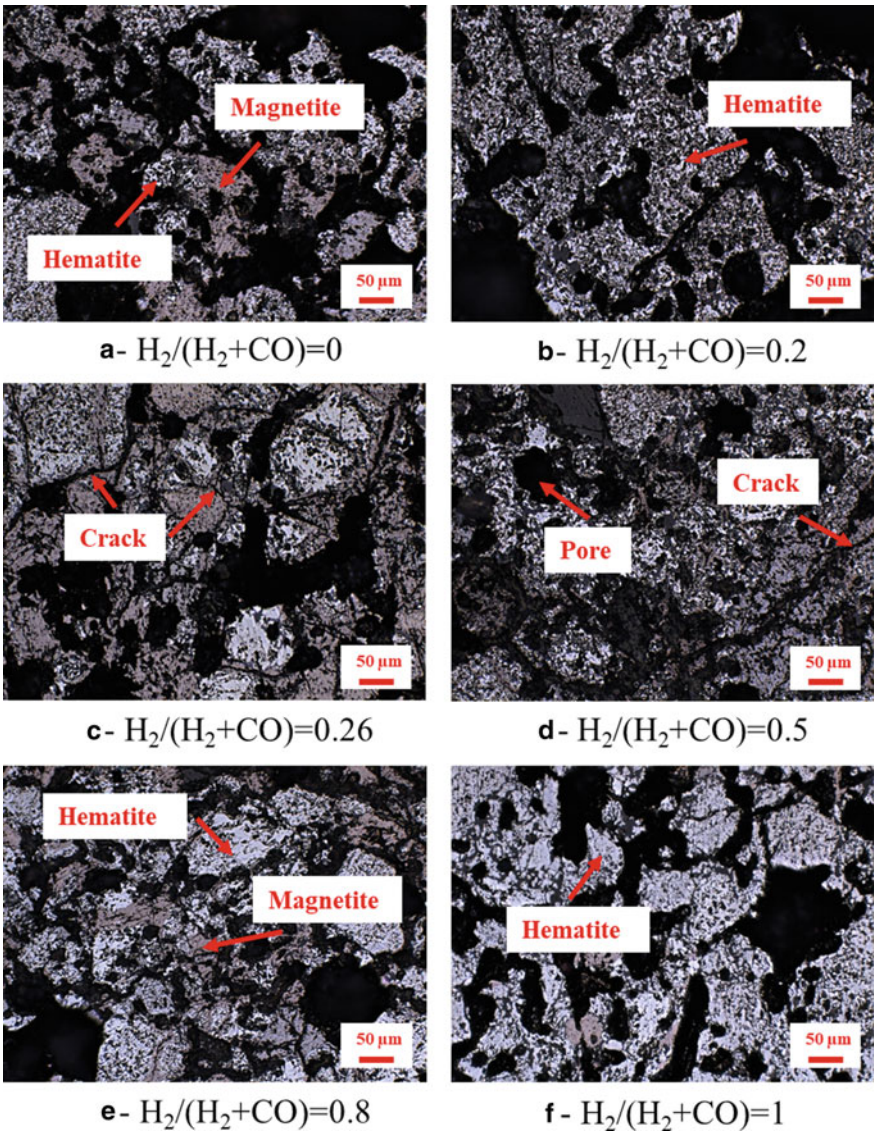

Fig. 9 Microstructure of samples reduced at different H_2 content

that the structure of VTM pellets was most seriously damaged at 550 °C. Increasing the reduction time would aggravate the damage to the structure of VTM pellets, while increasing the H_2 content has fewer damage to the structure. $RDI_{+3.15\ mm}$ first decreased and then increased with the increase of RI. The value of $RDI_{+3.15\ mm}$ was the lowest when RI was about 13%. The disintegration of VTM pellets mainly occurred in the process of hematite reduction to magnetite.

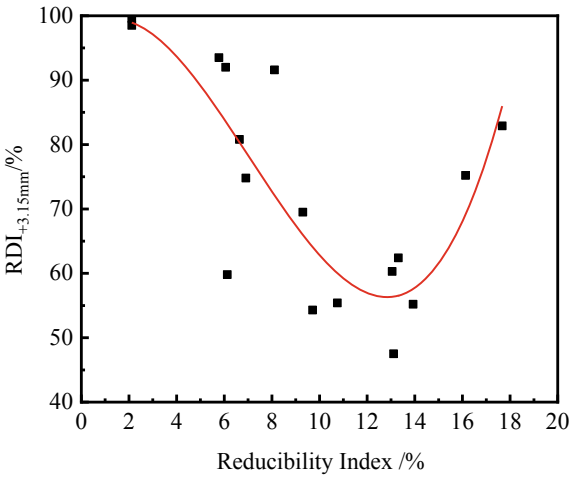

Fig. 10 Relationship between RDI and RI

Acknowledgements The authors wish to express their gratitude to the National Natural Science Foundation of China (51974053 and U2003215) and the Fundamental and Frontier Research Project of Chongqing, China (cstc2020jcyj–msxmX0515), for the financial support of this research.

References

1. Wang S, Guo Y, Jiang T et al (2016) Comprehensive utilization and industrial development direction of vanadium-titanium magnetite. China Metall 26(10):40–44
2. Chen L (2015) Current situation of vanadium-titanium magnetite resource utilization. China Resour Compr Utilization 33(10):31–33
3. Sun H, Zhu Q, Li H et al (2018) The technical state and development trend of the direct reduction of titanomagnetite by fluidized bed. Chin J Process Eng 18(6):1146–1159
4. Liu H, Fu J, Liu S et al (2016) Calculation methods and application of carbon dioxide emission during steel-making process. Iron Steel 51(4):74–82
5. Tang J, Chu M, Li F et al (2020) Development and progress on hydrogen metallurgy. Metall Mater 27(6):713–723
6. Kong L, Guo P, Wang L et al (2020) Reduction behavior of hydrogen injected in blast furnace. Sinter Pelletizing 45(6):1−4, 46
7. Wang L, Guo P, Kong L et al (2021) Analysis on carbon emission reduction ability of blast furnace tuyere with COG injection. Sinter Pelletizing 46(4):78−83, 98
8. Chen L, Zhang X, Liu X et al (2017) Discussion on direct reduction process of vanadium-titanium magnetite. Appl Chem Ind 46(1):150–153
9. Wang Z, Chen S, Chu M et al (2012) Simulation experiment on direct reduction of oxidized pellets of vanadium and titanium-bearing iron concentrates by gas-based shaft furnace. Iron Steel Vanadium Titanium 33(2):34–39
10. Chen M, Li J, Li X (2007) Experiment study on wustite reduction with compound gases of different hydrogen content at high temperature. Metal Mater Metall Eng 35(1):19–22
11. Yang L, Sui Y (2020) Experimental study on gas-based reduction pulverization and swelling of vanadium titano-magnetite pellets. Guangdong Chem Ind 47(6):25–27

12. Kuang C, Qian J, Cai B (1986) Research on the reduction swelling of indurated pellet from Tai-he V-bearing titaniomagnetite concentrate with or without sodium sulphate doping. Cent Iron Steel Res Inst Tech Bull S1:1–8
13. Wang Y, He Z, Zhan W et al (2020) Reduction behavior of iron-bearing burdens in hydrogen-rich stream. Iron Steel 55(7):34−40, 84
14. Liu C, Li J, Gao Y et al (2013) Low temperature reduction degradation characteristics of iron ores based on different ironmaking process. Iron Steel 48(12):25–29

Distribution of Inclusions in a IF Steel Continuous Casting Slab Casted During SEN-Clogged State

Qiuyue Zhou, Rikang Huang, and Lifeng Zhang

Abstract Inclusions in an interstitial-free (IF) steel slab from the loose side to the fixed side of the width center were detected to investigate the distribution of inclusions in the slab under the nozzle clogging state. The total oxygen (T.O) content of the slab was 11.07 ppm, and the total nitrogen (T.N) content of the slab was 24.96 ppm. Endogenous inclusions in IF steel were Al_2O_3 inclusions; TiN inclusions were precipitated with Al_2O_3 as the core during the cooling process of slab. In the thickness direction from the surface to the center of the slab, the area fraction of inclusions increased from 25.32 ppm to 267.78 ppm, and the maximum value of the inclusion area fraction was 405.62 ppm below the center of the slab. Due to the small cooling rate at the center of the slab, the number density of TiN larger than 10 μm reached 1.64 #/mm^2. Under the condition of nozzle clogging, the level fluctuation was large in the mold; contrary to the normal condition, the number density of inclusions at the fixed side of the slab was larger than that at the loose side.

Keywords IF steel · Cleanliness · Nozzle clogging · Distribution of inclusions

Introduction

Interstitial-free (IF) steel is a non-interstitial atomic steel with good deep-drawing performance. By adding strong carbonitride forming elements such as titanium to the steel, the content of carbon and nitrogen dissolved in the steel is reduced. IF steel was Al-killed, and the stable inclusion in the steel was Al_2O_3 [1]. TiN will precipitate during solidification and then grew into large particles in the case of low cooling rate [2]. TiN inclusions of large size formed in the slab will affect the fatigue

Q. Zhou · R. Huang
School of Metallurgical and Ecological Engineering, University of Science and Technology Beijing, Beijing 100083, China

L. Zhang (✉)
State Key Laboratory of Metastable Materials Science and Technology, Yanshan University, Qinhuangdao City 066004, Hebei Province, China
e-mail: zhanglifeng@ysu.edu.cn

Z. Peng et al. (eds.), *12th International Symposium on High-Temperature Metallurgical Processing*, The Minerals, Metals & Materials Series,
https://doi.org/10.1007/978-3-030-92388-4_44

Table 1 Chemical composition of IF steel (wt.%)

C	Mn	Ti	Al_s	P	Cr	Ni	V	Nb	Si	S
0.001	0.109	0.072	0.045	0.009	0.008	0.006	0.003	0.001	0.002	0.002

performance and toughness of the finished product [3]. TiN–MnS complex inclusions were primarily concentrated at the 1/4 position along the thickness direction [4]. The number and size of Al_2O_3 inclusions in the steel corresponded to the total oxygen content in the steel [5, 6]. In order to ensure the cleanliness of the IF steel, the content of total oxygen (T.O) and total nitrogen (T.N) in the IF steel should be controlled [7]. In the case of steady casting, the number of Al_2O_3 inclusions at the loose side of the slab was more than that at the fixed side of the slab because of the Al_2O_3 inclusions floating during the solidification process [8]. Strict requirements on the surface quality of the product were proposed for IF steels, and large-size inclusions in the cast slab were the main reason for the surface defect of the hot-rolled sheet. During the continuous casting process, Al_2O_3 inclusions in IF steels deposited to the submerged entry nozzle wall and caused a nozzle clogging [9, 10]. Nozzle clogging will lead to a large meniscus velocity and a large level fluctuation, which probably resulted in slag entrainment [11]. The distribution and composition of inclusions in the IF steel slab under the nozzle clogging condition should be clarified.

Methodology

The composition of the IF steel is shown in Table 1, which was produced by a basic oxygen furnace (BOF) → RH refining → continuous casting (CC) route. During the casting process, high melting point alumina inclusions were deposited on the nozzle wall, causing the nozzle clogging. The continuous casting slab under the serious nozzle clogging condition was sampled, the section size of the cast slab was 1700 mm × 240 mm, and the casting speed was 1.1 m/min. As shown in Fig. 1, inclusions in the width center of slab were detected by an automatic SEM-EDS scanning system. The slab was equally divided into 16 pieces from the loose side to the fixed side along the thickness direction, and the size of each piece was 12 mm * 15 mm. Inclusions larger than 3 μm were scanned. Contents of T.O and T.N in the steel were detected by Leco oxygen and nitrogen analyzer.

Distribution of Inclusions in the Slab

The content of T.O and T.N in the slab from the loose side to the fixed side is shown in Fig. 2. The content of T.O in the slab was about 11 ppm, and the content of T.N was about 25 ppm. Due to the floating of oxide inclusions during the solidification of

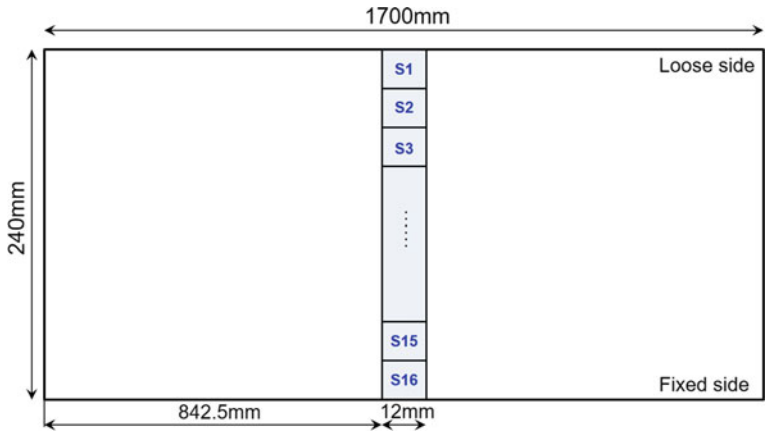

Fig. 1 Schematic diagram of sample processing

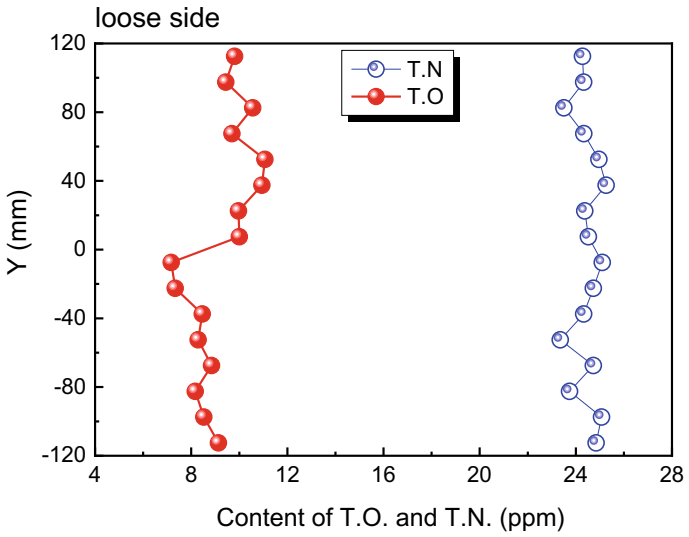

Fig. 2 Variations of T.O and T.N contents of the slab from the loose side to the fixed side

steel, the T.O content at the loose side was higher than that at the fixed side. During the casting process, the T.N content increased by 5 ppm due to the nitrogen pick-up of the molten steel, and the T.O content at the center of the ingot was higher than that at edges.

The morphology of inclusions in the IF slab is shown in Fig. 3. The stable inclusion in the IF steel was Al_2O_3 inclusion, and TiN inclusions were precipitated during the cooling process. In Fig. 3, the black phase was Al_2O_3, and the light gray phase was TiN. There were a few pure Al_2O_3 inclusions at the edge of the slab. During

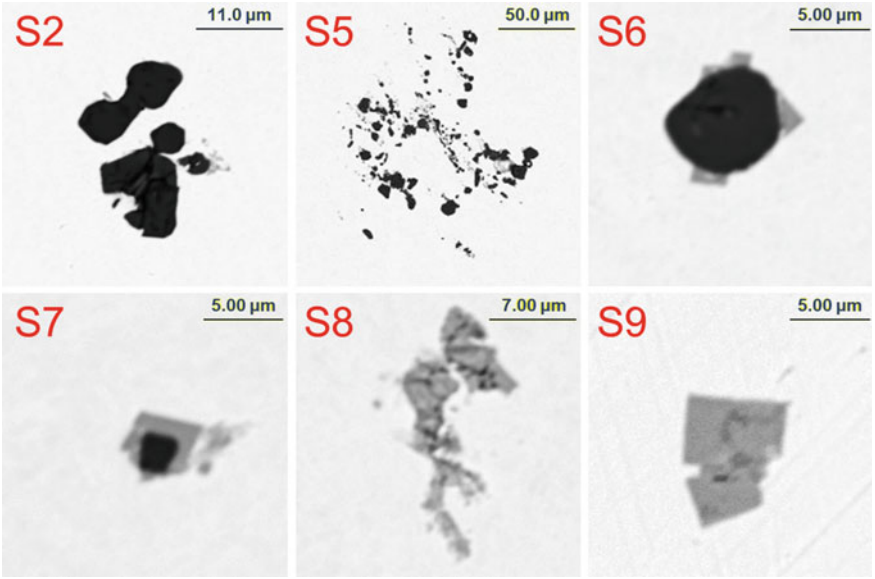

Fig. 3 Typical morphology of inclusions in the slab

the cooling process of the cast slab, TiN inclusions nucleated heterogeneously on Al_2O_3 inclusions. Homogeneous nucleated TiN inclusions with a diameter greater than 10 μm were formed at the center of the slab, due to the slow cooling rate.

Distribution of non-metallic inclusions in the IF steel continuous casting slab from the loose side to the fixed side is shown in Fig. 4. Non-metallic inclusions were divided into oxide inclusions and TiN precipitated during the cooling process. Oxide inclusions were mainly Al_2O_3 inclusions, of which the distribution is shown in Fig. 4a and the number density distribution is shown in Fig. 4b. Under the condition of nozzle clogging, the level fluctuation was large in the mold; contrary to the normal condition, the number density of Al_2O_3 inclusions at the fixed side of the slab was greater than that at the loose side. A large number of TiN inclusions were generated during the solidification of the continuous casting slab. The distribution of the size of the TiN inclusion precipitated in the slab is shown in Fig. 4c. The number density of the TiN inclusion is shown in Fig. 4d. The number and size of TiN inclusions at the edge of the slab were small due to the large cooling rate. The cooling rate at the center of the slab was small, and the growth time of TiN inclusions increased, so the size of TiN inclusions increased significantly. Because the cooling rate at the fixed side and the loose side were different, the precipitation of TiN inclusions on the fixed side was more serious.

The composition and the area fraction of inclusions are shown in Fig. 5. The inclusion at the edge of the slab was mainly Al_2O_3 inclusion, and there were a few TiN inclusions. The main composition of inclusions in the cast slab was about 80% TiN and 20% Al_2O_3. As the cooling rate decreased from the edge to the center of the

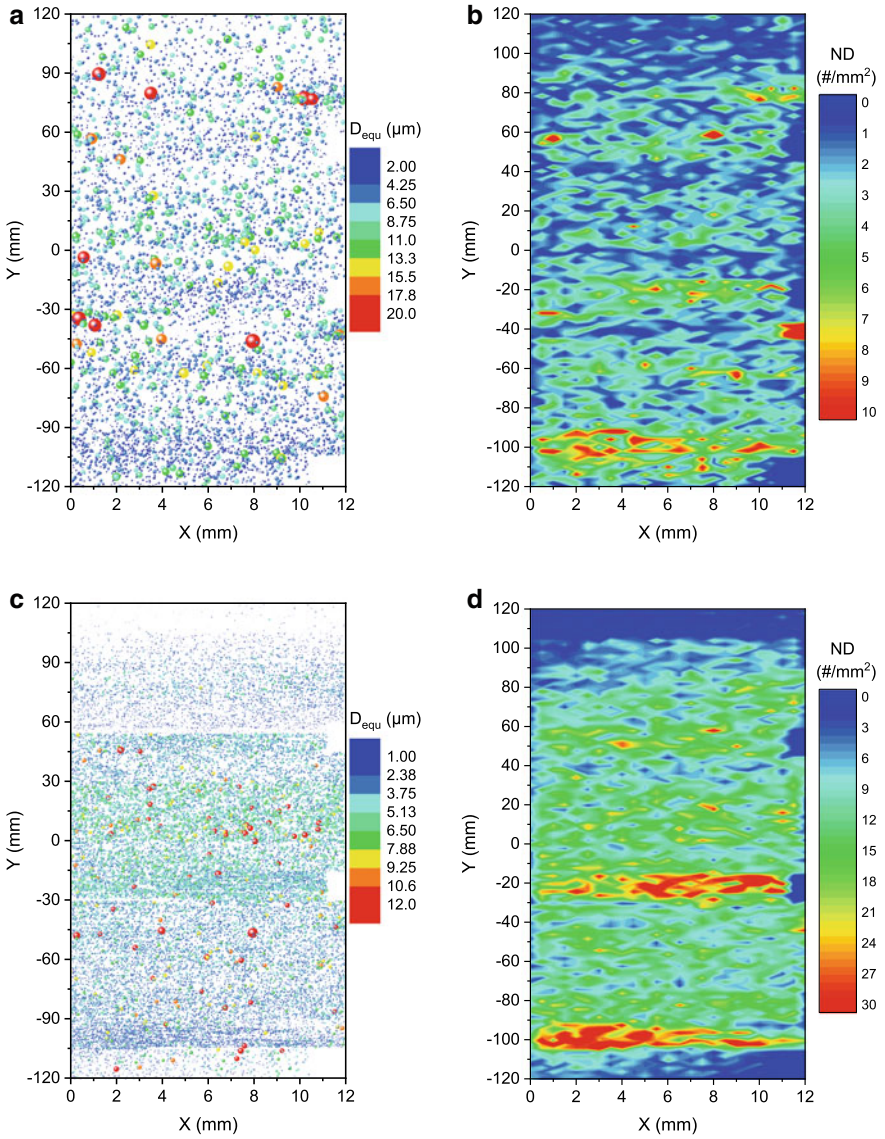

Fig. 4 Distribution of inclusions in the IF steel continuous casting slab. **a** Distribution of Al_2O_3 inclusions, **b** Number density of Al_2O_3 inclusions, **c** Distribution of TiN inclusions, **d** Number density of TiN inclusions

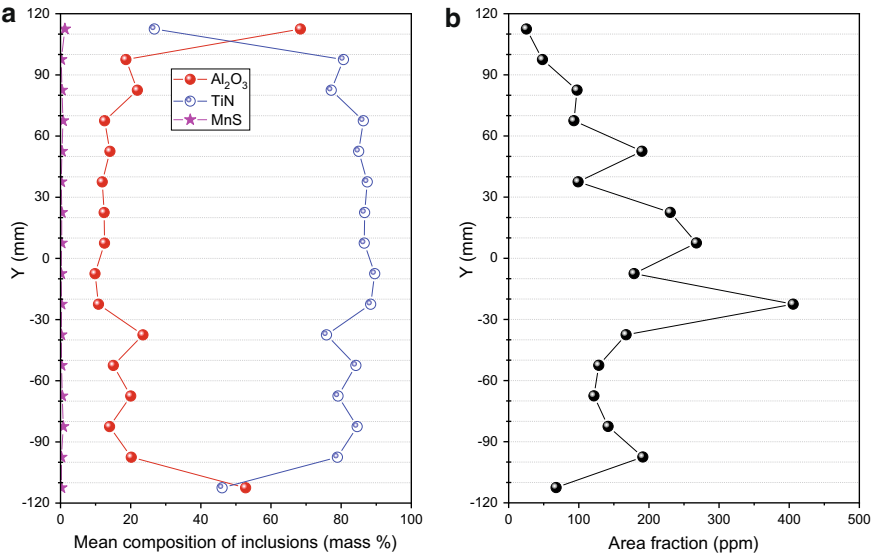

Fig. 5 Composition and area fraction of inclusions. **a** Composition of inclusions, **b** Area fraction of inclusions

slab, the precipitation of TiN inclusions increased, and the area fraction of inclusions increased. Along the thickness direction from the surface to the center of the slab, the area fraction of inclusions increased from 25.32 to 267.78 ppm, and the maximum area fraction of inclusions was 405.62 ppm below the center of the slab. Due to the small cooling rate at the center of the slab, the number density of TiN larger than 10 μm was 1.64 #/mm^2.

Precipitation of TiN Inclusions

The diagram of the TiN inclusion precipitation was calculated using FactSage 7.1 with FactPS, FToxid, and FTmisc databases and is shown in Fig. 6. With the increase of the T.N content, the precipitation temperature of TiN increased slightly, from 1514.8 to 1522.6 °C. The precipitation of TiN increased significantly with the increase of the T.N content in the steel. When the content of T.N in the steel increased from 15 to 35 ppm, the precipitation of TiN inclusions increased by 2.4 times. Under the current condition, MnS inclusions did not precipitate. By controlling the nitrogen pick-up of the molten steel, the formation of large TiN inclusions can be effectively controlled.

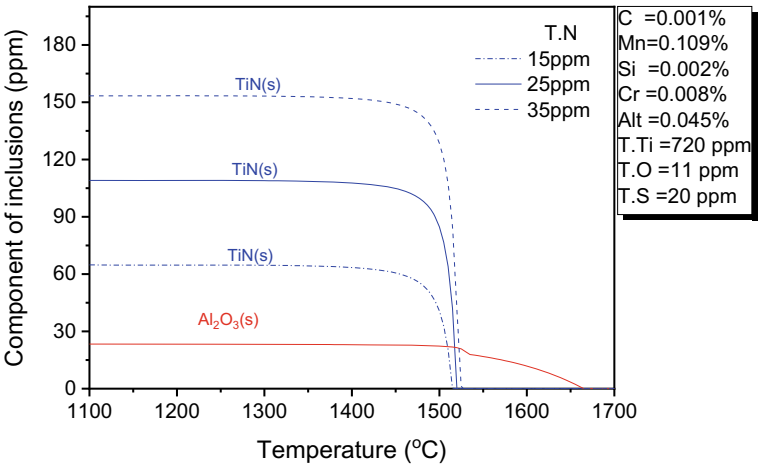

Fig. 6 Effect of T.N content in the steel on the precipitation of TiN inclusions

Conclusions

(1) Under the condition of nozzle clogging, the level fluctuation was large in the mold; contrary to the normal condition, the number density of oxide inclusions at the fixed side of the slab was larger than that at the loose side.

(2) The main composition of inclusions in the cast slab was about 80% TiN and 20% Al_2O_3. Under the current condition, MnS inclusions did not precipitate. As the cooling rate decreased from the edge to the center of the slab, the precipitation of TiN inclusions increased, and the area fraction of inclusions increased from 25.32 to 267.78 ppm.

(3) The precipitation of TiN increased significantly with the increase of the T.N content in the steel, and the precipitation temperature of TiN increased slightly. The nitrogen pick-up of the molten steel should be limited to reduce the formation of large TiN inclusions.

Acknowledgements The authors are grateful for support from the National Nature Science Foundation of China (Grant No. U1860206, No. 51725402), the S&T Program of Hebei (Grant No. 20311004D, 20591001D), the High Steel Center (HSC) at Yanshan University, and Beijing International Center of Advanced and Intelligent Manufacturing of High Quality Steel Materials (ICSM) and the High Quality Steel Consortium (HQSC) at University of Science and Technology Beijing (USTB), China.

References

1. Basu S, Choudhary SK, Girase NU (2004) Nozzle clogging behaviour of Ti-bearing Al-killed ultra low carbon steel. ISIJ Int 44(10):1653–1660
2. Qu T, Tian J, Chen K, Xu Z, Wang D (2019) Precipitation behaviour of TiN in Nb-Ti containing alloyed steel during the solidification process. Ironmaking Steelmaking 46(4):353–358
3. Wang R, Bao Y, Yan Z, Li D, Kang Y (2019) Comparison between the surface defects caused by Al_2O_3 and TiN inclusions in interstitial-free steel auto sheets. Int J Miner Metall Mater 26(2):178–185
4. Gao S, Wang M, Guo JL, Wang H, Zhi JG, Bao YP (2021) Extraction, distribution, and precipitation mechanism of TiN–MnS complex inclusions in Al-killed titanium alloyed interstitial free steel. Met Mater Int 27(5):1306–1314
5. Zhang L, Thomas BG (2003) State of the art in evaluation and control of steel cleanliness. ISIJ Int 43(3):271–291
6. Lee CM, Choi IS, Bak BG, Lee JM (1993) Production of high purity aluminum killed steel. La Revue de Metallurgie CIT. 90(4):501–506
7. Zhao Y, Yang Y, Barati M, McLean A (2018) Strategies for nitrogen control during the production of interstitial-free steel. Ironmaking Steelmaking 45(6):485–491
8. Chen W, Zhang L, Ren Q, Wang Q, Cai X, Ren Y, Yang W (2021) Three-Dimensional spatial distribution of non-metallic inclusions on the entire cross section of a steel continuous casting slab. Metall and Mater Trans B 52(5):3497–3514
9. Lee JH, Kang MH, Kim SK, Kim J, Kim MS, Kang YB (2019) Influence of Al/Ti ratio in Ti-ULC steel and refractory components of submerged entry nozzle on formation of clogging deposits. ISIJ Int 59(5):749–758
10. Deng Z, Zhu M, Zhou Y, Sichen D (2016) Attachment of alumina on the wall of submerged entry nozzle during continuous casting of Al-killed steel. Metall Mater Trans B 47(3):2015–2025
11. Zhou H, Zhang L, Zhou Q, Chen W, Jiang R, Yin K, Yang W (2020) Clogging-induced asymmetrical and transient flow pattern in a steel continuous casting slab strand measured using nail boards. Steel Res Int 92(4):2000547

Effect of Channel Heights on the Flow Field, Temperature Field, and Inclusion Removal in a Channel-type Induction Heating Tundish

Xi-qing Chen, Hong Xiao, Pu Wang, Peng Lan, Hai-yan Tang, and Jia-quan Zhang

Abstract The setting of a channel in a multi-strand induction heating (IH) tundish plays an important role in the metallurgical effect of the tundish. In the present work, the influence of channel heights with 300, 400, and 500 mm, respectively, on the flow, heat transfer, and non-metallic inclusions removal behavior in a dual-channel six-strand IH tundish was studied by establishing a three-dimensional coupled electromagnetic-flow-thermal numerical model and the Lagrangian Discrete Phase Model (DPM). The results show that as the channel height increases from 300 to 500 mm, the distribution of the effective magnetic field in the discharging chamber near the coil side gradually moves upwards, and the direction of the electromagnetic force at the exit of channel changes from downwards to upwards. When the IH turns on, the molten steel at the exit of channel flows from obviously downward to upward with the increase in the channel height, but the liquid level fluctuation becomes sharp under 500 mm of channel height. When the IH is turned off, the increase of channel height can reduce the degree of short-circuit flow at strand 2 and increase the inclusion removal ratio. In addition, turning on the IH can promote the removal of inclusions. Compared with IH turned off, the inclusion removal ratio under IH is increased by 10.13%, 14.27%, and 12.38%, respectively, for 300, 400, and 500 mm of channel height. According to the findings of the study, the height of 400 mm is suggested, which can not only avoid the short-circuit flow of strand No. 2 and improve the inclusion removal but also reduce the risk of slag entrapment by excessive liquid level fluctuations.

X. Chen · H. Xiao · P. Wang · P. Lan · H. Tang (✉) · J. Zhang (✉)
School of Metallurgical and Ecological Engineering, University of Science and Technology Beijing, Beijing 100083, People's Republic of China
e-mail: tanghaiyan@metall.ustb.edu.cn

J. Zhang
e-mail: jqzhang@metall.ustb.edu.cn

X. Chen
e-mail: xiqing_ustb@163.com

H. Xiao
Magnetoelectric Research Institute, Hunan Zhongke Electric Co., Ltd., Yueyang 414000, People's Republic of China

Z. Peng et al. (eds.), *12th International Symposium on High-Temperature Metallurgical Processing*, The Minerals, Metals & Materials Series,
https://doi.org/10.1007/978-3-030-92388-4_45

Keywords Induction heating tundish · Channel height · Electromagnetic force · Flow · Inclusion removal · Heat transfer

Introduction

The tundish is the last refractory container of liquid steel in the continuous casting process and consequently plays an important role to steel quality in the entire process. Heat loss is inevitable in the tundish during the casting process, and the fluctuations of casting temperature will not only affect the stability of the solidification structure but also have a direct impact on the quality of the continuous casting product [1]. Therefore, as a heat loss compensation, plasma heating [2, 3] and induction heating (IH) [4, 5] technologies emerged in the 1990s. The channel-type IH tundish has attracted more and more attention for its effectiveness in improving the flow field and temperature distribution and promoting the removal of non-metallic inclusions [6].

The patent for IH tundish was proposed by Ueda et al. [7] in 1984, and since then, IH tundish has been continuously investigated by scholars. Wang et al. [8, 9] stated that IH could compensate for the heat loss of the tundish but also pointed that the pressure gradient due to electromagnetic force facilitates the removal of inclusions. Yang and Lei et al. conducted a detailed study on the magnetic field [10], fluid flow, temperature fields [11], and inclusions removal [12] in IH tundish, which suggested that electromagnetic forces are more effective in changing the flow pattern of the molten steel and removing inclusions than Joule heat. All the above studies are of simple structured tundish without considering the effect of IH channels on the flow consistency of each strand. However, T-type multi-strand tundishes are mostly used in the long product bloom casting process. Yue et al. [13] investigated the seven-strand tundish and proposed that the location and shape of the channel must be considered in further studies to improve the consistency of each strand. Recent years, Tang et al. [14, 15] and Wang et al. [16, 17] optimized the structure of the multi-strand IH tundish in the discharging chamber and proposed a double-port channel structure.

Previous researches on the IH tundish mainly focused on the influence of the electromagnetic force and Joule heat on the flow field, temperature field, and inclusions removal behavior. However, that of the channel setting has rarely been considered. The channel in the channel-type IH tundish is not only the place where the heating takes place, but the channel itself is also a flow control device. Therefore, the location of the channel is very important. In this present work, the magnetic field, flow, temperature distribution, and inclusion removal behavior in a six-strand dual-channel IH tundish under different channel heights are comparatively investigated by establishing a three-dimensional coupled electromagnetic-flow-thermal numerical model and the Lagrangian Discrete Phase Model (DPM). It is expected to provide guidance for the setting of the channel of the IH tundish to be used in industry.

Mathematical Model

Figure 1 is a schematic diagram of the three-dimensional structure of the IH tundish. As shown in Fig. 1a, the electromagnetic calculation model includes an induction heater and molten steel. The induction heater consists of an iron core and a coil wound on it. Due to the structural symmetry of the six-strand tundish, half of the tundish is used for simulation calculation. Figure 1b is a schematic of the three-dimensional structure of the half of the tundish and the characteristic cross-section used in the analysis, and Fig. 1c is a side view of the tundish. It can be seen from the figure that the fluid domain in the simulation calculation is divided into the receiving chamber, the discharging chamber, and the channel connecting the two chambers. The distance between the centerline of the channel and the bottom of the discharging chamber is defined as the channel height (H), and 300, 400, and 500 mm are set in this work. The various geometrical parameters of the tundish are shown in Table 1.

The details of the electromagnetic-flow-thermal coupling model and the inclusions removal model in the induction heating tundish are well described by some scholars [8, 10], and our team has also published related papers in recent years [14, 16, 17]. Therefore, the model assumptions, governing equations, boundary conditions,

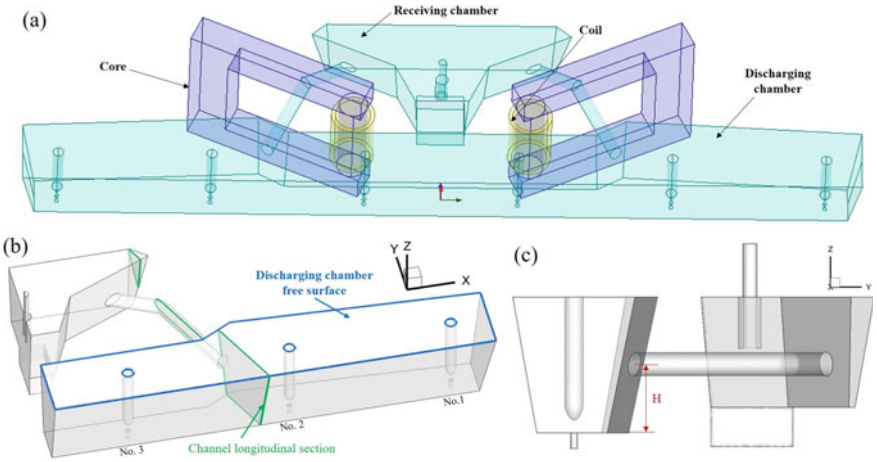

Fig. 1 Schematic diagram of tundish structure: **a** Electromagnetic model, **b** three-dimensional structure and characteristic surface, and **c** side view

Table 1 Geometry parameters of tundish with channel-type IH

Parameters	Values	Parameters	Values
Capacity of molten steel (tons)	34	Receiving chamber depth (mm)	790
Number of strand	6	Discharging chamber depth (mm)	640
Distance between the strand (mm)	1650	Channel diameter (mm)	140

relevant computational parameters, and model validation can be referred to the above-mentioned literature and will not be repeated here.

The electromagnetic field is solved by the Maxwell equation system, the flow field and temperature field are solved by the mass conservation equation, momentum equations, and energy equations. In addition, the inclusions removal model is solved by force balance analysis on particles. The electromagnetic-flow-thermal coupling calculation process and numerical simulation process of the inclusions removal in the six-strand IH tundish are as follows:

1. Use fluent to calculate the steady-state flow field and temperature field under without IH conditions. the convergence residual for the energy equation is 10^{-6}, and the others are 10^{-4}.
2. Use Ansys Maxwell to calculate the three-dimensional magnetic field, induced current field, and electromagnetic force field. Loading Lorentz force and Joule heat as source terms into the momentum and energy equations, respectively, and applying Fluent for 1800s transients to obtain the quasi-steady-state flow and temperature fields.
3. The DPM model is applied to calculate the inclusions removal behavior with IH turning off and turning on conditions, respectively, referring to the reference [14].

Results and Discussion

Effect of Channel Height on Electromagnetic Field

When an alternating current passes through a conductor, the current will concentrate on the surface of the conductor, which is called skin effect [18]. For the channel-type IH tundish, the induction current in the channel will tend to flow along the channel surface. There will also be a proximity effect in the channel, so the induced current is concentrated on the side close to the coil [19]. Figure 2 shows the magnetic flux intensity distribution in the longitudinal section of the channel for different channel heights. As can be seen from the figure, the magnetic flux intensity is mainly distributed in the channel and the side of the discharging chamber near the coil under the combined action of the skin effect and the proximity effect. The magnetic flux intensity on the surface of the channel is the largest, with a maximum of over 2400 Gs. The electromagnetic flux intensity in the center of the channel and most areas of the discharging chamber is below 480 Gs. As the height of the channel increases, the magnetic flux intensity on the upper side of the channel in the discharging chamber gradually increases, while that on the lower side gradually decreases, *i.e.*, the active region of the magnetic field gradually moves upward.

The direction of the electromagnetic force at the channel exit can affect the flow trend of the molten steel at the exit of the channel [16]. Figure 3 shows the distribution of the electromagnetic force vector on the centerline of the channel. As can be seen

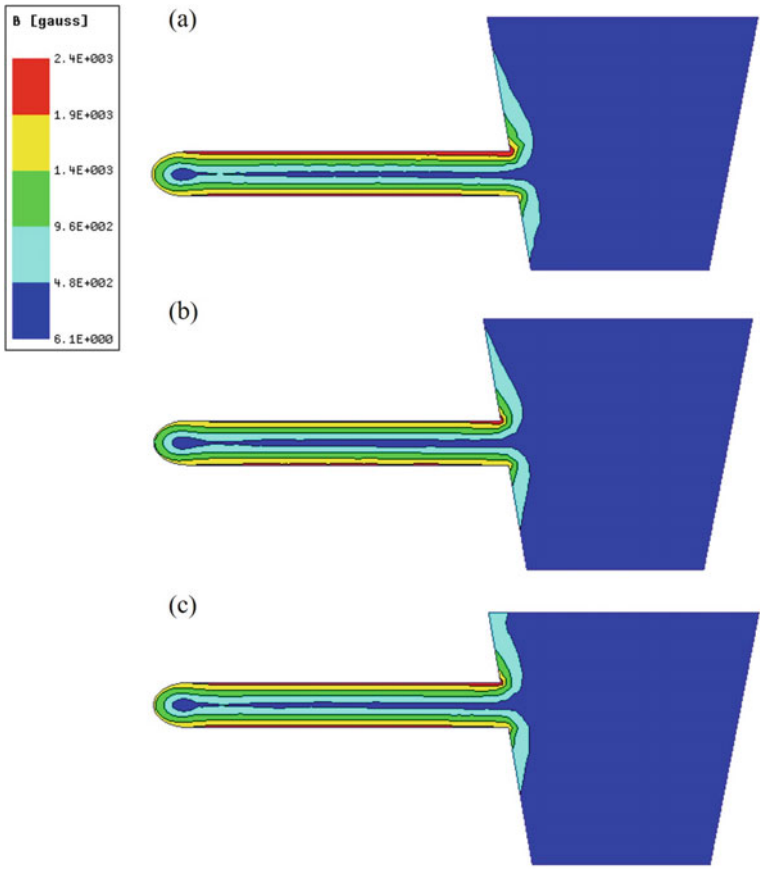

Fig. 2 Distribution of magnetic flux intensity in the longitudinal section of the channel: **a** $H =$ 300 mm; **b** $H = 400$ mm; **c** $H = 500$ mm

from the figure, when the channel height is 300 and 400 mm, the electromagnetic force at the channel exit is in the same direction as gravity, while when the channel height is increased to 500 mm, the direction of electromagnetic force at the channel exit changes from downwards to upwards, which will drive the molten steel at the exit flow in different directions.

Effect of Channel Height on Flow Field of Tundish

Figure 4 shows the velocity vector of the longitudinal section of the channel at different channel heights for heating 0 and 1800 s. As seen from the figure, before heating ($t = 0$ s), regardless of whether the channel height is increased or not, the

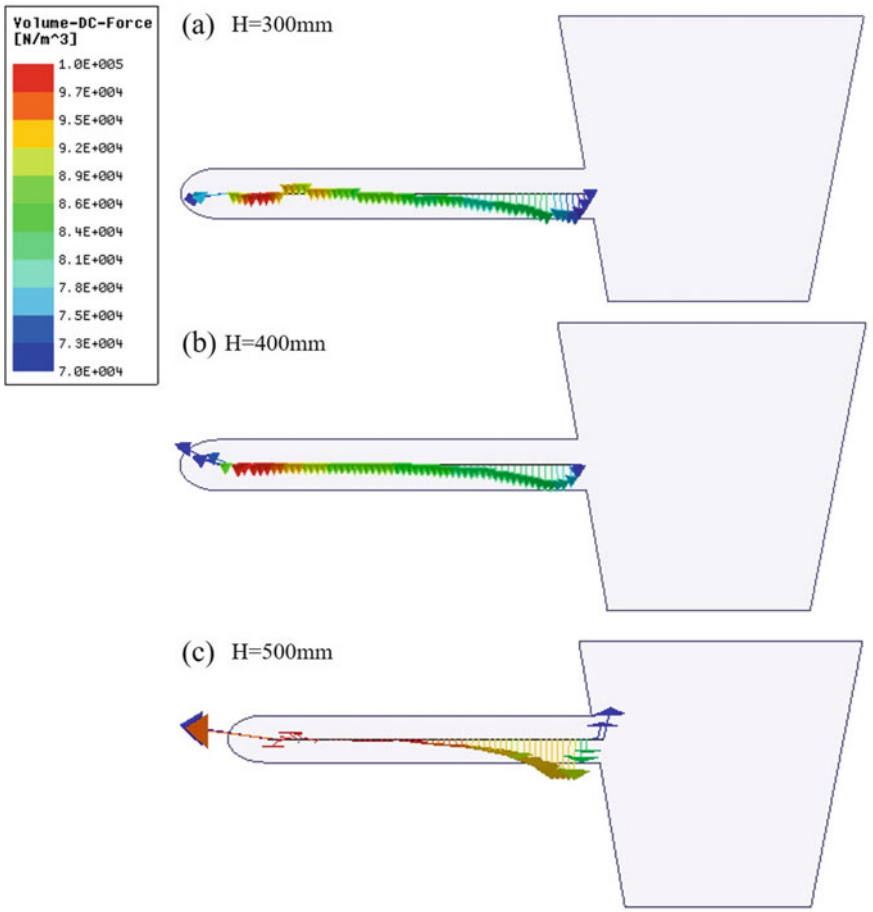

Fig. 3 Electromagnetic force vector diagram of the centerline of the longitudinal section of the channel: **a** $H = 300$ mm; **b** $H = 400$ mm; **c** $H = 500$ mm

flow velocity of the molten steel in the channel does not exceed 0.3 $m{\cdot}s^{-1}$, and the molten steel flows out horizontally from the exit of the channel to the front wall and then forms two large circulations. When heating for 1800 s, the electromagnetic force drives the molten steel in the channel to accelerate, and the flow velocity of the molten steel can reach 1 $m{\cdot}s^{-1}$ under all three channel heights. When the channel height is 300 and 400 mm, the steel at the channel exit is pulled by the downward electromagnetic force and has a downward flowing trend, especially for 300 mm. While the channel height is increased to 500 mm, the upward electromagnetic force is likely to drive the molten steel flowing upwards.

Figure 5 is a three-dimensional streamline diagram of molten steel in tundish when heated for 1800 s at different heights. As seen from the figure, when the height of the channel is 300 mm, the molten steel flowing out of the channel has a significant

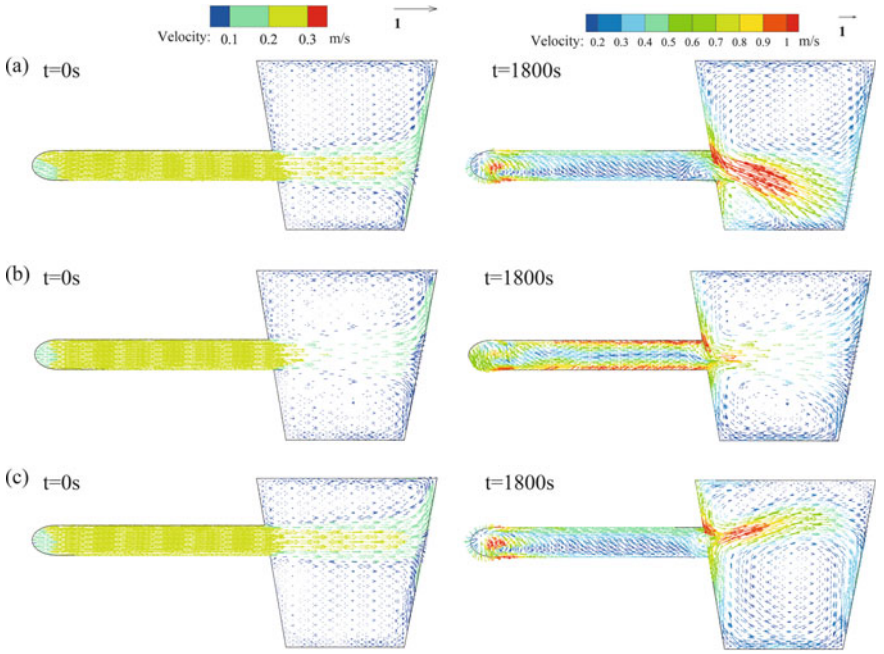

Fig. 4 Velocity vector diagram in the longitudinal section of the channel: **a** $H = 300$ mm; **b** $H = 400$ mm; **c** $H = 500$ mm

downward flow, and the speed is relatively fast. After the molten steel hits the wall of the tundish, it flows along the bottom of the tundish to strand No. 1. Under this case, the high-speed continuous flow is likely to erode the refractory lining at the bottom of the tundish and produce exogenous inclusions [20]. When the height of the channel is 400 mm, the molten steel flowing out of the channel will form a circular flow in upper and lower parts after a slightly downward jet to the wall of the tundish. When the height of the channel is 500 mm, the molten steel at the exit of the channel has an obvious upward flow after reaching the free surface and forms a circulating flow from top to bottom. It will take a longer time for the molten steel to reach nozzles No. 1 and No. 3 than No. 2.

Figure 6 shows the velocity distribution at the free surface of molten steel in the discharging chamber of the tundish with different channel heights when heating for 0 and 1800 s. Studies have shown that excessively high free surface velocity will destroy the stability of the steel-slag interface and cause slag entrapment [21, 22]. Kubota et al. [23] reported that the threshold of the free surface velocity should not exceed 0.40 m·s^{-1}. As seen from the figure, with the increase in channel height from 300 to 500 mm at heating 0 s, the region where the free surface flow velocity exceeds 0.11 m s^{-1} increases, but the maximum velocity does not exceed 0.15 m s^{-1}, that is, the increase in channel height is beneficial to activate the free surface but will not cause slag entrapment easily. When heating for the 1800 s, the electromagnetic force

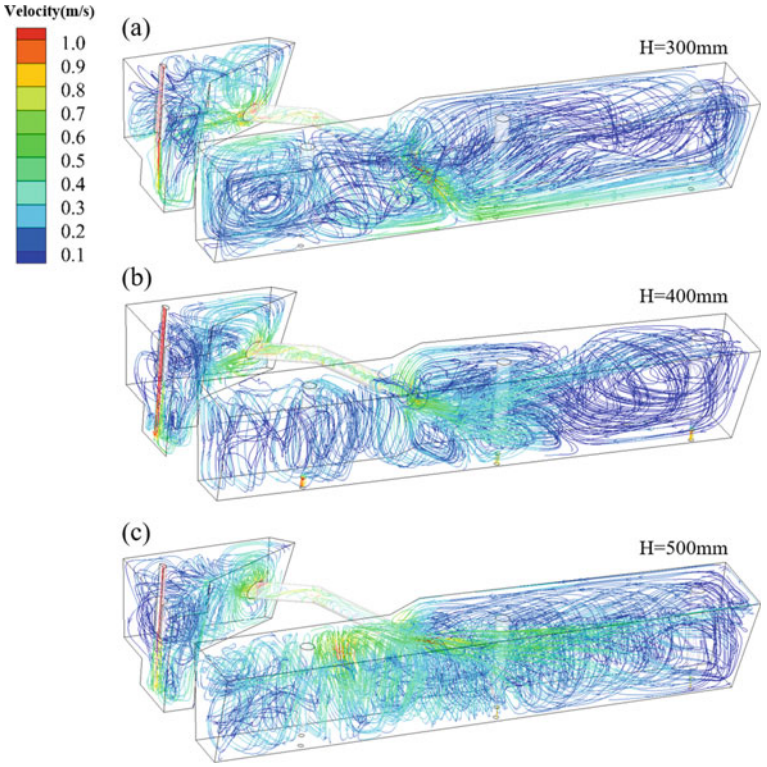

Fig. 5 Three-dimensional streamline diagram in the tundish after heating for 1800s: **a** $H = 300$ mm; **b** $H = 400$ mm; **c** $H = 500$ mm

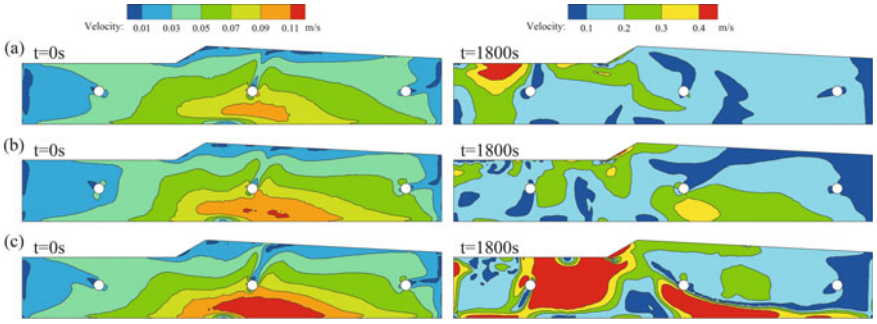

Fig. 6 Free surface velocity distribution in the discharging chamber of the tundish, left for 0 s and right for 1800 s: **a** $H = 300$ mm; **b** $H = 400$ mm; **c** $H = 500$ mm

drives the molten steel to accelerate out of the channel and thus produces turbulence, which makes the free surface velocity all higher than that without heated. When the channel height is 300 mm, although the velocity in more than half of the free surface is lower than 0.20 $m{\cdot}s^{-1}$, the velocity in some regions exceeds 0.40 $m{\cdot}s^{-1}$. When the channel height is 400 mm, the region which the velocity of the free surface in the discharging chamber over 0.20 $m{\cdot}s^{-1}$ is significantly larger than that in the case of 300 mm channel height, but there is almost no region where the flow velocity exceeds 0.40 $m{\cdot}s^{-1}$. With the channel height increasing to 500 mm, although the upward flow at the channel exit can bring the non-metallic inclusions in molten steel to the steel-slag interface and increases their contact chance with slag, it also makes the velocity of the free surface for a larger region exceeds 0.40 $m{\cdot}s^{-1}$. It is extremely easy to destroy the stability of the tundish cover, induce slag entrapment behavior, and even cause the exposed molten steel to be subjected to secondary pollution.

Effect of Channel Height on Temperature Field

Figure 7 shows the temperature distribution in the longitudinal section of the channel at different channel heights for heating 0, 900, and 1800 s. It is seen from the figure that the temperature of the top area of the tundish increases slightly from 1799 to 1800 °C with the increase of the channel height when heating for 0 s. The IH first rapidly heats the molten steel in the channel and then increases the overall temperature of the discharging chamber with the help of the flow of the molten steel. When the channel height is 300 mm and 400 mm and heating for 900 s, the high-temperature

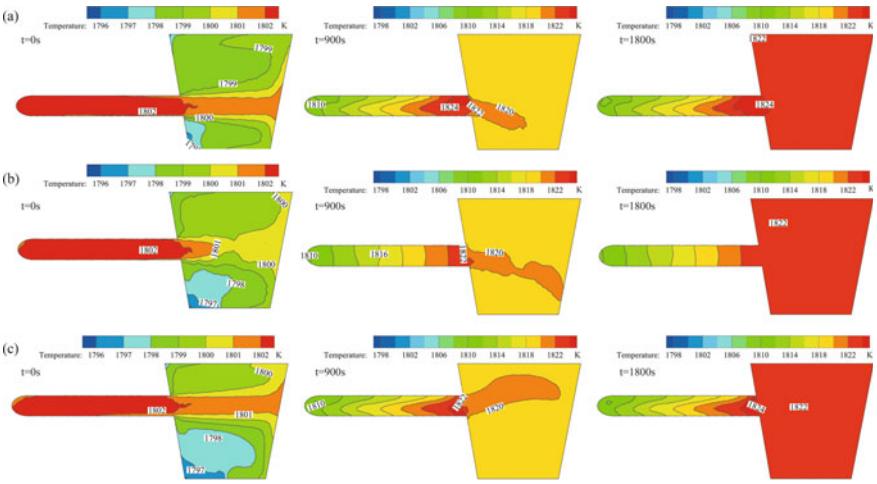

Fig. 7 Temperature field of the longitudinal section of the channel changes with time: **a** H = 300 mm; **b** H = 400 mm; **c** H = 500 mm

molten steel is diffused downward due to the fluid state in the above description, and the temperature at the bottom of the tundish is moderately higher than on the top area. When the channel height is 500 mm and heating for 900 s, the high-temperature molten steel flowing out of the channel exit is brought to the top area of the tundish by the up-rising flow, so that the upper area keeps the high temperature. As the heating continues to 1800 s, the temperature of the discharging chamber at different channel heights is gradually uniform and maintains a constant temperature state, and there is no significant difference in heating efficiency under different channel heights.

Effect of Channel Height on Inclusion Removal Ratio

Figure 8 compares the removal ratio of inclusions in various sizes when heating for 0 and 1800 s at different channel heights. Before heating ($t = 0$ s), the removal ratio of inclusions in various sizes all increases with the increasing particle size for every channel height. Because large inclusion size makes its buoyancy increase, which is more easily absorbed by the steel-slag interface. This shows that the size of the inclusions is a key factor affecting its removal. Moreover, the increase in channel height allows the outflow of inclusions to be closer to the free surface, thus improving the inclusion removal ratio.

It is also seen that the removal ratio of inclusions in all sizes after IH for 1800 s is significantly improved compared with that before heating ($t = 0$ s). Due to the presence of electromagnetic force and thermal buoyancy, the flow pattern of the molten steel changes significantly, and the inclusions in different sizes no longer

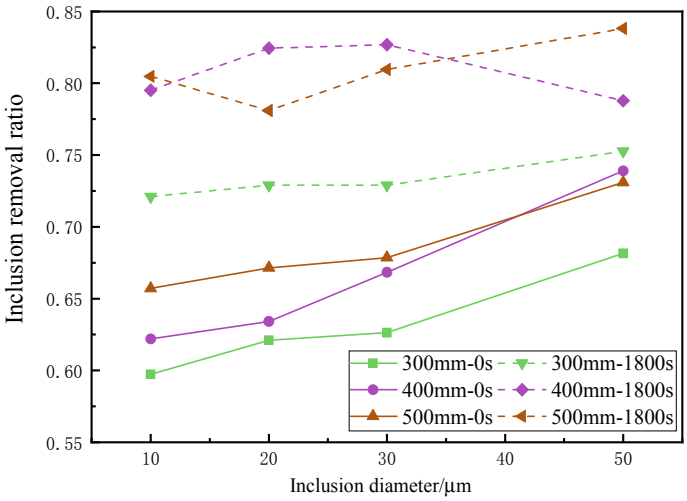

Fig. 8 Inclusion removal ratio of various sizes under different channel heights

show a single pattern of increasing removal ratio with the size or the channel height increasing. It also indicates that the influence of flow pattern on the inclusions removal cannot be ignored. And it can be seen that IH is more beneficial to increase the removal ratio of small size inclusions, which is consistent with the conclusion obtained by Xing et al. [5]. This is because that the IH increases the collision chance of inclusions each other.

When the channel heights are 300, 400, and 500 mm, the corresponding inclusion removal ratios before heating ($t = 0$ s) are 63.16, 66.59, and 68.45%, respectively, while they are 73.29, 80.85, and 80.83%, respectively, at IH for 1800 s. The removal ratio is increased by 10.13%, 14.26%, and 12.38% after heating for different channel heights, in which the channel height of 400 mm has the most superior effect on the IH to improve the inclusion removal ratio. Regardless of whether IH is turned on or not, the increase in the removal ratio is both the greatest when the channel height is increased from 300 to 400 mm. In summary, the channel height of 400 mm is the most favorable for the removal of inclusions and the most effective for IH to remove inclusions.

Conclusions

To improve the metallurgical effect of channel-type IH tundish, the effect of channel height on the magnetic field, flow, temperature distribution, and the inclusions removal in tundish are investigated using the coupled magnetic-flow-thermal model and the Lagrangian Discrete Phase Model. According to the findings of this study, the main conclusions can be listed as follows:

(1) As the height of the channel increases, the effective area of magnetic field distribution in the discharging chamber near the coil side gradually moves upward, and the direction of electromagnetic force at the exit of the channel changes from downwards to upwards.
(2) The effect of the electromagnetic force causes the molten steel at the channel exit to have a downward or upward flow trend. Compared with the channel heights of 300 and 500 mm, the slightly downward flow at 400 mm will neither wash the bottom of the tundish strongly nor cause excessive free surface velocity.
(3) When the IH is turned off, the increase in the channel height will make the molten steel flowing out of the channel closer to the free surface, which leads to an increase in the inclusion removal ratio for almost all sizes. When the IH is turned on, the maximum removal ratio of inclusions is 80.85% with the channel height 400 mm.

References

1. Tang HY, Liu JW, Wang KM et al (2021) Progress and perspective of functioned continuous casting tundish through heating and temperature control. Acta Metall Sin 57(10):1229–1245
2. Barron-Meza MA, Barreto-Sandoval J, Morales RD (2000) Physical and mathematical models of steel flow and heat transfer in a tundish heated by plasma. Metall Mater Trans B 31(1):63–74
3. Zhao MJ, Wang Y, Yang SF et al (2021) Flow behavior and heat transfer of molten steel in a two-strand tundish heated by plasma. J Market Res 13(7):561–572
4. Tang HY, Li XS, Zhang S et al (2020) Fluid flow and heat transfer in a tundish with channel induction heating for sequence casting with a constant superheat control. Acta Metall Sin 56(12):63–76
5. Xing F, Zhang SG, Zhu MY (2018) Motion and removal of inclusions in new induction heating tundish. Steel Res Int 89:1700542
6. Yoshii Y, Nozaki T, Habu Y et al (1995) Decreasing non-metallic inclusions in molten steel by use of tundish heating system in continuous casting. Tetsu-to-Hagane 71(11):1474–1481
7. Ueda T, Ohara A, Sakurai M et al (1984) A tundish provided with a heating device for molten steel. EU Pat, 0119853, 3 Mar 1984
8. Wang Q, Qi FS, Li BK et al (2014) Behavior of non-metallic inclusions in a continuous casting tundish with channel type induction heating. ISIJ Int 54(12):2796–2805
9. Wang Q, Li BK, Tsukihashi F (2014) Modeling of a thermo-electromagneto-hydrodynamic problem in continuous casting tundish with channel type induction heating. ISIJ Int 54(2):311–320
10. Yang B, Lei H, Bi Q et al (2018) Electromagnetic conditions in a tundish with channel type induction heating. Steel Res Int 89:1800145
11. Yang B, Lei H, Bi Q et al (2018) Fluid flow and heat transfer in a tundish with channel type induction heating. Steel Res Int 89:1800173
12. Lei H, Yang B, Bi Q et al (2019) Numerical simulation of collision-coalescence and removal of inclusion in tundish with channel type induction heating. ISIJ Int 59(10):1811–1819
13. Yue Q, Zhang CB, Pei XH (2016) Magnetohydrodynamic flows and heat transfer in a twin-channel induction heating tundish. Ironmaking Steelmaking 44(3):1–10
14. Tang HY, Guo LZ, Wu GH et al (2018) Hydrodynamic modeling and mathematical simulation on flow field and inclusion removal in a seven-strand continuous casting tundish with channel type induction heating. Metals 8(6):374
15. Tang HY, Wang KM, Li XS et al (2021) Improved metallurgical effect of tundish through a novel induction heating channel for multistrand casting. Metals 11(7):1075
16. Wang P, Xiao H, Chen XQ et al (2021) Influence of dual-channel induction heating coil parameters on the magnetic field and macroscopic transport behavior in T-type tundish. Metall Mater Trans B. https://doi.org/10.1007/s11663-021-02274-8
17. Wang P, Chen XQ, Xiao H et al (2021) Effect of flow control devices on the distribution of magnetic-flow-heat in the channel induction heating tundish. Ironmaking Steelmaking. https://doi.org/10.1080/03019233.2021.1948315
18. Northrup EF (1914) The skin effect and alternating-current resistance. J Franklin Inst 177(2):125–168
19. Karolina L K, Miroslav P, Nikola D, et al (2009) Proximity effect against skin effect in two coupled u-shaped busbars. Facta Universitatis. Series Electron Energetics 22(3):293–303
20. Wang Q, Tan C, Huang A et al (2021) Numerical simulation on refractory wear and inclusion formation in continuous casting tundish. Metall Mater Trans B 52(3):1344–1356
21. Singh R, Thomas BG, Vanka SP (2014) Large eddy simulations of double-ruler electromagnetic field effect on transient flow during continuous casting. Metall Mater Trans B 45(3):1098–1115
22. Watanabe K, Tsutsumi K, Suzuki M et al (2009) Effect of properties of mold powder entrapped into molten steel in a continuous casting process. ISIJ Int 49(8):1161–1166
23. Kubota J, Okimoto K, Suzuki M, et al (1990) Mechanism of level fluctuation and mold powder catching in slab continuous casting at high speeds. IISC. The sixth international iron and steel congress, vol 3. pp 356–363

Effect of Slag Basicity on Non-metallic Inclusions in a Heavy Rail Steel

Nan Liu, Lifeng Zhang, Yanping Chu, and Ying Ren

Abstract Experiments and thermodynamic calculations were performed to investigate the effect of slag basicity (CaO/SiO_2) on non-metallic inclusions in heavy rail steels. With the increased of the slag basicity from the 1.7 to 2.3, the composition of inclusions changed from the SiO_2-CaO to Al_2O_3-MgO-SiO_2-CaO. During the rolling process, the full liquid inclusions were rolled to the linear shape inclusions, which was harmful to heavy rail steels. It was proposed that the target of inclusions was the partial liquid inclusions instead of the full liquid inclusions to avoid the formation of the linear shape inclusions. Moreover, the relationship between the composition of the Al_2O_3-MgO-SiO_2-CaO slag and the composition of inclusions was calculated using FactSage thermodynamic software. The content of Al_2O_3 in inclusions gradually increased from less than 10% to above 30% with a higher slag basicity. The lower Al_2O_3 content in slag was beneficial to decrease the Al_2O_3 content in inclusions in heavy rail steels.

Keywords Heavy rail steel · Slag basicity · Inclusion

Introduction

The demand for higher performance steels has been increasing year by year, it is necessary to improve the cleanliness of heavy rail steels. Non-metallic inclusions have a detrimental effect on the property of heavy rail steels, such as their strength,

N. Liu · Y. Ren
School of Metallurgical and Ecological Engineering, University of Science and Technology Beijing, Beijing 100083, China

L. Zhang (✉)
State Key Laboratory of Metastable Materials Science and Technology, Yanshan University, Qinhuangdao 066004, Hebei, China
e-mail: zhanglifeng@ysu.edu.cn

Y. Chu
Steelmaking Branch, WISDRI Engineering & Research Incorporation Ltd., Wuhan 430223, China

Z. Peng et al. (eds.), *12th International Symposium on High-Temperature Metallurgical Processing*, The Minerals, Metals & Materials Series,
https://doi.org/10.1007/978-3-030-92388-4_46

toughness, and fatigue resistance. The Al_2O_3-rich inclusions after the Al deoxidation have a poor deformability during the rolling process, which is detrimental to the surface quality of heavy rail steels [1, 2]. Thus, Si-Mn deoxidation was adopted to suppress the formation of Al_2O_3-rich inclusions in heavy rail steels. However, a certain amount of Al added ferroalloys during the refining process obviously increased Al_2O_3 content in inclusions [3–5].

Control of inclusions is one of the main tasks of steelmakers. There are many ways developed to achieve the precise control of inclusions, including deoxidation [6, 7], calcium treatment [8–11], slag refining [12–14], argon blowing [15–17], etc. Therefore, the slag modification played an important role to control the composition, size, number, and distribution of inclusions in heavy rail steels. Inclusion composition was greatly influenced by the composition of the top slag [18]. The precise control of the composition of inclusions in steel could be achieved by choosing the proper top slag composition. For Al-killed steels, it was previously thought that alumina inclusions were modified to calcium aluminates by the Al reduction of CaO in the refining slag [19]. Recently, Kitamura et al. [20] proposed that the CaO in the CaO-Al_2O_3-SiO_2-MgO slag was hardly reduced by the Al in the molten steel with less than 0.25% Al. It was further proposed that the Al_2O_3 inclusions can hardly be modified to CaO-Al_2O_3 inclusions by the slag refining. The relationship between the slag composition and the cleanliness of Si-Mn-killed steel was widely studied through experimental studies. For Si-Mn-killed steels, the Al_2O_3 content in inclusions was obviously influenced by the slag basicity and Al_2O_3 content in slag [21–23]. Chen et al. [24] found that the slag basicity should be controlled around 1.0 to achieve plasticization of inclusions. Meanwhile, 10% content of Al_2O_3 in top slag gave aid to improve the cleanness of tire cord steel, which would not increase the Al_2O_3 content in inclusions. Park et al. [23] investigated the equilibrium of Si-Mn-killed steels, inclusions, and CaO-Al_2O_3-SiO_2-CaF_2-MgO(-MnO) slag with 30–50% content of Al_2O_3. It was reported that the mole ratio of MnO/SiO_2 in inclusions was approximately 0.8 and Al_2O_3 in inclusions increased from about 10 to 40 mol % with the increase of the slag basicity from 0.7 to 2.1.

The aim of the current work was to find a proper slag basicity to lower the content of Al_2O_3 in inclusions in heavy rail steels. Therefore, laboratory experiments with various slag basicity were performed, and non-metallic inclusions in steel after slag refining were analyzed and calculated.

Experimental

In the current laboratory experiments, approximately, 150 gramsheavy rail steel and 15 g refining top slag were melted in a MgO crucible. The initial steel composition was listed in Table 1. The experiments were performed using vertical electric resistance furnace under Ar atmosphere. After the temperature reaching 1873 K, the refining slag sealed by the pure iron foil was added on the top of the molten steel.

Table 1 Initial composition of heavy rail steels (wt %)

C	Si	Mn	V	S	T.O	Mg	Al	Ca	Fe
0.8	0.65	0.95	0.06	0.0040	0.0010	0.0004	0.0030	0.0010	Balance

Table 2 Final composition of refining slag

No.	R (CaO/SiO_2)	CaO	SiO_2	MgO	Al_2O_3	CaF_2
1	1.37	42.57	31.03	5.24	0.13	20.73
2	1.60	46.77	29.26	3.80	0.14	19.88
3	1.74	48.21	27.77	4.61	0.11	19.16
4	1.89	48.00	25.36	5.77	0.19	20.53
5	1.81	47.03	25.96	4.78	3.13	18.82
6	1.85	45.05	24.33	4.85	5.94	19.57

After the molten steel was hold in the furnace at 1873 K for 30 min, the crucible was cooled with a cooling rate of 5 K/min in the furnace. Slags were the mixture of analytically pure grade powders of CaO, SiO_2, MgO, Al_2O_3, and CaF_2. In the initial slag, the CaO/SiO_2 ratio was adjusted from 1.4 to 2.0, and the Al_2O_3 content was increased from 0 to 5%. In the current study, six experiments followed the same procedure except for adjusting CaO/SiO_2 and Al_2O_3. The synthetic slag was pre-melted at 1873 K for 2 h in a graphite crucible and then decarburized at 1273 K for 8 h to achieve a good homogeneity of the slag. After each experiment, steel and slag in the crucible were divided. The steel sample was sectioned two parts, one for the chemical analysis, and another was mounted and polished for automated SEM/EDS inclusion analysis system (ASPEX). The composition of slag was analyzed by an X-ray fluorescence spectrometer. The final composition of slag is listed in Table 2. The slag composition was determined based on a steelmaking plant. The refining slag contained roughly 15% CaF_2. To simulate the slag composition used in the steel plant and make sure the melting of the slag, the CaF_2 content in the current study was 20%.

Evolution of Inclusions After Slag Refining

Figure 1 shows the typical morphology of inclusions with various slag basicities. The morphology of $CaO\text{-}SiO_2\text{-}MgO\text{-}Al_2O_3$ inclusions with a slag basicity of 1.4 was in spherical shape, indicating that inclusions were liquid at the steelmaking temperature. With the increase of slag basicity from 1.4 to 2.0, the morphology of inclusions changed little. The morphology of inclusions was also in spherical shape.

The effect of the slag basicity on the number density and composition of inclusions in heavy rail steels was shown in Fig. 2. The CaO content of inclusions increased with a higher slag basicity from 1.4 to 2.0. Meanwhile, SiO_2 and MgO contents in

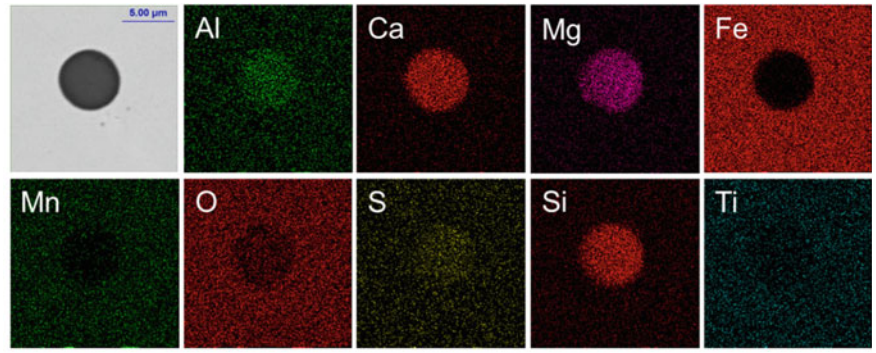

(a) R=1.4

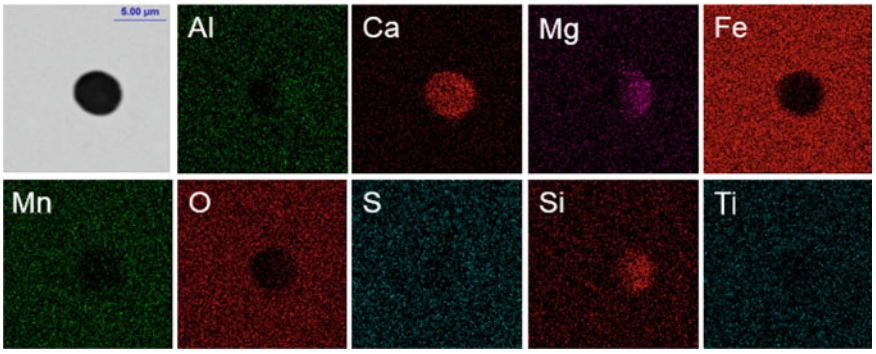

(b) R=2.0

Fig. 1 Typical morphology of inclusions with various slag basicity. **a** $R = 1.4$. **b** $R = 2.0$

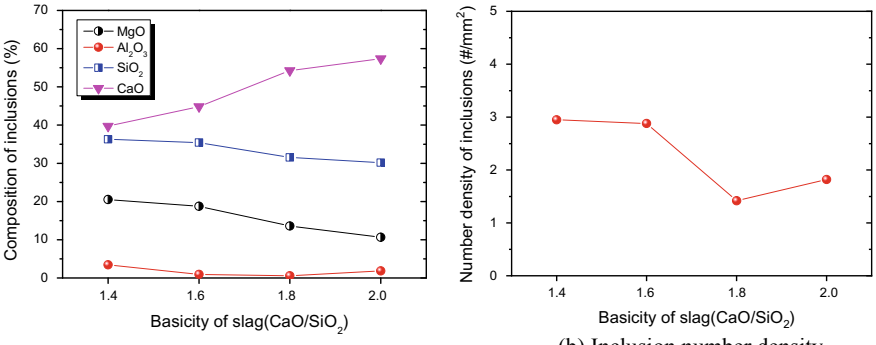

(a) Inclusion composition (b) Inclusion number density

Fig. 2 Effect of slag basicity on inclusions. **a** Inclusion composition. **b** Inclusion number density

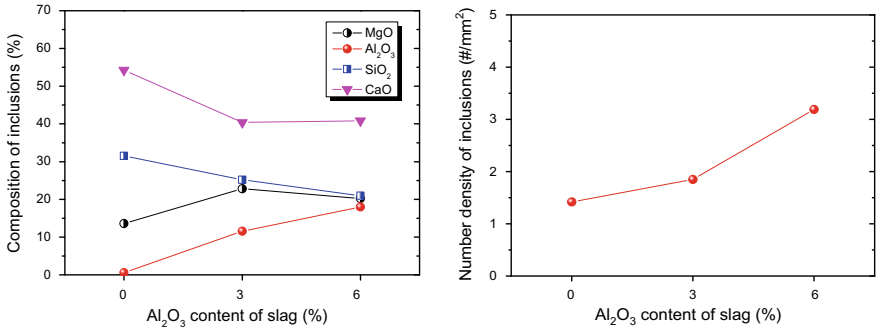

(a) Inclusion composition (b) Inclusion number density

Fig. 3 Effect of Al_2O_3 in slag on of inclusions. **a** Inclusion composition. **b** Inclusion number density

inclusions decreased with a higher slag basicty. It was noted that the Al_2O_3 content in inclusions was always lower than 5% with the change of slag basicity. The number density of inclusions decreased with the increase of slag basicity, indicating that the high basicity slag was beneficial to the removal of inclusions and lowering the oxygen in steel. For the refining process of heavy rail steels, it was suggested to lower the Al_2O_3 content in slag and increased the slag basicity to decrease the Al_2O_3 in inclusions and remove inclusions.

Figure 3 shows the effect of the Al_2O_3 in slag on the composition of inclusions in the steel. When the Al_2O_3 in slag increased from 0.1 to 5.9, contents of Al_2O_3 and MgO in inclusions gradually rose up, while contents of SiO_2 and CaO in inclusions apparently decreased. The aluminum transferred from the Al_2O_3 in slag to [Al] in steel, increasing the Al_2O_3 in inclusions. Meanwhile, the MgO in slag was reduced by the dissolved aluminum in the steel, leading to the increase of MgO in inclusions. The number density of inclusions was less than 3 per mm^2 with the increase of Al_2O_3 in slag. It was concluded that the lower Al_2O_3 content in slag was beneficial to decrease the Al_2O_3 content in inclusions in heavy rail steels.

Thermodynamic Calculation

The effect of the slag composition on steel and inclusion compositions was calculated using FactSage 7.1 with FactPS, FToxide, and FTmisc databases. Figure 4 shows the calculated effect slag basicity on steel compositions. The initial steel composition was listed in Table. In the initial slag, the CaO/SiO_2 ratio was adjusted from 1.2 to 2.0. The [Al] in steel increased from 5 ppm to more than 35 ppm with a higher slag basicity from 12 to 2.0, indicating that the higher slag basicity promoted the transfer of aluminum from the Al_2O_3 in slag to [Al] in steel. The [Mg] content slightly increased from 3 to 11 ppm with the higher slag basicity due to the reduction of MgO

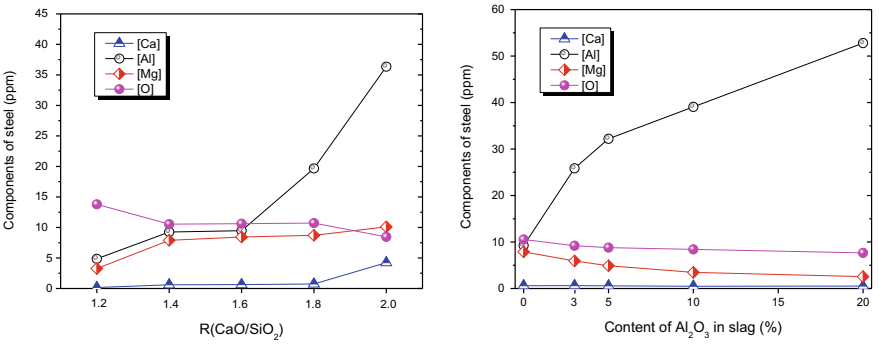

(a) Effect of slag basicity (b) Effect of Al_2O_3

Fig. 4 Calculated effect of slag composition on steel composition. **a** Effect of slag basicity **b** Effect of Al_2O_3

in slag by the [Al] in steel. With the increase of Al_2O_3 in slag from 0 to 6%, the [Al] in steel obviously increased from less than 10 ppm to over 50 ppm. Thus, the lower Al_2O_3 in slag was beneficial to decrease the [Al] in heavy rail steels.

Figure 5 shows the calculated effect slag basicity on inclusion compositions. In the initial slag, the Al_2O_3 content was increased from 0 to 5%. With the slag basicity in slag increasing from 1.2 to 2.0, the CaO content in inclusions increased from less than 40% to 55%, while contents of Al_2O_3, MgO, and SiO_2 in inclusions slightly decreased, which was corresponded with experimental results. There was little MnO in the inclusions after reactions due to the reduction of Al, Mg, and Ca in steel. With the increase of Al_2O_3 in slag from 0 to 6%, the Al_2O_3 content in inclusions obviously increased from less than 10% to more than 30%, and contents of CaO, MgO, and SiO_2 in inclusions slightly decreased, which was similar with the tendency of observed results. Thus, the high basicity slag was beneficial to lower the oxygen

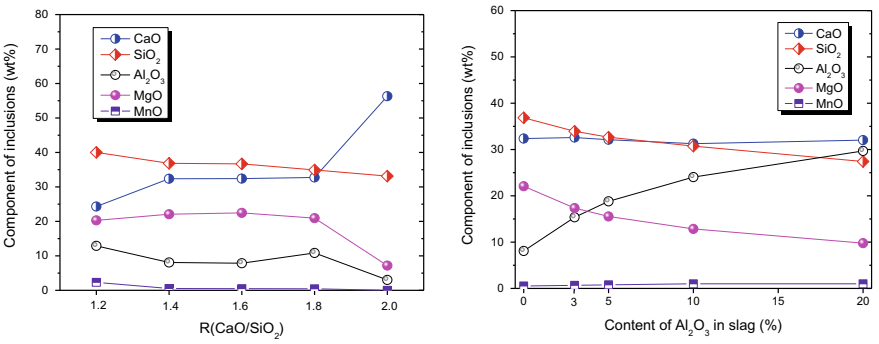

(a) Effect of slag basicity (b) Effect of Al2O3

Fig. 5 Calculated the evolution of inclusion composition with slag composition. **a** Effect of slag basicity. **b** Effect of Al_2O_3

in steel and the removal of inclusions in steel, while the formed inclusions contained a higher content of Al_2O_3. The low basicity slag refining was suggested to lower the Al_2O_3 in inclusions and improve the deformability of inclusions.

Conclusions

1. With a higher slag basicity in slag, the CaO content in inclusions increased, while contents of Al_2O_3, MgO, and SiO_2 in inclusions slightly decreased. The increase of slag basicity lowered the number density of inclusions.
2. The low slag basicity of less than 1.6 was suggested to lower the [Al] in steel to less than 10 ppm and Al_2O_3 in inclusions to lower than 10%, to improve the deformability of inclusions in heavy rail steel.
3. When the Al_2O_3 in slag increased, the content of Al_2O_3 and MgO in inclusions gradually rose up, while contents of SiO_2 and CaO in inclusions apparently decreased. The aluminum transferred from the Al_2O_3 in slag to [Al] in steel, increasing the Al_2O_3 in inclusions. The Al_2O_3 in slag should be lowered as low as possible to decrease the [Al] and Al_2O_3 in inclusions for heavy rail steels.

Acknowledgements The authors are grateful for support from the National Science Foundation China (Grant No. 51874032 and No. 51704018), Fundamental Research Funds for the Central Universities (Grant No.FRF-TP-17-001C2 and FRF-TP-19-037A2Z), the S&T Program of Hebei (Grant No. 20311004D, 20311005D, 20311006D 20591001D), the High Steel Center (HSC) at Yanshan University, and Beijing International Center of Advanced and Intelligent Manufacturing of High Quality Steel Materials (ICSM), and the High Quality Steel Consortium (HQSC) at University of Science and Technology Beijing (USTB), China.

References

1. Park JH, Todoroki H (2010) Control of MgO Al_2O_3 spinel inclusions in stainless steels. ISIJ Int 50(10):1333–1346
2. Park JH, Kang Y (2017) Inclusions in stainless steels—a review. Steel Res Int 88(12):1700130
3. Mizuno K, Todoroki H, Noda M, Tohge T (2001) Effect of Al and Ca in ferrosilicon alloys for deoxidation on inclusion composition in type 304 stainless steel. Iron Steelmaker 28(8):93–101
4. Park JH, Kang YB (2006) Effect of ferrosilicon addition on the composition of inclusions in 16Cr-14Ni-Si stainless steel melts. Metall Mater Trans B 5(37):791–797
5. Yan P, Pandelaers L, Zheng L, Blanpain B, Guo M (2015) Interfacial reaction and inclusion formation at early stages of FeMnSi addition to liquid Fe. ISIJ Int 55(8):1661–1668
6. Zhang L, Ren Y, Duan H, Yang W, Sun L (2015) Stability diagram of Mg-Al-O system inclusions in molten steel. Metall Mater Trans B 46(4):1809–1825
7. Yang W, Duan H, Zhang L, Ren Y (2013) Nucleation, growth, and aggregation of alumina inclusions in steel. JOM 65(9):1173–1180
8. Yang W, Zhang L, Wang X, Ren Y, Liu X, Shan Q (2013) Characteristics of inclusions in low carbon Al-Killed steel during ladle furnace refining and calcium treatment. ISIJ Int 53(8):1401–1410

9. Zhang L, Liu Y, Zhang Y, Yang W, Chen W (2018) Transient evolution of nonmetallic inclusions during calcium treatment of molten steel. Metall Mater Trans B 49(4):1841–1859
10. Ren Y, Zhang L, Li S (2014) Transient evolution of inclusions during calcium modification in Linepipe steels. ISIJ Int 54(12):2772–2779
11. Ren Y, Zhang Y, Zhang L (2017) A kinetic model for Ca treatment of Al-killed steels using FactSage macro processing. Ironmaking Steelmaking 44(7):497–504
12. Y Ren, L Zhang, W Fang (2017) Effect of addition of Al-based slag deoxidizer on $MgO{\cdot}Al_2O_3$ inclusions in 3Si-Fe steels. Metall Res Technol 114(1):108(1–9)
13. Harada A, Matsui A, Nabeshima S, Kikuchi N, Miki Y (2017) Effect of slag composition on $MgO{\cdot}Al_2O_3$ spinel-type inclusions in molten steel. ISIJ Int 57(9):1546–1552
14. Ren Y, Zhang L, Fang W, Shao S, Yang J, Mao W (2016) Effect of slag composition on inclusions in Si-deoxidized 18Cr-8Ni stainless steels. Metall Mater Trans B 47(2):1024–1034
15. Duan H, Ren Y, Zhang L (2019) Inclusion capture probability prediction model for bubble floatation in turbulent steel flow. Metall Mater Trans B 50(1):16–21
16. Duan H, Ren Y, Zhang L (2019) Fluid flow, thermal stratification, and inclusion motion during holding period in steel ladles. Metall Mater Trans B 50(3):1476–1489
17. Duan H, Ren Y, Thomas BG, Zhang L (2019) Agglomeration of solid inclusions in molten steel. Metall Mater Trans B 50(1):36–41
18. Suito H, Inoue R (1996) Thermodynamics on control of inclusions composition in ultraclean steels. ISIJ Int 36(5):528–536
19. Jiang M, Wang X, Chen B, Wang W (2010) Laboratory study on evolution mechanisms of non-metallic inclusions in high strength alloyed steel refined by high basicity slag. ISIJ Int 50(1):95–104
20. Liu C, Gao X, Ueda S, Kitamura S-y (2019) Change in composition of inclusions through the reaction between Al-killed steel and the slag of CaO and MgO saturation. ISIJ Int 59(2):268–276
21. Zhang L (2006) State of the art in the control of inclusions in tire cord steels—a review. Steel Res Int 77(3):158–169
22. Chen S, Wang X, He X, Wang W (2013) Industrial application of desulfurization using low basicity refining slag in tire cord steel. J Iron Steel Res Int 20(1):26–33
23. Park JS, Park JH (2014) Effect of slag composition on the concentration of Al_2O_3 in the inclusions in Si-Mn-killed steel. Metall Mater Trans B 45(3):953–960
24. Chen S, Jiang M, He X, Wang X (2012) Top slag refining for inclusion composition transform control in tire cord steel. Int J Miner Metall Mater 19(6):490–498

Enrichment of Amorphous B into $Mg_2B_2O_5$ Crystals Through Phase Transformation of B-bearing Blast Furnace Slag

Yu Li, Jintao Gao, and Zhancheng Guo

Abstract B-bearing blast furnace slag is a typical secondary resource of boron (B), which is produced from the ludwigite ore in ironmaking process. However, B is dispersed in the amorphous phase resulted to inefficiently recover from the B-bearing blast furnace slag. In this manuscript, the phase transformation behaviors of B-bearing blast furnace slag were investigated through varying of MgO contents and B_2O_3/SiO_2 (B/S) ratios based on the equilibrium phase diagram, and consequently, the amorphous B was adequately enriched into $Mg_2B_2O_5$ crystals. Firstly, $Mg_2B_2O_5$ crystals as the second precipitated phase were crystallized through adjusting MgO content to 50.00 wt.% and B/S ratio to 1.00 in the primary crystallization region of Mg_2SiO_4. In addition, the transformation of primary crystallization region from Mg_2SiO_4 to $Mg_2B_2O_5$ was achieved through varying B/S ratio to 1.80 and MgO content to 38.00 wt.%, and $Mg_2B_2O_5$ crystals as the first precipitated phase were fully crystallized.

Keywords B-bearing blast furnace slag · Amorphous boron · Boron enrichment · Phase transformation · $Mg_2B_2O_5$ crystals

Instruction

The ludwigite ore in Liaoning province, China, is one of the largest boron resources in the world [1]. However, this B-Mg-Fe symbiotic ore has been primarily adopted to refine iron by the mineral processing in combination with blast furnace ironmaking process [2]. As a result, almost all of the boron (B) and magnesium (Mg) are converted into the B-bearing blast furnace slag along with other gangue minerals [3, 4]. The B-bearing blast furnace slag contains up to 12–22 wt.% of B_2O_3 and 35–45 wt.%

Y. Li · J. Gao (✉) · Z. Guo (✉)
State Key Laboratory of Advanced Metallurgy, University of Science and Technology Beijing, Beijing 100083, People's Republic of China
e-mail: jintaogao@ustb.edu.cn

Z. Guo
e-mail: zcguo@ustb.edu.cn

Z. Peng et al. (eds.), *12th International Symposium on High-Temperature Metallurgical Processing*, The Minerals, Metals & Materials Series,
https://doi.org/10.1007/978-3-030-92388-4_47

of MgO [5–8], and its boron oxide content is higher than that of the raw ludwigite resource. However, the boron fails to be extracted from slag through the conventional beneficiation methods arising from the distribution of boron in amorphous phase [9]. Currently, plenty of B-bearing blast furnace slag is stacked in landfills, which causes a huge waste of high-value boron resources.

In order to recover boron resources, the B-bearing blast furnace slag is mainly adopted by hydrometallurgy methods through converting the B-containing compounds into boric acid or sodium borate, including acid leaching method [10], alkaline leaching method [11], and carbonate-alkaline leaching method [12]. However, boron is mainly existed in the amorphous phase resulting in the low extraction rate of boron [10–12], the large amounts of leachate used, slow leaching rate, and environmental pollution limited the hydrometallurgy methods for recovering boron from the B-bearing blast furnace slag. Actually, the boron element could be precipitated into some specific compounds (e.g. suanite ($Mg_2B_2O_5$) or kotoite ($Mg_3B_2O_6$)) from the molten slag, helping the subsequent separation of the B-containing compounds from others through the hydrometallurgy or beneficiation methods. Sui et al. [6] proposed that the extraction rate of boron from B-bearing blast furnace slag through hydrometallurgy methods was directly related to the precipitation characteristics of boron compounds. Moreover, the boron component existed in a form of $Mg_2B_2O_5$ or $Mg_3B_2O_6$ compound is conductive to improve the extraction rate of boron from the slag through leaching methods, as proposed by Zhang and Sui [5].

In addition, Gao et al. [13] studied the crystallization behaviors of B-bearing blast furnace slag and suggested that nothing was precipitated from the molten slag except the olivine phase, whereas the boron remained in slag phase overall at high temperatures. Liu et al. [14] reported that lower temperatures were beneficial for the formations of $Mg_2B_2O_5$ and $Mg_3B_2O_6$ crystals, which were precipitated from the molten slag together with olivine phase. Based on the phase equilibrium phase diagram of MgO-SiO_2-B_2O_3-CaO-Al_2O_3 and the various experiment results above, olivine is the first and main crystallization phase of B-bearing blast furnace slag. However, only a few boron is precipitated into the $Mg_2B_2O_5$ and $Mg_3B_2O_6$ crystals, whereas most of which exists in the slag phase of amorphous state. Furthermore, the content of B_2O_3 in $Mg_2B_2O_5$ (46.67 wt.%) is higher than that of $Mg_3B_2O_6$ (36.84 wt.%) in theory, so as to upper the extraction rate of boron. Hence, this work ascertains the selective precipitation conditions of B-bearing blast furnace slag melt to adequately enrich boron into the $Mg_2B_2O_5$ crystals, helping the extraction of boron from the slag.

In this study, the phase transformation behaviors of B-bearing blast furnace slag were investigated through varying of MgO contents and B_2O_3/SiO_2 (B/S) ratios based on the equilibrium phase diagram of MgO-SiO_2-B_2O_3-CaO-Al_2O_3, and consequently, the amorphous B was adequately enriched into $Mg_2B_2O_5$ crystals in B-bearing blast furnace slag.

Experimental

Materials

In this work, the B-bearing blast furnace slag was produced from ludwigite in the iron-making process of Fengcheng Iron and Steel Group Co. Ltd., in Liaoning province, China, and its chemical composition is shown in Table 1. The slag has a relatively high concentration of boron, and the mass fraction of B_2O_3 is up to 19.13 wt.%. However, only the significant diffraction peaks of Mg_2SiO_4 appear in the X-ray diffraction (XRD) pattern of the slag, as shown in Fig. 1a. Furthermore, the scanning electron microscopy with energy-dispersive X-ray spectroscopy (SEM-EDX) results of the B-bearing blast furnace slag is shown in Fig. 1b and Table 2, and numbers of equiaxed crystals of Mg_2SiO_4 is presented in the slag, while all boron is presented in the slag phase in an amorphous state.

Table 1 Chemical compositions (wt.%) of B-bearing blast furnace slag

Composition	MgO	SiO_2	B_2O_3	CaO	Al_2O_3	Others	B_2O_3/SiO_2(B/S)
B-bearing blast furnace slag	42.40	31.12	19.13	3.16	1.98	2.21	0.61

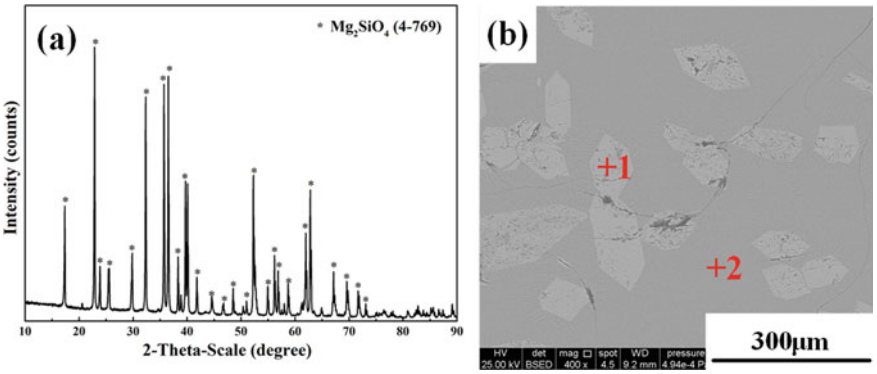

Fig. 1 XRD pattern and SEM image of B-bearing blast furnace slag

Table 2 EDX data of different phases in boron-bearing slag (wt.%)

Positions	No.	Mg	Si	O	Ca	Al	B	Fe	Phases
Figure 1b	Pt. 1	33.32	20.27	46.41	–	–	–	–	Mg_2SiO_4
Figure 1b	Pt. 2	21.23	11.94	49.02	3.47	2.48	10.25	1.61	slag phase

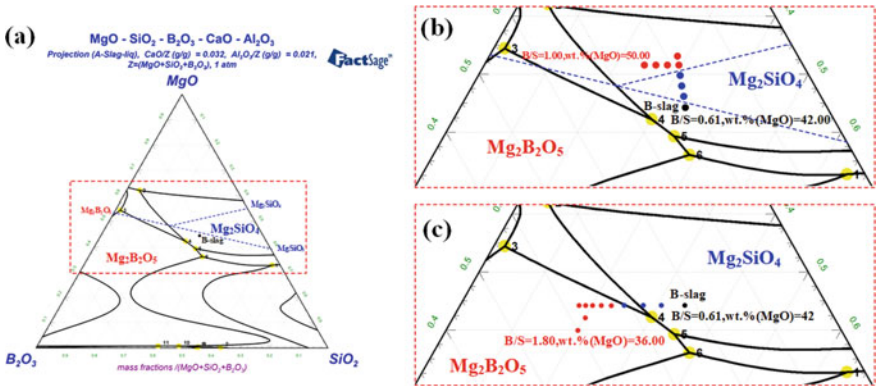

Fig. 2 Equilibrium phase diagram of MgO-SiO_2-B_2O_3-3wt.%CaO-2wt.%Al_2O_3

Enrichment of Amorphous B into $Mg_2B_2O_5$ Crystals as the Second Precipitated Phase

From the equilibrium phase diagram of MgO-SiO_2-B_2O_3-3wt.%CaO-2wt.%Al_2O_3 as calculated using FactSage 7.3 and shown in Fig. 2, the original composition of the B-bearing blast furnace slag was located within the primary crystallization region of Mg_2SiO_4. However, boron exists in the amorphous state in this region, which brings great difficulty to efficiently recover boron from the slag.

According to the phase equilibria of MgO-SiO_2-B_2O_3-3wt.%CaO-2wt.%Al_2O_3, MgO content and B/S ratio are the two main factors for the formation of the crystalline phase in B-bearing blast furnace slag. Therefore, the transformation behaviour of the crystalline phase with various MgO contents and B/S ratios was investigated. The crystallization behavior of B-bearing blast furnace slag was experimented by changing the MgO content from 42.00 to 52.00 wt.% and the B_2O_3/SiO_2 (B/S) ratio from 0.60 to 1.20, as shown in Fig. 2b. 10 g of each slag was thoroughly mixed and filled into a graphite crucible and heated to 1773 K for 30 min in a muffle furnace to ensure a complete melting and homogenization. Subsequently, the slags were cooled slowly to 1373 K with a cooling rate of 2 K/min and then water-quenched rapidly. Subsequently, XRD and SEM-EDX were utilized to analyze the crystalline phase and element migration behavior in the B-bearing blast furnace slag.

Enrichment of Amorphous B into $Mg_2B_2O_5$ Crystals as the First Precipitated Phase

The crystallization of $Mg_2B_2O_5$ crystals is greatly limited by the first precipitated olivine, and two primary crystalline regions consisting of $Mg_2B_2O_5$ and Mg_2SiO_4

are existed in the equilibrium phase diagram of MgO-SiO_2-B_2O_3-3wt.%CaO-2wt.%Al_2O_3. Therefore, the transformation of the primary crystalline phase in B-bearing blast furnace slag for directly enriching boron from the amorphous state into $Mg_2B_2O_5$ crystals is studied further.

The crystallization behavior of B-bearing blast furnace slag was experimented by changing the B/S ratio from 0.60 to 2.20 and the MgO content from 42.00 to 38.00 wt.%, as shown in Fig. 2c. A mass of 10 g of each slag was heated at 1773 K for 30 min. After that, the slags were cooled down slowly to 1373 K with a cooling rate of 2 K/min and then quenched in water rapidly. Subsequently, XRD and SEM-EDX were utilized to analyze the crystalline phase and element migration behavior in the B-bearing blast furnace slag.

Results and Discussion

Enrichment of Amorphous B into $Mg_2B_2O_5$ Crystals as the Second Precipitated Phase

The XRD patterns and SEM images for the crystalline phases in B-bearing blast furnace slag with various MgO contents (B/S = 0.60) are shown in Figs. 3 and 4. Obviously, only the Mg_2SiO_4 appears in the slag, and the diffraction peak intensity

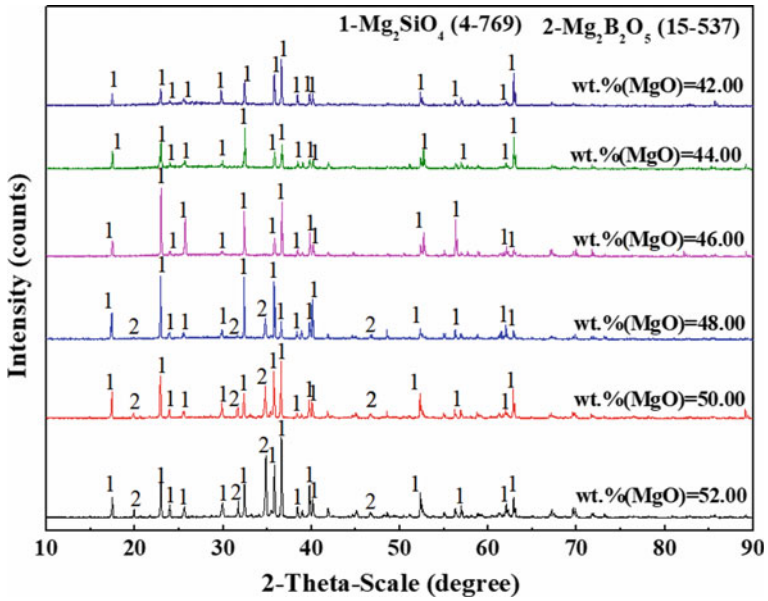

Fig. 3 XRD patterns of B-bearing blast furnace slag with various MgO contents (B/S = 0.60)

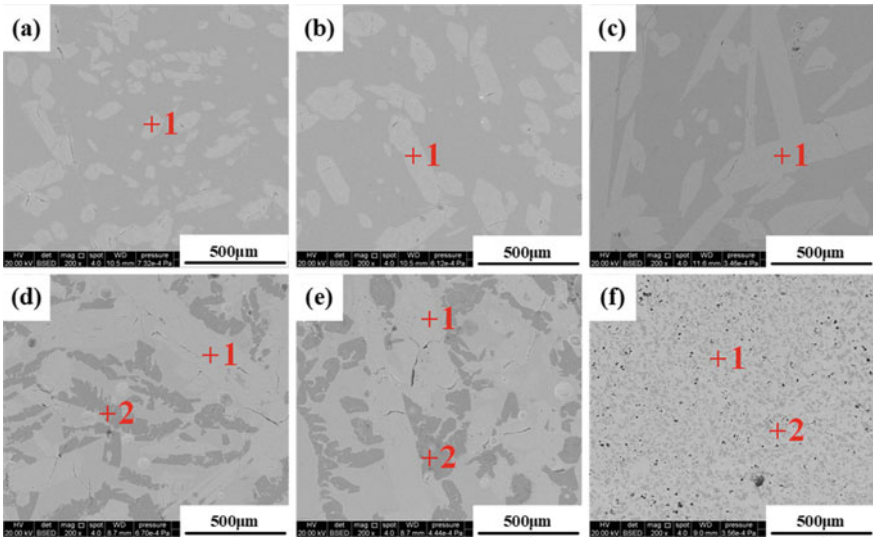

Fig. 4 SEM images of B-bearing blast furnace slag with various MgO contents (B/S = 0.60): **a** wt.% (MgO) = 42.00, **b** wt.% (MgO) = 44.00, **c** wt.% (MgO) = 46.00, **d** wt.% (MgO) = 48.00, **e** wt.% (MgO) = 50.00, **f** wt.% (MgO) = 52.00

and crystal size of Mg_2SiO_4 gradually increase with the MgO content increasing from 42.00 to 46.00. However, boron element is all dispersed in the slag phase, which shows that Mg^{2+} principally combined with SiO_4^{4-} and crystallized into Mg_2SiO_4. When the MgO content increased to 48.00, the diffraction peaks of $Mg_2B_2O_5$ appeared and its diffraction peak intensity gradually increase with the MgO content increasing from 48.00 to 50.00. In addition, fine crystals of $Mg_2B_2O_5$ with sizes of 200–300 μm were evenly distributed among the Mg_2SiO_4 crystals in the slag. As accordingly verified, more Mg^{2+} would react with $B_2O_5^{4-}$ to form $Mg_2B_2O_5$ crystals in the molten slag with the increase of MgO content. However, although the peak intensity of $Mg_2B_2O_5$ increased, the crystal size of $Mg_2B_2O_5$ and Mg_2SiO_4 became smaller and diffusely distributed in the slag phase when the MgO content was further increased to 52.00. It is verified that the appropriate increase of MgO content is beneficial to the nucleation of $Mg_2B_2O_5$ crystals and promotes the combination of Mg^{2+} and $B_2O_5^{4-}$, but the excessive MgO content will increase the slag viscosity and inhibit the growth of $Mg_2B_2O_5$ crystals in the primary crystallization region of Mg_2SiO_4. Therefore, it is favorable to enrich amorphous boron to $Mg_2B_2O_5$ crystals as the MgO content is 50.00 wt.% in the primary crystallization region of Mg_2SiO_4.

Figures 5 and 6 show further the XRD patterns and SEM images for the crystalline phases in the B-bearing blast furnace slag with various the B/S ratios (wt.% (MgO) = 50.00). Obviously, the diffraction peak intensity of $Mg_2B_2O_5$ gradually increases with the increase of B/S from 0.60 to 1.20, as shown in Fig. 5. On the contrary, the crystal size of $Mg_2B_2O_5$ crystals decreases gradually, and the crystal size of

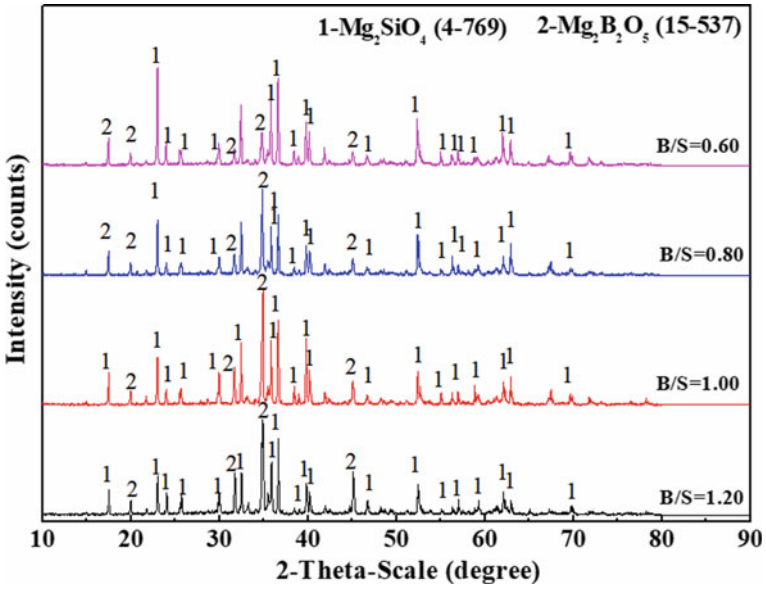

Fig. 5 XRD patterns of B-bearing blast furnace slag with various B/S ratios (wt.% (MgO) = 50.00)

$Mg_2B_2O_5$ crystals only 50–100 μm when the B/S exceeds 1.00, as shown in Fig. 6. In fact, the increase of B/S ratio is beneficial to the nucleation of $Mg_2B_2O_5$ crystals owing to more $B_2O_5^{4-}$ but will lead to the increase of slag viscosity so that the crystal growth of $Mg_2B_2O_5$ as the second precipitated phase is inhibited. Therefore, $Mg_2B_2O_5$ crystals as the second precipitated phase are crystallized through adjusting MgO content to 50.00 wt.% and B/S ratio to 1.00 in the primary crystallization region of Mg_2SiO_4.

Enrichment of Amorphous B into $Mg_2B_2O_5$ Crystals as the First Precipitated Phase

The crystallization of $Mg_2B_2O_5$ crystals is greatly limited by the first precipitated olivine in the primary crystallization region of Mg_2SiO_4, and it is not conducive to the subsequent extraction of boron from the B-bearing blast furnace slag. Therefore, the primary crystalline phase of slag is transformed for fully enriching boron from the amorphous state into $Mg_2B_2O_5$ crystals.

Figures 7 and 8 show the XRD patterns and SEM images for the crystalline phases in the B-bearing blast furnace slag with various the B/S ratios (wt.% (MgO) = 42.00). As the B/S ratio increases from 0.60 to 0.80, the diffraction peak intensity of Mg_2SiO_4 increases and the Mg_2SiO_4 crystals become larger, as presented in Fig. 8a, b. When the B/S ratio increases to 1.00, the diffraction peaks of $Mg_2B_2O_5$ appear

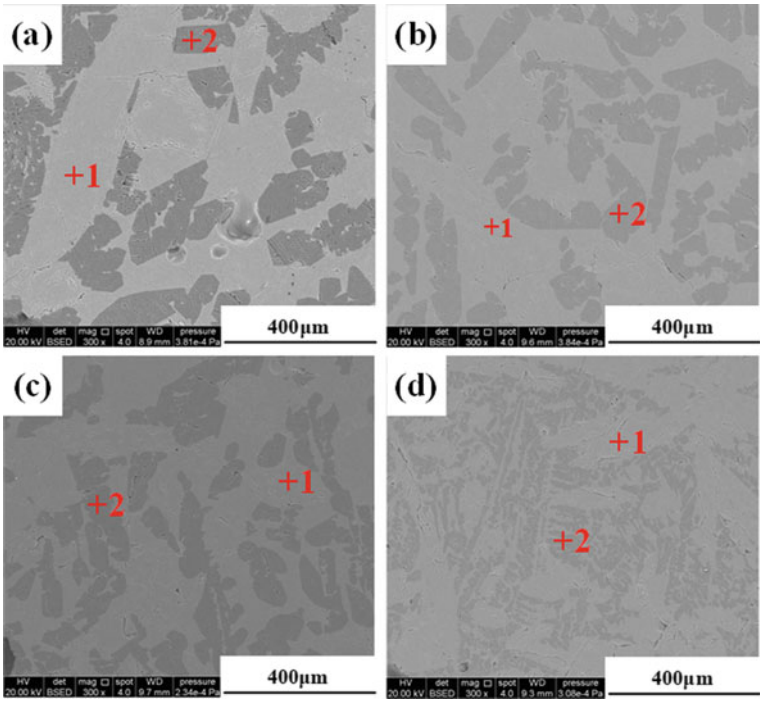

Fig. 6 SEM images of B-bearing blast furnace slag with various B/S ratios (wt.% (MgO) = 50.00): **a** B/S = 0.60, **b** B/S = 0.80, **c** B/S = 1.00, **d** B/S = 1.20

and the diffraction peak intensity of Mg_2SiO_4 decreases. In addition, $Mg_2B_2O_5$ fine crystals with sizes of 50–100 μm are uniformly distributed in the Mg_2SiO_4 crystals of the slag. In fact, based on the equilibria phase diagram of MgO-SiO_2-B_2O_3-3wt.%CaO-2wt.%Al_2O_3, the combination of B/S = 1.00 and wt.% (MgO) = 36.00 is in the primary crystallization region of Mg_2SiO_4. With the formation of Mg_2SiO_4 in the molten slag, the composition of the remaining melt is gradually transfer to the crystallization region of $Mg_2B_2O_5$, and $B_2O_5^{4-}$ start to crystallize with the Mg^{2+} to form $Mg_2B_2O_5$ in the melt. With the further increase in B/S ratio to 1.20, the primary crystallization region is transfer from Mg_2SiO_4 into $Mg_2B_2O_5$. Thus, more Mg^{2+} primarily react with $B_2O_5^{4-}$ in the molten slag, which causes the significant increase of the diffraction peak intensity of $Mg_2B_2O_5$ for B/S = 1.20. The crystal size of $Mg_2B_2O_5$ displays an obvious increase to 150–200 μm with the decrease of Mg_2SiO_4 as shown in Fig. 8d. Subsequently, $Mg_2B_2O_5$ is still the main crystalline phase in slag, and its diffraction peak intensity gradually decreases with the further increase of B/S. Accordingly, the crystal size of $Mg_2B_2O_5$ also increases when the B/S ratio increases from 1.20 to 1.80. However, the crystal size of $Mg_2B_2O_5$ begins to decrease after reaching the maximum crystal size with 200–400 μm at B/S = 1.80. As accordingly verified, the increase of B/S ratio will increase the concentration of $B_2O_5^{4-}$ in slag, which will promote the nucleation of $Mg_2B_2O_5$, but the further

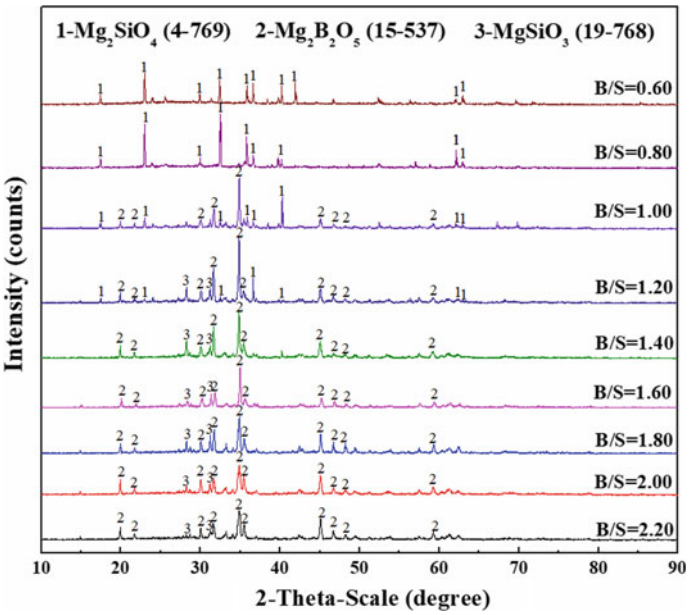

Fig. 7 XRD patterns of B-bearing blast furnace slag with various B/S ratios (wt.% (MgO) = 42.00)

increase of B/S ratio will lead to the inhibition of $Mg_2B_2O_5$ crystal growth. Therefore, it is conducive to enrich amorphous boron to $Mg_2B_2O_5$ crystals as the B/S ratio is 1.80 in the primary crystallization region of $Mg_2B_2O_5$.

In addition, the XRD patterns and SEM images for the crystalline phases in B-bearing blast furnace slag with various MgO contents (B/S = 1.80) are shown in Figs. 9 and 10. Obviously, the diffraction peak intensity of $Mg_2B_2O_5$ gradually increases, and the diffraction peak intensity of $MgSiO_3$ gradually decreases as MgO content decreases from 42.00 wt.% to 40.00 wt.%, as presented in Fig. 9. Moreover, the single diffraction peak of $Mg_2B_2O_5$ appears in the slag when the MgO content is 38.00 wt.%. Accordingly, $Mg_2B_2O_5$ crystal exhibits columnar crystal, and its crystal size increases gradually with decrease of MgO content, and the crystal size of $Mg_2B_2O_5$ is 300–600 μm when the MgO content is 38.00 wt.%. It is verified that the decrease of MgO content is beneficial to the growth of $Mg_2B_2O_5$ crystals and inhibits the combination of Mg^{2+} and SiO_3^{2-} in the primary crystallization region of $Mg_2B_2O_5$. Therefore, the transformation of primary crystallization region from Mg_2SiO_4 to $Mg_2B_2O_5$ was achieved through varying B/S ratio to 1.80 and MgO content to 38.00 wt.% for fully enriching boron into $Mg_2B_2O_5$.

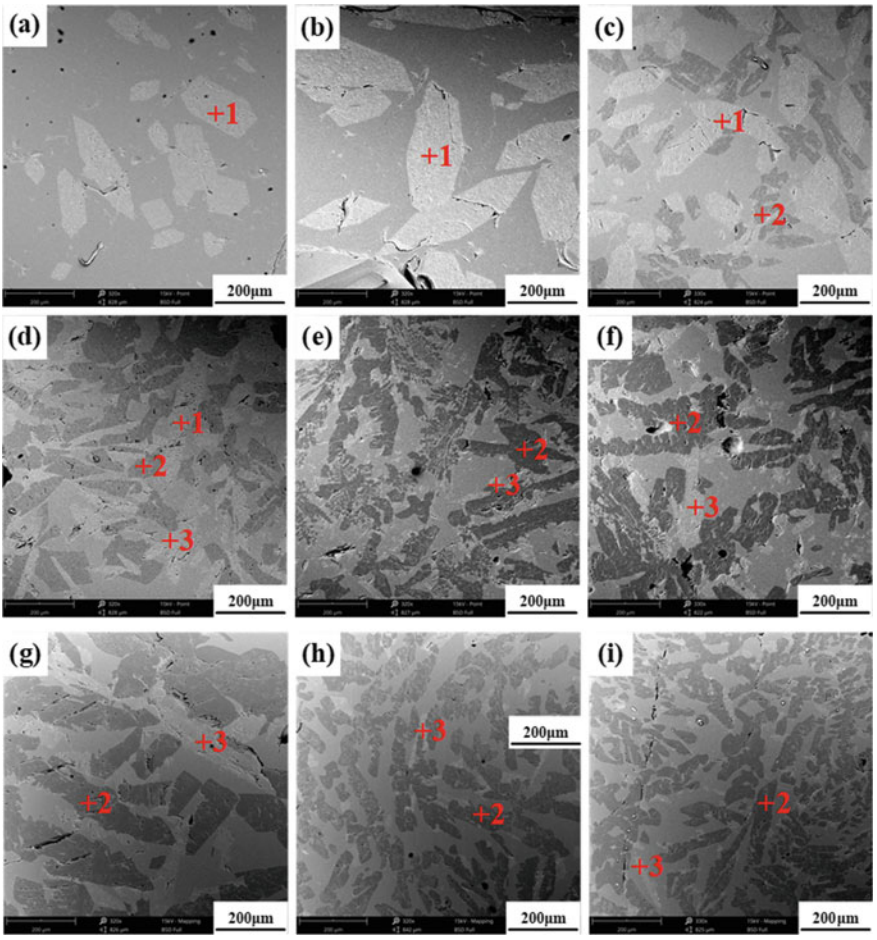

Fig. 8 SEM images of B-bearing blast furnace slag with various B/S ratios (wt.% (MgO) = 42.00): **a** B/S = 0.60, **b** B/S = 0.80, **c** B/S = 1.00, **d** B/S = 1.20, **e** B/S = 1.40, **f** B/S = 1.60, **g** B/S = 1.80, **h** B/S = 2.00, **i** B/S = 2.20

Conclusion

In this study, the phase transformation behaviors of B-bearing blast furnace slag were investigated through varying of MgO contents and B/S ratios based on the equilibrium phase diagram, and consequently, the amorphous B was adequately enriched into $Mg_2B_2O_5$ crystals. The following conclusions could be drawn:

(1) The increase of MgO content and B/S ratio was conductive to enrich amorphous boron into $Mg_2B_2O_5$ crystals in B-bearing blast furnace slag.

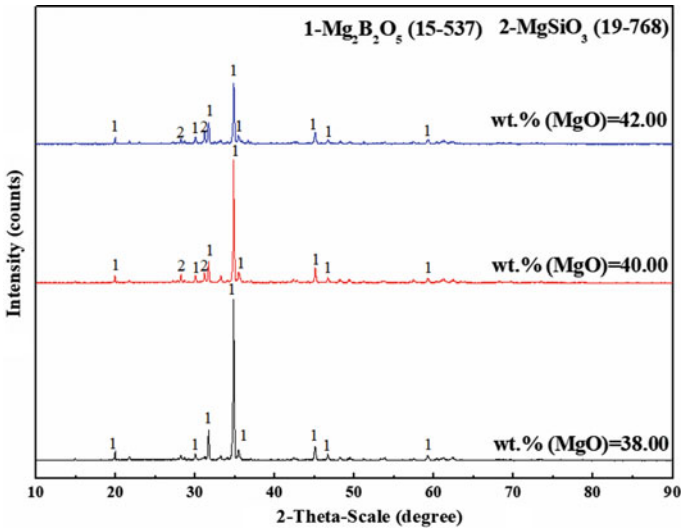

Fig. 9 XRD patterns of B-bearing blast furnace slag with various MgO contents (B/S = 1.80)

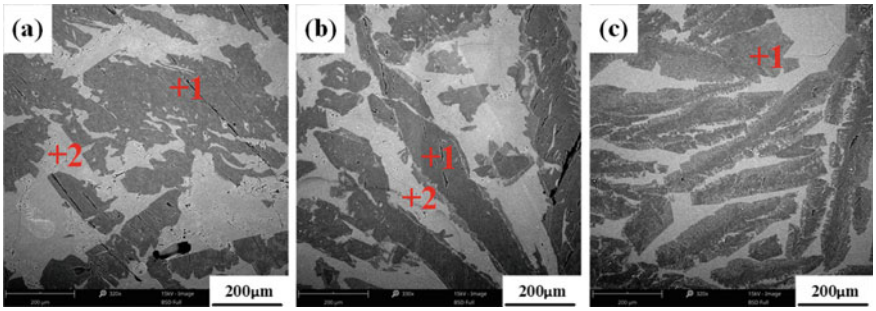

Fig. 10 SEM images of B-bearing blast furnace slag with MgO contents (B/S = 1.80): **a** wt.% (MgO) = 42.00, **b** wt.% (MgO) = 40.00, **c** wt.% (MgO) = 38.00

(2) $Mg_2B_2O_5$ crystals as the second precipitated phase were crystallized through adjusting MgO content to 50.00 wt.% and B/S ratio to 1.00 in the primary crystallization region of Mg_2SiO_4.

(3) The transformation of primary crystallization region from Mg_2SiO_4 to $Mg_2B_2O_5$ was achieved through varying B/S ratio to 1.80 and MgO content to 38.00 wt.%, and $Mg_2B_2O_5$ crystals as the first precipitated phase was fully crystallized.

References

1. Wang G, Wang JS, Yu XY, Shen YF, Zuo HB, Xue QG (2016) Innovative method for boron extraction from iron ore containing boron. Int J Miner Metal Mater 23(3):247–256
2. Li GH, Liang BJ, Rao MJ, Zhang YB, Jiang T (2014) An innovative process for extracting boron and simultaneous recovering metallic iron from ludwigite ore. Miner Eng 56:57–60
3. Ding YJ, Wang JS, Wang G, Ma S, Xue QG (2016) Comprehensive Utilization of Paigeite Ore Using Iron Nugget Making Process. J Iron Steel Res Int 19(6):9–13
4. Liu SL, Cui CM, Zhang XP (1998) Pyrometallurgical separation of boron from iron in ludwigite ore. ISIJ Int 38(10):1077–1079
5. Zhang PX, Sui ZT (1995) Effect of factors on the extraction of boron from slags. Metall Mater Trans B 26(2):345–351
6. Sui ZT, Zhang PX, Yamauchi C (1999) Precipitation selectivity of boron compounds from slags. Acta Mater 47(4):1337–1344
7. Li Y, Gao JT, Huang ZL, Guo ZC (2019) A green method for selective crystallization and extraction of suanite ($Mg_2B_2O_5$) crystals from boron bearing slag under super-gravity. Ceram Int 45(8):10961–10968
8. Li Y, Gao JT, Du Y, Guo, ZC (2020) Competitive crystallization of B, Si, and Mg and two-stage separation of olivine and suanite from boron-bearing slag in supergravity field. Miner Eng 155:106471
9. An J, Xue XX (2014) Life cycle environmental impact assessment of borax and boric acid production in China. Journal of cleaner production. J Clean Prod 66:121–127
10. Xie W, Zou CX, Tang ZY, Fu HG, Zhu XK, Kuang JC, Deng YJ (2017) Well-crystallized borax prepared from boron bearing tailings by sodium roasting and pressure leaching. RSC Adv 7(49):31042–31048
11. Xu YZ, Jiang T, Wen J, Chen WY, Xue XX (2017) Effects of mechanical activation on physicochemical properties and alkaline leaching of boron concentrate. Hydrometallurgy 173:32–42
12. Demirbas A, Yüksuk H, Cakmak I, Kucuk MM, Cengiz M, Alkan M (2000) Recovery of boric acid from boronic wastes by leaching with water, carbon dioxide- or sulfur dioxide-saturated water and leaching kinetics. Resour Conserv Recycl 28:135–146
13. Gao JT, Li Y, Xu GL, Wang FQ, Lu Y, Guo ZC (2017) Separation of olivine crystals and borate containing slag from $CaO–SiO_2–B_2O_3–MgO–Al_2O_3$ system by utilizing super-gravity. ISIJ Int 57(3):587–589
14. Liu LS, Liu WB, Zhan HR, Zhang LP (2014) Research on boron extraction rate of boron-containing slag and its industrial experimental conditions. Appl Mech Mater 467:138–145

Experimental Study on Thermal Shock Resistance of Magnesia Carbon Brick

Lv Changhai, Li Jing, Lv Renxiang, and Tian Shouxin

Abstract In this paper, five kinds of magnesia carbon refractories commonly used in the metallurgical industry were selected to explore their thermal shock resistance. The experiment results showed that the maximum residual flexural strength of sample 2# was 8.07 MPa after three thermal shock cycles under the stress of not more than 0.3 MPa, representing the best thermal shock resistance according to the standard. The accuracy of this result was verified through the tests for the linear expansion performance, ratio of high-temperature flexural strength (*Re*) to Elastic modulus (*E*). Sample 2# showed a basically identical linear expansion rate with that of the high-carbon sample at the test temperature of 1200–1500 °C. The *Re/E* index of sample 2# was relatively high at high temperatures. The comprehensive analysis identified that sample 2# performed the best thermal shock stability. Therefore, sample 2# can serve as qualified refractories of a converter bath.

Keywords Magnesia carbon brick · Thermal shock resistance · Linear expansion rate · *Re*/*E* index

Introduction

With the increasing furnace age of the converter, erosion to different degrees can be found in the steel furnace lining, especially in furnaces producing the steel of low carbon and phosphorus compared with those producing ordinary carbon steel. A laser thickness gauge was used to measure the residual thickness of the furnace lining,

L. Changhai · L. Jing (✉)
State Key Laboratory of Advanced Metallurgy, University of Science and Technology Beijing, Beijing 100083, China
e-mail: lijing@ustb.edu.cn

L. Renxiang
Jinan Ludong Refractories Company, Jinan 250100, China

T. Shouxin
Baosteel Group Central Research Institute, Shanghai 201900, China

Z. Peng et al. (eds.), *12th International Symposium on High-Temperature Metallurgical Processing*, The Minerals, Metals & Materials Series,
https://doi.org/10.1007/978-3-030-92388-4_48

with the result showing that the residual thickness of the molten pool of furnace lining was relatively small. After analyzing the causes of the lining erosion, it was found that due to the drastic changes in the surface temperature, premature damage and uncontrolled abrasion were unavoidable in the furnace lining.

Although no fixed standards are made for refractories used in the molten pool of the furnace lining and the steelmaking technology varies with different product structures, the thermal shock cycle exerts the same effect on the refractories in the molten pool, leading to severe abrasion of refractories and higher production costs. Therefore, it is necessary to choose a refractory product with sound thermal shock resistance; the key of the selection lies in the comparison and evaluation of the thermal shock resistance of different refractories. Thus, in this study, experiments were carried out to explore the thermal shock resistance of magnesia carbon bricks to provide a basis for selecting magnesia carbon bricks used in the molten pool.

Due to various refractory products and different thermal shock conditions, methods to test the thermal shock resistance are not fixed, which, instead, are flexible according to the actual situations [1]. Many of them have been conducted and widely accepted [2], following the test standards of thermal shock resistance of refractories, including DIN 51068, EN 993-11, ASTM-C-1171, and GB/T30873-2014. In this paper, tests were carried out with reference to EN 993-11 and GB/T30873-2014.

Experimental

Materials

Five kinds of magnesia carbon bricks widely used in the industry were selected to conduct thermal shock resistance tests. The raw materials of samples mainly included fused magnesia aggregate, flaky graphite, metallic Al, and Si powder. Phenol-formaldehyde resin liquid of the same amount as the raw material was chosen as the binder, as shown in Table 1. Then the raw materials in each sample were mixed in the high-speed mixer at 100 r/min, shaped using a 1500 t press, and dried at 200 °C for 24 h.

Table 1 Composition of magnesia carbon refractory sample /wt%

Raw materials composition	Samples number				
	1#	2#	3#	4#	5#
Fused magnesia aggregate	67.5	66	66.8	68	63.4
Magnesia powder	12	13	13	6.5	11
Flaky graphite	12	14	16	18	20
Si powder	2.5	1	0.2	2	0
Metallic Al	3	3	1	2.5	2.3

Experimental Method

Test samples were made from the same parts, with sample size: 120 mm × 50 mm × 50 mm and the test temperature of thermal shock resistance being 950 °C. The following test steps were repeated: A heat preservation, B heating, C rapid cooling, and D pressure. The test process is shown in Fig. 1, specifically: (a) First, the samples were held at 300 °C for heat preservation, until the weight was stable, waiting for the heating furnace to meet the test requirements. (b) The heating furnace preheated to 950 ± 10 °C and insulated for 15 min. Then, the samples were put into the heating furnace insulated at 950 °C for 30 min. (c) Emergency cooling was conducted using compressed air under a pressure of 0.1 MPa for 5 min. (d) After emergency cooling, the injection surface was taken as the tension surface to conduct a three-point bending stress test under the pressure of no more than 0.3 MPa.

If the samples break under the bending stress of 0.3 MPa, they will be considered to fail to pass the thermal shock test and vice versa. The residual strength was measured after three thermal shock cycles, while the flexural strength of the sample was measured before tests. According to the results, the residual strength ratio of each sample was calculated, as shown in Table 2.

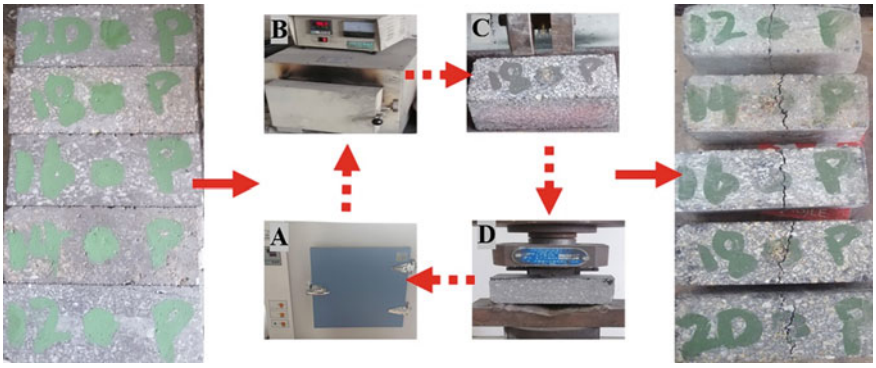

Fig. 1 Thermal shock resistance test

Table 2 Results of thermal shock resistance

Samples number	Mark	Bending stress/MPa	Residual flexural strength/Mpa)
1#	12	0.27–0.29	5.33
2#	14	0.27–0.29	8.07
3#	16	0.27–0.29	7.34
4#	18	0.27–0.29	4.08
5#	20	0.27–0.29	6.90

Results and Discussion

Residual Strength of the Sample

According to the EU standard EN 993-11, samples with higher residual strength represented better thermal shock resistance. The highest residual strength of sample 2# is 8.07 MPa, as shown in Table 2 and Fig. 2.

Figure 2 shows that sample 4# had the lowest residual strength 4.08 Mpa, followed by the residual strength of 1# sample was 5.33 Mpa, but 3# sample and 5# sample was relatively high. The carbon content of sample 5# was 20%. At 950 °C, the formation of carbides, and other substances densified the magnesia carbon brick, increased residual strength. The content of the metal additive Si in the 1# sample and the 4# sample was the highest. It will be oxidized inside the magnesia carbon brick at high temperature, and it was easy reaction for carbon, which lower the residual strength, while the residual strength of the 2#, 3# and 5# samples relatively high. The content of the metal additive Al in the 2# sample and the 5# sample was relatively high. The strength of magnesia carbon refractories containing properly proportioned Al and Si metal additives has been improved [3]. The low proportion of the magnesia powder in sample 4# (6.5%) impeded the wrapping of graphite and metal additives and the

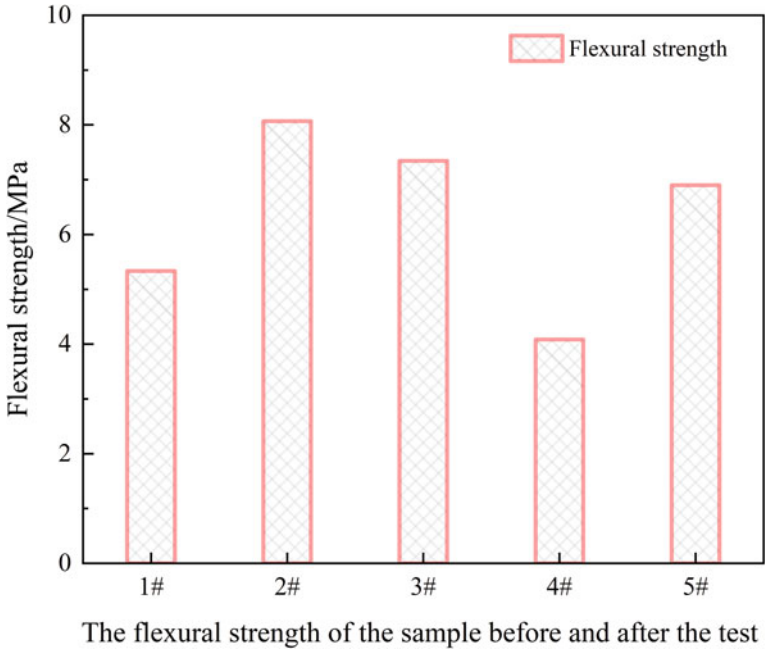

Fig. 2 Changes in flexural strength of samples before and after the test

reduction of the material's thermal expansion coefficient, thus affecting the thermal shock resistance of the sample.

Linear Expansion Rate of the Sample

To further verify the accuracy of the above test conclusions, a thermal dilatometer was used to test the linear expansion rate of the samples. Samples with lower linear thermal expansion rates at high temperatures represented smaller internal thermal stress affected by temperature changes, thus performing greater thermal shock resistance. The sample was collected along the direction parallel to that of shaping, and the size of the columnar sample was Φ10 mm × 50 mm. In order to prevent the oxidization, the sample was collected under the protection of N_2, with a heating rate of 5 °C/min. The test results are shown in Fig. 3.

Figure 3 shows that when the test temperature was 1500 °C, the maximum linear expansion rate of sample 1# was 1.950%, and the minimum linear expansion rate of sample 5# was 1.622%. Sample 3# showed the highest linear expansion rate at the temperature of 100–450 °C. Sample 1# showed the largest linear expansion rate at the temperature of 450–1200 °C. At the temperature of 1200–1500 °C, sample 1# represented the largest linear expansion rate, while the linear expansion rates of samples 2#–5# were basically the same. In the medium temperature range, the linear expansion rates of the samples were inversely proportional to their carbon content: the higher carbon content indicated the lower linear expansion rate. That revealed

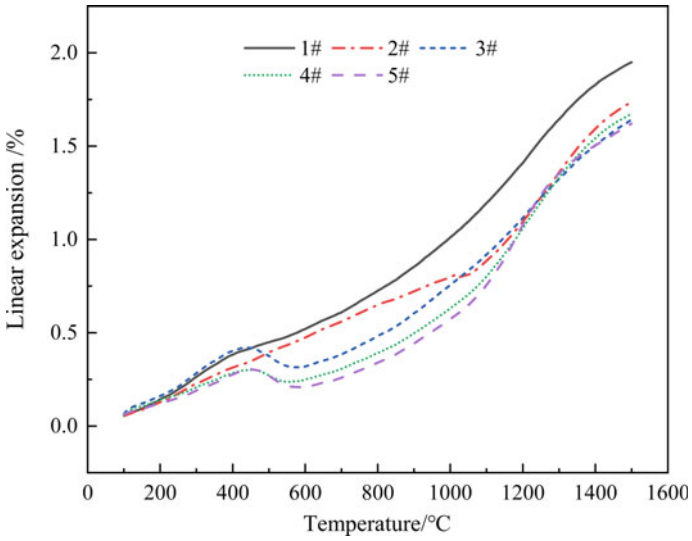

Fig. 3 Magnesia carbon brick linear expansion curve

one of the functions of carbon added in refractories: improving magnesia carbon bricks' thermal shock resistance by repressing its thermal expansion [4].

In practical steelmaking, the furnace lining temperature ranges between 1500 and 1400 °C from the end of steel production to iron mixing. When producing steels with low carbon and phosphorus, the slag splashing layer of the furnace lining is seriously melted due to their process characteristics, increasing the exposure of the furnace lining brick. Under this circumstance, refractory products with poor thermal shock resistance are most prone to damage. Figures 2 and 3 show that sample 1# has the largest linear expansion rate with relatively low residual strength, indicating poor thermal shock resistance.

Re/E *Index of the Sample*

In the previous study [5], the *Re/E* index was used to evaluate the thermal shock resistance of magnesia carbon bricks, identifying that the refractories with the higher strength represented stronger thermal stress resistance, thus were less likely to be destroyed and showed better thermal shock resistance. The material with a higher elastic modulus performed smaller elastic deformation, failing to mitigate and release the thermal stress and impeding its thermal shock resistance. In other words, the larger the *Re/E* index of the sample, the better its thermal shock resistance. In order to accurately evaluate the thermal shock resistance of magnesia carbon bricks, the stress and strain of the sample at 1400 °C were tested. As shown in Table 3 and Fig. 4.

Figure 4 shows that the relatively low *Re/E* value of sample 4# is mainly caused by its high elastic modulus and poor flexural strength. The relatively high *Re/E* value of sample 1# is mainly due to its high flexural strength at high temperatures. The thermal shock resistance of samples 2# and 3# was relatively good. The low *Re/E* value of sample 5# is mainly sparked by its overall low flexural strength before and after the test, high elastic modulus, and poor flexural strength.

Table 3 Elastic modulus and high-temperature flexural strength

Samples number	*Re/E*
1#	1.93
2#	1.88
3#	1.98
4#	1.04
5#	0.98

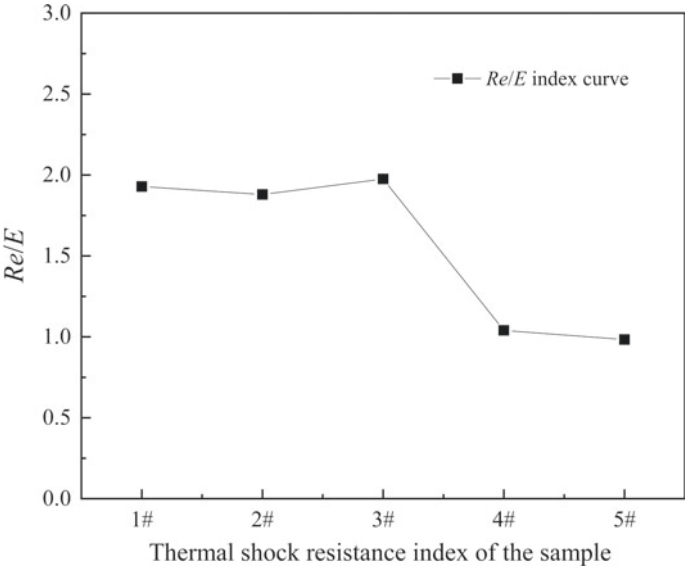

Fig. 4 Thermal shock resistance index of the magnesia carbon brick

Conclusion

In this paper, the thermal shock resistance of magnesia carbon brick samples at 950 °C was tested, and it was found that the residual flexural strength of sample 2# was the highest. According to the standard, the thermal shock stability of this sample should be the best. To verify the accuracy of this conclusion, linear expansion rate and high-temperature *Re*/*E* index were tested. The results show the accurate thermal shock resistance test at 950 °C. The carbon content of sample 2# is 14%. The analysis shows that this type of magnesium-carbon brick can meet the use requirements of refractories of the converter melting pool. The thermal shock stability of magnesium-carbon brick has a great relationship with graphite content, metal additives, magnesia fine powder content, etc. These factors influence the thermal shock stability of the materials by affecting the linear expansion rate and mechanical strength.

Acknowledgements We thank XM and LD company laboratories for the testing equipment provided.

References

1. Harada T (1993) Thermal shock resistance equipment. Taikabutsu Overseas 13:44–51

2. Brochen E., Clasen S, Dahlem E (2016) Determination of the thermal shock resistance of refractories. Refractories Worldforum: manufacturing & performance of high temperature materials. pp 1:79–85
3. Watanabe K, Yabuta K, Okamoto H, Yamamoto, H (1995) Oxidation behavior of MgO-C bricks with various additives. Unitecr'95 Congress. In: Proceedings of the unified international technical conference on refractories 4th biennial worldwide conference on refractories, Global development of refractories, Kyoto, 9–22 Nov 1995
4. Barthel H (1997) Carbon-containing magnesia and magnesia carbon bricks. Pocket manual refractory materials. Vulkan-Verlag, Essen/Germany
5. Fuping Q (2002) Development of low-carbon MgO-C bricks. Foreign refractory materials 5:56–57

Highly Efficient Iron Recovery from Low-Grade Refractory Iron Ores by Coal-Based Direct Reduction

Luxing Feng, Jiandong Chen, Xiao Zhang, Hongchuan Zuo, and Hanjie Guo

Abstract The coal-based direct reduction characteristics of low-grade iron ore during lignite pyrolysis were investigated. Especially, the coal used as reducing agent contains a high percentage of volatile matter and a low percentage of fixed carbon, which could produce a large amount of H_2 and CO during pyrolysis at high temperature and improve the speed of reduction reaction. The results show that appropriately increasing the reduction temperature, increasing the amount of reducing agent, and prolonging the reduction time can all improve the index of DRI. At reduction temperature of 1150 °C, lignite ratio of 20 wt.%, and reduction time of 40 min, the metallization degree of 92.71%, the index of DRI with iron grade of 90.94%, and iron recovery rate of 85.07% were obtained. The results could be useful for comprehensive utilization of low-grade refractory iron ore by the coal-based direct reduction process.

Keywords Direct reduction · Magnetic separation · Low-grade iron ore · Iron recovery

Introduction

Effective utilization of low-grade iron ore is essential in order to reduce production cost and solve the problem of gradual depletion of high-grade iron ore. There are abundant resources of low-grade iron ore in China; nevertheless, it commonly has

L. Feng · J. Chen
Jidong Development Group Co., Ltd, East of Linyin Road, Fengrun District, Tangshan 063000, China

X. Zhang · H. Zuo
Tangshan Jidong Equipment Engineering Co., Ltd, Tangshan Caofeidian District Equipment Manufacturing Industrial Park, Tangshan 063200, China

H. Guo (✉)
School of Metallurgical and Ecological Engineering, University of Science and Technology Beijing, 30 Xueyuan Road, Beijing 100083, China
e-mail: guohanjie@ustb.edu.cn

Z. Peng et al. (eds.), *12th International Symposium on High-Temperature Metallurgical Processing*, The Minerals, Metals & Materials Series,
https://doi.org/10.1007/978-3-030-92388-4_49

the characteristics of low iron content, fine iron minerals, complicated composition, and high content of harmful elements [1, 2]. More than 97% of iron ores need to be processed before entering the blast furnace for smelting. It also contains iron silicate gangue minerals with similar physical and chemical properties. As a result of these characteristics, it is difficult to concentrate the ore by conventional processing methods [3–5]. Efficient and economical use of these mineral resources remains a challenge [6–8].

Coal-based direct reduction followed by magnetic separation is an effective way to deal with this type of iron ore [9–12]. Iron oxides can be reduced to pure metallic iron and then separated from the ores by magnetic separation. Products with a degree of metallization exceeding 85% can be obtained from raw ores, which were reduced at high temperature (1100–1250 °C) for 60–100 min [9, 10, 13], from which 80% of the iron content could be recovered (TFe $\geq$ 90%) by magnetic separation. However, these laboratory studies recommend a high reduction temperature range, which is impractical for commercial production such as the high energy consumption and the formation of massive fayalite phases [14–17]. The fayalite is formed by the solid-phase reaction between SiO_2 and FeO during the reduction process, which is difficult to reduce, and its low magnetism can result in loss of iron during magnetic separation process. In addition, fayalite will melt at 1177 °C and form liquid phase [18], which will hinder the further reduction of iron oxides. So, accelerating reduction presence of iron oxide to iron and avoiding forming large numbers of fayalite are important.

It is well known that the amount of volatile matter produced by low-rank coals, such as lignite coal and subbituminous coal, is higher (25–65 wt.%) than that produced by high-rank coal. Based on the previous works, the low-rank coal showed high reactivity as a reducing agent, because volatile matter could produce large amounts of reducing gas and deposited carbon during pyrolysis process, which can ameliorate reducing atmosphere, improve reduction rate of the iron oxide, and decrease the generation of fayalite. In this study, a method of reduction roasting and magnetic separation of iron ore with high volatile coal as reducing agent was used to deal with a low-grade refractory iron ore. The reduction characteristics of low-grade iron ore during lignite pyrolysis were investigated to seek a feasible route for efficient utilization of low-grade iron resources.

Experimental

Materials

The iron ore sample used for this investigation was obtained from Xiaohebian Iron Mine in Yunnan Province of China. The chemical multi-element analysis for the compositions and the phase analysis of iron are given in Table 1 and Table 2, respectively. The results of multi-element analysis demonstrated that the main valuable

Table 1 Multi-element analysis of the iron ore sample

Compositions	Fe	FeO	Al_2O_3	SiO_2	CaO	MgO	P	S
Mass fraction (wt.%)	22.35	12.38	3.04	31.82	16.19	1.89	0.026	0.299

Table 2 Phase analysis of iron for sample

Phase name	Fe in magnetite	Fe in siderite	Fe in hematite and limonite	Fe in pyrite	Fe in silicate	Total
Content (wt.%)	12.08	1.21	5.00	0.426	3.64	22.35
Percentage (%)	54.04	5.41	22.37	1.90	16.28	100

Table 3 Proximate analysis results of lignite

Compositions	Fixed carbon	Volatile matter	moisture	Ash
Mass fraction (wt.%)	43.60	41.05	4.61	10.74

metal in the sample was Fe, with a content of 22.35 wt.%. The amounts of impurities like P and S were very low by 0.026 wt.% and 0.299 wt.%, respectively.

From Table 2, the iron elements were mainly found to exist in the form of magnetite, hematite, and limonite in the low-grade iron ore sample, and nearly half of the iron is difficult to recover by conventional methods.

The lignite, a low-rank coal, used in this study was obtained from Xinjiang Province of China. The proximate analyses were based on GB/T212-2008 in China as shown in Table 3, respectively. Table 3 shows that the lignite has a low fixed carbon content of 43.60 wt.%, high volatile content of 41.05 wt.%, and low ash content of 10.74 wt.%, which is suitable for coal-based reduction of iron ores. The low-rank coal is able to produce deposited carbon at temperatures of 400–600 °C and a large amounts of reducing gas (H_2 and CO) above 700 °C, which significantly promotes the reduction reaction [19]. The gasification rate of fixed carbon in coal has reached to 87.98% at temperatures of 950 °C, respectively, guaranteeing the process will achieve rapid reduction. The coal was crushed to 5–20 mm size.

Methods

Four group experiments were designed to investigate the effects of different parameters on iron recovery from iron ore, such as reduction temperature, the ratio of coal to iron ore, reduction time, and gringing time. The experimental flowsheet included preheating, electric heating rotary kiln reduction, cooling, grinding, and magnetic separation procedures, as shown in Fig. 1. Firstly, 1000 g of low-grade ore had a

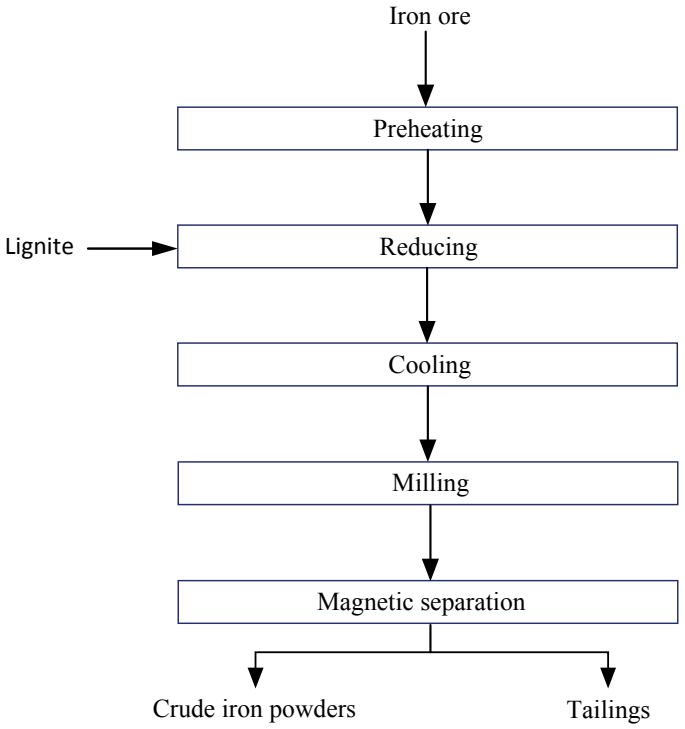

Fig. 1 Schematic diagram of reduction and magnetic separation process of low-grade iron

controlled particle size distribution from 0 to 15 mm. Secondly, the iron ore was charged into a laboratory scale electric heating rotary kiln with a diameter of 80 mm and a length of 1000 mm, rotating at 1 rpm when the temperature was raised to a given value. Ten min later, divide the lignite into ten parts on average and put them into the rotary kiln, respectively. After a given time, the reduced samples were taken out when cooling down to 100 °C in the airtight kiln. Next, the cooled reduced sample was ground with a ball grinding mill to a given particle size. Finally, the ground material was separated to produce crude iron powders with the Davis magnetic tube at an optimized intensity of 0.1 T. Eventually, the wet iron powders and the tailing were filtered and dried in a vacuum oven. The grades of magnetic concentrate were analyzed by chemistry method.

Results and Discussion

The effects of main process parameters, which included reduction temperature, lignite ratio (the mass ratio of lignite to raw ore), reduction time, and milling time, on the separation and recovery of iron were examined.

Effects of Reduction Temperature on Iron Recovery

Reduction temperature is the main factor that impacts the reaction. In this experiment, reduction temperatures were selected as 950, 1050, 1150, and 1250 °C. Other parameters were kept constant as following: lignite ratio of 20 wt.% (200 g lignite: 1000 g raw ore), reduction time of 40 min, milling time of 10 min. Results were shown in Fig. 2.

From Fig. 2, with the increasing of reduction temperature, the metallization degree of roasted samples and iron grade of crude iron powders (magnetic concentrate) and iron recovery rate increased gradually. The recovery rate of iron increased rapidly

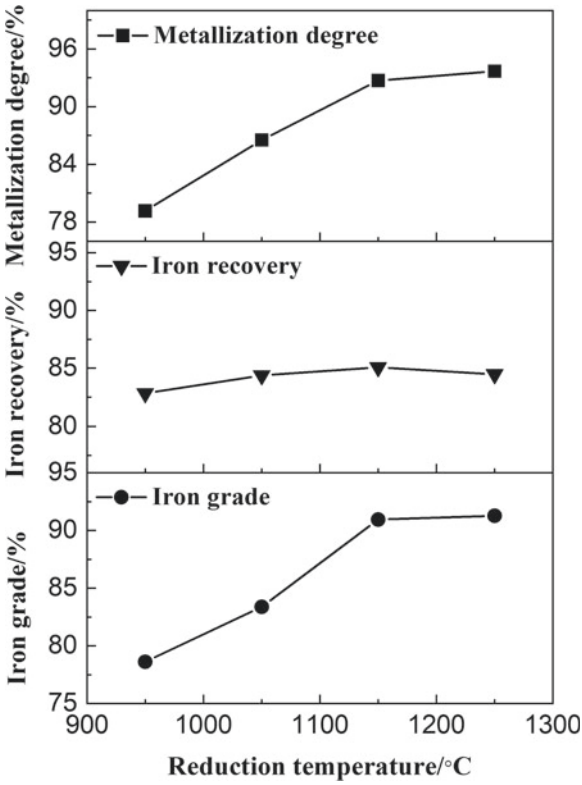

Fig. 2 Effects of reduction temperature on iron recovery (lignite ratio: 200:1000, reduction time: 40 min, milling time: 10 min)

as the reduction temperature increased from 950 to 1250 °C, and then decreased slightly. The maximum recovery rate of iron is about 85.07%, the metallization degree is 92.71%, and iron grade is 90.94 wt.%.

It is well known that coal pyrolysis generates gas products such as H_2, CO, CO_2, and CH_4, which were strongly effected by the pyrolysis conditions such as temperature, gas flow rate, and type of catalyst [20–22]. At high temperatures, coal pyrolysis resulted in a larger amount of gas products; hence, the indirect reaction of iron ore with gas components such as CO and H_2 was accelerated. As a result, the metallization degree of iron ore increased at higher temperatures, which was beneficial to improve iron recovery and iron grade.

Effects of Lignite Ratio on Iron Recovery

In order to investigate the optimum content of lignite, different ratios of lignite to iron ore were studied, respectively. Under the conditions of reduction temperature 1150 °C, reduction time 40 min, and milling time 10 min, the effect of lignite ratio on the separation and recovery of iron was studied, and the ratio of lignite to iron ore was selected as 100:1000, 150:1000, 200:1000, and 250:1000. Results were shown in Fig. 3.

As shown in Fig. 3, with the increasing of lignite ratio, iron grade and iron recovery rate of magnetic concentrate slowly increased. The metallization degree of roasted product rapidly increased as the lignite ratio increased from 10 to 20 wt.%, and then leveled off after lignite ratio at above 20 wt.%. Theoretically, the higher the quality of coal, the longer the duration of strong reduction atmosphere, which is more conducive to the reaction. However, the high quality of coal will also bring a series of problems. First, the increase of cost. Secondly, the sulfur content in coal is generally high, which not only pollutes the environment, but also may lead to the problem of too high sulfur in the final iron concentrate. Hence, the optimal lignite ratio was determined to be 20 wt.%.

Effects of Reduction Time on Iron Recovery

By keeping lignite ratio of 20%, the samples were roasted at 1150 °C for different time. The effect of reduction time on the recovery of iron is shown in Fig. 4.

As shown in Fig. 4, the metallization degree of roasted samples and iron grade of crude iron powders (magnetic concentrate) and iron recovery rate increased rapidly as the reduced time increased from 20 to 40 min, but leveled off after reduced time passing 40 min. It was inferred that when the reduction temperature was 1150 °C, the optimum reduction time was about 40 min, during which iron oxides reducing was mostly completed except for some difficult reduction phases such as $Ca_2Fe_2O_5$ and $CaFe_2O_4$ [23].

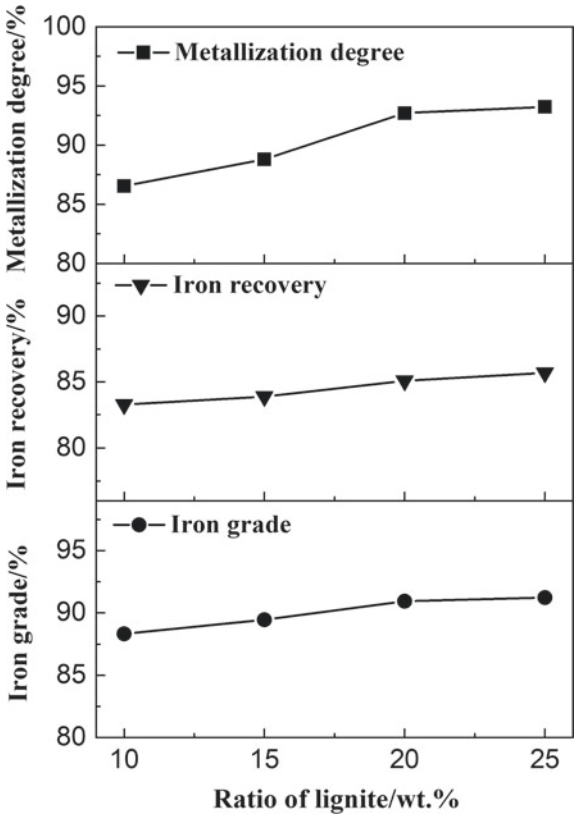

Fig. 3 Effects of the lignite ratio on iron recovery (reduction temperature: 1150 °C, reduction time: 40 min, milling time: 10 min)

Effects of Milling Time on Iron Recovery

Because of the complex dissemination characteristics of roasted products, they needed to be milled before magnetic separation. The effect of milling time of the roasted samples on the recovery of iron was tested here. The conditions of magnetic reducing were as the following: the reduction temperature of 1150 °C for 40 min, with the proportion of lignite and iron ore at 200:1000. The results were shown in Fig. 5.

With the increasing of milling time, the percentage of minus 74 μm and iron grade in the concentrate increased rapidly, while recovery rate of iron decreased slightly. The decrease of particle size was beneficial to monomer dissociation of metallic iron particles in reduced product feeding to magnetic separation. The monomer dissociation is extremely important to metallic iron particles to be effectively recovered by magnetic separation. At 97.32% of particles less than 74 μm, sufficient monomer dissociation of metallic iron particles was obtained. The crude iron powders, produced under this particle size, contained 90.94% iron grade with iron recovery rate of 86.13%.

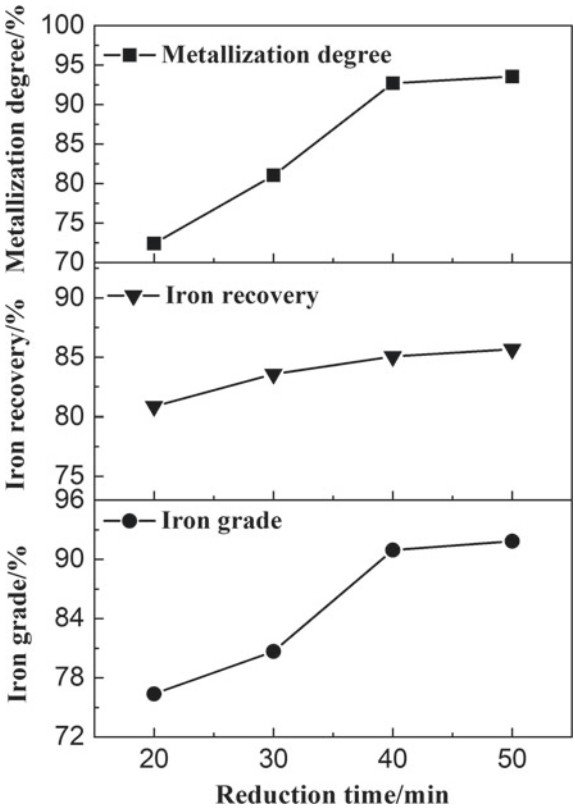

Fig. 4 Effects of reduction time on iron recovery (reduction temperature: 1150 °C, lignite ratio: 200:1000, milling time: 10 min)

Conclusion

This iron ore is characterized by its low iron grade, high silicate content. Quartz, magnetite, hematite, limonite, calcite, mica, and kaolinite existed in the iron ore as main phases, and nearly half of the iron is difficult to recover by conventional methods. Effective utilization of low-grade iron ore by lignite pyrolysis was proposed to increase the degree of reduction and iron recovery. The behavior of the reduction reaction during lignite pyrolysis over low-grade iron ore was evaluated. The reduction temperature, lignite ratio, reduction time, and milling time of roasted samples are four main factors which affect the iron recovery. Optimized process conditions are obtained by one factor at a time tests for recovery iron from low-grade iron as the following: roasting at 1150 °C for 40 min, lignite ratio of 20 wt.%, milling 10 min, and particle size of 97.32% less than 74 μm in the roasted product. Under the optimum reducing conditions, the metallization degree of roasted samples was 92.71%, and the iron grade of magnetic concentrate was 90.94% with iron recovery rate of 85.07%.The results demonstrate that coal-based direct reduction followed by magnetic separation for recovery iron from low-grade iron is the feasibility using

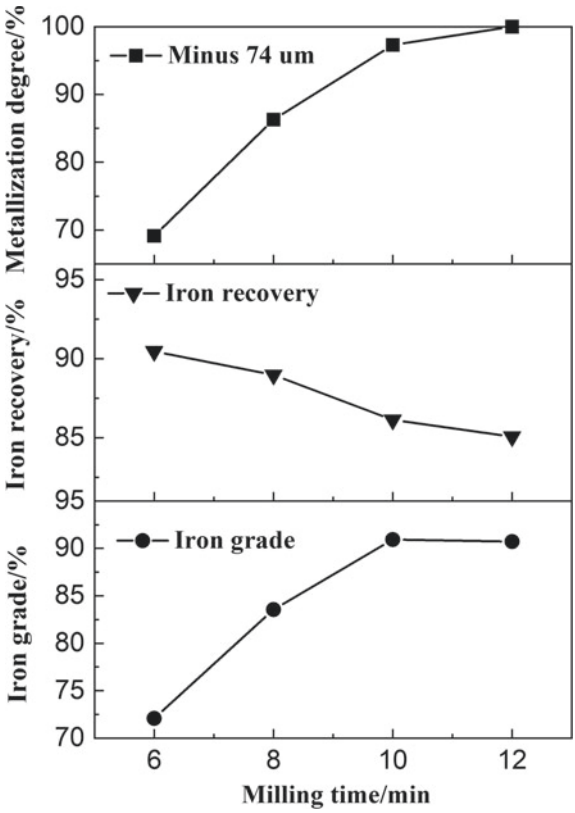

Fig. 5 Effects of milling time on iron recovery (reduction temperature: 1150 °C, reduction time: 40 min, lignite ratio: 200:1000)

lignite as reductant. Lignite pyrolysis at high reduction temperatures is beneficial to accelerate the conversion of iron oxides to iron.

References

1. Man Y, Feng JX, Li FJ et al (2014) Influence of temperature and time on reduction behavior in iron ore-coal composite pellets. Powder Technol 256:361–366
2. Park H, Sahajwalla V (2014) Effect of alumina and silica on the reaction kinetics of carbon composite pellets at 1473 K. Trans Iron Steel Inst Jpn 54(1):49–55
3. Zhang JS (2007) Status and trend of exploitation and utilization of iron ore resources in China. Iron Steel 17(1):1–6
4. Yuan ZT, Gao T, Yin WZ et al (2007) Status quo and development orientation of China's refractory ore resource utilization. Metal Mine 367(1):1–6
5. Hou ZL (2005) Current situation and potential of iron ore resources in China. Exposition Geol Prospect 20(4):242–247
6. Yu W, Sun TC, Hu TY (2015) Desulfuration behavior of low-grade iron ore-coal briquette during the process of direct reduction followed by magnetic separation. ISIJ Int 55(1):329–331

7. Seifelnassr AAS, Moslim EM, Abouzeid AZM (2013) Concentration of a Sudanese low-grade iron ore. Int J Miner Process 122:59–62
8. Rath SS, Rao DS, Mishra BK (2016) A novel approach for reduction roasting of iron ore slime using cow dung. Int J Miner Process 157:216–226
9. Yang CC, Zhu DQ, Pan J et al (2017) Simultaneous recovery of iron and phosphorus from a high-phosphorus oolitic iron ore to prepare Fe-P alloy for high-phosphorus steel production. JOM 69:1663–1668
10. Swagat S, Hrushikesh R, Sahoo B et al (2013) Optimization of flotation variables for the recovery of hematite particles from BHQ ore. Int J Miner Metall Mater 20(7):605–611
11. Rashid R, Salleh HM, Ani MH et al (2014) Reduction of low-grade iron ore pellet using palm kernel shell. Renew Energy 63:617–623
12. Sun YS, Han YX, Gao P et al (2014) Distribution behavior of phosphorus in the coal-based reduction of high-phosphorus-content oolitic iron ore. Int J Miner Metall Mater 21(4):331–338
13. Sun YS, Han YX, Peng G et al (2013) Recovery of iron from high phosphorus oolitic iron ore using coal-based reduction followed by magnetic separation. Int J Miner Metall Mater 20(5):411–419
14. Ye Q, Peng ZW, Li GH et al (2019) Microwave-assisted reduction of electric arc furnace dust with biochar: an examination of transition of heating mechanism. ACS Sustain Chem Eng 7:9515–9524
15. Ma BZ, Xing P, Yang WJ et al (2017) Solid-state metalized reduction of magnesium-rich low nickel oxide ores using coal as the reductant based on thermodynamic analysis. Metall Mater Trans B 48:2037–2046
16. Liu WC, Yang JK, Xiao B (2009) Application of Bayer red mud for iron recovery and building material production from alumosilicate residues. J Hazard Mater 161:474–478
17. Kim WH, Lee YS, Suh IK et al (2012) Influence of CaO and SiO_2 on the reducibility of wustite using H_2 and CO gas. ISIJ Int 52:1463–1471
18. Fu JY et al (1996) Sintering and pelletizing. Central South University Press, Changsha
19. Cahyono RB, Rozhan AN, Yasuda N et al (2013) Catalytic coal-tar decomposition to enhance reactivity of low-grade iron ore. Fuel Process Technol 113:84–89
20. Folgueras MB, Díaz RM, Xiberta J (2005) Pyrolysis of blends of different types of sewage sludge with one bituminous coal. Energy 30(7):1079–1091
21. Pütün E (2010) Catalytic pyrolysis of biomass: effects of pyrolysis temperature, sweeping gas flow rate and MgO catalyst. Energy 35(7):2761–2766
22. Park SW, Jang CH (2012) Effects of pyrolysis temperature on changes in fuel characteristics of biomass char. Energy 39:187–195
23. Yang HF, Jing LL, Zhang BG (2011) Recovery of iron from vanadium tailings with coal-based direct reduction followed by magnetic separation. J Hazard Mater 185:1405–1411

Numerical Simulation of Dispersion Behavior of Modifier Particle in Hot Slag with Mechanical Stirring

Chunming Zhang, Nan Wang, and Min Chen

Abstract To improve the modification efficiency and effect of hot slag with mechanical stirring, the dispersion behavior of modifier particles with stirring time is investigated by numerical simulation. The hot slag is divided into six regions, and the particle number concentration in different regions of hot slag is evaluated and discussed further. In addition, the effects of particle size and adding position on the distribution of modifier particle are also elucidated. The results show that four circulation streams on each side of a cross-shape impeller which are beneficial to complete mixing between modifier particles and hot slag. A dynamic steady state of particle motion in each region can be obtained within 10 s by mechanical stirring. The particle diameter of 5 mm and adding modifier particle directly to the vortex core of hot slag are more conducive to hot slag modification.

Keywords Hot slag · Mechanical stirring · Modification · Particle number concentration

Introduction

Large amounts of steel slag is generated during the process of steel production, which accounts for about 10% to 15% of steel output [1]. Steel slag has a high-potential industrial value and contains many valuable elements such as Fe, Cu, Zn, Mn, Ca, Mg, Si. However, steel slag also contains a little of CaO and MgO, which may cause volume expansion due to reaction with water, and this seriously affects the effective recovery and utilization of steel slag [2–4]. Therefore, effective modification of steel slag is an effective way to improve the recycling rate of steel slag. The modified slag could be used as the raw material for road construction, engineering backfilling, and glass–ceramics preparation. Therefore, the effective utilization of steel slag is an urgent issue to achieve emission reduction in the metallurgical industries [5–8].

C. Zhang · N. Wang (✉) · M. Chen
School of Metallurgy, Northeastern University, Shenyang 110819, Liaoning, China
e-mail: wangn@smm.neu.edu.cn

Z. Peng et al. (eds.), *12th International Symposium on High-Temperature Metallurgical Processing*, The Minerals, Metals & Materials Series,
https://doi.org/10.1007/978-3-030-92388-4_50

To improve the modification efficiency, using an impeller to stir the hot slag can effectively promote the mixing effect of steel slag and modifier. Mechanical stirring is a conventional method in the metallurgical industries, and the most representative one is the KR stirring process for hot steel desulfurization. The desulfurizer particles added to the hot steel surface could be efficiently entrained into the lower part of hot steel by mechanical stirring to achieve a good desulfurization effect [9–11]. Ji et al. [12] studied the influence of variable speed stirring on the dispersion of desulfurizer in KR process. The results showed that the stirring mode of 50–90 rpm can achieve the best mixing of desulfurizer.

Sukawa et al. [13] studied the influence of impeller shape and size on dispersion characteristics of desulfurizer through water model experiments, and the lightness change of particle image is used to reflect the mixing degree of particles. Wu et al. [14] studied a new desulphurization technology using pulsed and rotary stirring-injection, and the results showed that the mixing time of the melting bath was apparently shortened. Additionally, the practical hot metal experiments were also carried out to investigate the desulfurizer behavior [9, 15–17].

For modification of hot slag, it is very necessary to improve the utilization ratio of modifiers and even dispersion in hot slag, which are the key factors to develop a feasible hot slag modification process. In the present work, the dispersion behavior of modifier particles with stirring time was investigated by numerical simulation. The hot slag is divided into six regions, and the number concentration of modifier particle in different regions of hot slag was evaluated and discussed further. In addition, the effects of particle size and adding position on the distribution of modifier particle were also elucidated. The research results are of great significance for improving the modification effect of hot slag, and further promoting the comprehensive utilization of metallurgical slag.

Model Description

Geometrical Model and Numerical Methods

The weight of hot slag is 25 t which is stirred with a cross-shaped impeller, and the stirring speed is constant of 60 rpm. Three thousand modifier particles of the same size are added to the surface of hot slag after the slag surface forming a stable vortex, and analyze the influence of particle size and adding position on dispersion characteristics of modifier. The commercial software ANSYS FLUENT 16.0 was used in this study. The numerical simulations were carried out based on around four hundred thousand cells. The three-dimensional mesh of hot slag and impeller is shown in Fig. 1. The height of hot slag surface is 1.76 m, and the distance from upper surface of impeller to slag surface (immersion depth) is 500 mm. The dimensions and physical properties used in the numerical simulation are listed in Table 1. The

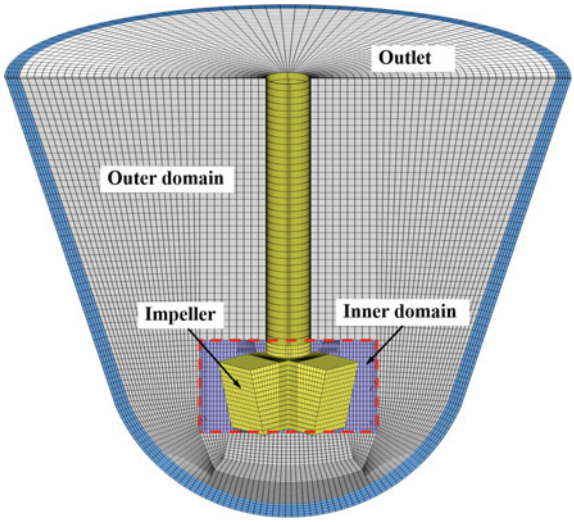

Fig. 1 Structure and computational mesh of the hot slag and impeller

Table 1 Main parameters used in numerical simulation

Parameter	Value
Height of hot slag, (mm)	1760
Blade height, (mm)	360
Blade width, (mm)	570
Impeller immersion depth, (mm)	500
Impeller rotation speed, (rpm)	60
Density of hot slag, (kg·m^{-3}), (1773–1823 K)	3000
Viscosity of hot slag, (Pa·s), (1773–1823 K)	0.13
Diameter of modifier particle, (mm)	1–10
Density of modifier particle, (kg·m^{-3})	2500

number of computational grids in mathematical model is about 400,000, and the sliding-mesh (SM) method [18, 19] is used to couple the inner and outer domains. All solid surfaces are set as non-slipping walls, and the mouth of slag pot is set to pressure-outlet boundary condition. The boundary condition type of modifier particle is "reflected", and the particle retains all the normal or tangential momentum after rebound.

Mathematical Model

Basic Assumptions

The mathematical model was formulated based on the following assumptions:

(1) The hot slag is considered to be an incompressible fluid;
(2) Heat transfer in hot slag is not considered;
(3) The modifier particles are assumed to be rigid spheres, and the density and size of particles do not change with stirring time;
(4) Chemical reactions and solidification in hot slag are not considered.

Fluid Flow Model

In the present work, the volume of fluid model (VOF) is used to simulate the vortex caused by mechanical stirring on the surface of hot slag. For hot slag, the continuity equation and transient Navier–Stokes equation can be expressed in Eqs. (1)–(2).

$$\frac{1}{\rho_1}\left[\frac{\partial}{\partial t}(\alpha\rho_1) + \nabla\cdot(\alpha\rho_1 v_1)\right] = 0 \tag{1}$$

$$\frac{\partial}{\partial t}(\rho v) + \nabla\cdot(\rho v v) = -\nabla p + \nabla\cdot(\mu\cdot\nabla v) + \rho g + F_\sigma + F_{\text{other}} \tag{2}$$

where ρ_1 is the slag density; v_1 is the flow velocity of hot slag; α is the volume fraction of hot slag; p is static pressure; g is gravity; ρ and μ are the density and viscosity of the air-slag mixture, respectively. F_σ is the surface tension between air and slag, and F_{other} is the interaction momentum per unit mass transferred from the discrete phases.

Standard k–ε model can be expressed in Eqs. (3)–(5).

$$\frac{\partial}{\partial t}(\rho_1 k) + \nabla\cdot(\rho_1 k v_1) = \nabla\cdot\left[\left(\mu_1 + \frac{\mu_t}{\sigma_k}\right)\nabla k\right] + G_k + G_b - \rho_1\varepsilon \tag{3}$$

$$\frac{\partial}{\partial t}(\rho_1\varepsilon) + \nabla\cdot(\rho_1\varepsilon v_1) = \nabla\left[\left(\mu_1 + \frac{\mu_t}{\sigma_\varepsilon}\right)\nabla\varepsilon\right] + C_{1\varepsilon}\frac{\varepsilon}{k}(G_k + C_{3\varepsilon}G_b) - C_{2\varepsilon}\rho_1\frac{\varepsilon^2}{k} \tag{4}$$

$$\mu_t = \frac{\rho_1 C_\mu k^2}{\varepsilon} \tag{5}$$

where G_k and G_b represent the generation of turbulence kinetic energy due to the mean velocity gradients and buoyancy, respectively. $C_{1\varepsilon}$, $C_{2\varepsilon}$, $C_{3\varepsilon}$, and C_μ are constants, and σ_k and σ_ε are turbulent Prandtl numbers.

The discrete particle model (DPM) is used to describe the motion behavior of particles. The drag force, gravity, and other forces that cannot be ignored of particles are considered in this paper. The force balance equation of particle is as follows

$$m_d \frac{dv_d}{dt} = F_d + F_g + F_b + F_p + F_{\text{vm}} \tag{6}$$

where m_d is the mass of modifier particle and v_d is the velocity of modifier particle. The forces of particle (F_d, F_g, F_b, F_p, and F_{vm}) are expressed in Eqs. (7)–(11).

Drag force

$$F_d = C_d \frac{\rho |v - v_d|(v - v_d)}{2} \cdot \frac{\pi d_d^2}{4} \tag{7}$$

where d_d is the particles diameter and C_d is the drag coefficient.

Gravity force

$$F_g = \frac{1}{6}\pi d_d^3 \rho_d \cdot g \tag{8}$$

Buoyancy force

$$F_b = \frac{1}{6}\pi d_d^3 \rho \cdot g \tag{9}$$

Pressure gradient force

$$F_p = \frac{1}{6}\pi d_d^3 \rho v_d \Delta v \tag{10}$$

Virtual mass force

$$F_{\text{vm}} = \frac{\pi}{6}\rho d_d^3 C_{\text{vm}} \left(v_d \Delta v - \frac{dv_d}{d_t} \right) \tag{11}$$

where C_{vm} is the virtual mass coefficient of 0.5.

Results and Discussion

Flow Field of Hot Slag

Figure 2 shows the streamlines of hot slag when the flow has been achieved to a stable state, and the particle diameter is 1 mm. Fig. 2a shows the streamlines of slag upper surface. It can be seen that the hot slag has a strong swirling flow around the

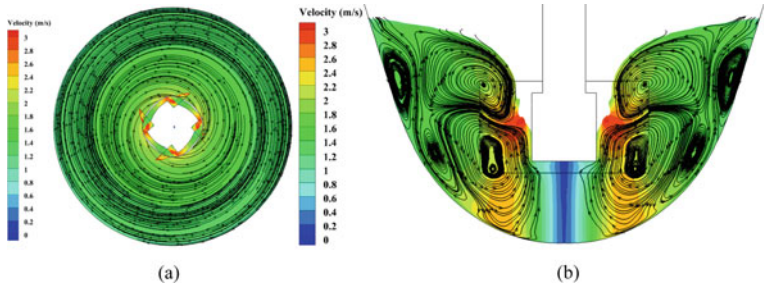

Fig. 2 Streamline and velocity distribution of hot slag with mechanical stirring: **a** Upper surface of hot slag; **b** velocity distribution and streamlines along longitudinal section

stirring axis, and the flow velocity is about 1.8 m/s. An obvious vortex appeared at the center of slag upper surface. Figure 2b shows the velocity distribution and streamlines of hot slag along longitudinal section. It can be observed that the flow velocity of hot slag between the blades is the largest, about 3 m/s. The flow velocity of hot slag is the smallest under the impeller, which is difficult to mix the modifier particles evenly. There are four circulation streams on each side of the impeller. The circulation streams near the upper part of impeller would entrain the modifier particles near the wall into the vortex core, which are beneficial to the even mixing of modifier particles in the hot slag.

Dispersion of Modifier Particle

Figure 3 shows the dispersion of modifier particles with stirring time which is directly added into the vortex core. The hot slag is demarcated into six regions, and the particle number concentration (defined as the number of modifier particles in a unit volume of hot slag) is used to quantitatively evaluate the dispersion degree of modifier particles. The hot slag is divided into Regions (I) and (O) along the radial direction and divided into Regions O1, O2, and O3 along the axial direction. It can be noted that the particles are mainly distributed on the vortex core (Region I1) of hot slag after 1 s stirring, as shown in Fig. 3a. Then, the modifier particles move quickly to the outer (Regions O1, O2, and O3) and bottom regions (Regions I2 and I3) with the circulation stream, as shown in Figs. 3b and c, respectively. The modifier particles completely diffused before 10 s, and the dispersion is more even, as shown in Fig. 3d. Figure 4 shows the variation of particle number concentration with stirring time in each region. After 2 s, the particle number concentrations in Regions O1, O3, and I3 increases gradually, while those in Regions I1, I2, and O2 decrease until attaining a constant in each region before 10 s. Therefore, it takes about 10 s for the particles in each region to reach a steady-state motion.

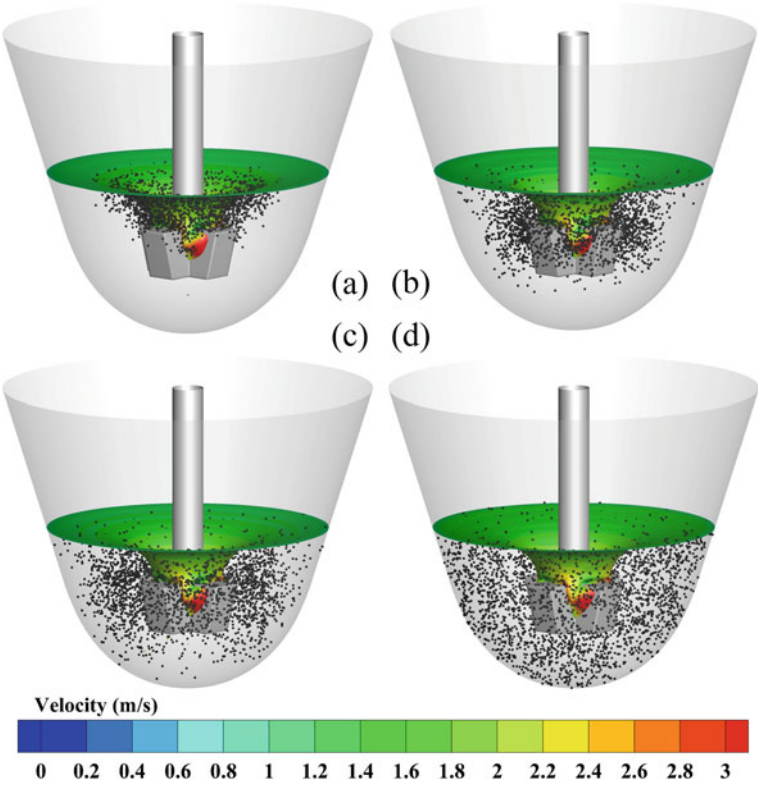

Fig. 3 Dispersion characteristic of modifier particle after different stirring time: **a** 1 s; **b** 2 s; **c** 3 s; **d** 10 s

Effect of Particle Size

Figure 5 shows the dispersion of modifier particles with different sizes for 2 s. It can be seen that the particles with the diameter of 1 mm mainly distribute in Region O3, as shown in Fig. 5a, which could be considered that the smaller particles easily be entrained into the lower part by the circulation streams and difficultly float to the slag surface. When the diameters of particles are 5 mm and 10 mm, the particles are mainly concentrated in Regions I1, O1, as shown in Figs. 5b and c, respectively. Figure 6 shows the particle number concentration in each region after 10 s stirring time for different particle diameters. The particle concentration between each region is very uneven when the particle diameter is 10 mm, and the maximum particle concentration difference between Regions 1 and 3 is 311 per m^3 hot slag. This is because the particle density is less than that of hot slag, and the larger diameter particles are easier to float. When the particle diameter is 5 mm, the particle concentration between each region is more even, and the maximum concentration difference is 246 per m^3 that

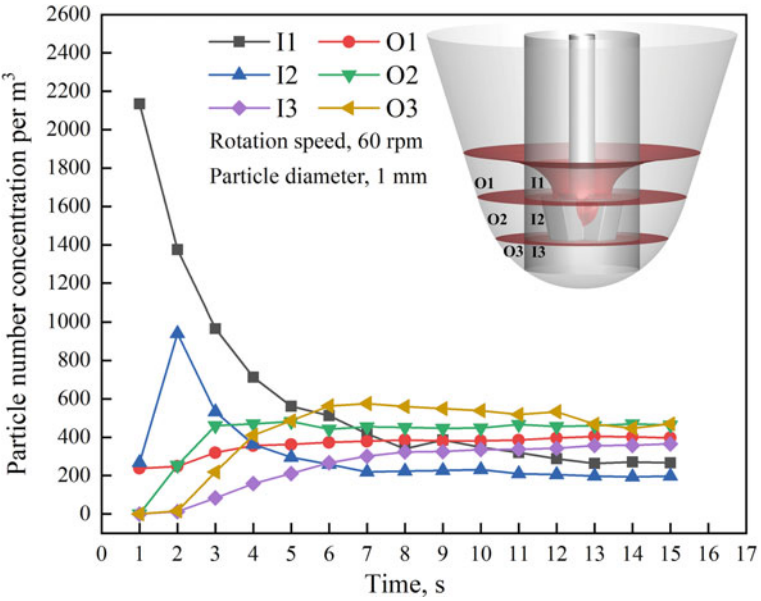

Fig. 4 Variations of particle number concentration in different six regions with stirring time

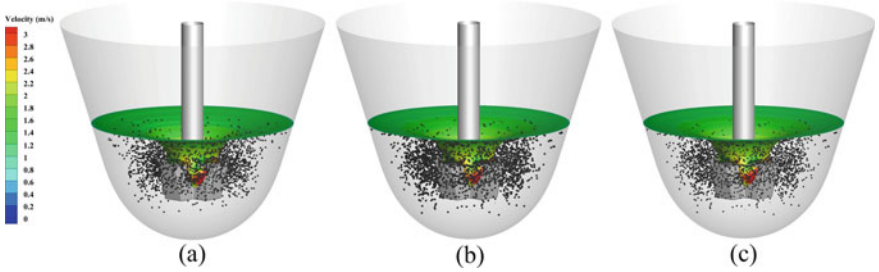

Fig. 5 Dispersion characteristic of the modifier particles with different sizes: **a** 1 mm; **b** 5 mm; **c** 10 mm

occurs between the Regions O1 and I2. Therefore, the modifier particles of 5 mm diameter are more conducive to the hot slag modification.

Effect of Particle Adding Position

Figure 7 shows the dispersion characteristic for different particle adding positions after 2 s stirring, in which the diameter of particle is 1 mm. When the modifier particles are added to the vortex core, they evenly diffuse toward the wall of slag

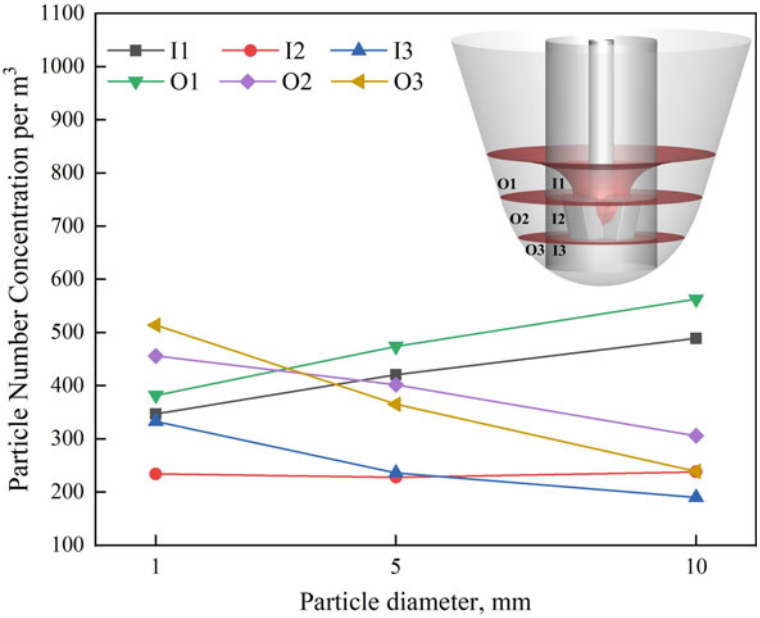

Fig. 6 Particle number concentration in different regions for different particle diameters

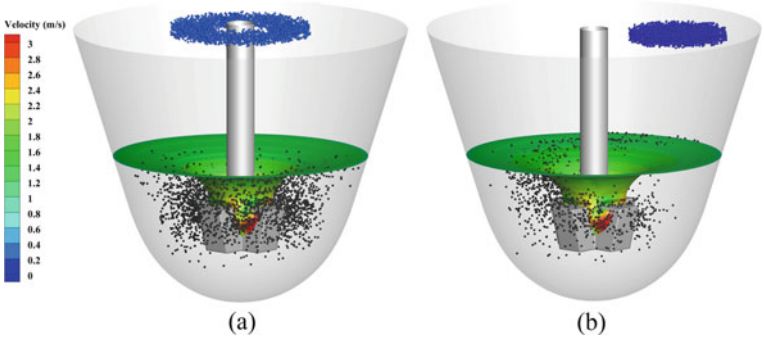

Fig. 7 Particle distribution for different adding positions: **a** Vortex core; **b** side surface

pot, as shown in Fig. 7a. However, when the particles are added to the side surface, a few particles are entrained into the vortex core from the side surface, but the other particles are entrained into the side circulation streams. The particle dispersion is very uneven within a short time when the particles are added to the side surface, as shown in Fig. 7b. Figure 8 shows the typical motion trajectories of particles for different adding positions after 15 s stirring. When the particles are added to the vortex core, some particles rotate in the whole slag due to the forced rotational flow near the impeller, as shown in Fig. 8a. For the particles added to the side surface, a

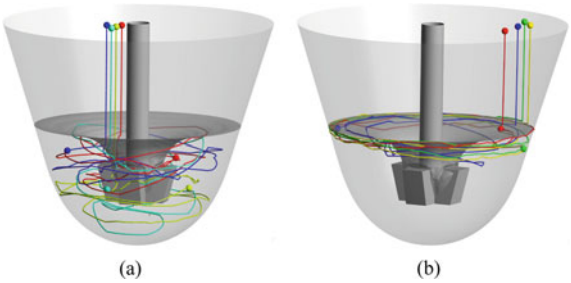

Fig. 8 Trajectories of modifier particles for different adding positions: **a** Vortex core; **b** side surface

portion of the particles rotates in Region O1 during the whole stirring process due to the smaller density than molten slag, as shown in Fig. 8b.

Figure 9 shows the particle number concentration in each region for different adding modes after 10 s stirring. Compared with the side-surface addition, the concentration of particles in each region is more even when the particles are added to the vertex core, and the average particle number concentration in Region O3 (514 per m^3) is about 2.2 times that in Region I2 (234 per m^3). When the particles are added to the side surface, the particle number concentration reaches the maximum in Region O1 (587 per m^3), while in Region I2, the concentration reaches the minimum (160 per m^3), and the particle number concentration ratio is 3.67. Therefore, adding particles directly to the vortex core is better than that of side-surface addition, and the particles can be evenly distributed in hot slag in a short time.

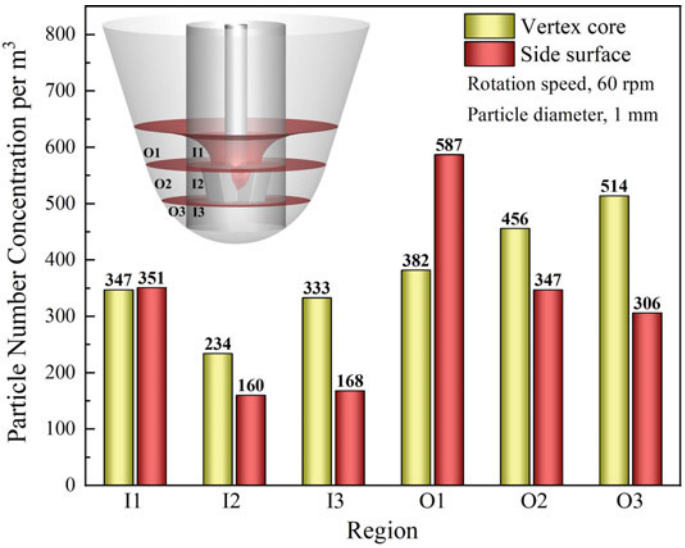

Fig. 9 Particle number concentration in each region for different adding positions

Conclusions

The dispersion characteristics of modifier particles in hot slag with mechanical stirring were investigated by numerical simulation in this work, and the particle number concentration in different regions of hot slag was discussed. In addition, the effects of particle size and adding position on the distribution of modifier particles were also elucidated. The main conclusions are as follows:

(1) Four circulation streams existing on each side of cross-shape impeller are beneficial to the thorough mixing between modifier particles and hot slag. The motion of modifier particles in each region of hot slag reaches a dynamic steady state within 10 s by mechanical stirring.
(2) The particle number concentration in each region of hot slag is more even when the particle diameter is 5 mm, which is more conducive to the hot slag modification.
(3) Adding modifier particle directly to the vortex core is recommended, and modifier particles can be evenly distributed in hot slag within a short time.

Acknowledgements The authors gratefully acknowledge the National Natural Science Foundation of China. [Grant numbers: 51974080, 52074077 and 52174301], the Fundamental Research Funds for the Central Universities was supported by Chinese Education Ministry [Grant number. N2125018].

References

1. Lin GP (2007) Summary and prospects of sensible heat recovery technology of molten slag. Iron Steel Scrap China 4:30–36
2. Xu HJ, Fu GQ, Zhu MY (2006) Experimentation on distensibility of steel slag. Environ Eng 24(6):62–63
3. Vaverka J, Sakurai K (2014) Quantitative determination of free lime amount in steelmaking slag by X-ray diffraction. ISIJ Int 54(6):1334–1337
4. Waligora J, Bulteel D, Degrugilliers P et al (2010) Chemical and mineralogical characterizations of LD converter steel slags: a multi-analytical techniques approach. Mater Charact 61(1):39–48
5. Das B, Prakash S, Reddy PSR et al (2007) An overview of utilization of slag and sludge from steel industries. Resour Conserv Recycl 50(1):40–57
6. Wang X (2006) Recovery and utilization of steel-making slag. Wuhan Iron Steel Corporation Technol 44(5):51–54
7. Li CW, Wang L, Sun BL et al (2007) The treatment and comprehensive utilization of steel slag. Energy Metall Ind 26(4):54–57
8. Zhao J, Yan PY, Wang DM (2017) Research on mineral characteristics of converter steel slag and its comprehensive utilization of internal and external recycle. J Clean Prod 156:50–61
9. Nakai Y, Sumi I, Kikuchi N et al (2017) Powder blasting in hot metal desulfurization by mechanical stirring process. ISIJ Int 57(6):1029–1036
10. Ren XD, Zhang TA, Dou ZH et al (2011) Study of new hot metal desulfurization process on 1t desulfurization experiments. J Iron Steel Res Int 18(2):125–128
11. Shao P, Zhang TA, Liu Y et al (2011) Numerical simulation on fluid flow in hot metal pretreatment. J Iron Steel Res Int 18(2):29–134

12. Ji JH, Liang RQ, He JC (2016) Simulation on mixing behavior of desulfurizer and high-sulfur hot metal based on variable-velocity stirring. ISIJ Int 56(5):794–802
13. Sukawa T, Iguchi M (2005) Promotion of uniform dispersion of fine particles into a mechanically agitated steel bath. ISIJ Int 45(8):1145–1150
14. Wu W, Hu YB, Liu L et al (2008) Physical simulation of new desulphurization technology using pulsed and rotary stirring-injection. J Iron Steel Res Int 15(1):15–18
15. Nakai Y, Hino Y, Sumi I et al (2015) Effect of flux addition method on hot metal desulfurization by mechanical stirring process. ISIJ Int 55(7):1398–1407
16. He JC, Zhang TA, Masamichi S et al (2011) Experimental research of external desulfurization in situ mechanical stirring. J Iron Steel Res Int 18(2):119–124
17. Nakai Y, Sumi I, Kikuchi N et al (2013) Aggregation behavior of desulfurization flux in hot metal desulfurization with mechanical stirring. ISIJ Int 53(8):1411–1419
18. Luo JY, Gosman AD, Issa RI et al (1993) Full flow field computation of mixing in baffled stirred vessels. Chem Eng Res Des 71(3):342–344
19. Ng K, Fentiman J, Lee KC et al (1998) Assessment of sliding mesh CFD predictions and LDA measurements of the flow in a tank stirred by a Rushton impeller. Chem Eng Res Des 76(6):737–747

Numerical Simulation of Inclusion Coagulation During Soft Blowing Process of Ladle Furnace

Haotian Wang, Nan Wang, Xiaoao Li, and Min Chen

Abstract Ladle soft blowing plays an important role in the removal of non-metallic inclusions in liquid steel. In the present work, a CFD-PBM coupling model was established to simulate the soft blowing process in a 180t ladle. The turbulence behavior of gas and liquid phases in the ladle was accurately described, and the turbulent collision and coagulation of medium and small size inclusions in liquid steel were investigated. The results show that the inclusion size is generally smaller than the Kolmogorov microscale with the argon blowing rate of 100–200 NL/min, and the inclusion motion mainly depends on the molecular viscous action. After soft blowing for 5 min, the collision and coagulation behaviors are obvious, and the number density of small inclusions is significantly reduced. For the gas flow rate of 200 NL/min, the average diameter of inclusion increases from 3.94 to 4.25 μm, and the number density of 2-10 μm inclusions decreases from 1.0383×10^{13} to 4.4847×10^{12} per m^3, which decreases by 56.81%.

Keywords Inclusion · Coagulation and growth · Soft blowing · Turbulence · Numerical simulation

Introduction

With the continuous progress of modern science and technology and the development of industry, the demand for high quality steel and clean steel is increasing. Non-metallic inclusions in steel will damage the continuity of steel matrix, resulting in the inhomogeneity of steel structure and seriously affecting the properties of steel [1]. Zhou et al. [2] studied the effect of argon flow rate on the removal of non-metallic inclusions and its removal mechanism through a physical modeling of argon-stirred refining ladle. Liu et al. [3] used Euler–Lagrange method to simulate the argon blowing process of 100t ladle and carried out mathematical calculation of

H. Wang · N. Wang (✉) · X. Li · M. Chen
School of Metallurgy, Northeastern University, Shenyang, Liaoning Province, China
e-mail: wangn@smm.neu.edu.cn

Z. Peng et al. (eds.), *12th International Symposium on High-Temperature Metallurgical Processing*, The Minerals, Metals & Materials Series,
https://doi.org/10.1007/978-3-030-92388-4_51

inclusion removal under different argon blowing flow rates. Duan [4] used the component transport equation to simulate the movement and removal process of inclusion particles. Zheng et al. [5] studied the mechanism of inclusion removal from molten steel by bubbles during the refining process with argon blowing through a physical model. Based on the hydraulic model experiment of the 60t refining furnace, Ju et al. [6] studied the effects of air blowing, time, and particle size on the removal of inclusions and spatial distribution of inclusions by using high-speed camera and professional image processing software (Image Pro Plus). However, collision and aggregation of inclusions are not considered. In this paper, the inclusion collision polymerization model based on turbulent collision mechanism was established by coupling the gas–liquid-solid three-phase CFD model with the PBM model, and the aggregation, growth, and removal behaviors of small size inclusions during the weak argon blowing process of ladle were simulated.

Governing Equations for CFD-PBM Coupled Model

Assumptions

The mathematical model for fluid flow and inclusion behavior in gas-stirred systems is based on the following assumptions:

(1) The molten steel in the ladle is an incompressible viscous fluid, and its flow is unsteady.
(2) The argon bubbles are spherical with a diameter of 15 mm, and the diameter of the bubble remains unchanged during bubbles rising in ladle.
(3) The inclusions are spherical particles and uniformly distributed in liquid steel without affecting the movement of molten steel.
(4) The interaction between the inclusion and the argon bubble is ignored.
(5) A flat, free surface was assumed at the top surface of ladle, and inclusions reaching the top surface are considered ideal absorption by the slag layer and not to revert back into the ladle at a later time.

CFD Model

In the present study, based on Euler-Euler method, the mass and momentum conservation equations are used for gas–liquid-inclusion three phases, respectively.

Mass conservation equation for each phase:

$$\frac{\partial(\alpha_k \rho_k)}{\partial t} + \nabla \cdot \left(\alpha_k \rho_k \overrightarrow{u_k}\right) = S_k \tag{1}$$

where ρ_k, α_k, $\vec{u}_k$, and S_k are the density, volume fraction, averaged velocity vector, and mass source term of liquid phase ($k = l$), gas phase ($k = g$), and inclusion particle phase ($k = p$), respectively. In the current model, both S_l and S_g are zero, and the inclusion mass source term S_p needs to be solved by the PBM model. Because the computational domain is shared by gas–liquid-inclusion three phases, the constraint condition $\alpha_l + \alpha_g + \alpha_p = 1$ must be satisfied.

Momentum conservation equation for each phase:

$$\frac{\partial\left(\alpha_k \rho_k \overrightarrow{u_k}\right)}{\partial t} + \nabla \cdot \left(\alpha_k \rho_k \overrightarrow{u_k}\,\overrightarrow{u_k}\right) = -\alpha_k \nabla p + \nabla \cdot \left(\alpha_k \mu_{eff}\left(\nabla \overrightarrow{u_k} + \left(\overrightarrow{u_k}\right)^T\right)\right) + \alpha_k \rho_k \overrightarrow{g} + \overrightarrow{M_k} \tag{2}$$

$$\mu_{\text{eff}} = \mu_l + \mu_t = \mu_l + C_u \rho_l \frac{k^2}{\varepsilon} \tag{3}$$

where $\overrightarrow{g}$ is the gravity acceleration; μ_l, μ_t, and μ_{eff} are the molecular viscosity, turbulent viscosity, and effective viscosity of liquid phase, respectively; p is the pressure, which is shared by all the phases; and M_k is interaction force among the three phases.

In the process of ladle soft argon blowing, the existence of bubbles generates additional turbulence, which is called bubble-induced turbulence by some scholars [7]. The gas–liquid two-phase turbulence behavior has an important influence on the collision polymerization of inclusions. In this paper, the turbulence k-ε model is modified by user-defined functions (UDFs), and the bubble-induced turbulence is loaded into the source term of the k-ε model. The modified k-ε turbulence model is shown as follows.

$$\frac{\partial}{\partial t}(\alpha_l \rho_l k) + \nabla \cdot (\alpha_l \rho_l \overrightarrow{u_l} k) = \nabla \cdot (\alpha_l \frac{\mu_{t,l}}{\sigma_k} \nabla k) + \alpha_l G_{k,l} + \alpha_l G_b - \alpha_l \rho_l \varepsilon + \alpha_l \rho_l \prod_{k,l} \tag{4}$$

$$\frac{\partial}{\partial t}(\alpha_l \rho_l k) + \nabla \cdot (\alpha_l \rho_l \overrightarrow{u_l} \varepsilon) = \nabla \cdot (\alpha_l \frac{\mu_{t,l}}{\sigma_k} \nabla \varepsilon) + \alpha_l \frac{\varepsilon}{k}(C_{1\varepsilon}(G_{k,l}+G_b) - C_{2\varepsilon} \rho_l \varepsilon) + \alpha_l \rho_l \prod_{\varepsilon,l} \tag{5}$$

where k and ε are the turbulent kinetic energy and the dissipation rate of the liquid phase, respectively; $G_{k,l}$ is the turbulent kinetic energy generated by the average velocity gradient in the liquid phase; and G_b denotes the additional bubble-induced turbulent kinetic energy generated, which is expressed as follows.

$$G_{k,l} = \mu_t (\nabla \overrightarrow{u_l} + (\nabla \overrightarrow{u_l})^T) : \nabla \overrightarrow{u_l} \tag{6}$$

$$G_b = C_b \frac{\mu_t}{\mu_{\text{eff}}} (\rho_l - \rho_g) g \alpha_g \overrightarrow{u_{\text{rel}}} \tag{7}$$

where C_b denotes the fraction of bubble-induced energy converted into the liquid phase turbulence, and the value is 0.85 [7].

Inclusion Population Balance Model

In the current work, PBM model is used to describe the transport, coagulation, and size distribution of inclusions in liquid steel. Only the collision and coalescence behaviors of inclusions are considered, and the population balance equation is given by

$$\frac{\partial n(V_i)}{\partial t} + \nabla \cdot (\overrightarrow{u_p} n(V_i)) = \frac{1}{2} \int_0^{V_i} \beta(V_i - V_j, V_j) n(V_i - V_j) n(V_j) \mathrm{d}V_j - \int_0^{V_{\max}} \beta(V_i, V_J) n(V_i) n(V_j) \mathrm{d}V_j + S_i \tag{8}$$

where $\beta(V_i, V_j)$ represents the inclusion coalescence rate, and $n(V_i)$ and V_i are the number density and volume of the inclusions in group i, respectively. S_i denotes the inclusion removal rate.

The turbulent flow of molten steel produces eddies, and the large eddies gradually split into small eddies. The size of the smallest eddies is called Kolmogorov microscale η, which is expressed as follows:

$$\eta = \left(\frac{\nu^3}{\varepsilon} \right)^{\frac{1}{4}} \tag{9}$$

where ν is the kinematic viscosity of liquid steel; ε is the turbulent dissipation rate of molten steel.

The coagulation of inclusions in molten steel can be divided into two steps. First, the inclusions move close to and collide under the action of various aggregation driving forces, and then the inclusion overcomes the external forces to complete the aggregation behavior. These two steps are described by the collision frequency and effective aggregation coefficient in the aggregation. Due to the small size of inclusions and the good fluidity following the liquid steel, the collision growth is mainly due to the turbulent collision generated by the turbulent flow of liquid steel. Therefore, the turbulent model is used in this study.

When the inclusion size is smaller than Kolmogorov microscale, the inertia force on inclusion is very weak, and the inclusion mainly flows with the liquid steel under the action of viscous force, and the inclusion collisions are influenced by the local shear within the eddy. According to the work by Saffman and Turner [8], the collision rate of inclusions is expressed as:

$$\beta(V_i, V_j) = \alpha\sqrt{\frac{8\pi}{15}}\frac{(d_i + d_j)^3}{8}\sqrt{\frac{\varepsilon}{\nu}} \tag{10}$$

When the inclusions are bigger than the smallest eddy, the aggregation behavior of inclusions is mainly influenced by the inertia force. In this case, the aggregation rate is expressed using Abrahamson's model [9].

$$\beta(V_i, V_j) = 2^{\frac{3}{2}}\alpha\sqrt{\pi}\frac{(d_i + d_j)^3}{4}\sqrt{U_i^2 + U_j^2} \tag{11}$$

where α is the empirical capture efficiency coefficient of turbulent collision, which describes the hydrodynamic and attractive interaction between colliding particles. Higashitani et al. [10] proposed the following relationship:

$$\alpha = 0.732\left(\frac{5}{N_T}\right)^{0.242} \tag{12}$$

where N_T is the ratio between the viscous force and the van der Waals force.

Boundary Conditions and Important Parameters

In the current work, the CFD-PBM coupled model was solved using the commercial computational fluid dynamics software Fluent 2021 R1 combined with user-defined function (UDF). The argon gas inlet is set as the velocity inlet. There are two argon blowing inlets at the bottom of the ladle, located at 0.5r from the center of the ladle bottom, and the angle between the two inlets is 90°. Non-slip wall conditions were adopted for the bottom and side walls of the ladle, and the standard wall function was used to calculate the turbulence characteristics near the wall surface. The top surface of the ladle is set as free shear wall boundary condition, and the argon bubble will escape when it reaches the top surface. At the initial time, the liquid steel was at rest, and inclusions were evenly distributed in the liquid steel, with a volume fraction of 0.0015.

The inner diameter of the bottom of the 180-ton ladle is 3011 mm, the inner diameter of the upper end of the ladle is 3438 mm, the inner height of the ladle is 4230 mm, and the depth of the liquid steel is 3150 mm. Soft blowing argon flow rate is 100–200 NL/min. Since the flow inside the ladle is symmetric, half geometry

Table 1 Physical property of different materials

Physical property	Parameters
Density of molten steel	7100 kg/m^3
Density of inclusions	3900 kg/m^3
Density of gas	1.6228 kg/m^3
Molecular viscosity of molten steel	0.0055 Pa s
Surface tension between molten steel and argon gas	1.4 N/m

Table 2 Characteristic diameter, initial quantity density, and volume fraction of inclusion in each group

Groups	Characteristic diameter (μm)	Initial quantity density($1 \times m^{-3}$)	Volume fraction
1	2.00	3.58E+12	0.01
2	2.64	3.12E+12	0.02
3	3.48	2.04E+12	0.03
4	4.59	2.95E+11	0.01
5	6.06	9.00E+11	0.07
6	8.00	4.48E+11	0.08
7	10.60	4.87E+11	0.20
8	13.90	2.44E+11	0.23
9	18.40	1.62E+11	0.35

is selected for modeling. The physical properties of gas–liquid-solid three-phase materials in the simulation calculation are shown in Table 1.

The sample analysis shows that the size of inclusions is mainly 2–20 μm. The inclusions are divided into nine groups according to the grouping method $v_{i+1}/v_i = 2^{1/q}$ proposed by Lister et al. [11]. The characteristic diameter, initial quantity density, and integration rate of each group of inclusions are shown in Table 2.

Results and Discussion

Fluid Flow Analysis

Figure 1 shows the simulation results of gas–liquid two-phase flow in a 180-ton gas-stirred ladle, where Fig. 1a is the gas volume fraction distribution. As the bubble rises, the gas volume fraction gradually decreases, and the size of the bubbly plume gradually widens. Figure 1b shows turbulent kinetic energy of molten steel. In the region with large turbulent kinetic energy, the probability of inclusion collision growth is greater. As can be seen from Fig. 1c, driven by bubble buoyancy, liquid flows upward,

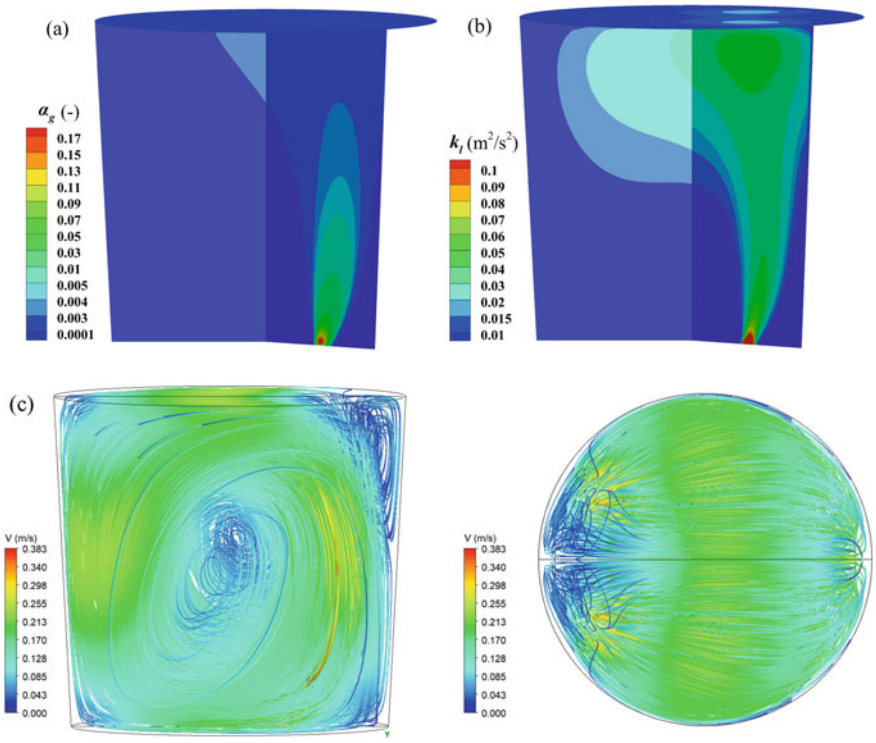

Fig. 1 Bubbly plume flow of gas-stirred ladle: **a** gas volume fraction, **b** turbulent kinetic energy, **c** flow field

while the two plume regions attract each other, meet at the symmetric plane, and bend toward the near-wall side. When liquid steel flows to the top surface, it continues to flow horizontally and radially, and then down the ladle wall. At the side far away from the argon blowing position, a large circulating flow is formed, which drives most of the molten steel flow in the ladle. At the same time, two small circulations are formed at the upper part of the argon blowing position and adjacent to the ladle wall.

Figure 2 shows the contour map of local Kolmogorov microscale η predicted by the current model under a different gas flow rate. It is clear that the η gradually decreases with the gas flow rate increases. The inclusion size is generally smaller than η under the three gas conditions, and is larger than η only near the gas inlet. This phenomenon shows that the inclusions flow with the molten steel mainly under the action of viscous force. The inertial force only plays a leading role in a small area near the argon gas inlet, and the inclusions show turbulent random motion.

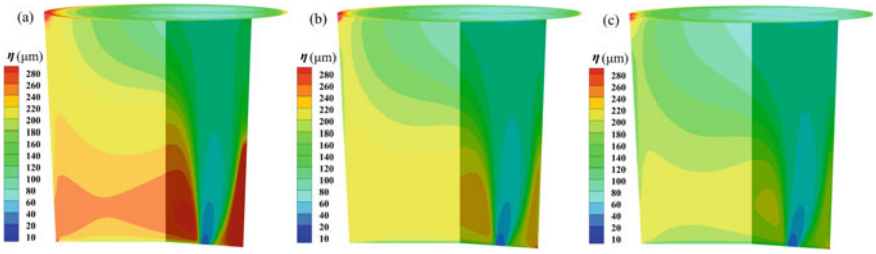

Fig. 2 Kolmogorov microscale η in liquid steel under different gas flow rates: **a** 100 NL/min; **b** 150 NL/min; **c** 200 NL/min

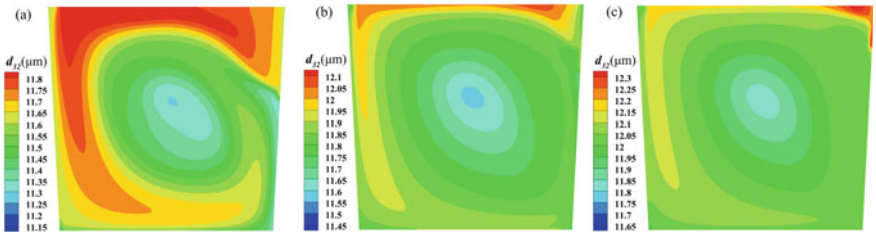

Fig. 3 Sauter mean diameter d_{32} of the inclusions at different gas flow rates: **a** 100 NL/min; **b** 150 NL/min; **c** 200 NL/min

Average Diameter and Quantity Density of Inclusions

Figure 3 shows the average diameter distribution of inclusions at the symmetrical surface of ladle under different gas flow rates after 5 min. The average diameter of inclusions is represented by Sauter average diameter (d_{32}). It can be seen that the distribution of inclusions is consistent with the large circulating flow, and the behavior of inclusions following the flow of liquid steel is obvious, which is consistent with the conclusion obtained above. In addition, the average diameter of inclusions increases with the increase of argon flow rate. On the outside of the large circulating flow, the flow rate of molten steel is stronger than that at the center of the circulating flow, resulting in the average diameter of the inclusion on the outside is larger than that at the center. However, with the increase of gas volume, the average diameter difference between the inside and outside inclusions decreases. This indicates that the circulating flow of liquid steel is stronger with the larger gas blowing at the same time, and the inclusion in the ladle is more fully grown by collision polymerization.

Figure 4 shows the variation of the average diameter of inclusions in ladle with soft argon blowing time. It can be seen that for the inclusions with an initial average diameter of 3.94 μm, the average diameter of the inclusions increases significantly after 5 min of soft argon blowing at 100, 150, and 200 NL/min. The average diameter of inclusions increases from 3.94 μm to 4.17 μm, 4.21 μm, and 4.25 μm, respectively, with the increased rates of 5.84%, 6.85%, and 7.87%, respectively.

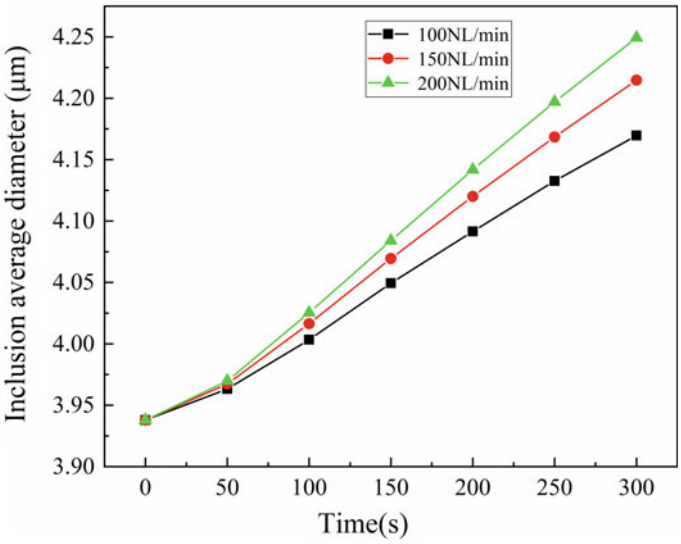

Fig. 4 Evolution of inclusion average diameter with blowing time

Figure 5 shows the variation of inclusions quantity density in each group at the initial time and after soft blowing for 5 min when the argon blowing flow rate is 200 NL/min. One of the effects of gas stirring is to promote the collision of inclusions in molten steel and to coalesce and grow up. With the development of soft blowing

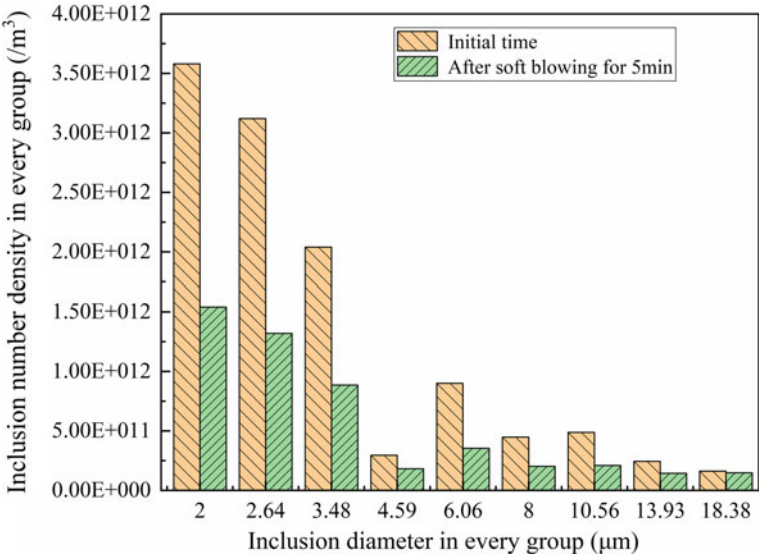

Fig. 5 Inclusion number density in every group

process, the collision and growth process of inclusions in the whole ladle also goes on. It can be seen from the simulation results that the number density of inclusions decreases in each group. The smaller the size of inclusions, the more obvious the number of inclusions decreased, and the number density of 2–10 μm inclusions decreased from 1.0383×10^{13} to $4.4847 \times 10^{12}/m^3$, with a reduction rate of 56.81%. The reason for this result is that the smaller the number of inclusions is, the more likely they are to aggregate and grow up under the action of gas stirring.

Conclusions

(1) Through the establishment of CFD-PBM coupling model, the gas–liquid two-phase turbulence phenomenon and the movement behavior of inclusions in a 180-ton gas-stirred ladle were simulated. The results show that the inclusions with a diameter of 2–20 μm are generally smaller than Kolmogorov microscale, and the inclusions mainly follow the flow of molten steel under the action of molecular viscous force.

(2) The results show that the growth behavior of inclusion collision polymerization becomes more obvious with the increase of soft blowing argon flow rate. The average diameter of the inclusions increased from 3.94 μm to 4.17 μm, 4.21 μm, and 4.25 μm, respectively, with the increased rates of 5.84%, 6.85%, and 7.87%, respectively, after 5 min of soft argon blowing at 100–200 NL/min.

(3) Under the condition of soft blowing argon stirring, the simulation results of the change of the number density of the inclusions in the liquid steel show that the smaller the size of the inclusions, the more the number of inclusions and the easier to aggregate and grow up under the action of gas stirring. The number density of 2–10 μm inclusions decreased from $1.0383 \times 10^{13}/m^3$ to $4.4847 \times 10^{12}/m^3$, with a reduction rate of 56.81%.

Acknowledgments The authors gratefully acknowledge the National Natural Science Foundation of China [Grant numbers: 51974080, 52074077 and 52174301], the Fundamental Research Funds for the Central Universities was supported by Chinese Education Ministry [Grant number N2125018].

References

1. Li JJ, Xin XQ, Li Q, Zhang YZ (2019) Research on key factors affecting non-metallic inclusions in steel. Heavy Cast Forging 1:13–14
2. Zhou YL, Zhu MY, Liu JB, Chen JJ, Zheng SG (2016) Mechanism of nonmetallic inclusion removal in argon-stirred refining ladles. Iron Steel 51(06):39–46
3. Liu FG, Ren Y, Duan HJ, Zang LF (2019) Mathematical simulation and plant trial on soft blowing process of ladle furnace. Steelmaking 35(06):24–30

4. Duan HJ (2018) Fundamental on interfacial phenomena of non-metallic inclusions in molten steel. PhD thesis, University of Science and Technology Beijing
5. Zheng SG, Zhu MY (2008) Mechanism of inclusion removal from molten steel by bubbles during the refining process with argon blowing. Iron Steel 6:25–29
6. Ju JT, Wei JQ, Liu WG (2017) Hydraulic model experiment of non-metallic inclusion distribution in a bottom-blown argon ladle furnace. Iron Steel 52(10):45–50
7. Lou WT (2016) Study on the multiphase flow transport behavior and reaction kinetics in the refining ladle. PhD thesis, Northeastern University
8. Saffman PG, Turner JS (1956) On the collision of drops in turbulent clouds. J Fluid Mech 1:16–30
9. Abrahamson J (1975) Collision rates of small particles in a vigorously turbulent fluid. Chem Eng Sci 30(2):1371–1379
10. Higashitani K, Yamuchi K, Matsuno Y et al (1983) Turbulent coagulation of particles dispersed in a viscous fluid. J Chem Eng Jpn 16(4):299–304
11. Lister JD, Smit DJ, Hounslow MJ (1995) Adjustable discretized population balance for growth and aggregation. Am Inst Chem Eng 41(3):591–603

Prediction Model of Calcium Addition in SPHC Steel Refining Process

Zhiqiang Du, Nan Wang, Min Chen, and Xiaoao Li

Abstract The high melting point Al_2O_3 inclusions in steel can be modified to low melting point calcium aluminate by the calcium treatment process, which makes the inclusions easy to grow up by collision and float to remove, thus improving the cleanness of liquid steel. Taking the treatment of molten steel by SPHC in a steel mill as the research object, the budget models of molten steel composition and temperature, calm time, top slag composition, and the amount of molten steel calcium were established based on RH refining data using multiple linear and multiple nonlinear regression analysis methods. The results show that the hit ratio of the multiple linear and multiple nonlinear budget models is 83.8% and 94.6%, respectively, and the multiple nonlinear regression model has better fitting ability and higher hit ratio. The amount of calcium is mainly determined by the content of [Ca] and $[Al]_O$ and [S] in molten steel before calcium treatment. Therefore, in the actual process of calcium treatment, the amount of calcium should be precisely adjusted according to the specific composition of molten steel.

Keywords Calcium treatment · The amount of calcium · Multiple linear regression · SPHC steel

Introduction

SPHC steel is a low carbon and low silicon aluminum-killed steel with low carbon content, good plasticity, toughness, machining performance, and welding performance, etc. It is widely used in deep processing materials such as stamping and panel forming of an automobile, home appliance, and instrument shell [1] and has strict requirements on its surface quality and composition. Since aluminum deoxidation alloying is adopted in SPHC steel extraction process [2], calcium feeding line denaturing of Al_2O_3 inclusions in liquid steel must be carried out in the RH refining process. Modification of non-metallic inclusions in molten steel by calcium treatment

Z. Du · N. Wang (✉) · M. Chen · X. Li
School of Metallurgy, Northeastern University, Shenyang, Liaoning Province, China
e-mail: wangn@smm.neu.edu.cn

Z. Peng et al. (eds.), *12th International Symposium on High-Temperature Metallurgical Processing*, The Minerals, Metals & Materials Series,
https://doi.org/10.1007/978-3-030-92388-4_52

can effectively control the composition, shape, and size of inclusions in aluminum-killed steel, which is one of the important technical means to improve the cleanliness of molten steel, ensure the smooth running of continuous casting, and improve steel properties [3–8]. However, the control of calcium addition is mainly based on thermodynamic calculation and field experience data, and the calcium recovery rate fluctuates greatly, which seriously restricts the effect of inclusion modification. Therefore, how to obtain a stable calcium recovery rate and achieve accurate control of inclusion modification effect has become the bottleneck problem restricting the development of calcium treatment technology. To enhance the level of inclusion SPHC steel production process control, based on the multiple linear regression analysis methods, considering SPHC steel refining process the steel condition (molten steel composition and temperature), the top slag composition, molten steel composed process variables such as time, build a budget model of molten steel for the amount of calcium, for SPHC steel refining process provides the reference for the precise control of the amount of calciumTable 1.

Process variables can be divided into two categories: process variables before calcium treatment and process variables after calcium treatment. Among them, molten steel [S] content, molten steel $[Al]_O$ content ($[Al]_O$ is the difference between $[Al]_T$ and $[Al]_S$), molten steel [Ca] content, and molten steel temperature are the composition and temperature of molten steel before calcium treatment; the content of top slag (FeO) and top slag (CaO)/(Al_2O_3) are the component content of top slag when entering the station; the sedation time of molten steel is the total time of soft blowing and static stirring of molten steel after calcium treatment.

According to the actual production conditions in RH refining process, the calcium addition is mainly determined by seven process variables such as molten steel [S] content, $[Al]_O$ content, and [Ca] content. X1–X7 symbols represent input variables, and Y is output variables. The Pearson correlation coefficients of these variables

Table 1 Statistical information of process variables

Variable	Symbol	Unit	Mean value	Maximum	Minimum	Standard deviation
Molten steel [S] content	x_1	%	0.00136	0.0027	0.0005	0.0005
Molten steel [Al]o content	x_2	%	0.0020	0.0036	0.0011	0.0006
Molten steel [Ca] content	x_3	%	0.0004	0.0001	0.0008	0.0002
Temperature	x_4	°C	1600	1608	1589	4
Sedation time	x_5	Min	48	56	36	5
Content of (FeO) in top slag	x_6	%	0.416	1.761	0.056	0.347
(CaO)/(Al_2O_3) in top slag	x_7	/	1.80	2.34	1.29	0.30
Calcium addition	Y	kg/t	0.19	0.31	0.08	0.06

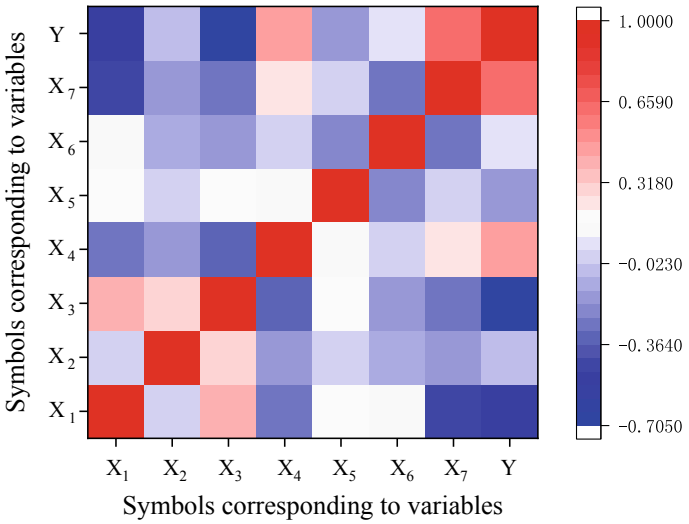

Fig. 1 Pearson correlation coefficient between process variables

are shown in Fig. 1. Pearson correlation coefficient reflects the influence degree between the two variables to a certain extent. According to Fig. 1, it is found that the correlation between calcium addition and molten steel [S] content, $[Al]_O$ content, [Ca] content, and sedation time is negative, and the correlation coefficients are −0.50, −0.07, −0.70, and −0.17, respectively. Among them, the correlation between calcium addition and [S] content and [Ca] content in molten steel is strong, while the correlation between calcium addition and $[Al]_O$ content and sedation time in molten steel is weak. It also shows that the increase of [S], $[Al]_O$, and [Ca] content in molten steel and the increase of sedation time will lead to the decrease of calcium addition. At the same time, the correlation between calcium addition and temperature, FeO content in top slag, and $(CaO)/(Al_2O_3)$ content in top slag is positive, and the correlation coefficients are 0.47, 0.05, and 0.63, respectively. The correlation between calcium addition and temperature and $(CaO)/(Al_2O_3)$ content in top slag is strong, but the correlation with (FeO) content in top slag is weak, and it shows that on the basis of reasonable smelting temperature, the increase of temperature, the increase of (FeO) content in top slag, and the increase of $(CaO)/(Al_2O_3)$ in top slag will lead to the increase of calcium addition.

Model Evaluation Method

In order to determine the accuracy of the model regression, the regression performance of the model is verified through the determination coefficient (R^2), mean absolute error (MAE), mean square error (MSE), and root mean square error (RMSE).

The calculation formulas are shown in Eqs. (1)–(4). The closer the value of R^2 is to the value of 1, the better the regression performance of the model, while the smaller the values of MAE, MSE, and RMSE, the better the regression performance of the model.

Coefficient of determination

$$R^2 = \frac{\sum_{i=1}^{n} (y_i - \hat{y}_i)^2}{\sum_{i=1}^{n} (y_i - \overline{y}_i)^2} \tag{1}$$

Mean absolute error

$$\mathrm{MAE} = \frac{1}{n} \sum_{i=1}^{n} \left| y_i - \hat{y}_i \right| \tag{2}$$

Mean square error

$$\mathrm{MSE} = \sum_{i=1}^{n} \left(y_i - \overline{y}_i \right)^2 \tag{3}$$

Root mean square error

$$\mathrm{RMSE} = \sqrt{\frac{1}{n} \sum_{i=1}^{n} \left(y_i - \hat{y}_i \right)^2} \tag{4}$$

Analysis of Regression Results

Analysis of Multiple Linear Regression Results

When the multiple linear regression equation contains a constant term, the specific fitting formula is shown in Formula (5), where x_1 is the content of molten steel [S]; x_2 is the content of $[\mathrm{Al}]_{\mathrm{O}}$ in molten steel; x_3 is the content of molten steel [Ca]; x_4 is the temperature; x_5 is the sedation time; x_6 is the content of top slag (FeO); x_7 is $(\mathrm{CaO})/(\mathrm{Al_2O_3})$ in top slag; a_1, $a_2 \ldots a_7$ is the corresponding coefficient of each variable. a_0 is a constant term.

$$y = a_0 + a_1 x_1 + a_2 x_2 + a_3 x_3 + a_4 x_4 + a_5 x_5 + a_6 x_6 + a_7 x_7 \tag{5}$$

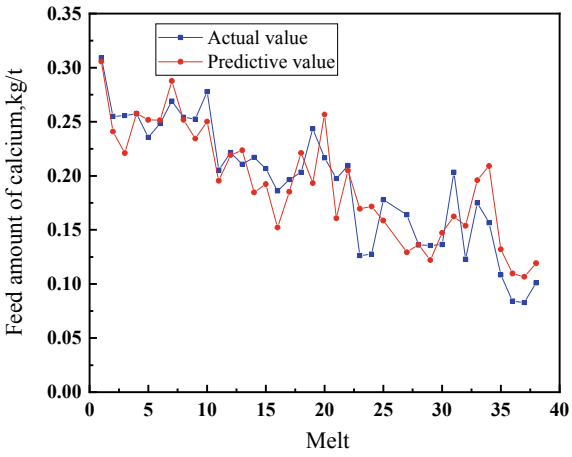

Fig. 2 Comparison between actual value and predicted value of multiple linear regression with constant term

$$y = -5.2746 - 0.8233x_1 + 22.3043x_2 - 161.5460x_3 + 0.0034x_4 - 0.0011x_5 + 0.0210x_6 + 0.0953x_7 \quad (6)$$

From the fitting results, $a_0 = -5.2746$, a_1 = -0.8233, $a_2 = 22.3043$, $a_3 = -161.5460$, $a_4 = 0.0034$, $a_5 = -0.0011$, $a_6 = 0.0210$, $a_7 = 0.0953$. The specific fitting equation is shown in Eq. (6).

The comparison curve between the prediction result obtained by fitting the multiple linear regression equation and the field value is shown in Fig. 2, and the predicted results are consistent with the changing trend of field values, which shows that the prediction model can also effectively predict the calcium feeding rate of molten steel. The positive and negative relationship of the regression coefficient in Formula (6) can be obtained, the increase of [S] content in molten steel will lead to the decrease of calcium feeding, the increase of $[Al]_O$ content will lead to the increase of calcium addition, and the increase of [Ca] content in molten steel will also lead to the decrease of calcium addition. For the molten steel temperature during calcium feeding, under reasonable smelting conditions, the increase of molten steel temperature will lead to the increase of calcium addition. At the same time, for the sedation time after calcium feeding, the increase of sedation time will slightly reduce the amount of calcium. The increase of $(CaO)/(Al_2O_3)$ and (FeO) content in top slag will also lead to the increase of calcium addition. Through the further analysis of the regression coefficient in Formula (6), it can be concluded that the [Ca] content in the molten steel before calcium feeding has the greatest impact on the calcium addition, followed by the $[Al]_O$, [S] content in the molten steel and the $(CaO)/(Al_2O_3)$ in the top slag, while the content of the top slag (FeO), the cooling time of the molten steel, and the temperature of the molten steel have little impact on the calcium addition. Therefore, when the calcium addition is budgeted in the actual refining process, it should be mainly controlled in combination with the composition of molten steel (Tables 2 and 3).

Table 2 Statistical table of evaluation indexes of multiple linear regression model

Evaluating indicator	Regression model
R^2	0.79
MAE	0.0218
MSE	0.1219
RMSE	0.0262

Table 3 Comparison of hit rate of multiple linear regression model

Model	Prediction relative error (%)				
	±25	±20	±15	±10	±5
Multiple linear regression model (%)	83.8	70.3	59.5	45.9	18.9

As can be seen from Tables 2 and 3 R^2 of the multiple linear regression equation is 0.79, and the relative error range of ±10%, ±15%, and ±20% is 15.9%, 59.5%, and 70.3%, respectively. It can be concluded from the results that the multiple linear regression equation has a high precision in predicting the amount of calcium.

Analysis of Multiple Nonlinear Regression Results

When multiple nonlinear regression equations are selected, the specific fitting formula is shown in Formula (7), where x_1 is the content of molten steel [S]; x_2 is the content of $[Al]_O$ in molten steel; x_3 is the content of molten steel [Ca]; x_4 is the temperature; x_5 is the sedation time; x_6 is the content of top slag (FeO); x_7 is (CaO)/(Al_2O_3) in top slag; a_1, $a_2 \ldots a_7$ is the corresponding coefficient of each variable. a_0 is a constant term.

$$y = a_0 + a_1 x_1^{-0.3039} + a_2 x_2^{-7/12} + a_3 x_3 + a_4 x_4 + a_5 x_5 + a_6 x_6^{7/4} + a_7 e^{0.5859 x_7} \quad (7)$$

The functional relationship between molten steel [S] content and (CaO)/(Al_2O_3) in top slag is determined by the optimal fitting results obtained by fitting the calcium feeding amount with molten steel [S] content and (CaO)/(Al_2O_3) in top slag, respectively. At the same time, the power of molten steel $[Al]_O$ content and top slag (FeO) content is calculated from the heat balance when calcium modifies alumina inclusions, and the formula is shown in Formulas (8)–(11). The role of (FeO) in the top slag can be regarded as the oxygen transfer of the top slag to the molten steel. The specific relationship is shown in Eqs. (13)–(15). Among them, it is calculated from (12)–(15) that $w_{Ca} \rightarrow w_{FeO}^{\frac{7}{4}}$. For [Ca] content, temperature, and sedation time of molten steel, the linear relationship between molten steel [Ca] content, temperature, sedation time, and calcium addition is selected through the comprehensive consideration of the best

fitting results and Pearson correlation.

$$w_{\mathrm{Ca}} = \left(\frac{a_{12\mathrm{CaO}\cdot 7\mathrm{Al_2O_3}}}{f_{\mathrm{Ca}}^{12}\cdot f_{\mathrm{Al}}^{14}\cdot a_{\mathrm{O}}^{33}\cdot e^{\frac{7113224-189.4\mathrm{T}}{\mathrm{RT}}}}\right)^{\frac{1}{12}}\cdot w_{\mathrm{Al}}^{-\frac{7}{6}} \tag{8}$$

$$3[\mathrm{Ca}] + (\mathrm{Al_2O_3})_{\mathrm{inc}} = 3(\mathrm{CaO})_{\mathrm{inc}} + 2[\mathrm{Al}] \quad \Delta G^{\theta} = -664577 + 40.45\mathrm{T} \tag{9}$$

$$w_{\mathrm{Al}} = \left(\frac{a_{(\mathrm{CaO})_{\mathrm{inc}}}^{3}\cdot f_{(\mathrm{Al_2O_3})_{\mathrm{inc}}} e^{\frac{664577-40.45\mathrm{T}}{\mathrm{RT}}}}{f_{\mathrm{Al}}^{2}}\right)^{\frac{1}{2}}\cdot w_{(\mathrm{Al_2O_3})_{\mathrm{inc}}}^{\frac{1}{2}} \tag{10}$$

$$w_{\mathrm{Ca}} = \left(\frac{a_{12\mathrm{CaO}\cdot 7\mathrm{Al_2O_3}}}{f_{\mathrm{Ca}}^{12}\cdot f_{\mathrm{Al}}^{14}\cdot a_{\mathrm{O}}^{33}\cdot e^{\frac{7113224-189.4\mathrm{T}}{\mathrm{RT}}}}\right)^{\frac{1}{12}} \cdot \left(\frac{a_{(\mathrm{CaO})_{\mathrm{inc}}}^{3}\cdot f_{(\mathrm{Al_2O_3})_{\mathrm{inc}}} e^{\frac{664577-40.45\mathrm{T}}{\mathrm{RT}}}}{f_{\mathrm{Al}}^{2}}\right)^{-\frac{7}{72}}\cdot w_{(\mathrm{Al_2O_3})_{\mathrm{inc}}}^{-\frac{7}{12}} \tag{11}$$

$$[\mathrm{Fe}] + [\mathrm{O}] = (\mathrm{FeO}) \quad \Delta G^{\theta} = -225500 + 41.3\mathrm{T} \tag{12}$$

$$w_{\mathrm{FeO}} = \left(\frac{a_{\mathrm{Fe}}\cdot f_{\mathrm{O}}\cdot e^{\frac{225500-41.3\mathrm{T}}{\mathrm{RT}}}}{f_{\mathrm{FeO}}}\right)\cdot w_{O} \tag{13}$$

$$2[\mathrm{Al}] + 3[\mathrm{O}] = \mathrm{Al_2O_3} \quad \Delta G^{\theta} = -867370 + 222.5\mathrm{T} \tag{14}$$

$$w_{\mathrm{Al}} = \left(\frac{a_{\mathrm{Al_2O_3}}}{f_{\mathrm{Al}}^{2}\cdot f_{\mathrm{O}}^{3}\cdot e^{\frac{867370-222.5\mathrm{T}}{\mathrm{RT}}}}\right)^{\frac{1}{2}}\cdot w_{\mathrm{O}}^{-\frac{3}{2}} \tag{15}$$

From the fitting results, $a_0 = -5.7696$, $a_1 = -0.0045$, $a_2 = -0.0021$, $a_3 = -169.4914$, $a_4 = 0.0038$, $a_5 = -0.0016$, $a_6 = 0.0113$, $a_7 = 0.0582$. The specific fitting equation is shown in Eq. (16).

$$\begin{aligned} y = {} & -5.7696 - 0.0045x_1^{-0.3039} - 0.0021x_2^{-7/12} - 169.4914x_3 \\ & + 0.0038x_4 - 0.0016x_5 + 0.0113x_6^{7/4} + 0.0582e^{0.5859x_7} \end{aligned} \tag{16}$$

The comparison curve between the prediction result obtained by fitting the multiple nonlinear regression equation and the field value is shown in Fig. 3. The change trend of the prediction result is consistent with the field value, which shows that the prediction model can also effectively predict the calcium feeding amount of liquid steel. According to the multivariate nonlinear fitting equation of Eq. 16, the increase of [S] content and $[\mathrm{Al}]_{\mathrm{O}}$ content in liquid steel will lead to the increase of calcium feeding, and the increase of [Ca] content in liquid steel will also lead to the decrease of calcium addition. For the molten steel temperature during calcium feeding, under reasonable smelting conditions, the increase of molten steel temperature will lead to the increase of calcium addition. At the same time, for the sedation time after calcium feeding, the increase of sedation time will slightly reduce the

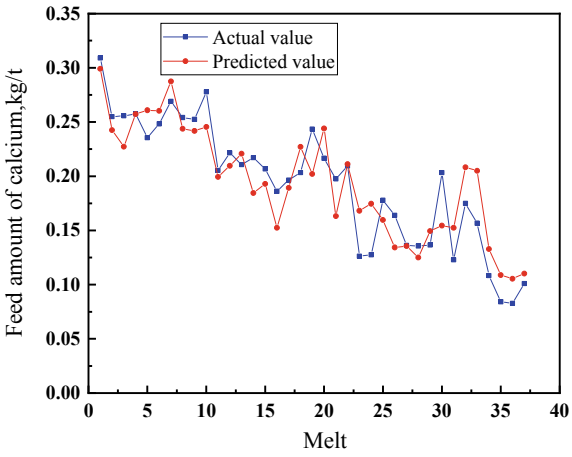

Fig. 3 Comparison between actual value and predicted value of multivariate nonlinear regression with constant term

amount of calcium. The increase of $(CaO)/(Al_2O_3)$ and (FeO) content in top slag will also lead to the increase of calcium addition. After analyzing the regression coefficient in Formula (10), it can be seen that the [Ca] content in molten steel before calcium feeding has the greatest influence on the calcium addition, followed by the $[Al]_O$, [S] content in molten steel, and the $(CaO)/(Al_2O_3)$ of top slag, while the content of top slag (FeO), molten steel sedation time, and molten steel temperature have little influence on the calcium addition. The specific model evaluation indicators are shown in the Tables 4 and 5.

As can be seen from Table 4, the R^2 values of the multiple nonlinear regression model are 0.81, respectively. From the values of MAE, MSE, and RMSE, the model has higher prediction accuracy. It can be seen from Table 5 that when the relative errors are in the range of ±15%, ±20%, and ±25%, the hit rates reach 62.2%, 73.0%,

Table 4 Statistical table of evaluation indexes of multivariate non-regression model

Evaluating indicator	Regression model
R^2	0.80
MAE	0.0215
MSE	0.1203
RMSE	0.0253

Table 5 Hit rate of multiple nonlinear regression model

Model	Prediction relative error (%)				
	±25	±20	±15	±10	±5
Multiple linear regression model (%)	94.6	73.0	62.2	51.4	29.7

Table 6 Statistical table of evaluation indexes of multiple linear and nonlinear regression models

	Evaluating indicator	Evaluation results
Multiple linear regression model	R^2	0.79
	MAE	0.0218
	MSE	0.1219
	RMSE	0.0262
Multivariate nonlinear regression model	R^2	0.80
	MAE	0.0215
	MSE	0.1203
	RMSE	0.0253

Table 7 Comparison of hit rate between multiple linear and nonlinear regression models

Model	Prediction relative error (%)				
	±25	±20	±15	±10	±5
Multiple linear regression model (%)	83.8	70.3	59.5	45.9	18.9
Multivariate nonlinear regression model (%)	94.6	73.0	62.2	51.4	29.7

and 94.6%, respectively. Compared with the multiple linear regression model, the hit rate is significantly improved (Table 6).

Tables 7 show the comparison of the results of the multivariate liner moder and the multivariate nonlinear model. From the above results, it is obvious that the fitting result of the multivariate nonlinear model is better than that of the multivariate linear model. It shows that the fitting results of multiple nonlinearity have more guidance for the process.

Conclusion

Considering the actual molten steel composition and temperature, molten steel sedation time, top slag composition, and other factors in SPHC steel refining process, based on multiple linear regression and multiple nonlinear regression methods, the budget model of molten steel calcium addition is constructed, the influence law of process parameters is analyzed, and the hit rate of the model is compared. The results are as follows:

(1) The multiple linear regression budget model and multiple nonlinear regression budget model are constructed, respectively. The determination coefficients (R^2) of the two models are 0.79 and 0.80, respectively.
(2) The hit rates of multiple linear regression and multiple nonlinear regression budget models with a relative error of ±25% are 83.8% and 94.6%, respectively.

(3) Before calcium feeding, the content of [Ca] in molten steel has the greatest influence on the amount of calcium, followed by the content of $[Al]_O$ and [S] in molten steel and $(CaO)/(Al_2O_3)$ in top slag, while the content of top slag (FeO), molten steel sedation time, and molten steel temperature have little influence on the amount of calcium.
(4) According to the comprehensive evaluation indexes and the hit rate of the model, the multiple nonlinear regression model has a good fitting ability and high hit rate.

Acknowledgements The authors gratefully acknowledge the National Natural Science Foundation of China [Grant numbers: 51974080, 52074077 and 52174301], the Fundamental Research Funds for the Central Universities was supported by Chinese Education Ministry [Grant number N2125018].

References

1. Deng XY, Su DX, Zhou YZ, Ma JC (2014) Steelmaking process optimization of SPHC steel produced by BOF→RH→CC. Steelmaking 30(05):26–29
2. Gao ZP (2011) Technology of steelmaking. Metallurgical Industry Press 236
3. Xing WH, Teng M, Zhang BY, Song FL, Wu TF, Zhang TG (1995) Influence of Ca-cored wire feeding on steel quality. J Iron Steel Res 06:15–19
4. Sun YH, Fang ZQ (2014) Formation of intermediate products during calcium treatment and modification routes of alumina inclusions by intermediate products. J Univ Sci Technol Beijing 36(12):1615–1625
5. Zheng W, Li TY, Wang CF, Xiong S, Li GQ, Zhu CY (2018) Development and prospect of calcium treatment process. Steelmaking 34(02):1–7
6. Zhang LF (2016) Several important scientific research points of non-metallic inclusions in steel. Steelmaking 32(04):1–16
7. Wang LZ, Li JQ, Yang SF, Chen CY, Jin HX (2019) Effect of calcium treatment on characteristics of non-metallic inclusions in steel containing high Al. Iron Steel 54(11):27–32
8. Gao SY, Jiang M, Hou ZW, Wang XH (2017) Effect of calcium treatment on inclusions in high carbon aluminum killed steel. Iron Steel 52(04):25–30

Preparation of Spherical Iron Powder by High-Temperature Re-melting and Spheroidizing

Qipeng Bao, Lei Guo, and Zhancheng Guo

Abstract Spherical metal powders are in great demand in the novel manufacturing industry, such as 3D printing, plasma spraying, and metal powder injection molding. For the efficient production of spherical metal powder, an innovative method to prepare spherical metal powder was proposed in this paper through re-melting and spheroidizing the irregular shape metal powders at high temperatures. And, the spherical iron powder is successfully prepared using direct reduced iron powder. The morphology, particle size distribution, spheroidization rate, and gas content of the powders prepared were characterized. When the gas ratio of hydrogen increases in the spheroidizing atmosphere, the oxygen content of the treated powder decreases subsequently. Meanwhile, the change in nitrogen and hydrogen content is not obvious. After treatments at 1833 K, the particles below 100 μm present smooth surfaces, and no hollow particles and satellite spheres exist. And, the spheroidization rate is close to 100%, which is greatly beneficial to improve the flowability.

Keywords Spherical iron powder · Spheroidization · 3D printing · Flowability

Introduction

Spherical metal powder has many unique properties, such as isotropy, excellent flowability, and high density [1, 2]. In recent years, spherical metal powders are in great demand in the novel manufacturing industry, such as 3D printing, plasma spraying, and metal powder injection molding [3, 4]. But, there are still some defects in the existing production process of spherical metal powder.

For example, satellite particles and hollow particles inevitably appear in metal powders produced by atomization methods. However, the powder-preparing process

Q. Bao · L. Guo · Z. Guo (✉)
State Key Laboratory of Advanced Metallurgy, University of Science and Technology Beijing, Beijing 100083, P. R. China
e-mail: zcguo@ustb.edu.cn

L. Guo
e-mail: leiguo@ustb.edu.cn

Z. Peng et al. (eds.), *12th International Symposium on High-Temperature Metallurgical Processing*, The Minerals, Metals & Materials Series,
https://doi.org/10.1007/978-3-030-92388-4_53

involving plasma as heat source usually has some problems, such as high cost and volatilization of alloy elements [5]. Thus, for the efficient production of spherical metal powder, an innovative method to prepare spherical metal powder was proposed in this paper through re-melting and spheroidizing the irregular shape metal powders at high temperatures [6]. The direct reduction iron powder is a widely useful raw material in the field of metallurgy [7]. Its production process is mature, the output is huge, and the cost is low. Therefore, we choose direct reduction iron powder as raw material. And, the spherical iron powder was successfully prepared by high-temperature re-melting and spheroidizing.

In order to study the optimal spheroidizing conditions, we have set different spheroidizing parameters such as temperature and particle size. And, the morphology, particle size distribution, spheroidization rate, and gas content of the powders prepared were characterized. When the gas ratio of hydrogen increases in the spheroidizing atmosphere, the oxygen content of the treated powder decreases subsequently. Meanwhile, the change in nitrogen and hydrogen content is not obvious. After treatments at 1833 K, the particles below 100 μm present smooth surfaces, and no hollow particles and satellite spheres exist. And, the spheroidization rate is close to 100%, which is greatly beneficial to improve the flowability. Furthermore, after calculating the theoretical model, it is also basically consistent with the experimental results. This theoretical model can be used to predict the spheroidization results of other metals.

Experimental

Materials

The iron powder used in this paper is gas-based direct reduction iron powder produced by the Beijing Xingrongyuan company. The chemical composition of the raw powder is shown in Table 1. It can be seen from the table that the oxygen content is high, and the content of other impurity elements is at the general level. And, the iron powder is silver-gray macroscopically, with poor flowability, and in irregular porous sponge shape microscopically. The particle size ranges from about 10–150 μm.

Table 1 Chemical composition (wt.%) of the experimental materials

Composition	TFe	Mn	Si	C	P	S	O
Conc	Bal	0.146	0.237	0.009	0.013	0.015	0.306

Apparatus

As shown in Fig. 1, the experimental device can be divided into four parts: heating, feeding, temperature control, and gas supply. The heat source of the furnace is a molybdenum silicide rod. The limit heating temperature can reach 1873 K. The length and inner diameter of the pipe are 1600 mm and 70 mm, respectively, and a corundum furnace tube is adopted. The temperature is controlled by a programmable controller with a B thermocouple. The observation accuracy is within ±3 °C.

In Fig. 1, the spheroidization process is explained in detail. The raw iron powder in the storage hopper is continuously fed into the furnace tube by the screw feeder. After that, the powder is evenly dispersed in the air. When the flying metal particles pass through the high-temperature zone, they are quickly heated and melted into water droplets. Under surface tension, metal droplets spontaneously shrink into spheres. The whole spheroidization process was carried out in atmosphere of 75% argon and 25% hydrogen. The powder disperses spontaneously in space due to the size difference size. The molten metal droplets are cooled and solidified in the middle and lower parts of the furnace tube.

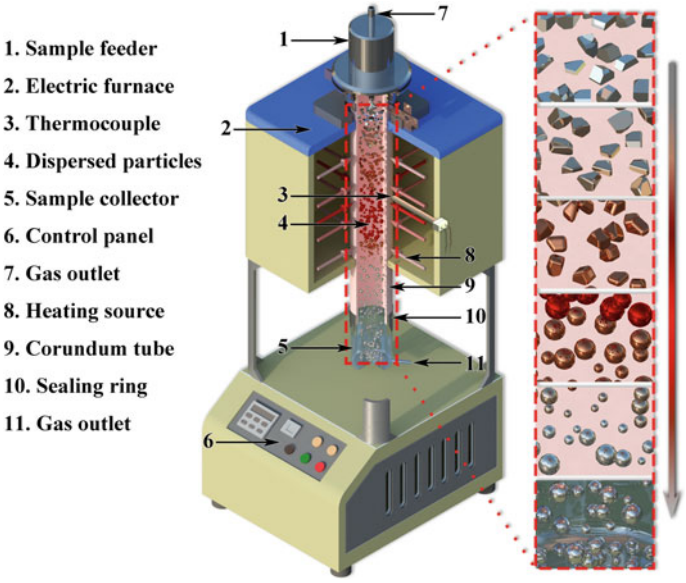

Fig. 1 Systematic diagram of experimental apparatus

Characterization

In order to observe the particle morphology, scanning electron microscopy (SEM, phenom prox) was used. For the cross-sectional morphology, the powder was installed in the resin and polished first. The gas content is detected by oxygen/nitrogen/hydrogen analyzer (EMGA-830). The particle size distribution was measured using a laser particle size analyzer (Malvern clf-2). Hall flowmeter (xf-02) was used to measure powder flowability.

Results and Discussion

The Results of the High-Temperature Re-melting and Spheroidizing

The particle surface morphologies after high-temperature re-melting and spheroidizing are shown in Fig. 2. It involves temperatures ranging from 1733 to 1833 K (20° intervals). All particles are perfect spheres with smooth surfaces. There are no obvious defects such as satellite particles on the surface. At the temperature of 1833 K, the prepared small particles (below 100 μm) are uniform, perfect sphere, and free of pores.

By counting the proportion of spheroidized particles, the spheroidization rate data can be obtained, as shown in Fig. 2. Below the temperature of 1793 K, the spheroidization rate of particles is low, which means that the particles are not spheroidized at all. When the temperature increases to 1833 K, the spheroidization rate of particles improves with the decrease of particle size. At 1833 K, the particles below 60 μm are close to 100%. Therefore, the change is not obvious with the decrease of particle size (Fig. 3).

The Effect of Spheroidization Temperatures

The surface morphology of the powder varies with temperature is shown in Fig. 2. Within a reasonable range, the spheroidization quality is obviously improved with the increase in temperature. At 1833 K, the small particles (below 60 μm) are nearly complete spheroidized. But, the large particles (greater than 100 μm) at 1833–1813 K are still incompletely spheroidized. Through Fig. 2 (d5), these particles are in the shape of short rods or irregular droplets. Differing from the particle treated at 1733–1793 K, these particles have already melted a little on the surface and produced a small amount of liquid phase. But before complete melting, it has entered the cooling stage. Because of the fast cooling rate, there is no enough time for concentrating as sphere shapes. When the temperature rises to 1623 K, all particles show as perfect

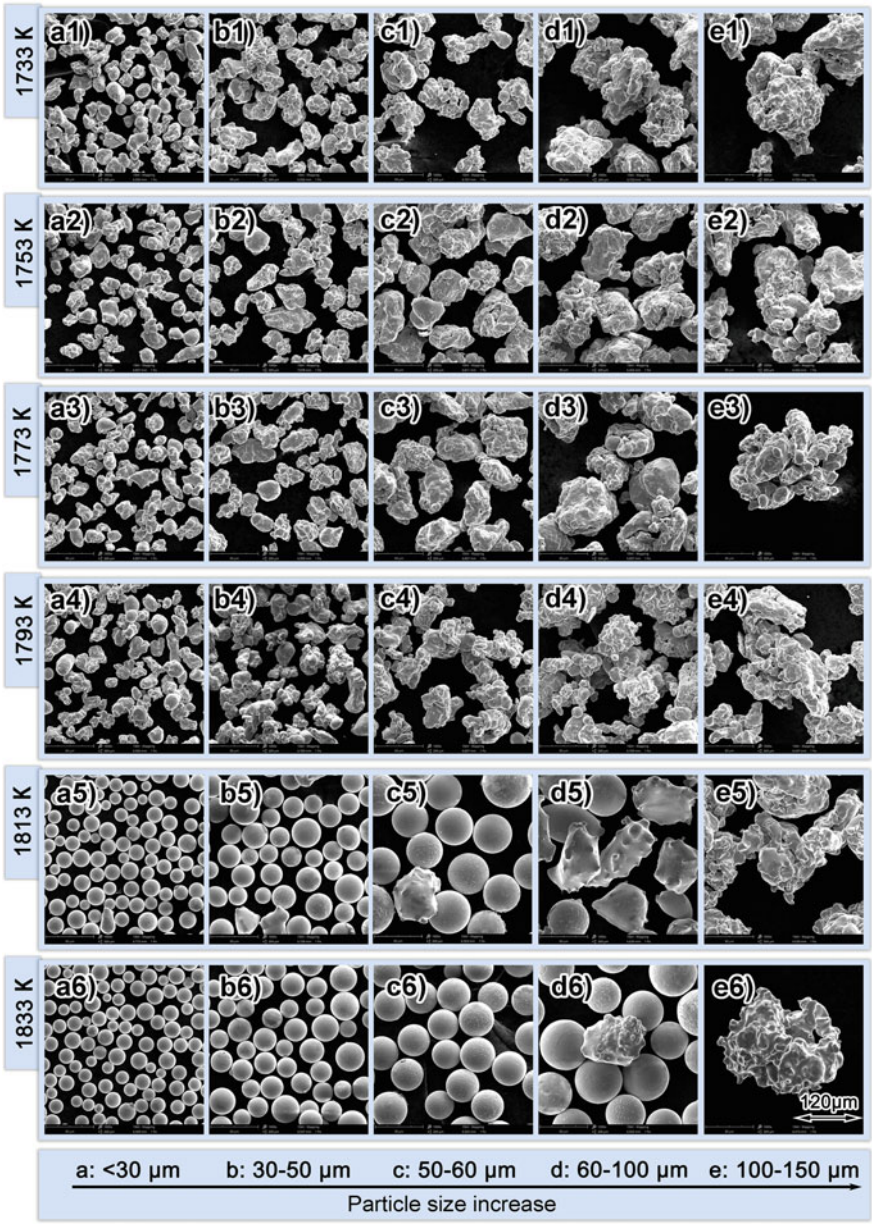

Fig. 2 Surface morphology of spheroidized particles under different conditions

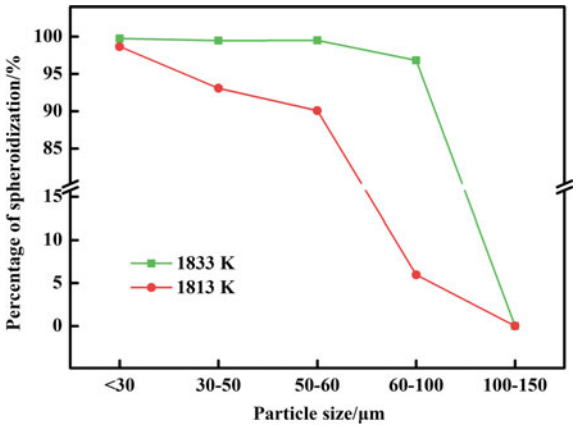

Fig. 3 Spheroidization rate of spheroidized particles under different conditions

spheres and bright smooth surfaces. At 1833 K, as shown in Fig. 2 (e6), the melting extent is lower. While at 1793 K and below, the particles show no signs of melting.

According to the oxygen/nitrogen/hydrogen analysis, the oxygen content of the raw powder is about 0.312%. The detailed data are shown in Fig. 4. For the prepared powder, the oxygen content is basically reduced. With the increase of temperature, the oxygen content of spheroidized powder increased slightly. The main reason for the decrease of oxygen content is the reducing activity of hydrogen. The reduction of the surface area also contributes to the reduction of adsorbed oxygen. The nitrogen content and hydrogen content are basically the same as raw materials, at a low level.

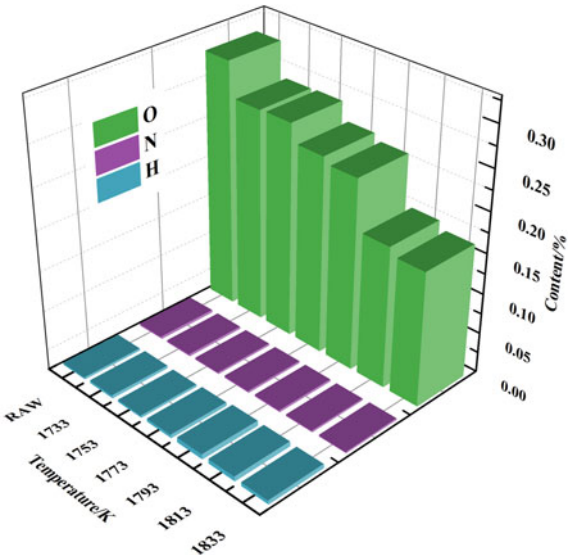

Fig. 4 Gas content of spheroidized particles at different temperatures and raw powder

The Effect of Particle Sizes

The cross-section morphologies of spheroidized particles with different particle sizes at 1833 K are shown in Fig. 5. There are some pores inside the raw powder. While in the treated particles, they are dense without defects. The composition is uniform without segregation or impurities. However, when the particle size rises to 150 μm, the incomplete shrinkage and melting would bring some pores inside particles.

Particle size distribution is also one of the important parameters to characterize metal powder [8]. Narrow particle size distribution means uniform particle size and better the flowability. Figure 6 shows the particle size distribution of spheroidized particles with different sizes and raw powder. The particle size of the raw powder is in a bimodal distribution. Most of the particles are distributed in the range of 50–100 μm, and a small part are distributed near 30 μm. The spheroidized particles basically have a normal distribution, and the particle size is relatively uniform.

The gas content of particles also has an obvious relationship with particle size. As shown in Fig. 7, it is the particle gas content of each particle size after spheroidization at 1813 K. The oxygen content decreases with the decrease of particle size. Especially when the particle size is reduced to 60 μm, the oxygen content is greatly reduced. This is because the particles below 60 μm melt well and are reduced more fully at this temperature. The content of hydrogen and nitrogen has been very low, and the change is not obvious.

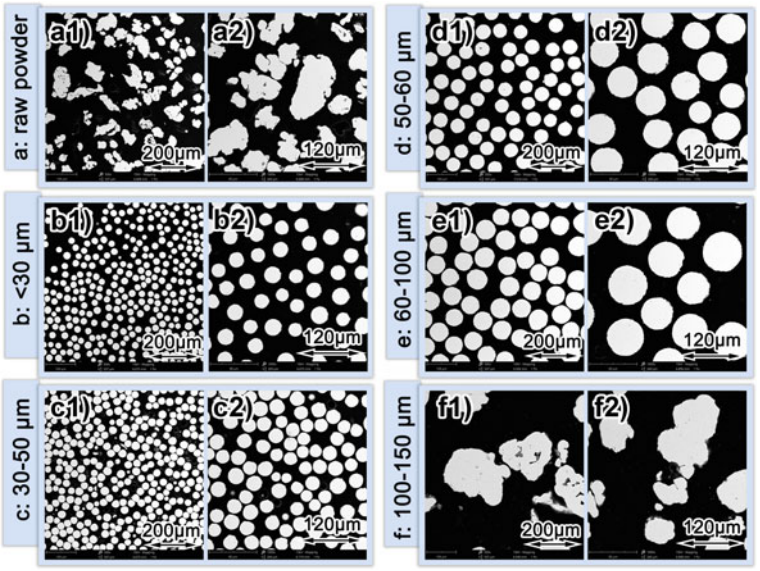

Fig. 5 Cross-section morphology of spheroidized particles with different sizes and raw powder

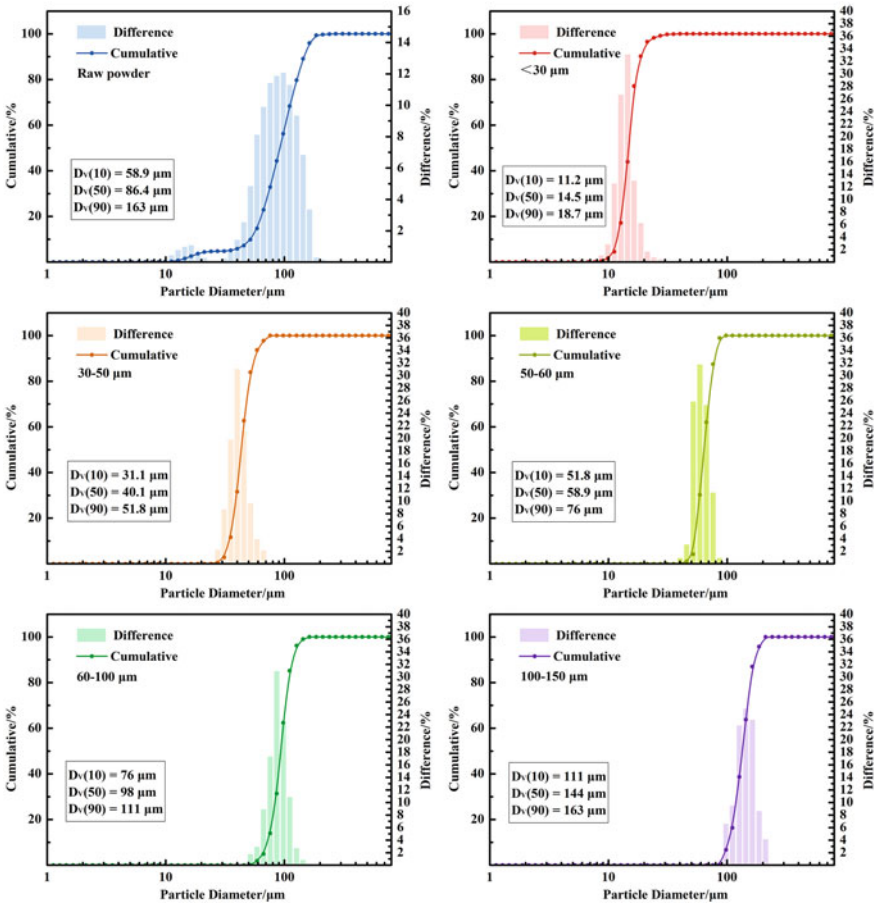

Fig. 6 Particle size distribution of spheroidized particles with different sizes and raw powder

The Verification of Theoretical Heat Transfer Model

In order to predict the spheroidization process, we need to understand the heat exchange between metal particles and the gas environment. Researching the heat exchange process, the particles' falling behavior also needs to be studied. Thus, the instantaneous velocity and temperature of particles under different conditions could be calculated, based on the Stokes formula [9] and enthalpy balance:

$$\mathrm{d}u_\mathrm{p}/\mathrm{d}t = F_D\left(u_\infty - u_\mathrm{p}\right) + \mathrm{g}_\mathrm{x}\left(\rho_\mathrm{p} - \rho_\infty\right)/\rho_\mathrm{p} + F_\mathrm{X} \tag{1}$$

$$\frac{\pi}{6}\rho_\mathrm{p} d_\mathrm{p}^3 C_\mathrm{p}\frac{\mathrm{d}T_\mathrm{p}}{\mathrm{d}t} = h_\mathrm{c} A_\mathrm{p}(T_\infty - T_\mathrm{p}) + \varepsilon_\mathrm{p} A_\mathrm{p}\sigma_\mathrm{sb}(T_\mathrm{a}^4 - T_\mathrm{p}^4) \tag{2}$$

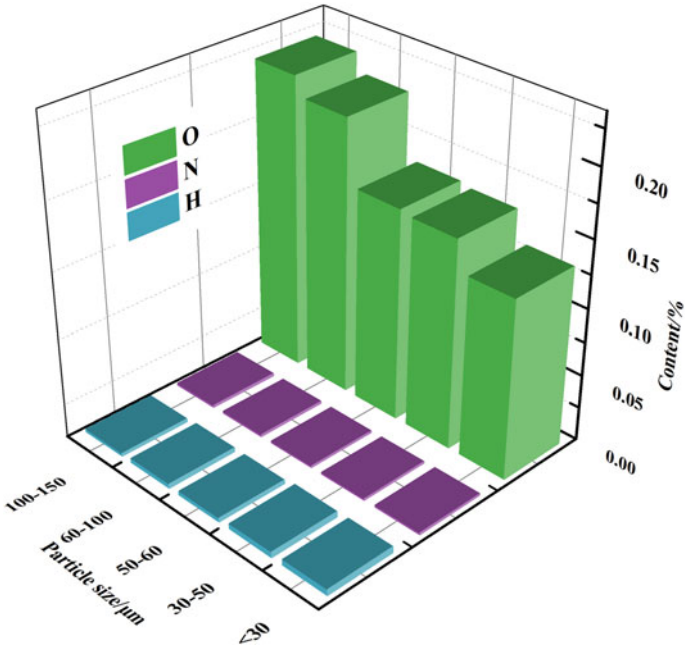

Fig. 7 Gas content of spheroidized particles with different sizes

However, the physical parameters [10, 11] of metallic iron at high temperatures are constantly changing, as shown in Fig. 8. Therefore, the analytical solution cannot be obtained directly. However, the numerical solution can be obtained by finite difference iteration.

This part is taken the iron powder with particle sizes of 30, 50, 60, 100, and 150 μm as an example. This result can provide a reference for the setting of experimental conditions for other metals.

Figure 9 shows the particle temperature at an ambient temperature of 1813 K. At start, the 30–60 μm particles quickly reach the ambient temperature. And, there is little difference in the subsequent high-temperature region. And, 100 μm particles have a great difference before entering the high-temperature zone and then quickly reach the ambient temperature in the temperature zone above T_m. The 150 μm particles are quite different, completely below T_m. This means that the heat obtained from the environment is not enough to make 150 μm; the particles are completely melted (Fig. 10).

When the ambient temperature is reduced to 1793 K, 100 μm particles cannot reach above the melting point temperature. Therefore, when the ambient temperature is 1793 K, 100 μm particles cannot be completely spheroidized. It is worth noting that all particle temperature curves are bent near T_C, which is mainly caused by the drastic change of heat capacity near Curie temperature.

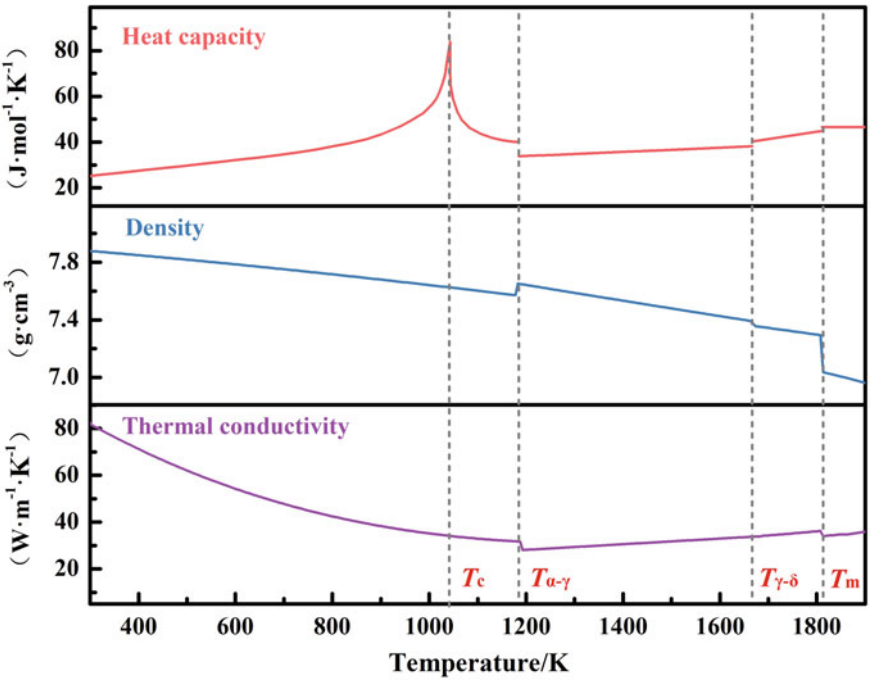

Fig. 8 Basic physical parameters of iron related to heat transfer process. T_c: Curie point; $T_{\alpha\text{-}\gamma}$: phase transition point of α to γ; $T_{\gamma\text{-}\delta}$: phase transition point of γ to δ; T_m: melting point

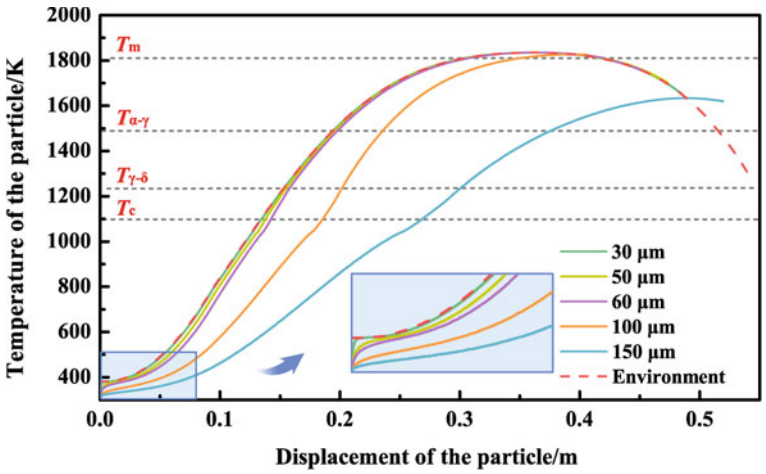

Fig. 9 Particle temperature in spheroidizing process under the ambient temperature of 1813 K

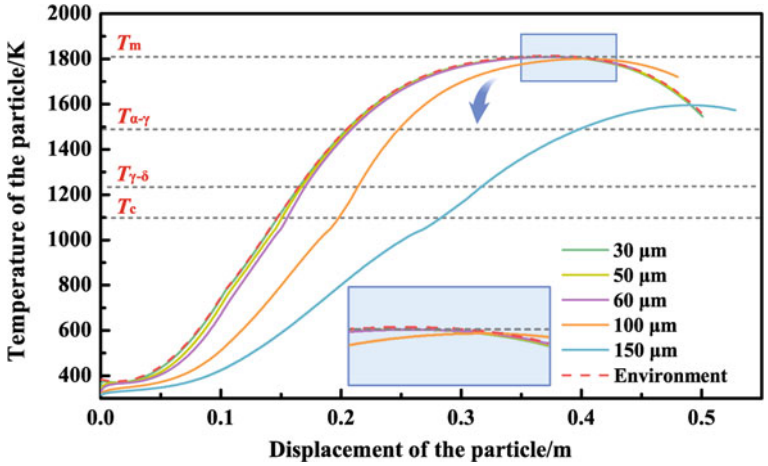

Fig. 10 Particle temperature in spheroidizing process under the ambient temperature of 1793 K

Conclusion

In this paper, a novel method was proposed for the production of high-quality spherical metal powder. The spheroidization regular of particles and the numerical solution model have been established and studied. The following conclusions could be drawn. This process greatly reduces the defects of hollow particles and satellite particles. The spheroidization process is mild, avoiding the influence of the atomization medium. This is a crucible-free re-melting process without contamination from inclusions. The reduction atmosphere in spheroidization can reduce the oxygen content of the metal powder. Theoretically, the spheroidization temperature can be controlled near the melting point by using a suitable high-temperature section. The gas consumption can be significantly reduced only by maintaining the micro-reduction atmosphere without using the atomizing medium gas.

Acknowledgements The authors acknowledge the financial support from the Key Projects of the State Key Research and Development Plan (No. 2016YFB0601304), the Open Project (SKLASS 2019-13) of State Key Laboratory of Advanced Special Steel, and Shanghai Key Laboratory of Advanced Ferrometallurgy, Shanghai University.

References

1. Sun P, Fang ZZ, Zhang Y, Xia Y (2017) Review of the methods for production of spherical Ti and Ti alloy powder. JOM 69:1853–1860
2. Narra SP, Wu Z, Patel R, Capone J, Paliwal M, Beuth J, Rollett A (2020) Use of non-spherical hydride-dehydride (HDH) powder in powder bed fusion additive manufacturing. Add Manuf 34:101188

3. Sungail C, Abid A (2018) Spherical tantalum feed powder for metal additive manufacturing. Met Powder Rep 73:316–318
4. Li XG, Zhu Q, Shu S, Fan JZ, Zhang SM (2019) Fine spherical powder production during gas atomization of pressurized melts through melt nozzles with a small inner diameter. Powder Technol 356:759–768
5. Dzur B (2008) Plasma puts heat into spherical powder production. Met Powder Rep 63:12–15
6. Bao QP Yang YR, Wen XC, Guo L, Guo ZC (2021) The preparation of spherical metal powders using the high-temperature remelting spheroidization technology. Mat Des 199:109382
7. Anameric B, Kawatra SK (2007) Properties and features of direct reduced iron. Miner Process Extr M 28(1):59–116
8. Lagutkin S, Achelis L, Sheikhaliev S, Uhlenwinkel V, Srivastava V (2004) Atomization process for metal powder. Mat Sci Eng A Struct 383:1–6
9. Sjöberg LE (2003) A general model for modifying Stokes' formula and its least-squares solution. J Geodesy 77:459–464
10. Helsing J, Grimvall G (1991) Thermal conductivity of cast iron: models and analysis of experiments. J Appl Phys 70(3):1198–1206
11. Austin JB, Pierce JR (1933) The linear thermal expansion and alpha-gamma transformation temperature of pure iron. Physics 4(12):409–410

Phosphorus Migration Behavior in the Process of Converter Slag Gasification Dephosphorization

Chenxiao Li, Yuekai Xue, Shuai Tong, and Kaixuan Zhang

Abstract To realize the gasification dephosphorization process in the converter slag splashing stage for avoiding the P enrichment, the dephosphorized slag can be left for recycling in subsequent furnaces. The migratory behavior of P during the slag gasification dephosphorization was studied. The results show that the P element in converter slag is mainly enriched in the silicate phase. The FeO in the converter slag is reduced by the coke into a large-diameter granular elemental Fe phase. The P_2O_5 in the slag is reduced to P_2 steam by coke at high temperature. Most of the P_2 steam passes through the gas-slag interface and enters the furnace gas. A small part of the P_2 steam will be adsorbed by the nearby elemental Fe phase to form iron phosphide.

Keywords Converter slag · Gasification dephosphorization · Phosphorus migration · Occurrence state

China is the world's largest steel producer, and the steel industry is also a high consumption and high emission industry. According to the National Bureau of Statistics, China's steel slag output in 2020 is about 160 million tons, and the utilization rate of steel slag resources is less than 30%, causing environmental pollution and resource waste. With the introduction of the "Environmental Protection Tax Law" and "Recycling Development Leading Action" and other regulations, it shows that the recycling of steel slag in steel enterprises is imminent [1–3]. "Control at the source" is an important direction to effectively reduce converter slag emissions, while the current production of residual slag can achieve low slag converter smelting, but the cyclic enrichment of P in the slag will directly lead to the utilization of slag in the furnace. Therefore, if the P in the steel slag can be removed, its phosphorus capacity

C. Li (✉) · Y. Xue · S. Tong · K. Zhang
Metallurgy and Energy College, North China University of Science and Technology, Tangshan 063210, China
e-mail: lichenxiao34@163.com

Tangshan Key Laboratory of Special Metallurgy and Material Manufacture, Tangshan 063210, China

Z. Peng et al. (eds.), *12th International Symposium on High-Temperature Metallurgical Processing*, The Minerals, Metals & Materials Series,
https://doi.org/10.1007/978-3-030-92388-4_54

can be increased, the slag retention operation can be carried out, and the slag recycling economy can be realized. For this reason, domestic and foreign scholars have made breakthrough progress in the dephosphorization of steel slag, and their methods of gasification dephosphorization of steel slag have been developed rapidly. JIANG [4] added SiO_2 or Al_2O_3 to the steel slag, and the phosphorus of the slag was gasified and removed and then returned to the steelmaking process for smelting. Wang [5] studied the dephosphorization reaction kinetics and showed that under microwave heating conditions, gasification dephosphorization is a secondary reaction and its limiting link in the possible interface chemical reaction. Xue [6] used coke powder for gasification dephosphorization industrial test on a 60t converter of Tangshan Iron and Steel, and the results showed that the gasification dephosphorization of coke powder reduction slag is feasible and superior.

The above studies have shown that part of the P_2O_5 in the slag can be removed by gasification dephosphorization and has attracted the attention of many domestic and foreign scholars. However, there are few studies on the whereabouts of phosphorus in the process of gasification dephosphorization. Therefore, the author makes a theoretical analysis of the reaction mechanism of gasification dephosphorization and phosphorus migration behavior through FactSage software simulation and thermal experiment and provides technical guidance for metallurgical industry production.

Experimental Materials and Methods

Experimental Materials

The compositions of converter slag and coke are shown in Table 1 and Table 2, respectively. Before the experiments, the steel slag and carbon were crushed to less than 200 mesh and with electromagnetic crusher. To strengthen the effect of gasification dephosphorization and take into account the consumption of coke powder in the experiment, all the experiments of the furnaces used two units of carbon to reduce 100 g of converter slag. One unit of carbon equivalent is defined as the total mass of carbon used when FeO, MnO, and P_2O_5 of the slag are reduced to the corresponding elements.

Table 1 Composition of converter slag (wt.%)

FeO	CaO	SiO_2	MgO	MnO	P_2O_5	R
15.82	42.85	12.55	7.15	3.35	3.08	3.41

Table 2 Composition of coke (wt.%)

C	CaO	SiO_2	MgO	P_2O_5	S	Other
86.55	1.37	6.42	0.33	0.36	0.98	3.99

Experimental Method

The main equipment for experimental heating is (HLLG1217) a vertical high-temperature-resistance furnace, bipolar silicon molybdenum rod as heating element. The schematic diagram of the experimental equipment structure is shown in Fig. 1, a total of three sets of thermal experiments was carried out, and the experimental data were all average values. All heat experiments are carried out under the protection of nitrogen, and the nitrogen flow is controlled by the equipment rotor flowmeter, and the N_2 flow rate is 0.4 m^3/h.

Before the experiment, put mix the slag and coke powder into the corundum crucible with the outer graphite crucible. Turn on the circulating cooling water before starting the heating program to ensure the cooling protection of the furnace. Since the converter slag gasification dephosphorization is carried out before the slag splashing, the reference industrial smelting temperature at this stage is about 1540 °C. To simulate industrial production temperature, the temperature of this experiment is 1540 °C, then keep it warm for 1 h. After the experiment, when the slag is lowered to room temperature, slag samples are taken for testing. The composition of gasification dephosphorization slag is shown in Table 3.

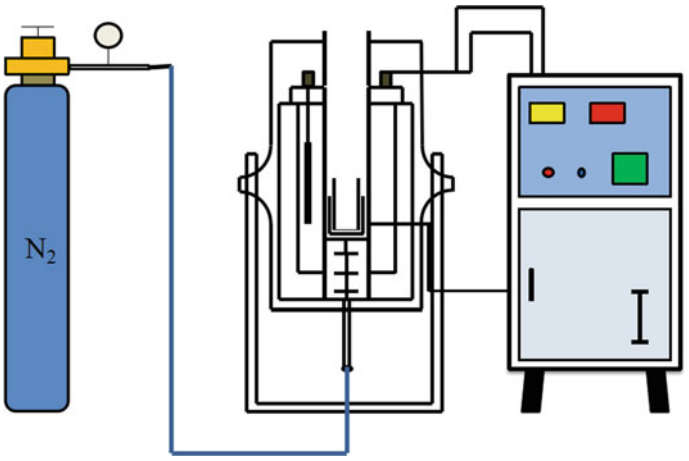

Fig. 1 Schematic diagram of high-temperature-resistance furnace

Table 3 Composition of gasification dephosphorization slag (wt.%)

FeO	CaO	SiO_2	MgO	MnO	P_2O_5
13.56	44.22	16.32	8.30	3.19	2.22

Analysis of Results

Thermodynamic Analysis of Gasification Dephosphorization Reaction

This experiment uses coke as the reducing agent, in the standard state. There are four gas products of carbon reduction P_2O_5, namely P, P_2, P_4, and PO. To determine the specific gasification dephosphorization products, the FactSage software was used to simulate the thermal carbon reduction of slag at different temperatures. As shown in Fig. 2, it can be seen from Fig. 2 that the equilibrium partial pressure of gas P_2 is much higher than the equilibrium partial pressures of P, P_4, and PO, and the equilibrium partial pressure of gas shows an upward trend with the increase of temperature. It can be inferred that the gas product of the carbon reduction of P_2O_5 is P_2.

To better study the slag components involved in the reaction, the slag composition before and after reduction at 1540 °C was compared, as shown in Table 4. It can be seen from Table 4 that the mass fraction of P_2O_5, FeO, and MnO in the slag is significantly reduced, indicating that it will react with coke at 1540 °C. The reaction formula is as (1)–(3).

$$P_2O_{5(l)} + 5C_{(s)} = P_{2(g)} + 5CO_{(g)} \quad \Delta G^{\theta} = 603609 - 648.94T \tag{1}$$

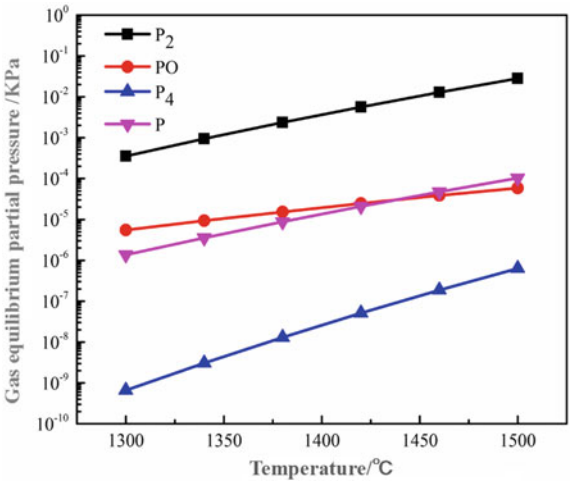

Fig. 2 Diagram of the change of the equilibrium partial pressure of phosphorus gas

Table 4 Slag composition before and after reduction (wt.%)

Slag	FeO	CaO	SiO_2	MgO	MnO	P_2O_5
Final slag	15.82	42.85	12.55	7.15	3.35	3.08
Gasification dephosphorization slag	13.56	44.22	16.32	8.30	3.19	2.22

$$FeO_{(l)} + C_{(s)} = Fe_{(l)} + CO_{(g)} \quad \Delta G^{\theta} = 141660 - 139.45T \tag{2}$$

$$MnO_{(s)} + C_{(s)} = Mn_{(l)} + CO_{(g)} \quad \Delta G^{\theta} = 292954 - 174.14T \tag{3}$$

From Table 2, the addition of coke powder will bring in a certain amount of P_2O_5, so the actual reaction amounts of P_2O_5, FeO, and MnO in this experiment are 3.12 g, 15.82 g, and 3.35 g, respectively. The average theoretical reduction rates of P_2O_5, FeO, and MnO are 27.9%, 20.6%, and 4.78%, respectively. But, the actual reduction rate of P_2O_5 is 28.3%, which is 0.4% different from the theoretical reduction rate. Because there is a certain gap between laboratory reaction conditions and theoretically good kinetic and thermodynamic conditions, within the allowable range of experimental error, it can be considered that the experimental reduction rate is basically the same as the theoretical calculation value.

At the temperature of 1540 °C in the experiment, the standard state Gibbs free energy of P_2O_5, FeO, and MnO reduction were calculated from the thermodynamics of the reaction Formulas (1), (2), and (3) to be −572.9, −111.2, and −22.8 kJ/mol. The driving force for P_2O_5 to be reduced is greater, which can indicate that carbon will preferentially reduce P_2O_5, followed by FeO and MnO. The consumption of coke has been calculated theoretically, the theoretical added amount of coke fixed carbon is 8.88 g, and the theoretical value of P_2O_5, FeO, and MnO being completely reduced by C is 4.6 g. So, the unmelted C phase appears in the gasification dephosphorization slag.

Phosphorus Occurrence Behavior Before and After Gasification Dephosphorization Reaction

Analysis of Final Slag Mineral Phase Composition and Phosphorus-Rich Phase

Analyze the microscopic morphology and phase of the final slag by SEM–EDS, as shown in Fig. 3. From Fig. 3a, it can be seen that the slag is composed of four phases, the first is that the black matrix has a claw-like structure with a large distribution area; the second is that the bright white, gray matrix is randomly dispersed in particles or strips and is embedded in the gray and black matrix; the third is a large-diameter granular dark gray matrix, part of which is distributed on the white matrix, and the other part is attached to the black matrix; the fourth type is an off-white matrix with the irregular distribution. To quantitatively study the phase characteristics of the slag, the analysis data of different microzones are summarized and analyzed, the dot position is shown in Fig. 3b, and the mass scores of each element at the corresponding points are shown in Table 5. Area1 phase contains high amounts of Ca, Mn, Si, Mg, and other elements, and it is inferred that this phase is fostered. Area

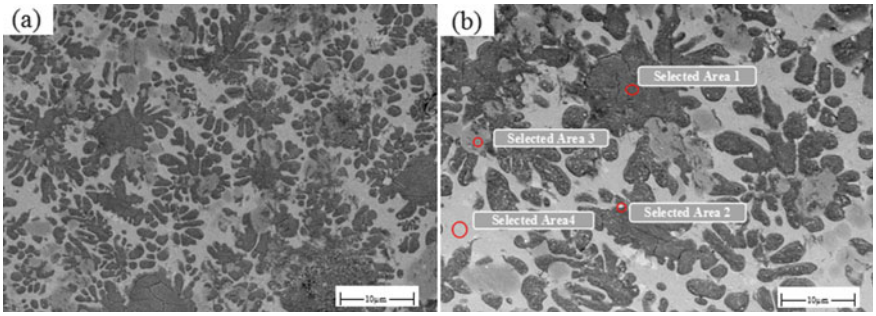

Fig. 3 Microscopic morphology and phase diagram of the final slag sample

Table 5 Composition of each phase element in the final slag (wt.%)

Area	Element	C	O	Mg	Si	P	Ca	Fe	Phase
1	Mass%	19.70	33.80	1.45	3.81	0.43	28.82	10.22	Forsterite
	Atom%	35.53	41.59	1.23	2.57	0.26	18.60	3.27	
2	Mass%	4.35	28.68	1.64	3.01	0.61	13.30	42.60	RO phase
	Atom%	10.28	50.87	1.76	3.04	0.56	9.42	21.64	
3	Mass%	3.33	28.19	0.36	12.80	2.30	42.24	9.22	C_2S phase
	Atom%	7.17	45.52	0.38	11.78	1.92	23.76	3.07	
4	Mass%	9.47	31.69	0.56	6.25	0.40	23.66	24.54	Calcite olivine
	Atom%	18.07	47.90	0.56	4.73	0.37	18.21	19.83	

2 phase contains a large amount of Ca, Mn, Fe, and Mg elements. It is inferred that this phase is a typical RO phase, and the P content is relatively high. The dark gray phase is dominated by Area 3 phase, and its proportion in the slag has increased. This phase contains high content of Ca, Si, O elements, the mass fraction are 23.76%, 11.78%, and 45.52%, respectively, and the mass fraction of P element is as high as 2.30%, and the stoichiometric atom ratio of Ca, Si, and O in C_2S is 2:1:4. The actual atomic ratio of Ca, Si, O in this phase is very close to that of C_2S. Therefore, it can be inferred that the dark gray matrix is the C_2S phase, which is the phosphorus-rich phase. The Fe, Si, and Ca elements in Area 4 phase are relatively high, which can be inferred to be possible calcite olivine.

To further study the occurrence of P in the final slag, the silicate phase area with high P content was quantitatively analyzed, that is, the relationship between the content of P, Ca, and Si in the micro-area is shown in Fig. 4. As shown in Fig. 4, the Ca content in the C_2S phase microzones is generally between 25 and 40%, the Si content is concentrated in the 11–14% range, and the P content is between 1.4 and 2.2%. P content increases with the increase of Ca and Si content, respectively. P exists in silicate phase regions with high Ca and high Si content, but it also exists in low Ca and low Si content micro-regions individually.

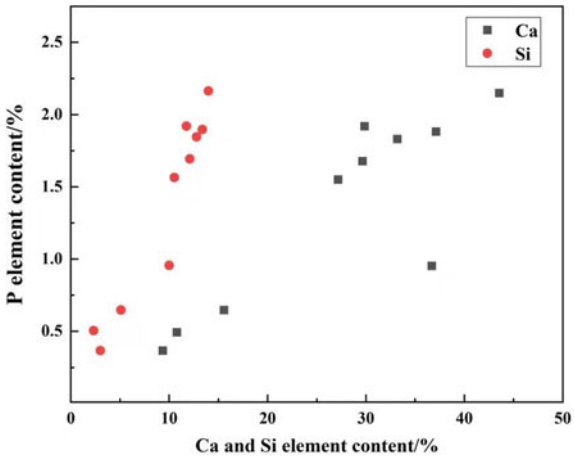

Fig. 4 Relationship between P, Ca, and Si content in C_2S phase of final slag

Phosphorus Migration in Gasification Dephosphorization Reaction

The slag before and after reduction was detected by SEM–EDS, and it was found that the RO phase in the final slag was small white particles and long strips. After reduction, it becomes bright white large-diameter granular and dispersed distribution, which may be due to the FeO in the RO phase being reduced to elemental Fe phase by C at a high temperature of 1540 °C, as shown in Fig. 5.

In the process of EDS analysis, it was found that there is a large amount of P element in the Fe phase of gasification dephosphorization slag. The RO phase of the final slag and the Fe phase of the gasification dephosphorization slag are separately analyzed, as shown in Fig. 6.

It can be seen from Fig. 6, that the P content in the RO phase microzone of the final slag is within the range of 0.4–0.8%, and the Fe element content is within the range of 10–50%. With the increase of Fe content in the final slag, the P content fluctuates slightly, but there are some high P micro-regions in the Fe content between 10 and

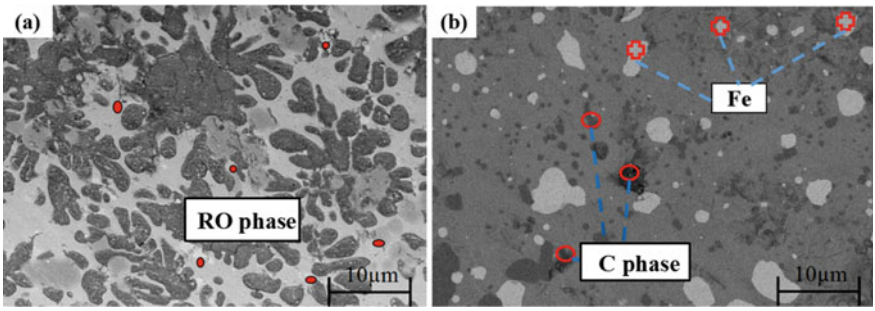

Fig. 5 SEM before and after the converter slag gasification dephosphorization reaction

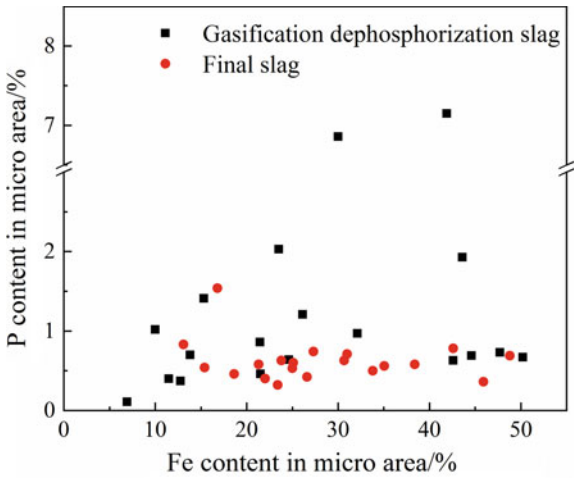

Fig. 6 Relationship between P content and Fe content in RO phase and Fe phase microdomain

20%. The content of P in the Fe phase microzones of the gasification dephosphorization slag is uneven in the range of 0.15–7.5%, and the content of Fe element is in the range of 0–60%. On the whole, the Fe content and P content in the Fe phase microzones of the gasification dephosphorization slag are not obviously linear, but when the Fe content is less than 30%, as the Fe content increases, the P content also has an upward trend; when the Fe content is greater than 30%, as the Fe content increases, the P content has a downward trend, but there will still be high P micro-regions.

The content of P in the Fe phase microdomains of the gasification dephosphorization slag is generally higher than that in the RO phase microdomains of the final slag. It can be inferred that part of the P is excluded from the furnace in the form of P_2 gas during the gasification dephosphorization. In addition, part of P_2 will encounter the liquid elemental Fe phase during the floating process. Due to the high density of the Fe phase, the P_2 gas will be drawn into it under the action of gravity, and the Fe phase will react with the elemental Fe to form Fe_2P and Fe_3P, FeP, and other iron phosphide compounds [7]. As a result, the illustration of migration behavior of P during slag gasification dephosphorization of coke reduction converter slag can be obtained as shown in Fig. 7. According to the quantitative analysis of microzone P and the migration behavior of P during gasification dephosphorization, it can be known that as the content of elemental Fe produced by coke reduction of FeO increases, the content of P present in the Fe phase will also increase. However, if the FeO content in the final slag is too high, a large amount of FeO will be reduced by C into the elemental Fe phase and more P will occur, which will inevitably lead to a decrease in the quality of molten steel. Therefore, maintaining an appropriately high FeO content in the final slag will facilitate the gasification dephosphorization reaction, and the presence of FeO will increase the activity coefficient of P_2O_5 [8].

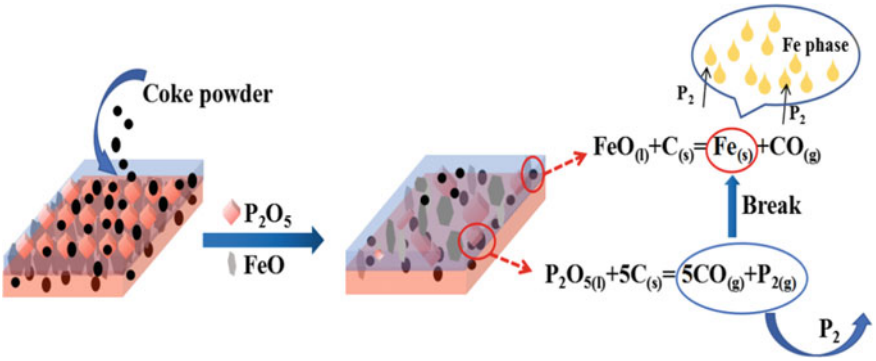

Fig. 7 Illustration of migration behavior of P during slag gasification dephosphorization

Conclusion

The P in the final slag generally exists in the silicate phase micro-regions with high Ca and high Si content. The part of the P_2O_5 of the converter slag can be reduced by coke. Within the allowable error range of the experiment, the reduction rate of P_2O_5 in the experiment is basically the same as the theoretical calculation value. And, the reduction product may be P_2. The FeO in the converter slag is reduced by the coke to Fe phase, and the Fe phase will adsorb the released P_2. As the Fe content increases, the P content in the Fe phase will also increase. Therefore, most of the P_2 steam enters the furnace gas through the gas-slag interface. A small part of the P_2 will be adsorbed by the nearby element Fe phase.

Acknowledgements The presented research was supported by The National Natural Science Foundation of China (52004097).

References

1. Wang SR, Zhang WD (2017) Solid waste resources treatment mode and development tendency of iron and steel enterprises in China. Iron and Steel 52(04):1–6
2. Wang XX, Cao HM (2019) Exploration on industrialization development path of comprehensive utilization of solid waste in iron and steel industry 37(07):60–62
3. Wang YY, Liang HY, Cheng Y (2014) Discussion on the industrialization development route of comp rehensive utilization of solid wastes of iron and steel industry 32(S1):777–780
4. Jiang MF, Cui YY et al (2013) Effect of modification treatment for reduction of dephosphorization slag in hot metal bath. J Iron Steel Res Int 20(1):1–20
5. Wang YC, Li HY, Luo GP, et al (2017) Microwave carbothermic reduction converter slag gasification and dephosphorization reaction macro-kinetics 29(02):93–97
6. Xue YK, Wang SH, Li CX et al (2018) Experimental study on recycling of 60 t converter slag after gasification and dephosphorization 34(01):20–24

7. Dong YC, Wang HC (2012) Dephosphorization of steel production process. Metallurgical Industry Press, Beijing
8. Guo RH, Wang SH, Li CX et al (2020) Gasification dephosphorization test of converter slag for coke reduction dephosphorization 55(09):123–129

Removal of Heavy Metals from Sn-bearing Lead Slag: Effect of Reductant Dosage

Mingyuan Gu, Yiwei Zhong, and Zhancheng Guo

Abstract A carbothermic reduction process was proposed to recover valuable metals from Sn-bearing lead slag. The microstructure evolution and phase transition of the carbon-containing pellets during the reduction process were investigated via XRD and SEM–EDS analysis. Results revealed that with the increasing of the reducing agent dosage, the metallization rate of Fe and the volatilization ratio of Zn increased. The metallic iron particles obtained at lower reductant dosage can aggregate much bigger than those obtained with higher reductant dosage due to more liquid phase (Fe_2SiO_4, Fe–FeS) and lower ash residue. However, excessive reductant dosage can easily lead to the generation of Fe–Pb–Sn alloy in the reduction process, which hindered the further removal of Sn and Pb. When the reductant agent dosage was 22% and roasting at 1200 °C for 20 min, the volatilization ratio of Zn, Pb, and Sn can reach 93.31%, 92.5%, and 66.8%, respectively. Valuable flue dust rich in heavy metals was also obtained.

Keywords Sn-bearing lead slag · Carbothermic reduction · Reductant agent dosage · Waste recovery

Introduction

Large amounts of lead slag are produced during the production of primary lead and secondary lead industries. Considering lead concentrate smelting as an example, a primary lead smelting system production of 1 t of lead will discharge 7.1 t of lead slag [1]. As an environmentally hazardous waste, lead smelting slag was considered as a potential secondary resource of valuable metals (Zn, Pb, Fe, Cu, and Sn) if recycled.

Several metallurgical processes have been proposed, such as pyrometallurgy, one-step smelting, Ausmelt, and fuming were commonly used to recover heavy metals in industry. In recent years, gas-based or coal-based direct reduction technology has

M. Gu · Y. Zhong (✉) · Z. Guo
State Key Laboratory of Advanced Metallurgy, University of Science and Technology Beijing, Beijing 100083, P. R. China
e-mail: ywzhong@ustb.edu.cn

Z. Peng et al. (eds.), *12th International Symposium on High-Temperature Metallurgical Processing*, The Minerals, Metals & Materials Series,
https://doi.org/10.1007/978-3-030-92388-4_55

been widely used to process metallurgical dust or slag [2]. During this process, highly metalized pellets for iron recovery can be obtained, and valuable flue dust containing heavy metals can be recovered through the direct reduction and volatilization process [3]. In the carbothermic reduction, the reductant agent dosage (usually is coal or carbon) plays an important role in the reduction of iron and heavy metals. It is generally agreed that carbon gasification plays an extremely important role in the reduction of iron oxide by carbon because it provides reducing gas for reduction [4]. For iron and zinc compounds, to achieve the reduction of FeO and deep volatilization of Zn, a strong reduction atmosphere is favorable, which needs a more reductant dosage [5]. For the volatilization of the Pb, as it can volatile through Pb, PbO, and PbS, so the strong reduction atmosphere is non-essential [6]. However, for the volatilization of Sn element, the dosage of reductant agent was not as high as possible, and it had been found that lignite and semi-coke with good reactivity accelerated the generation of metallic iron and metallic tin and caused Fe-Sn alloy to easily form in the reduced pellets [7], resulting in a decline in the volatilization.

In this study, the Sn-containing lead slag which also containing Fe, Pb, and Zn was used as the raw material, adopting the containing carbon pellet direct reduction method. Effect of reductant agent dosage on the metallization rate of iron and volatilization ratio of heavy metals was investigated. More importantly, the objectives of this research were to determine the phase transformation of iron compounds and heavy metals elements, to observe the microstructure evolution of iron particles, and how the impact of the metallic iron morphology affects the removal of Sn and Pb.

Experimental

Materials

Sn-bearing lead slag used in this study is from a lead smelter plant in Yunnan, China, which compositions are shown in Table 1. Fine coke powder was used as a reductant with fixed carbon of 76.21% with a particle size of <0.074 mm (Xinjiang Province, China). Limestone was used as an additive to enhance the carbothermic reduction of the lead slag, and the particle size was <0.074 mm. Bentonite was used as a binder to increase the falling strength of pellets. Then, several kinds of pellets with different molar ratios of C/O (correspond with the reductant agent dosage) were made in a disk-granulating machine, where the molar weight of the element O refers to those combined with elements Fe, Zn, Pb, and Sn. The size of green pellets was controlled

Table 1 Chemical compositions of the lead slag by XRF (wt. %)

Component	Pb	Zn	Sn	TFe	S	As	SiO_2	Al_2O_3	CaO	MgO
Content	2.58	4.24	0.63	29.75	1.29	0.33	24.56	6.69	13.73	2.02

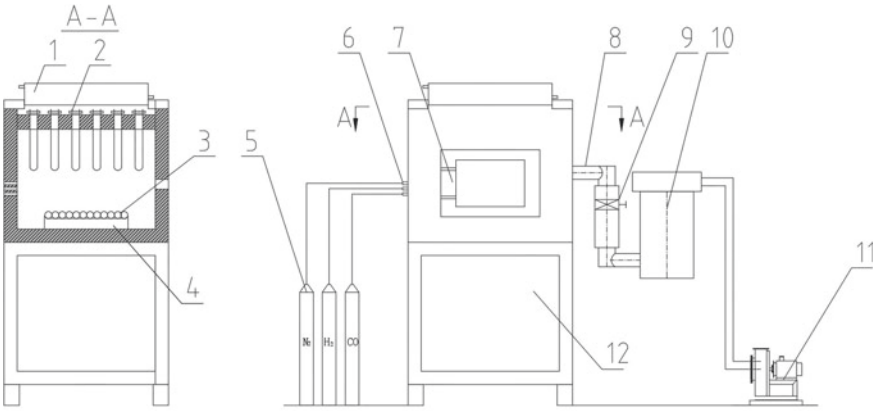

1-water-cooled cover; 2-heating element in the furnace; 3-carbon-containing lead slag pellets; 4-refractory plate; 5-gas cylinder; 6-gas inlet; 7-furnace door; 8-exhaust pipe; 9- ajustable air valve; 10-bag filter; 11-induced draft fan; 12-controlling cabinet

Fig. 1 Schematic diagram of experimental apparatus for carbothermic reduction and flue dust collection

about 10–12 mm through a circular screen. The wet pellets were dried at 110 °C for 4 h before being loaded in the furnace.

Experiment Methods

The experimental apparatus is shown in Fig. 1. The dry pellets were firstly loaded on the preheated refractory plate and then were placed in the furnace. Weigh the dry pellets before reduction. After a designated period time, the pellets were taken out and cooled under N_2 flow to room temperature. The metalized pellets were weighed, ground, and analyzed. The flue dust arising from the carbothermic reduction process was collected by a bag filter device connected to the flank outlet of the furnace.

Analysis Method

After carbothermic reduction, the metallization degree (η) was determined by chemical titration analysis, which was defined as:

$$\eta = w(\text{MFe})/w(\text{TFe}) \times 100\% \quad (1)$$

where w(TFe) is the total content of Fe after reduction and w(MFe) is the content of metallic iron after reduction. Sn, Pb, and Zn contents in the dry pellets and reduced

pellets were measured by chemical analysis. Subsequently, the volatilization ratio of Pb, Sn, and Zn was calculated according to the following equation:

$$\lambda = (m_0 w_0 - m_1 w_1)/m_0 w_0 \times 100\% \quad (2)$$

where m_0 is the mass of dry pellets before reduction, w_0 is the Pb, Sn, or Zn content in the dry pellets, m_1 is the mass of the metalized pellets, and w_1 is the content of Pb, Sn, or Zn in the metalized pellets. The phase composition of the metalized pellets was analyzed by X-ray diffraction (TTR III, Rigaku Corporation, Japan), and microstructure evolution was observed by SEM–EDS (MLA250, FEI Quanta).

Results and Discussion

Effect of Reductant Dosage on the Metallization Rate

Figure 2 shows the effect of reductant dosage on the metallization rate of iron, carbon residue, and macroscopic appearance of metalized pellets. The pellets were reduced at 1200 °C for 20 min. It can be seen that the metallization rate and carbon residue increased with the increase of the C/O molar ratio. And, the metallization rate reaches nearly 90%. The gasification reaction will proceed at a faster rate when increasing the reductant dosage. It will generate more CO, which improves the reduction [8]. From the macroscopic appearance of metalized pellets, when the C/O molar ratio is below 1.8, the pellets presented a melting state, and the pellets adhere to each other. Some low melting point substances are formed when the reductant exhausts, and the reduction atmosphere becomes weak. Under a higher C/O ratio, reducing atmosphere is stronger, and the pellets are fully reduced [9].

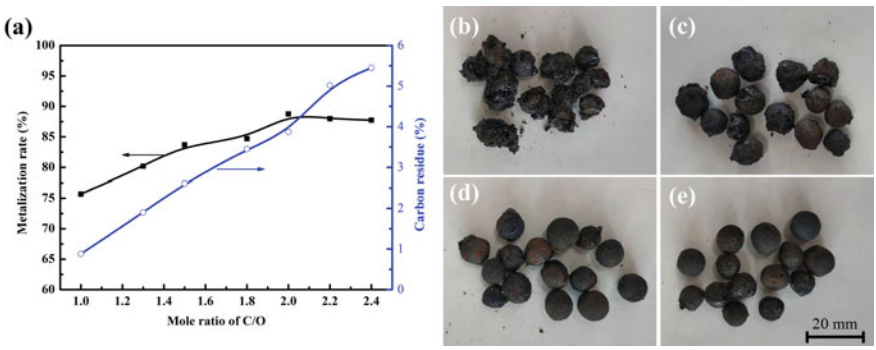

Fig. 2 Effects of C/O molar ratio on the reduction of pellets: **a** curves of metallization rate and carbon residue, **b** C/O = 1.3, **c** C/O = 1.8, **d** C/O = 2.0, **e** C/O = 2.4

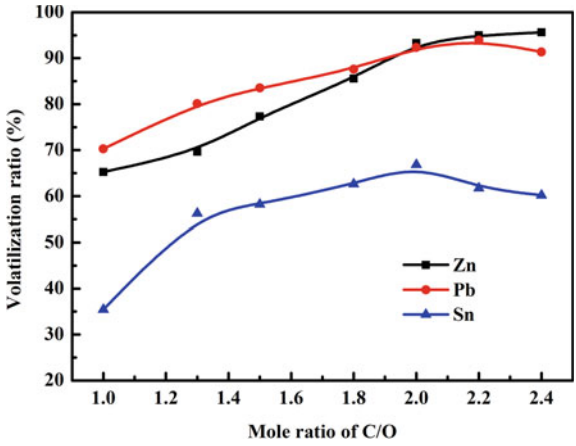

Fig. 3 Effect of mole ratio of C/O on the volatilization ratio of heavy metals

Effect of Reductant Dosage on the Removal of Heavy Metals

The influence of reductant dosage on heavy metal removal was also studied at the temperature of 1200 °C. As showed in Fig. 3, the volatilization ratio of Zn increased significantly as the C/O molar ratio increased from 1.0 to 2.4. This is because the reductive atmosphere of the system is gradually strengthened with the improvement of the C/O mole ratio, which is beneficial to the reduction of zinc oxides [10]. However, the volatilization ratio of Sn increases firstly and then decreases from 66.823 to 60.207% as the molar ratio increasing from 2.0 to 2.4. It is well known that Sn element can volatile out of the pellets in the form of SnO, which can volatile at the temperature of 1127 °C [6]. But, it should be noticed that SnO_2 and SnO can be further reduced to metallic Sn, and the vapor pressure of which was very low. The decrease of Sn volatilization ratio at higher C/O was mainly attributed to the reaction of SnO_2 reduced to metallic tin under stronger reduction atmospheres [11].

Lead can volatile as Pb, PbO, and PbS, of which the saturated vapor pressure is 1937 Pa, 5912 Pa, and 43,169 Pa at 1200 °C, respectively [6, 7]. When the reduced coal is excessive, the lead compounds were easier to reduce and produce liquid Pb, leading to a slight decrease in the volatilization ratio [12]. As a result, volatilization of the Pb and Sn is inhibited.

Microstructure Evolution and Phase Transition of the Pellets

SEM–EDS analysis of the metalized pellets obtained under different C/O molar ratio is presented in Fig. 4. The metallic iron particles (bright white particles) obtained at lower reductant dosage were much bigger than those obtained with higher reductant. As can be seen from Fig. 4a, Point 1 and Point 4 are gangue (calcium iron silicate) and iron sulfide (FeS), and the FeS phase (which initially exists in the lead slag) acts

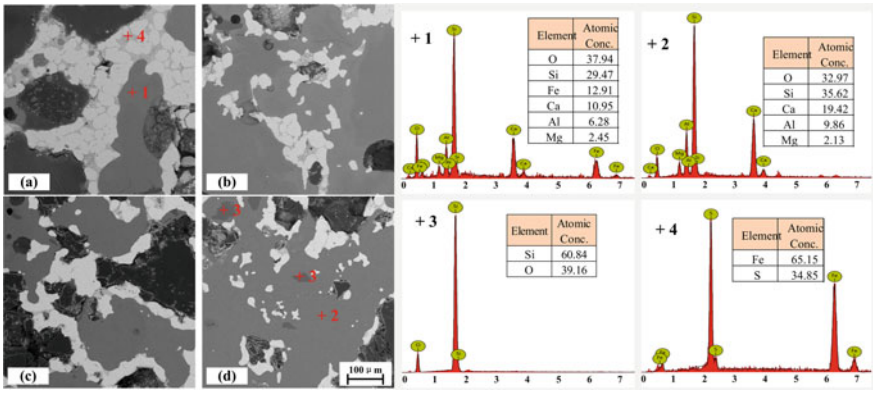

Fig. 4 Microstructures of the metalized pellets for different C/O molar ratio prepared at 1200 °C for 20 min: **a** 1.0, **b** 1.5, **c** 1.8, **d** 2.4

as a "binder" and combine the metallic iron together. FeS has a lower melting point (1188 °C), which can accelerate the aggregation of metallic iron; on the other hand, the eutectic mixture of Fe–FeS (melting point is 985 °C) can be easily generated at the temperature of 1200 °C; hence, aggregation of the iron particles was accelerated by this liquid phase [13]. Therefore, the metalized pellets made in a lower C/O molar ratio presented a melting state according to the macroscopic appearance (Fig. 2b, c). With the increase of C/O molar ratio, iron particles become smaller and disperse. Large-size aggregation comprised of Fe and FeS is barely found. That is because, ash and carbon residue in the anthracite impede aggregation of the metallic particles.

The XRD patterns of the samples reduced at 1200 °C for different C/O molar ratios are shown in Fig. 5. Fayalite (Fe_2SiO_4) was gradually reduced to metallic iron during the process, and the peak of metallic iron appeared. At a C/O molar ratio of 1.0, the fayalite peak is clearly detected. It indicated that Fe_2SiO_4 cannot be reduced sufficiently under a weak reduction atmosphere. Another reason is that metallic iron is reoxidized due to lack of carbon, and the newly formed FeO reacted with SiO_2 again [9]. At a molar ratio of 1.3, quartz (SiO_2) peak as a transition phase is clearly detected, and the intensity became stronger as the C/O raised (Eq. 3). The quartz phase can also be identified from SEM–EDS analysis (Fig. 4d). Comparing with the lower C/O pellets, the peak of fayalite disappeared at the C/O molar ratio higher than 2.0. Meanwhile, the peak of higher smelting point phases such as SiO_2, $Ca_3Al_2(SiO_4)_3$ is strengthened as the reductant dosage increased. It was evident that the phases present in the reduced samples identified by XRD were in good agreement with SEM–EDS analysis results.

$$Fe_2SiO_4 + 2C = 2Fe + SiO_2 + 2CO \tag{3}$$

To further investigate the removal mechanism of heavy metals, SEM–EDS analysis was used to examine the residue phase in the metalized pellets. As seen from

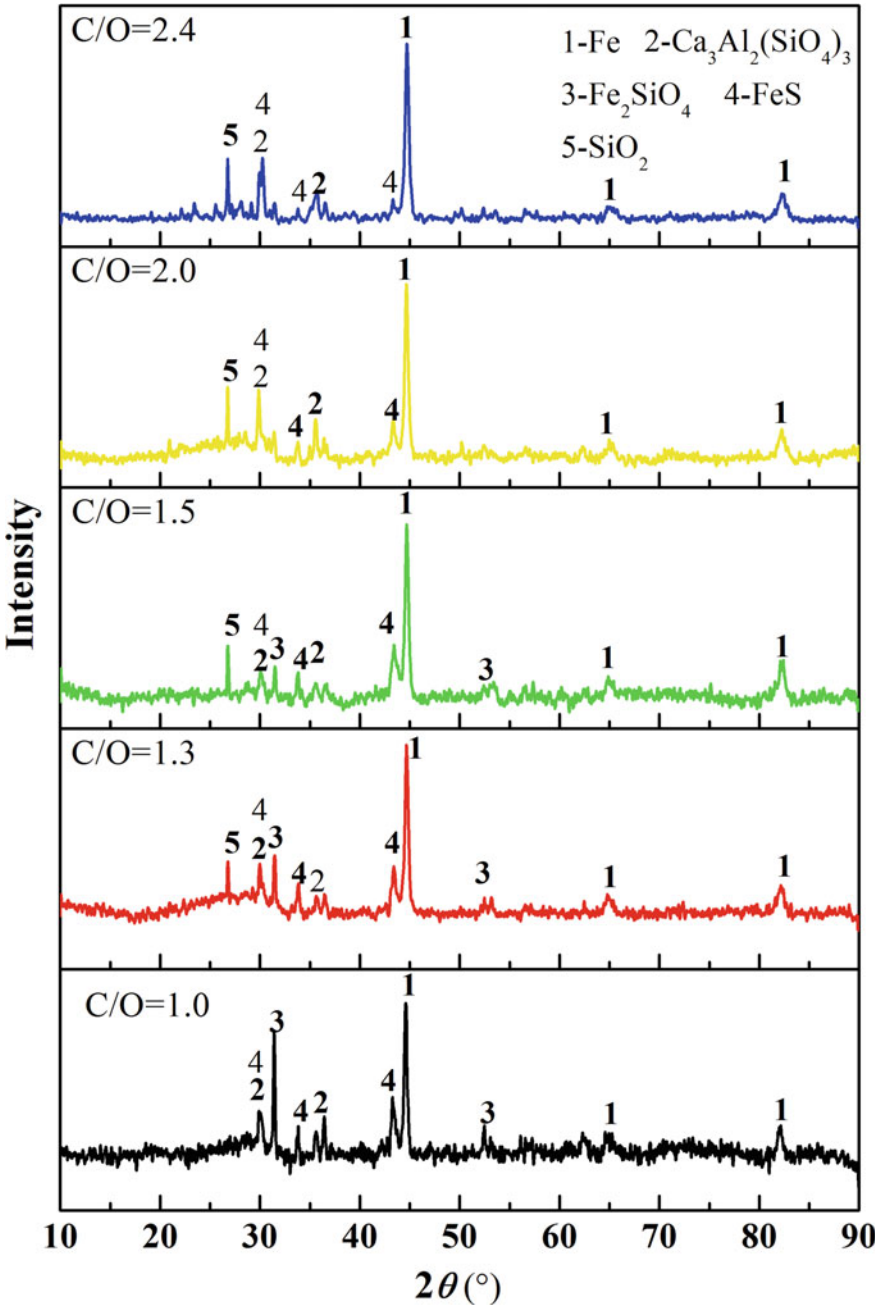

Fig. 5 XRD patterns of the metalized pellets reduced at 1200 °C for different C/O molar ratio

Fig. 6a, when the C/O molar ratio was 1.0, the reduction and volatilization of heavy metal-containing phases are not sufficient. From the energy spectrum, the main components of **Point 1** are Fe, O, Si, Pb, Zn, Sn, and Ca, et al., which are wrapped in the aggregated iron particles. It is difficult to react completely under this enclosed structure, generating under a weaker reducing atmosphere. Further, the partial amplification of Fig. 6a was examined. It can be seen from Fig. 6a1 that some tiny white particles disperse in the FeS matrix (**Point 2**), the main elements of the bright white particles in **Point 3** are Fe, S, and Pb, and analysis shows that it is poly-metallic sulfide. From this perspective, when the C/O molar ratio is 1.0, the calcium iron silicate, Fe_2SiO_4, and low smelting point phases such as Fe–FeS resulted in the melting phenomenon of the pellets, which in return impede the volatilization of heavy metals diffuse from the low porosity pellets [14]. Similar microstructure and phases can be also observed at the C/O molar ratio of 1.3 and 1.5. Figure 6b showed the morphology of reduced pellets prepared at a C/O molar ratio of 2.4. It is noted that the main elements in **Point 4** are Fe, Pb, and Sn, which are determined to be alloy and adhere to the surface of metallic iron. Increasing of C/O molar ratio results in a higher concentration of CO in the pellets, and SnO_2 can be reduced to non-volatile metallic Sn [15]. Meanwhile, more PbO is easily reduced to metallic Pb with lower vapor pressure. And because of the metallic affinity, Fe–Sn–Pb alloy is generated, which results in a decrease in the volatilization of Sn and Pb.

Characterization of the Flue Dust

XRD patterns of the flue dust are shown in Fig. 7. Three major phases are identified: ZnO, $PbSO_4$, and Zn_2SnO_4. The formation of the flue dust was that: $ZnFe_2O_4$ in the pellets was reduced to metallic Zn for volatilization, and then the Zn vapor was oxidized again to ZnO by oxygen in the flue gas [16]. Lead-iron-bearing silicate may decompose into PbO and then was reduced to Pb by carbon. PbO and PbS can directly volatilize into the flue without chemical reaction due to its high vapor pressure. Pb and PbS can also be oxidized in the flue [17]. SnO_2 can combine with ZnO to form Zn_2SnO_4 in the flue gas [6]. The XRF results (Table 2) indicate that Zn, Pb, and Sn are 52.45%, 16.89%, and 3.79%, respectively.

Conclusion

In this study, the effect of reductant dosage on the phase transformation of pellets and removal of heavy metals was analyzed. The following four conclusions could be drawn: (1) When C/O molar ratio of 2.0 (reductant dosage of 22%), the temperature of 1200 °C, and reduction time of 20 min, the metallization degree was 88.75%, and the volatilization ratio of Zn, Pb, and Sn was 93.31%, 92.5%, and 66.8%, respectively. In addition, highly valuable flue dust containing 52.45% Zn, 16.89% Pb, and 3.79%

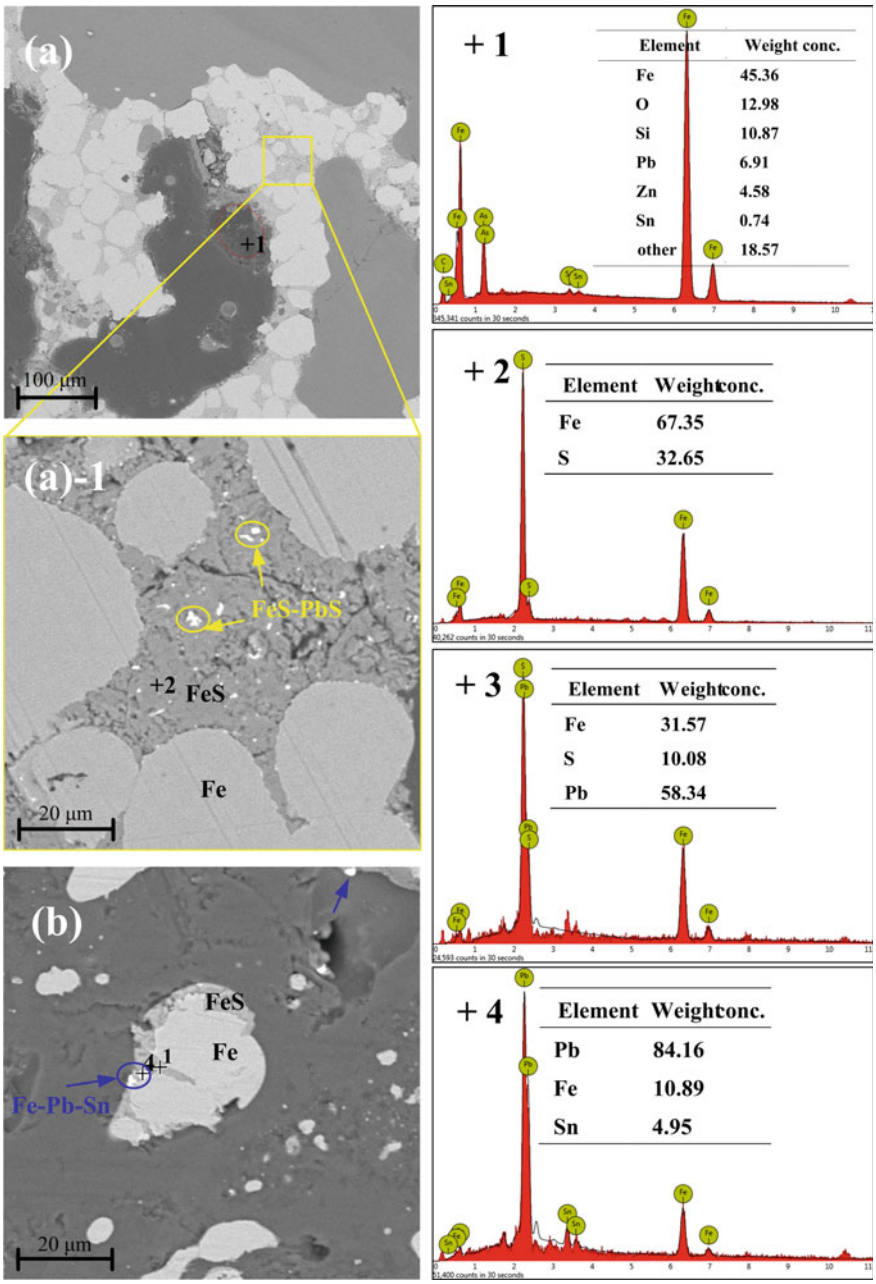

Fig. 6 SEM–EDS observations of the metalized pellets: **a-**1 C/O molar ratio 1.0, **b** C/O molar ratio 2.4

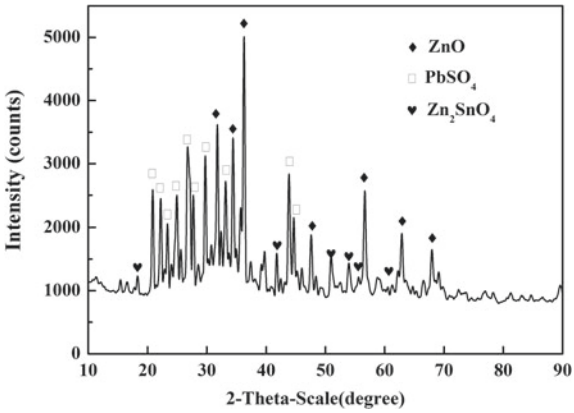

Fig. 7 XRD patterns of the flue dust

Table 2 Chemical compositions of the flue dust by XRF (wt.%)

Component	Zn	Pb	Sn	TFe	S	SiO_2	Al_2O_3	CaO	MgO
Content	52.45	16.89	3.79	0.75	1.71	0.61	0.22	0.25	0.19

Sn was obtained. (2) Reductant dosage has a significant impact on the size of metallic iron. The metallic iron particles obtained at lower reductant dosage were much bigger than those obtained with higher reductant due to more liquid phase (Fe_2SiO_4, Fe-FeS), lower ash and carbon residue. (3) Volatilization ratio of Sn and Pb tended to be decreased under a too low or too high reductant dosage. Heavy metals can be encapsulated by the low smelting point Fe–FeS phase which is generated in a weaker reducing atmosphere. (4) Overdose of reductant can result in the formation of non-volatile Fe–Pb–Sn alloy, which hindered further removal of Sn and Pb.

Acknowledgements This work was supported by Key Research and Development Program of China (No. 2019YFC1905705).

References

1. Pan DA, Li LL, Tian X, Wu YF, Cheng N, Yu HL (2019) A review on lead slag generation, characteristics and utilization. Resour Conserv Recy 146:140–155
2. Xia LG, Mao R, Zhang JL, Xu XN, Wei MF, Yang FH (2015) Reduction process and zinc removal from composite briquettes composed of dust and sludge from a steel enterprise. Int J Miner Metall Mater 22(2):122–131
3. Wu YL, Jiang ZY, Zhang XX, Xue QG, Miao Z, Zhou ZY, Shen YS (2018) Process optimization of metallurgical dust recycling by direct reduction in rotary hearth furnace. Powder Technol 326:101–113
4. Fruehan RJ (1977) The rate of reduction of iron oxides by carbon. Metall Trans B 8(1):279–286
5. Wang CL, Li KQ, Yang HF, Li CH (2017) Probing study on separating Pb, Zn, and Fe from lead slag by coal-based direct reduction. ISIJ Int 57(6):996–1003

6. Peng RQ (ed) (2005) Tin metallurgy. Central South University Press, Changsha
7. Su ZJ, Zhang YB, Liu BB, Zhou YL, Jiang T, Li GH (2016) Reduction behavior of SnO_2 in the tin-bearing iron concentrates under CO–CO_2 atmosphere. Part I: efect of magnetite. Powder Technol 292:251–259
8. Wang G, Wang JS, Ding YG, Ma S, Xue QG (2012) New separation method of boron and iron from ludwigite based on carbon bearing pellet reduction and melting technology. ISIJ Int 52(1):45–51
9. Takashi M, Natsuo I, Yoshiaki H (2004) Influence of gangue composition on melting behavior of coal reduced iron mixture. ISIJ Int 44(12):2105–2111
10. Liu Y, Su FY, Wen Z, Li Z, Yong HQ, Feng XH (2013) Mathematical simulation of direct reduction process in zinc-bearing pellets. Int J Miner Metall Mater 20(11):1042–1049
11. Zhang YB, Li GH, Jiang T, Guo YF, Huang ZC (2012) Reduction behavior of tin-bearing iron concentrate pellets using diverse coals as reducers. Int J Miner Process 110–111:109–116
12. Wang DY, Wang WZ, Chen WQ, Zhou RZ, Lin ZC (2000) Kinetics of evaporation of Zn and Pb from carbon-bearing pellets made of dust containing Zn-Pb-Fe oxides. Int J Miner Metall Mater 7(3):178–183
13. Yao GZ, Li YL, Guo Q, Qi T, Guo ZC (2021) Preparation of reduced iron powder for powder metallurgy from magnetite concentrate by direct reduction and wet magnetic separation. Powder Technol 392:344–355
14. Zhao HY, Chen YL, Duan XQ (2021) Study on the factors affecting the deep reduction of coal gangue containing high contents of iron and sulfur. Fuel 288:119571
15. Zhang YB, Su ZJ, Zhou YL, Li GH, Jiang T (2013) Reduction kinetics of SnO_2 and ZnO in the tin, zinc-bearing iron ore pellet under a 20%CO–80%CO_2 atmosphere. Int J Miner Process 124:15–19
16. Peng C, Zhang FL, Li HF, Guo ZC (2009) Removal behavior of Zn, Pb, K and Na from cold bonded briquettes of metallurgical dust in simulated RHF. ISIJ Int 49(12):1874–1881
17. Di JC, Li WF (2015) Comprehensive recovery of valuable metals in lead and copper smelting flue dust. China Nonferr Metal 44(3):50–53

Simulation Study on Top Blowing Combustion in Iron Bath Smelting Reduction

Panfeng Wang, Nan Wang, Jin Xu, and Haiyang Yu

Abstract In this paper, the smelting reduction furnace is taken as the research object, and by establishing the "upper space" combustion model, the effects of different top lance positions, different top blowing oxygen enrichment flow, and different inclination angles of top lance inlet on gas velocity distribution and temperature distribution in the furnace were studied. This paper provides guidance for non-blast furnace ironmaking process theoretical and computational basis on aspects of scale-up design, process optimization, and process control.

Keywords Iron bath melting reduction · Top jet · Secondary combustion · Numerical simulation

Introduction

Smelting reduction ironmaking process is an important branch of non-blast furnace ironmaking process [1]. It is a very important development direction of ironmaking process. Gou et al. [2, 3] conducted numerical simulation of 300t top blown oxygen lance converter, using $k - \varepsilon$ turbulence model and finite chemical reaction model, and DeMarco-Lockwood melt model [4] simulates the gas flow, combustion reaction, and heat transfer in the injection process. Shin et al. [5] simulated the combustion of smelting reduction furnace, mainly simulated the effects of oxygen lance position and inlet velocity on flow field, heat transfer, and secondary combustion rate in the furnace. Panjkovic [6] used CFD to simulate the secondary combustion rate, gas temperature, and heat transfer efficiency between gas, iron, and slag in the iron bath reactor. The results show that the heat transfer from the upper gas-phase space to the lower molten pool mainly depends on the radiation heat transfer to the molten pool surface and the convective heat transfer between gas and small droplets. Baowei and Youduo [7] developed a mathematical model of droplet generation, movement, and heat transfer in top blown converter. Based on the study of gas flow, combustion, and

P. Wang · N. Wang (✉) · J. Xu · H. Yu
School of Metallurgy, Northeastern University, Shenyang, Liaoning Province, China
e-mail: wangn@smm.neu.edu.cn

Z. Peng et al. (eds.), *12th International Symposium on High-Temperature Metallurgical Processing*, The Minerals, Metals & Materials Series,
https://doi.org/10.1007/978-3-030-92388-4_56

heat transfer in the furnace, it is concluded that the secondary combustion process of droplets in the furnace is an important heat transfer mode.

Numerical Simulation Research Method

Model Hypothesis

When solving the mathematical model of top blowing jet combustion of smelting reduction furnace, its combustion reaction is very complex. In order to explore its combustion characteristics, only the chemical reactions of CO, H_2, and O_2 are considered, and the following assumptions are made:

(1) It is assumed that all fluids are incompressible viscous fluids;
(2) Convective heat transfer during combustion is not considered, but only radiation heat transfer is considered;
(3) It is assumed that the bottom of the calculation domain is the release position of CO and H_2, which is the slag level;
(4) The wall surface of the smelting reduction furnace has no penetration and no slip boundary.

Model Formulation

Fluid flow is governed by the law of conservation of physics. The basic conservation laws include the law of continuity equation, the law of momentum equation, and the law of energy equation. If the flow contains mixed interactions of different components, the system should also abide by the law of component conservation. If the flow is in a turbulent state, the system also abides by additional turbulent transport equations. The calculation in this chapter involves turbulent gas-phase combustion reaction, so the mathematical model should consider all the above basic control equations, which are the mathematical description of these conservation laws.

Continuity equation

$$\frac{\partial \rho}{\partial t} + \nabla\left(\rho \overrightarrow{u}\right) = 0 \tag{1}$$

where ρ is the density, kg/m^3; $\vec{u}$ is the speed, m/s; T is the time, s.

Momentum equation

$$\frac{\partial\left(\rho \overrightarrow{u}\right)}{\partial t} + \nabla\left(\rho \overrightarrow{u}\,\overrightarrow{u}\right) = -\nabla p + \nabla\left[\mu\left(\nabla \overrightarrow{u} + \nabla \overrightarrow{u}^{\mathrm{T}}\right)\right] + \rho g + \boldsymbol{F} \tag{2}$$

where P is the pressure, Pa; G is gravity acceleration, m/s^2; μ is viscosity, Pa s; F is the source term force, N.

Energy equation

$$\frac{\partial(\rho T)}{\partial t} + \nabla\left[\overrightarrow{u}(\rho T + p)\right] = \nabla\left(k_{eff}\nabla T\right) + S_h \tag{3}$$

where T is the temperature value, K; k_{eff} is the heat transfer coefficient; S_h is the internal heat source of the fluid and the part of the fluid mechanical energy converted into heat energy due to viscosity.

Realizable k − ε turbulence model equation

$$\frac{\partial}{\partial t}(\rho k) + \frac{\partial}{\partial x_i}(\rho u_i k) = \frac{\partial}{\partial x_j}\left[\left(\mu + \frac{\mu_t}{\sigma_k}\right)\frac{\partial k}{\partial x_j}\right] + G_k + G_b - \rho\varepsilon - Y_M \tag{4}$$

$$\frac{\partial}{\partial t}(\rho\varepsilon) + \frac{\partial}{\partial x_i}(\rho u_i \varepsilon) = \frac{\partial}{\partial x_j}\left[\left(\mu + \frac{\mu_t}{\sigma_\varepsilon}\right)\frac{\partial \varepsilon}{\partial x_j}\right] + C_{1\varepsilon}\frac{\varepsilon}{k}(G_k + C_{3\varepsilon}G_b) - C_{2\varepsilon}\rho\frac{\varepsilon^2}{k} \tag{5}$$

$$\mu_{\text{t}} = \rho C_{\mu}\frac{k^2}{\varepsilon} \tag{6}$$

$$C_\mu = \frac{1}{A_0 + A_S U^* \frac{k}{\varepsilon}} \tag{7}$$

where G_k is the turbulent kinetic energy generated by the average velocity gradient, kg/m s^3; G_b is the turbulent kinetic energy due to buoyancy, kg/m s^3; Y_M is the effect of compressible turbulent wave expansion on dissipation rate; μ_{t} is turbulent viscosity; C_μ is the average shear rate function; $C_{1\varepsilon}, C_{2\varepsilon}, \sigma_k, \sigma_\varepsilon$ are constants, where $C_{1\varepsilon} = 1.44$, $C_{2\varepsilon} = 1.9$, $\sigma_k = 1.0$, $\sigma_\varepsilon = 1.2$.

Component transport equation

The reaction rate appears in the component transport equation in the form of source term. In this paper, the method of calculating the reaction rate is used based on the Arrhenius velocity expression, as shown in the Table 1

$$\frac{\partial}{\partial t}(\rho Y_{\text{i}}) + \nabla\cdot\left(\rho\overrightarrow{u}Y_{\text{i}}\right) = -\nabla J + R_{\text{i}} + S_{\text{i}} \tag{8}$$

Table 1 Calculation expression of chemical reaction rate

Chemical reaction	Reaction rate (kmol/$(\text{m}^3\text{gas})^{-1}\text{s}^{-1}$)
$CO + 0.5O_2 = CO_2$	$1.3 \times 10^8 C_{CO} C_{O_2}^{0.5} C_{H_2O}^{0.5} \exp(-1.8169 \times 10^3/RT)$
$H_2 + 0.5O_2 = H_2O$	$10^{11} C_{H_2} C_{O_2} \exp(-4.19857 \times 10^5/RT)$

Radiation model

$$\nabla \cdot \left(I\left(\vec{r}, \vec{s}\right)\vec{s}\right) + (a+\sigma_s)I\left(\vec{r}, \vec{s}\right) = an^2\frac{\sigma T^4}{\pi} + \frac{\sigma_s}{4\pi}\int_0^{4\pi} I\left(\vec{r}, \vec{s}\right)\phi\left(\vec{s}\cdot\vec{s}\right)d\Omega \quad (9)$$

Boundary Conditions

Initial inlet boundary: the inlet boundary condition of the top blowing gas jet of the smelting reduction furnace is the pressure inlet, the inlet gas is 35% O_2, the rest is N_2, and the gas inlet temperature is 1473 K; the release position of CO and H_2 at the slag liquid level is the velocity inlet, the gas content is 77.1% CO and 1.8% H_2, the rest is N_2, and the gas inlet temperature is 1573 K.

Initial outlet boundary: the boundary condition at the outlet of the smelting reduction furnace is the pressure outlet boundary condition.

Symmetry plane boundary: the symmetry plane boundary is set as the symmetry boundary condition.

Wall boundary conditions: the solid wall is no slip and no penetration boundary (wall), that is, at the solid wall, the velocity perpendicular to the wall and tangential velocity is 0.

Simulation Scheme

Required experimental means, research conditions, and experimental conditions:

Simulation platform: the server

Processor: Intel(R) Xeon(R) CPU E5-2687v4@3.00GhHz 3.00 GHz (two processer)

Install memory: (RAM): 96.0 GB

System type: 64-bit operating system

Simulation software: ICEM16.1, FLUENT16.1, TECPLOT2017.

This paper mainly simulates the effects of different operating conditions (top blowing gas jet flow, top blowing lance position, and lance inclination) on the flow field and combustion characteristics of top blowing jet, and analyzes the jet combustion characteristics such as jet distribution, velocity distribution, temperature distribution under different conditions. It is concluded that the combustion characteristics of the upper space under the action of oxygen enriched top blowing jet change with

Table 2 Gas composition and physical parameters of molten pool

Composition of molten pool gas	Volume fraction (%)	Density (kg/m^3)
CO	77.1	1.1233
N_2	21.1	1.138
H_2	1.8	0.08189
Hot air composition	–	–
O_2	35	1.2999
N_2	65	1.138

Table 3 Numerical simulation scheme

Parameter	Numerical value
Gun position H (mm)	800, 1000, 1200, 1400
Flow Q_m (kg/s)	0.2, 0.25, 0.3, 0.35
Dip angle θ (°)	10, 15, 20, 25

different parameters. Relevant gas physical parameters and numerical simulation schemes are shown in Tables 2 and 3.

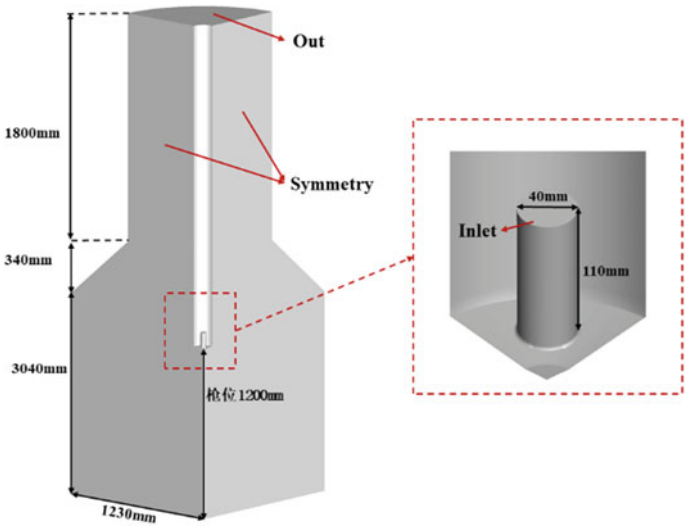

Fig. 1 Geometric model and dimensions upper space of smelt reduction furnace

Results and Discussion

Analysis of Results of Different Gun Positions

It can be seen from Fig. 2a that under the condition of consistent height from the liquid level of the molten pool, with the increase of the lance position of the oxygen lance, the velocity of the air flow gradually decreases. It can be seen from Fig. 2b: on the cross section with H = 0.2 m, the velocity change trend of the air flow is consistent under different oxygen lance position parameters. In the process of approaching the furnace center from the edge of the furnace wall, the velocity first increases slowly to the maximum value and then decreases rapidly. The maximum value of velocity is different under different oxygen lance position parameters. With the increase of oxygen lance position, the maximum value gradually decreases. H = 0.4 m cross-section and H = 0.6 m cross-section have the same distribution law as H = 0.2 cross-section.

It can be seen from the Fig. 3 that with the increase of the distance between the top lance and the liquid level of the molten pool, the length of the combustion flame gradually increases, which is conducive to the transfer of the heat released by

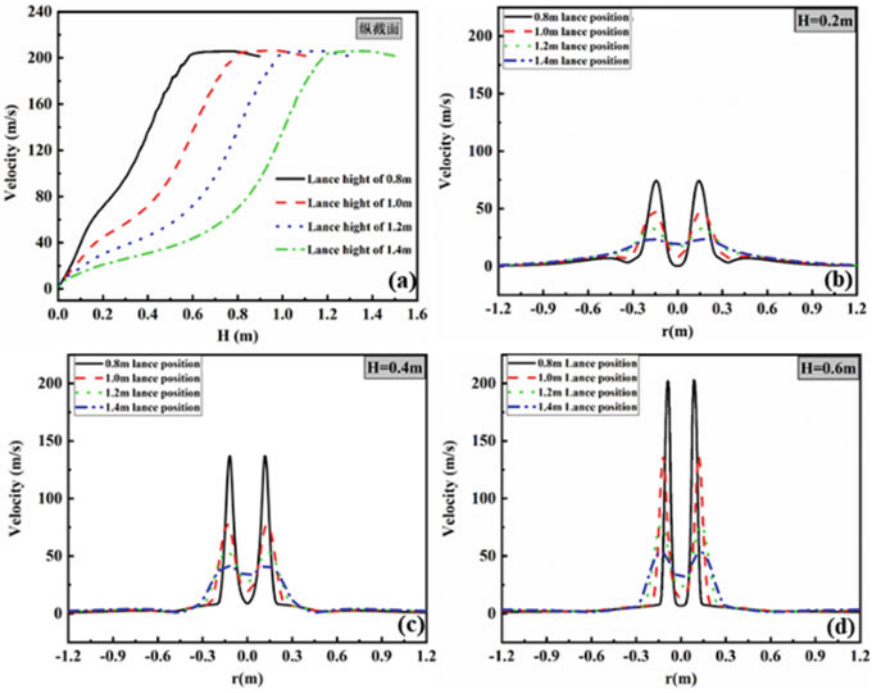

Fig. 2 Axial velocity distribution of longitudinal section of different oxygen gun height **a** radial distribution along the cross-section **b** H = 0.2 m, **c** H = 0.4 m, **d** H = 0.6 m

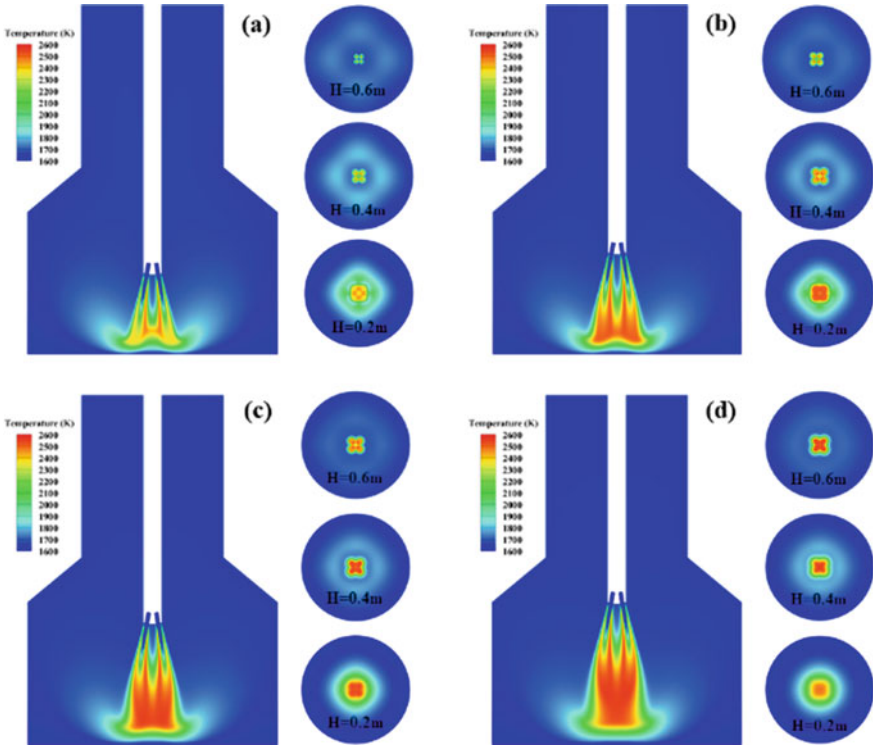

Fig. 3 Different oxygen lance heights **a** 0.8 m; **b** 1.0 m; **c** 1.2 m; **d** temperature nephogram of 1.4 m longitudinal section and cross-section at different heights

combustion to the lower part of the molten pool, and the flame temperature is also gradually increasing to accelerate the reduction of iron ore. The above phenomenon is mainly because with the upward movement of the gun position, the space between the top gun and the liquid level of the molten pool increases, and more gas is added to the combustion reaction to maximize the use of the chemical energy of the gas escaping from the molten pool and improve the secondary combustion rate. The high-temperature zone of flame combustion is mainly concentrated in the furnace center, which can reduce the erosion of high heat flow gas to the furnace wall lining.

It can be seen from Fig. 4a: with the increase of the height from the liquid level of the molten pool, the temperature of the flame center first increases rapidly and then decreases gradually. The maximum temperature of the combustion flame of the iron bath smelting reduction furnace at the height of 0.8 m is 2300 K, and the maximum temperature of the combustion flame under other parameters is 2500 K. The main reason is that the distance between the top gun at the height of 0.8 m and the liquid level of the molten pool is too small. It is caused by insufficient gas combustion, so the distance between the oxygen lance and the molten pool liquid level is at least 1.0 m. It can be seen from Fig. 4b: on the cross section with a height of H = 0.2 m from the

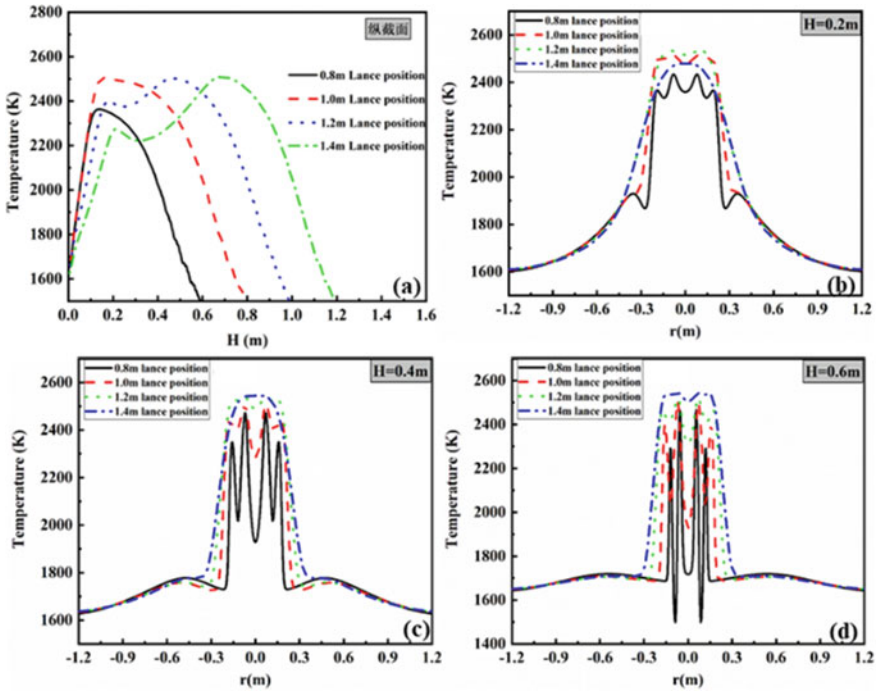

Fig. 4 Axial temperature distribution in longitudinal section **a** radial temperature distribution in cross-section **b** H = 0.2 m, **c** H = 0.4 m, **d** H = 0.6 m

molten pool liquid level, the flame temperature trend diagram with an oxygen lance position of 0.8 m fluctuates more frequently, while the flame temperature with an top lance position of 1.4 m increases all the time and finally reaches the maximum value.

Analysis of Results of Different Top Blowing Flows

As can be seen from Fig. 5a, under the condition of consistent height from the liquid level of the molten pool, with the increase of oxygen enriched gas flow, the speed of gas flow gradually increases. It can be seen from Fig. 5b: on the cross-section with H = 0.2 m, the velocity change trend of the air flow is consistent under different flow parameters. In the process of approaching the furnace center from the edge of the furnace wall, the velocity first increases slowly to the maximum value and then decreases rapidly. The maximum value of velocity is different under different gas flow parameters. With the increase of gas flow, the maximum value decreases gradually.

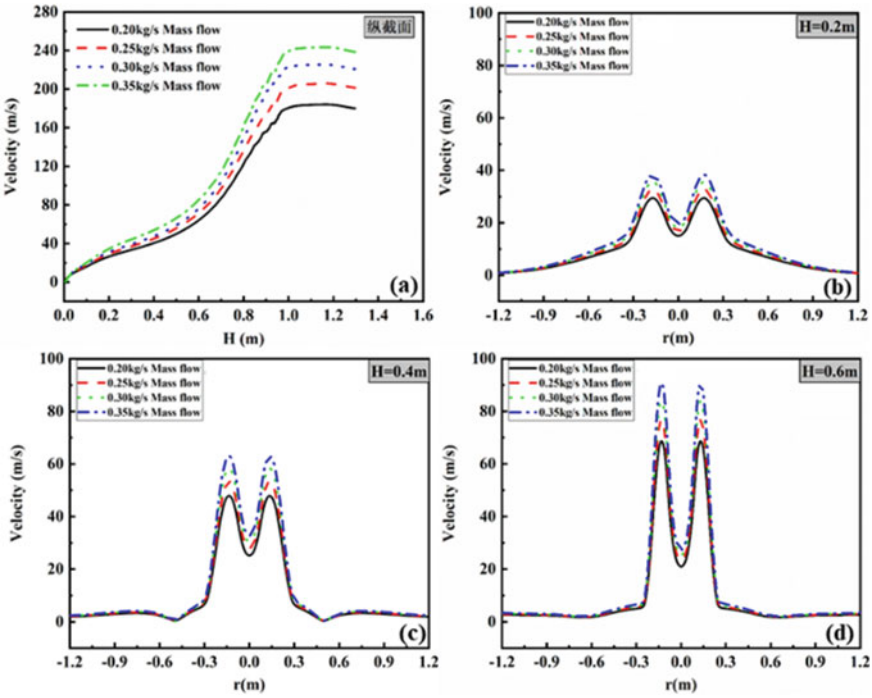

Fig. 5 Axial velocity distribution in longitudinal section **a** radial distribution in cross-section **b** H = 0.2 m, **c** H- = 0.4 m, **d** H- = 0.6 m under different flow parameters

Conclusions

Through the above analysis of the simulation results, the conclusions are as follows:

(1) With the increase of the distance between the top lance and the liquid level of the molten pool, the length of the combustion flame increases gradually, and the temperature of the flame also increases gradually. However, the distance between the top lance and the liquid level of the molten pool should not be too large. The position of the top lance is too high, and the high-temperature flue gas is directly discharged from the upper space, resulting in the increase of coal consumption and heat loss. Therefore, the height of the top lance should be between 1.2 and 1.4 m.

(2) With the increase of oxygen enrichment flow rate, the temperature of combustion flame gradually decreases, and with the increase of gas flow rate, the maximum temperature of combustion flame gradually moves down. Therefore, when the oxygen-enriched gas flow is 0.2 kg/s, the temperature in the upper space of the furnace is the highest.

(3) When the inclination angle of the oxygen lance inlet is 10°, the temperature increases continuously from the furnace wall close to the furnace to the

center. However, under other parameters, the temperature inside the furnace first increases and then decreases, and the temperature in the furnace center gradually decreases with the increase of the inclination angle. Therefore, the inclination angle of the top lance inlet shall not be greater than 15°.

Acknowledgements The authors gratefully acknowledge the National Natural Science Foundation of China [Grant numbers: 51974080, 52074077 and 52174301], the Fundamental Research Funds for the Central Universities was supported by Chinese Education Ministry [Grant number: N2125018].

References

1. Chou JM, Chuang MC, Yeh MH et al (2003) Effects of process conditions on mixing between molten iron slag in smelting reduction vessel via water model study. Ironmaking Steelmaking 30(3):195–202
2. Gou H, Irons GA, Lu WK (1993) Mathematical modeling of post-combustion in a KOBM converter. Trans B 24(1):179–188
3. Chuang H, Kuo J, Huang C et al (2006) Multi-phase flow simulations in direct iron ore smelting reduction process. ISIJ Int 46(8):1158–1164
4. Guo DC, Gu L, Irons GA (2002) Developments in modelling of gas injection and slag foaming. Appl Math Model 26(2):263–280
5. Shin MK, Lee SD, Joo SH et al (1996) A numerical study on the combustion phenomena occurring at the post combustion stage in bath-type smelting reduction furnace. ISIJ Int 33(3):369–375
6. Panjkovic V, Truelove J, Ostrovski O (2002) Analysis of performance of an iron-bath reactor using computational fluid dynamics. Appl Math Model 26(2):203–221
7. Baowei L, Youduo H (1994) A mathematical model of flow, combustion and heat transfer in top blown converter. J Inner Mongolia Univ Sci Technol 13(4):30–40

Study on Burden Mineral Phase Identification System and Prediction Model of Metallurgical Properties Based on BP Neural Network

Qingqing Hu, Donglai Ma, Yue Wang, Zhixiong You, and Xuewei Lv

Abstract Sinters and pellets are the main burden of blast furnace in ironmaking industry, and their phase compositions (hematite, magnetite, perovskite, calcium ferrite, silicates, glass phase) will affect the metallurgical properties (low-temperature reduction degradation index, reducibility, and softening-melting properties). In this paper, based on optical microscope, RGB model, and image analysis, the gray range of each mineral phase is preliminarily determined, while the composition and content of different mineral phases in burden can be reasonably calculated by reflectance calculation model. Furthermore, BP neural network method is used to investigate the mapping relationship between mineral phase composition and metallurgical properties. Therefore, a prediction model of burden mineral phase-metallurgical properties is established which has reached a certain accuracy, and the influence of the content of each phase on metallurgical properties is qualitatively analyzed. To enhance the accuracy of the model, it is necessary to enrich the database and improve the modeling method.

Keywords BP neural network · RGB model · Mineral phase · Metallurgical properties

Introduction

In ironmaking industry, iron ores are processed to sinter and pellet and added into blast furnace as iron-bearing burden [1, 2]. The chemical compositions and mineral phase structures of burden have great impact on its metallurgical properties which determine operating conditions and product quality of blast furnace [3, 4]. In terms of chemical components, many scholars [5, 6] investigated the effect of the proportion of simple oxides in burden on metallurgical properties, including SiO_2, CaO, MgO, Al_2O_3, and TiO_2. For example, higher content of TiO_2 in burden would cause slag foaming, higher viscosity of slag, and slag-iron difficult to separate, which worsens

Q. Hu · D. Ma · Y. Wang · Z. You (✉) · X. Lv
College of Materials Science and Engineering, Chongqing University, Chongqing 400044, China
e-mail: youzx@cqu.edu.cn

Z. Peng et al. (eds.), *12th International Symposium on High-Temperature Metallurgical Processing*, The Minerals, Metals & Materials Series,
https://doi.org/10.1007/978-3-030-92388-4_57

the operation efficiency of BF [7]. These basic chemicals form complex mineral phases, such as hematite, magnetite, perovskite, calcium ferrite, silicate, glass phase, and so on. In addition, the composition and structure of these phases are significantly related to metallurgical properties such as low-temperature reduction degradation index, reducibility, and softening melting properties. At present, some studies [8] have discussed the relationship between metallurgical properties and mineral phase structure, but mostly focus on the single factor, which lack of systematic research.

In this paper, the phase microstructure of charge is obtained by optical microscope, the phase composition is determined by scanning electron microscope, and the phase identification model is established. In addition, the mapping relationship between ore phase composition and metallurgical properties is studied by BP neural network method, and a high-precision prediction model of ore phase metallurgical properties of burden is established. The model is applied to study the effects of mineral phases on metallurgical properties.

Mineral Phase Identification

Sampling Method

The microstructure of the sample was observed under 500 times by optical microscope (LEICA DM RXp). As shown in Fig. 1, to ensure the representativeness of each sample, 16 points evenly on the surface of the burden were chosen to take micrographs. Counting the relatively area occupied (%) by every mineral phase in each picture and taking the average value. Hence, the proportion of each phase in the burden can be obtained, that is, the input of the neural network model.

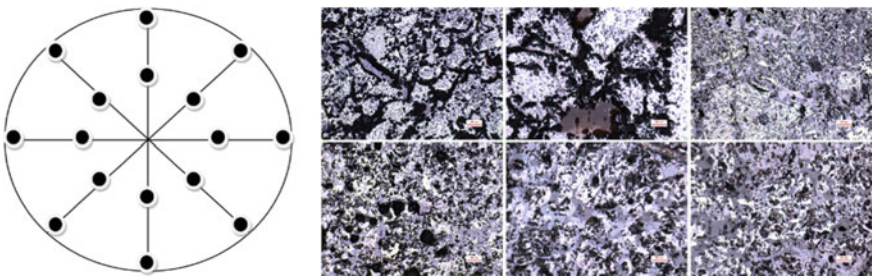

Fig. 1 Sampling position and microscope pictures

Automatic Cognition Theory of Mineral Phase

Under the field of view of optical microscope, different phases will show different colors. Based on RGB color model [9], the pictures can be grayed by using the average method, and the brightness values (I) of different minerals can be obtained.

$$I = \frac{1}{3}(\mathrm{R} + \mathrm{G} + \mathrm{B}) \tag{1}$$

Through the conversion of Eq. (1), the relationship between the reflectivity of minerals and the pixel gray level on the digital mineral phases picture is established.

$$\mathrm{Reflect} = k \times I/255 \tag{2}$$

In Eq. (2), k is the proportional correction factor. According to the above two equations, the relationship between reflectivity and R, G, and B values is acquired:

$$\mathrm{Reflect} = k \times \frac{1}{255} \times \frac{1}{3}(\mathrm{R} + \mathrm{G} + \mathrm{B}) \tag{3}$$

When the value of k is determined, the reflect of different minerals can be calculated conveniently. Table 1 shows the gray value distribution of different mineral through this method, which provides evidence to analysis micrograph information accurately.

BP Neural Network

Back propagation (BP) neural network model is composed of BP network and data processor. It is a highly nonlinear dynamic system with strong self-adaptive and self-learning functions. BP network is generally composed of input layer, hidden layer, and output layer. The data processor is used to process the data to form input and output samples. In the whole learning process of neural network, the forward propagation of signal and the reverse propagation of error are carried out repeatedly, and its connection weight and node threshold are continuously updated until the network output error is gradually reduced to an acceptable degree, and finally the output results are obtained.

Table 1 Gray value distribution for different mineral

Mineral phase	Hematite	Magnetite	Perovskite	Calcium ferrite	Silicates and glass phases
Gray value distribution	141–145	115–125	111–116	107–115	<75

Modeling and Training

In this paper, the structural parameters of neural network are determined. The number of hidden layer nodes is mostly determined by experience. Some studies [10] proposed a formula for calculating the optimal number of hidden layer nodes:

$$l = \sqrt{x + y} + \alpha \tag{4}$$

where x and y are the number of nodes in the input layer and the output layer, respectively. And α is an integer constant in [1, 10], which is taken here $\alpha = 5$.

The number of input layer nodes x of BP neural network is 5. Due to the lack of partial data, the number of output layer nodes y is taken as 1 or 5, that is, the reducibility and low-temperature reduction pulverization rate (2) and softening-melting properties (5) are predicted separately. When y is1or 5, l is 7 or 8, respectively. Hence, the structure of BP neural network x:l:y is 5:7:1 or 5:8:5 in Fig. 2.

$$Y = f(X1, X2, X3, X4, X5) \tag{5}$$

Y-metallurgical properties include low-temperature reduction degradation index, reducibility, and softening-melting properties. X_1—ilmenite, X_2—titanomagnetite, X_3—perovskite, X_4—calcium ferrite, X_5—silicates + glass phases.

As shown in Tables 2 and 3, the original data are obtained through experiments and literatures [11–13]. The above obtained mineral phases composition and metallurgical properties are divided into three groups randomly, as training samples, testing samples, and predicting samples, respectively. As shown in Table 4, normalize the input samples to the [−1, 1] interval before network training. The function of normalization is to accelerate the convergence of training network. Normalization equation is as follows:

$$\hat{z}_i = \frac{2(z_i - z_{\min})}{z_{\max} - z_{\min}} - 1 \tag{6}$$

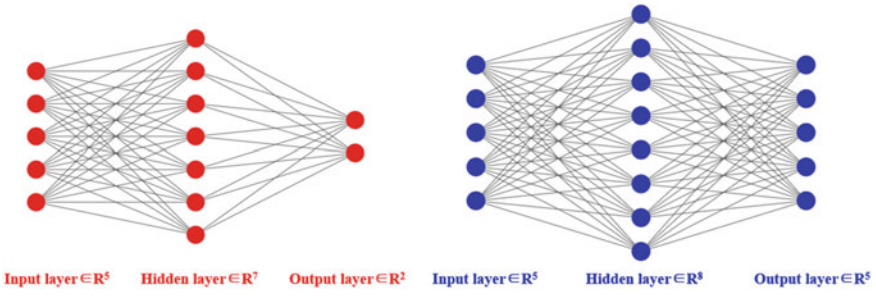

Fig. 2 Structure diagram of neural network: 5:7:2 and 5:8:5

Table 2 Mineral phases composition and metallurgical properties (%)

Number	Hematite	Magnetite	Perovskite	Calcium ferrite	Silicates and glass phases	$RDI_{-3.15}$	RI
1 [11]	32.56	25.34	2.19	22.66	17.25	68.30	83.62
2 [11]	31.87	25.69	2.33	21.33	18.78	67.87	83.50
3 [12]	25.50	29.63	0.53	22.36	21.98	84.91	86.75
4 [12]	24.51	32.12	0.80	20.90	21.67	74.85	84.44
5 [13]	25.93	16.05	1.65	19.34	37.04	40.89	84.70
6 [13]	18.07	28.57	5.04	13.87	34.45	34.87	80.80

*$RDI_{-3.15}$: Low-temperature reduction degradation index (the mass ratio of burden which diameter less than 3.15 mm) RI: Reduction Index. Due to space constraints, only partial data is shown in this paper

Table 3 Corresponding softening-melting properties

Number	Softening property/°C			Dropping property/°C				S value
	t_a	t_b	Δt_{ba}	t_s	t_d	Δt_{ds}	ΔP_{max}/Pa	
1 [11]	1190.00	1285.00	95.00	1290.00	1430.00	140.00	6762.00	878.00
2 [11]	1201.00	1292.00	91.00	1303.00	1440.00	137.00	5488.00	685.00
3 [12]	1223.00	1310.00	87.00	1325.00	1452.00	127.00	5684.00	659.00
4 [12]	1218.00	1307.00	89.00	1320.00	1450.00	130.00	5880.00	700.00
5 [13]	1216.00	1290.00	74.00	1326.00	1450.00	124.00	5712.00	659.00
6 [13]	1205.00	1317.00	112.00	1297.00	1440.00	143.00	7100.00	936.00

Table 4 Partial data after normalization

Number	Hematite	Magnetite	Perovskite	Calcium ferrite	Silicates and glass phases	$RDI_{-3.15}$	RI
1 [11]	0.37	−0.47	−0.81	−0.06	−0.28	0.49	0.29
2 [11]	0.34	−0.46	−0.79	−0.12	−0.18	0.48	0.28
3 [12]	0.07	−0.31	−0.95	−0.07	0.02	1.00	0.61
4 [12]	0.03	−0.22	−0.93	−0.14	0.00	0.69	0.37

In Eq. (6), $\hat{z}_i$—normalized value, z_i—raw data, z_{max}—maximum value in raw data, z_{min}—minimum value in raw data.

The BP neural network is established by using MATLAB (2019a) software, and the Levenberg–Marquardt backpropagation algorithm is used, which the mineral phase composition and metallurgical properties data are imported to make the network model self-learning, training, and fitting.

Table 5 Artificially constructed mineral phases composition data (Partial)

Mineral phase	Relatively content of each phase (%)					Total content (%)
Hematite	1.00	40.73	3.55	30.58	24.15	100.00
	1.50	40.52	3.53	30.42	24.03	100.00
Magnetite	29.24	11.00	3.64	31.36	24.77	100.00
	29.08	11.50	3.62	31.18	24.63	100.00
Perovskite	23.03	32.84	0.00	24.66	19.47	100.00
	23.02	32.83	0.05	24.64	19.46	100.00
Calcium ferrite	26.21	37.38	3.25	11.00	22.16	100.00
	26.06	37.17	3.24	11.50	22.03	100.00
Silicates and glass phases	25.96	37.02	3.22	27.79	6.00	100.00
	25.82	36.83	3.21	27.65	6.50	100.00

Application of Model

After successfully training the neural network model, based on the average data of each phase of burden collected in the literature, changing the content of a specified mineral phase evenly while keeping the relative content of other phases unchanged. In order to investigate the influence of the content of each phase on the metallurgical properties qualitatively and quantitatively, the data is obtained in Table 5 and imported to the model.

Results and Discussion

Analysis of Network Model 1

As shown in Fig. 3, using BP neural network can predict the low-temperature reduction degradation index and reducibility of BF burden. According to Table 6, the R values of training samples, test samples, and prediction samples are obtained that all of them excess 0.98. Meanwhile, the mean square errors (MSE) of $RDI_{-3.15}$ and RI reach 9.146 and 0.357, respectively. Furthermore, the average error between the prediction group and the raw data is 0.69%, which means the error is within the acceptable range. Therefore, the neural network model 1 has achieved high accuracy and can be further used to analyze the relationship between various phases and related metallurgical properties which the result will be discussed on next part.

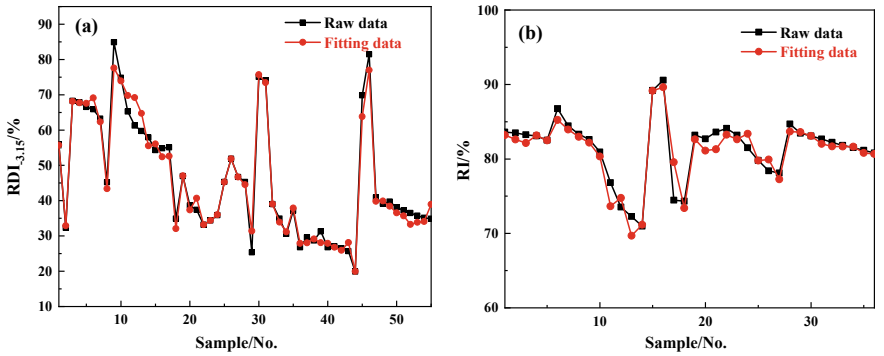

Fig. 3 Comparison between fitting data and raw data: **a** $RDI_{-3.15}$, **b** RI

Table 6 Statistic indexes of neural network

Neural Network	Property	Correlation coefficient (R)			MRE	MSE
		Training	Validation	Test		
Network 1 (5:7:2)	RDI-3.15	0.9918	0.9829	0.9867	0.078	0.0121
	RI				0.007	0.0401
Network 2 (5:8:5)	S-M P	0.9669	0.9359	0.9151	0.022	0.0369

Analysis of Network Model 2

There are few relevant literatures containing the valid data of the softening-melting property of burden, and many indexes are involved in this performance, so we design model 2 by changing the network structure parameters (5:8:5). According to Fig. 4 and Table 6, model 2 is used to predict the softening-melting property which the trained network can well approach the given target. In addition, the values of MRE and MSE are 0.022 and 0.0369, respectively. Furthermore, the R values of training

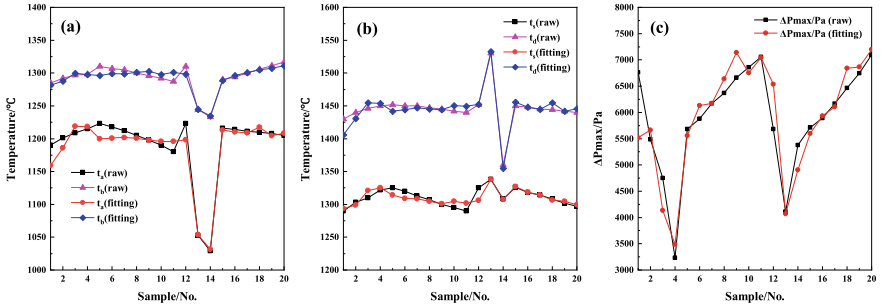

Fig. 4 Comparison between fitting data and raw data: **a** softening temperature, **b** dropping temperature, **c** ΔP_{max}

samples, test samples, and prediction samples are between 0.9151 and 0.9669 that the accuracy is slightly lower than that of model 1. Ergo, the model has no further application in this paper, although it can do some qualitative analysis.

Effect of Mineral Phases on Metallurgical Properties

Combining the value range of each mineral phase in actual production, their effects on the metallurgical properties are evaluated by using model 1 due to its better accuracy. The results are shown in Fig. 5, every mineral phase increases within a rational range as an independent variable. With the increase of the content of these mineral phases (excluding perovskite), the value of $RDI_{-3.15}$ will first increase and then decrease. When perovskite increases from 0 to 5%, the values of $RDI_{-3.15}$ and RI decrease because perovskite is a brittle material with high melting point that does not have bonding effect and difficult to be reduced [14]. Many studies [15, 16] have shown that the volume expansion of skeletal hematite when it is reduced to cubic magnetite is the main reason for the low-temperature reduction degradation of burden. In addition, hematite is easier to reduce than magnetite. Calcium ferrite [17] is a kind of binder phase, while the increase of its content will also promote the reduction of burden. This needs to be improved through experiments. Silicates and glass phases have a certain bonding effect, with the increase of their content, $RDI_{-3.15}$ of burden will decrease, but the metallization degree will decrease by forming hardly reducible Fe_2SiO_4 meanwhile [18]. Most of the results of the qualitative analysis of the model are consistent with the actual situation. Nevertheless, considering the complexity of mineral phase composition, it is necessary to further refine the indicators and expand the database to improve the prediction accuracy.

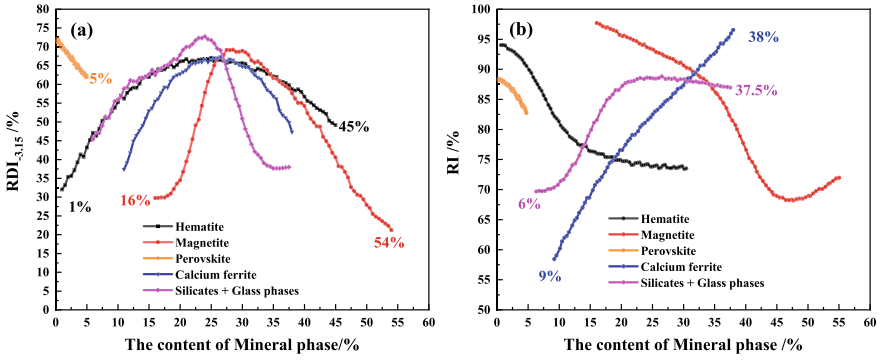

Fig. 5 Effects of mineral phases on metallurgical properties: **a** $RDI_{-3.15}$, **b** RI

Conclusions

The gray range of each mineral phase is preliminarily determined by RGB-gray model, which can reasonably calculate the proportion of each mineral phase and be used for automatic identification of mineral phase. Based on BP neural network, the mineral phase composition-metallurgical properties model is established, which can predict metallurgical properties when taking the mineral phase composition as the input. Model 1 is used to predict $RDI_{3.15}$ and RI, and the predicted value is highly consistent with the raw data. The influence of mineral phase structure on metallurgical properties is analyzed qualitatively; most of the results agree with the real situation. Further research will be performed in the future, which extra influencing factors, model algorithm, and basic database will be taken into account, so as to improve the prediction accuracy of metallurgical properties.

Acknowledgements The authors wish to express their gratitude to the National Natural Science Foundation of China (U2003215 and 51974053), the Fundamental and Frontier Research Project of Chongqing, China (cstc2020jcyj–msxmX0515) for the financial support of this research.

References

1. Cheng Z, Tan Z, Guo Z et al (2020) Recent progress in sustainable and energy-efficient technologies for sinter production in the iron and steel industry. Renew Sust Energ Rev 131:110034
2. Tatsuro A, Michitaka S (2006) Optimization of ironmaking process for reducing CO_2 emissions in the integrated steel works. ISIJ Int 46(12):1736–1744
3. Wu S, Su B, Liu X et al (2018) Optimisation of the blast furnace burden based on its primary slag formation behaviour. Ironmaking Steelmaking 45(1):50–57
4. Iljana M, Kemppainen A, Paananen T et al (2016) Evaluating the reduction-softening behaviour of blast furnace burden with an advanced test. ISIJ Int 56(10):1705–1714
5. Li W, Fu G, Chu M, Zhu M et al (2020) Investigation of the oxidation induration mechanism of Hongge vanadium titanomagnetite pellets with different Al_2O_3 additions. Powder Technol 360:555–561
6. Zhou Z, Luo Y, Zhu D (2019) Enhancing the reduction of high-aluminum iron ore by synergistic reducing with high-manganese iron ore. Metal 9(1):15
7. Paananen T, Kinnunen K (2010) Effect of TiO_2-content on reduction of iron ore agglomerates. Steel Res Int 80(6):408–414
8. Zhu D, Chou J, Shi B et al (2019) Influence of MgO on low temperature reduction and mineralogical changes of sinter in simulated COREX shaft furnace reducing conditions. Minerals 9(5):272
9. Ravi S, Suman M, Kishore P et al (2019) Multi modal spatio temporal co-trained CNNs with single modal testing on RGB–D based sign language gesture recognition. J Comput Lang 52:88–102
10. Wei L, Dong J, Chen Z et al (2020) Prediction model of urban freight generation based on BP neural network. J Shanghai Maritime Univ 41(4):50–54
11. Gan Q (2008) Study on influence of MgO on mineral composition and metallurgical properties of V-bearing titaniferous magnetite sinter. Iron Steel 08:7–11

12. Gan Q, He Q, Wen Y (2009) Study on the influence of FeO content on quality and quantity of V-Ti-bearing sinter. Sintering Pelletizing 34(01):14–19
13. He M (2016) Effect of w(TiO_2) on sintering properties of high titanium vanadium-titanium magnetite. Iron Steel 51(05):9–16
14. Yang S, Zhou M, Jiang T et al (2015) Effect of basicity on sintering behavior of low-titanium vanadium−titanium magnetite. Trans Nonferrous Met Soc China 25:2087–2094
15. Wu S, Liu X, Zhou Q et al (2011) Low temperature reduction degradation characteristics of sinter, pellet and lump ore. J Iron Steel Res Int 18(8):20–24
16. Lan R, Wang J, Han Y et al (2012) Reduction behavior of sinter based on top gas recycling-oxygen blast furnace. J Iron Steel Res Int 19(9):13–19
17. Ran L, Wang L, Yan Z et al (2018) Present situation of research on impact of chemical composition on low temperature reduction degradation of sinter. Sintering Pelletizing 43(01):1–5
18. Zeng R, Wang N, Li W (2021) Influence of SiO_2 on the gas-based direct reduction behavior of Hongge vanadium titanomagnetite pellet by hydrogen-rich gases. Powder Technol 386:90–97

Thermodynamic Study on Modification of Converter Slag by Using Hot Blast Furnace Slag

Yuzhu Pan, Dajun Luo, Xiang Yuan, Pengcheng Zhang, Jingxin Wang, and Gaoming Liang

Abstract Blast furnace slag (BFS) and converter slag (CS) are the main by-products of the BF-BOF long-process steel production model. In China, the utilization ratio of BFS is high. CS cannot be widely used in the building materials industry due to its characteristics, which is an important issue for the sustainable development of Chinese steel companies. In this article, FactSage software is used to study the conversion of CS by using the heat of BFS, and the research results provide a theoretical basis for improving the utilization ratio of CS. The thermodynamic calculation results show that when the temperature is lower than 1200 °C, the liquid phase ratio of the CS is higher than that of the BFS. When the temperature is higher than 1250 °C, the liquid phase ratio of BFS is much higher than that of CS. When the mass ratio of BFS to CS is increased from 5:5 to 9:1, the liquid phase ratio of the mixed slag at the same temperature will gradually increase. The molten BFS can absorb the free CaO and MgO in the CS through a variety of eutectic phase and peritectic phase melting reactions, and melt part or all of the high melting point Ca_2SiO_4. When the proportion of BFS is relatively high, the fluidity of the mixed slag can be maintained, which provides a guarantee for subsequent processing.

Keywords Blast furnace slag · Converter slag · Thermodynamic · Convert · Liquid phase

Y. Pan (✉) · D. Luo · X. Yuan · P. Zhang · J. Wang · G. Liang
Hunan ValinXiangtan Iron & Steel Co., Ltd., Hunan, Xiangtan City 411100, China

D. Luo
e-mail: luodajun35@163.com

X. Yuan
e-mail: yx2058@163.com

P. Zhang
e-mail: ustbzpc@163.com

G. Liang
e-mail: lianggaomingxisc@163.com

Z. Peng et al. (eds.), *12th International Symposium on High-Temperature Metallurgical Processing*, The Minerals, Metals & Materials Series,
https://doi.org/10.1007/978-3-030-92388-4_58

Introduction

In China, steel production is dominated by the BF-BOF long process, in which blast furnace slag (BFS) and converter slag (CS) are the main by-products. BFS is widely used in construction fields such as cement, concrete, glass, and ceramics. Due to the composition and formation characteristics of CS, CS contains a large amount of f-CaO, f-MgO and hard-to-break phases, which makes it difficult to refine and stabilize the quality. This makes it difficult for CS to be widely applied to the construction industry and the utilization ratio of CS in China is far lower than that of Japan, the European Union, and the United States [1]. Finally, most of the CS is unused, causing environmental pollution.

In China, molten BFS is quenched by high-pressure water, and a large amount of heat cannot be recovered, which results in a waste of energy. If CS can be added to the molten BFS in the blast furnace process, or use the molten BFS in a special refractory container to change the properties of CS, eliminate or reduce the f-CaO, f-MgO, and hard-to-crush phases in the CS, then the utilization ratio of CS will be improved, and at the same time the heat of BFS will be utilized.

This article mainly uses thermodynamic calculations to study using of BFS heat and composition to transform CS, so as to provide a theoretical basis for Chinese steel companies to make full use of the heat energy of BFS and increase the utilization ratio of CS.

Research Methods

In this article, the thermodynamic calculation software FactSage was used for research. FactSage thermodynamics software is one of the largest computing systems with integrated databases in the field of thermochemistry. The basic principles and developments were specifically introduced in the literature [2–4]. In this study, the FToxid (The FACT Oxide Database) database is used for thermodynamic calculations. The thermochemical data of the CaO-SiO_2-MgO-Al_2O_3-$FeOx$ oxide system in the database has been optimized to a considerable extent. The calculation module used is a multi-element multi-phase balance calculation module. The specific conditions set for the calculation include: $P_{O_2} = 21\%$; compound species includes pure solids and pure liquids; equilibrium is set to "normal + transition" mode. The solution phase parameters set in the calculation process is shown in Table 1.

This article refers to the composition of the BFS of Xiangtan Iron and Steel Company No. 2 blast furnace and the CS of the steelmaking plant for the calculations. The main components are shown in Table 2. The calculation results include the liquid phase ratio of BFS and CS at 1000 °C–1600 °C, and the calculation step is 50 °C. In addition, it also includes the liquid phase ratio of mixed slag, in which mass ratios of BFS and CS is 5:5, 6:4, 7:3, 8:2, and 9:1 respectively. The mixed slag compositions are shown in Table 3.

Table 1 Solution phase parameters set for calculation

Base phase	Full name
FT-oxid-SLAGA	A-Alag-liq all oxids + S
FT-oxid-MeO A	A-Monoxide
FToxid-αC2SA	A-α-Ca_2SiO_4
FToxid-OlivA	A-Olivine

Table 2 Main components of Xiangtan iron and steel company no. 2 BFS and CS of the steelmaking plant

Components	CaO	SiO_2	Al_2O_3	MgO	FeO	T/°C	R_2
BFS	41.68	35.16	15.8	7.36	–	1510 ± 10	1.19
CS	51.87	16.31	4.43	10.75	16.64	25 °C	3.18

Table 3 Main components of mixed blast furnace slag and converter slag in different proportions

BFS: CS	CaO	SiO_2	Al_2O_3	MgO	FeO	R_2
9:1	42.70	33.28	14.66	7.70	1.66	1.28
8:2	43.72	31.39	13.53	8.04	3.33	1.39
7:3	44.74	29.51	12.39	8.38	4.99	1.52
6:4	45.76	27.62	11.25	8.72	6.66	1.66
5:5	46.78	25.74	10.12	9.06	8.32	1.81

Calculation Results and Analysis

Analysis of Liquid Phase Formation Mechanism of CS and BFS

The calculation results of the liquid phase ratio of CS and BFS are shown in Fig. 1. It can be seen from Fig. 1 that when the temperature is lower than 1200 °C, the liquid phase ratio of the CS is higher than that of the BFS. When the temperature is between 1200 °C and 1250 °C, the liquid phase ratio of the BFS is more than CS.

The melting of the mineral phase includes eutectic phase melting, peritectic melting, dissolution, and temperature reaching the melting point of the mineral phase. It is necessary to discuss the composition of the solid phase before the appearance of the liquid phase of BFS and CS, and determine the melting reaction of BFS and CS. It is used to determine the proportion of suitable mixed slag phases, which promote the melting and recrystallization of CS, and achieve the purpose of eliminating f-CaO, f-MgO and difficult-to-break phases in CS.

The phase types and ratios shown in the calculation results before liquid phase production are shown in Table 4. It can be seen from Table 4 that the main phases

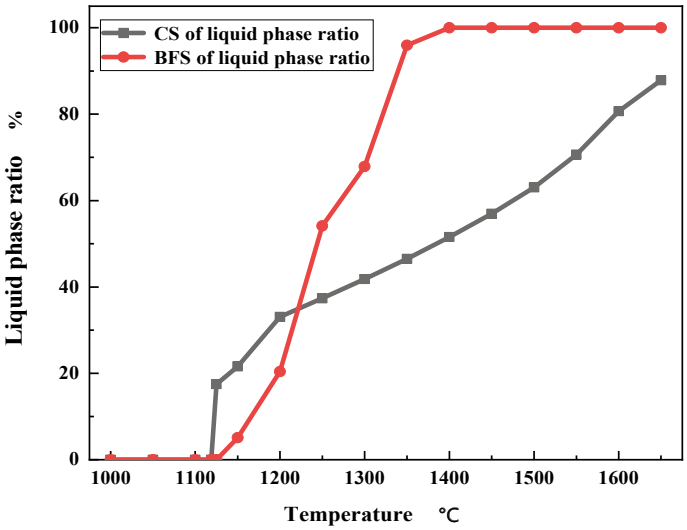

Fig. 1 Change of liquid phase ratio of CS and BFS

Table 4 Main phases of BFS before the appearance of liquid phase

Phase	Olivine	$Ca_2MgSi_2O_7$	$Ca_2Al_2SiO_7$	$CaSiO_3$	$Ca_3MgSi_2O_8$
Proportion	3.32	44.61	41.15	8.58	2.36

before the appearance of the blast furnace slag liquid phase were $Ca_2MgSi_2O_7$ and $Ca_2Al_2SiO_7$, which reached 44.61% and 41.15%, respectively. The main reactions of blast furnace slag liquid phase formation are shown in formulas (1) and (2). Among them, reaction (1) is a eutectic phase melting reaction, and reaction (2) is a peritectic phase conversion reaction:

$$Ca_2MgSi_2O_7 + Ca_2Al_2SiO_7 + CaSiO_3 = L \quad 1214\ ^\circ C \tag{1}$$

$$Ca_2MgSi_2O_7 + Ca_2Al_2SiO_7 = Ca_3MgSi_2O_8 + L \quad 1214\ ^\circ C \tag{2}$$

Table 5 shows the phase composition before the appearance of the CS liquid phase. Among them, Ca_2SiO_4 accounted for 46.68%. There are two oxide solid solutions in the phase, accounting for 25.27% and 19.17% respectively, and the rest is $Ca_3Al_2O_6$ phase, accounting for 8.88%. Table 6 shows the main components

Table 5 Main phases of CS before the appearance of liquid phase

Phase	Ca_2SiO_4	Monoxide#1	Monoxide#2	$Ca_3Al_2O_6$
Proportion	46.68	25.27	19.17	8.88

Table 6 Main components of Monoxide#1 and Monoxide#2

Components	CaO	SiO_2	Al_2O_3	MgO	FeO
Monoxide#1	0.48	–	–	38.21	61.30
Monoxide#2	93.92	–	0.20	0.15	5.73

of Monoxide#1 and Monoxide#2. Both Monoxide#1 and Monoxide#2 are solid solution phases composed of oxides such as MgO, FeO, and CaO. Monoxide#1 is mainly composed of FeO and MgO, accounting for 61.3% and 38.21% respectively. Monoxide#2 is mainly composed of CaO and FeO, accounting for 93.92% and 5.73%, respectively.

Through the analysis of the CaO-SiO_2-FeO phase diagram, it can be known that the liquid phase of the CS is caused by the CaO-SiO_2-FeO system, and the lowest temperature of the liquid phase appearance can reach 1093 °C [5–9]. From the results of thermodynamic calculations, it can be known that during the melting of CS, Ca_2SiO_4 cannot disappear completely, resulting in the liquid phase rate of CS lower than BFS. It can be seen that due to the high basicity of CS, it is difficult for Ca_2SiO_4 to continue to melt after FeO is completely consumed, which makes it difficult for CS to melt. Since the oxygen blowing time in the converter steelmaking process is about 13 min-15 min, the steel-slag reaction in the converter cannot reach equilibrium. In the process of converter steelmaking, P element causes Ca_2SiO_4 to fail to phase change and pulverize. A part of CaO, MgO, and FeO formed by iron oxidation form an oxide solid solution, that is, the RO phase. There is still a part of metallic iron in CS, and these reasons make it difficult to handle and apply.

BFS cannot generate liquid phase at lower temperature through CaO-SiO_2-FeO system like CS. The main phases of BFS, $Ca_2MgSi_2O_7$ and $Ca_2Al_2SiO_7$, which can produce a large amount of liquid phase through reaction (1) and reaction (2), resulting in a higher liquid phase ratio of BFS than CS.

Liquid Phase Formation After Mixing BFS and CS with Different Mass Ratios

Figure 2 shows the change trend of liquid phase ratio after mixing different proportions of BFS and CS. It can be seen from Fig. 2 that as the proportion of BFS in the mixed slag increases, the liquid phase ratio of the mixed slag at the same temperature increases. Figure 3 shows the change rule of the phase content before the appearance of the liquid phase of CS and mixed slag. It can be seen from Fig. 3a, b that as the proportion of BFS in the mixed slag increases, the content of Ca_2SiO_4 and monoxide phases gradually decreases. This is due to the increase in the proportion of BFS, which reduces the basicity and FeO content of the mixed slag.

According to the information given in Fig. 3c–e, the proportions of $Ca_2Al_2SiO_7$, $Ca_2MgSi_2O_7$, and $CaSiO_3$ in the mixed slag increase as the proportion of BFS in the

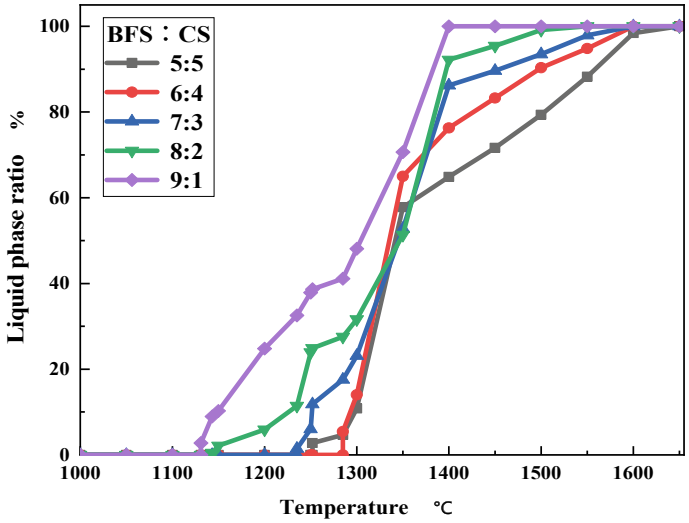

Fig. 2 Change rule of liquid phase ratio after mixing BFS and CS in different proportions

mixed slag increases. According to Fig. 3f, it can be seen that the ratio of $Ca_3MgSi_2O_8$ increases first and then decreases with the increase of the BFS ratio. When the ratio of BFS to CS reached 8:2 and 9:1, the olivine phase appeared in the mixed slag, and the $CaFeSiO_4$ phase accounted for more than 30% of the olivine phase.

Comparing Figs. 2 and 3, it can be seen that when the temperature is lower than 1350 °C, the liquid phase ratio of all mixed slags is lower than CS. This is because the proportion of BFS increases and the FeO content of the mixed slag decreases, and the amount of liquid phase produced by the CaO-SiO_2–FeO system decreases. As the temperature increases, the new phase reacts with the original phase. As shown in reaction (3)–(6), when BFS:CS is 5:5, 6:4, and 7:3, compared with CS, mixed slag can produce more liquid through reaction (3), (4), and (5). When BFS:CS is 8:2 and 9:1, compared with CS, the mixed slag produces more liquid phase through reaction (5) and reaction (6).

$$Ca_3MgSi_2O_8 + FeO = L \quad 1288\ ^\circ C \tag{3}$$

$$Ca_2Al_2SiO_7 + FeO = L \quad 1158\ ^\circ C \tag{4}$$

$$CaSiO_3 + Ca_2Al_2SiO_7 = L \quad 1273\ ^\circ C \tag{5}$$

$$Ca_3MgSi_2O_8 + CaSiO_3 + Ca_2Al_2SiO_7 = L \quad 1224\ ^\circ C \tag{6}$$

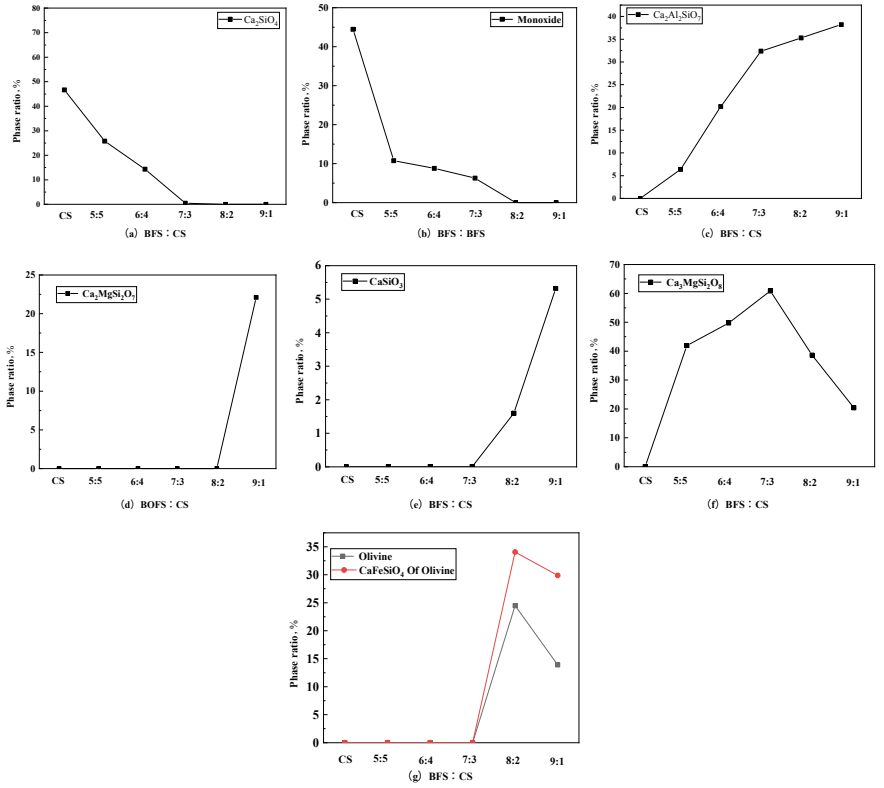

Fig. 3 Phase change before the liquid phase is produced at different ratios of BFS and CS

According to the calculation results, the most suitable BFS:CS ratio in this study is 9:1. The reason is that the mixed slag of this ratio can produce a liquid phase through reactions (1), (2), (5), and (6). In the solid phase, there is a $CaFeSiO_4$ phase with a lower melting point, and the liquid phase ratio reaches 100% at 1350 °C. In addition, adding less normal temperature CS to the molten BFS is beneficial to maintain the temperature of the mixed slag, thereby ensuring the temperature at which the above-mentioned liquid phase reaction occurs, and ensuring the fluidity of the mixed slag.

Conclusion

In this article, using BFS to reform CS was studied by thermodynamic calculations. The main conclusions as follows:

(1) Thermodynamic calculations show that due to the different compositions of BFS and CS, the solid phase composition is different before the liquid phase appears, which results in the different formation of BFS and CS liquid phase, and liquid phase ratio of BFS with low basicity is higher than CS when the temperature exceeds 1250 °C.
(2) The calculation results show that the lower basicity can make the mixed slag produce more liquid phase. As the proportion of BFS in mixed slag increases, the solid phase composition of the mixed slag changes, resulting in more liquid phase generation paths, and the liquid phase ratio gradually increases at the same temperature.
(3) When the ratio of BFS to CS is 9:1, the liquid phase ratio of the mixed slag is high, and it is beneficial to maintain the temperature of the mixed slag, which is a more suitable ratio.

References

1. Guo J, Bao Y, Min W (2018) Steel slag in China: treatment, recycling, and management. Waste Manag 78:318–330
2. Bale CW, Chartrand P, Degterov SA et al (2002) FactSage thermochemical software and databases. Calphad 26(2):189–228
3. Bale CW, Bélisle E, Chartrand P et al (2009) FactSage thermochemical software and databases—recent developments. Calphad 33(2):295–311
4. Bale CW, Bélisle E, Chartrand P et al (2016) FactSage thermochemical software and databases, 2010–2016. Calphad 54:35–53
5. Bowen NL, Schairer JF, Posnjak E (1933) The system CaO–FeO–SiO_2. Am J Sci s5–26(153):193–284
6. Wu S, Han H, Xu H et al (2010) Increasing lump ores proportion in blast furnace based on the high-temperature interactivity of iron bearing materials. ISIJ Int 50(5):686–694
7. Wu S, Han H, Liu X (2010) Mathematical model for blast furnace burden optimization based on the high-temperature reactivity. ISIJ Int 50(7):987–993
8. Pan YZ, Zuo HB, Wang BX et al (2020) Effect of reduction degree on cohesive zone and permeability of mixed burden. Ironmaking Steelmaking 47(3):1–6
9. Pan YZ, She XF, Wang G et al (2019) Melting behavior and interaction of gangue phase of iron-containing burden. ISIJ Int 59(7):1192–1197

Author Index

Z. Peng et al. (eds.), *12th International Symposium on High-Temperature Metallurgical Processing*, The Minerals, Metals & Materials Series,
https://doi.org/10.1007/978-3-030-92388-4

Subject Index

Z. Peng et al. (eds.), *12th International Symposium on High-Temperature Metallurgical Processing*, The Minerals, Metals & Materials Series,
https://doi.org/10.1007/978-3-030-92388-4